Universitat Autònoma de Barcelona

MOLECULAR, BIOLOGICAL AND CLINICAL IMPLICATIONS OF HYDROXYOLITE SYSTEM IN BREAST CANCER

Anna M. Rodríguez Rivero

Universitat Autònoma de Barcelona

Department of Surgery

PhD program in Surgery and Morphological Sciences

MOLECULAR, BIOLOGICAL AND CLINICAL IMPLICATIONS OF HYDROXYOLITE SYSTEM IN BREAST CANCER

Doctoral Thesis

Anna M. Rodríguez Rivero

Supervised by:

Dr. Dr. Pau Turon Dols

Dr. Joan Francesc Julián Ibáñez

Tutor

Prof. Dr. Jaume Fernández Llamazares

Barcelona, May 2021

MOLECULAR, BIOLOGICAL AND CLINICAL IMPLICATIONS OF HYDROXYOLITE SYSTEM IN BREAST CANCER

This work has been carried out and presented by Anna M. Rodríguez Rivero to obtain the doctoral degree in the University Autonoma of Barcelona under the supervision of Dr. Dr. Pau Turon Dols and Dr. Joan Francesc Julián Ibáñez.

Tutor: Prof. Dr. Jaume Fernández Llamazares

University Autonoma of Barcelona

Department of Surgery

Dr. Dr. Pau Turon Dols

Supervisor

Dr. Joan Francesc Julián Ibáñez

Supervisor

Anna M. Rodríguez Rivero

ACKNOWLEDGMENTS

ACKNOWLEDGMENTS

First and foremost, I would like to express my gratitude to my supervisors Dr. Pau Turon and Dr. Joan Francesc Julián for providing me the opportunity to perform my PhD thesis being part of the OLi Project. I am grateful for their guidance, their tireless and tenacious way of working. I am thankful for all the determination into making this thesis what it is. I really appreciate all their passion in the work we have shared together during all these years. I would also like to thank Dr. Jaume Fernández-Llamazares for accepting to be my tutor with enthusiasm and without hesitation.

I specially thank to Hospital Germans Trias i Pujol (HUGTiP) team: Dr. Jordi Navinés, Dr. Maite Fernández-Figueras, Dr. Eva Castellà, Dr. Pedro Fernández, Dr. Antonio Mariscal, Mrs. Irian Lorences and Dr. Laia Pérez-Roca for their contribution in the pathological diagnosis, obtaining and preparation of the samples. I also want to thank the initial work shared with Ms. Ana García at IGTP facilities. I would like to extend my gratefulness to Dr. Sara Bystrup, Dr. Arce García-Jaraquemada, Mr. Eugeni Aragall, Dr. Edurne Pedrosa and Dr. Eva Martínez-Balibrea. Very special thanks to all the patients who have participated in this study with their invaluable contribution, whose generosity has made it also possible.

I am thankful to Dr. Mónica Marro for her perseverance and sharing her expertise in Raman spectroscopy, Dr. Vanesa Sanz for her contribution to identify hydroxyolites, as well as Dr. Pablo Loza, Prof. Dr. Romain Quidant, Dr. Cuauhtemoc Araujo, Mr. Roger Guiu, Mrs. Marina Cunquero, Dr. Jordi Andilla, Dr. Maria Marsal and Mr. César Alonso for their involvement, expertise and collaboration during this work at ICFO facilities.

Moreover, I acknowledge for the contribution that UPC team has made. I wish to show my gratitude to Prof. Dr. Carlos Alemán for his invaluable knowledge which made possible part of this thesis, Dr. Jordi Puiggalí, Dr. Luís J. del Valle, Dr. Manuel Rivas, Dr. M. T. Casas, Dr. Guillem Revilla-López and, in particular, I very much appreciate to (almost Dr.) Jordi Sans for his helpful effort and contribution.

A special mention to B. Braun Group and the Braun family for supporting the OLi Project in their firm. I thank Dr. Meinrad Lugan, Dr. Joachim Schulz, Dr. Hans-Otto Maier, Dr. Sonja Rauschwalve, Dr. Jens von Lackum, Dr. Katrin Sternberg, Prof. Boris Hofmann and Mr. Jesús Donado and Mr. Manuel Jiménez. Many thanks also sent to B. Braun Surgical R&D team

for their support, especially to Dr. Christine Weis, Ms. Irene Prieto, Mrs. Silvia Herrezuelo, Mrs. Kamelia Traeger, Ms. Anna Satlari, Mrs. Beatrice Cernei, Ms. Paula Abellán also for her cooperation, and Dr. Vanesa Sanz once again for her contribution. In particular, I would like to express my gratitude to Dr. Cristina Rodríguez who was always giving her best in the last studies with invaluable hard effort.

There are a large number of people without whom I could not have performing this work. Also, I would like to express my gratitude to every person whom I could not have a chance in the past to thank their contribution to my training as a researcher.

I am extremely grateful to my parents and family for their constant unconditional support and encouraging me with their love. A special mention to the breast cancer fighters Inma and Rosalía. To my aunt Isabel, who always believed in me and she has not been able to see this work finished. To my friends, for being there, despite the distance.

To conclude, I also would like to thank Roger. He was always there stood by me through the good times and bad. Roger, these lines fall short to thank you for your patience and love during all these years, and especially to let me understand what is most important in life. You are the best travel companion I would have ever dreamed of. An amazing life awaits us being Marc's parents. And my last words are to my beloved son, who shared with me part of this journey. Marc, I hope someday you will be proud of me. Remember: "It always seems impossible until it's done."

Barcelona, May 2021

SUMMARY

SUMMARY

Breast cancer is the most frequent cancer among women with two million new cases diagnosed in 2018. The understanding of its origin and progression through new approaches is of outmost interest. In this thesis, we contribute with a new line of research based on natural biomineralization of nucleic acids, transferring knowledge from materials science to clinical research. We focus on the molecular content of breast cancer calcifications, their role as natural non-viral vectors of transfection (NVT) and their expected relationship with breast cancer multifocality.

The feasibility of the nucleic acid biomineralization has recently been demonstrated by our group using experimental and computational methods with the ultimate intention to explore the relationship among calcifications found in tumor tissue, the process of DNA biomineralization and its biological function. We demonstrate in Revilla et al. (2019),[1] by means of Molecular Dynamics simulation, that adsorption of nucleic acids in both hydroxyapatite (HAp) and calcium oxalate (CaOx) is feasible. However, only HAp can encapsulate those biopolymers. Such a hybrid structure composed of HAp and nucleic acids, we termed as *hydroxyolite* (HOLi), is identical to an inorganic NVT which is able to introduce the nucleic acids carried by the mineral into a target cell. We prove that DNA biomineralization, independently of its degree of methylation, is favored on HAp compared to CaOx. Moreover, we study the influence of Mg^{2+} ions and we unveil that Mg^{2+} facilitates DNA encapsulation in HAp but disables it in CaOx.

Secondly, we explore the existence of hydroxyolites in human breast cancer tissue freshly excised by using Raman spectroscopy. Through new advanced Raman imaging algorithm in combination with advance multivariate analysis (Marro et al., 2021)[2] we confirm that HAp microcalcifications contain DNA adsorbed and encapsulated demonstrating the hypothesis that living tissue creates hybrid structures equal to a NVT.

Thirdly, we investigate if natural calcifications (i.e. amorphous calcium phosphate (ACP), HAp and CaOx) can act as NVT (Rodríguez-Rivero et al., 2021 – ready for submission).[3] We conclude, using a known transfection model (A549 human lung epithelial cells), that all of

them are able to transfect but transfection efficiency of ACP, a precursor of HAp, is much higher than HAp and CaOx. We study the effect of supplying Ca^{2+} and Mg^{2+}, demonstrating that Ca^{2+} enhances the transfection of all of them and even makes feasible the transfection of naked DNA. On the other hand, we confirm that such NVT can migrate to a certain distance (up to 50 mm) before transfecting, simulating the clinical scenario of multifocality.

The study of DNA biomineralization in tumor tissue, the migration of HAp-DNA particles that protect DNA from enzymatic degradation and the capacity of transfection of natural NVT open new avenues in cancer research. The findings of this thesis contribute to the understanding of the clinical scenario related to breast cancer multifocality.

References

1. Revilla-López, G., Rodríguez-Rivero, A. M., Del Valle, L. J., Puiggalí, J., Turon, P., & Alemán, C. Biominerals formed by DNA and calcium oxalate or hydroxyapatite: a comparative study. *Langmuir*. 2019; *35*(36): 11912-11922. https://doi.org/10.1021/acs.langmuir.9b01566
2. Marro, M., Rodríguez-Rivero, A. M., Araujo-Andrade, C., Fernández-Figueras, M.T., Pérez-Roca, L., Castellà, E., Navinés, J., Mariscal, A., Julián, J.F., Turon, P., & Loza-Alvarez, P. Unravelling the encapsulation of DNA and other biomolecules in HAp microcalcifications of human breast cancer tissues by Raman imaging. *Cancers.* 2021; *13*(11): 2658. https://doi.org/10.3390/cancers13112658
3. Rodríguez-Rivero, A. M., Rodríguez-Miguel, C., Sans, J., Alemán, C., Julián, J. F., & Turon, P. Cell transfection mediated by breast cancer nanocalcifications of hydroxyapatite and calcium oxalate. 2021 (ready for submission).

RESUM

El càncer de mama és el càncer més freqüent entre les dones amb dos milions de casos nous diagnosticats el 2018. La comprensió del seu origen i la seva progressió a través de nous enfocaments té un gran interès. En aquesta tesi, contribuïm amb una nova línia de recerca basada en la biomineralització natural dels àcids nucleics, que transfereix coneixements de la ciència dels materials a la investigació clínica. Ens centrem en el contingut molecular de les calcificacions que s'observen en el càncer de mama, el seu paper com a vectors de transfecció no virals naturals (NVT) i la relació esperada amb la multifocalitat del càncer de mama.

La viabilitat de la biomineralització dels àcids nucleics ha estat demostrada recentment pel nostre grup mitjançant mètodes experimentals i computacionals amb la intenció última d'explorar la relació entre les calcificacions que es troben en el teixit tumoral, el procés de biomineralització de l'ADN i la seva funció biològica. Ho demostrem a Revilla et al. (2019),[1] mitjançant les simulacions de Dinàmica Molecular, on es reporta que l'adsorció d'àcids nucleics és viable tant en hidroxiapatita (HAp) com en oxalat de calci (CaOx). Tot i això, només la HAp pot encapsular aquests biopolímers. Aquesta estructura híbrida integrada per HAp i àcids nucleics, anomenada *hidroxiolita* (HOli), és idèntica a un NVT inorgànic que és capaç d'introduir els àcids nucleics transportats pel mineral a una cèl·lula diana. Demostrem que la biomineralització de l'ADN, independentment del seu grau de metilació, és afavorida en HAp en comparació amb CaOx. A més, estudiem la influència dels ions Mg^{2+} i revelem que faciliten l'encapsulació de l'ADN a l'HAp però l'inhibeix a CaOx.

En segon lloc, explorem l'existència d'hidroxiolites en teixits humans de càncer de mama recentment extirpats mitjançant l'espectroscòpia Raman. Fent ús d'un nou algoritme avançat d'imatge Raman en combinació amb tècniques d'anàlisi multivariant avançada (Marro et al., 2021),[2] confirmem que les microcalcificacions d'HAp contenen ADN adsorbit i encapsulat demostrant la hipòtesi que el teixit natural crea estructures híbrides equivalents a un NVT.

En tercer lloc, investigem si les calcificacions naturals (és a dir, el fosfat de calci amorf (ACP), HAp i CaOx) poden actuar com a NVT (Rodríguez-Rivero et al., 2021 – preparat per enviar).[3] Concloem, utilitzant un model de transfecció conegut (cèl·lules humanes epitelials de pulmó

A549), que tots els vectors són capaços de transfectar, però l'eficiència de transfecció de l'ACP, precursor de les calcificaciones d'HAp, és molt superior a l'HAp i el CaOx. Estudiem l'efecte de l'addició de Ca^{2+} i Mg^{2+}, demostrant que el Ca^{2+} millora la transfecció de tots ells i fins i tot fa factible la transfecció d'ADN nu. D'altra banda, confirmem que aquest NVT poden migrar a una distància determinada (fins a 50 mm), abans de transfectar la cèl·lula destí, simulant l'escenari clínic de multifocalitat.

L'estudi de la biomineralització de l'ADN en el teixit tumoral, la migració de partícules de DNA-HAp que protegeixen l'ADN de la degradació enzimàtica i la capacitat de transfecció de NVT naturals obren noves vies en la investigació del càncer. Els resultats d'aquesta tesi contribueixen a la comprensió de l'escenari clínic relacionat amb la multifocalitat del càncer de mama.

Referències

1. Revilla-López, G., Rodríguez-Rivero, A. M., Del Valle, L. J., Puiggalí, J., Turon, P., & Alemán, C. Biominerals formed by DNA and calcium oxalate or hydroxyapatite: a comparative study. *Langmuir*. 2019; *35*(36): 11912-11922. https://doi.org/10.1021/acs.langmuir.9b01566
2. Marro, M., Rodríguez-Rivero, A. M., Araujo-Andrade, C., Fernández-Figueras, M.T., Pérez-Roca, L., Castellà, E., Navinés, J., Mariscal, A., Julián, J.F., Turon, P., & Loza-Alvarez, P. Unravelling the encapsulation of DNA and other biomolecules in HAp microcalcifications of human breast cancer tissues by Raman imaging. *Cancers.* 2021; *13*(11): 2658. https://doi.org/10.3390/cancers13112658
3. Rodríguez-Rivero, A. M., Rodríguez-Miguel, C., Sans, J., Alemán, C., Julián, J. F., & Turon, P. Cell transfection mediated by breast cancer nanocalcifications of hydroxyapatite and calcium oxalate. 2021 (preparat per enviar).

RESUMEN

El cáncer de mama es el cáncer más frecuente entre las mujeres, con dos millones de nuevos casos diagnosticados en 2018. La comprensión de su origen y progresión a través de nuevos enfoques es de gran interés. En esta tesis contribuimos con una nueva línea de investigación basada en la biomineralización natural de ácidos nucleicos, transfiriendo conocimientos de la ciencia de los materiales a la investigación clínica. Nos centramos en el contenido molecular de las calcificaciones del cáncer de mama, su papel como vectores naturales no virales de transfección (NVT) y su relación esperada con la multifocalidad del cáncer de mama.

Nuestro grupo ha demostrado recientemente la viabilidad de la biomineralización de ácidos nucleicos utilizando métodos experimentales y computacionales con la intención última de explorar la relación entre las calcificaciones encontradas en el tejido tumoral, el proceso de biomineralización del ADN y su función biológica. Demostramos en Revilla et al. (2019),[1] mediante simulaciones de Dinámica Molecular, que la adsorción de ácidos nucleicos tanto en hidroxiapatita (HAp) como en oxalato de calcio (CaOx) es factible. Sin embargo, sólo la HAp puede encapsular esos biopolímeros. Esta estructura híbrida compuesta de HAp y ácidos nucleicos, que denominamos *hidroxiolita* (HOli), es idéntica a un NVT inorgánico que es capaz de introducir los ácidos nucleicos transportados por el mineral en una célula diana. Demostramos que la biomineralización del ADN, independientemente de su grado de metilación, se ve favorecida en HAp en comparación con CaOx. Además, estudiamos la influencia de los iones Mg^{2+} y desvelamos facilitan la encapsulación del ADN en HAp pero lo inhibe en CaOx.

En segundo lugar, exploramos la existencia de hidroxiolitas en tejido de cáncer de mama humano recién extirpado mediante espectroscopia Raman. A través de un nuevo algoritmo avanzado de imágenes Raman en combinación con un análisis multivariado avanzado (Marro et al., 2021)[2] confirmamos que las microcalcificaciones de HAp contienen ADN adsorbido y encapsulado, lo que demuestra la hipótesis de que el tejido vivo es capaz de crear estructuras híbridas equivalentes a un NVT.

En tercer lugar, investigamos si las calcificaciones naturales (es decir, fosfato cálcico amorfo (ACP), HAp y CaOx) pueden actuar como NVT (Rodríguez-Rivero et al., 2021 – preparado para presentar).[3] Concluimos, utilizando un modelo de transfección conocido (células humanas epiteliales de pulmón A549), que todos ellos son capaces de transfectar pero la eficiencia de transfección del ACP, precursor de HAp, es mucho mayor que el de la HAp y CaOx. Estudiamos el efecto de aportar Ca^{2+} y Mg^{2+}, demostrando que los iones Ca^{2+} potencian la transfección de todos ellos e incluso hacen factible la transfección del ADN desnudo. Por otro lado, confirmamos que tales NVT pueden migrar hasta cierta distancia (hasta 50 mm), antes de transfectar la célula diana, simulando el escenario clínico de multifocalidad.

El estudio de la biomineralización del ADN en el tejido tumoral, la migración de partículas HAp-ADN que protegen al ADN de la degradación enzimática y la capacidad de transfección del NVT natural abren nuevas vías en la investigación del cáncer. Los hallazgos de esta tesis contribuyen a la comprensión del escenario clínico relacionado con la multifocalidad del cáncer de mama.

Referencias

1. Revilla-López, G., Rodríguez-Rivero, A. M., Del Valle, L. J., Puiggalí, J., Turon, P., & Alemán, C. Biominerals formed by DNA and calcium oxalate or hydroxyapatite: a comparative study. *Langmuir*. 2019; *35*(36): 11912-11922. https://doi.org/10.1021/acs.langmuir.9b01566
2. Marro, M., Rodríguez-Rivero, A. M., Araujo-Andrade, C., Fernández-Figueras, M.T., Pérez-Roca, L., Castellà, E., Navinés, J., Mariscal, A., Julián, J.F., Turon, P., & Loza-Alvarez, P. Unravelling the encapsulation of DNA and other biomolecules in HAp microcalcifications of human breast cancer tissues by Raman imaging. *Cancers.* 2021; *13*(11): 2658. https://doi.org/10.3390/cancers13112658
3. Rodríguez-Rivero, A. M., Rodríguez-Miguel, C., Sans, J., Alemán, C., Julián, J. F., & Turon, P. Cell transfection mediated by breast cancer nanocalcifications of hydroxyapatite and calcium oxalate. 2021 (preparado para presentar).

TABLE OF CONTENTS

TABLE OF CONTENTS

GLOSSARY

GLOSSARY

The most commonly used abbreviations in this work have been listed in this list.

A	Adenine
ACP	Amorphous calcium phosphate [$Ca_3(PO_4)_2.nH_2O$]
AJCC	American Joint Commission of Cancer
ALP	Alkaline phosphatase
Asc	Ascorbic acid
ATP	Adenosine 5′-triphosphate
Avg	Average
BCA	Bicinchoninic acid
BCS	Breast-conserving surgery
β-Gly	β-Glycerophosphate
BMPs	Bone matrix proteins
BSP	Bone sialoprotein
C	Cytosine
CaOx	Calcium oxalate (CaC_2O_4)
CaP	Calcium phosphate
cm	Centimeter
CO_2	Carbon dioxide (CO_2)
DCIS	Ductal Carcinoma *in situ*
DD	Dickerson dodecamer 5'-CGCGAATTCGCG-3'
Dex	Dexamethasone
DLVO	Boris Derjaguin, Lev Landau, Evert Verwey, Theodoor Overbeek theory

DMEM	Dulbecco's modified Eagle's medium
DMSO	Dimethyl sulfoxide
DNA	Deoxyribonucleic acid
DNase	Deoxyribonuclease
ECM	Extracellular matrix
EMT	Epithelial to mesenchymal transition
FBS	Fetal bovine serum
FWHM	Full width at half maximum
G	Guanine
h	Hours
HAp	Hydroxyapatite [$Ca_{10}(PO_4)_6(OH)_2$]
HEPES	4-(2-hydroxyethyl)-1-piperazineethanesulfonic acid
HER2	Human epidermal growth factor receptor 2
HOLi	Hydroxyolite
HUGTiP	University Hospital Germans Trias i Pujol Badalona, Barcelona. Spain
H&E	Hematoxylin and eosin stain
ICFO	The Institute of Photonic Sciences, Castelldefels, Barcelona. Spain
IDC	Invasive ductal carcinoma
IGTP	Research Institute Germans Trias i Pujol, Badalona, Barcelona. Spain
ILC	Invasive lobular carcinoma
L	Liter
LCIS	Lobular carcinoma *in situ*
l.d.	Limit of detection
Luc	Luciferase
M	Molar

MD	Molecular dynamics
MFMC	Multifocality and multicentricity
min	Minute
mm	Millimeter
mmol	Millimole
nm	Nanometer
NVT	non-viral vectors of transfection
OCT	Optimal cutting medium
OCN	Osteocalcin
OD	Optical density
OPN	Osteopontin
OSN	Osteonectin
PCA	Principal component analysis
pDNA	Plasmid DNA
PenStrep	Penicillin-Streptomycin
P_i	Inorganic phosphate
PolyP	Polyphosphate
PP	Polypropylene ($(C_3H_6)_n$)
PP_i	Inorganic pyrophosphate ($P_2O_7^{4-}$)
QM	Quantum mechanics
RASSF1A	Ras association domain family 1 isoform A
RDF	Radial distribution function
Ref.	Reference
RMSD	Root mean square deviation
RNA	Ribonucleic acid

RPMI	Roswell Park Memorial Institute medium
ROS	Reactive oxygen species
RS	Raman spectroscopy
RT	Room temperature
SAH	S-adenosylhomocysteine
SAM	S-adenosylmethionine
SEM	Scanning electron microscopy
T	Thymine
TEM	Transmission electron microscopy
TNM	Classification of malignant tumors according to AJCC: primary Tumor, Lymph Node and Metastasis
UV-vis	Ultraviolet-visible

Transfection Efficiency rates

V.L.	Very low
L	Low
M	Medium
H	High
V.H.	Very high

CELL LINES

- **4T1 (ATCC® CRL-2539™)**

Organism: *Mus musculus*, mouse / Tissue: mammary gland, epithelial / Disease: This tumor is an animal stage IV human breast cancer.

- **4T1-Luc2 (ATCC® CRL-2539-LUC2™)**

Organism: *Mus musculus*, mouse / Tissue: mammary gland, epithelial / Disease: This produced tumor mimics an animal stage IV human breast cancer / Express luciferase encoded by Luc2 gene (pGL4).

- **A549 (ATCC® CCL-185™)**

Organism: *Homo sapiens*, human / Tissue: lung, epithelial / Disease: Carcinoma.

INTRODUCTION

1 INTRODUCTION

1.1 BREAST CANCER

1.1.1 BREAST CANCER FIGURES

Breast cancer is the most common type of cancer, and it is the fifth cause cancer-related death in the world. Female breast cancer is the most commonly diagnosed cancer, with an estimated 2.3 million new cases (11.7 %) in 2020 according to the World Health Organization.[1] As a result of the high disease burden of breast cancer in women (Table 1), it is expected to reach 3.2 million cases per year in 2050. Breast cancer screening programs are being conducted for women with higher risk, and they have been implemented in the most developed countries since some years ago.

Table 1. Incidence and mortality for annual breast cancer worldwide. Figure extracted from GLOBOCAN,[1] The Global Cancer Observatory (2020), with permission from John Wiley and Sons.

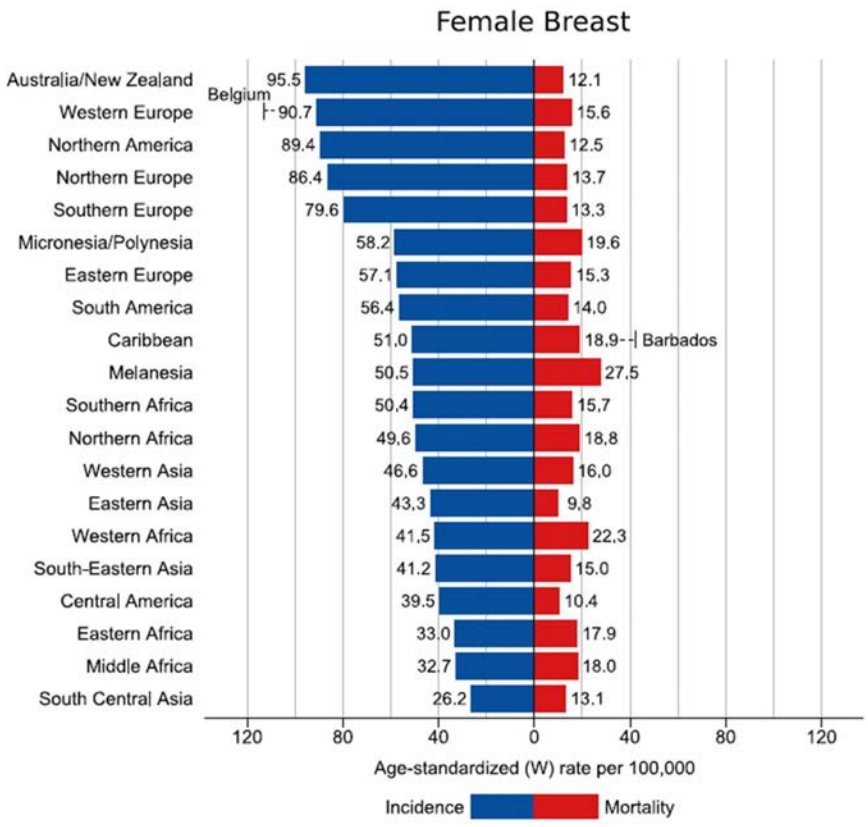

In Spain, an incidence of 77.5 cases of females per 100,000 inhabitants was observed last year, thus being the most frequent malignant tumor. Such ratio has been increasing in recent years, estimating that 1 in 8 women will suffer from breast cancer during her lifetime. In 2015, nearly a quarter of a million new invasive cancer cases were diagnosed. The most common cancer in woman was breast (28.0 %),[2] with 27,747 cases according to the Spanish Network of Cancer Registries (REDECAN), which placed Spain in an intermediate situation compared to European countries. In Spain, the first screening program was rolled out in 1990. According to breast cancer detection programs in Catalonia (Spain), more than 4,600 new cases are diagnosed every year. Participation rate was over 73 % during 2011, and these programs are performing mammograms every 2 years to women with ages within 50 and 69 years. Up to now, early detection programs have significantly decreased mortality due to this cancer,[3] a 2.6 % decrease each year because of improvements in treatments and early detection. The five-year survival rate of women diagnosed has improved in the last years, and now it stands at 90 %, a survival similar to the best rated European countries. Considering the significance of mammographic mammary microcalcifications for the early detection of breast cancer, it would be required further research to determine the origin and role of those mammary microcalcifications formed in the tumor environment.

Diagnosis of breast cancer is made though a sequence termed *triple assessment*, which includes the following components: clinical examination, imaging procedures and biopsy. Breast cancer is a progressive disease, but it can be restrained through research, prevention, early detection, and treatment at initial stages.

1.1.2 ETIOLOGY OF BREAST CANCER

Breast cancer is a multi-factorial disease and can rarely be attributed to a single factor. Many factors can increase the risk of developing breast cancer. It has been suggested that breast cancer is a disease related to several risk factors, clinical presentations, pathological features, response to therapy and outcomes. Additionally, some risk factors cannot be controlled such as gender, age, and hereditary aspects. Etiologic factors[4,5,6,7] as family history, dietary, hormonal, metabolic and secretory, as well as age, previous benign disease, geographical variation, age at first birth, obesity, lactation, early menarche, hormone replacement therapy, alcohol consumption, smoking, and exposure to ionizing radiation are factors associated with a feasible risk for breast cancer. All these factors can be classified into **environmental**, **endocrine** or **genetic** and **epigenetic** groups. These factors do not act in isolation but show a clear interdependence among them.

- **Environmental factors**

Exogenous factors are also implicated in the development of breast cancer, as obesity or diet.[8] Alcohol consumption has proven to increase the risk in female drinkers.[9] Environmental factors[10] as exposure to ionizing and non-ionizing radiation or exposure to organic chemicals compounds and by-products of industrial and vehicular combustion are considered risk factors. Some examples are hormones and endocrine-disrupting compounds (including oestrogens or dioxins), higher accumulations of metals (Fe, Ni, Cr, Zn, Cd, or Hg), chemicals (benzene, ethylene oxide, vinyl chloride or aromatic amines), among others.

- **Endocrine factors**

High body fat levels increases the risk in postmenopausal women.[11] Moreover, hormones as Hormone Replacement Therapy (HRT),[12] contraceptives[13] and a high age of beginning of menopause or a high age at first pregnancy[5] in combination with other factors increment the risk. On the other hand, longer breastfeeding[14] or a later age at menarche[15] might reduce the risk as they are considered protective factors.

- **Genetic and epigenetic factors**

A hereditary component is a significant non-modifiable risk factor. Some examples are well documented in mutations observed in genes as BRCA1 and BRCA2,[16,17,18] being high risk factors for developing breast cancer, as well as epigenetic mechanisms. RASSF1A (Ras association domain family 1 isoform A)[19] is a tumor suppressor whose inactivation is implicated in the development of several cancers. *Epigenetic*[20,21,22] studies the inheritable modifications in gene function without alteration of the nucleotide sequence of DNA. These modifications occur all over the genome and, taken together, they are called the epigenome. Several pathologies are associated to alterations in epigenetic processes, including cancer.[23] Contrary to genetic alterations, epigenetic changes are reversible, and can be modified by environmental factors.

METHYLATION OF DNA

The main studied epigenetic modifications comprise histone changes and DNA methylation.[24,25] The foremost form of epigenetic information is DNA methylation in mammalian cells (Figure 1), or the covalent addition of a methyl group to the 5-position of cytosine (C) mainly within the CG dinucleotides (CpG), acting principally as a repressive tag to inhibit transcription and silence chromatin.[26] Abnormal DNA methylation patterns are normally observed in cancer disease.

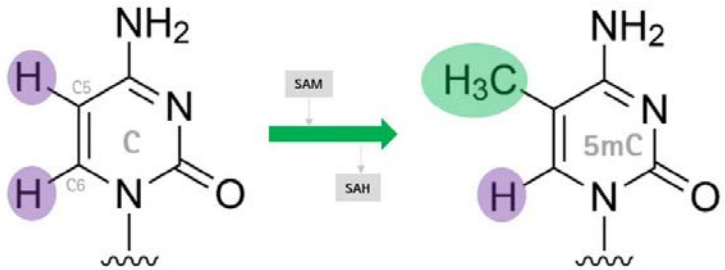

Figure 1. Schematic representation of DNA methylation to the 5' position of the cytosine ring through the S-adenosyl-L-methionine (SAM).

DNA methyltransferases are the enzymes responsible for DNA methylation. These enzymes catalyze the transfer of a methyl group from the donor S-adenosyl-L-methionine (SAM) to the 5' position of the C ring, obtaining the base 5-methylcytosine (5mC). DNA (cytosine-5)-methyltransferases (DNMTs) pass the methyl group at the DNA C ring carbon C5 by using S-adenosylmethionine (SAM) as methyl donor,[27] whereas S-adenosylhomocysteine (SAH) is the cofactor product DNA methylation has deep effects on the mammalian genome.

The leading epigenetic alteration in higher eukaryotes is methylation at the 5-cytosine positioned within the CpG islands, normally 300–3,000 base pairs in length. CpG islands are considered to be mutation hotspots since C is susceptible to deamination obtaining a thymine, where the conversion may merely be fixed by a very ineffective mismatch reparation.[28]

In general, *hypomethylation*[29] is related to damage of imprinting and chromosomal instability, as proto-oncogene promoter regions deriving in the activation of its expression. On the other hand, *hypermethylation* is linked with promoters and may appear secondary to gene (oncogene suppressor) silencing, where in suppressor genes their consequence is silencing.

A diminution in the overall methylation level of the DNA that attends tumor evolution has been defined as global hypomethylation. Hence, the global hypomethylation of the genome is a typical and prompt circumstance in numerous neoplasms, as well as breast cancer,[30] and considered one more hallmark event of cancer (for additional information, see section *Metastasic progression of cancer*). Tumor cells display **global hypomethylation** but **gene-specific hypermethylation**, as the DNA methylation distribution all over the genome is not uniform. Finally, hypermethylation has been described in genes involved in angiogenesis, apoptosis, adhesion and invasion, and cell proliferation as BRCA1 and RASSF1A (highly methylated),[31] among others.

The prognostic factors of breast cancer are objective characteristics related to the tumor or the patient that directly influence their natural evolution and, therefore, can predict the results of their follow-up, as well as the possible response to a specific therapeutic measure. Prognostic factors include histological type, tumor size and location, lymph node involvement, hormone receptors expression, index of angiogenesis, proliferation and

apoptosis, expression of epidermal growth receptors (EGPR), cell cycle regulators, adhesion molecules and oncogenes, among others.

Further research needs to be performed as many of the upcoming foreseeable advances in diagnosis and treatment depend on it. Prevention strategies, new therapeutic approaches and changes in lifestyle, are considered the most effective strategies to increase the number of breast cancer survivors (BCSs),[32,33] principally in younger women.

1.1.3 TYPES AND STAGES OF BREAST CANCER

1.1.3.1 TYPES OF BREAST CANCER

Breast cancers can be classified into subgroups according to histological type:[34]

- **Histological type** assigns the growth pattern of the tumors through specific cytological and morphological patterns, typically related with characteristic clinical presentations.
- **Histological grade** is a rating of the degree of differentiation and proliferative activity of a tumor, and reflects its aggressiveness.

The most frequent carcinoma of the breast has an epithelial origin and usually appears in the ducts that carry the nipple (Figure 2), or in the lobes (milk-producing glands).

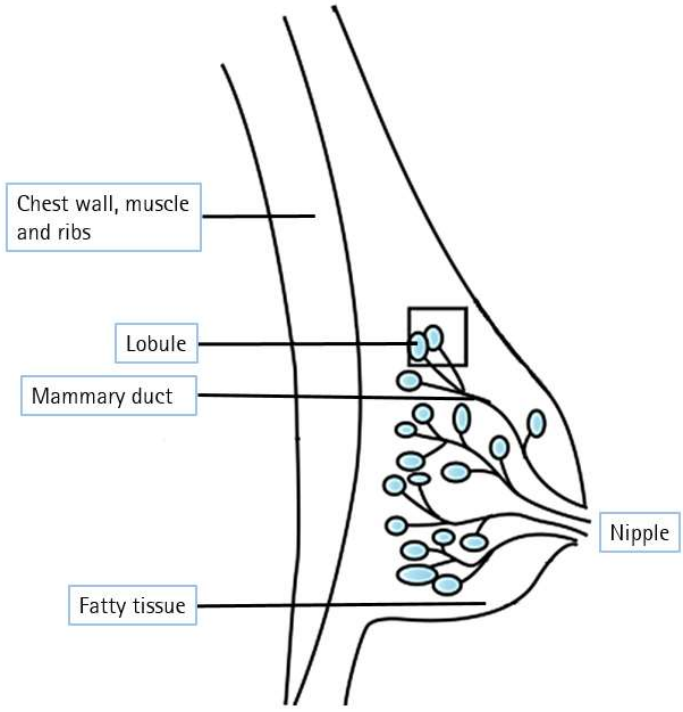

Figure 2. Schematic cross-section view of breast. Image adapted with permission from E. Wong, J. Rebelo, M. Rossi and S. Chaundry (McMaster Pathophysiology Review).

Depending on its histological origin, invasive character and structural pattern, malignant tumors can be classified into different subtypes (Table 2).

Table 2. Breast cancer histological subtypes.

Histological subtypes	Ductal	Lobular
Pre-invasive cancer	Ductal carcinoma in situ (DCIS)	Lobular carcinoma in situ (LCIS)
Invasive cancer	Invasive ductal carcinoma (IDC)	Invasive lobular carcinoma (ILC)

Most malignant tumors can be **non-invasive** (or pre-invasive), where cells that are confined to the ducts and do not invade surrounding fatty and connective tissues of the breast. On the other hand, if breast cancer is **invasive,** cells break through the duct and lobular wall and invade the surrounding fatty and connective tissues of the breast, even without being metastatic (spreading) to the lymph nodes or other organs.

- **Ductal carcinoma in situ (DCIS),** the most common type of non-invasive breast cancer is confined to the breast ducts. DCIS is considered the earliest form of breast cancer and it is normally diagnosed on screening mammography.[35] Cancer cells are located inside a duct and have not invaded the adipose tissue surrounding the breast. The changes in patterns of gene expression,[36] during breast tumorigenesis, appear throughout the transition from normal tissue to ductal carcinoma in situ (Figure 3). For example, the p53 tumor-suppressor gene is mutated in almost 25 % of all ductal carcinoma in situ lesions[37] but is rarely mutated in benign (or normal) proliferative breast tissue.

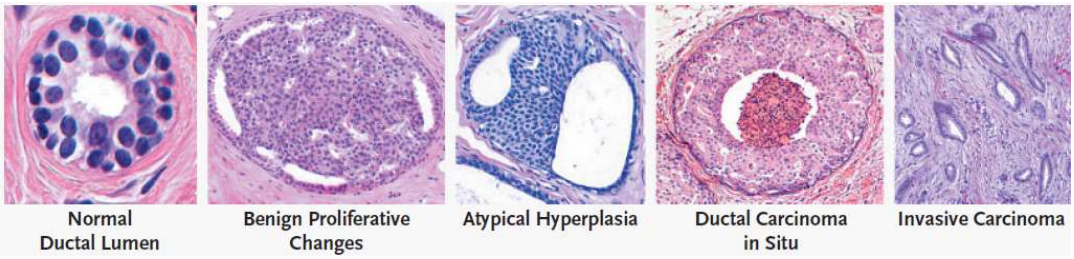

Figure 3. Transformation from healthy tissue to pre-invasive lesions (duct cross sections). Reproduced with permission from Burstein, H. et al. (2014),[35] New England Journal of Medicine, 350(14), 1430-1441, Copyright Massachusetts Medical Society.

Comedocarcinoma, a subtype of DCIS, is characterized by linear and branched calcifications. It is considered the most aggressive DCIS and it is most often associated with micro invasions. This term is often used to describe DCIS with a lot of necrosis.

- **Invasive ductal carcinoma (IDC)** or infiltrating ductal carcinoma, is the most common type of breast cancer. This type grows in a milk duct and invades the surrounding fatty tissue of the breast.

- **Lobular carcinoma in situ (LCIS**) refers to breast cancer that has not spread beyond the area where it initially developed. LCIS is a sharp increase in the number of cells within the milk glands (lobules) of the breast. LCIS is less common and considered a marker that the patient has a higher than average risk of breast cancer in the future. For this reason, some specialists prefer the term "lobular neoplasia" rather than "lobular carcinoma." Neoplasia is an accumulation of abnormal cells.

- **Invasive lobular carcinoma (ILC)** or infiltrating lobular carcinoma, is the second most common type of invasive breast cancer. This type starts in the lobules where milk is produced, and later on the cells infiltrate (or invade) the adjacent tissue outside of the lobe. As IDC, these types have the capability to spread to other parts of the body (metastasis).

1.1.3.2 STAGES OF BREAST CANCER

Individual cases of breast cancer are generally ranked by stages using the TNM classification system[38] of the American Joint Commission on Cancer (AJCC), a classification developed within 1943 and 1952. TNM is based on the fact that the type of treatment and the probabilities of survival are related to the extension of the primary tumor (T), the presence or absence of a tumor in the regional lymph nodes (N), and the presence or absence of metastasis (M) beyond the lymph nodes (Table 3).

Table 3. Summary of the TNM guidelines to classify the stages of breast cancer.

Stage	5 year survival rate	Tumor (T)	Nodule (N)	Metastasis (M)
0	100 %	Tis*	N0	M0
IA	100 %	T1	N0	M0
IB		T0	N1mi**	M0
		T1	N1mi**	M0
IIA	Around 93 %	T0	N1	M0
		T1	N1	M0
		T2	N0	M0
IIB		T2	N1	M0
		T3	N0	M0
IIIA	Around 72 %	T1	N2	M0
		T2	N2	M0
		T3	N1-2	M0
IIIB		T4	N0	M0
		T4	N1	M0
		T4	N2	M0
IIIC		Any T	N3	M0
IV	22 %	Any T	Any N	M1

(*) Tis: Tumor in situ

(**) N1mi: micrometastasis

Then, according to the size of the tumor (T) of the breast:

- T1 is equal to or less than 2 cm,
- T2 if it is between 2-5 cm,
- T3 if it is greater than 5 cm,
- T4 if there is expansion in the skin or thoracic wall.

It is numbered from 0 to 3 if it has reached the near lymph nodes (nodules, N):

- 0 indicates absence of lymph node infiltration,
- N1 if 1-3 ganglia,
- N2 4-9 nodes are affected,

- N3 if there are 10 or more ganglia affected by the internal or supraclavicular breast; and, finally, if the cancer has metastasized (M) to other organs, enumerating 0 in the absence of metastasis, or 1 with metastasis.

Once the categories T, N and M have been determined, it will be classified by stages. Stage classification is closely linked to the prognosis of the disease. The percentage of survival is 100 % in stage I at 5 years, and about 20 % in stage IV. At stage 0 (Tis, N0, M0), cancer has not spread to lymph nodes or distant areas. In stage IV (any T, any N, M1), cancer may or may not have spread to the adjacent lymph nodes. In addition, it has spread to distant organs or distal lymph nodes from the breast (M1). The organs where cancer spreads more frequently are bones, liver, brain or lungs.

1.1.3.3 INTRINSIC MOLECULAR SUBTYPES OF BREAST CANCER

Nearly all breast tumors are characterized by the expression of estrogen receptor (ESR1), progesterone receptor (PR), or human epidermal growth factor receptor 2 [HER2 (alias ERBB2)] proto-oncogene. In 2000, Perou et al.[39] identified 'intrinsic genes', which presented a slight alteration in expression but high variance across different tumors, having important clinical implications. This 'intrinsic' gene list is referred to genes that vary the most among tumors from different patients compared to samples from the same tumor / patient.

Five *intrinsic molecular subtypes* of breast cancer have been identified according to their gene expression profile.[34,40,41] It has been proposed that each of them might initiate in different types of stem/progenitor cells. The intrinsic molecular subtypes[42] (i.e. Luminal A, Luminal B, HER2, Basal-like, Normal breast-like) are described in Table 4. Breast biopsies allow the determination of the histological and molecular subtypes, which have key consequences for therapy. Intrinsic molecular profiling offers clinically significant data beyond existing pathology-based classifications.[39]

Table 4. Immunohistochemical (IHC) staining for the intrinsic breast cancer molecular subtypes.

Intrinsic molecular subtype	% of breast cancers	HR*	HER2	Ki-67	Prognosis
Luminal A	40 %	+	+	Low	Better
Luminal B	20 %	+	- or +	Low or high	Marginally worse
HER2-enriched	10-15 %	-	+	Not needed	Poor
Basal-like or Triple-negative	15-20 %	-	-	Not needed	Worse
Normal-like	No data	+	-	Low	Slightly worse than *Luminal A*

(*) HR: hormone receptor (ER: estrogen receptor and / or PR: progesterone receptor); (+): positive and (-): negative.

- **Luminal A.** It is characterized by higher levels of estrogen receptors (ER), low expression of HER2, and low expression of proliferation markers including Ki-67. *Luminal A* represents the phenotype of better prognosis and is the most common subtype.

- **Luminal B.** These tumors generally present high levels of proliferation markers, p53 mutations (a type of tumor suppressor gene), and lower expression of ER. *Luminal B* generally grows slightly faster than *Luminal A* and its prognosis is marginally worse.

HER2-positive (or enriched). This subgroup presents high expression of HER2 providing more aggressive clinical and biological behavior. Tumors with *HER2-positive* are also positive for ER but they express lower ER levels. They have a tendency to be tumors with a high degree of proliferation. Without treatment, *HER2-positive* tumors have a poor prognosis.

- **Basal-like (or Triple-negative).** It refers to tumors that do not express progesterone receptor (PR), ER and HER2, therefore referred to as *triple-negative*. However, terms *triple-negative* and *basal-like* are not entirely synonymous. The term *triple-negative* refers to the immunohistochemical classification of breast tumors lacking ER, PR and

HER2 protein expression, whereas the *basal-like* subtype is defined via gene expression microarray analysis. The *basal-like* classification is presented merely in the research scenery and thus the *triple-negative* phenotype currently is a consistent substitute in the clinical setting.[43] It is more common in patients with BRCA1 mutations. The *basal subtype* has been associated with a worse prognosis. Most of these tumors have an aggressive clinical behavior, high rate of metastasis to the lung and brain, and they are infiltrating ductal tumors with solid growth pattern.

Sørlie et al.[44] suggested that luminal and basal-like cancers would originate from luminal and basal cells, respectively. Other authors as Lehmann et al.[45] have identified six triple-negative subtypes: two *basal-like* (BL1, BL2), *immunomodulatory* (IM), *mesenchymal* (M), *Luminal Androgen Receptor* (LAR), and *claudin-low* phenotype or *mesenchymal stem-like* (MSL).

- **Normal-like.** It is characterized to be HER2 negative, low levels of Ki-67, and HR positive as *Luminal A*, but they are not considered to be basal-like cancers as they are negative for CK5 and EGFR. Additionally, its prognosis is slightly worse than *Luminal A*.

1.1.4 SURGICAL TREATMENTS OF BREAST CANCER

The detection and surgical removal of breast tumors in its initial phase before viable metastasis has been established improve significantly the development of the disease, before it become a systemic disease. Breast cancer is considered as a systemic disease due to its high capacity to produce distant metastasis. Presently, there are several therapeutic strategies available to treat it with different alternatives that can be combined in different sequences.

Therapeutic methods at a late stage of cancer development have a considerably smaller impact on the prognosis. One of the limitations of the current TNM classification of malignant tumors is the use of the size of the largest invasive focus as an important descriptive factor, regardless of multifocality[46] (see Section Breast cancer multifocality and multicentricity). Consequently, although some patients are diagnosed with good prognosis according to traditional factors, the actual result might be worse than expected. The preoperative image study that uses the multimodal approach has the ability to describe the total extent of the disease. Such an approach includes mammography, mammary ultrasonography and magnetic resonance. It offers the best opportunity to describe the real extent of the disease.

Different strategies are focused on different evolutionary phases of the disease. The type of surgery will depend on the size, location and extent of the tumor. In breast cancer, loco-regional treatment is contemplated through breast surgery, mastectomy or conservative surgery, and systemic complementary treatment through hormone therapy and chemotherapy, and treatment with radiotherapy.

Breast-conserving surgery (BCS) with radiation therapy is today a standardized therapy for low grade breast cancer.[47] The complementary or adjuvant treatment aims to reduce the possibility of the existence of tumor cells disseminated in other organs minimizing the reappearance over time. The tendency to use conservative surgery, such as **tumorectomy** (resection of a localized tumor or a tumor mass, and a margin of healthy tissue), **segmentectomy** (resection of a segment of the breast) or **quadrantectomy** (removal of a quadrant of breast tissue in which the tumor is located), will depend on factors such as the location of the tumor and the size of the breast. Those treatments would be associated with radiotherapy of the rest of the breast, and they can be applied to patients with small tumors (not larger than 4 cm).[48]

In former times, surgery such as mastectomy (or 'Halsted radical mastectomy', a surgical excision of the whole mammary gland associated with a complete axillary lymphadenectomy, and including pectoral muscles) was reserved where locally advanced tumors. Over time, such extensive surgeries have been abandoned, replacing them with the 'Madden technique' (radical mastectomy modified) that preserve the pectoral muscles.

Breast-conserving surgery is the best option in those cases of cancer at initial stages, since it allows to safeguard a breast aesthetically correct. The main risk in this treatment is the eventual appearance of local recurrences and the risk of distant metastases that recurrence would cause. In 1991,[49] The National Institutes of Health Consensus Conference recommended that breast conservation treatment is an appropriate method of primary therapy for the majority of women with breast cancer at Stage I and II, and is preferred because it provides a survival equivalent rate to total mastectomy and axillary dissection while preserving the breast. Moreover, the majority of patients with node negative breast cancer are treated by surgery or by a combination of surgery and radiation without further therapy. On the other hand, sentinel lymph node biopsy technique, the current paradigm in the management of regional basin in breast cancer due to its efficacy and cost-effectiveness, can allows to avoid complete lymphadenectomy when it is negative.[50]

In an attempt to avoid the morphological and morphometric destructuring of the mammary gland in conservative surgery, oncoplastic surgery has been developed that allows the gland to be remodeled in order to obtain a better aesthetic result. A novel immediate volumetric replacement system has recently been described in conservative surgery using platelet-enriched plasma (PRP).[51]

1.1.4.1 PREOPERATIVE LOCATION OF NON-PALPABLE BREAST LESIONS

Breast-conserving surgery (BCS) is considered the gold-standard treatment for early breast cancer, which comprises DCIS and stage I, stage IIA, stage IIB, and stage IIIA. The lump needs to be localized properly prior to surgical excision to execute a BCS. An excellent procedure for accurate location of non-palpable breast lesions would permit the surgeon to

perform a complete surgical excision, averting unnecessary normal tissue removal and preventing aesthetic defects.

Some of the preoperative procedures used consist of two parts: an imaging technique to locate the lesion using localization methods (manual or geometric, by fenestrated compressor, ultrasonography, mammography or magnetic resonance imaging) and perform the preoperative marking of the lesion that allows the surgeon to locate it using dyes, metallic suture or radioactive materials, such as Radioguided Occult Lesion Localization (ROLL) and Sentinel Node and Occult Lesion Localization (SNOLL) techniques which are intended to intraoperative identification of both non-palpable lesion and sentinel lymph node, respectively. Moreover, the wire-guided localization (WGL) technique can simply be performed under localization methods guidance, and offers real-time control of the wire-needle position, permitting precise location of the lesion, introducing a wire to the core of the lump.

1.1.5 BREAST CANCER MULTIFOCALITY AND MULTICENTRICITY

Multifocality and multicentricity (MFMC, Figure 4) are used as captions to evaluate the magnitude of disease in breast cancer. *Multifocal* breast cancer is named when the same breast quadrant presents two or more foci of cancer or tumor foci within 5 cm of each other, while if the focis are present in different quadrants of the same breast or tumor foci separated by more than 5 cm is defined as *multicentric.*[52] The nomenclature is broadly used to describe various tumors clinically diagnosed.

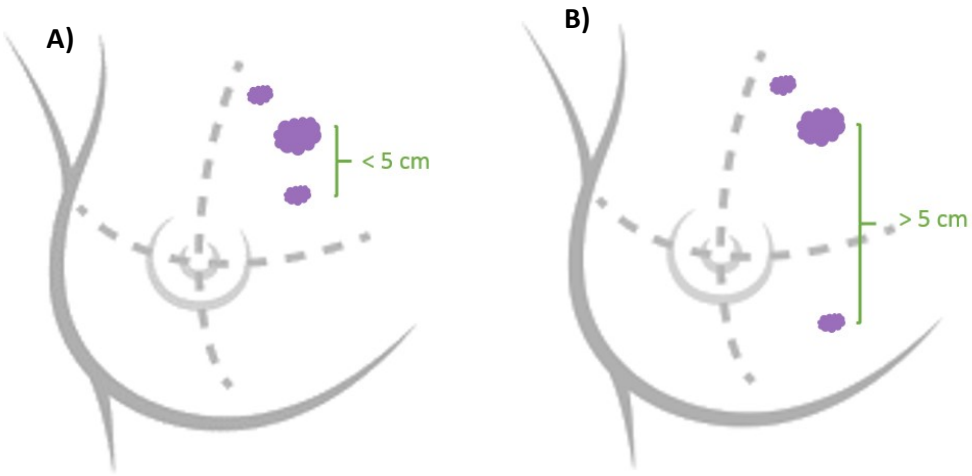

Figure 4. Breast cancer multifocality (A) and multicentricity (B).

A significant prognostic factor for multifocal and multicentric breast cancer is the tumor size.[53] Additionally, multifocal tumors might be non-invasive or invasive. Non-invasive cancers remains in the milk-producing glands (lobules) or milk ducts of the breast, while invasive cancers spread to other organs. MFMC breast cancers are related to augmented locoregional recurrence rates and that breast conservation treatment is a safe alternative for patients with multifocal tumors.[54] The different types of breast cancer recurrence are explained in the next section of this thesis.

1.1.6 BREAST CANCER RECURRENCE

Recurrence is the term used for reappearance of a tumor after previous removal. When breast cancer has been detected in an early stage in or around the breast (or regional lymph nodes), it can be removed by surgery.[55] However, undetected deposits of disease could persist locally or at distant sites that might progress into life-threatening situation if not treated.[56] Several types of breast cancer are likely to develop a recurrence and they are defined as local, regional or secondary breast cancer.

- **Local recurrence.** If breast cancer recovers in the breast, armpit area or chest is termed as local recurrence.

- **Regional recurrence.** Regional recurrence is also known as locally advanced breast cancer. If breast cancer recovers and spreads to the lymph nodes and tissues around the neck, chest or breastbone, it is named locally advanced breast cancer. This type of recurrence enhances the risk of concurrent or late systemic dissemination.[57] The patient's survival is substantially diminished within 2 years after salvage therapy with an important augmented risk of metastases, depending on numerous parameters, as molecular subtype of the original tumor or the metastatic disease.[58]

- **Secondary breast cancer.** Secondary or metastatic breast cancer (stage IV) refers to a breast cancer that might disseminate from breast (where the primary tumor is located) to other parts of the body. Secondary breast cancer usually affects lungs, bones, brain and liver. The metastatic progression of cancer is explained more in detail in the following section.

1.1.7 METASTATIC PROGRESSION OF CANCER AND TUMOR MICROENVIRONMENT

1.1.7.1 METASTATIC PROGRESS

Hanahan and Weinberg[59] published the *hallmarks of cancer,* where they proposed how normal cells turn into cancer cells, including: tumor-promoting inflammation, genome instability and mutation, evading of the immune response, reprogramming of metabolism energy, activation of the tissue invasion and metastasis, induction of angiogenesis, replicative immortality, apoptosis resistance, insensitivity to anti-growth signals and self-sufficiency in growth signals.

In most patients, the metastases at distant sites are the main cause of death. They might develop distant metastases three years after the initial detection of the primary tumor. Metastatic breast cancer is considered not curable but treatable. Nevertheless, the presence of metastases at distant sites ten years or more after the initial diagnosis is a common situation. Each type of tumor only proliferates and generates metastasis in certain organs, a process known as *organ-specificity of metastasis.*[60] Principal sites of metastasis for breast tumors are bone, lungs, liver, lymph node and brain.

Stephen Paget's[61] suggested that metastasis were not spread randomly, due to certain tumor cells (the 'seeds') have an affinity for a specific organ microenvironments (the 'soil'). According to this explanation, the identification of secondary tumors would be possible following a predefined distribution pattern,[62] showing that metastases preferentially affect the same organs. Moreover, diverse models[63,64] describing the metastatic process in cancer have been suggested, and some of them are detailed in this section:

- The *traditional model* of metastasis suggests that merely subpopulations of tumor cells acquire metastatic capacity late in tumorigenesis.
- *Spontaneous metastasis* indicates that all tumor cells have the capability to develop a metastasis.
- The *dynamic heterogeneity* model proposes that the regularity to which metastatic variations arise within the primary tumor defines its metastatic potential.
- The *clonal dominance* theory proposes that metastatic subclones within a primary tumor could overgrow and control the tumor mass.

- The *genometastasis hypothesis* proposes that metastasis occurs through transfection of cells in distant organs with circulating oncogenes, based on *in vitro* work from Garcia-Olmo et al.,[65] proposing that metastasis occurs through transfection of susceptible cells, through plasma-circulating oncogenes from the primary tumor.
- The *parallel evolution model* suggests that only breast cancer stem cells have the capacity to metastasize and form new tumors, as its dissemination happens independently from tumor cells at the primary site. Additionally, it has been described that primary tumor factors secretion induce the formation of a premetastatic niche in the new organ before the arrival of metastatic cells. An additional model of the metastatic process describes in what way oncogenic mutations on breast stem cell could cause tumors due to the transformation to a breast cancer stem cell. A tissue-specific profile from disseminated cancer stem cells could induce an analogous response equally from the primary tumor.
- The *integrative model* speculates the metastatic potential is an inherent characteristic of breast cancer and might be recognized their gene-expression profiles in the primary breast carcinoma.
- In the mid-90s, the *Oligometastasis hypothesis*[66] was proposed, describing the metastasis by a variety of biologic behavior that ranges from a single metastasis to an intermediate state of spread to widespread disease. This hypothesis proposes that patients with metastasis restricted in number and organ site might be treated by surgery and radiotherapy.

1.1.7.2 TUMOR MICROENVIRONMENT (TME)

The cellular microenvironment where the tumor cells are located is named tumor microenvironment (TME). This includes the extracellular matrix (ECM), signaling molecules, surrounding blood vessels, and tumor and other non-malignant cells (Figure 5).

High levels of growth factors and cytokines released by tumor cells induce angiogenesis, increase the survival and proliferation of cancer stem cells, and recruit tumor-associated cells, promoting tumor cell invasion and metastasis. Some studies have suggested that the TME

seems to considerably contribute to tumorigenesis. The relationship between tumor cells and TME is required to understand tumor progression and development.[67]

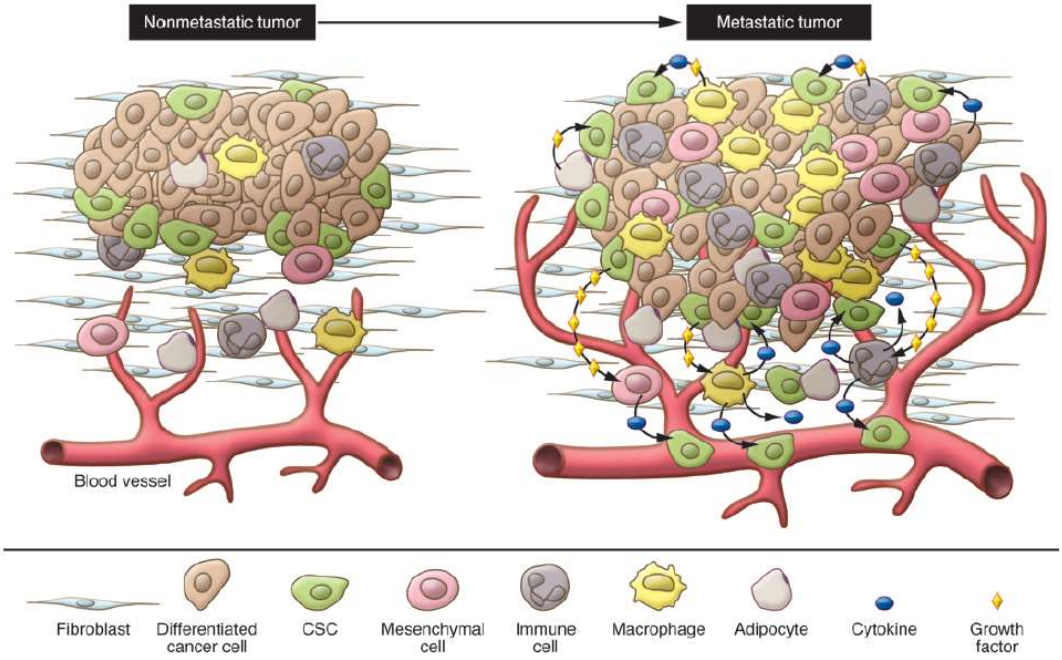

Figure 5. Tumor microenvironment (TME) representation, which includes the extracellular matrix (ECM), signaling molecules, blood vessels, and tumor and other non-malignant cells. Image extracted from Korkaya et al. (2011)[68] with permission from American Society for Clinical Investigation.

The way in which a normal mammary cell becomes a malignant tumor cell is still being investigated. A neoplasm could be formed due to an uncontrolled cell division, where a successive epigenetic and genetic alterations characterize its development. The scientific community has debated about the aforementioned hypotheses remaining a poorly understood concept. Given the controversy generated, it seems to be clear that the key to this complex process remains to be disclosed.

1.2 MICROCALCIFICATIONS

1.2.1 TYPE OF BREAST MICROCALCIFICATIONS

Albert Salomon was the first physician to study X-rays of breast tissue, and he made the earliest report about the existence of calcifications associated with breast cancer in 1913.[69] Calcifications can be potentially used as a marker for patients having a poor outcome despite the fact that all other factors might have a good prognosis.

Breast calcifications are calcium deposits within breast tissue. Macrocalcifications are large white dots (> 0.5 mm in diameter) and are most often found in non-cancerous tissues.[70,71] On the other hand, the term microcalcification refers to calcifications whose diameter is less than 1 mm. Microcalcification may correlate with increased cancer progression and metastasis of breast cancer.[72,73,74] Microcalcifications can be present up to 30 % of all malignant breast lesions, and account for 85-95 % of all cases of DCIS in detection campaigns.[71]

Diagnosis of breast cancer is made though a sequence termed *triple assessment*, which includes the following components:

- Clinical examination.
- Imaging procedures: mammography, ultrasonography, or both.
- Biopsy: excisional, needle, fine needle aspiration, core needle, vacuum-assisted, large core, sentinel node, axillary node dissection.

A mammographic image is a consistent reflection of the breast structure, although it tends to simplify the histological heterogeneity of breast cancer to some mammographic tumor characteristics shown on Figure 6.

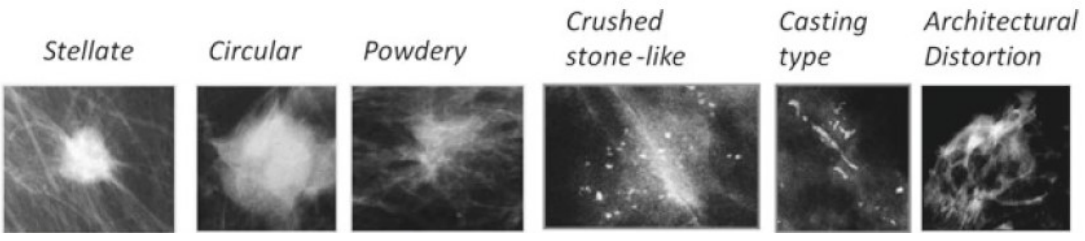

Figure 6. Microcalcification mammographic appearance characteristics. Image extracted from Tabár et al. (2014)[79] with permission from Springer New York.

Based on their mammographic appearance, they can be described as stellate (spiculated), circular or oval, powdery, crushed stone-like, casting type or architectural distortion. This terminology corresponds to the American College of Radiology's BI-RADS® mammographic classification (Table 5). BI-RADS is an acronym for Breast Imaging-Reporting and Data System,[75,76] a tool used with mammography to standardize terminology, making explicit characterization of significant data as:

a. **Mass:** Size, morphology (shape, margin), density, associated calcifications, associated features, location.

b. **Calcifications:** Morphology — describe typically benign type or describe shape of particles, distribution (may not be appropriate for typically benign calcifications), associated features, location.

c. **Architectural Distortion:** Associated calcifications, associated features, location.

d. **Asymmetries** (asymmetry, global asymmetry, focal asymmetry, developing asymmetry): associated calcifications, associated features, location.

e. **Intramammary lymph node** (rarely important): Location.

f. **Skin lesion** (rarely important): Location.

g. **Solitary dilated duct** (rarely present): Location.

Table 5. BI-RADS® Assessment Categories and management recommendations.

Category	BI-RADS® assessment categories	Management
0	**Mammography**: Incomplete – Need additional imaging evaluation and / or prior mammograms for comparison.	Recall for additional imaging and/or comparison with prior examination(s).
1	Negative	Routine mammography screening
2	Benign	Routine mammography screening
3	Probably benign	Short-interval (6-month) follow-up or continued surveillance mammography
4	Suspicious	Tissue diagnosis
	Category 4A: Low suspicion for malignancy	

Category	BI-RADS® assessment categories	Management
	Category 4B: Moderate suspicion for malignancy	
	Category 4C: High suspicion for malignancy	
5	Highly suggestive of malignancy	Tissue diagnosis
6	Known biopsy-proven malignancy	Surgical excision when clinically appropriate

Radiographic characteristics[77] of breast calcifications are differentiated in **malignant** or **benign** lesions. Thus, calcifications in malignant lesions are infrequently larger than 1 mm, they have irregular density, size and shape, they are most often intraductal, or ductal casts (material solidified in ducts) and often branched (Y-, M-, N- or W- shaped as broken needle, grains of salt, crushed stone and sand-like).

Analysis of these characteristics proves to be additional prognostic tools to predict the long-term outcome of initial breast cancers.[78] They can be classified according to size, appearance and distribution as benign or suspected malignancy. According to Tabár et al.,[79] tumors around 1-14 mm has a prognostic importance, except for tumors with casting-type calcifications. The tissue with large microcalcifications, of approximately 1 mm, tends to be diagnosed as more benign than those with a size inferior to 0.5 mm. However, there are exceptions, since thicker heterogeneous or dystrophic calcifications of more than 1 mm have been found related to malignant lesions. Numerous studies have shown that survival of patients with mammographic microcalcifications was significantly shorter than those without.[80]

1.2.2 PROPERTIES OF BREAST CALCIFICATIONS TYPE I AND TYPE II

In the decade of the 1980s, the first studies describing the composition and structure of breast microcalcifications were carried out, showing two different forms of microcalcifications associated with breast disorders. These two forms are distinguished by their chemical and physical properties. Frappart et al.[81] categorized such microcalcifications in type I and type II through scanning electron microscopy (SEM) and transmission (TEM), X-ray diffraction analysis, and other techniques (Table 6).

Table 6. Properties of type I and II microcalcifications. Table adapted from Morgan et al. (2005)[82] with permission from Springer New York LLC.

	Type I	Type II
Chemical composition	Calcium oxalate	Hydroxyapatite
Light microscope	Partially transparent	Opaque
Color	Amber	Grey-white
Polarized light	Birefringent	Non-birefringent
Stains with hematoxylin	No	Yes (purple)
SEM	Pyramids	Ovoid or fusiform, irregular
TEM	Homogenous structure, well defined limits	Needles arranged in rosettes
Associated lesions	Predominately benign	Benign and malignant

Type I microcalcifications are made of calcium oxalate (CaOx).[83] These calcifications were described as partially transparent with amber color, and birefringent under polarized light[84] (Figure 7), feature commonly used to identify them in histopathologic assessment. They form pyramids and their surface is relatively flat if it is observed by SEM.

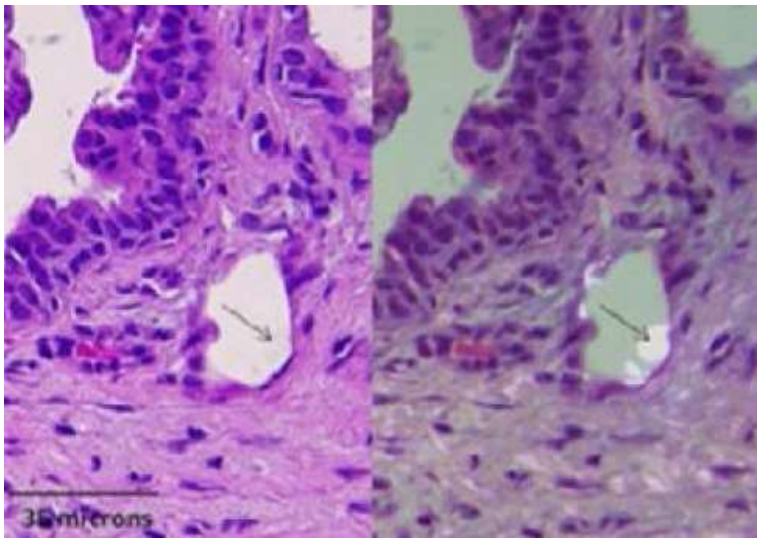

Figure 7. Histopathology of breast lesions with calcifications type I that do not bind H&E and appear as colorless crystals (arrows) that are birefringent when viewed under polarized light (right). Reprinted with permission from Saha, A., Barman, I., Dingari, N. C., McGee, S., Volynskaya, Z., Galindo, L. H., et al.[84] Raman spectroscopy: a real-time tool for identifying microcalcifications during stereotactic breast core needle biopsies. *Biomedical optics express*. 2011; *2*(10): 2792-2803 ® The Optical Society.

On the other hand, type II microcalcifications are composed of some calcium phosphate (CaP) phases, mostly hydroxyapatite (HAp) but also by its precursors. They were defined as grey-white, opaque and form ovoid or fusiform shapes with irregular surfaces. Some authors related their opacity with incrementing the probability of malignancy, frequently related to an invasive carcinoma.[71] Calcium hydrogen phosphate dihydrated (Brushite; $CaHPO_4 \cdot 2H_2O$) and octacalcium phosphate (OCP) have also been identified as precursors to the formation of HAp in mineralized tissue,[85] mostly in an slightly acidic environment,[86] which is a feature of the microenvironment of solid tumors.[87]

CaOx is usually associated with benign breast tumors[81] or at most with non-invasive lobular carcinoma *in situ*, while HAp is associated with both benign and malignant breast disorders,[88,89] as a proliferative lesion such as sclerosing adenosis where HAp is also associated with benign conditions in the breast. However, CaOx are rarely found in carcinomas, suggesting[72] that type I microcalcifications are a product of secretions, whereas type II calcium deposits are the result of cell death processes such as necrosis, apoptosis and cellular degradation.

1.2.3 FORMATION OF BREAST MICROCALCIFICATIONS

There are three described mechanisms for microcalcification formation: regulated, unregulated and dysregulated pathways. In the regulated, microcalcifications are expected to be formed through a physiologically regulated process, similar to bone-like mineralization, where epithelial cancer differentiates to osteoblasts-like cells[90], the mesenchymal bone-forming cells. Unregulated mineralization is the result of increments in calcium and phosphate concentrations that leads to apatite formation and cellular debris, usually related to necrotized cells and abnormal homeostasis. Finally, dysregulated mineralization is related to an imbalance between inhibitors and promoters of mineralization.

Numerous initiation sites for the formation of breast calcifications have been suggested, comprising apoptotic bodies, ECM, and matrix vesicles, or a combination. Some authors[91] pointed out the significance of calcifications as part of the breast cancer microenvironment. Microcalcifications are regularly detected in necrotic parts of human breast tumors as a consequence of a non-regulated process of mineralization, usually observed in regions of cell death and most likely as a result of a combination of anomalous homeostasis in necrotic or damaged cells due to local increases in inorganic phosphate (P_i) and Ca^{2+} concentrations, and favored apatite nucleation on organic waste remaining once a cell dies by lysis or apoptosis (cellular debris).

1.2.3.1 *IN VITRO* MINERALIZATION MODELS

In order to understand the biomineralization process, some *in vitro* models have been proposed and reviewed by O'Grady and Morgan (2018).[92] The first model [93] has been related to an "*osteogenic cocktail"* (OC) based on exogenous addition of β-glycerophosphate (β-Gly) as phosphate source, ascorbic acid (Asc) and dexamethasone (Dex),[94,95] where alkaline phosphatase (ALP) hydrolyses phosphate monoesters to release inorganic phosphate (P_i). However, the original source of PO_4^{3-} ions used by mammary cells to develop microcalcifications *in vivo* remains unknown but phosphate is abundant in the organisms in the form of nucleic acids, in adenosine phosphates (AMP, ADP and ATP) and in the form of polyphosphates (i.e. pyrophosphate) than can release phosphate monomers after enzymatic hydrolysis by ALP.

A second model is based on the effect of Bone morphogenetic protein 2 (BMP2), a protein belonging to the transforming growth factor superfamily. It was added to osteoblast cultures in order to induce mineralization. Its action has been correlated with the increase in ALP activity, which is deemed to have a significant role in the mineralization process in physiological environments.

A third model for *in vitro* mineralization is proposed by O'Grady and Morgan (2019)[96] and describes also the activation of mineralization signaling pathways and influx of Ca^{2+} by transport proteins as TRPM7 (Figure 8).

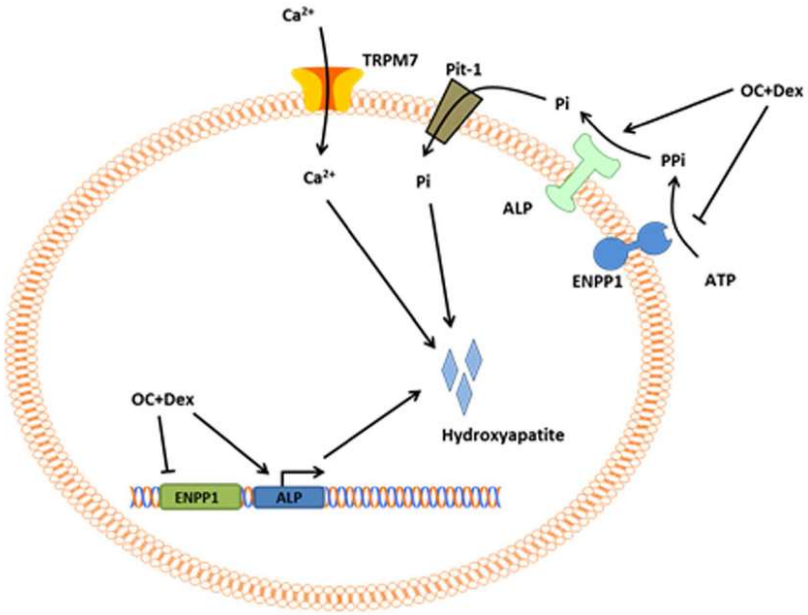

Figure 8. A recent proposed mechanism of *in vitro* microcalcification formation. Image extracted from O'Grady and Morgan (2019, Creative Commons License).[96]

Such a model proposes that ATP (or extracellular nucleotide triphosphates) is hydrolyzed by the protein coding gene Ectonucleotide Pyrophosphatase/Phosphodiesterase 1 (ENPP1) to release inhibitory pyrophosphate (PP_i) which is degraded by alkaline phosphatase enzyme (ALP). Inorganic phosphate (P_i) is introduced into the cell via the Pit-122 (Na-dependent phosphate transporter), where it can associate with Ca^{2+} through the TRPM7 channel to initiate nucleation of HAp. The OC + Dex media formulation raises downregulation of the ENPP1 (anti-mineralization), and upregulation of ALP and RUNX2 (pro-mineralization). On the other hand, an ALP-independent mechanism of mineralization is triggered if P_i is used, as the

phosphate required for Ca^{2+} deposition is accessible to the cells without needing ALP facilitated degradation of β-Gly.

Beyond those mineralization models, Vidavsky et al. (2018)[97] proposed a mechanism to explain how mineralization was linked to malignancy (Figure 9), using a 3D *in vitro* breast cancer model of multicellular spheroids. This pathway suggests that the calcifications increase with an increase of malignancy potential, showing a correlation with the increment in OPN and a decrease in ALP expression.

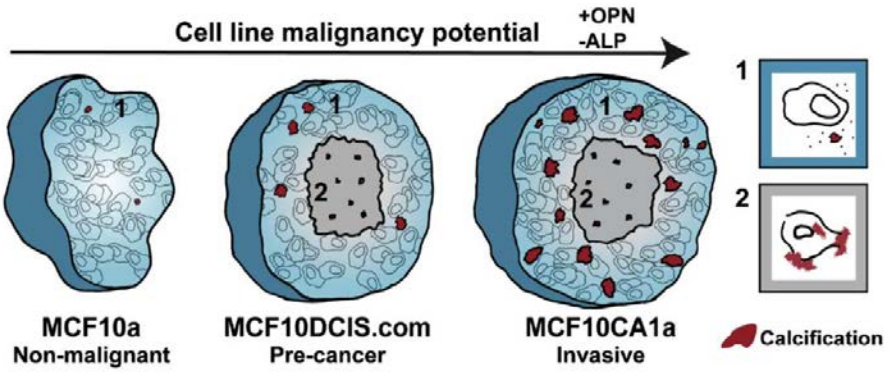

Figure 9. Schematic description proposed by Vidavsky et al. (2018)[97] with permission from PERGAMON, showing mineralization pathways in the 3D *in vitro* breast cancer model of multicellular spheroids. Alkaline phosphatase (ALP) expression increase and Osteopontin (OPN) expression decrease with an increase of cell line malignancy potential, where: viable cell area (cyan, 1), necrotic core (grey, 2), and calcification (red).

1.2.3.2 INDUCTORS AND INHIBITORS OF BIOMINERALIZATION

Several ions, molecules or metabolites are involved in physiological mineralization in breast cancer as: Type I collagen, Alkaline phosphatase (ALP), Osteopontin (OPN), pyrophosphate (PP_i) and bone matrix proteins (BMPs) as Bone Sialoprotein (BSP), Osteonectin (OSN), Osteocalcin (OCN), and transcription factors as RUNX2 and MSX2.

Several genes that are highly expressed in tissue related to breast cancer tumors containing microcalcifications and their probable connection with breast cancer are listed in Table 7.

Table 7. Several mineralization associated genes and their role in breast cancer. Table adapted from O'Grady and Morgan (2018)[92] with permission from ELSEVIER BV.

Gene	Role in mineralization	Role in breast cancer
ALP	Hydrolysis of pyrophosphate or polyphosphate to release phosphate.	Serum with ALP increased in patients with metastatic disease.
BMP2	BMP2 activates pro-mineralization signaling pathways.	Remains unclear. It has been associated with both altered proliferation, apoptosis and migration.
BSP	Promotes HAp nucleation.	High BSP expression associated with bone metastasis.
OPN	Inducible inhibitor of mineralization.	Overexpression promotes lymphatic invasion. High expression associated with decreased disease-free survival and overall survival.
OSN	Regulates osteoblast differentiation and promotes mineralization.	Remains unclear. It has been associated with both positive and negative prognosis factors.

Highly expression of OPN and OSN have been related to microcalcifications associated with breast cancer. In addition, increased expression of BSP and upregulated OPN expression was found in infiltrating carcinomas with microcalcifications. Also, the increased levels of BSP and osteocalcin (OCN) were found in the serum of breast cancer patients, similar to ALP. Bellahcène and Castronovo (1995)[98] showed immunostaining for OPN and OSN in invasive and *in situ* breast carcinomas. Furthermore, these authors proposed that microcalcifications found in breast cancer patients are fossils of cancer cells, hypothesizing also that high expression of BSP may be involved by creating a suitable microenvironment for the crystallization of calcium and phosphate into HAp.

Currently, some authors propose that all these evidences suggest that in the pathophysiologic condition, breast cancer cells could switch to osteoblast-like cells during Epithelial to Mesenchymal Transition (EMT). Epithelial breast tumor cells potentially acquires the mesenchymal phenotype through EMT, and use it by epithelial cancer cells to promote local invasion and dissemination to distant organs.[99] These mesenchymal cells acquire osteoblast like properties under BMPs induction,[100] and secret HAp crystals which are formed through an analogous process to the physiologic bone formation. The coexistence of mesenchymal markers (i.e. vimentin, β-Catenin and CD-44) and osteoblastic proteins (BMP-2 and OPN) was

found larger in infiltrating carcinomas with microcalcifications. Consequently, some authors argue that neoplastic osteoblast-like cells are probably responsible for the pathophysiological mineralization. Additionally, it has been suggested that a subpopulation of cancer cells through EMT displayed the osteoblast-like phenotype, apparently motivated by BMP-2. Some studies have showed that BMPs influence invasion and migration of breast cancer cells.[101,102] As a result, BMP-2 and ectopic expression of RUNX2 induces EMT of epithelial breast cancer cells acquiring mesenchymal characteristics during tumorigenesis, and transdifferentiate EMT-cells to osteoblast-like cells, as well as expression of RUNX2 could enhance invasive capacity in breast cancer cells,[103] being responsible for metastasis.

Fetuin-A, a glycoprotein is an inhibitor of calcium phosphate deposition as well. Such fact is supported by *in vivo* studies in mice, where its deficiency resulted an increased bone formation through time and growth plate defects. Fetuin is expected to facilitate the formation of colloidal calciprotein particles reducing the concentration of free calcium to a great extent and inhibiting the formation of crystals of calcium phosphate.[104,105]

1.3 HYDROXYOLITE (NUCLEIC ACID - HYDROXYAPATITE SYSTEM)

1.3.1 HYDROXYAPATITE

Hydroxyapatite (HAp), a mineral with formula $Ca_{10}(PO_4)_6(OH)_2$ and hexagonal symmetry, is the main inorganic component of bones, tendons and teeth in order to give them hardness and stability. Pure HAp contains 39.68 % calcium and 18 % phosphorus by weight resulting in a molar ratio Ca/P = 1.67.[106] HAp is the most stable form of calcium phosphate at room temperature and at a pH range within 4-12.

Biomedical applications of calcium phosphates,[107,108,109] such as HAp, are based on advantages based on their ability to induce bone formation and vascularization, and to cover assorted uses such as bone augmentations, artificial bone grafts, maxillofacial reconstruction, vertebral fusion, periodontal disease, repairs and bone filler after tumor surgery.

Suitable properties for *in vitro* and *in vivo* use in the biomedical field make possible its use as a bioactive and osteoconductive bone substitute material in clinical surgery and as a system for the delivery of antitumor agents and antibodies in the treatment of cancer. In addition, HAp also has the advantage of absorbability and a great affinity for binding with a variety of molecules.[110]

1.3.1.1 CALCIUM PHOSPHATE PRECURSOR PHASES OF HYDROXYAPATITE

Several calcium phosphate phases are formed during the hydroxyapatite mineral formation in a physiological environment. The main precursor calcium phosphate phases are:

1. octacalcium phosphate (OCP, $Ca_8H_2(PO_4)_6{\cdot}5(H_2O)$)
2. tricalcium phosphate (α-TCP and β-TCP, $Ca_3(PO_4)_2$)
3. calcium hydrogen phosphate dihydrate (Brushite - $CaHPO_4{\cdot}2(H_2O)$)
4. calcium hydrogen phosphate anhydrous (Monetite - $CaHPO_4$)
5. tetracalcium phosphate ($Ca_4(PO_4)_2O$)
6. amorphous calcium phosphate (ACP, $Ca_3(PO_4)_2{\cdot}nH_2O$)

Brushite and OCP have been identified as the main precursors of HAp[111] in mineralized tissue as teeth enamel and bone, during pathological mineralization induced by trauma, but

predominantly in an acidic environment, as solid tumors.[112] OCP and Brushite dissolve easily,[67,113] they contain water in the crystal lattice and do not incorporate impurity ions as HAp does. During *in vivo* mineralization, ACP is normally observed as a consequence of the presence of Mg^{2+} ions, which stabilize acidic calcium phosphate phases during *in vitro* precipitation. Particularly for pathological mineralization processes, it was shown that the Mg^{2+} ion significantly inhibits HAp crystal growth but it has a modest influence on the kinetics of OCP growth and had practically no effect on Brushite crystallization. A probable cause for this widespread range of inhibition properties could be by the existence of lattice water in Brushite and OCP, reducing the adsorption of foreign ions. Finally, it was demonstrated that these more acidic phases grow at significantly increased rates when compared to HAp.

1.3.2 HYDROXYOLITE: DNA – HAp HYBRID SYSTEM

Revilla et al. (2013)[114] and Bertrán et al. (2014)[115] demonstrated that nucleic acids can act as nucleating agents of a HAp crystal. This HAp crystal can adsorb and or encapsulate sequences of deoxyribonucleic acid (DNA) or ribonucleic acid (RNA) without introducing a significant distortion to the biopolymer strands. In particular, the tertiary structure of the nucleic acid is preserved while maintaining the hydrogen bonds that bind the two parallel strains in the structure of DNA (i.e. B-DNA). Turon et al. (2015)[116] termed such a hybrid system as '**hydroxyolite'** (Figure 10). Therefore, a hydroxyolite is formed by the combination of a generic sequence of nucleic acid (i.e. DNA or RNA) in contact, adsorbed or encapsulated, with HAp. Such a system merges the features of an outstanding family of biopolymers and a multifaceted mineral as HAp.

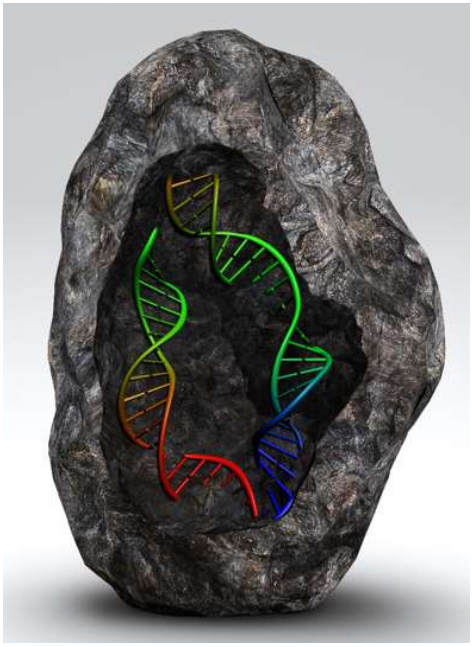

Figure 10. Hydroxyolite (DNA-HAp system) representation. Reproduced from Turon et al. (2015)[116] with permission from John Wiley and Sons.

1.3.2.1 HYDROXYOLITE BY CO-PRECIPITATION AND ADSORPTION

In vitro synthesized hydroxyolites might have a wide range of particle sizes and morphologies caused by the synthesis conditions, their aggregation during the growing phase and partially by their slow rate of crystallization, which makes it difficult to avoid overlapping between the stages of nucleation and growth. Thus, finding the propitious conditions to synthesize hydroxyolites nanoparticles with reproducible sizes and morphologies is a research challenge, taking into consideration that the morphology of the particles determines to a certain extent their behavior. In such a co-precipitation process, nucleic acids act as a template of a HAp crystal, attracting constituting ions Ca^{2+}, PO_4^{3-} and OH^- ions from the mother solution. *In vitro* synthesis revealed HAp nanoparticles are usually constituted by spherical particles or nanorods (Figure 11), however other morphologies are possible depending on the synthesis conditions (i.e. pH, Temperature and type of ions present in the solution). In order to obtain spherical nanocapsules of DNA, solutions containing Ca^{2+} and PO_4^{3-} ions have to be rapidly mixed at high pH, which favor rounded morphologies.

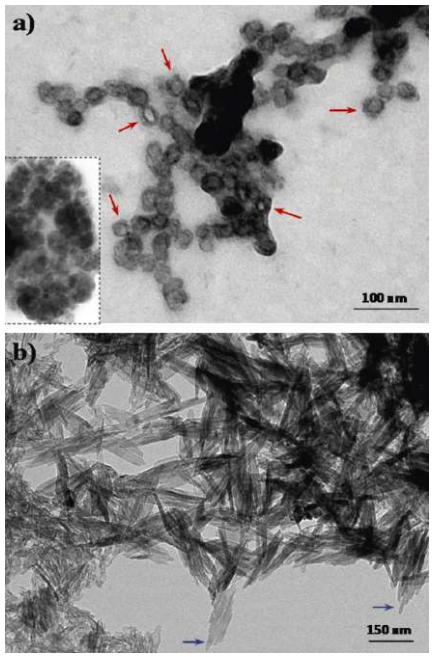

Figure 11. TEM micrographs showing hydroxyolites as: a) nanoparticles and b) nanocrystals. The red arrows show capsules with the incorporation of the DNA inside. Images extracted from Bertran et al. (2014),[115] with permission from Royal Society of Chemistry.

Hydroxyolites synthesized by absorption are formed from an already synthesized HAp substrate that adsorbs the nucleic acid on its surface. As del Valle et al. (2014)[117] demonstrated, through synthesis under controlled environments, their main features (i.e. Ca/P ratio, size, Z-potential, surface and crystallinity) are affected (Table 8), changing their properties. DNA can be incorporated in different ratios in HAp (i.e. from DNA:HAp from 1:10 to 1:250 w/w).

Table 8. Ca/P ratio, Z-potential (ZP), particle dimensions (w = width; *l* = length; h = height; and R = radius), surface area (S), crystallite size (L) and crystallinity (cc) obtained for HAp1–HAp4 particles. Average ± standard deviation values were derived from 6 independent measures. Table extracted from del Valle et al. (2014),[117] with permission from Royal Society of Chemistry.

Sample	Ca/P ratio	ZP (mV)	Particle dimensions (nm)	S (nm^2)	L (nm)	χ_c (%)
HAp1	1.71 ± 0.25	−2.5 ± 0.2	Sheets: $w = 273 \pm 37$, $\ell = 693 \pm 114$, $h = 19 \pm 2$ Rods: $R = 17 \pm 3$, $\ell = 105 \pm 12$	Sheets: 10 968 ± 2129 Rods: 420 330 ± 117 802	12 ± 2	50 ± 4
HAp2	1.37 ± 0.07	−3.6 ± 0.2	$w = 262 \pm 95$, $\ell = 227 \pm 68$, $h = 15 \pm 4$	125 950 ± 12 656	22 ± 3	100
HAp3	1.69 ± 0.05	−1.3 ± 0.1	$R = 32 \pm 4$	13 050 ± 3060	6 ± 1	3 ± 1
HAp4	1.94 ± 0.08	0.6 ± 0.1	$R = 42 \pm 5$, $\ell = 276 \pm 15$	1498 ± 189	14 ± 3	68 ± 5

HAp morphology can be shaped as amorphous nanospheres, sheets, fusiform rods, flower like and spicules as shown in Figure 12 depending on the reaction conditions. HAp particles with different morphologies (labeled as HAp#) were identified as sheet crystals (HAp2), amorphous nanospheres (HAp3) and fusiform rods (HAp4), whereas commercial HAp Bio-Gel® HTP Gel from BIO-RAD (HAp1) was used as the control in all assays.

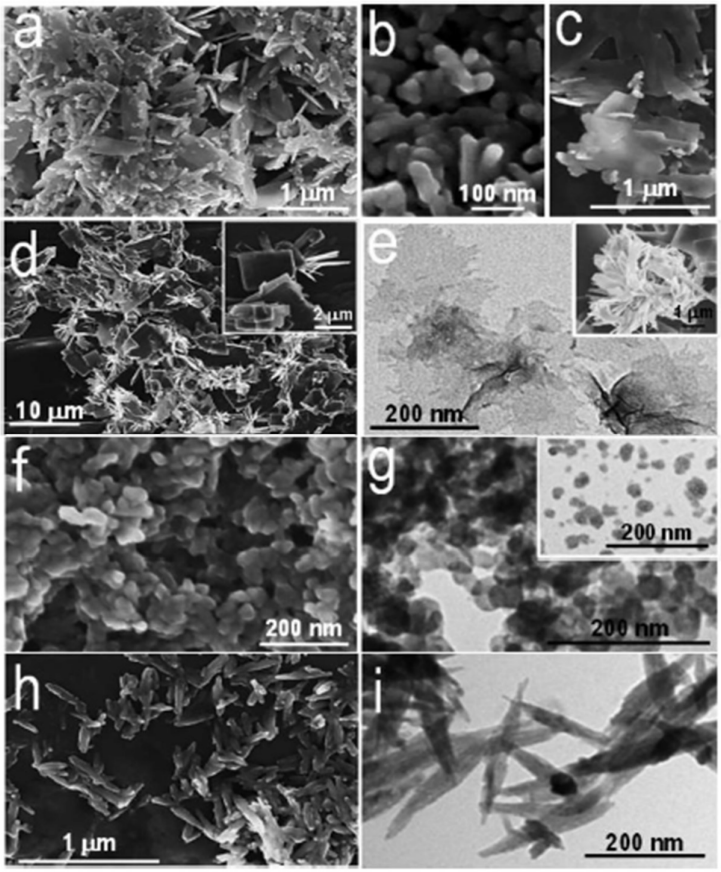

Figure 12. Morphology of hydroxyapatite (HAp) particles: HAp1 (a-c) refers to commercial samples; HAp2 (d-e), HAp3 (f-g) and HAp4 (h-i) correspond to samples prepared by chemical precipitation. SEM images: (a-d), (f) and (h). TEM images: (e), (g) and (i). Image extracted from del Valle et al. (2014),[117] with permission from Royal Society of Chemistry.

Such a variability in the morphology gave the opportunity to study the adsorption properties in different HAp crystal faces leading to interesting conclusions. The nature of DNA–HAp interaction on the crystal surface depends on the exposed face of the crystal[117] (Figure 13).

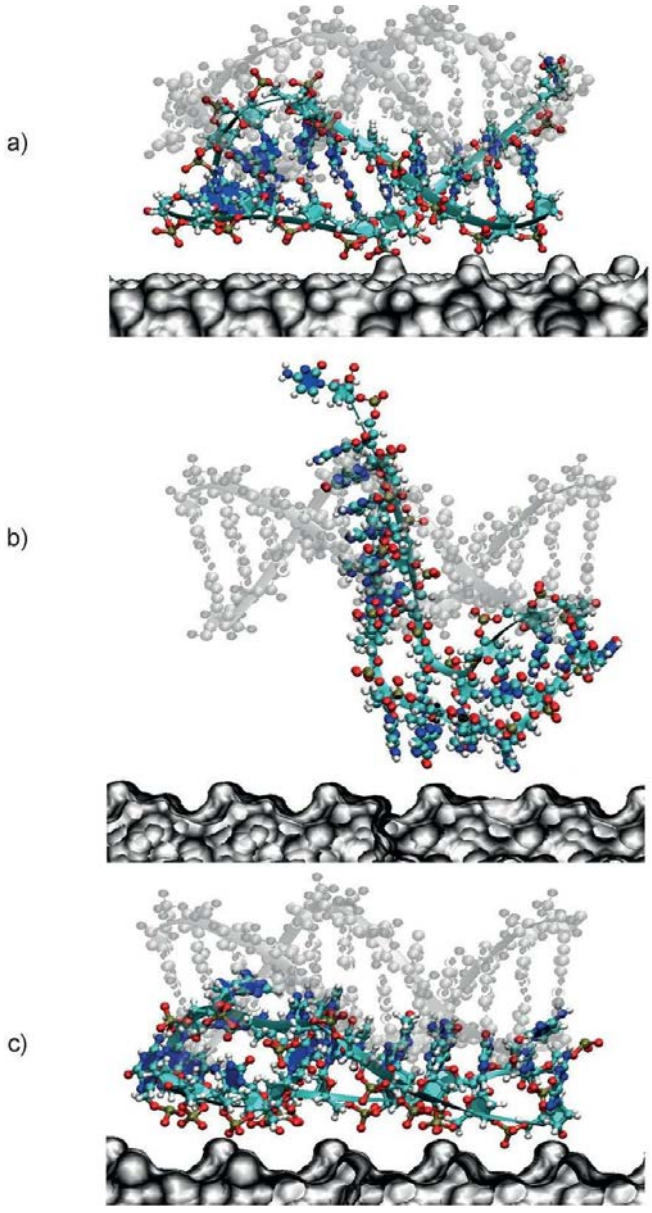

Figure 13. Interaction of DNA with three different HAp surfaces (in grey the initial state, in color the final state): a) DNA is attracted to the surface of face (001) and DNA double helix is not distorted, b) DNA is distorted and repelled when it interacts with the face (010 ; Ca^{2+} - OH^-) terminated with Ca^{2+} , OH^- , and PO_4^{3-}, c) DNA is strongly attracted to the side (010 ; Ca^{2+}) causing double helix distortion and pushing the molecule towards the surface. Image extracted from Turon et al. (2015),[116] with permission from John Wiley and Sons.

The binding site on the (001) face is the most favorable, and maintains the B-DNA double helix conformation without significant distortions. In opposition, the interaction on the (010) face terminated with Ca^{2+}, OH^-, and PO_4^{3-}—termed (010; $Ca^{2+}OH^-$)— results in DNA structural

distortions and repulsive interactions. Finally, the binding on (010) face, terminated with Ca^{2+} and PO_4^{3-} ions (010; Ca^{2+}), displays intense attractive interactions, which are able to distort the three dimensional double helix structure and fold the molecule towards the surface. Additionally, amorphous nanospheres (HAp3) and spicules (HAp4), synthesized under controlled reaction conditions (Figure 14), presented improved protection against enzymatic degradation by DNase compared to nanorods (HAp1) and sheet crystals (HAp2).

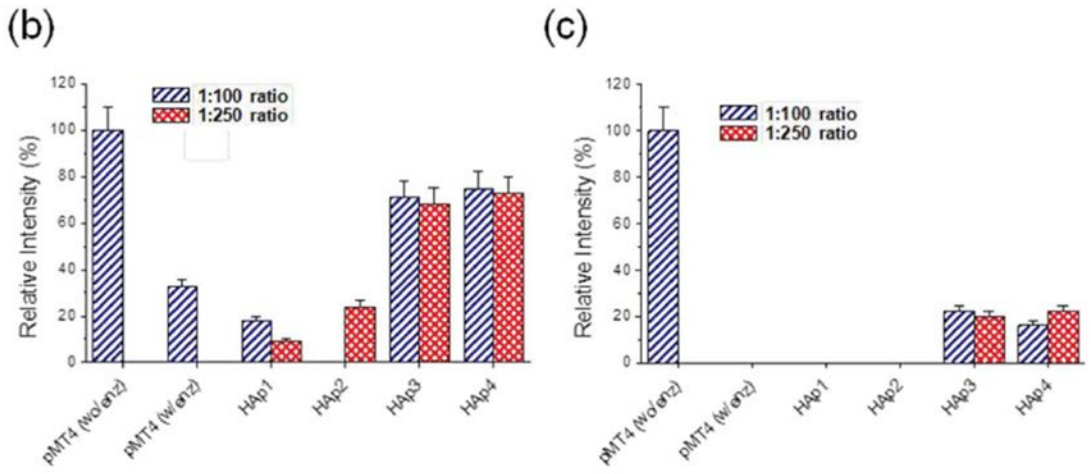

Figure 14. Enzymatic digestion of the DNA:HAp complexes: (a) agarose gel electrophoretograms of complexes derived from 1:100 and 1:250 mixtures after digestion with *Sal*I and *DNase* I. The pMT4 plasmid was used as the control in the absence of the enzyme (-enz) and digested with the enzyme (+enz); (b) quantification of DNA that remains in the complexes after digestion with *Sal*I restriction enzyme; and (c) quantification of DNA that remains in the complexes after digestion with *DNase* I unspecific nuclease. Image extracted from del Valle et al. (2014),[117] with permission from Royal Society of Chemistry.

Interestingly, a high buffering effect was observed in rods (HAp1) and spheres (HAp3) presenting the highest buffering effect, while sheets (HAp2) showed an intermediate situation (Figure 15). The effect is very low for spicules (HAp4). On the other hand, the buffering response is about two-fold faster for rods than for spheres. The summary of these results evidences that the chemical composition, especially the CO_3^{2-}/PO_4^{3-} ratio, plays a major role in the proton-buffering capacity of HAp particles. Such a buffering effect might have an impact if hydroxyolites are endocyted by cells (see Transfection section).

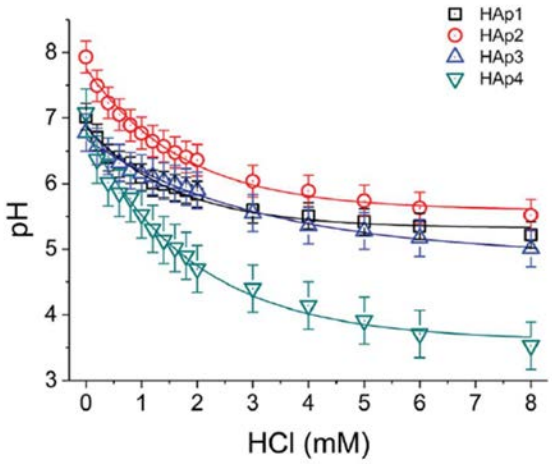

Figure 15. Proton-buffering capacity of HAp particles studied by del Valle et al. (2014),[117] with permission from John Wiley and Sons.

1.4 RAMAN SPECTROSCOPY IN BREAST CANCER

Clinical efficacy of screening mammography has some limitations that lead to a low positive predictive value and push the researchers to seek for more powerful techniques to be applicable to breast cancer diagnosis.[91] Traditional clinical imaging techniques do not totally discriminate type I from type II calcifications and important clinical information is missed in the early stages of diagnosis. However, if feasible, the number of patients requiring invasive biopsies could be minimized. [100,118] For that reason, researchers struggle looking for non-invasive techniques[119,120,121] that can give high quality information that can be complementary to mammography.

Raman spectroscopy is a technique that uses inelastic photon scattering to describe specific molecular bonds. When a sample is illuminated by an optical beam, a small portion of photons is dispersed inelastically due to the intramolecular bonds present. When this happens, a photon either transfers energy to, or receives energy from the molecule, producing a change in its vibrational state. When the photon escapes from the sample, it exhibits an altered energy level and, thus, an altered wavelength. This energy change is known as the *Raman shift* and is specific to each type of chemical bond. Thus, each molecule has its own Raman spectrum, a graph representing the intensity of the Raman shift as a direct function of the molecular composition of the specimen being studied. Raman spectroscopy is a very useful technique for the determination of the identity of chemical entities in complex environments. It has been substantiated that Raman is a successful technique to study biological samples, as a non-invasive technique, providing information concerning their molecular structure. Raman is a non-destructive technique that does not require staining and enables direct analysis of biological samples both *in vitro* and *ex vivo* from whole organisms or specific tissues, including both the cellular and biomolecular level. These characteristics postulate it as an ideal technique for multiple biomedical applications,[122] such as in the field of cancer, due to its ability to detect nucleic acids, proteins or other biological relevant molecules.

Raman spectroscopy is expected to be a clinical tool for real-time *in vivo* cancer diagnosis through the distinction of malignant lesions from healthy lesions.[123] Moreover, at the cellular level, can monitor the intracellular processes occurring in blood circulation.[124, 125,126] Finally, at the biomolecular level, is able to detect tumor biomarkers associated to the tumor surface

and evaluate the efficacy of anticancer drugs. Furthermore, the non-regular distribution of key molecules and deposits (i.e. proteins, lipids, metabolites and microcalcifications) give better understanding of the mechanisms behind breast cancer.[127,128]

Raman spectroscopy discriminates among normal, benign, and malignant lesion based on spectral features and intensity differences. After processing, it delivers a diagnosis of the tissue achieving high scores of accuracy compared to conventional pathological examinations.[129,130,131,132] In regards of Raman applications for breast cancer, we note that Raman has been used to provide *in situ* diagnostic information, as the one developed by Haka et al.[130,133, 134] Tissue penetration of Raman signal has been an topic of research as initially only few millimeter deep were able to be scanned (i.e. Stone (2007) reported a 10 mm, Stone and Matousek (2008) reached up to 27 mm[135] and Kersens et al. (2010)[136] up to 56 mm in porcine tissue).[118] Raman spectral analysis has also been successfully used to identify the mineral composition in some calcifying diseases as *renal calculi* in kidney,[137] identifying HAp, CaOx monohydrated and dihydrated, calcium hydrogen phosphate dihydrate (Brushite), magnesium ammonium phosphate hexahydrate and uric acid. The same approach was followed to determine the chemical composition of calcifications observed in malignant tumors. Raman spectroscopy can easily distinguish the two types of microcalcifications in breast diseases (Figure 16), HAp and CaOx, and some authors reported the molecular composition on its surface as we discuss in Section 8.2, however the detection of nucleic acids encapsulated in the mineral is still a challenge due their low quantities and the size of the calcified particles and a matter of research in this thesis.

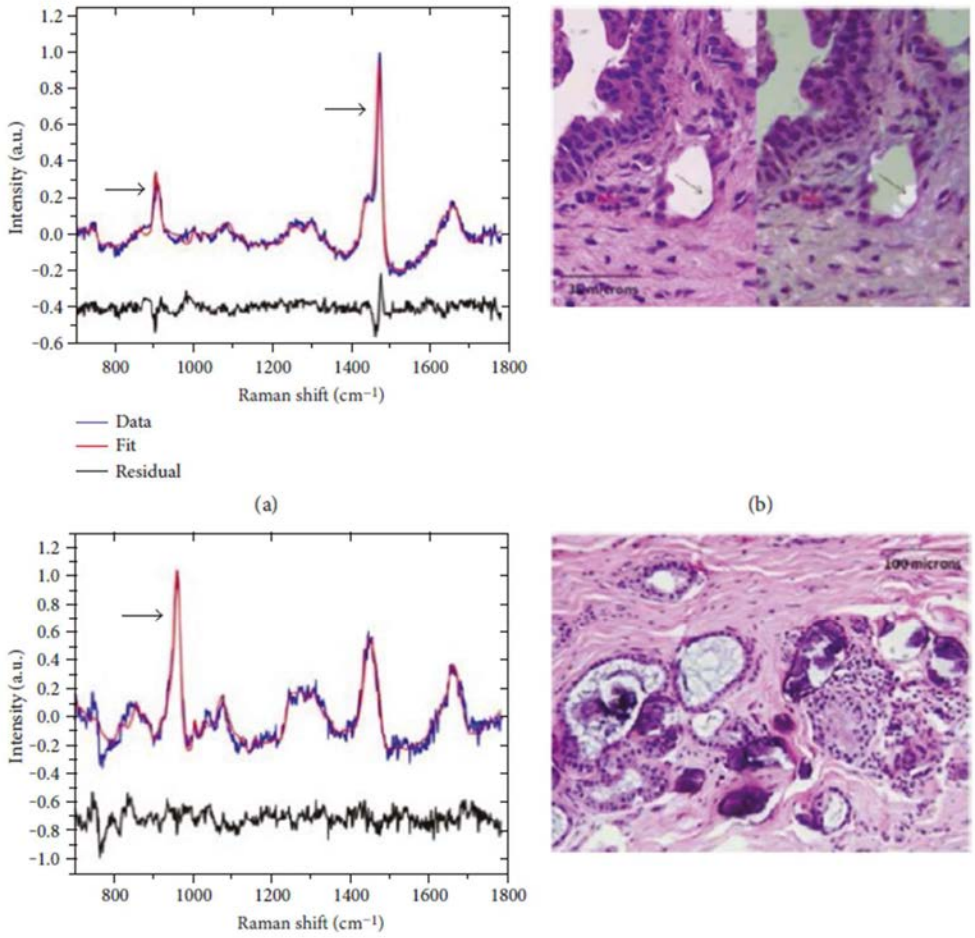

Figure 16. Typical Raman spectra and histopathology of breast lesions (fibrocystic change) with type I and II microcalcifications. The Raman spectrum of the breast lesion with type I microcalcifications in (a) shows prominent bands at 912 cm^{-1} and 1477 cm^{-1} (arrows) characteristic of calcium oxalate; the calcium oxalate crystals comprising the type I microcalcifications (b) do not bind H&E (left panel) and appear as colorless crystals (arrows) that are birefringent when viewed under polarized light (right panel). In contrast, the Raman spectrum of the breast lesion with type II microcalcifications in (c) shows a prominent band at 960 cm^{-1} (arrow) characteristic of calcium hydroxyapatite; the calcium hydroxyapatite rich type II microcalcifications appear as basophilic concretions on the H&E stain (d) and are nonbirefringent. Figure extracted from Gao et al. (2017, Creative Commons Attribution License).[123]

1.5 TRANSFECTION

Transfection is a singular process. It represents an invasion of a fine-tuned regulated cell environment by a vector that transports encoded information. Transfection might result in the healing of a defective gene (as intended by gene therapy)[138,139] or be the origin of a mutation, leading to the expression or down-regulation of the encoded proteins, that might bring fatal consequences for the host as tumor formation, leukemia or death, as it was observed in some failed clinical trials performed since 1990s using transfection vectors.[140,141,142] Safety issues in gene delivery are related to immunogenicity and toxicity but is commonly agreed that toxicity is more difficult to be solved than immunogenicity.[143] Up to now, no DNA carrier for gene therapy purposes has been approved by the US Food and Drug Administration.[144] Gene therapy is the intended variation of gene expression in specific cells to treat pathological conditions. Genetic engineering techniques are based on the introduction of exogenous genetic material to the cells inside. Transfection is defined as the artificial introduction of nucleic acids (DNA or RNA) into a cell. Thus, as the cell membrane consists of a phospholipid bilayer with negative charge and embedded proteins, it is presented as an impenetrable barrier to charged molecules, such as the phosphate skeletons of the nucleic acids (also negatively charged). It can be discerned between a *transient transfection*, where the foreign DNA is not incorporated into the host genome, and a *stable transfection*, where exogenous DNA is integrated into the host genome and replicated to the next cell generation.[145,146]

The nucleic acids introduction through the cell membrane can be done by biological, physical or chemical methods,[147,148] resulting in a change in the properties of the cell:

- Biological methods rely on genetically modified viruses to transfer non-viral genes to cells. The use of viral vectors has several disadvantages as their carcinogenesis, cytotoxicity, immunogenicity, limited DNA packaging capacity, and difficult vector manufacture. On the other hand, the main advantage of using non-viral vectors is their biosafety and biocompatibility due to their less immunotoxicity. Non-viral vectors have significant advantages over viral methodologies due to its demonstrated reduced pathogenicity, low cost and easier production. Nevertheless, the use of non-viral agents have been forgotten for a long time due to their poorer efficiency.

- Physical methods deliver nucleic acids directly into the cytoplasm or nucleus of the cell, which include microinjection, ballistic DNA, electroporation, sonoporation, phonoporation, magnetofection, hydroporation, mechanical massage and thermoporation.

- Chemical methods use carrier molecules to neutralize or impart a positive charge to nucleic acids, which are charged negatively. Once reached to the cytoplasm or nucleus, the carrier is degraded and releases the nucleic acids transfecting the cell. These carriers include inorganic particles such as calcium phosphate (mainly hydroxyapatite and Brushite), silica or gold; lipid based (lipoplexes), and polymer based (polyethylenimine (PEI), chitosan, dendrimers, polymethacrylate, Poly DL-Lactide (PLA) and Poly (DL-lactide-*co*-glycolide (PGLA)). A chemical method requires two main elements:[149] a carrier agent and the genetic material to be delivered. The carrier agent usually protects the genetic material through the transfection process and facilitates the introduction of genetic material allowing a controlled release kinetics. This feature is usually designed to increase the efficacy of transfection, which is correlated with the proportion of encapsulated nucleic acids that have the ability to transform a target cell into a desired state. Regarding its transfection properties, the fundamental challenge is to develop effective, non-toxic, non-immunogenic, and non-carcinogenic vectors to deliver genetic material into cells.

Since nucleic acids cannot transfect a cell because they are quickly degraded by the lysosomes in the endocytic pathway, it is necessary to encapsulate them in a carrier system to protect the genetic material against enzymatic degradation. The circular DNA can perform a superior transfection efficiency than the linear DNA, but the explanation is still not clear. The adsorption of the nucleic acids in a carrier vehicle involves the use of electrostatic interactions between the negatively charged nucleic acids backbone and the carrier agent with positive charge. Upon arrival at or cytoplasm or the cell nucleus, the carrier must protect the genetic material from enzymatic degradation of the environment and release the nucleic acids, generally after the carrier degradation when exposed to the inner cell environment (i.e. low pH) and finally the released nucleic acids transfect the cell (Figure 17).

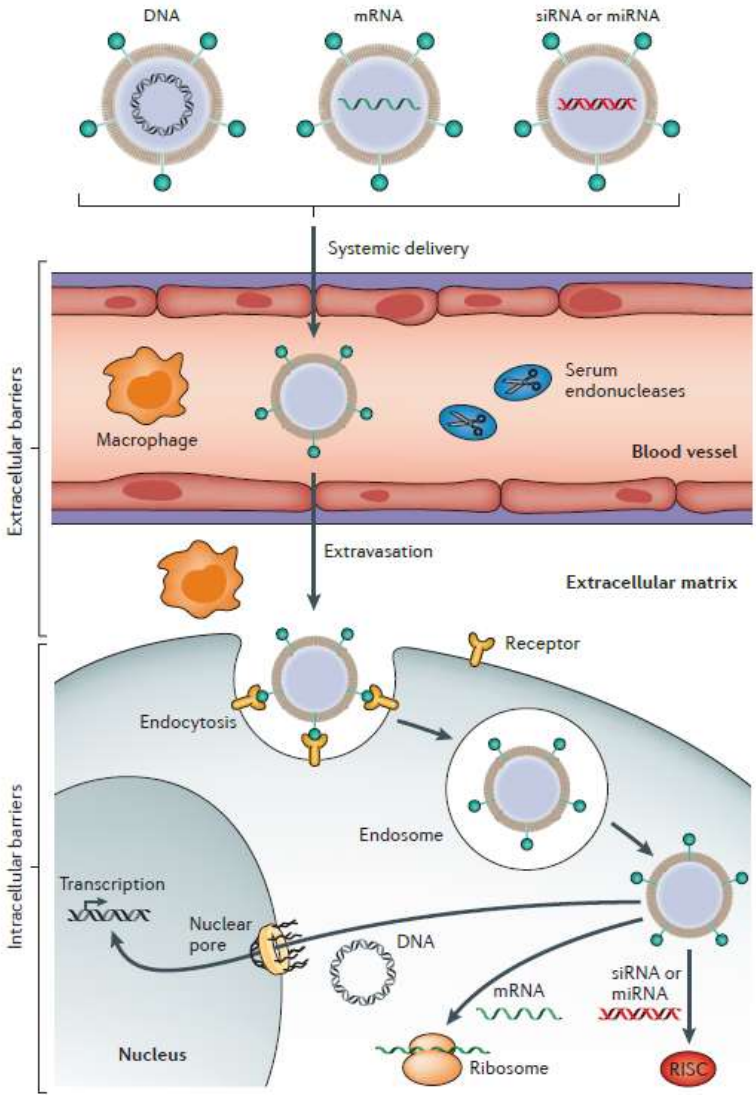

Figure 17. Barriers to successful *in vivo* delivery of nucleic acids using non-viral vectors. Image extracted from Yin et al. (2014)[150] with permission from Nature Research.

Numerous non-viral vectors[151] can be used to deliver DNA, mRNA and short double-stranded RNA. These vectors must resist degradation by serum endonucleases, avoid renal clearance from the blood, prevent non-specific interactions and elude immune detection, which can be reached by chemical modifications of nucleic acids and encapsulation of vectors. In addition, these vectors need to reach target tissues requiring certain features, and facilitate cell entry and endosomal escape by specific ligands and key components of carriers.

It has to be noted that naked DNA cannot successfully enter into cells. DNA by itself needs the support of an appropriate vector. It has been described in the literature the direct injection of naked DNA into diverse tissues is very inefficient. For example, a tail-vein injection of naked DNA into mice do not result in gene expression in major organs because of its rapid degradation by nucleases in the blood. The half-life of plasmid DNA has been estimated to be ten minutes following intravenous injection in mice.[152] For this reason, DNA into a particle carrier is required to afford protection from endonuclease. It has been shown that the naked plasmid DNA injected into the rodent muscle[153] was not able to transfect a significant number of cells using the plasmid to induce the expression of foreign genes.

Other authors considered the effect of horizontal DNA transfer[154] on tumor progression. They showed that apoptotic bodies resultant from tumor cells induce formation of p53-deficient cells *in vitro* and tumor formation *in vivo*. They suggested that the uptake of DNA via apoptotic bodies could be a potential mechanism where genetic diversity and instability is produced inside a tumor. They hypothesized that the genetic alterations required for malignancy could store inside tumor cells by the use of horizontal transfer of DNA.

1.5.1 CALCIUM PHOSPHATE TRANSFECTION VECTORS

In this thesis, we focus on chemical transfection of non-viral vectors, centered in calcium phosphate as transfection vectors equivalent to what we termed hydroxyolites. For extensive information in regards of non-viral vectors of transfection, we refer to the reviews of Mintzer and Simanek (2009),[155] Yin et al. (2014),[150] Keles et al. (2016)[149] and Gigante et al. (2019).[156]

Calcium phosphate mediated transfection was one of the earliest mechanisms used to transfect cells.[157] It relies in a simple method based on co-precipitation of DNA with calcium and phosphate ions. It was developed by Graham and van der Eb (1973)[158] and such a transfection method was only preceded by transfections using virus, such as poliovirus RNA, by Alexander et al. (1958)[159] and by the first non-viral transfection method developed by Vaheri and Pagano (1965), mediated by diethylaminoethyl–dextran (DEAE-D), a polycationic substance.[160] Inorganic nanoparticles have demonstrated encouraging potential as carriers and drug delivery systems[161,162,163,164,165] in biomedical engineering. Among the inorganic

particles currently considered as non-viral vectors of transfection (i.e. silicates, gold nanoparticles and nanotubes),[155,156] calcium phosphate vectors are made of different phases (i.e. amorphous calcium phosphate, calcium hydrogen phosphate dihydrate, and hydroxyapatite). Furthermore, hydroxyapatite (HAp) is the most stable phase and the most studied[143] due to its stability under biological conditions, and its similarity to the mineralized matrix of natural bone. Hydroxyapatite is considered a smart route for gene delivery due to its biocompatibility, biodegradability and affinity to DNA.[146,166,167] Amorphous calcium phosphate and Brushite are considered precursors of HAp, particularly in physiological environments. They are known to be able to transfect as well. Several published works report[168,169] a low transfection efficiency when non-viral vectors are used compared to viral vectors. Among them, calcium phosphate vectors are considered to show one of the lowest transfection efficiencies. However, they are appreciated by their biocompatibility, low toxicity, low cost and easiness to transfect a high amount of cells and effectiveness with many different cultured cell types,[145,148,170,171] a fact that is useful for production and purification of some type of proteins and virus.[148] As other inorganic particles, calcium phosphates are not likely to be attacked by microorganisms.[145] On the other hand, using nucleic acids as a nucleating agent of non-viral vectors of transfection represents an alternative to conventional gene therapy strategies, in which plasmids are transported at the surface of the mineral and, consequently, are exposed to undergo enzymatic attacks. Once the vector is internalized, it must release the nucleic acids inside the cell. Consequently, foreign genetic information interacts with cellular decodification process, for instance, in order to silence genes or to synthesize the new proteins encoded in its sequence (i.e. small interfering siRNA or mRNA, release happens in the cytosol) or be recombined with the own genome of the cell if DNA sequences reach the cell nucleus, completing the transfection process. We note that DNA is more stable than RNAs because the last has an additional hydroxyl group that allows its hydrolysis and additionally, RNAs are more easily reached by degrading enzymes.[172]

There are some cellular barriers that any transfection vector must overcome before DNA reaches to the nucleus for further transcription. Relevant barriers and factors to be considered when designing and using a non-viral vector of transfection are: i) crossing the cell membrane during cell uptake phase (i.e. specific superficial charge of the particle, particle morphology[164] and synchronize the action of specific ligands in the cell surface that drives the

endocytosis), ii) escape from endosomes and lysosomes (i.e. strong pH buffering of lysosome, contribute to the osmotic swelling and rupture) until nucleic acid is released to the cytosol, iii) migration towards the nucleus, avoiding or resisting the degrading action of cell enzymes and finally, and iv) nucleus entry achievement (i.e. nucleic acid size and interaction with ligands that allow the entrance in the nucleus).[156]

The groups that investigated the uptake mechanism of calcium phosphate particles reached to the conclusion that the endocytic pathway is prevalent but there could be some differences on the specific path depending on the cell type. Endocytosis is typically classified in five groups: phagocytosis, clathrin-mediated endocytosis, caveolae-mediated endocytosis, clathrin- and caveolae-independent endocytosis and micropinocytosis. Researchers explain the transfection mainly by two main mechanisms of endocytosis: i) receptor-mediated endocytosis and ii) nonspecific endocytic process, termed micropinocytosis.[143] Clathrin- and caveolae-dependent pathways share the feature of relying in specific receptor recognition or ligand interactions after recruiting them on the cell surface. They have been reported by some authors as Olton et al.[173] and Batard et al.[174] Giger et al.[175] although micropinocytosis was reported by Sokolova et al.[170]

To proceed with the transfection, once the calcium phosphate vector is inside of an endosome, it must escape from the mature endosome in order to start the migration through the cell and reach to the nucleus. A fact that usually occurs caused by the maturing process of endosome to lysosome that increase the osmotic pressure. Through that process, pH drops inside of the endosome as a consequence of ATPase proton pumps that transfer protons from cytosol to endosome. They usually activate hydrolytic enzymes and acidify the compartment. Such an acidification initiates the dissolution of the calcium phosphate vectors. Their solubility and speed of dissolution is defined by the phase of the calcium phosphate carrier. As a general trend, amorphous calcium phosphate is more soluble than Brushite, and HAp is the most insoluble. However it becomes more soluble as the content of carbonate in its lattice increases. Hydroxyapatite dissolution results in simultaneous detachment of Ca^{2+} and HPO_4^{2-} species from the particle surface, as our group demonstrated by *in silico* studies where the protonation of PO_4^{3-} ions is a crucial step regulating its dissolution and further nucleic acid release.[176] Furthermore, a natural buffer is created by HPO_4^{2-} and $H_2PO_4^-$ delivered by the hydroxyapatite that protects the nucleic acid from the action of hydrolytic enzymes activated

at low pH. The proton transfer is followed by passive migration of chloride ions that finally lead to the water entry to compensate the high osmolality. The high concentration of those ions inside the vesicle finally results in the massive income of water molecules that facilitates the rupture of the lysosome, and releases the nucleic acid into de cytosol. pH buffering was shown to be a relevant characteristic for non-viral vectors. It can be related to endosomal disruption and protection of nucleic acids form lysosomal degrading effect in order to inhibit the lysosome nuclease. Additionally, it changes the osmolality of acidic vesicles that is directly related to the swelling and rupture of the acidified endosome. That process, known as proton sponge effect, was also observed in vectors made of cationic polymers that are able to buffer the pH in a wide range. The increase of osmotic pressure triggers the swelling and rupture of the lysosome, and finally, the release of the nucleic acid to the cytosol occurs.[177,178] It is expected that the dissolution quickness and buffering capacity of the vector might affect the time until the endosome is disrupted and as a consequence the efficiency of the transfection process. However, this factor is still under research.

Finally, the entry of the nucleic acid into nucleus is required for DNA to express the encoded genes. The transport of the nucleic acid into the nucleus occurs through the nuclear pore complexes (NPC) that facilitate the internalization of nanoparticles as the large size of DNA hinders its direct internalization through the nucleus envelop through the existing small pores. NPCs are highly permeable to small molecules but they contain the crossing of larger molecules across the nuclear membrane. To overcome this restriction, macromolecules carrying a nuclear localization sequence (NLS) are identified by importins, and they facilitate their transport into the nucleus, making feasible the cross of nuclear membrane. After transportation, DNA bind to specific peptide complexes, must be dissociated efficiently in order to proceed with the transcription or recombination. Lastly, not degraded DNA needs at that point to be separated from the cationic complexes before or after entering the nucleus of the host cells.[179] Entry is supposed to take place through nuclear pores (~10 nm in diameter) or during cell division.

Transfection efficiency has been one of the most documented topics in transfection research as the usefulness for gene therapy purposes. The transfection efficiency of calcium phosphate is a well-studied process where several factors influence such a ratio: cell type,[180] cell cycle,[181] reagent concentration, precipitation time, size of particles, way of mixing (manual vs

automated dropwise), temperature, size of the particles being those within 20-200 nm the optimal ones,[143,156,182,183] that leads to poor reproducibility,[184] presence of dispersants,[185] even the presence of soluble calcium ions facilitate the DNA uptake and further endosomal escape.[186] We expect that such behavior might be emphasized in the context of a potential transfection process in real tissue by natural hydroxyolites being the transfection ratio extremely low but not negligible.

The concentrations of calcium and phosphate and pDNA plasmid have been identified as relevant characteristic to control the vector size and morphology but other important parameters cannot be underestimated as temperature and reaction time as time results in aggregation of the particles and a reduction of the transfection efficiency.[178] pDNA condensation and binding are directly correlated with DNA protection[168] and transfection efficiency. However, the delivery across the cell membrane has not been correlated with transfection efficiency that is more related to other factors as the charge and buffering capacity of the vector. Loghman et al.[187] reported a transfection efficiency within 2-10 % in a transfection between 2-18 h and estimated the toxicity following non-viable cells levels of nonviable cells: 24 % (calcium phosphate, CaP).

Orrantia and Chang[188] speculated about the low transfection efficiency of CaP-DNA vectors indicating that the majority of endocytosed DNA is degraded in a short period of time and excreted to the cytosol and only a small fraction of the remaining DNA may be delivered directly to the nucleus by intermediary vesicles without migrating through the cytosol.[189] Sokolova et al. (2006)[170,190] showed that multi-shell CaP/DNA nanoparticles improved the transfection efficiency due to the protection of DNA against degrading nuclease enzymes. One of the restrictions of traditional CaP transfection technique is unbalancing of the calcium homeostasis inside the cell. However, the intracellular calcium level continued in the normal range after transfection with the multi-shell nanoparticles. This helpful performance can be a sign for a greater biocompatibility of these nanoparticles. Functional Ca^{2+} pumps in cells eliminate the calcium toxicity induced by CaP nanoparticles when dissolving. Hydroxyapatite is generally used to deliver antibiotics and other drugs to hard tissues, such as anti-inflammatory, anti-cancer, anti-osteoporotic substances and others, such as proteins, hormones, vitamins, and growth factors. However, its main disadvantages are associated to low levels of gene expression due to endosome exhaustion, primary cell toxicity, the partial

protection of DNA degradation by nucleases, and the lack of control of the final particle size that leads to poor experimental reproducibility.[191] In addition, the precipitate formation is sensitive to changes in pH, DNA concentration, temperature or concentrations of salts in the environment, such as high concentrations of phosphates, as RPMI medium (Roswell Park Memorial Institute). Therefore, to ensure effectiveness in *in vitro* transfection,[192] the physicochemical properties of DNA-HAp system must be controlled as biodegradability, load, density, solubility, molecular weight, crystallinity, hydrophobicity, rigidity, and pKa values of cationic nanoparticles. The transfection efficiency has been frequently related to cell division (mitosis) but Kirchenbuechler et al.[193] demonstrated that a transfection is still feasible in non-dividing cells, but their efficiency is lower and it takes a longer time lapse.[194]

Nevertheless, different improvements in encapsulation have been described, which take into account the prevention of particle aggregation, Ca^{2+} replacement for Mg^{2+} ions and / or Sr^{2+}, and phosphates (PO_4^{3-}) and hydroxyl (OH^-) replacement for carbonate (CO_3^{2-}) ions and / or fluoride (F^-). The ionic substitution can be beneficial since it can inhibit aggregation, increasing the load efficiency as a consequence of a higher load density, and increasing the dissolution rate of endocytosed particles. Particles smaller than 100 nm[195] are barely recognized by the immune system and can be without difficulty captured by cells. Additionally, these particles might be used in cancer therapy as they are dissolved at low pH,[196] e.g. in the environment of solid tumors, in this manner releasing incorporated biomolecules or drugs.

Some authors described *in vitro* transfection using HAp particles associated to plasmid DNA in bone explants. HAp particles were loaded with a plasmid containing a galactosidase reporter gene by incubation. HAp particles were placed in contact with the bone explants for 8 and 30 days,[197] and the galactosidase activity was detected. Several studies have been published about the CaP nanoparticles used as non-viral vector for DNA delivery in lungs, liver and spleen.[189] Therefore, the release of unrestrained DNA from the core of damaged cells, along with calcium and phosphate ions also available in cells, can initiate a biomineralization process that preserves DNA from physical aggression or chemicals. Consequently, DNA will be not degraded, denatured or modified in spite of being an extremely fragile molecule, and the genetic information that it contains can be transferred to the next generation.

Calcium phosphate vector for gene delivery *in vivo* has been severely restricted mainly due to the lack of tissue specificity, low transfection efficiency and uncontrollable growth of particles in a physiological solution over time.[198] However, some studies report calcium phosphates *in vivo* experiments (i.e. young Swiss albino mice).[188]

The feasibility of natural synthesis of non-viral vectors of transfection and their transfection efficiency, in the context of a breast tumor microenvironment, is reported in the next chapters. Additionally, the capacity of microcalcifications containing nucleic acids to transfect is explored in order to investigate their role in spreading the tumor DNA to different cells. A detailed description of the objectives and their justification can be found in Justification Section.

APPROACH

2 APPROACH

Mineralization of organic molecules has been an intensive research topic for scientists in last decades in the field of Chemistry of Materials. They intend to design new hybrid systems with enhanced properties, by mimicking Nature and consequently, inspiring industrial applications in diverse areas as chemistry, photonics and electronics but also in the medical sector.[199] For that reason, through this thesis, we use a similar approach, combining *in silico* and *in vitro* experiments, in order to understand: i) what is the origin of such a hybrid mineralized system, in our case made of a nucleic acid and a hydroxyapatite (HAp) mineral, ii) how to identify and characterize it in a physiological environment, and iii) how to interpret the results in order to make possible the transference of concepts from basic research in Chemistry to other disciplines as Biology and Medicine.[200]

In this section, we summarize our approach about how the theoretical framework developed here can be transferred to Medicine. We describe our area of interest as biomineralization of nucleic acids in living tissue and its consequences in the context of breast cancer. We outline the basics of the potential role and implications of the foreseen existence of naturally synthesized hydroxyolite particles in tumor tissue in connection with breast cancer disease and the multifocality scenario.

2.1 BIOMINERALIZATION

Biomineralization is a frequent process usually related to both organic-inorganic interactions in the biological interphases (e.g. development of shells and growth of bone) and crystallization of a mineral, directly templated by an organic molecule (e.g. filling the spaces, directing structures or balancing charges).[201] On the other hand, *biocrystallization*, a particular subtype of biomineralization, describes how some important biomolecules are encapsulated by organisms when they suffer life threatening aggressions (i.e. co-crystallization of DNA and Dps protein is observed in *E. Coli* under stress).[202,203]

Such protection of DNA is considered as a reminiscence of the ancestral ordered states of the inanimate world and a last strategy to avoid degradation of highly specialized molecules (i.e.

biopolymers as nucleic acids and proteins).[204] How those biomineralization processes work is still poorly understood and merit further research. The present work is linked to that research as we focus on the hybrid system made of HAp and nucleic acids, termed as hydroxyolite. We looked for them in the context of a natural biomineralization that protects and keeps functional the DNA and RNA when cells undergo a cell death process. However, we consider that our work goes beyond the scope of biomineralization because we aim to study such a process in the framework of breast cancer, focusing on the origin and role of microcalcifications in the context of breast cancer multifocality.

2.2 TRANSFERENCE OF CONCEPTS FROM CHEMISTRY TO MEDICINE

The concepts we aim to transfer from the Chemistry of Materials to Medicine are the result of the previous research of our group and they are summarized in the following subsections:

a. Synthesis of a hydroxyolite triggered by a common shared crystallization plane by DNA and HAp.
b. Influence of nitrogenous base sequences on the synthesis of a hydroxyolite crystal.
c. Effect of Mg^{2+} in hydroxyolite synthesis.
d. Dissolution mechanism of a hydroxyolite under acidic conditions.
e. Hydroxyolite as a non-viral vector of transfection.

a) Existence of a crystallization plane shared by DNA and HAp

DNA presents a polyphosphate backbone that supports the 3D structure of DNA strands and holds the nucleosides. Such links (–PO_3^-–) are similar in structure and hold negative electrical charge, as phosphate monomers (PO_4^{3-}) that participate in the HAp lattice. We note that any of the polyphosphate backbone links might act as a nucleating agent of a HAp crystal as a consequence ionic attractions between negatively charged polyphosphate and positive calcium ions (Ca^{2+}). It is worth noting that a crystallization plane formed by four phosphate groups in HAp lattice matches the spatial coordinates of four links of the nucleic acid backbone, two of them belonging to each DNA strand (Figure 18) facilitating the aggregation of calcium, phosphate and hydroxyl ions around it.

The mineralization process, which depends on time and environmental conditions (type of ions and their relative concentrations, pH and temperature among others), leads to an ordered HAp crystal that contains DNA adsorbed or encapsulated.[114,115] We aim to transfer such a concept extracted from Chemistry to Biology and Medicine by foreseeing that such process will occur in natural scenarios, particularly in the context of cell death processes where nucleic acids are released to the extracellular matrix and the HAp forming ions are in the same location at the same time. Therefore, we looked for several scenarios in calcifying diseases where HAp is known to be naturally formed despite the mechanisms behind such calcification are not completely understood.

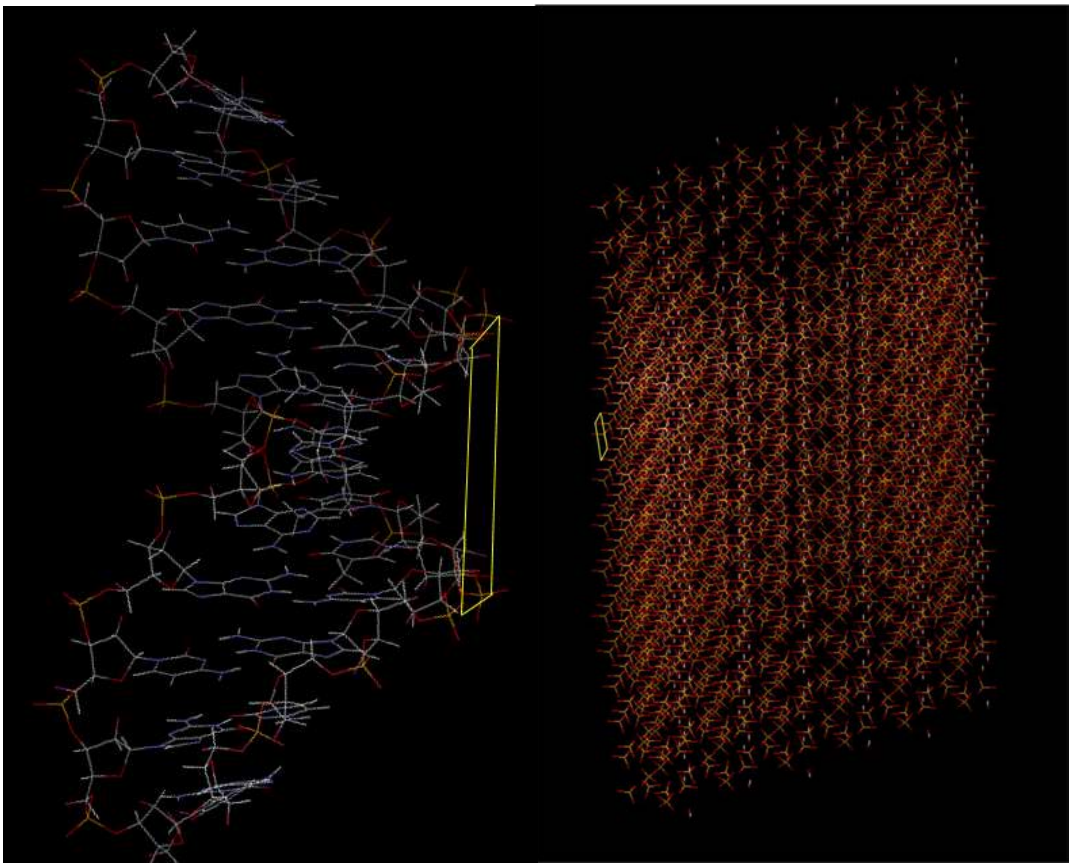

Figure 18. Common crystallization plane shared by DNA and HAp. Courtesy of UPC and B. Braun Surgical.

b) Influence of nucleic acid nitrogenous base sequence

In a previous research, our group confirmed that all nucleic acid sequences could be adsorbed or encapsulated in HAp without losing their functionality by performing several *in*

silico studies. We considered nucleic acids were still functional if hydrogen bonds that link the two strands of DNA or RNA were preserved despite their interaction with HAp. DNA and RNA dodecamers with different nitrogenous base sequences were tested against fluorapatite (FAp) and HAp, including worst case scenarios (see Figure 19). FAp, where OH^- ions were substituted by F^- changed the 3D structure of DNA or RNA and hydrogen bonds were not feasible anymore. Conversely, when nucleic acid dodecamers interacted with HAp, the 3D structure was only distorted but still preserved (Figure 19). The feasibility of adsorbing and encapsulating any DNA and RNA sequence without disrupting the hydrogen bonds between the pairs A-T and C-G of each strand was proven independently of the sequence, confirming that any sequence of DNA/RNA could play the role of a nucleating agent of a hydroxyolite crystal.

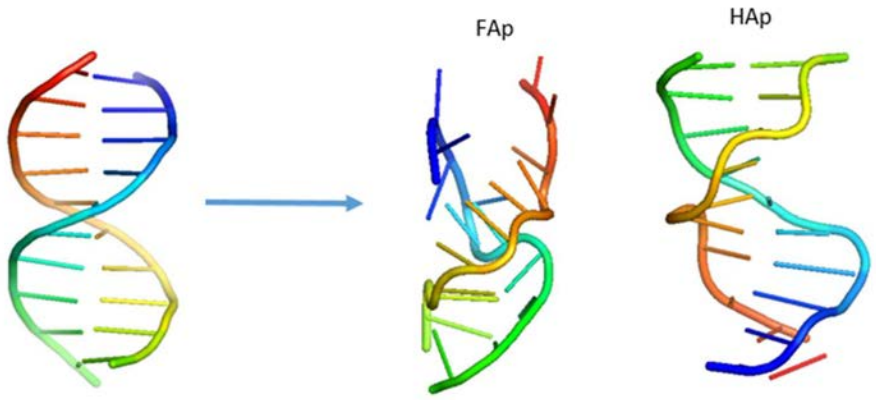

Figure 19. Effect of fluorapatite (FAp) and hydroxyapatite (HAp) on DNA functionality when encapsulated in a FAp or HAp pore. Hydrogen bonds between two strands are destroyed in FAp but only are distorted in HAp. Image courtesy of UPC and B. Braun Surgical.

c) Effect of Mg^{2+} in hydroxyolite synthesis

The effect of Mg^{2+} ions in the mother solution of a hydroxyolite crystal was studied by using *in silico* studies and by empirical assays. We concluded that Mg^{2+} ions play a role in stabilizing DNA double helix. Moreover, Mg^{2+} facilitates the formation of hydroxyolites of reduced size. Mg^{2+} ions tend to migrate to the outer surfaces of the newly formed hydroxyolite and restrict the further growth of the crystal[205] resulting in particles of smaller size, more frequently at submicrometric range. Additionally, we proved that Mg^{2+} becomes integrated in a HAp substrate in similar concentration independently of Mg^{2+} concentration in the mother

solution when a certain threshold is surpassed. We transfer such fact to our research because Mg^{2+} is ubiquitous in physiological environments and it should be expected that any natural hydroxyolite we find in biological tissue should contain Mg^{2+} ions in its lattice.

d) Dissolution mechanism of a hydroxyolite

We considered that once the hydroxyolite system is formed, particularly relevant is the case of a change in the pH if it becomes more acidic. For that reason, we clarified the dissolution mechanism of a hydroxyolite and confirmed that it is feasible under acidic conditions.[176] We note the clinical relevance of this fact in the context of decalcifying diseases as osteoporosis or bone cancer. However, we focused on demineralization of nucleic acids after endocytosis, as this process is of outmost interest for gene therapy applications and transfection processes. Gene therapy struggles with the design of biocompatible carriers of nucleic acids, as a hydroxyolite is, for gene delivery in order to replace and repair damaged DNA. Calcium phosphates are known to be a suitable carrier for nucleic acids delivery. They belong to the non-viral vectors of transfection (NVT) family and show a high biocompatibility and minor secondary effects. Simulations at atomistic level revealed that the dissolution process does not affect the functionality of the encapsulated nucleic acid. Mechanistic studies determined that under acidic conditions (usually < pH 6.6), hydration of the HAp surface leads to hydrogenation of phosphates at the surface of HAp that result in the formation of hydrogen phosphate ion (HPO_4^{2-}). The newly formed HPO_4^{2-} ion detaches from the HAp surface favoring the simultaneous detachment of calcium ions. Such process starts in several places across the HAp surface, driving a polynuclear process that results in the final release of the nucleic acid.

We transfer such basic research knowledge to the dissolution process expected to occur after endocytosis of calcium phosphate NVT. During the transfection process, NVT are internalized by the cell, the vesicle formed (endosome) migrates into the cytoplasm and become a lysosome into which its content is acidified and digested by acid hydrolases. Considering the dissolution mechanism, we concluded that the simultaneous detachment of hydrogen phosphate ions from a hydroxyolite provides enough hydrogen phosphate ions to buffer the surrounding environment inside the lysosome protecting the nucleic acid from the acidic environment that could degrade it.

e) Hydroxyolites as non-viral vectors of transfection

We proved that HAp protects nucleic acids and avoids their degradation,[117] keeping them functional for further reuse, encapsulated or adsorbed, hidden them from the action of DNase degrading enzymes. HAp behaves as a reservoir of nucleic acids intended to maintain intact or with minor degradation such important molecules, contributing to a natural recycling process of DNA and RNA. Nucleic acids can last in such protected condition for a long time, waiting to be reintroduced in a cell. We consider those hydroxyolite particles as natural calcium phosphate non-viral vectors of transfection (NVT). It is known since 1970s, that they are able to cross cell membranes and deliver the adsorbed or encapsulated nucleic acid to a cell through a transfection process. For that reason, any natural hydroxyolite may theoretically be part of a transfection process if their size is in the optimal range for crossing the cell membrane.

Transferring these concepts to our research in this work, we expect that any sequence of DNA or RNA could be part of a naturally formed hydroxyolite. Furthermore, we expect they can participate in transfection processes, when feasible. Through this thesis we aim to explore the implications of such naturally synthesized non-viral vectors of transfection made of calcium phosphate in the context of breast cancer where the available DNA is likely to be originally part of a tumor cell.

As a conclusion of the previous paragraphs, we established a conceptual framework that allowed us to hypothesize that hydroxyolites will be naturally formed in living tissue. Particularly interesting is the case when DNA or RNA is released to the extracellular matrix (i.e. cell death processes related to necrosis) free to interact with Ca^{2+} and PO_4^{3-} ions. Ca^{2+} ions are expected to be released from the endoplasmic reticulum deposits and, PO_4^{3-} ions expected to be supplied after cleavage of polyphosphate polymers under the effect of some enzymes (i.e. alkaline phosphatase; ALP). Such simultaneous processes are expected to occur inside of a tumor. As a consequence, we focused in breast cancer tumors where calcifications of HAp are observed as we considered them candidates to contain nucleic acids to confirm the natural formation of hydroxyolites in breast cancer tissue.

JUSTIFICATION

3 JUSTIFICATION

Recent studies at atomic level have shown that nucleic acids can be encapsulated or adsorbed in hydroxyapatite (HAp), a highly biocompatible mineral usually found in bone, enamel and teeth but also found in breast cancer microcalcifications.[114,115] Results obtained in *in silico* studies were confirmed by *in vitro* studies showing that the process of adsorption or encapsulation in the mineral does not modify the functional properties of nucleic acids.[206] Furthermore, such a process allows nucleic acids to be carried and delivered to a cell and continue to be functional after release (transfection). *In vitro* synthesized HAp particles encapsulating or adsorbing nucleic acids (i.e. DNA), named *hydroxyolites*, are capable of transfecting both prokaryotic[117] and eukaryotic cells[207] by introducing DNA into the nucleus, making feasible its recombination with the cell genome and further gene expression. Moreover, HAp acting as a carrier protects DNA against environmental aggressions of physical and chemical agents, including among them the degrading effect of DNase enzymes.

Transferring such knowledge to the breast cancer tissue microenvironment, we note that processes of cell degeneration, in particular the necrotic or apoptotic, are known to lead to calcium phosphate calcifications.[208] We note that necrotic processes might produce uncontrolled release of nucleic acids into the extracellular matrix. Such fact, combined with the presence of phosphate groups and calcium ions that are released as a consequence of the cell death process, can naturally result in calcium phosphate calcifications that capture DNA or RNA into their lattice, resulting in a naturally formed hybrid system made of nucleic acids and HAp, a combination we defined as hydroxyolite. On the other hand, we note that HAp calcifications (type II) in breast neoplasms[131,209] are frequently associated with worse prognosis compared to calcium oxalate (CaOx, type I)[210] calcifications. In addition, worse prognosis has been associated when necrosis and calcifications are observed simultaneously.[211,212] We expect that such calcifications observed in breast cancer tissue might contain nucleic acids adsorbed in their surface or encapsulated in their interior. Thus, in this thesis we aim to identify such calcifications in breast cancer tissue, analyze their molecular content by using advanced spectroscopic techniques and study their behavior as a non-viral vectors of transfection.

Raman spectroscopy has proven to be a very powerful tool for the determination of biochemical compounds due to its specificity and ability to discriminate some molecules in complex biological environments such as *ex vivo* tissues.[129,213,214] There are some precedents in the literature reporting calcifications with absorption bands related to proteins or nucleic acids without having carried out an undoubtful assignment.[73] For that reason, we scrutinize those calcifications using the more advanced algorithms in 3D Raman imaging with the objective to univocally assign their molecular content and, if applicable, discuss their role as natural transfection vectors.

Transfection using calcium phosphate vectors is known since the 1970s in the context of gene therapy.[158] Transfection process is based on the ability of HAp, as a non-viral vector of transfection, to transport nucleic acids inside the cell, specifically to the nucleus, where the genetic information contained in HAp is delivered. As a consequence, the released nucleic acid can recombine with the cell's own and insert a specific sequence of nucleotides in order to correct a defective gene, the objective of gene therapy. Conversely, other mechanisms of transfection, such as viral vectors,[215] are more efficient than HAp but they have undesired side effects. For this reason, the use of HAp has recently regained the interest of the scientific community despite the low rates of transfection efficiency. Various attempts have been reported in the literature to improve the efficiency of this process by modifying HAp particles, by creating several layers of HAp[190] or by coating them with biocompatible materials.[216] On the other hand, CaOx calcifications have not been studied from the transfection perspective.

Based on the previous premises, in this thesis, we hypothesize that breast calcifications, particularly HAp, may contain nucleic acids and act as a natural non-viral vector of transfection. Potentially, such natural vector of transfection might have the capacity of transfecting nearby cells. Taking into consideration the *in vitro* transfecting studies reported in the literature,[145] the particles with the highest transfection capacity are in the range within 20-200 nm,[217,218] at the edge of the range of optical microscopy and near the edges of resolution of microscopes coupled with Raman or confocal spectroscopy being a challenge to detect and analyze them. Such small size facilitates their migration through the tissue or even the natural conducts (i.e. vascular and lymphatic vessels) following the mainstream gradient flow or just by Brownian movement.

We performed the research focusing on the origin and role of hydroxyolites, taking as a reference the breast cancer scenario. We aim to confirm whether natural hydroxyolites are formed and if the can act as transfection vectors. Secondly, we study if CaOx can perform as a transfection vector and the effect of Ca^{2+} and Mg^{2+} ions. Thirdly, we include in the transfection study, the precursors of HAp (i.e. amorphous calcium phosphate) and the biopolymers containing phosphates, from pyrophosphate (n=2) to polyphosphate (n=25) as the affinity of such molecules for HAp is high.[219] Finally, we aim to investigate, in the clinical context of breast multifocality, if the family of calcium phosphate NVT are able to migrate to a certain distance (up to 5 cm) and still efficiently deliver nucleic acids to the target cells.

HYPOTHESES

4 HYPOTHESES

The hypotheses we aim to contrast through this thesis are the following:

Hypothesis I. Hydroxyolites, nucleic acids adsorbed or encapsulated in hydroxyapatite, are naturally synthesized in the context of a human breast cancer tumor.

Hypothesis II. Non-viral vectors of transfection made of calcium phosphate are able to transfect, in particular focusing on natural hydroxyolites.

Hypothesis III. Non-viral vectors of transfection made of calcium oxalate are able to transfect.

Hypothesis IV. Non-viral vectors of transfection are able transfect cells after migration up to 5 cm. (We consider migration distance ≤ 5 cm taken into consideration the context of this thesis around breast tumor multifocality).

OBJECTIVES

5 OBJECTIVES

5.1 MAIN OBJECTIVE

The main objective of this thesis is to demonstrate that *Hydroxyolites,* hybrid particles made of hydroxyapatite and nucleic acids, are naturally formed in breast cancer tissue. Furthermore, those hydroxyolites are considered to behave as non-viral vectors of transfection able to migrate and transfect surrounding cells. We study such a process in the clinical context of breast cancer multifocality.

5.2 SECONDARY OBJECTIVES

This thesis has been structured in several secondary objectives as outlined below:

1. Development of a conceptual background that explains why hydroxyapatite calcifications might contain nucleic acids adsorbed or encapsulated in breast cancer tissue.
2. Characterization of hydroxyolites *in vitro* and *ex vivo* by Raman spectroscopy.
3. Feasibility of calcium oxalate to adsorb and/or encapsulate nucleic acids in comparison with hydroxyapatite.
4. Determination of the transfection capabilities of *in vitro* synthesized hydroxyolites. Influence of additional Ca^{2+}.
5. Determination of Mg^{2+} ion effect on adsorption, encapsulation and transfection efficiency of hydroxyolites.
6. Determination of the transfection capabilities of calcium oxalate.
7. Determination of the transfection capabilities of precursors of hydroxyapatite (amorphous calcium phosphate, Brushite, pyrophosphate, triphosphate and polyphosphate).
8. Study of the effect of the mineral substrate of transfection vector.
9. Determination of the migration feasibility of non-viral vectors of transfection.

The work to achieve the sub-objectives described beforehand has been distributed into chapters. The first chapter is a general introduction into breast cancer and types of mammary microcalcifications. Some common sections are the chapter describing Materials and Methods, Conclusions, Appendix, and References. Finally, the articles are listed in section Annex 3.

MATERIALS AND METHODS

6 MATERIALS AND METHODS

Permission to use figures, illustrations and tables extracted or adapted from scientific publications included in this manuscript has been obtained from Copyright Clearance Center. In addition, thanks to Dr. Wong (McMaster Pathophysiology Review); Dr. Fernández-Figueras; Dr. Marro, Dr. Loza, Dr. Sanz, Dr. Quidant (ICFO); Prof. Dr. Alemán, Dr. Puiggalí, Dr. Revilla-López, Dr. Casas, Dr. Rivas, Mr. Sans (UPC); and Dr. Rodríguez and Dr. Dr. Turon (B. Braun Surgical) for permission to use their figures and tables. Figures with Creative Commons License have been also indicated.

6.1 DESIGN AND METHODOLOGY FOR THE OBTENTION OF TISSUE SAMPLES FROM PATIENTS

6.1.1 ETHICAL ASPECTS

Before the study was launched, the project was approved by the University Hospital Germans Trias i Pujol (HUGTiP) Research Ethics Committee, obtaining the relevant authorizations from the center's managers. This study was carried out following the basic ethical principles contained in the Declaration of Helsinki, Fortaleza (Brazil), October 2013. Samples and data from patients included in this study were provided by the IGTP-HUGTiP Biobank integrated in the Spanish National Biobank Network of *Instituto de Salud Carlos III* (PT13/0010/0009) and Tumor Bank Network of Catalonia, and they were processed following standard operating procedures with the appropriate approval of the Ethical and Scientific Committees (CCEBB IGTP-HUGTiP Request: BB14004, EBB18004 and evaluation Ref: BB-C-1402).

For all cases it was necessary the collaboration of all the medical departments involved in the treatment of the patients: surgeons, radiologists, nuclear medicine and pathological anatomy laboratory.

6.1.1.1 INFORMATION AND INFORMED CONSENT FORM

Surgeons informed the participants about the objectives of the study. The patients had to have the legal capacity to give their consent and exercise their freedom of decision. Written consent was obtained before the patient was included in the study (see Annex 2).

6.1.1.2 DATA CONFIDENTIALITY

Confidentiality of the data was guaranteed, both in their collection, and in any communication or publication derived from this investigation. Promoter and the researchers of the study guaranteed the confidentiality of patient data and ensured that the provisions of Organic Law 15/1999 on Protection of Personal Data were complied with at all times. The processing of the data that the Promoter of the study collected during the same was subject to the current legislation regarding data protection. Patients were identified in the records only with the code number.

6.1.2 POPULATION AND SIZE OF THE SAMPLE

Tissues from patients with calcifications of the HUGTiP. Given the exploratory nature of the procedure, a formal calculation of the size of the sample was not performed. All subjects to study met the inclusion and exclusion criteria.

6.1.2.1 INCLUSION CRITERIA

Subjects that could be included in this study were those who met the following conditions:

1. Breast tissue with calcifications.
2. Benign and malignant neoplasms of the breast (any histological type).
3. Any number of calcifications.
4. Voluntary acceptance to participate in the study and signature of informed consent (see document on Annex 2).
5. Age ≥ 18 years.

6.1.2.2 EXCLUSION CRITERIA

The subjects that could not be included in this study were those who did not met any of the following conditions:

1. Tumor size that not allows taking a sample for the study.
2. Psychiatric illness or personal condition that does not allow the understanding or acceptance of participating in the study.
3. Other neoplasms at the time of selection.
4. Human Immunodeficiency Virus (HIV).
5. Hepatitis B or C.

6.1.3 DESIGN OF THE STUDY

6.1.3.1 SAMPLING PROTOCOL

Due to the exploratory nature of the procedure, no formal calculation of the sample size has been made. Subjects to be studied meet the inclusion and exclusion criteria.

In the case where the samples were obtained by thick needle biopsy, the standard radiology protocol was followed. On the other hand, when the samples were obtained from the extirpated tumor, the regulations established by the Pathological Anatomy Service (HUGTiP) were followed.

6.1.3.2 EXTRACTION OF THE SAMPLES FROM PATIENTS

The standard surgical procedure for the treatment of breast cancer was performed by experienced surgeons with the patient under general anesthesia. Patients went through conventional or specific surgery according to the protocols of the Breast Pathology Unit (HUGTiP).

The extracted piece was spatially oriented and sent to the Radiology Department (HUGTiP), where an X-ray was performed to confirm the inclusion of the neoplasia and calcifications of the piece.

An expert pathologist of Pathological Anatomy Department (HUGTiP) determined the part of the tumor that should be assigned for the study.

6.1.4 HISTOPATHOLOGY

Selected tissue specimens containing calcifications were identified in order to characterize calcifications by spectroscopic techniques. They were frozen in liquid nitrogen and stored at -85 ºC until analysis. These histological samples were fixed with optimal cutting temperature (OCT), cut to 5 µm and mounted on quartz slides, in order to avoid substrate interferences among spectroscopic signals. These biological samples were frozen in isopentane using a Bright Clini-RF freezer before 30 minutes after extraction.

6.2 RAMAN SPECTROSCOPY

Thawed tissue sections of 5 µm thickness were measured in quartz slides after conditioning at room temperature for 30 min. An inVia Renishaw Raman microscope was used at Institute of Photonic Sciences (ICFO) facilities. A visible 532 nm laser excitation with 10 mW and a 50x objective was used. Raman images were acquired with 1s acquisition time and 1 µm pixel size. To extract the chemical composition, for the Raman images, Multivariate curve resolution (MCR) was used. MCR-ALS algorithm is detailed in our article M. Marro, A. M. Rodríguez-Rivero, C. Araujo-Andrade, M.T. Fernández-Figueras, L. Pérez-Roca, E. Castellà, J. Navinés, A. Mariscal, J.F. Julián, P. Turon and P. Loza-Alvarez. Unravelling the encapsulation of DNA and other biomolecules in HAp microcalcifications of human breast cancer tissues by 3D Raman imaging. *Cancers.* 2021; *13*(11): 2658. https://doi.org/10.3390/cancers13112658 (see Annex 3, Creative Common CC BY license).

For MCR analysis a MATLAB toolbox was used: PLS toolbox (from Eigenvector Research). First, an exploration of the spectral dataset was performed using Principal Component Analysis (PCA). The initial number of components selected was the number in which the cumulative variance explained was more than 99 %. Two independent analyses (PCA and MCR) were performed on the same dataset, which contained the spectra of the breast cancer tissues in rows. The use of this method allowed the interpretation of both DNA content and the composition of the calcifications extracting relevant information.

On the other hand, a 532 nm laser was used for excitation and the laser power was 80 mW 0.1 s (large scan area) which is focused onto the sample via a microscope with 10x or 50x objective (WITec Alpha 300R confocal Raman microscope) at B. Braun facilities. Raman images and spectra were processed and analyzed using WITec Project FOUR software (version 4.1). A piezo stage was used to move the sample in order to obtain the Raman spectra. A spectrum was recorded at every point, with a scan area according to the size of the calcification.

Fluorescence signals in the background of Raman spectra obtained from biological samples are common and differ among samples. To avoid the possibility of inhibiting our ability to interpret the spectra, it must be eliminated before analyzing the data. Hence, to treat the data obtained, a subtraction for background removal have been used. On the other hand, the size of the particles of interest is expected to be in the edge of the detection range of Raman

spectroscopy (~ 200 nm). For that reason, bigger calcifications than desired should be used making more difficult the confirmation of the existence of the non-viral vectors of transfection. When using low size calcifications, the focal range of the microscope is bigger than the particle and the signals have lower intensity, making more difficult their correct identification.

6.2.1 *IN VITRO* SYNTHESIS OF DNA-HAP PARTICLES

Suspensions of HAp particles (5 $mg \cdot mL^{-1}$) were prepared following the procedure described elsewhere[115] and subsequently sonicated to improve their dispersion. DNA was extracted from 4T1-luc2 cells (Perkin Elmer, 124087). DNA-HAp complexes were formed to reach 1 % DNA, on HAp w/w. DNA-HAp particles were incubated for 90 min at 37 ºC and 200 rpm, shaking them with a vortex every 30 min. Complexes were separated from the solution by centrifugation at 10,000 rpm for 10 min. Sediments were re-suspended in 10 mL of sterile water.

6.2.2 FOURIER-TRANSFORM INFRARED (FTIR) SPECTROSCOPY

Infrared absorption spectra were recorded from powder samples with a Fourier Transform FTIR 4100 Jasco spectrometer in the 1800–700 cm^{-1} range. Specac model MKII Golden Gate attenuated total reflection (ATR) equipment with a heated Diamond ATR Top-Plate was used.

6.2.3 STATISTICAL ANALYSIS

Patients' data was introduced to a database system designed for this study, with restricted access and provided with traceability of the data until its closure. Study results were presented in a precise way, including tables of the individual gross data that are understandable. The main component statistical analysis (PCA) will be used to build predictive models.

6.3 MOLECULAR DYNAMICS (MD) AND QUANTUM MECHANICAL (QM) CALCULATIONS

Experimental part is detailed in our published article. Reprinted with permission from Revilla-Lopez, G., Rodríguez-Rivero, A. M., del Valle, L. J., Puiggali, J., Turon, P., & Alemán, C. Biominerals Formed by DNA and Calcium Oxalate or Hydroxyapatite: A Comparative Study. *Langmuir.* 2019*; 35* (36): 11912-11922 (see ANNEX 3). Copyright (2019) American Chemical Society.

https://doi.org/10.1021/acs.langmuir.9b01566

6.4 CELL CULTURE AND *IN VITRO* TRANSFECTION STUDIES

6.4.1 CELL LINES

- **4T1 (ATCC® CRL-2539™)**

Organism: *Mus musculus*, mouse / Tissue: mammary gland, epithelial / Disease: This tumor is an animal stage IV human breast cancer.

- **4T1-Luc2 (ATCC® CRL-2539-LUC2™)**

Organism: *Mus musculus*, mouse / Tissue: mammary gland, epithelial / Disease: This tumor produced mimics an animal stage IV human breast cancer / Express luciferase encoded by Luc2 gene (pGL4).

- **A549 (ATCC® CCL-185™)**

Organism: *Homo sapiens*, human / Tissue: lung, epithelial / Disease: Carcinoma.

6.4.2 SUBCULTURING ADHERENT CELLS

All materials and equipment were clean and sterile. Information for the appropriate medium for a given cell type was obtained from the source of the cells.

6.4.2.1 GENERAL CELL MAINTENANCE

i. Complete Media- per 50 mL

Penicillin-Streptomycin (PenStrep, Sigma Aldrich, Ref. P4458) and Fetal Bovine Serum (Hi-FBS, ThermoFisher, Ref. 10082147) were thawed, and media (RPMI-1640, ThermoFisher, Ref. A1049101 or DMEM, ThermoFisher, Ref. 31966021) was warmed in a 37 ± 2°C water bath. 45 mL of media was placed into a conical centrifuge PP tube (50 mL), with 5 mL of FBS and 0.5 mL of PenStrep. Content was mixed by inverting the closed container at least five times.

ii. Maintenance of a cell line

1. Trypsinization and passage of adherent cells

All complete media was pre-warmed in a 37 ± 2 ºC water bath. All media from a confluent culture flask (e.g. T-25 flask) was removed using a sterile serological pipette. Cells were washed with PBS 1x (ThermoFisher, Ref. 10010015), and 1-2 mL of Tryple Express (ThermoFisher, Ref. 12604-021) were added to detach cells. Then, cells were incubated for approximately 10 minutes in the CO_2 incubator. After incubation, cells were checked under inverted microscope to make sure cells were detached. At that point, enough complete media was added to the flask (3 mL), and the content was placed into conical centrifuge PP tube (50 mL). This conical centrifuge tube was centrifuged for 5 min at 1200 rpm. After centrifugation, the media containing Tryple was removed, and cells (pellet) was resuspended in complete media, according to the split ratio decided (from 1:2 to 1:20). The total volume of the cell suspension was divided by the split ratio, and distributed into the desired number of new flasks. Enough complete media was added to each flask to end up with a 3 mL solution of complete media / cells per flask.

2. Cell counting and viability

A confluent culture was trypsinized following steps previously described. 10 µL of cell suspension was removed and added to a culture tube with 10 µL of Trypan Blue solution 0.4 % (Sigma Aldrich, Ref. T8154). This mixture was gently resuspended. A cover slip was placed over the counting chambers of a Neubauer chamber. 10 µL of the stained cell suspension was added to each side of the hemocytometer, and the cells were counted in the four corners (16 squares each of one grid) according to Figure 20.

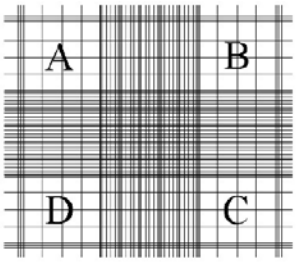

Figure 20. Neubauer chamber (hemocytometer).

The number of counted live cells was divided by 8 (representing the four corners of the grid, both sides). The number of cells was multiplied by 10^4 mL to determine the concentration of the cells per mL. Each large square represents an area of 1 mm^2 at a depth of 0.1 mm. Therefore, each large square corresponds to a volume of 0.1 mm^3 or 10^{-4} mL. To account for the addition of Trypan Blue to the cell suspension, the cells per mL must be multiplied by a dilution factor of 2.

3. Cryopreservation
    a. Cell Freezing

Using a confluent T-75 culture flask, the media was removed with a serological pipette, washed the cells with 10 mL of 1x PBS and trypsinized. Cells were counted (using steps previously described) to determine cell viability.

The suspension was centrifuged at 1200x for 5 minutes at room temperature. Medium was removed, and the cells were suspended in cell freezing medium (a mixture of FBS containing 10 % DMSO) at about 10^6 to 10^7 cells/mL and aliquot 1 mL into cryovials. After label with date, batch number, and passage number, the cryovials were placed into a 'Mr. Frosty' container to transfer it into a -80 ± 5 ºC freezer. Final storage was done in cryoboxes into liquid nitrogen.

    b. Thawing

Cryovials were thawed with 1 mL of pre-warmed complete media (up & down gently with pipette). Cells were resuspended immediately into a conical centrifuge tube containing 10 mL of pre-warmed complete media. This conical centrifuge tube was centrifuged for 5 min at 1200 rpm. After centrifugation, the media with

cryoprotectant was removed. Cells were resuspended immediately in a T-25 flask containing 3 mL of pre-warmed complete media.

4. Mycoplasma test

When a new cell line was started, a sample was analyzed with a Mycoplasma detection kit (Lonza, Ref. LT07-701) according to manufacturer instructions. To perform this analysis, cells were cultured in media with FBS (without antibiotics) during 15 days before analysis.

Additionally, this procedure was repeated every two months with all cultured cell lines.

6.4.3 ISOLATION OF DNA FROM CELLS

4T1-luc2 cells were cultured *in vitro* with RPMI 1640 medium (Gibco by Thermofisher, Ref. A1049101) in T-175 flasks, supplemented with 10 % FBS (ThermoFisher, Ref. 10082147) and 1 % PenStrep (Sigma Aldrich, Ref. P4458) at 37 ºC in a moist environment with 5 % CO_2. Cells were detached with Tryple Express (ThermoFisher, Ref. 12604021) and centrifuged at 1,200 rpm for 5 min. The supernatant was completely removed and discarded. Then, the cell pellet was resuspended in sterile water to a final volume of 7 mL. DNA was purified from these samples using a magnetic beads DNA isolation system at BioBank facilities (IGTP-HUGTiP) with the Chemagic Magnetic Separation Module I (Perkin Elmer). Qualitative and quantitative analysis of DNA was performed with Epoch™ spectrophotometer (BioTek). Integrity analysis of DNA was performed with TapeStation System 2200 (Agilent Technologies).

6.4.4 CELL STAINING FOR CONFOCAL MICROSCOPY IMAGING

Cultured cells were fixed with formalin 10 % for 20 min. After washing three times with PBS, cells were stained with a HAp probe of alendronate fluorescently labelled with fluorescein (6-[Fluorescein-5(6)-carboxamido] hexanoic acid N-hydroxysuccinimide ester (Sigma Aldrich, Ref. 46940), and alendronate sodium trihydrate (Sigma Aldrich, Ref. A4978) at 2.5 µg/mL in PBS (ThermoFisher, Ref. 10010023) for 1 h. After washing three times with

PBS, cells were incubated with DRAQ5 (ThermoFisher DRAQ5™ Fluorescent Probe Solution (5 mM), Ref. 62251) as DNA probe at 5 µM in PBS without washing step. Cells were imaged in a Leica confocal microscope using 63x immersion oil objective, a 488 nm laser for HAp probe (emission filter at 500-532 nm) and a 633 nm laser for DNA probe (emission filter at 650-780). Images at different depths were obtained for each calcification found.

6.4.5 MEASUREMENT OF DNA CARRIED BY TRANSFECTION VECTORS (BISBENZIMIDE ASSAY)

Total DNA free in solution was determined by a bisBenzimide H 33258 assay (Hoechst 33258) using a DNA Quantitation Kit (Sigma-Aldrich®, Catalog number DNAQF), according to the instructions provided by the manufacturer and measured using a microplate reader (Cytation 5, Biotek Instruments, Inc.) at ambient temperature, and at a wavelength of 360 nm excitation and 460 nm emission. Hoechst 33258 assay requires a DNA standard calibration curve to determine the DNA content of samples. Transfection vectors were prepared containing 500 ng DNA in 400 µL in all cases.

6.4.6 *IN VITRO* TRANSFECTION OF EUKARYOTIC CELLS

A549 cells (ATCC® CCL-185™, LGC Standards) were cultured in 75-cm^2 flasks in Dulbecco's modified Eagle's medium (DMEM, ThermoFisher, Ref. 31966021) supplemented with 10 % fetal bovine serum (Hi-FBS, ThermoFisher, Ref. 10082147), 1 % Penicillin-Streptomycin (PenStrep, Sigma Aldrich, Ref. P4458) at 37 ºC in a humidified 5 % CO_2-containing atmosphere. Cells were seeded at 40,000 cells per well into 24-well plates the day before transfection. Replacement of media with Opti-MEM® media (ThermoFisher, Ref. 11058021) without serum was done 2 hours before the transfection. Then, 0.5 µg of plasmid DNA containing a luciferase gene (NanoLuc™, a pNL vector using a pGL4-based backbone; Promega, Ref. N1091, Figure 21) was added to a solution containing the HAp nanoparticles.

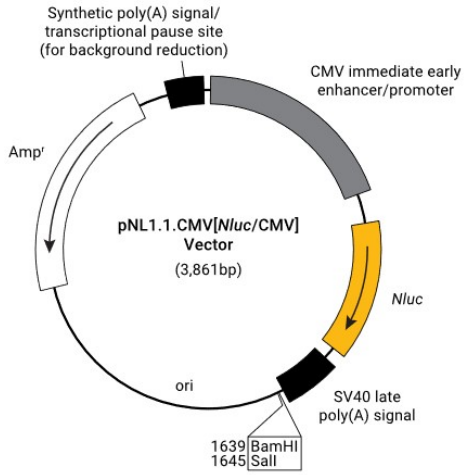

Figure 21. pNL1.1.CMV[NLUC/CMV] Vector map and sequence reference points. Image extracted from Promega.

Naked plasmid DNA was used as a negative control, and conventional CaP transfection reagent was added as a positive control (see Preparation of amorphous calcium phosphate – DNA system). After addition of 50 µL of the incubated mixture dropwise to each well, cells were incubated for 6 h, and once replacement with 400 µL of fresh serum complet media. Each experiment was repeated in triplicate. The cells were lysed after incubation. Luciferase gene expression was monitored by using a commercial kit (Promega, Ref. N1110) and Cytation 5 microplate reader (BioTek), according to the instructions provided by the manufacturer Transfection efficiency was determined 24 and 48h-post transfection, expressed as mean Relative Light Units (RLU) per microgram of cell protein (normalized against protein content) using a Pierce BCA protein assay kit (see section 6.4.7. for more details).

6.4.7 PREPARATION OF MINERAL DNA - NANOPARTICLES SYSTEM

6.4.7.1 Preparation of hydroxyolites (HAp – DNA system)

- *Co-precipitate HAp – DNA (*HAp-*c*DNA*)*

Hydroxyapatite nanoparticles were synthesized *in situ* from a solution of 500 mM calcium nitrate tetrahydrate (Sigma Aldrich, Ref. C4955) and 500 mM ammonium phosphate dibasic (Sigma Aldrich, Ref. 09839), adjusting volumes to reach a molar relation Ca/P = 1.67. Then,

0.5 µg of plasmid DNA (NanoLuc™, a pNL vector using a pGL4-based backbone; Promega, Ref. N1091) was added to hydroxyapatite nanoparticles *in situ* diluted with Opti-MEM® media (ThermoFisher, Ref. 11058021).

- *Adsorbed HAp – DNA (*HAp-*a*DNA*)*

0.5 µg of plasmid DNA (NanoLuc™, a pNL vector using a pGL4-based backbone; Promega, Ref. N1091) was added to 1 M hydroxyapatite suspension and diluted with Opti-MEM® media (ThermoFisher, Ref. 11058021). 1 M hydroxyapatite (Sigma Aldrich, Ref. 289396) solution was prepared using water for molecular biology (Merck Millipore, Ref. H20MB0506).

- HAp-*c*DNA(Ca^{2+}) and HAp-*a*DNA(Ca^{2+})

Exogenous Ca^{2+} was supplied to hydroxyolite vectors once the particles were already formed through the addition of $CaCl_2$ to reach a concentration of 0.0524M $CaCl_2$.

6.4.7.2 Preparation of oxalate – DNA system

- *Co-precipitate CaOx – DNA (*CaOx-*c*DNA*)*

Calcium oxalate nanoparticles were synthesized from a solution of 0.04 M sodium oxalate (Sigma Aldrich, Ref. 223433) and 0.04 M calcium chloride (Scharlab, Ref. CA01920500). Then, 0.5 µg of plasmid DNA (NanoLuc™, a pNL vector using a pGL4-based backbone; Promega, Ref. N1091) was added to oxalate nanoparticles *in situ* diluted with Opti-MEM® media (ThermoFisher, Ref. 11058021).

- *Adsorbed CaOx – DNA (*CaOx-*a*DNA*)*

0.5 µg of plasmid DNA (NanoLuc™, a pNL vector using a pGL4-based backbone; Promega, Ref. N1091) was added to 1 M calcium oxalate suspension and diluted with Opti-MEM® media (ThermoFisher, Ref. 11058021). 1 M calcium oxalate (Sigma Aldrich, Ref. 455997) solution was prepared using water for molecular biology (Merck Millipore, Ref. H20MB0506).

- CaOx-*c*DNA(Ca^{2+}) and CaOx-*a*DNA(Ca^{2+})

Exogenous Ca^{2+} was supplied to vectors once the particles were already formed through the addition of $CaCl_2$ to reach a concentration of 0.0524M $CaCl_2$.

6.4.7.3 Preparation of amorphous calcium phosphate – DNA system

- Positive control (PC)

DNA co-precipitated HAp and HEPES. Amorphous calcium phosphate was synthesized using the "Calcium Phosphate Transfection Kit" (ThermoFisher, Ref. K278001) and according to the manufacturer's instructions.

Briefly, 0.5 µg of plasmid DNA (NanoLuc™, a pNL vector using a pGL4-based backbone; Promega, Ref. N1091) was mixed directly with a concentrated solution of 2 M calcium dichloride ($CaCl_2$) and water for molecular biology (Merck Millipore, Ref. H20MB0506). This mixture was then added dropwise to a HEPES Buffered Saline (HBS) solution in a ratio 1:1, and diluted with Opti-MEM® media (ThermoFisher, Ref. 11058021) while bubbling air through the solution over 1-2 minutes. The final solution was incubated at room temperature for 30 minutes prior to use.

- *Co-precipitate ACP – DNA (*ACP-*c*DNA*)*

DNA co-precipitated with ACP. The procedure was identical to that previously described but replacing the volume of HBS by a solution of 274 mM sodium chloride (NaCl; Scharlab, Ref. SO02250500), 10 mM potassium chloride (KCl; Scharlab, Ref. PO02000500) and 1.4 mM disodium hydrogen phosphate (Na2HPO4; Sigma Aldrich, Ref. 795410).

- *Adsorbed ACP – DNA (*ACP-*a*DNA*)*

DNA adsorbed on ACP. According to the proportions detailed in the "Calcium Phosphate Transfection Kit" (ThermoFisher, Ref. K278001), a solution of 2 M calcium dichloride ($CaCl_2$; Scharlab, Ref. CA01920500) and water for molecular biology (Merck Millipore, Ref. H20MB0506) was mixed with 274 mM sodium chloride (NaCl; Scharlab, Ref. SO02250500), 10 mM potassium chloride (KCl; Scharlab, Ref. PO02000500) and 1.4 mM disodium hydrogen

phosphate (Na_2HPO_4; Sigma Aldrich, Ref. 795410) in a ratio 1:1. Then, the mixture was added dropwise to 0.5 µg of plasmid DNA (NanoLuc™, a pNL vector using a pGL4-based backbone; Promega, Ref. N1091) and diluted with Opti-MEM® media (ThermoFisher, Ref. 11058021) while bubbling air through the solution over 1-2 minutes. The final solution was then incubated at room temperature for 30 minutes prior to use.

- ACP-*c*DNA(Ca^{2+}) and ACP-*a*DNA(Ca^{2+})

Exogenous Ca^{2+} was supplied to vectors once the particles were already formed through the addition of $CaCl_2$ to reach a concentration of 0.0524M $CaCl_2$.

6.4.7.4 Preparation of Brushite – DNA system

- *Co-precipitate Brushite – DNA (*Bru-*c*DNA*)*

Brushite nanoparticles were synthesized from a solution of 0.05 M Sodium phosphate dibasic (Sigma Aldrich, Ref. 795410) and 0.05 M calcium chloride dihydrate (Sigma Aldrich, Ref. 223506), adjusting volumes to reach a molar relation Ca/P = 1. Then, 0.5 µg of plasmid DNA (NanoLuc™, a pNL vector using a pGL4-based backbone; Promega, Ref. N1091) was added to brushite nanoparticles *in situ* diluted with Opti-MEM® media (ThermoFisher, Ref. 11058021).

- *Adsorbed Brushite – DNA (*Bru-*a*DNA*)*

0.5 µg of plasmid DNA (NanoLuc™, a pNL vector using a pGL4-based backbone; Promega, Ref. N1091) was added to 1 M calcium hydrogen phosphate dihydrate ($CaHPO_4{\cdot}2H_2O$) suspension and diluted with Opti-MEM® media (ThermoFisher, Ref. 11058021). 1 M calcium hydrogen phosphate dihydrate (Scharlau, Ref. CA02100500) solution was prepared using water for molecular biology (Merck Millipore, Ref. H20MB0506).

6.4.7.5 Preparation of calcium pyrophosphate – DNA system

0.5 µg of plasmid DNA (NanoLuc™, a pNL vector using a pGL4-based backbone; Promega, Ref. N1091) was added to 1 M calcium pyrophosphate ($Ca_2P_2O_7$) diluted with Opti-MEM® media (ThermoFisher, Ref. 11058021). 1 M calcium pyrophosphate (Sigma Aldrich, Ref.

401552) solution was prepared using water for molecular biology (Merck Millipore, Ref. H20MB0506).

6.4.7.6 Preparation of triphosphate – DNA system

0.5 µg of plasmid DNA (NanoLuc™, a pNL vector using a pGL4-based backbone; Promega, Ref. N1091) was added to 1 M penta-sodium triphosphate ($Na_5P_3O_{10}$) diluted with Opti-MEM® media (ThermoFisher, Ref. 11058021). 1 M penta-sodium triphosphate (Supelco, Ref. 1069991000) solution was prepared using water for molecular biology (Merck Millipore, Ref. H20MB0506).

6.4.7.7 Preparation of polyphosphate – DNA system

0.5 µg of plasmid DNA (NanoLuc™, a pNL vector using a pGL4-based backbone; Promega, Ref. N1091) was added to 1 M sodium polyphosphate (Graham's salt) diluted with Opti-MEM® media (ThermoFisher, Ref. 11058021). 1 M sodium polyphosphate (Graham's salt, Merck, Ref. 1.06529.1000) solution was prepared using water for molecular biology (Merck Millipore, Ref. H20MB0506).

6.4.7.8 SYNTHESIS OF 30 % Mg SUBSTITUTED MINERALS

The synthesis of 30 % Mg substituted minerals was prepared[220] for doped hydroxyapatite, amorphous calcium phosphate, calcium oxalate and Brushite.

- 30 % Mg doped Hydroxyapatite – DNA system (HAp(Mg^{2+})-*c*DNA)

0.5 µg of plasmid DNA (NanoLuc™, a pNL vector using a pGL4-based backbone; Promega, Ref. N1091) was added to 0.15 mol of 1 M magnesium dichloride (Sigma Aldrich, Ref. 1002071925). 0.35 mol of 0.5 M calcium nitrate tetrahydrate (Sigma Aldrich, Ref. C4955) and 0.5 M ammonium phosphate dibasic (Sigma Aldrich, Ref. 09839), adjusting volumes to reach a molar relation Ca/P = 1.67, were added to the solution and diluted with Opti-MEM® media (ThermoFisher, Ref. 11058021).

- 30 % Mg doped Hydroxyapatite – DNA system (HAp(Mg^{2+})-aDNA)

0.5 µg of plasmid DNA (NanoLuc™, a pNL vector using a pGL4-based backbone; Promega, Ref. N1091) was added to 0.15 mol of 1 M Magnesium dichloride ($MgCl_2$; Sigma Aldrich, Ref. 1002071925). Then, this mixture was added to 1 M hydroxyapatite particles suspension and diluted with Opti-MEM® media (ThermoFisher, Ref. 11058021).

- 30 % Mg doped Amorphous calcium phosphate (with or without HEPES) – DNA system PC(Mg^{2+}), ACP(Mg^{2+})-*c*DNA and ACP(Mg^{2+})-*a*DNA

Particles were synthesized using the "Calcium Phosphate Transfection Kit" (ThermoFisher, Ref. K278001) following the methodology previously detailed for each particle, but adding 0.15 mol of 1 M magnesium dichloride ($MgCl_2$; Sigma Aldrich, Ref. 1002071925) to 0.5 µg of plasmid DNA (NanoLuc™, a pNL vector using a pGL4-based backbone; Promega, Ref. N1091) prior to the addition of the rest of reagents.

- 30 % Mg doped calcium oxalate – DNA system (CaOx(Mg^{2+})-*c*DNA)

0.5 µg of plasmid DNA (NanoLuc™, a pNL vector using a pGL4-based backbone; Promega, Ref. N1091) was added to 0.012 mol of 1 M magnesium dichloride (Sigma Aldrich, Ref. 1002071925). 0.028 M sodium oxalate (Sigma Aldrich, Ref. 223433) and 0.04 M calcium chloride (Scharlab, Ref. CA01920500), were added to the solution and diluted with Opti-MEM® media (ThermoFisher, Ref. 11058021).

- 30 % Mg doped Brushite – DNA system (Bru(Mg^{2+})-*c*DNA)

0.5 µg of plasmid DNA (NanoLuc™, a pNL vector using a pGL4-based backbone; Promega, Ref. N1091) was added to 0.015 mol of 1 M $MgCl_2$ (Sigma Aldrich, Ref. 1002071925). 0.035 mol of calcium chloride dihydrate (Sigma Aldrich, Ref. 223506) and 0.05 M sodium phosphate dibasic (Sigma Aldrich, Ref. 795410), adjusting volumes to reach a molar relation Ca/P = 1, were added to the solution and diluted with Opti-MEM® media (ThermoFisher, Ref. 11058021).

6.4.8 BICINCHONINIC ACID (BCA) PROTEIN ASSAY

Pierce™ BCA Protein Assay Kit (ThermoFisher, Ref. 23225) was used to measure total protein concentration from cell lysate according to manufacturer's instructions. First, a set of diluted Albumin (BSA) Standards was prepared using a working range = 20 – 2,000 µg / mL. Then, 25 µL of each standard or unknown sample was pipette into a clear 96-microplate well. 200 µL of the working reagent was added to each well. The plate was mixed thoroughly on a plate shaker for 30 seconds, covered and incubated at 37°C. After 30 minutes, the plate was cooled to RT, and the absorbance was measured at 562 nm on a plate reader. The standard curve was used to determine the protein concentration of each unknown sample.

6.4.9 OSTEOGENIC MEDIA DESCRIPTION

4T1 cell line (ATCC® CRL-2539™, LGC Standards) was cultured in standard conditions with DMEM (ThermoFisher, Ref. 21063-029) supplemented with 10 % FBS (ThermoFisher, Ref. 10082147) and 1 % penicillin/streptomycin (PenStrep, Sigma Aldrich, Ref. P4458). Osteogenic conditions using the same standard conditions media, supplemented with 10 mM β-Glycerophosphate (Sigma-Aldrich, Ref. G9422) and 50 µg/mL ascorbic acid (Sigma-Aldrich, Ref. A92902).

Cells were seeded at 15,000 cells per well in 6-wells plate (Nunc, ThermoFisher, Ref. 140675) and cultured several weeks until HAp crystals were produced, typically more than 3 weeks.

6.4.10 PARTICLE SIZE (DLS) AND Z-POTENTIAL

Measurements were performed on a NanoBrook 90Plus Zeta equipped with an AQ-1321 cell for the zeta potential measurement. The synthesized samples were re - suspended and diluted 5,000 times in ultrapure milli-Q water (Millipore) and 1 mM KCl water solution respectively, and sonicated (when specified) for 10 minutes. Particle size (DLS) was set to collect and average data every 3 minutes and Zeta potential (ELS) was obtained from averaging two series of 10 measurements to ensure representative data. All measurements were performed at room temperature.

6.4.11 STATISTICS

All series of average size (S), percentage of particles below 500 nm (Γ_{500}), Z-potential (Z), and free DNA (C_{DNA}) measurements were performed in triplicate. For each time point, the average and standard deviation were calculated. Furthermore, due to the intrinsic characteristics of the transfection assay, mostly related to the kind of cells, their life cycle and the internalization process of transfection vectors, a significant variability among replicates is expected that makes difficult the interpretation of the quantitative results. For that reason, assays were performed three independent days by triplicate each condition. Average and standard deviation (n–1) of the each test were calculated to compare the daily series. Average of the all data was calculated to classify the transfection ratio in intervals. The transfection efficiency intervals have been classified by magnitude orders as very low (V.L.), low (L), medium (M), high (H) and very high (V.H.) are defined in Table 9. Principal Components Analysis (PCA) was performed in Minitab® v.18.1 statistic software package.

Table 9. Intervals of transfection efficiency by magnitude order.

Transfection efficiency		RLU/µg protein	Score
No transfection		0	0
Very low	V.L.	1 - 9	2
Low	L	10 - 99	4
Medium	M	100 - 999	6
High	H	1,000 – 9,999	8
Very high	V.H.	10,000 – 99,999	10

6.5 DETERMINATION OF Mg^{2+} ION EFFECT

6.5.1 TURBIDITY MEASUREMENT OF HYDROXYOLITES PARTICLES WITH MAGNESIUM

A 96-well microplate was filled with 300 µL of the samples or blanks. The samples were prepared diluting HOLi (DNA encapsulated in HAp) in sterile water (B. Braun Medical, Ref. 262858), and adding 0-8 mM $MgCl_2$ 1 M ± 0.01 M (Sigma Aldrich, Ref. 1002071925). Three wells were left as blank, containing only sterile H_2O. The absorbance of the solutions in contact with the samples was controlled at λ= 320 nm, at time points of 1 hour in the Synergy HT microplate reader (BioTek) until a maximum of 96 hours (4 days). Between readings, the microplate was shaken and incubated at 23 ºC and 37 ºC.

6.5.2 OSTEOGENIC QUANTIFICATION: Ca^{2+} CONTENT (MINERALIZATION)

4T1 cell line (ATCC® CRL-2539™, LGC Standards) was cultured in standard conditions with DMEM (ThermoFisher, Ref. 21063-029) supplemented with 10 % FBS (ThermoFisher, Ref. 10082147) and 1 % penicillin/streptomycin (PenStrep, Sigma Aldrich, Ref. P4458). Osteogenic conditions using the same standard conditions media, supplemented with 10 mM β-Glycerophosphate (Sigma-Aldrich, Ref. G9422) and 50 µg/mL ascorbic acid (Sigma-Aldrich, Ref. A92902). DMEM complete media containing 2 and 8 mM Magnesium chloride (Sigma Aldrich, Ref. 1002071925) was added to the corresponding wells.

Cells were seeded at 15,000 cells per well in 6-wells plate (Nunc, ThermoFisher, Ref. 140675) and cultured several weeks until HAp crystals were produced, and the osteogenic quantification was performed after 21 and 45 days. Cells containing mineral deposits were stained bright red by the Alizarin Red Solution, according to the manufacturer's protocol (Osteogenesis Assay Kit, Merck Millipore, Ref. ECM815).

6.5.3 STATISTICAL ANALYSIS

Statistical data analysis was performed using Minitab® 18.1 (2017, Minitab Inc.) on n = 3 replicates. Two-tailed unpaired student's T-tests and Two-way Anova were carried out to compare treatments groups. A p-value of less than 0.05 was considered statistically significant. Details on statistical tests are presented in the figure legends. All graphs show mean + standard deviation of the mean as indicated in the figure legends.

6.6 TRANSFECTION AFTER MIGRATION

A549 cells (ATCC® CCL-185™, LGC Standards) were cultured in 25-cm^2 flasks in Dulbecco's modified Eagle's medium (DMEM, ThermoFisher, Ref. 31966021) supplemented with 10 % fetal bovine serum (Hi-FBS, ThermoFisher, Ref. 10082147), 1 % Penicillin-Streptomycin (PenStrep, Sigma Aldrich, Ref. P4458) at 37 ºC in a humidified 5 % CO_2-containing atmosphere.

The transfection methodology described in the previous section was adapted in order to study how the migration distance of the vectors through the culture media affects the transfection rate. In this sense, the volume of Opti-MEM® media (ThermoFisher, Ref. 11058021) without serum added 2 hours before the transfection was adjusted to guarantee a migration distance of 3 mm (200 µL of Opti-MEM® media per well). An *in vitro* vertical migration setup was specifically designed for the assay to perform 7, 20 and 50 mm migration distance tests (Figure 58).

The set-up was built using 24-well plates assembled with conical sterile polypropylene tubes in order to ensure a defined migration distance before entering in contact with the target cells seeded at the bottom of the well. The transfection procedure was identical to that described previously. Opti-MEM® media (ThermoFisher, Ref. 11058021) was used to fill the tube until the selected migration distance. 50 µL of the incubated mixture corresponding to each vector was added dropwise to each well.

RESULTS

7 RESULTS

7.1 TRANSFERENCE OF HYDROXYOLITE CONCEPTUAL BACKGROUND TO BREAST CANCER TISSUE CLINICAL SCENARIO

Through this thesis we focused our work on breast cancer tissue, where the formation of hydroxyapatite (HAp) and calcium oxalate (CaOx) calcifications is often observed. Consequently, in this section, we detail the results of the transference of our conceptual approach and knowledge about hydroxyolites accumulated in the field of Chemistry of Materials to the Medicine.

We consider as a first result of this section, the identification of a clinical scenario where natural hydroxyolites could be synthesized as a consequence of a pathology. We looked for scenarios where biomineralization of nucleic acids might occur. We reached to the conclusion that hydroxyolites should be naturally formed in some diseases that usually develop HAp calcifications as we are going to explain in the following paragraphs. We concluded that the best option for that clinical scenario was breast cancer tissue that usually present HAp calcifications.

The second result is related to the appearance and continuous growth of a HAp crystal whether contains or does not contain a nucleic acid. As we demonstrated that such processes are thermodynamically favored, we should expect a continuous growth when enough ions are present in the mother solution (*in vitro*) or in the surrounding tissue (*in vivo*). For that reason, we understand that HAp calcifications, observed in a mammogram scan for diagnosis purposes or in an optical microscope for pathological assessment, are big enough to be seen without difficulties by traditional techniques. The thermodynamics behind HAp crystals favor the growth until the range of micrometers is achieved. At the end of the growing process, the breast cancer tissue shows large calcifications as the ones we will analyze the following section.

A third result is about HAp calcifications containing nucleic acids can also be found in the submicrometric or nanometer range due to the effect of some environmental factors (i.e. lack of enough constituting ions in the surroundings or by the effect of other ions and molecules

that hinder the growth, for instance Mg^{2+}). Transferring our previous knowledge to this context, we highlight the relevance of those smaller hydroxyolite particles, as confirmed in next section, in breast cancer tissue as they can be considered as natural non-viral vectors of transfection (NVT) with the capacity of protect and deliver DNA and RNA to a new cell.

As a fourth result of this section, we consider the thermodynamics of the two main processes of a hydroxyolite synthesis. Following our simulations, we could expect two different situations a hydroxyolite by DNA adsorption and a hydroxyolite by DNA encapsulation. Regarding the first, nucleic acid becomes adsorbed on an already formed HAp crystal. In that case, it is only necessary that RNA or DNA are free to interact with existing HAp microcalcification in breast before being degraded by enzymes (i.e. DNase family) that cleave their bonds and degrade them. On the other hand, if the nucleic acid is taken as nucleating agent, it will start the process to develop a hydroxyolite encapsulating DNA/RNA. In this case, the one who triggers the formation of the particle is the nucleic acid, not the existing HAp. For that reason, to complete the clinical scenario we looked for, a cell mechanism should be identified that results in the release of the nucleic acids. We found such mechanism as related to cell death processes (i.e. necrosis) where the release of DNA to the extracellular matrix is usually observed. Additionally, the release of constituting ions of HAp (Ca^{2+} and PO_4^{3-}) is triggered by the cell death process as well. The combination of both should lead to a natural hydroxyolite in the breast cancer tissue. It is known that in the center of breast tumors are necrotized areas containing HAp microcalcifications, usually around the nest (see Figure 22).

Figure 22. Calcifications around the nest. Courtesy of ICFO and B. Braun Surgical.

Finally, we recall that patients under a screening diagnostic process through regular mammography may show both calcium oxalate (type I) and calcium phosphate (type II) microcalcifications. Currently, in spite of their radiological interest, mammograms cannot discriminate between type I and type II microcalcifications.[88] Furthermore, in order to overcome such a fact, calcifications are regularly assessed through specific biopsies using optical microscopy by using their optical properties (i.e. CaOx presents birefringence but HAp not) and the use of specific stains. However, radiologist and pathologist are unable to detect nucleic acids deposited on them using the traditional optical methodologies. Taking into consideration such challenge, we looked for available alternative techniques to detect the presence of hydroxyolites. We reviewed TEM microscope archive images (Figure 23). Under TEM microscope, calcifications give an opaque fingerprint easy to differentiate from the surrounding tissue. Nevertheless, if organic molecules would be adsorbed or encapsulated on them, they would be degraded by the high energy electron beam irradiating the samples, making impossible their molecular identification.

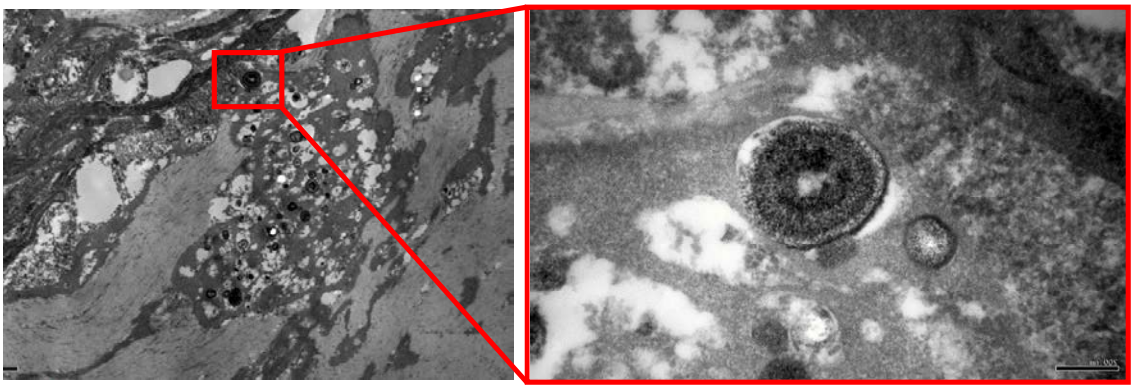

Figure 23. Papillary carcinoma of thyroids by TEM (left). Zoom of the red marked area showing a spherical structure similar to a hydroxyolite as a white area is in the center of the opaque calcified spheroid (right). Image courtesy of Dr. M. Fernández-Figueras.

TEM images obtained from several tumor tissue (Figure 24) showed circular or spherical structures, similar to the ones we obtained after *in vitro* synthesis of hydroxyolites. On the other hand, focusing on our field of interest, Figure 24 also shows calcifications in a TEM image of breast cancer tissue with circled blackened areas marked with red arrows that might indicate the presence of organic matter inside of some HAp calcifications.

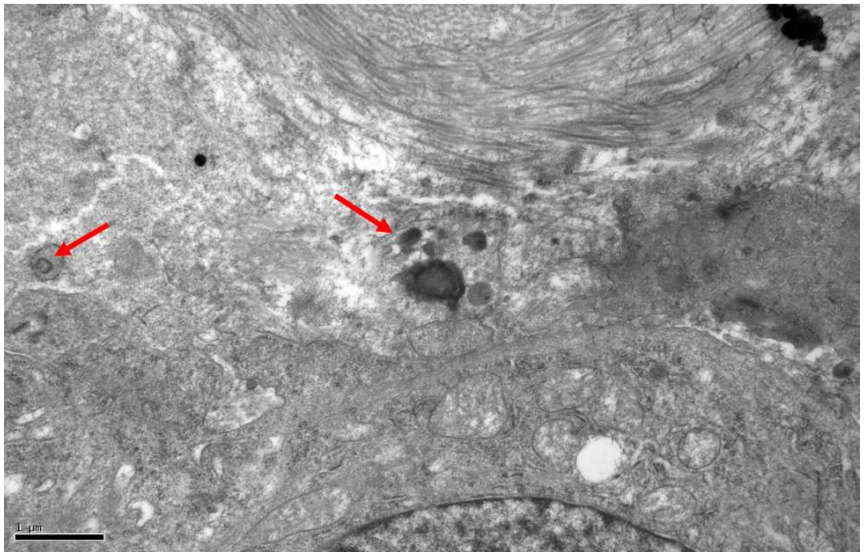

Figure 24. Red arrows highlight calcifications observed by TEM in a breast cancer tissue sample. Dark areas corresponds to high density substances (i.e. HAp). Image courtesy of Dr. M. Fernández-Figueras.

As a consequence, taking into account the theoretical considerations exposed in this section about the feasibility of hydroxyolite synthesis in living breast cancer tissue and considering the possibility that TEM images obtained from calcifications in breast tissue samples would correspond to hydroxyolites, we have investigated the existence of natural hydroxyolites in a breast tumor microenvironment. Furthermore, we consider a fifth result of our conceptual approach to identify the need of having available more specific and powerful techniques, as the ones we propose in this thesis (i.e. Raman spectroscopy and fluorescent labelling) to identify natural hydroxyolites in living tissue.

In the following sections, we expose the empirical results obtained after assessment with Raman spectroscopy to detect nucleic acids of fresh samples excised from breast cancer tumors (section 7.2). Furthermore, we explore the consequences of such discovery in terms of the potential role of hydroxyolite as a non-viral vector of transfection. Moreover, we study the feasibility of CaOx to behave as non-viral vector of transfection. We analyze and compare their transfection efficiency in several scenarios, including their capacity of migration in order to contribute to the understanding of the role of such particles in the context of breast cancer multifocality.

As a conclusion, our translational approach around the hydroxyolite concept resulted in emphasizing the importance to explore the existence of natural hydroxyolites and their potential role in a clinical scenario that we define breast tissue environment. The results of that research are detailed in the next sections.

7.2 CHARACTERIZATION OF HYDROXYOLITE CALCIFICATIONS BY RAMAN SPECTROSCOPY

In this section, we aim to characterize the microcalcifications obtained from breast cancer tissue samples in order to determine if hydroxyolites are naturally synthesized.

Firstly, we intend to collect a library of spectra related to a hydroxyolite in order to identify the bands that can be univocally related to the nucleic acids, hydroxyapatite (HAp) and their combinations depending on if they are adsorbed or encapsulated. Secondly, we analyze several related compounds to determine their specific Raman fingerprint. Such preliminary work is intended to allow us to identifying the most relevant bands of a hydroxyolite in a complex tissue environment where many other molecules might be present. Despite Raman spectroscopy is an extremely powerful technique to identify metabolites in a biological environment is still necessary to determine if some interferences coming from surrounding molecules and ions are affecting the interpretation of the spectra. For that reason, we have collected an extended Raman database of pure substances intended to be used as a framework for the interpretation of Raman spectra obtained from fresh tumor tissue. We have recorded spectra of nucleic acids (i.e. DNA and RNA), calcium phosphate minerals that might act as precursors of HAp or natural hydroxyolites and, from hydroxyolites synthesized *in vitro*. Additionally, we have recorded spectra of other relevant substances that might be present in the tumor tissue (i.e. sodium and calcium oxalate) or become adsorbed on naturally synthesized HAp or hydroxyolites (i.e. polyphosphates, amino acids or proteins) that might impede the correct interpretation of the spectrum, including some substituting ions (i.e. Mg^{2+} or CO_3^{2-}) of Ca^{2+} or PO_4^{3-} respectively, as dopants of HAp.

7.2.1 LIBRARY OF RAMAN SPECTRA

We compiled the Raman spectra of hydroxyolite related substances in order to build the database included in Annex 1. The list of compounds included in the database is the following:

a) Basic components of a hydroxyolite

- Hydroxyapatite [$Ca_{10}(PO_4)_6(OH)_2$]
- Deoxyribonucleic acid (DNA)

- Ribonucleic acid (RNA)

b) Precursors of HAp

- Amorphous calcium phosphate [$Ca_3(PO_4)_2 \cdot nH_2O$]
- Calcium hydrogenphosphate dihydrate. Brushite [$CaHPO_4 \cdot 2H_2O$]
- Sodium dihydrogen phosphate [NaH_2PO_4]
- Calcium pyrophosphate [$Ca_2P_2O_7$]
- Sodium triphosphate [$Na_5P_3O_{10}$]
- Sodium hexametaphosphate [$Na_6P_6O_{18}$]
- Sodium hexametaphosphate +200 mesh [$(NaPO_3)n$]
- Sodium polyphosphate (Graham's salt) [$(NaPO_3)n$ n=ca.25]
- Adenosine 5'-triphosphate magnesium salt [$C_{10}H_{16}N_5O_{13}P_3 \cdot xMg^{2+}$]

c) Effect of substituting ions

- Hydroxyapatite doped with Mg^{2+}

d) HAp with polyphosphates

- Hydroxyapatite with triphosphate
- Hydroxyapatite doped Mg^{2+} and adsorbed polyphosphates [$Ca_{1-x}Mg_x(PO_4)_6(OH)_2$]

d) Compounds related to type I breast cancer microcalcifications

- Calcium oxalate [CaC_2O_4]
- Calcium oxalate hydrate [$CaC_2O_4 \cdot H_2O$]
- Calcium oxalate dihydrate [$CaC_2O_4 \cdot 2H_2O$]
- Sodium oxalate [$Na_2C_2O_4$]
- Calcium carbonate [$CaCO_3$]

e) Other metabolites of interest

- L-Phenylalanine. $C_6H_5CH_2CH(NH_2)CO_2H$ [$C_9H_{11}NO_2$]
- Collagen

f) Hydroxyolites synthesized *in vitro*

- Hydroxyolite with DNA encapsulated
- Hydroxyolite with DNA adsorbed in (001) facet
- Hydroxyolite with DNA adsorbed in (010-Ca^{2+}) facet
- Hydroxyolite with DNA adsorbed in (010-OH^-) facet

Though the following subsections we highlight some relevant features of the Raman Spectra we use for the identification of hydroxyolites in tumor tissue.

7.2.1.1 RAMAN SPECTRUM OF HYDROXYAPATITE

The Raman spectrum of HAp shows the internal vibrational PO_4^{3-} modes. The vibrational frequencies used to identify HAp are related four vibrational modes of free PO_4^{3-} and OH^- ions (Table 10).

Table 10. HAp vibrational bands in Raman spectra.

Band modes for HAp		Wavenumbers, cm^{-1}	
		Literature[221]	Experimental
PO_4^{3-}	V_2	431, 447	431, 447
	V_4	579, 590, 607, 614	579, 591, 606, 615
	V_1	962	963
	V_3	1028, 1040 (shoulder), 1047, 1052 (shoulder), 1076	1025, 1034, 1044, 1050, 1075
OH^-	Translational mode	329	-
	Stretching mode	3573	3574

We find the most relevant of them at v_1 = 962.73 cm^{-1}, v_2 = 436.15 cm^{-1}, v_3 = 1045.86 cm^{-1}, and v_4 = 589.93 cm^{-1} and OH^- stretching mode at 3573.86 cm^{-1} (see Figure 25). Those frequencies correspond[221] to the symmetric P-O stretching mode, the doubly degenerate P-O stretching modes, the doubly degenerate asymmetric P-O stretching modes, and the triply degenerated modes of P-O stretching modes, respectively. Additionally, the stretching mode of hydroxyl ion (OH^-) expected at 3571 cm^{-1} is observed at 3573.86 cm^{-1} and its translational mode is found at 329 cm^{-1}. The vibrational bands of OH^- predicted by C_6 factor group

symmetry analysis at 630 cm^{-1} are not detected as it has been reported in the literature.[222] The vibrational mode v_1 at ~ 962 cm^{-1} is the most intense and most visible band in complex biological environments. Moreover, it can be expected a shift depending on the chemical surrounding conditions of PO_4^{3-} in HAp as it is caused by the presence of substituting ions in its lattice or adsorption of organic molecules.

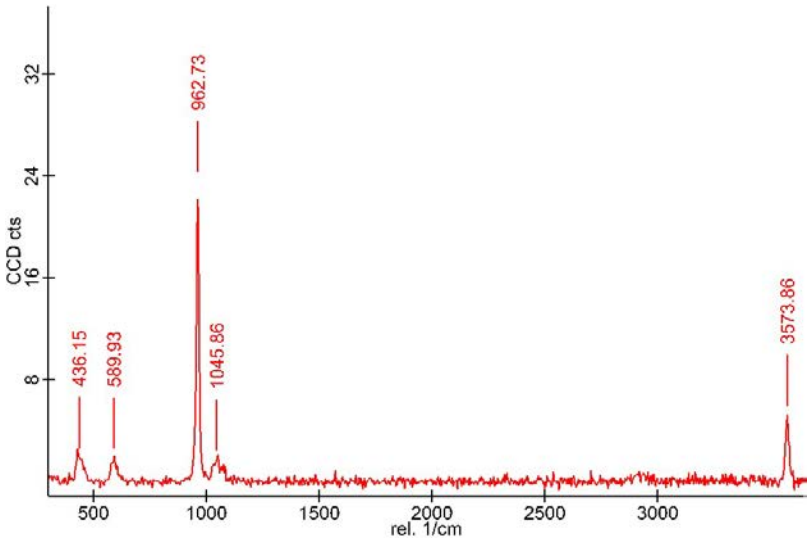

Figure 25. Raman spectra of hydroxyapatite (Sigma Aldrich, Ref. 04238).

7.2.1.2 DNA RAMAN SPECTRUM

In this subsection we highlight the main features of DNA Raman spectrum because through this thesis we put the focus on hydroxyolites made of HAp and DNA. We consider they are the most likely to be naturally synthesized as a result of cell death processes where significant amounts of DNA are released to the surrounding environment. Nevertheless, the RNA Raman spectra and its characteristic bands are shown in Annex 1. However, such spectra shows a higher fluorescence than the spectrum with DNA and the identification of the univocal bands is more complex. Thus, we focused our work on DNA. Henceforth, when we use hydroxyolite we mean hydroxyolites with DNA adsorbed or encapsulated.

Raman micro spectroscopic measurements were performed on calf thymus DNA (ct-DNA) samples. The normalized mean Raman spectrum of ct- DNA is shown in Figure 26.

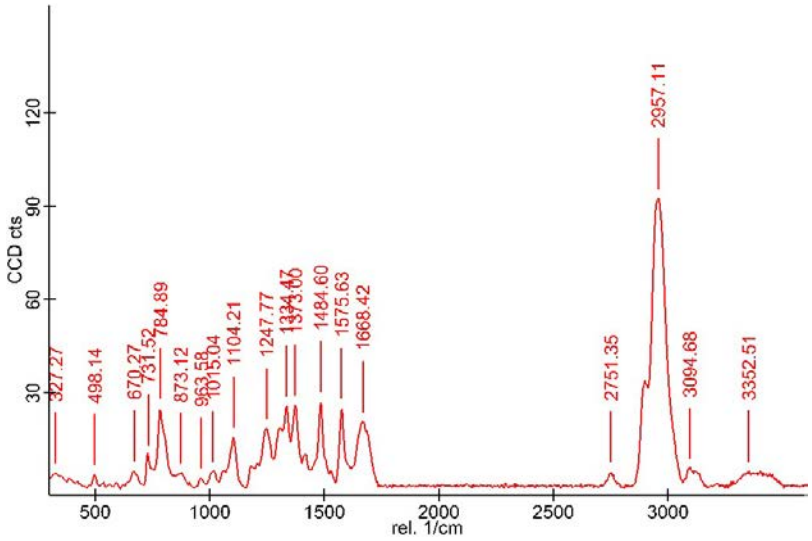

Figure 26. Raman spectra of ct-DNA: calf thymus (Sigma Aldrich, Ref. D1501).

According to literature,[124,223] the vibrations of purines (adenine (A), guanine (G)) and pyrimidines (cytosine (C), thymine (T)) nucleobases are characteristic of the Raman spectrum of DNA. All noticeable bands are marked in the figure and explicitly assigned to vibrational modes of DNA nucleobases as shown in Table 11.

Table 11. Experimental data from five spectra (n = 5) and assignments for vibrational bands of ct-DNA Raman spectrum, compared to assignments found in literature.

Assignment	ct-DNA (rel. 1 / cm)	
	Experimental (n=5)	Literature
Ring breathing - G-dRib	671	675
Ring breathing - A	732	726
Ring breathing - T	746	744
Ring breathing - C	**785**	**779**
ν(CO) – dRib-P	868	870
T, G, C, dRib	1015	1012
ν(CO5') – dRib	1064	1060
Vs(PO_2^-) - bk	1104	1096
G, T, C	1180	1177
Ring mode – C, T	1248	1243
Ring mode – A, C	1307	1300
ν(C2N3) – A, G	**1334**	**1334**
Ring mode δ_s (C5H3) – T, A, C	1372	1371
δ (2´CH2) – dRib	1416	1417
δ (5´CH2) – dRib	1450	1458
Ring mode N7 – G, A	1485	1484
ν(C4C3), ν(C5C4) – G, A	**1576**	**1574**
ν(C4=O) – T, G, C	1668	1665

The experimental data was based on five independent spectra and compared to data obtained from literature. All important peaks displayed in Figure 27 are corresponding to those described in literature. It is worth noting that the main characteristic peaks as: i) ring breathing – C (785 cm^{-1}), ii) ν(C2N3) – A, G (1334 cm^{-1}), and, iii) ν(C4C3), ν(C5C4) – G, A (1575 cm^{-1}) were taken as a reference to identify DNA content interacting with HAp when recording Raman spectra in complex environments as tissue samples.

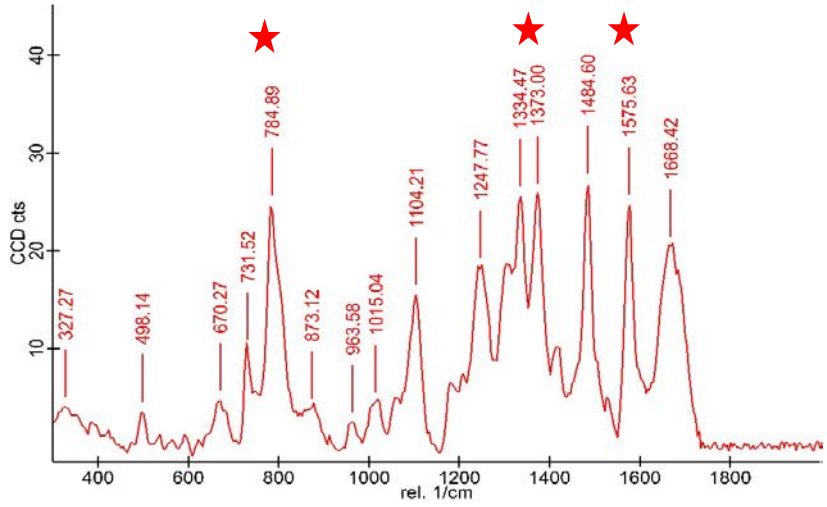

Figure 27. Area of interest of Raman spectra of ct-DNA: calf thymus (Sigma Aldrich, Ref. D1501). DNA specific bands marked with stars in red.

7.2.1.3 RAMAN SPECTRUM OF HYDROXYOLITES SYNTHESIZED *IN VITRO*

DNA intended to be part of the hydroxyolites synthesized *in vitro* was extracted from 4T1-luc2 cells, a luciferase expressing adenocarcinoma cell line derived from mouse mammary gland. They were harvested *in vitro* in T-75 flasks and purified using the magnetic beads DNA isolation system at BioBanc (IGTP-HUGTiP). Concentration, purity and DNA integrity number (DIN) of nucleic acid was determined. The total amount of DNA present in the samples are detailed on Table 12.

Table 12. Example for the data obtained from the DNA isolation system.

#	Volume (µL)	260/280	260/230	ng/µL	ng	µg
DNA 1	1350	2.007	2.154	734.805	991986.8	**992**
	1350	1.994	2.145	735.701	993196.4	**993**
DNA 2	1270	2.013	2.177	1275.952	1620459	**1620**
	1270	2.014	2.179	1281.149	1627059	**1627**

Nucleic acids and proteins have an absorbance maxima at 260 and 280 nm, respectively. The ratio of absorbance at 260 and 280 nm have been used to assess the purity of DNA. A ratio of

A_{260} / A_{280} ≥ 1.8 is generally considered as an acceptable level of DNA purity. If the ratio is appreciably lower, in either case, it may indicate the presence of protein, phenol or other contaminants that absorb strongly at or near 280 nm. The ratios observed in Table 12 show an acceptable A_{260}/A_{280} ratio as they are within 1.994 and 2.014. Moreover, DNA integrity number (DIN) was determined to demonstrate the genomic DNA (gDNA) quality. The DIN was calculated by the Genomic Service of IGTP with the Bioanalyzer TapeStation 2200 (Agilent Technologies Inc.) automated platform from the electrophoretic trace. The ranges from 1 to 10 indicate degradation of gDNA, typically from a gradual process in which high-molecular weight DNA could be fragmented into smaller species. The results obtained are detailed on Figure 28, which DIN were determined as 8.2 and 9.2 in the samples. Obtaining larger quantity of DNA were accomplished through the magnetic beads DNA isolation system at BioBanc (IGTP-HUGTiP).

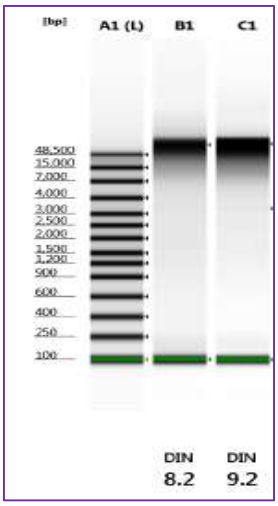

Figure 28. Example of the raw data from DIN measurement; where A1: ladder, B1: DNA1 and C1: DNA2.

The synthesis of hydroxyolites was performed according to the method described by Bertran et al. (2014).[115] A Transmission Electronic Microscopy (TEM) image of a group of hydroxyolites (HAp-DNA) synthesized *in vitro* is shown in Figure 29 (left). We note the opaque capsules made of HAp that surrounds organic matter (light grey). Conversely, HAp particles are shown as dark spheres under the microscope, meaning that HAp blocks the electron beam impeding them to reach the detector.

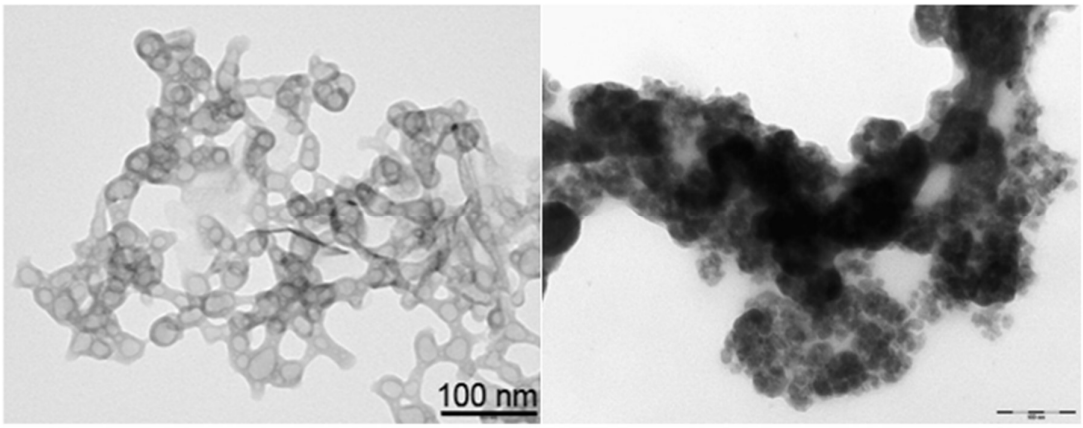

Figure 29. TEM image of hydroxyolites synthetized in the laboratory (left) and hydroxyapatite (right) Image courtesy of B. Braun Surgical and UPC.

On the other hand, FTIR spectra of HAp and hydroxyolites samples were compared in to highlight that DNA is incorporated to the mineral. All spectra in Figure 30 show typical PO_4^{3-} bands at the region comprised within 950 and 1200 cm^{-1}, the characteristic IR vibrational modes of PO_4^{3-} at v_1 = 962 cm^{-1} and v_3 = 1014 and 1089 cm^{-1} of HAp. Moreover, we note that FTIR spectrum of both batches of *in vitro* hydroxyolite samples show at 1632 cm^{-1} a band assigned to Amide I groups belonging to the encapsulated DNA.[224] The band at around 1416 cm^{-1} corresponds to the partial substitution of phosphate PO_4^{3-} by carbonate (CO_3^{2-}) of the HAp, showing that in such mineralization process, even *in vitro*, carbonate only derived from the presence of CO_2 in the reaction atmosphere is an expected ion to be considered in the system when hydroxyolites are naturally synthesized.

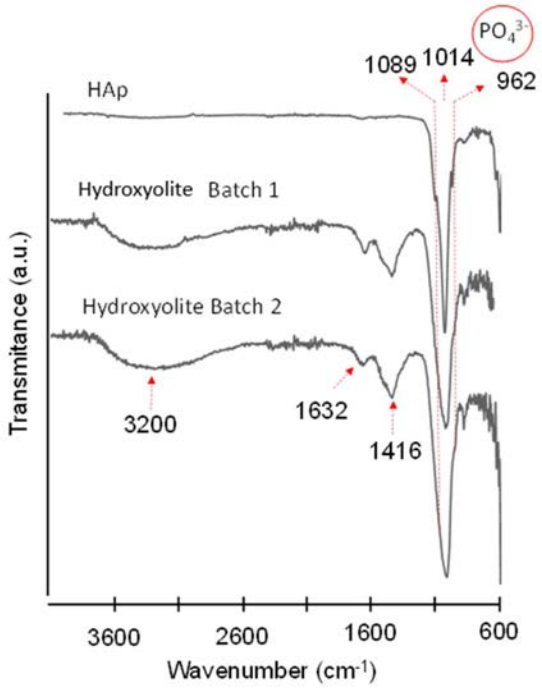

Figure 30. FTIR spectra of HAp and two different batches of hydroxyolites (HOLi) made of HAp and DNA synthesized *in vitro*. Courtesy of B. Braun Surgical and UPC.

Raman spectra were collected in order to characterize the main features of a hydroxyolite (Figure 31) with DNA encapsulated in low quantities (294 µg/ 30 mg HAp). We observe that the main band of HAp is clearly visible at 959.10 cm^{-1} and the most intense bands related to DNA are displayed within the range 2900-3100 cm^{-1}. However, the selected bands of DNA for its identification in more complex environment (i.e. 785 cm^{-1}, 1372 cm^{-1} and 1575 cm^{-1}) are difficult to be observed because they are much less intense and the concentration of DNA inside the hydroxyolite is quite low. We note that such sensitivity would not be useful when looking for hydroxyolites in a physiological environment due to the interference of many other metabolites in that region.

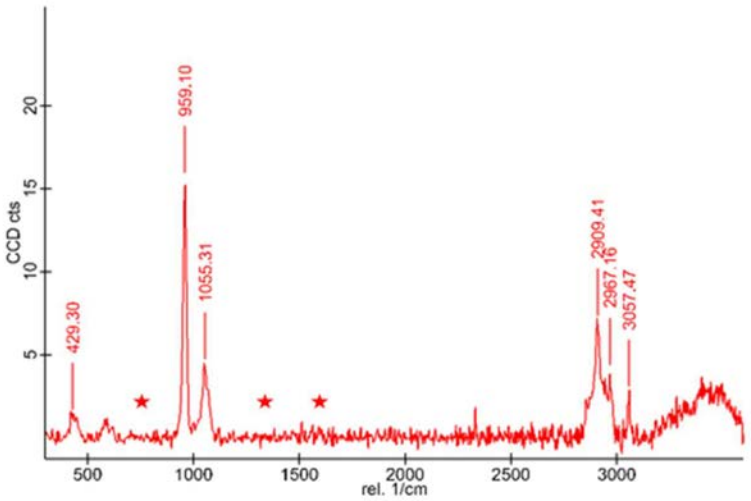

Figure 31. Raman spectrum of a hydroxyolite containing DNA encapsulated synthesized *in vitro*. DNA specific bands marked with stars in red.

With the objective to determine if the presence of some ions as Mg^{2+} or other molecules as carbonates or polyphosphates, that could be precursors of HAp, might influence the identification of HAp or DNA bands, we recorded the Raman spectra of hydroxyolites synthesized *in vitro* (encapsulated) containing DNA, Mg^{2+} and polyphosphates as they individual ones. As shown in Figure 32, Mg^{2+} incorporated (1.5 %) is not affecting the pattern of the Raman spectrum.

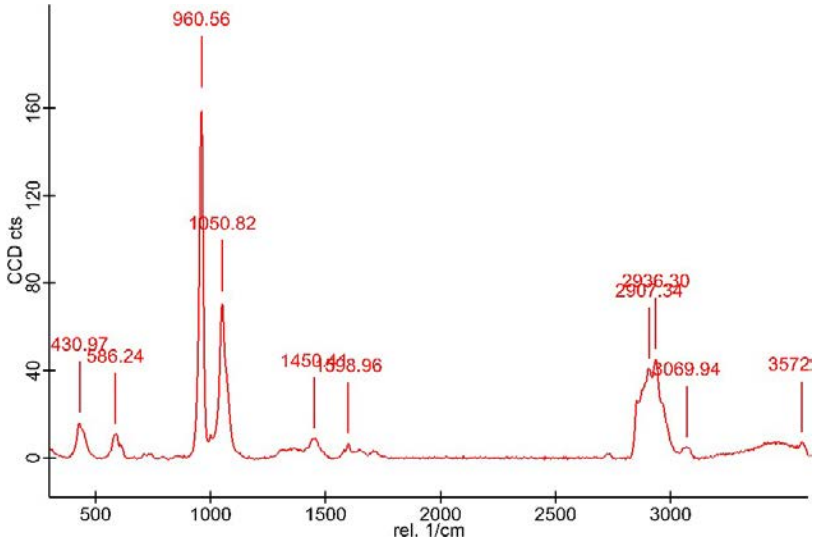

Figure 32. Raman spectra of HOLi + Mg^{2+}.

The identification bands are located in the same position (± 2 cm^{-1}) that is not considered a relevant shift in this context. This fact is confirmed when polyphosphate (PolyP) was added (0.2 M) to the hydroxyolite containing Mg^{2+}. Figure 33 displays the area of interest of such a modified hydroxyolite.

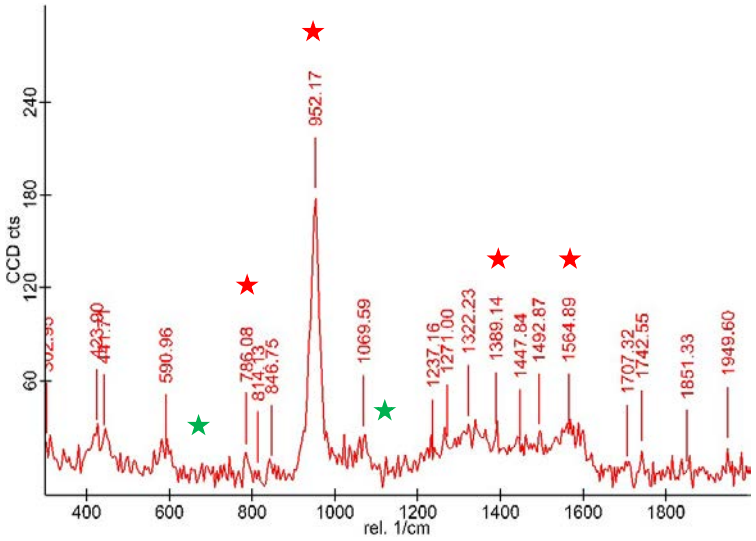

Figure 33. Raman spectra of HOLi + Mg^{2+} + PolyP. DNA specific bands marked with stars in red. PolyP specific bands marked with stars in green.

The main bands of PolyP (684, 162.98 and 1268.92 cm^{-1}) and v1 CO_3^{2-}mode at 1070 cm^{-1} and the carbonate v4 bands at 715 and 689 cm^{-1} assigned to B-type carbonated apatite are not expected to interfere.

Figure 34 shows the Raman microscopic mapping of a hydroxyolite *in vitro* synthesized containing Mg^{2+} and PolyP. Raman images were generated during data acquisition by integrating over the P-O stretching band (962 cm^{-1}) from HAp, and the main characteristic peaks of DNA (785, 1372 and 1575 cm^{-1}).

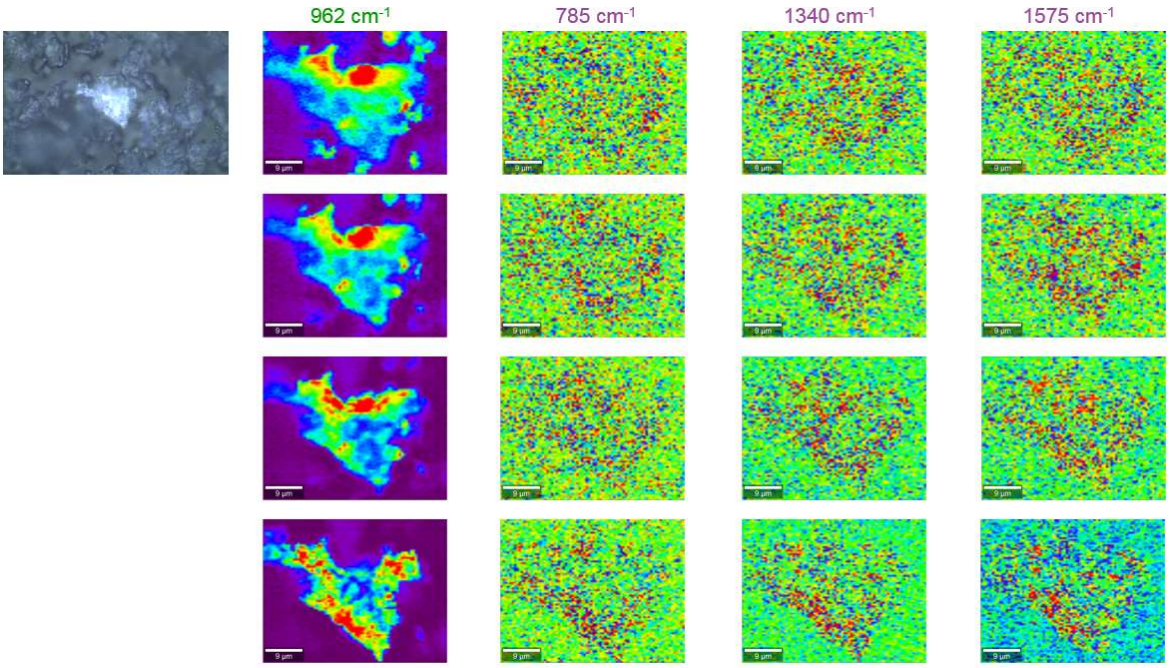

Figure 34. Raman image-stacking in z of HOli+Mg^{2+}+PolyP, where the data acquisition was performed by integrating over HAp: 962 cm^{-1} and DNA: 785, 1340 and 1575 cm^{-1}, and red signal indicates more intensity for each integrating peak. Experimental parameters: 45 x 35 µm with 80 points and lines per image (Scale bar = 9 µm).

As Figure 34 shows the area occupied by HAp is clearly identified by its 962 cm^{-1} showing areas of the hydroxyolite that HAp absorption is intense. Each row of maps in the Figure is separated by 2 µm and shows that DNA and HAp are overlapped and distributed all over the particle. Some areas show of more concentration of DNA or HAp depending on the depth of the scan demonstrating that DNA is encapsulated in HAp. Then, we conclude that Raman spectroscopy is a suitable technique for the study of hydroxyolites *in vitro*, however if the amount of DNA encapsulated in HAp is low, specific DNA bands in Raman spectrum can be too weak to be easily detected and more powerful algorithms to deconvolute the signals might be necessary or the use of more selective techniques (i.e. selective fluorescent probes for HAp and DNA) might be necessary.

7.2.2 HYDROXYOLITES IN BREAST CANCER TISSUE SECTIONS

7.2.2.1 RAMAN SPECTROSCOPIC *EX VIVO* STUDIES IN BREAST CANCER TISSUE SECTIONS

In this section are shown the main results in characterization of hydroxyolite calcifications by Raman spectroscopy of the work written by:

> M. Marro, A. M. Rodríguez-Rivero, C. Araujo-Andrade, M.T. Fernández-Figueras, L. Pérez-Roca, E. Castellà, J. Navinés, A. Mariscal, J.F. Julián, P. Turon & P. Loza-Alvarez. Unravelling the encapsulation of DNA and other biomolecules in HAp microcalcifications of human breast cancer tissues by Raman imaging. *Cancers.* 2021; *13*(11): 2658. https://doi.org/10.3390/cancers13112658 (Creative Common CC BY license). See ANNEX 3.

As we concluded in the previous section, Raman spectroscopy is an appropriate technique to study microcalcifications in breast tissue, as it provides a univocal chemical identification of those calcium related compounds as calcium oxalate (CaOx) and hydroxyapatite (HAp), and hydroxyolites *in vitro* but it remains a challenge to determine if natural hydroxyolites can be identified among breast tissue microcalcifications.

In this section, we report the results of Raman spectroscopic studies we performed with the objective to identify the molecular composition of different breast microcalcifications observed in tumor tissue samples, particularly with the objective to identify the natural hydroxyolites containing nucleic acids adsorbed or encapsulated in HAp. For that reason, we focus our studies first on identifying the type of calcification (i.e. calcium oxalate, calcium carbonate or calcium phosphate) and in a second stage, and using more precise techniques we intend to confirm if DNA is naturally deposited on HAp surface or if it is trapped in its inner part. For that reason, we looked for more sensitivity using specifically developed algorithms developed by The Institute of Photonics in Catalonia (ICFO).

All studies involving human tissue samples were approved HUGTiP Ethics Committee. Fresh tissue samples used in these studies were obtained from patients following surgical procedures (HUGTiP). After removal, the samples were sectioned, frozen and stored at -85 ºC until examination without any further treatment to preserve them to minimize this risk of damaging the hydroxyolites. The extracted pieces were spatially oriented and sent to the Radiology Department (HUGTiP), where an X-ray assay was performed to confirm the

inclusion of the neoplasia and calcifications of the piece. An expert pathologist from Pathological Anatomy Department (HUGTiP) determined the part of the tumor that was assigned for the hydroxyolite detection study. Those samples were embedded in OCT compound and frozen in isopentane using a Bright Clini-RF freezer before 30 minutes after extraction. The specimens were cut into sections from 5 µm using a microtome and mounted on quartz slides to reduce background signals in Raman spectroscopy. Moreover, the fixed tissue samples were also stained with H&E (Figure 35).

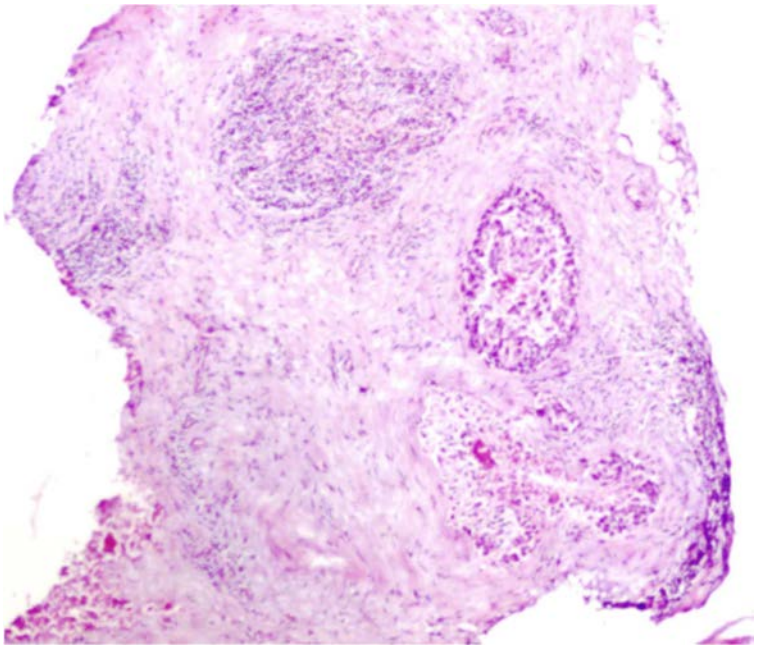

Figure 35. Calcification in an H&E stained section from a non-infiltrating intraductal carcinoma sample (carcinoma in situ).

In a representative sample, we selected the area of calcifications around the nest up to 2,000 µm. We analyzed the composition of the calcifications to confirm the suitability of the approach regarding the tissue samples to be assessed (Figure 36).

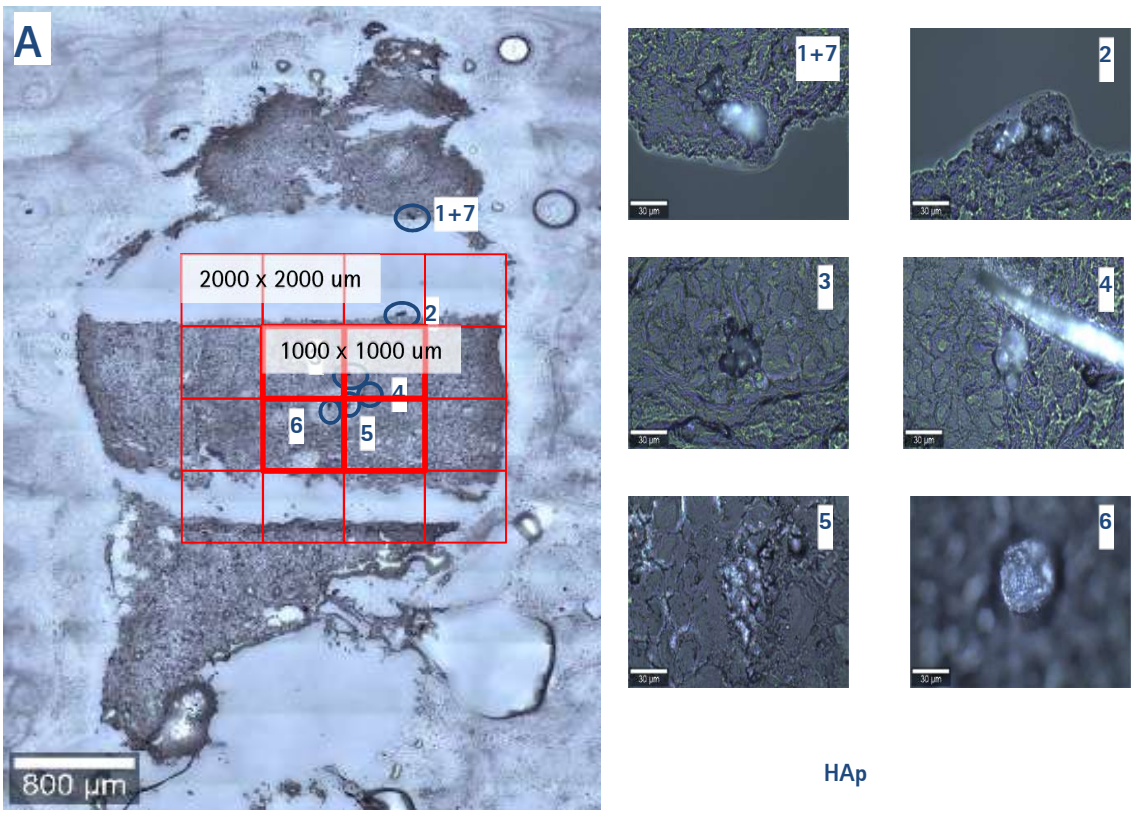

Figure 36. Hydroxyapatites found in specimen with ductal carcinoma in situ up to 2,000 µm from the central point of the nest of calcifications.

Calcifications from n=1 to n=6 were identified as mainly based of HAp (959.60 cm^{-1}). The presence of other bands not corresponding to HAp is easily observed. However, DNA or RNA bands previously selected by us (785 cm^{-1}, 1340 cm^{-1} and 1575 cm^{-1}) were not well defined, only the band at 1664.66 cm^{-1} matched the 1662.22 cm^{-1} assigned to DNA v(C4=O)-T,G,C in the literature. We recorded a map at 1340 cm^{-1} but the presence of DNA on the HAp calcification cannot be totally stated.

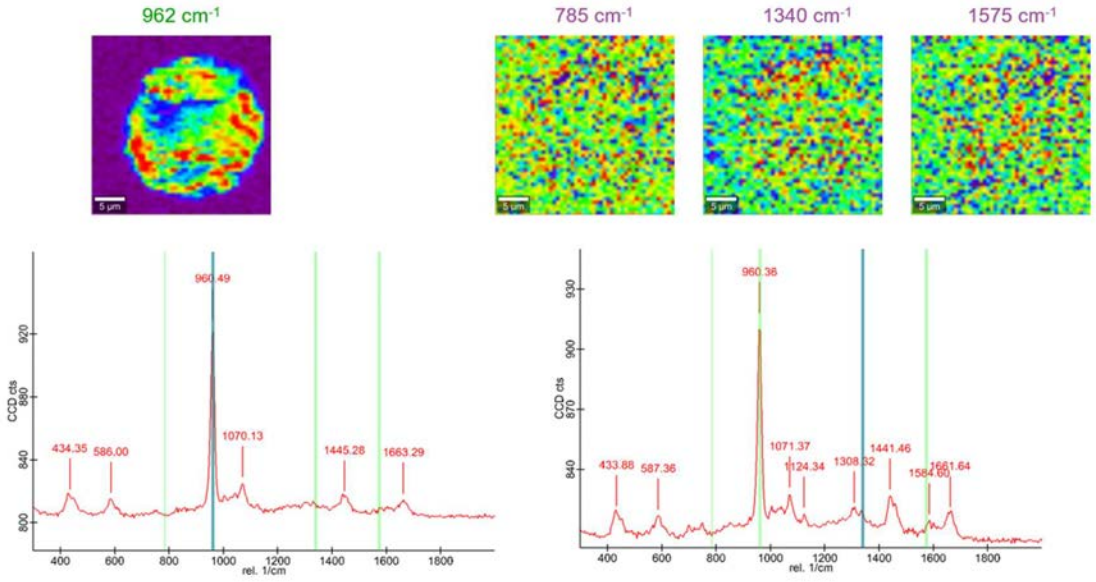

Figure 37. Raman images where the data acquisition was performed by integrating over 962 cm^{-1} (HAp) and 785, 1340 and 1575 cm^{-1} (DNA) in specimen calcification nº 6. Red signal indicates more intensity for each integrating peak. Experimental parameters: 30 x 30 µm with 50 points and lines per image (Scale bar = 5 µm).

Furthermore, we concluded that we needed a refinement of the Raman technique in order to confirm the presence of nucleic acids that was achieved by the application of more advanced algorithms to deconvolve the recorded signal. Such algorithm was developed by ICFO, thanks to the contributions of Dr. Mónica Marro, Dr. Cuauhtémoc Araujo-Andrade and Dr. Pablo Loza from ICFO under to cooperation framework with B. Braun Surgical. Using a Multivariate Curve Resolution (MCR) approach was possible to extract molecular components existing in the calcifications and its spatial distribution. Then, the molecular components obtained by MCR with the Raman database collected from HAp-DNA synthesized *in vitro* and the Raman images in different optical sections (in x, y, z) are able to elucidate if HAp calcifications from malignant lesions contain DNA.

Figure 38 shows a representative sample and their histological slides with the corresponding H&E stained sections and the slides used to perform Raman analysis.

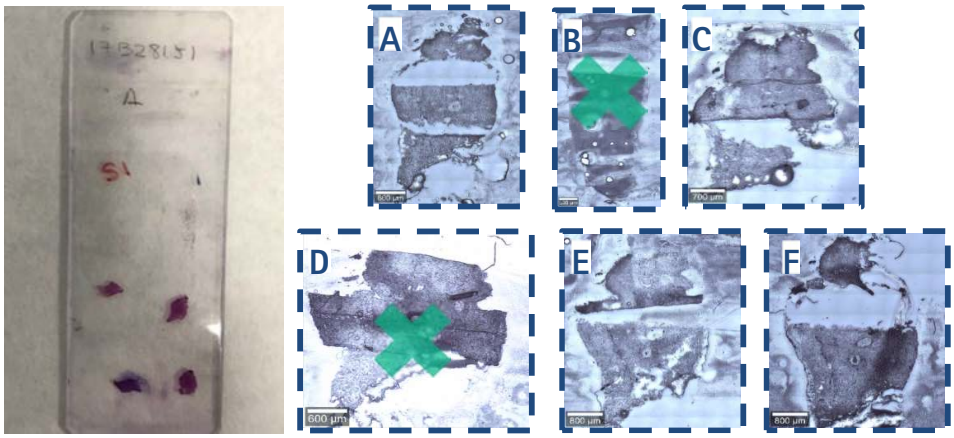

Figure 38. Histological slides from a specimen with ductal carcinoma in situ. B, D did not contain calcifications.

Tissue sections (n= 26 patients) from freshly excised human breast biopsies were examined by the pathologists. After their assessment, samples were diagnosed as infiltrating ductal (n=23) and lobular carcinomas (n=3) and included in the Raman study (Table 13).

Table 13. Summary of main features of tissue calcifications found from breast cancer patients included in the study.

Patient	Diagnosis	CaOx	HAp	DNA	Size[a]	Shape[b]	Localization[c]
1	Infiltrating ductal carcinoma	No	Yes	Yes	m, D= 20 µm	S	t
2	Infiltrating ductal carcinoma	No	Yes	Yes	m, D= 20 µm	R	t
3	Infiltrating ductal carcinoma	No	Yes	No	m, D= 10 µm	S	t
		No	Yes	Yes	m	R	t
4	Infiltrating ductal carcinoma	No	Yes	Yes	m, D= 20 µm	R	d
5	Infiltrating ductal carcinoma	No	Yes	Yes	m, D= 20 µm	S	t
	Infiltrating ductal carcinoma	No	Yes	Yes	m, 30 x 20 µm	R	t
6	Infiltrating ductal carcinoma	No	No	No	-	-	-
7	Infiltrating ductal carcinoma	No	Yes	Yes	m, D= 10 µm	R	t
8	Infiltrating ductal carcinoma	No	No	No	-	-	-
9	Infiltrating ductal carcinoma	No	Yes	Yes	m, 25 x 15 µm	R	t

Patient	Diagnosis	CaOx	HAp	DNA	Size[a]	Shape[b]	Localization[c]
		No	Yes	Yes	m, 20 µm	S	t
10	Infiltrating ductal carcinoma, multifocal	No	Yes	Yes	m, 30 µm	R	t
11	Infiltrating ductal carcinoma	No	Yes	Yes	m	R	t
12	Infiltrating ductal carcinoma	No	No	-	-	-	-
13	Infiltrating ductal carcinoma	No	Yes	No	b	R	t
14	Infiltrating ductal carcinoma	No	Yes	Yes (nc)	S	R	t
15	Infiltrating ductal carcinoma	No	Yes	Yes	b	R	t
16	Infiltrating ductal carcinoma	No	Yes	Yes	m, 100 µm	R	d
17	Infiltrating ductal carcinoma	No	Yes	Yes	m, 40 x 50 µm	R	t
18	Infiltrating ductal carcinoma	No	Yes	Yes	s, D=7 µm	S	t
19	Infiltrating ductal carcinoma	No	Yes	Yes	m	R	t
20	Infiltrating ductal carcinoma	No	Yes	Yes	m	R	d
21	Infiltrating ductal carcinoma	No	Yes	Yes	m	R	d
22	Infiltrating ductal carcinoma	No	Yes	Yes	m, 20 x 10 µm	R	t
23	Infiltrating ductal carcinoma	No	Yes	Yes	b	R	t
24	Infiltrating lobular carcinoma	No	Yes	Yes	m, D= 20 µm	R	t
25	Infiltrating lobular carcinoma	Yes	No	No	s	S	t
		No	Yes	Yes	m	R	t
26	Infiltrating lobular carcinoma	No	Yes	Yes	m	R	t

[a] Size: small, s (<10 µm); medium, m (10 µm < m < 100 µm); big, b (> 100 µm). [b] Shape: rock, R; sphere, S; needle, N. [c] Localization: duct, d; tissue, t.

Type II microcalcifications were found in 23 of 26 patients. Only one sample out of 26 patients presented type I calcifications. Calcifications were not found in 3 patients. A high percentage

of calcifications analyzed were identified as HAp. We highlight that most of them contained DNA (92.3 %) including both diagnostics, most of them diagnosed as infiltrating ductal carcinoma (91.3 % out of 23 patients) and infiltrating lobular carcinoma (100 % out of 3 patients). Such finding is aligned with this thesis main hypothesis that calcifications containing nucleic acids (hydroxyolites) are naturally formed. Additionally, ten Raman images were obtained from these CaOx calcifications and no traces of DNA were identified in them. Regarding the morphology, rocky aspect (21 out of 27) is more frequent than spheres (6 out of 27) and no needle shaped calcifications were observed. In regards of the size, most of the particles where classified as medium size (10 μm < m < 100 μm) and they were mainly located in the tissue. Nevertheless, 4 of them were located in the duct.

HAp calcifications found in tissue samples of the patients included in the Raman study were analyzed using and advanced algorithm specifically developed for that purpose by ICFO researchers. A representative sample, Figure 39 shows the microcalcification image obtained with Bright-field microscope. In Figure 40 is represented how the MCR algorithm decompose the spectral signal in three main components (i.e. HAp, DNA and others), making more precise the identifications of the chemical components of the calcification. Figure 41 shows the Raman spectra in z-axis.

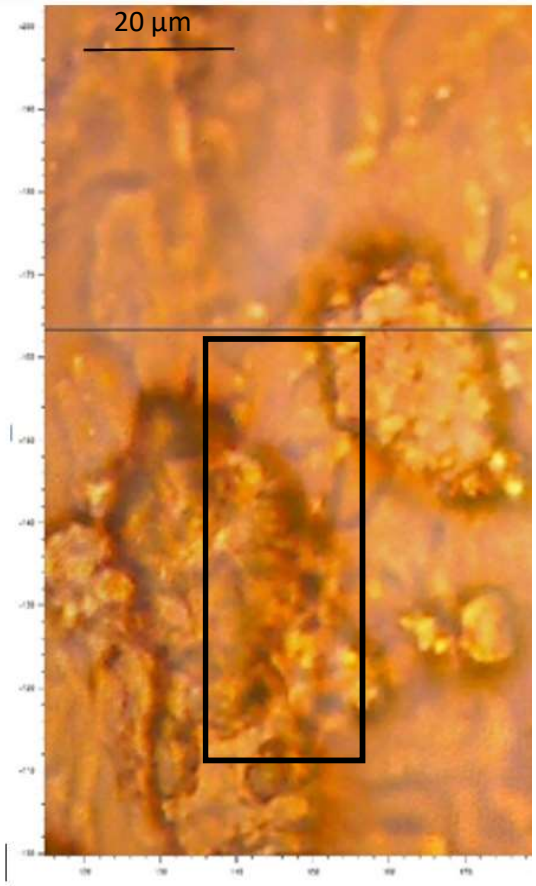

Figure 39. Bright-field image of the analyzed calcification. Courtesy of ICFO and B. Braun Surgical.

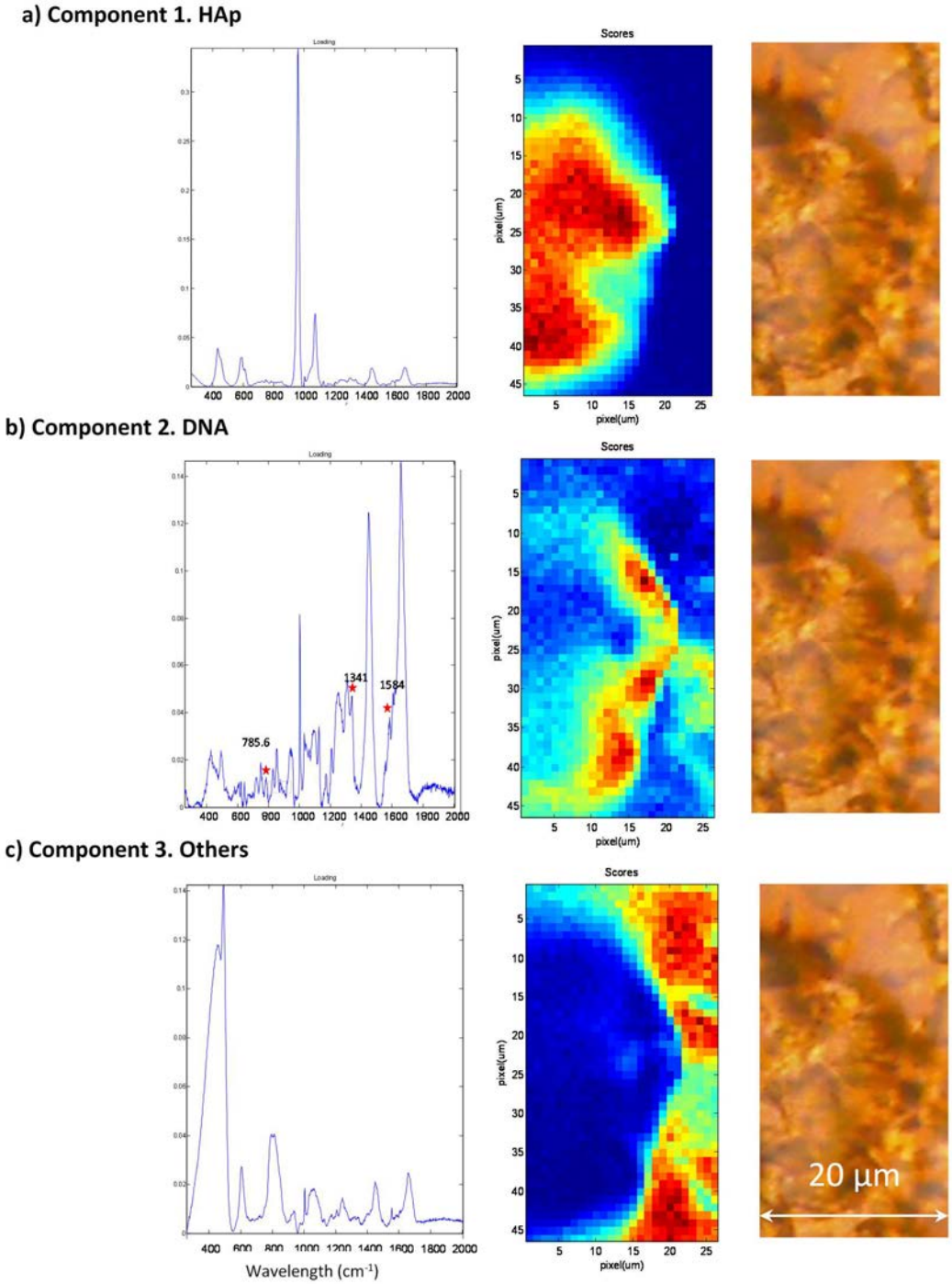

Figure 40. Raman spectral images showed the presence of DNA in HAp tissue calcifications. By using MCR algorithm, several molecular components (such as HAp, DNA and other molecules) were deconvolved (left) from the Raman spectra as well as their corresponding abundance maps for each component (center). Bright-field image of the analyzed calcification (right). The assignment of bands for HAp and DNA were performed based in our constructed database and literature (Scale bar = 20 µm). Courtesy of ICFO and B. Braun Surgical.

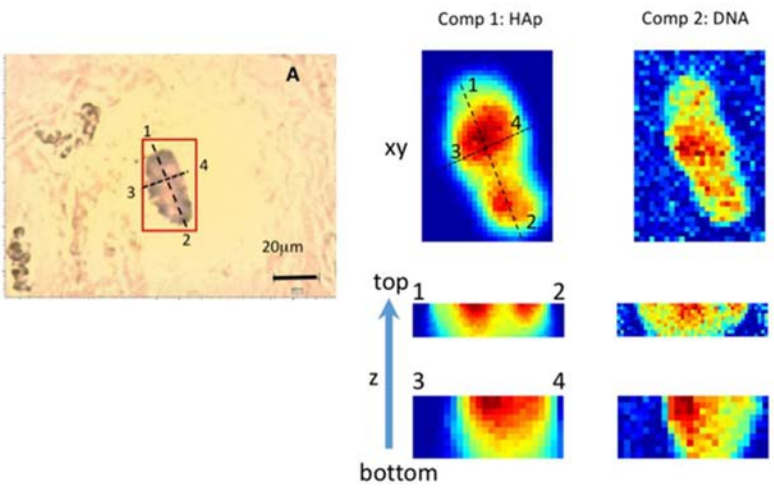

Figure 41. Hydroxyolite by encapsulation found in breast cancer tissue. Bright-field image of a HAp calcification (left). Raman map of HAp and DNA components (right) in y, z-axes using MCR algorithm. Courtesy of ICFO and B. Braun Surgical.

7.3 COMPARISON OF CALCIUM OXALATE AND HYDROXYAPATITE FEASIBILITY TO ADSORB AND ENCAPSULATE NUCLEIC ACIDS

In this section are summarized the main results of the work published by:

> Reprinted with permission from Revilla-Lopez, G., Rodríguez-Rivero, A. M., del Valle, L. J., Puiggali, J., Turon, P., & Alemán, C. Biominerals Formed by DNA and Calcium Oxalate or Hydroxyapatite: A Comparative Study. *Langmuir.* 2019*; 35* (36): 11912-11922 (see ANNEX 3). Copyright (2019) American Chemical Society. https://doi.org/10.1021/acs.langmuir.9b01566

We have used a synergistic approach to compare DNA mineralization in hydroxyapatite (HAp) and calcium oxalate (CaOx). Particularly, the capacity of DNA to interact with HAp and CaOx has been examined theoretically and experimentally. Molecular Dynamics (MD) simulations have been carried out in order to analyze: the adsorption of DNA onto the most stable facet of HAp and CaOx, the growing of HAp and CaOx minerals around the DNA template (i.e. the nucleating effect of DNA), and the stability of biominerals formed by DNA encapsulated inside nanopores of HAp or CaOx. Finally, Quantum Mechanical (QM) calculations have been conducted to provide a comprehensive chemical explanation of the results derived from both MD simulations and UV-vis spectroscopy, which are fully consistent. It is worth mentioning that special attention has been given to the discussion of the biominerals involving CaOx, which have been much less studied than those that contain HAp, and to the role of Mg^{2+}.

7.3.1 ADSORPTION OF DNA ON THE MINERAL SURFACES

MD simulations were focused on the adsorption of two DNA dodecamers on the surface of the HAp and monohydrated CaOx minerals. The first dodecamer was selected from the gene RASSF1A (5'-CG4GTCG5CCG6TCG7-3'), henceforth R1A, and the second is the Dickerson dodecamer (5'-CGCGAATTCGCG-3'). We focused on the interaction formed when such dodecamers are adsorbed onto the most stable facet of HAp[225] and monohydrated CaOx,[226] which is the (001) and (100), respectively. Almora-Barrios et al.[227] reported that the calculated surface energies of the (001) and the average (010) surfaces are 1.01 and 1.32 J/m, respectively, indicating that the former is more stable than the latter, in agreement with

previous literature.[228,229] Indeed, the less stable (010) surface, which was proposed to be much less populated than the (100), quickly accumulating more material that grow out of the crystal morphology because of the reactivity associated to such instability. Besides, the (100) was identified by atomic force microscopy experiments not only as the most populated facet of CaOx[230,231] but also as the surface that forms the strongest interactions with carboxylate and amidinium groups, which are abundantly present in biomolecules, including DNA.

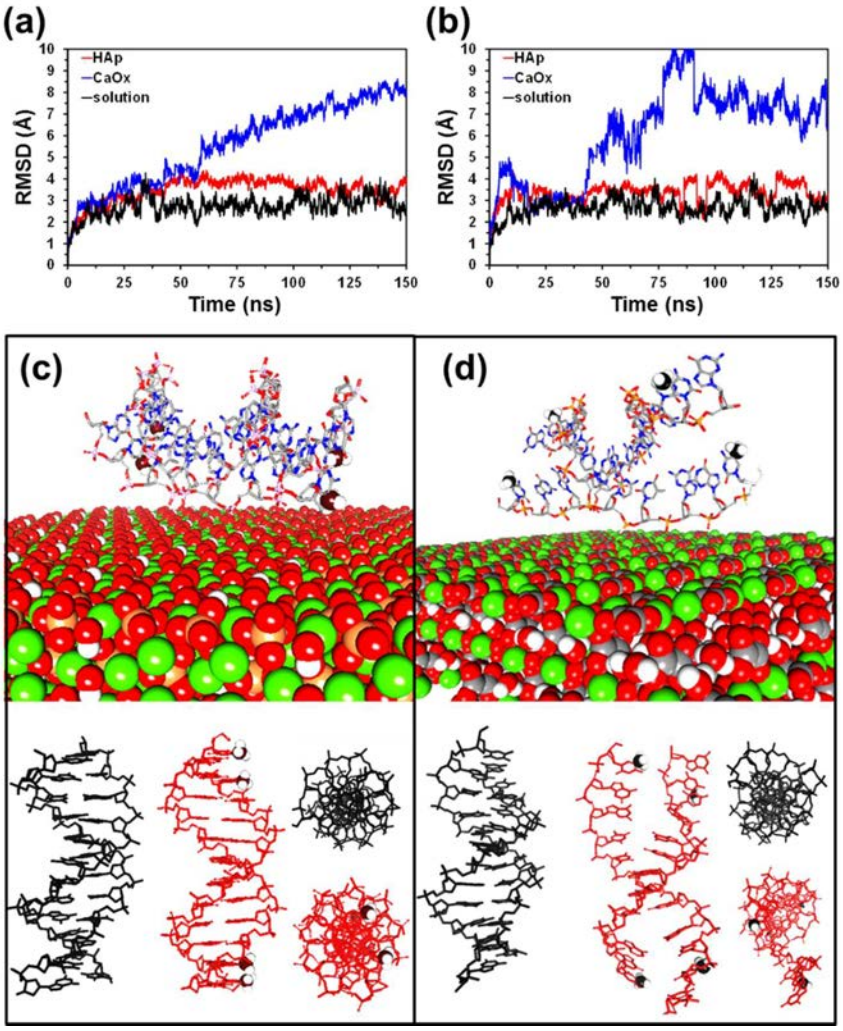

Figure 42. Comparison of DNA adsorption on HAp and monohydrated CaOx. Temporal evolution of the RMSD with respect to the canonical B-DNA double helix for (a) R1A (5'-CG4GTCG5CCG6TCG7-3') and (b) DD (5'-CGCGAATTCGCG-3') adsorbed onto the (001) HAp and (100) CaOx facets. The RMSD obtained for the DNA in aqueous solution has been included for comparison. Axial view of the R1A dodecamer adsorbed onto (c) the (001) surface of HAp and (d) the (100) surface of monohydrated CaOx. Oversized black balls highlight the position of carbon of methyl groups in the methylated DNA. For each system, the axial and equatorial views of the canonical double helix (in black) and the R1A double helix adsorbed onto the HAp or CaOx surface (in red) are compared at the bottom.

Although the methylated and non-methylated sequences showed a similar behavior when interacting separately with HAp or monohydrated CaOx, simulations demonstrated that the structural stability of DNA is totally different when interacting with each mineral. The stability of the adsorbed sequences was evaluated by examining the temporal evolution of the root mean square deviation (RMSD), which was calculated comparing each atom position of the B-DNA canonical double helix with the dodecamer structures recorded from MD trajectories. As shown below, the RMSD converged for all systems preserving the B-DNA structure, whereas the RMSD was high enough to guarantee complete de-structuration for all systems in which the double helix is lost. However, in the latter cases convergence of the RMSD was not considered a requisite since the dynamics and structure of unfolded B-DNA is out of the scope of this work. Figure 42a and 36b, which include the results obtained in aqueous solution (control), compare the RMSDs obtained for R1A and DD, respectively. The average RMSD obtained for R1A and DD adsorbed onto the (001) HAp (3.5 ± 0.6 Å and 3.4 ± 0.4 Å, respectively) is close to that obtained for the same sequence in aqueous solution (2.7 ± 0.5 Å and 2.7 ± 0.4 Å, respectively), evidencing that the B-DNA double helix remains stable when adsorbed onto HAp.

In contrast, the average RMSD increases progressively for the R1A and DD sequences adsorbed on the (100) facet of monohydrated CaOx, reaching in both cases to values higher than 8 Å after 150 ns. Thus, the CaOx surface causes a drastic destabilization of the adsorbed double helix due to the electrostatic repulsions between the oxalate ion (Ox^{2-}) and polyphosphate DNA backbone, which are directly confronted. The effect of Ox^{2-} ···polyphosphate repulsive interactions in the double helix is illustrated in Figure 42d for R1A and DD. As it can be seen, electrostatic repulsions tend to deploy the DNA double helix, separating the two strands. This destabilizing effect is not offset by the water molecules of the internal monohydration layer, which practically does not interact with the superficial DNA.

7.3.2 NUCLEATION OF DNA TEMPLATED BIOMINERALS

The behavior of R1A in an ionic solution to assess the feasibility of DNA to nucleate CaOx and/or HAp biominerals and act as a template was modelled using solution-like systems containing Ox^{2-} or PO_4^{3-} ions together with the DNA dodecamer, Ca^{2+} and Mg^{2+}. Figure 43a shows the radial distribution functions (RDFs) derived from the simulation with Ox^{2-} for the following pairs: Mg^{2+}–DNAp (where DNAp refers to the center of masses of the phosphate groups from the DNA backbone), Ca^{2+}–DNAp, Mg^{2+}–Ox^{2-} (where Ox^{2-} refers to the center of masses of Ox^{2-} anions), Ca^{2+}–Ox^{2-} and DNAp–Ox^{2-}. For a given pair, α–β, the Radial Distribution Function (RDF) curve gives a measure of the relative probability that β resides at a radial distance r from α centered at the origin of coordinates.

The profile obtained for Mg^{2+}–DNAp pair (black) shows a sharp peak at r= 1.9 Å, evidencing the high affinity of Mg^{2+} towards DNA. Besides, the first peak for the Ca^{2+}–DNAp pair, which appears at r= 2.6 Å, apparently displays a lower area under the curve (red), revealing a weak attraction force. On the other hand, the area under the Ca^{2+}–Ox^{2-} peak at r= 2.6 Å (light blue) is much higher, reflecting that the attraction of Ca^{2+} by the Ox^{2-} is very favored in comparison to the affinity by the phosphate groups from DNA. Interestingly, Ox^{2-} anions do not exhibit any affinity towards DNA, an equi-probable distribution being found once an exclusion threshold at r= 5.5 Å is exceeded.

Considering the possibility of forming triads like DNAp···X···Ox^{2-}, where X refers to Ca^{2+} or Mg^{2+} coordination ions, analysis of the RDFs shows that Ca^{2+} cannot play this role. Once Ca^{2+} is bound to DNAp or to Ox^{2-} prefers the interaction with surrounding explicit water molecules instead of forming the triad. Thus, the sum of the r values for the first peak of the Ca^{2+}–DNAp and Ca^{2+}–Ox^{2-} RDFs totals 5.2 Å, this value being lower than the threshold distance of cation-mediated DNAp–Ox^{2-} carboxyl interaction (i.e. 5.5 Å). The addition of the distances associated to the first peak of Mg^{2+}–DNAp and Mg^{2+}–Ox^{2-} RDFs renders a value of 6.0 Å, which is bigger than the cation mediated threshold. However, the absence of peaks in the RDF of the DNAp-Ox^{2-} pair suggests that DNAp···Mg^{2+}···Ox^{2-} interactions are extremely weak in highly hydrated environments. The above mentioned tendencies are reflected in Figure 43b, which displays a snapshot from the MD simulation of the modelled system (red box). As it can be seen, Ox^{2-} anions tend to form clusters with Ca^{2+} cations separated from the DNA. Apparently, the polyphosphate groups from DNA do not play any significant role in the formation of CaOx.

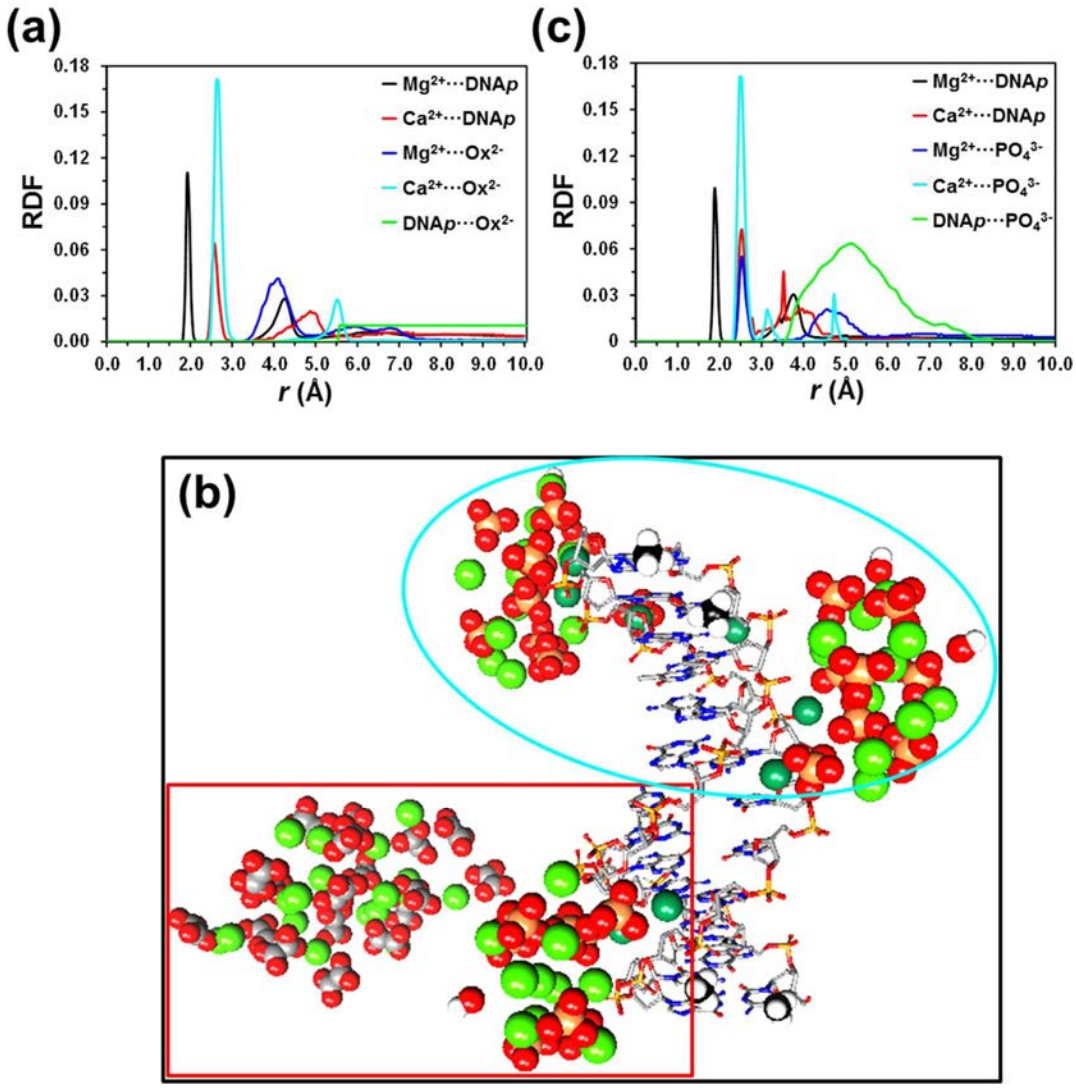

Figure 43. (a) RDFs extracted from the MD simulation of the solution containing R1A, water, Mg^{2+}, Ca^{2+} and Ox^{2-}. DNAp refers to the DNA phosphate backbone. (b) Superposed snapshot extracted from the simulations with Ox^{2-} (red box) and PO_4^{3-} (blue ellipsoid) ions. (c) RDFs extracted from the MD simulation of the solution containing R1A, water, Mg^{2+}, Ca^{2+} and PO_4^{3-}.

Figure 43c displays the RDFs derived from the simulation with PO_4^{3-} for the Mg^{2+}–DNAp, Ca^{2+}–DNAp, Mg^{2+}–PO_4^{3-} (where PO_4^{3-} refers to the center of masses of PO_4^{3-} anions), Ca^{2+}–PO_4^{3-} and DNAp–PO_4^{3-} pairs. The profiles obtained for Mg^{2+}–DNAp and Ca^{2+}–DNAp pairs (black and red, respectively) show sharp peak at r= 1.9 and 2.5 Å, respectively. Thus, although the affinity of the DNA dodecamer towards Mg^{2+} is higher than towards Ca^{2+}, the latter ion interacts more with the phosphate groups of DNA than in the simulation with Ox^{2-}. Besides, the Ca^{2+}–PO_4^{3-} profile shows a sharp peak at r= 2.5 Å (light blue), indicating that the attraction of Ca^{2+} by

PO_4^{3-} anions and DNAp is very similar. However, the most important difference between simulations with Ox^{2-} and PO_4^{3-} is detected in the RDF calculated for the DNAp–PO_4^{3-} pair (green), which shows a broad peak centered at r= 5.00 Å. This peak evidences that PO_4^{3-} anions tend to be distributed around the DNA, which acts as a template and facilitates the growing of the mineral around it. Moreover, in this case the formation of both DNAp···Ca^{2+}···PO_4^{3-} and DNAp···Mg^{2+}··· PO_4^{3-} triads is consistent with the peaks observed in the RDFs. Thus, the addition of the r values for the first peak of the Ca^{2+}–DNAp and Ca^{2+}–PO_4^{3-} RDFs sums 5.0 Å, which matches the maximum of the broad peak obtained for the DNAp–PO_4^{3-} RDF (i.e. 5.0 Å). Besides, the sum of the distances associated to the first peak of Mg^{2+}–DNAp and Mg^{2+}–PO_4^{3-} is 4.3 Å, which is within the area of the broad peak obtained for DNAp-PO_4^{3-}. These results indicate that PO_4^{3-} anions tend to form clusters around the polyphosphate backbone of DNA, repulsive interactions being shielded by the Ca^{2+} and Mg^{2+} ions located between them. This clustering distribution is shown in Figure 43b, which displays a representative snapshot from the MD simulation of the PO_4^{3-} containing system (blue ellipsoid) superposed to that from simulation with Ox^{2-}. Overall, the formation of calcium phosphate clusters surrounding the DNA backbone is fully consistent with previous experimental observation, in which the DNA was found to act as template for the nucleation and growth of crystalline HAp.[115]

7.3.3 ENCAPSULATION OF DNA INSIDE MINERAL NANOPORES

In order to elucidate whether DNA can be present inside HAp and CaOx in microcalcifications, the encapsulation of R1A and DD in mineral nanopores was modelled. Figure 44 represents the structure of R1A and DD dodecamers embedded in HAp and CaOx nanopores after relaxation through energy minimizations and MD, as is described in the Methods section.

In the case of HAp, the DNA double helix occupies practically the whole pore, independently of its methylation degree. Although interactions with mineral ions induce some distortions in the backbone, the DD and R1A double helix with their intra-strand stacking and the inter-strand hydrogen bonds are clearly preserved. This is illustrated in Figure 44, which also depicts the double helix without the mineral. As it can be seen, initial double helices do not undergo

significant distortions, which is fully consistent with the simulations discussed in the previous sub-section.

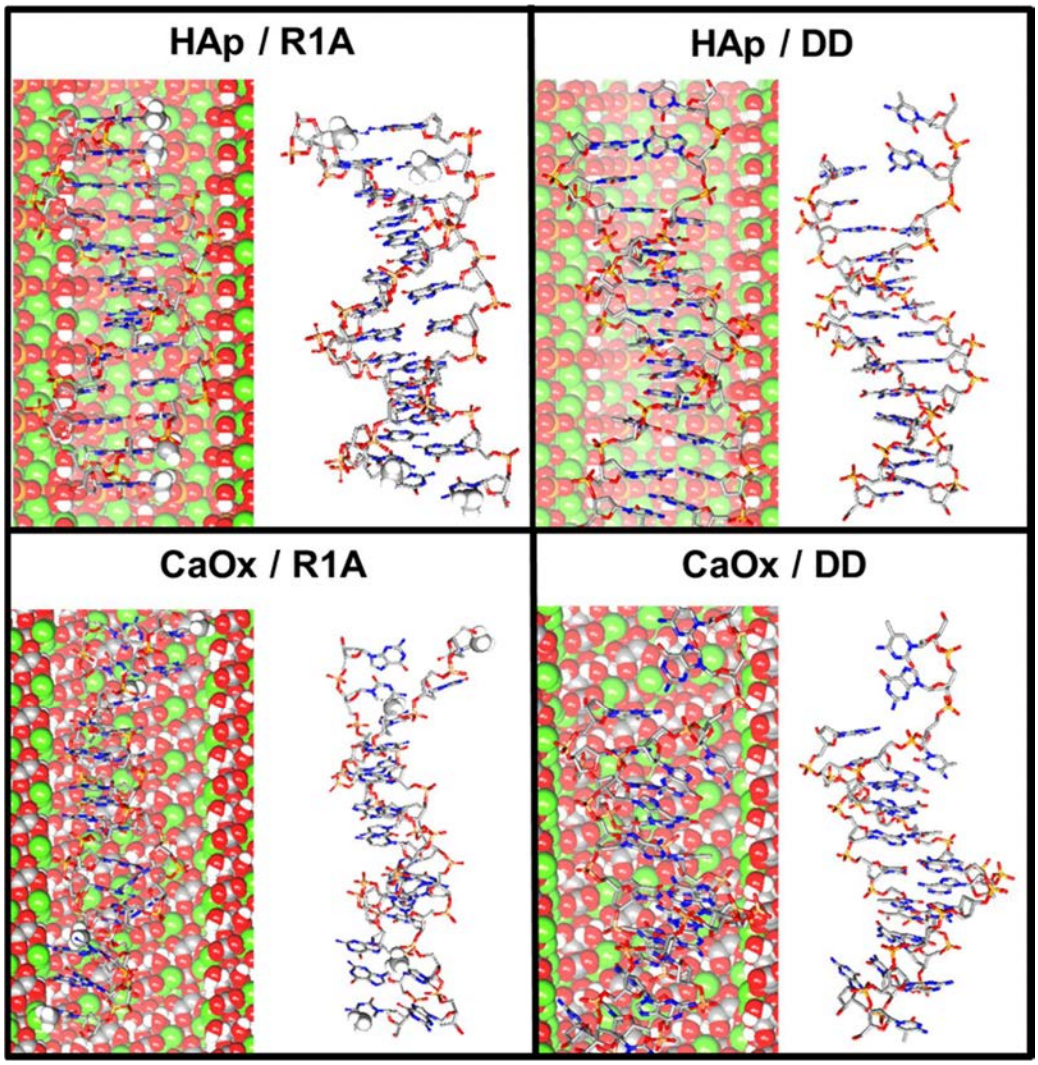

Figure 44. Axial perspective of the R1A and DD double helix embedded in HAp and CaOx nanopores after relaxation through energy minimization and MD. The double helix is also displayed without mineral to show the different degree of distortion induced by the minerals.

Thus, the attractive interaction between the Ca^{2+} ions of HAp and the polyphosphate chain of the DNA allows maintaining the stability of the B-DNA inside the pore. The RMSD between the canonical double helix (i.e. the starting structure) and the relaxed double helix, which was calculated considering all the atoms, is relatively small: 1.9 and 3.5 Å for R1A and DD, respectively.

Relaxation of R1A and DD dodecamers embedded in CaOx induced drastic geometric distortions that affected significantly both the inter-strand hydrogen bonds and the intra-strand π-π stacking, as is displayed in Figure 44.

7.3.4 QUANTUM MECHANICAL (QM) SIMULATIONS

Interactions between the different species involved in DNA-CaOx complexes were further studied to completely understand the poor affinity of DNA by CaOx in comparison to HAp. For this purpose, QM calculations in vacuum and within the framework of an implicit solvation model were performed on small representative model complexes involving two or three interacting species, which are depicted in Figure 45. The estimated ΔG_b and ΔG_{hyd} values, which were calculated as it is indicated in the Methods section, are expected to complete the scenario described by classical MD simulations. The ΔG_b informs about the strength of the interactions that maintain the species involved in the complex assembled in aqueous solution, while ΔG_{hyd} gives the free energy change associated with the transfer of the complex between vacuum and bulk water. The ΔG_b and ΔG_{hyd} values included in Figure 45 completely support the conclusions derived from MD simulations and experimental observations.

First inspection of the ΔG_b and ΔG_{hyd} values reveals that the strength of the binding is more exothermic in complexes with Mg^{2+} than with Ca^{2+}, whereas hydration favors the latter with respect to the former. Careful analysis reveals that when differential energies are considered for the calculated complexes, this behavior can be explained. The ΔG_b is more attractive for $Mg^{2+}\cdots$DNAp than for $Ca^{2+}\cdots$DNAp (i.e. $\Delta\Delta$Gb= -32.5 kcal/mol), indicating that the phosphates from DNA tend to coordinate Mg^{2+} instead of Ca^{2+} when both ions are present. The same trend is observed for $Mg^{2+}\cdots Ox^{2-}$ and $Ca^{2+}\cdots Ox^{2-}$ complexes, the strength of the binding being higher in the former than in the latter (i.e. $\Delta\Delta G_b$= -46.0 kcal/mol). However, ΔG_{hyd} indicates the opposite, the solvation being significantly more favored for complexes with Ca^{2+} than with Mg^{2+} (i.e. $\Delta\Delta G_{hyd}$= -42.0 and -49.5 kcal/mol for complexes with DNAp and Ox^{2-}, respectively).

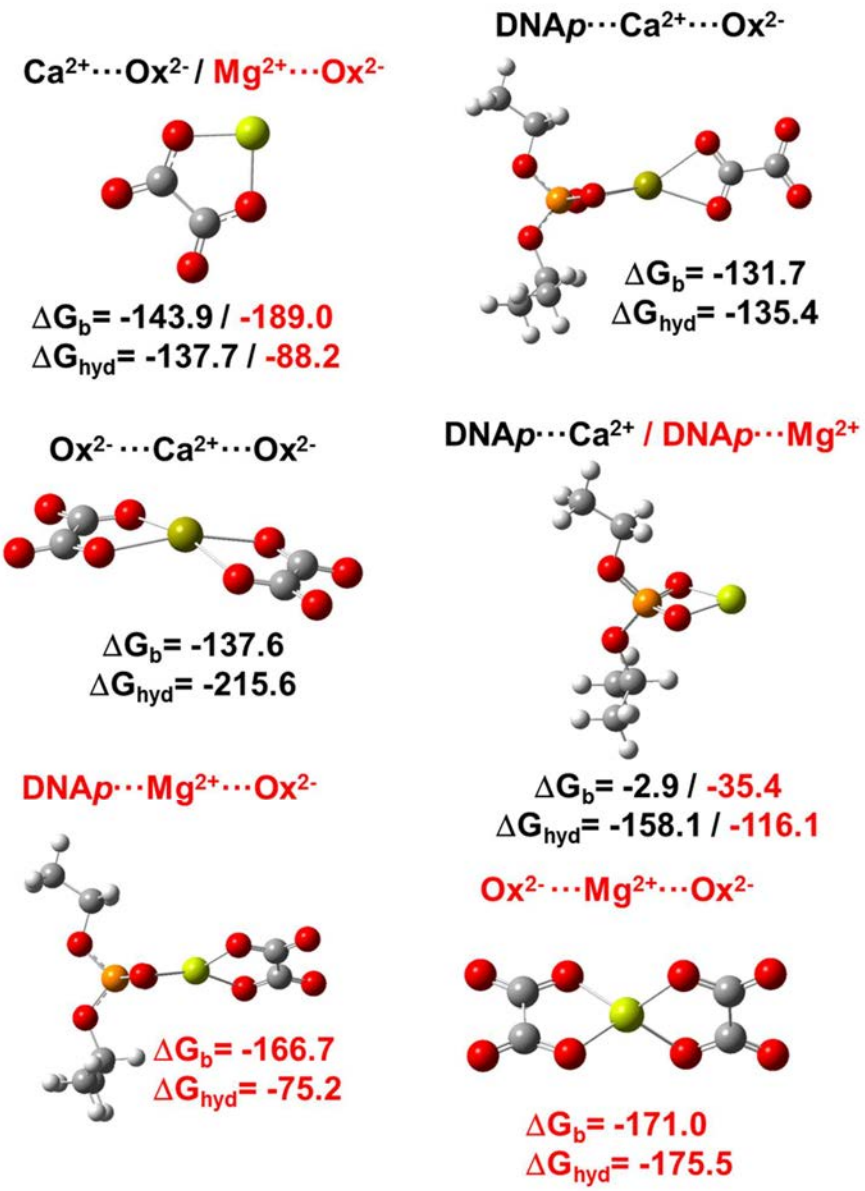

Figure 45. Quantum mechanics calculated binding free energy in aqueous solution (ΔG_b; kcal/mol) and hydration free energy (ΔG_{hyd}; kcal/mol) for different complexes including either Ca^{2+} or Mg^{2+}, oxalate (Ox^{2-}) and DNA phosphates (pDNA): black color letters stands for Ca^{2+} whereas red color ones for Mg^{2+}. Calculations were performed within the SMD-B3LYP/6-311G++(2d,2p) framework.

The balance between $\Delta\Delta G_b$ and $\Delta\Delta G_{hyd}$ values indicates that, in a solution containing all the considered species, Ox^{2-} preferentially interacts with Ca^{2+} while DNA phosphate prefers Mg^{2+}. Additional calculations on model complexes involving three interacting species provide complete understanding of the in lab experiments described in the previous sub-section for CaOx and MgOx. Thus, the strength of the binding in $Ox^{2-}\cdots Mg^{2+}\cdots Ox^{2-}$ is stronger than in Ox^{2-}

$\cdots Ca^{2+}\cdots$ Ox^{2-} by $\Delta\Delta G_b$= -33.4 kcal/mol, while the hydration of the latter is favored with respect to that of the former by $\Delta\Delta G_{hyd}$= -40.1 kcal/mol. Therefore, the sum of these free energy gaps indicates that Ox^{2-} anions tend to surround and coordinate with Ca^{2+} instead of Mg^{2+}. Amazingly, this tendency is much more pronounced for DNAp$\cdots Mg^{2+}\cdots$ Ox^{2-} and DNAp$\cdots Ca^{2+}\cdots$ Ox^{2-} complexes. Thus, although the binding is favored in the former complex by $\Delta\Delta G_b$= -35.0, hydration stabilizes the latter by $\Delta\Delta G_{hyd}$= -60.2 kcal/mol.

7.4 DETERMINATION OF THE TRANSFECTION CAPABILITIES OF HYDROXYOLITES

This section aim to report the ability of hydroxyolites to transfect cells. As mentioned in previous sections, we consider a hydroxyolite to be a non-viral vector of transfection which is expected to carry a nucleic acid sequence across the cell membrane and deliver nucleic acids in the cytosol and reach to the cell nucleus. First, we focus on the feasibility of the cellular uptake of hydroxyapatite (HAp) because endocytosis of calcium phosphate (ACP) particles is a crucial step of the transfection process. It determines if a hydroxyolite can be a suitable carrier for nucleic acids to achieve their target as a transfection vector. Second, we aim to demonstrate that such hydroxyolites, containing DNA encapsulated made by co-precipitation of HAp and DNA, are able to transfect. Third, we aim to demonstrate that hydroxyolites holding adsorbed DNA on their surface are able to transfect as well. Fourth, we study the influence of an excess of Ca^{2+} ion on the transfection efficiency. Fifth, we aim to demonstrate HAp particles generated by cells cultured *in vitro* are able to adsorb DNA and behave as a non-viral vectors of transfection.

7.4.1 HYDROXYPATITE CELL UPTAKE BY A549 CELLS

Murine mammary adenocarcinoma cell line 4T1 (ATCC® CRL-2539™) was selected to obtain *in vitro* hydroxyapatite (HAp) calcifications. 4T1 cells were cultured for several weeks until natural HAp calcifications were observed. It took more than three weeks in average under osteogenic conditions (Figure 46), and typically more than two months for standard conditions (see Methods).

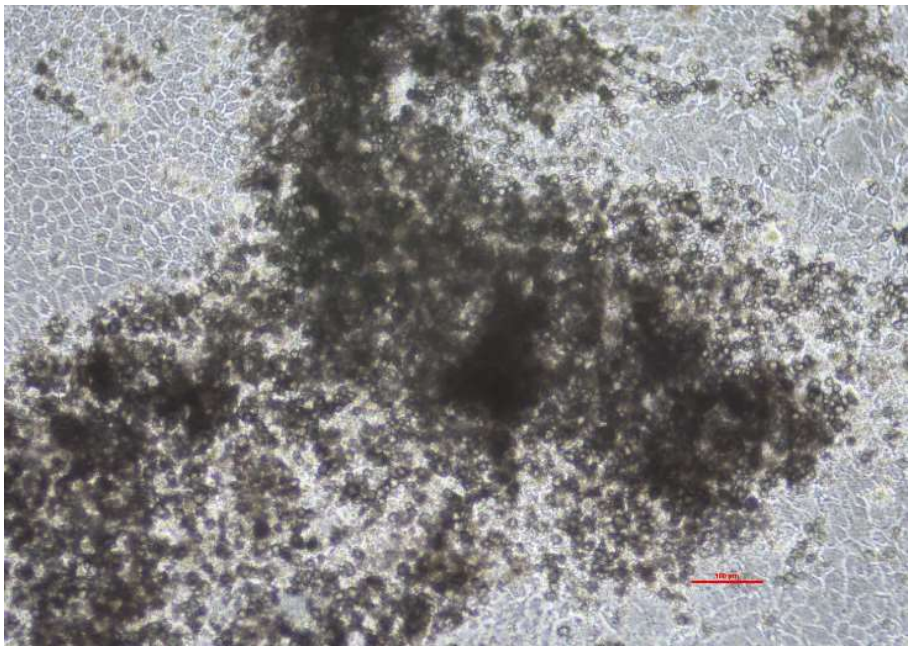

Figure 46. Mineralization observed in 4T1 cells on day 25th using osteogenic induction (Scale bar = 100 µm).

In a second stage, human lung epithelial A549 cells (ATCC® CCL-185™) were put in contact with HAp calcifications obtained from 4T1 cells in order to demonstrate A549 cells are able to uptake naturally synthesized HAp calcifications. The localization of those submicrometric particles inside the cell was studied by confocal laser scanning microscopy by using specific fluorescent probes selectively targeting HAp and DNA. HAp calcifications were stained using a fluorescently labelled alendronate, a known ligand for HAp[232,233,234] whose selectivity towards the mineral was confirmed experimentally by co-staining with a commercial probe targeting HAp. Far-red fluorescent probe (DRAQ5)[235] was selected to selectively stain DNA. Fluorescent nanoparticles corresponding to labelled HAp (green) were identified inside the cells by using a laser scanning confocal microscope (Figure 47), showing the successful uptake after 24 and 48 hours since the beginning of the endocytosis assay.

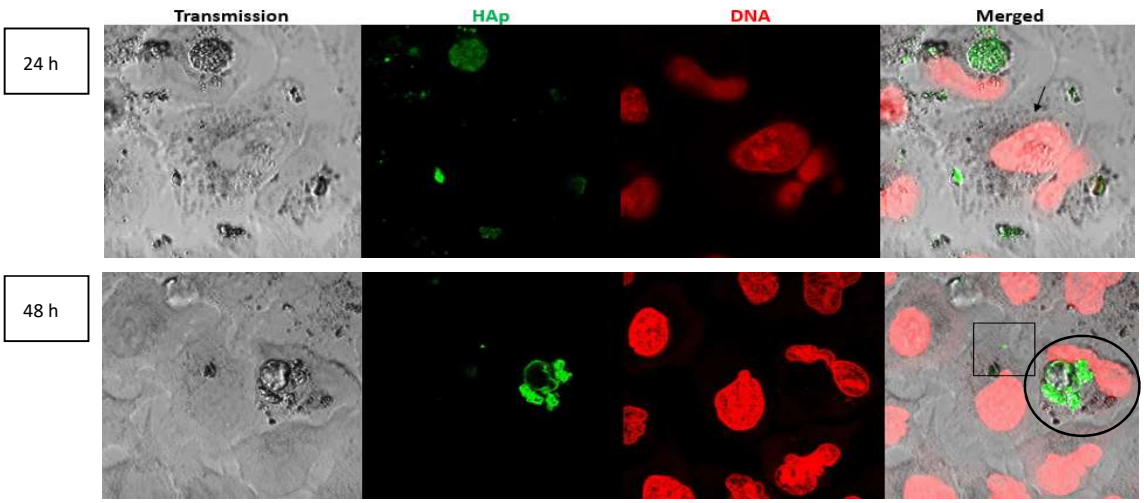

Figure 47. Localization of hydroxyapatite (HAp) inside A549 cells by confocal laser scanning microscopy after 24 and 48 h. From left to the right: Transmission (Bright field image), green channel (HAp probe of alendronate fluorescently labelled), red channel (DNA stained with DRAQ-5 probe) and merged (green and red channel overlapped). Arrow and square indicate HAp into the cytoplasm. Circle indicates overlapping of DNA and HAp in the area of cell nucleus.

HAp particles were found randomly distributed in the cytoplasm and a Z-axis scan was performed in order to confirm their chemical identity. Additionally, HAp particles were found overlapped with stained DNA (red) located in the cell nucleus, suggesting that some of them were able to reach to the target, the cell nucleus and its surroundings. In summary, we confirm the feasibility of HAp cellular uptake and the suitability of the method to detect HAp and DNA inside cells.[a]

[a] We thank Dr. Vanesa Sanz and Prof. Dr. Romain Quidant from ICFO, who established and validated the methodology of fluorescent probes to target HAp calcifications containing DNA under the collaboration agreement with B. Braun Surgical.

7.4.2 *IN VITRO* TRANSFECTION STUDIES OF HYDROXYOLITES ON EUKARYOTIC CELLS

In the next sections are shown the results in transfection assays of the work published by:

> Rodríguez-Rivero, A. M.; Rodríguez-Miguel, C.; Sans, J.; Alemán, C.; Julián, J. F. and Turon, P. Cell transfection mediated by breast cancer nanocalcifications of hydroxyapatite and calcium oxalate. 2021 (ready for submission).

We use hydroxyolites synthesized *in vitro* to transfect A549 cells (ATCC® CCL-185™). A549 cells are epithelial adherent cells often used as a host in transfection models.[236,237,238] As a preliminary step, we obtained the hydroxyolites by chemical synthesis, where equal quantities of DNA were co-precipitated (HAp-*c*DNA) and adsorbed (HAp-*a*DNA-HAp) on HAp. The protocol for transfection studies is described in section Materials and Methods. The transfection efficiency intervals, which have been classified by magnitude orders as Very Low (V.L.), Low (L), Medium (M), High (H) and Very High (V.H.) are defined in Abbreviations and described in Table 9.

Hydroxyolites by DNA encapsulation were synthesized by the co-precipitation method (see Methods), mixing the nLuc gene with a solutions containing Ca^{2+} and PO_4^{3-} at pH > 7. The transfection protocol was started after 30 min since the synthesis of those transfection vectors. On the other hand, hydroxyolites by adsorption were synthesized by leaving the plasmid DNA (pDNA) interact with already formed HAp calcifications synthesized *in vitro* (see Methods). We use an equal concentration of DNA in order to prepare both types of hydroxyolites. As part of the transfection protocol, A549 cells were seeded onto 24-wells plates with 40,000 cells per well for all experiments. Hydroxyolites were added to wells containing 200 µL Opti-MEM® and incubated for 6 hours, then the whole cell culture medium was removed. After replacement with fresh medium, the gene transfection efficacy and its ratio of efficiency was evaluated at 24 h, 48 h-post transfection using a luciferase reporter gene (NanoLuc) into A549 cells. Luciferase activity was normalized against protein content using a Pierce BCA protein assay kit. We note that the distance that hydroxyolites have to migrate until they reach to the cells is the minimum possible (~ 3 mm) in this assay, a short migration through the culture media from the place where they are deposited until the cell membrane. As migration distance is a relevant parameter, we study its effect in more detail

in section 7.9. Transfection assays reveal three important features, which are summarized in Table 14.

Table 14. Transfection efficiency (RLU/µg protein) of HAp through time with DNA adsorbed and co-precipitated through time (n=3 at each time point).

	Transfection Efficiency (RLU / µg protein)			
	24 h	Transfection	48 h	Transfection
Negative Control (NC)	0	No transfection	0	No transfection
Positive Control (PC) ***St. Dev.***	49527 *7428*	**Very High**	79330 *26533*	**Very High**
HAp-*c*DNA ***St. Dev.***	**225** *130*	**Medium**	**106** *61*	**Medium**
HAp-*a*DNA ***St. Dev.***	**138** *3*	**Medium**	**35** *3*	**Low**

Firstly, we note that NC assay demonstrates that no luminescence signal was originated by cells and cell culture media in absence of reactants. Secondly, PC based on a standardized transfection vector made of calcium phosphate in combination with HEPES Buffer Solution (HBS) and luciferase pDNA supplied in the transfection kit scored the highest transfection rate (V.H.) at 24 and 48 h, indicating the correct application of the transfection protocol and the feasibility of A549 cells transfection with the protocol used. According to these results, HAp-*c*DNA and HAp-*a*DNA are capable to transfect A549 cells with a M transfection ratio, showing hydroxyolites are able to introduce DNA inside target cells when it is absorbed or co-precipitated on them.

7.4.2.1 *IN VITRO* TRANSFECTION STUDIES OF HYDROXYOLITES ON EUKARYOTIC CELLS WITH $CaCl_2$

We analyzed the effect of an additional exogenous source of Ca^{2+} in the transfection media. Ca^{2+} was supplied once the particles were already formed (Table 15).

Table 15. Transfection efficiency (RLU/µg protein) of naked DNA and HAp with DNA adsorbed and co-precipitated doped with calcium (n=3 at each run).

	Transfection efficiency (RLU / µg protein)									
	24 h					48 h				
	Run 1	Run 2	Run 3	Avg. (n=9)	Transfection	Run 1	Run 2	Run 3	Avg. (n=9)	Transfection
Negative Control (NC)	0	0	0	**0**	**No transfection**	0	0	0	**0**	**No transfection**
Positive Control (PC)	25036	10522	12929	16162	**Very High**	64285	17537	23944	35255	**Very High**
St. Dev.	*4347*	*1131*	*456*			*13111*	*2670*	*3276*		
Naked DNA	0	0	0	**0**	**No transfection**	0	0	0	**0**	**No transfection**
St. Dev.	*0*	*0*	*0*			*0*	*0*	*0*		
Naked DNA (Ca^{2+})	714	9231	3297	**4414**	**High**	585	9942	3278	**4602**	**High**
St. Dev.	*48*	*518*	*283*			*22*	*1633*	*1203*		
HAp-*c*DNA	0	3	4	**3**	**Very Low**	1	4	1	**2**	**Very Low**
St. Dev.	*0*	*3*	*0*			*1*	*1*	*1*		
HAp-*c*DNA (Ca^{2+})	6	106	456	**189**	**Medium**	209	82	903	**398**	**Medium**
St. Dev.	*0*	*52*	*136*			*10*	*8*	*292*		
HAp-*a*DNA	15	9	6	**10**	**Low**	49	25	6	**27**	**Low**
St. Dev.	*5*	*5*	*2*			*35*	*4*	*2*		
HAp-*a*DNA (Ca^{2+})	1815	187	95	**699**	**Medium**	7021	162	309	**2497**	**High**
St. Dev.	*490*	*157*	*51*			*726*	*65*	*230*		

The first noticeable effect is that naked DNA with Ca^{2+} was able to transfect, rating H at 24 and 48 h. Naked DNA showed no luminescence signal above the threshold confirming that there is no transfection when DNA naked is used as a vector. Furthermore, HAp-*a*DNA enhance the transfection ratio with the additional supply of Ca^{2+} ions, increasing from L to M transfection ratio. Consistent with Pedraza el al.,[239] we confirmed that calcium chloride plays a critical role in effective gene transfection, we report the influence of an excess of Ca^{2+} ion when hydroxyolites by encapsulation or adsorption are already synthesized. As expected Ca^{2+} ions interact with the negatively charged backbone of DNA, facilitating the endocytosis of the DNA.

7.4.3 *IN VITRO* TRANSFECTION STUDIES OF HYDROXYOLITES MADE WITH DNA ADSORBED ON NATURALLY HYDROXYAPATITE SYNTHESIZED BY 4T1 CELLS

We followed the same protocol described in Section 7.4.1 in order to obtain calcifications naturally generated by 4T1 cells. In order to obtain hydroxyolites with DNA adsorbed on the surface, plasmid DNA was mixed with calcifications generated from *in vitro* cell culture following the protocol described in Methods. These calcifications were identified as hydroxyapatite (HAp) by Raman spectroscopy. Then, cells were seeded onto 24-wells plates with 40,000 cells per well for all experiments. Hydroxyolites by adsorption using *in vitro* synthesized HAp by 4T1 cells were added to wells containing 200 µL Opti-MEM® and incubated for 6 hours, then the whole cell culture medium was removed. After replacement with fresh medium, luciferase activity was determined 24 and 48 h-post transfection and normalized against protein content using a Pierce BCA protein assay kit (Table 16).

Table 16. Transfection efficiency (RLU/µg protein) of HAp natural calcifications *in vitro* generated from 4T1 cells after 24 and 48 h (n = 3).

	Transfection efficiency (RLU / µg protein)			
	24 h	Transfection	48 h	Transfection
Negative Control (NC)	0	No transfection	0	No transfection
Positive Control (PC) ***St. Dev.***	22078 *583*	**Very High**	75792 *2525*	**Very High**
HOLi from 4T1 cells ***St. Dev.***	**13705** *2070*	**Very High**	**10631** *3668*	**Very High**

According to these results, calcifications generated by 4T1 cells in an *in vitro* cell culture environment that contains 5 % CO_2 in the atmosphere, and exposed to a plasmid DNA are capable to transfect A549 cells with a V.H. transfection ratio (13,705 and 10,631 RLU/ µg protein at 24 h and 48 h. respectively). This fact is in agreement with the good internalization test of HAp particles (see images in Figure 47). Additionally, it confirms that DNA can be internalized by a natural calcium phosphate carrier made of HAp naturally synthesized by cells both with and without osteogenic media.

7.5 DETERMINATION OF Mg^{2+} ION EFFECT ON ADSORPTION, ENCAPSULATION AND TRANSFECTION OF HYDROXYOLITES

Several *in vitro* transfection assays were performed including in the presence of Mg^{2+} ions, as it is ubiquitous in physiological environments. The effect of Mg^{2+} was included in the transfection study with the objective to elucidate if the behavior of the transfection vectors based on HAp studied as Ca^{2+} ion has done in the previous assay.

7.5.1 *IN VITRO* MONITORING OF HYDROXYOLITES AGGREGATION IN PRESENCE OF MAGNESIUM

The inhibitory effect of Mg^{2+} on particle growth was explained by replacement of Ca^{2+} with Mg^{2+}. Chowdhury et al. (2004)[240] observed that the addition of gradually elevated concentrations of Mg^{2+} (0–8 mM) progressively slowed the growth of the particles. In order to observe the effect of Mg^{2+} addition on aggregation of hydroxyolite particles several measurements at 320 nm were performed using a kinetic turbidimetric method at 37 ºC.

Figure 48 shows the growth profile of those precipitates generated in the presence of incremental concentrations of Mg^{2+} (0-8 mM) by incubating them at 37 ºC and 23 ºC for 96 h.

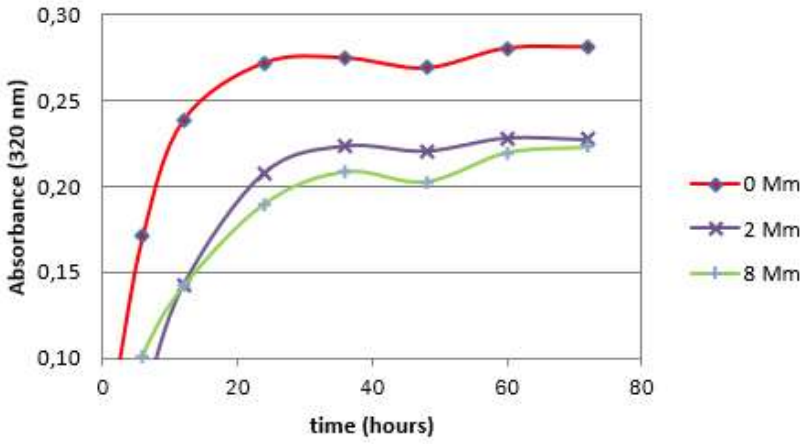

Figure 48. Turbidity measurements at 320 nm of hydroxyolites in H_2O at 37 ºC in presence of Mg^{2+} (0, 2 and 8 mM) (n = 3).

As shown in Figure 49, turbidity dropped constantly when increasing Mg^{2+} concentrations, confirming that Mg^{2+}, once is incorporated in the particle, reduces the crystal growth after 96 hours at 37 ºC and 23 ºC.

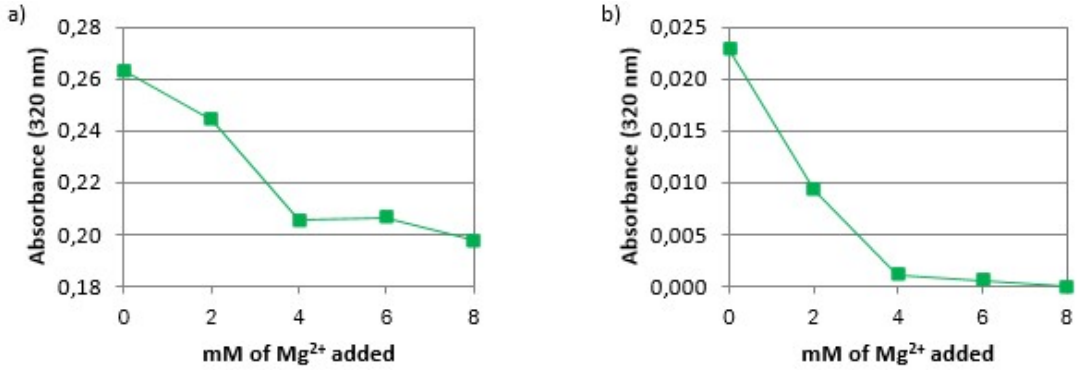

Figure 49. Turbidimetry measurements at 320 nm of hydroxyolites in H_2O in the presence of Mg^{2+} (0-8 mM) for 96 hours at a) 37 ºC and b) 23 ºC (n = 3).

Hydroxyolite precipitation or growth were measured though the turbidity of suspensions containing those particles by Optical Density (OD) at 320 nm. The results obtained are similar to data found in the literature, even at room temperature (23 ºC) after 96 h. Chowdhury et al. (2004)[240] observed the effects of Mg^{2+} prior to initiation of precipitation after 30 min of incubation. In our results is observed the same effect after 96 hours with particles already formed, even at room temperature.

7.5.2 EFFECTS OF MAGNESIUM ON 4T1 CELLS MINERALIZATION

Calcium deposits are a sign of *in vitro* bone formation and can distinctively be stained using Alizarin Red Staining as qualitative analysis. The Alizarin Red Solution stained 4T1 cells (ATCC® CRL-2539™) containing mineral deposits red after 45 days of osteogenic induction (Figure 50). According to the manufacturer's protocol, quantitative analysis of Alizarin Red Staining can be performed by determining OD_{405} values of a set of known Alizarin Red concentrations and comparing these values with those obtained from test samples.

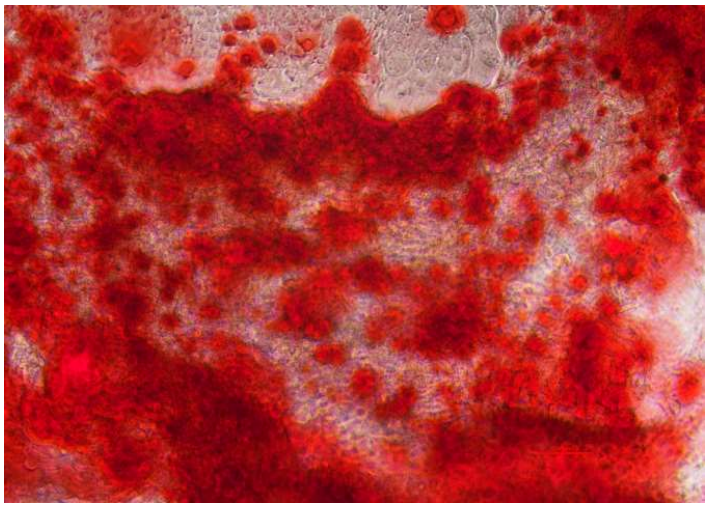

Figure 50. Mineralization detected in Alizarin Red staining of 4T1 cells on day 45 of osteogenic induction (Scale bar = 100 µm).

Quantification of samples using Alizarin Red standards were calculated using three replicates for each Alizarin Red concentration. Sample readings have been applied to the standard curve to calculate the amount of Ca^{2+} in the samples. Quantification results using Alizarin Red after 45 days are shown in Figure 51.

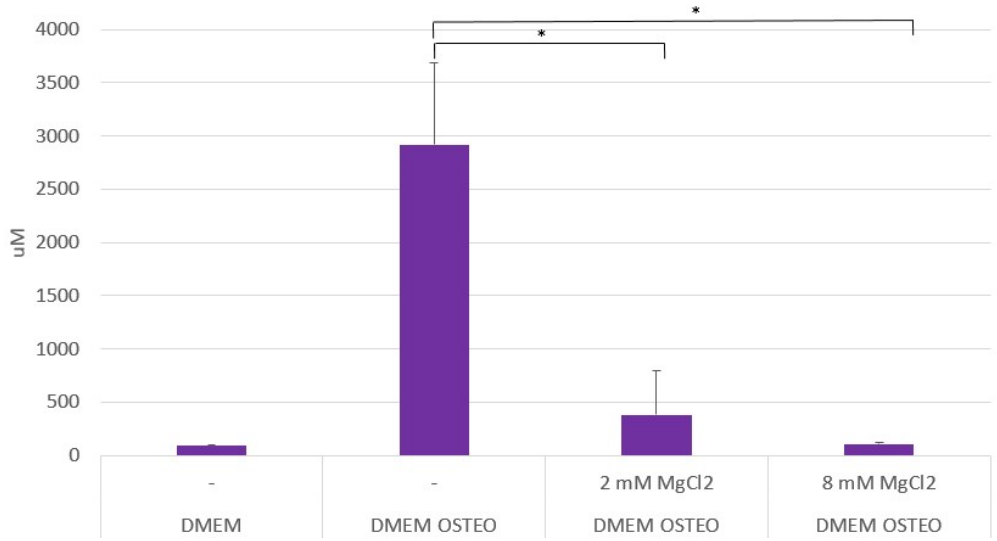

Figure 51. Mineralization in 4T1 cells was analyzed by quantitative analysis of Alizarin Red staining after 45 days in DMEM medium, DMEM osteogenic medium, DMEM osteogenic medium containing 2 mM $MgCl_2$ and DMEM osteogenic medium containing 8 mM $MgCl_2$. Each point represents the mean + SD (n = 3), one-way ANOVA. *p < 0.05.

The final results with three replicates after 45 days, calculated from the Alizarin Red quantitation data set was 2920 µM for samples of Osteogenic induction, 378 µM Osteogenic medium with 2 mM $MgCl_2$ ($p < 0.05$), 104 µM Osteogenic medium with 8 mM $MgCl_2$ ($p < 0.05$), and 86 µM for samples incubated with DMEM as control.

7.5.3 EXPERIMENTAL DNA MINERALIZATION

As a consequence of the previous *in silico* results (see section 7.3), DNA mineralization with calcium oxalate (CaOx), magnesium oxalate (MgOx) and hydroxyapatite (HAp) was investigated forming DNA-CaOx, DNA-MgOx and DNA-HAp complexes through the procedure described in our published article:

> Reprinted with permission from Revilla-Lopez, G., Rodríguez-Rivero, A. M., del Valle, L. J., Puiggali, J., Turon, P., & Alemán, C. Biominerals Formed by DNA and Calcium Oxalate or Hydroxyapatite: A Comparative Study. *Langmuir.* 2019*; 35* (36): 11912-11922 (see ANNEX 3). Copyright (2019) American Chemical Society.
> https://doi.org/10.1021/acs.langmuir.9b01566

It is worth noting that DNA was incorporated into aqueous inorganic solutions and, therefore, the biomolecule could be absorbed onto the surface of the formed mineral particles or encapsulated into them. The non-physiological conditions used in these experiments have been used as a proof of concept for the underlying physicochemical mechanism considering monohydrated CaOx and HAp, which are the minerals employed in the simulations. Thus, the conditions used for the *in vitro* synthesis of minerals have avoided mixed effects of other crystalline forms, as for example dihydrated and trihydrated in the case of CaOx and Brushite, tricalcium phosphate or amorphous calcium phosphate in the case of HAp.

Figure 52a compares the UV-vis spectra recorded for: a1) as obtained DNA-CaOx samples; a2) digested DNA-CaOx samples, in which superficially adsorbed DNA is removed by digesting as obtained DNA-CaOx complexes with DNase; a3) as obtained DNA-CaOx samples from a1 are re-dissolved with sodium citrate (5 mM); and a4) digested DNA-CaOx samples dissolved with sodium citrate (5 mM). The UV-vis spectrum of as prepared DNA-CaOx complexes (a1) clearly demonstrates the presence of DNA since a characteristic absorption peak is observed at 266

nm. However, the absorbance at 266 nm decreases considerably after enzymatic degradation treatment (a2). This absorbance increases after dissolution of the as obtained DNA-CaOx complexes (a3), while it remains very small when the digested samples are dissolved (a4).

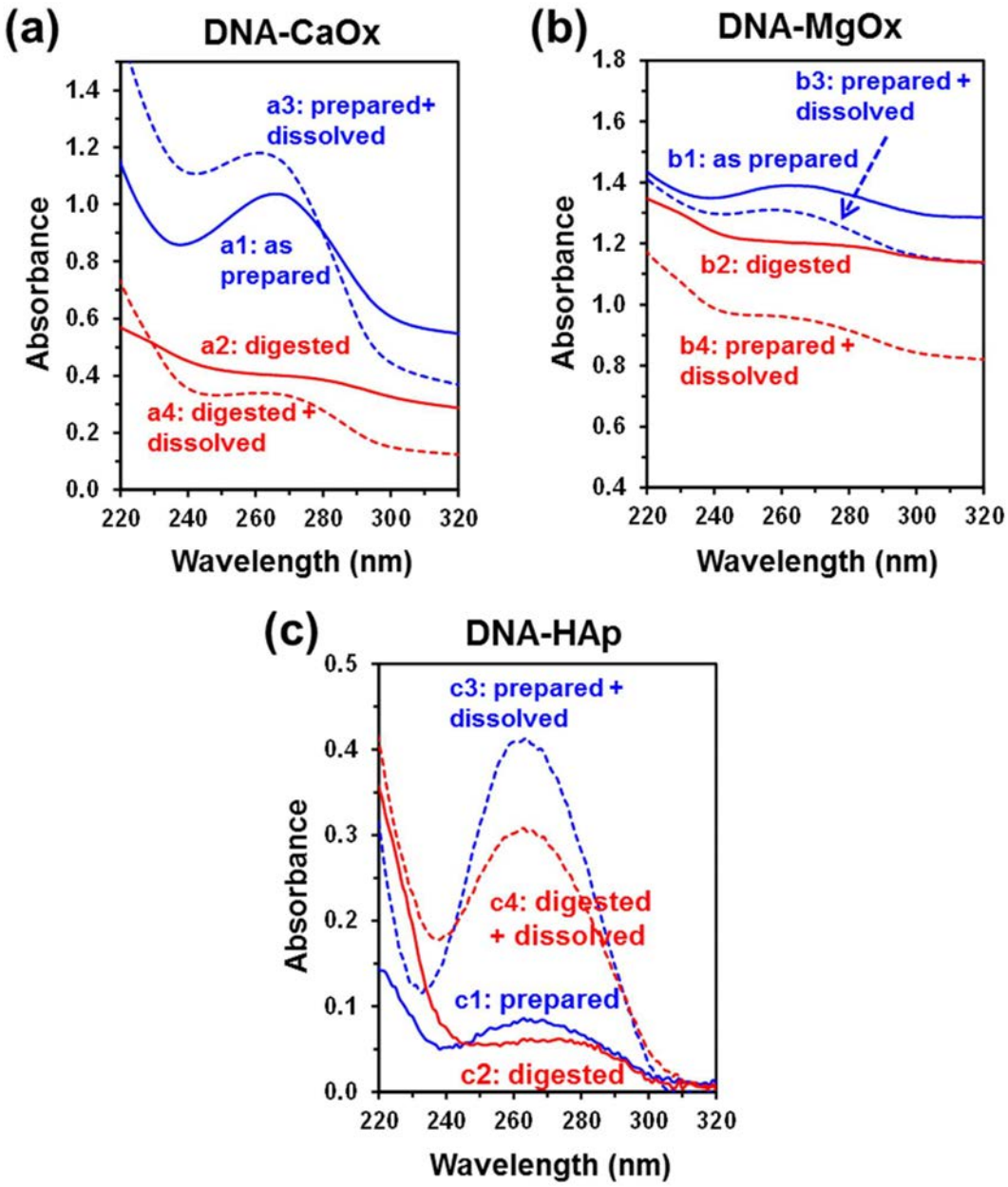

Figure 52. UV-vis absorption spectra of the (a) DNA-CaOx, (b) DNA-MgOx and (c) DNA-HAp complexes. Spectra of: as prepared samples (#1, blue solid lines); samples digested with DNase to eliminate DNA adsorbed on the surface (#2, red solid lines); dissolved as prepared samples (#3, blue dashed lines); and dissolved digested samples (#4, red dashed lines), where # refers to a, b or c.

Trying to promote the affinity of Ox^{2-} towards DNA, DNA-MgOx complexes were prepared following the procedure previously used to obtain DNA-CaOx complexes (see Methods). As the electrostatic binding of Mg^{2+} in the grooves of DNA is essential for the stability of the double helix, substitution of Ca^{2+} by Mg^{2+} was hypothesized to favor the mineralization of DNA.

The UV-vis spectra recorded for as prepared, digested and dissolved DNA-MgOx samples are displayed in Figure 52b. Surprisingly, the absorption peak at 266 nm is very small for the as obtained samples, before and after dissolution (b1 and b3, respectively) and inexistent for the digested ones, before and after dissolution (b2 and b4, respectively). Accordingly, the adsorption of DNA onto the mineral surface is lower for MgOx than for CaOx, whereas the DNA encapsulation was very limited in both cases. These experimental observations are fully consistent with MD simulations on the nucleation of DNA biominerals, in which the formation of DNAp···Ca^{2+}···Ox^{2-} and DNAp···Mg^{2+}···Ox^{2-} interacting triads were not detected, indicating that Ox^{2-} anions hinder the mineralization of DNA, independently of the identity of the divalent metallic cation.

Conversely, UV-vis spectra obtained for DNA-HAp complexes shows the presence of both DNA absorbed on the surface and encapsulated inside the particles. Thus, the DNA absorption peak is clearly observed in as prepared complexes, before and after dissolution (c1 and c3, respectively) and in samples dissolved after digestion with the DNase (c4). Interestingly, the absorbance is much higher for dissolved samples (c3 and c4) than that of as prepared samples (c1 and c2), evidencing the very high tendency of HAp to grow surrounding the DNA molecule that acts as the nucleating template.

7.5.4 TRANSFECTION STUDIES WITH HYDROXYOLITES DOPED WITH MAGNESIUM

Since Mg^{2+} inhibits the growth of the HAp particles, we investigated DNA uptake by the cells, mediated by particles doped with Mg^{2+}. Several *in vitro* transfection assays using pDNA encapsulated in HAp doped with Mg^{2+} were conducted on A549 cells (ATCC® CCL-185™). The general procedure for transfection studies is described on section Materials and Methods. The gene transfection efficiency of the HAp doped with Mg^{2+} was evaluated using a

luciferase reporter gene (nLuc) into A549 cells. Cells were seeded onto 24-wells plates with 40,000 cells per well for all experiments. Hydroxyolites doped with Mg^{2+} were added to wells containing 200 µL Opti-MEM® and incubated for 6 hours, then the whole cell culture medium was removed. After replacement with fresh medium, luciferase activity was determined 24 and 48 h-post transfection and normalized against protein content (Table 17).

Table 17. Transfection efficiency (RLU/µg protein) of HAp with DNA adsorbed and co-precipitated doped with magnesium (n=3 at each run).

	Transfection efficiency (RLU / µg protein)									
	24 h					48 h				
	Run 1	Run 2	Run 3	Avg. (n=9)	Transfection	Run 1	Run 2	Run 3	Avg. (n=9)	Transfection
Negative Control (NC)	0	0	0	**0**	**No transfection**	0	0	0	**0**	**No transfection**
Positive Control (PC)	30511	36651	10983	26048	**Very High**	34404	47305	10330	30680	**Very High**
St. Dev.	*10531*	*4682*	*3768*			*2478*	*6716*	*1675*		
Naked DNA	0	0	0	**0**	**No transfection**	0	0	0	**0**	**No transfection**
St. Dev.	*0*	*0*	*0*			*0*	*0*	*0*		
Naked DNA (Mg^{2+})	1	2	1	**1**	**Very Low**	1	2	2	**2**	**Very Low**
St. Dev.	1	2	0			1	1	1		
HAp-*c*DNA	0	3	4	**3**	**Very Low**	1	4	1	**2**	**Very Low**
St. Dev.	*0*	*3*	*0*			*1*	*1*	*1*		
HAp(Mg^{2+})-*c*DNA	2	2	2	**2**	**Very Low**	1	1	1	**1**	**Very Low**
St. Dev.	*2*	*3*	*2*			*0*	*1*	*0*		
HAp-*a*DNA	15	9	6	**10**	**Low**	49	25	6	**27**	**Low**
St. Dev.	*5*	*5*	*2*			*35*	*4*	*2*		
HAp(Mg^{2+})-*a*DNA	16	54	27	**35**	**Low**	15	18	19	**18**	**Low**
St. Dev.	*8*	*32*	*20*			*3*	*5*	*6*		

The presence of Mg^{2+} in the synthesizing solution of co-precipitated hydroxyolites is expected to reduce the size of the particles and this effect is expected to be influenced by the concentration of Mg^{2+} until certain threshold as the ions tend to migrate to the surface of the particle hindering its further growth.[241] The synthesis was performed adding 30 % Mg^{2+} ion to substitute Ca^{2+} ion during the synthesis process. According to the obtained results, HAp

calcifications absorbed doped with Mg^{2+} were capable to transfect A549 cells (L), one order of magnitude higher, in comparison to naked pDNA also doped with Mg^{2+} (V.L.).

7.6 DETERMINATION OF THE TRANSFECTION CAPABILITIES OF CALCIUM OXALATE (TYPE I)

As a consequence of the *in silico* study reported in section 7.3, we wondered if calcium oxalate (CaOx) calcifications type I might behave as transfection vectors under certain circumstances (i.e. lack of Mg^{2+}) as in such a case the mineral is able to adsorb the nucleic acid. In this section we focus on CaOx as a carrier of nucleic acids in order to confirm whether calcifications type I in breast cancer have the potential to be a non-viral vector of transfection. To our knowledge, this is the first time that CaOx is tested for that purpose.

7.6.1 TRANSFECTION STUDIES WITH CALCIUM OXALATE (CaOx)

In vitro transfection assays using pDNA adsorbed and encapsulated in CaOx *in situ* synthesized were conducted on A549 cells (ATCC® CCL-185™). The general procedure for transfection studies is described on section Methods. After replacement with fresh medium, luciferase activity was determined 24 h, 48 h, 72 h and one week post transfection and normalized against protein content (Table 18).

Table 18. Transfection efficiency (RLU/µg protein) of CaOx through time with DNA adsorbed and co-precipitated through time (n=3 at each time point).

	Transfection efficiency (RLU / µg protein)			
	24 h	**48 h**	**72 h**	**1 week**
Negative Control (NC)	0	0	0	0
Positive Control (PC) ***St. Dev.***	22078 *583*	75792 *2525*	29998 *5847*	5017 *495*
CaOx-*c*DNA ***St. Dev.***	**8** *6*	**6** *6*	**1** *1*	**0** *0*
CaOx-*a*DNA ***St. Dev.***	**37** *7*	**57** *15*	**52** *57*	**13** *8*

These results revealed CaOx with adsorbed DNA (CaOx-*a*DNA) is showed as new non-viral transfection vector.

7.6.1.1 TRANSFECTION STUDIES WITH CALCIUM OXALATE (CaOx) DOPED WITH CALCIUM

In this section, calcium chloride is added to the synthesis solution of once DNA is already co-precipitated with calcium oxalate (CaOx-*c*DNA(Ca^{2+})) and the transfection vectors formed. We analyzed the effect of an additional exogenous source of Ca^{2+} in the transfection media. Results are shown in Table 19.

Table 19. Transfection efficiency (RLU/μg protein) of CaOx with DNA adsorbed and co-precipitated doped with calcium (n=3 at each run).

	Transfection efficiency (RLU / μg protein)									
	24 h					48 h				
	Run 1	Run 2	Run 3	Avg. (n=9)	Transfection	Run 1	Run 2	Run 3	Avg. (n=9)	Transfection
Negative Control (NC)	0	0	0	**0**	**No transfection**	0	0	0	**0**	**No transfection**
Positive Control (PC)	25036	10522	12929	16162	Very High	64285	17537	23944	35255	Very High
St. Dev.	*4347*	*1131*	*456*			*13111*	*2670*	*3276*		
CaOx-*c*DNA	1	7	5	**4**	**Very Low**	3	2	3	**2**	**Very Low**
St. Dev.	*0*	*4*	*3*			*1*	*0*	*1*		
CaOx-*c*DNA (Ca^{2+})	153	1443	2727	**1441**	**High**	328	1731	2461	**1507**	**High**
St. Dev.	*15*	*718*	*372*			*44*	*197*	*588*		
CaOx-*a*DNA	27	13	12	**17**	**Low**	208	35	21	**88**	**Low**
St. Dev.	*9*	*9*	*2*			*76*	*23*	*9*		
CaOx-*a*DNA (Ca^{2+})	575	263	714	**518**	**Medium**	819	618	526	**654**	**Medium**
St. Dev.	*419*	*59*	*147*			*406*	*162*	*144*		

We analyzed the effect of an additional exogenous source of Ca^{2+} in the transfection media. An enhanced transfection ratio was observed for CaOx, resulting in an increment of three orders of magnitude for CaOx-*c*DNA (Ca^{2+}), from V.L. to H. It corroborates that the presence of Ca^{2+} enhances the transfection process as we reported in section 7.4.2.1 when using hydroxyolites. On the other hand, when DNA is adsorbed on CaOx only one order of magnitude was incremented due to the influence of additional Ca^{2+}, resulting from L. to M.

7.6.1.2 TRANSFECTION STUDIES WITH CALCIUM OXALATE (CAOX) DOPED WITH MAGNESIUM

Afterwards, *in vitro* transfection assays using pDNA encapsulated in calcium oxalate (CaOx) doped with Mg^{2+} were conducted. Experimental conditions are described on Methods section. CaOx doped with Mg^{2+} ion by adding 30 % Mg^{2+} ion to substitute Ca^{2+} ion during the synthesis process of the mineral was performed (Table 20).

Table 20. Transfection efficiency (RLU/µg protein) of CaOx with DNA adsorbed and co-precipitated doped with magnesium (n=3 at each run).

	Transfection efficiency (RLU / µg protein)									
	24 h					48 h				
	Run 1	Run 2	Run 3	Avg. (n=9)	Transfection	Run 1	Run 2	Run 3	Avg. (n=9)	Transfection
Negative Control (NC)	0	0	0	**0**	**No transfection**	0	0	0	**0**	**No transfection**
Positive Control (PC)	30511	36651	10983	26048	**Very High**	34404	47305	10330	30680	**Very High**
St. Dev.	*10531*	*4682*	*3768*			*2478*	*6716*	*1675*		
CaOx-*c*DNA	1	7	5	**4**	**Very Low**	3	2	3	**2**	**Very Low**
St. Dev.	*0*	*4*	*3*			*1*	*0*	*1*		
CaOx(Mg^{2+})-*c*DNA	7	3	5	**5**	**Very low**	1	2	0	**1**	**Very Low**
St. Dev.	*7*	*1*	*5*			*1*	*1*	*0*		
CaOx-*a*DNA	27	13	12	**17**	**Low**	208	35	21	**88**	**Low**
St. Dev.	*9*	*9*	*2*			*76*	*23*	*9*		
CaOx(Mg^{2+})-*a*DNA	19	20	21	**20**	**Low**	28	23	25	**26**	**Low**
St. Dev.	*12*	*9*	*2*			*14*	*4*	*3*		

In the case of Mg^{2+} included in the mineral lattice as CaOx(Mg^{2+})-aDNA and CaOx(Mg^{2+})-cDNA, the effect is almost negligible for both when compared to the vector without Mg^{2+} (Figure 54). We note that we concluded in the *in silico* study (section 7.3) that DNA cannot be physically encapsulated in CaOx but it can be adsorbed in the absence of Mg^{2+}.

7.7 DETERMINATION OF THE TRANSFECTION CAPABILITIES OF HYDROXYAPATITE PRECURSORS

In this section, we compare the transfection capabilities of hydroxyapatite precursors. Firstly, we take into consideration amorphous calcium phosphate (ACP) and Brushite as intermediate in the synthesis of HAp in a physiological environment. In the second subsection, we are going to study the effect of the polyphosphate family that are able to yield free orthophosphates after cleavage of the polymer by specific enzymes (i.e. ALP and Lambda protein phosphatase). We selected three representative substances: i) calcium pyrophosphate containing two phosphate monomers, ii) sodium triphosphate and iii) a long chain polyphosphate, termed Graham's salt with n=25, representative of such polymer family. We wondered if such molecules would be able to behave a transfection vectors by themselves before they are converted into HAp after polymer degradation and subsequent precipitation.

Hence, this subsection refers to the ability of HAp precursors to transfect A549 cells. Our results confirm that submicrometric spherical (Figure 53) vectors using ACP-cDNA and ACP-aDNA are able to transfect A549 cells scoring as the highest. Although its ratio is lower than the positive control is much higher compared to HAp-DNA and CaOx-DNA.

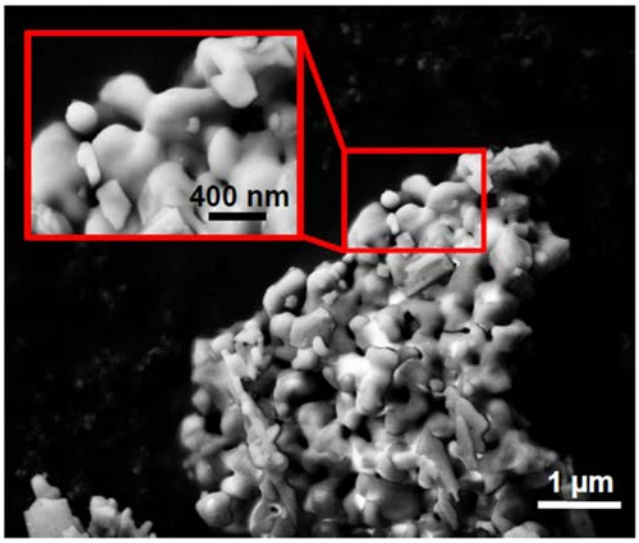

Figure 53. SEM micrograph of the ACP simple synthesized. The inset confirms the spherical morphology of the initial ACP particle. Image courtesy of J. Sans (UPC) and B. Braun Surgical.

7.7.1 TRANSFECTION STUDIES WITH AMORPHOUS CALCIUM PHOSPHATE (ACP)

In vitro transfection assays using pDNA encapsulated and adsorbed in amorphous calcium phosphate (ACP) *in situ* synthesized were conducted on A549 cells (ATCC® CCL-185™). The general procedure for transfection studies is described on section Methods. After replacement with fresh medium, luciferase activity was determined 24 h, 48 h, 72 h and one week-post transfection and normalized against protein content (Table 21).

Table 21. Transfection efficiency (RLU/µg protein) of ACP through time with DNA adsorbed and co-precipitated through time (n=3 at each time point).

	Transfection efficiency (RLU / µg protein)			
	24 h	**48 h**	**72 h**	**1 week**
Negative Control (NC)	0	0	0	0
Positive Control (PC) ***St. Dev.***	22078 *583*	75792 *2525*	29998 *5847*	5017 *495*
ACP-*c*DNA ***St. Dev.***	**18347** *4332*	**8364** *2458*	**1128** *683*	**184** *28*
ACP-*a*DNA ***St. Dev.***	**16556** *4221*	**12452** *3294*	**1142** *193*	**255** *151*

It should be noted that the positive control rated V.H., similar compared to ACP at 24 h even for the effect of HEPES buffer that enhances the transfection of the reference vector.

7.7.1.1 TRANSFECTION STUDIES WITH AMORPHOUS CALCIUM PHOSPHATE (ACP) DOPED WITH CALCIUM

In this section, we add calcium chloride to the synthesis solution of co-precipitated DNA with amorphous calcium phosphate (ACP-*c*DNA). We analyzed the effect of an additional exogenous source of Ca^{2+} in the transfection media. Ca^{2+} was supplied once the particles were already formed (Table 22).

The additional Ca^{2+} showed a negative effect on the transfection with ACP-*c*DNA(Ca^{2+}) and ACP-*a*DNA(Ca^{2+}), the ratio decreasing one order of magnitude from H to M at 24 h and two orders of magnitude from V.H. to M at 48 h.

Table 22. Transfection efficiency (RLU/µg protein) of ACP with DNA adsorbed and co-precipitated doped with calcium (n=3 at each run).

	Transfection efficiency (RLU / µg protein)									
	24 h					48 h				
	Run 1	Run 2	Run 3	Avg. (n=9)	Transfection	Run 1	Run 2	Run 3	Avg. (n=9)	Transfection
Negative Control (NC)	0	0	0	**0**	**No transfection**	0	0	0	**0**	**No transfection**
Positive Control (PC)	11047	26146	23221	20138	**Very High**	46416	31325	27829	35190	**Very High**
St. Dev.	*1528*	*2853*	*3288*			*7356*	*2158*	*2175*		
ACP-*c*DNA	1227	13645	11960	**8944**	**High**	558	19996	18886	**13147**	**Very High**
St. Dev.	*830*	*1042*	*3156*			*251*	*5556*	*3568*		
ACP-*c*DNA (Ca^{2+})	310	273	966	**516**	**Medium**	286	338	1026	**550**	**Medium**
St. Dev.	*32*	*77*	*581*			*15*	*87*	*286*		
ACP-*a*DNA	1191	7514	13836	**7514**	**High**	760	9595	20897	**10417**	**Very High**
St. Dev.	*619*	*3673*	*2980*			*378*	*4562*	*2255*		
ACP-*a*DNA (Ca^{2+})	305	256	1305	**622**	**Medium**	138	542	1340	**674**	**Medium**
St. Dev.	*14*	*69*	*600*			*63*	*102*	*415*		

7.7.1.2 TRANSFECTION STUDIES WITH AMORPHOUS CALCIUM PHOSPHATE (ACP) DOPED WITH MAGNESIUM

Afterwards, *in vitro* transfection assays using pDNA encapsulated in amorphous calcium phosphate (ACP) doped with Mg^{2+} were conducted. Experimental conditions are described on Methods section. Calcium phosphate doped with Mg^{2+} ion by adding 30 % Mg^{2+} ion to substitute Ca^{2+} ion during the synthesis process was performed (Table 23).

In the case of Mg^{2+} included in the mineral lattice as ACP(Mg^{2+})-*a*DNA and ACP(Mg^{2+})-*c*DNA, the effect is almost negligible compared to the vector without Mg^{2+}.

Table 23. Transfection efficiency (RLU/µg protein) of ACP with DNA adsorbed and co-precipitated doped with magnesium (n=3 at each run).

	Transfection efficiency (RLU / µg protein)									
	24 h					48 h				
	Run 1	Run 2	Run 3	Avg. (n=9)	Transfection	Run 1	Run 2	Run 3	Avg. (n=9)	Transfection
Negative Control (NC)	0	0	0	**0**	**No transfection**	0	0	0	**0**	**No transfection**
Positive Control (PC)	30511	36651	10983	26048	**Very High**	34404	47305	10330	30680	**Very High**
St. Dev.	*10531*	*4682*	*3768*			*2478*	*6716*	*1675*		
ACP-*c*DNA	1227	13645	11960	**8944**	**High**	558	19996	18886	**13147**	**Very High**
St. Dev.	*830*	*1042*	*3156*			*251*	*5556*	*3568*		
ACP(Mg^{2+})-*c*DNA	249	2465	1310	**1478**	**High**	154	4093	1147	**1798**	**High**
St. Dev.	*33*	*506*	*192*			*39*	*1210*	*564*		
ACP-*a*DNA	1191	7514	13836	**7514**	**High**	760	9595	20897	**10417**	**Very High**
St. Dev.	*619*	*3673*	*2980*			*378*	*4562*	*2255*		
ACP(Mg^{2+})-*a*DNA	510	2672	1077	**1533**	**High**	112	5851	820	**2261**	**High**
St. Dev.	*85*	*977*	*319*			*40*	*1274*	*179*		

7.7.2 TRANSFECTION STUDIES WITH POLYPHOSPHATES

In vitro transfection assays using pDNA adsorbed with calcium pyrophosphate (n=2), sodium triphosphate (n=3) and polyphosphate Graham's salt (n=25) were performed (Table 24). Experimental conditions are described on section Methods. In this case, DNA was adsorbed on already synthesized particles of polyphosphate family.

Table 24. Transfection efficiency (RLU/µg protein) of calcium pyrophosphate, sodium triphosphate and polyphosphate Graham's salt with DNA adsorbed (n=3).

	Transfection efficiency (RLU / µg protein)			
	24 h	Transfection	48 h	Transfection
Control (negative)	0	No	0	No
St. Dev.	*0*	transfection	*0*	transfection
Positive Control (PC)	49527	Very High	79330	Very High
St. Dev.	*7427*		*26533*	
CaPyr- *a*DNA	**56**	**Low**	**161**	**Medium**
St. Dev.	*14*		*23*	

	Transfection efficiency (RLU / µg protein)			
	24 h	Transfection	48 h	Transfection
TriP- *a*DNA *St. Dev.*	**1** *1*	**Very Low**	**1** *1*	**Very Low**
PolyP- *a*DNA *St. Dev.*	**1** *1*	**Very Low**	**0** *0*	**No transfection**

We highlight that transfection does not occur when sodium triphosphate (n=3) and sodium polyphosphate (n=25) were used but calcium pyrophosphate (n=2) presented a significant transfection scored M, even increasing from 24h to 48 h, a relevant fact that merits further research.

7.7.2.1 TRANSFECTION STUDIES WITH POLYPHOSPHATES DOPED WITH CALCIUM

As performed in previous sections, calcium chloride was added to the media to observe the effect of an excess of Ca^{2+} and the presence of Cl^- (Table 25). Experimental conditions are described on section Materials and Methods.

Table 25. Transfection efficiency (RLU/µg protein) of calcium pyrophosphate, sodium triphosphate and polyphosphate Graham's salt with DNA adsorbed doped with calcium (n=3).

	Transfection efficiency (RLU / µg protein)			
	24 h	Transfection	48 h	Transfection
Control (negative) *St. Dev.*	0 *0*	No transfection	0 *0*	No transfection
Positive Control (PC) *St. Dev.*	25036 *4947*	Very High	64285 *13111*	Very High
CaPyr- *a*DNA *St. Dev.*	**56** *14*	**Low**	**161** *23*	**Medium**
CaPyr- *a*DNA(Ca^{2+}) *St. Dev.*	**2407** *1665*	**High**	**6941** *1174*	**High**
TriP- *a*DNA *St. Dev.*	**1** *1*	**Very Low**	**1** *1*	**Very Low**
TriP- *a*DNA(Ca^{2+}) *St. Dev.*	**3** *1*	**Very Low**	**7** *2*	**Very Low**
PolyP- *a*DNA *St. Dev.*	**1** *1*	**Very Low**	**0** *0*	**No transfection**
PolyP- *a*DNA(Ca^{2+}) *St. Dev.*	**0** *0*	**No transfection**	**3** *1*	**Very Low**

The transfection ratio has been significantly increased using pDNA adsorbed in calcium pyrophosphate (CaPyr-*a*DNA(Ca^{2+}) and adding an excess of Ca^{2+} ions in the transfection media and scores in H. Again, it is worth noting that V.L. or no transfection were obtained when using sodium triphosphate (n=3) and sodium polyphosphate (Graham's salt, n=25), respectively.

7.7.2.2 TRANSFECTION STUDIES WITH POLYPHOSPHATES DOPED WITH MAGNESIUM

In this section, we add magnesium chloride to the synthesis solution of adsorbed DNA with calcium pyrophosphate (n=2), sodium triphosphate (n=3) and polyphosphate Graham's salt (n=25). Results with polyphosphates doped with magnesium are shown in Table 26.

Table 26. Transfection efficiency (RLU/µg protein) of calcium pyrophosphate, sodium triphosphate and polyphosphate Graham's salt with DNA adsorbed doped with magnesium (n=3).

	Transfection efficiency (RLU / µg protein)			
	24 h	Transfection	48 h	Transfection
Negative Control (NC)	0	No transfection	0	No transfection
Positive Control (PC) ***St. Dev.***	30511 *10531*	Very High	34404 *2478*	Very High
CaPyr- *a*DNA ***St. Dev.***	**56** *14*	**Low**	**161** *23*	**Medium**
CaPyr(Mg^{2+})- *a*DNA ***St. Dev.***	**6** *7*	**Very Low**	**8** *2*	**Very Low**
TriP- *a*DNA ***St. Dev.***	**1** *1*	**Very Low**	**1** *1*	**Very Low**
TriP(Mg^{2+})- *a*DNA ***St. Dev.***	**0** *0*	**No transfection**	**0** *0*	**No transfection**
PolyP- *a*DNA ***St. Dev.***	**1** *1*	**Very Low**	**0** *0*	**No transfection**
PolyP(Mg^{2+})- *a*DNA ***St. Dev.***	**0** *0*	**No transfection**	**0** 0	**No transfection**

We analyzed the effect of an additional exogenous source of Mg^{2+} in the transfection media. However, V.L. or no transfection were obtained using calcium pyrophosphate (V.L.), sodium triphosphate (n=3) and sodium polyphosphate (Graham's salt, n=25).

7.7.3 TRANSFECTION STUDIES WITH BRUSHITE

In vitro transfection assays using pDNA encapsulated and adsorbed in Brushite *in situ* synthesized were conducted on A549 cells (ATCC® CCL-185™). The general procedure for transfection studies is described on section Methods. After replacement with fresh medium, luciferase activity was determined 24 h and 48 h-post transfection and normalized against protein content (Table 27).

Table 27. Transfection efficiency (RLU/µg protein) of Brushite through time with DNA adsorbed and co-precipitated through time (n=3 at each time point).

	Transfection efficiency (RLU / µg protein)			
	24 h	Transfection	48 h	Transfection
Negative Control (NC)	0	No transfection	0	No transfection
Positive Control (PC) ***St. Dev.***	49527 *7428*	Very High	79330 *26533*	Very High
Bru-*c*DNA ***St. Dev.***	**144** *20*	**Medium**	**657** *287*	**Medium**
Bru-*a*DNA ***St. Dev.***	**30** *1*	**Low**	**35** *4*	**Low**

According to these results, Brushite calcifications are capable of performing as transfection vectors and to transfect A549 cells, showing a M transfection ratio when is co-precipitated (Bru-*c*DNA). We note that the ratio of Bru-*c*DNA (M) is higher than Bru-*a*DNA (L).

7.7.3.1 TRANSFECTION STUDIES WITH BRUSHITE DOPED WITH CALCIUM

In this section, we analyzed the effect of an additional exogenous source of Ca^{2+} in the transfection media. Ca^{2+} was supplied once the particles were already formed (Table 28).

Table 28. Transfection efficiency (RLU/µg protein) of Brushite with DNA adsorbed and co-precipitated doped with calcium (n=3).

	Transfection efficiency (RLU / µg protein)			
	24 h	Transfection	48 h	Transfection
Negative Control (NC)	0	No transfection	0	No transfection
Positive Control (PC) *St. Dev.*	25036 *4947*	Very High	64285 *13111*	Very High
Bru-*c*DNA *St. Dev.*	**144** *20*	**Medium**	**657** *287*	**Medium**
Bru-*c*DNA (Ca^{2+}) *St. Dev.*	**3** *0*	**Very Low**	**110** *12*	**Medium**
Bru-*a*DNA *St. Dev.*	**30** *1*	**Low**	**35** *4*	**Low**
Bru-*a*DNA (Ca^{2+}) *St. Dev.*	**326** *182*	**Medium**	**585** *150*	**Medium**

Additional Ca^{2+} showed a mild decreasing effect on the transfection Bru-*c*DNA(Ca^{2+}) as the ratio is kept is the same range (M) at 48 h but showed a different pattern at 24 h, indicating that the transfection was delayed in comparison with the vector without Ca^{2+}. On the other hand, a positive effect was observed in Bru-*a*DNA(Ca^{2+}), where the transfection ratio increased one magnitude order and scored M.

7.7.3.2 TRANSFECTION STUDIES WITH BRUSHITE DOPED WITH MAGNESIUM

In this section, *in vitro* transfection assays using pDNA encapsulated in Brushite doped with Mg^{2+} were conducted. Experimental conditions are described on Methods section. Brushite doped with Mg^{2+} ion by adding 30 % Mg^{2+} ion to substitute Ca^{2+} ion during the synthesis process was performed. We analyzed the effect of an additional exogenous source of Mg^{2+} in the transfection media (Table 29).

Table 29. Transfection efficiency (RLU/µg protein) of Brushite with DNA adsorbed and co-precipitated doped with magnesium (n=3).

	Transfection efficiency (RLU / µg protein)			
	24 h	Transfection	48 h	Transfection
Negative Control (NC)	0	No transfection	0	No transfection
Positive Control (PC) *St. Dev.*	30511 *10531*	Very High	34404 *2478*	Very High
Bru-*c*DNA *St. Dev.*	**144** *20*	**Medium**	**657** *287*	**Medium**
Brushite(Mg^{2+})-*c*DNA *St. Dev.*	**9** *12*	**Very Low**	**11** *1*	**Low**
Bru-*a*DNA *St. Dev.*	**30** *1*	**Low**	**35** *4*	**Low**
Brushite(Mg^{2+})-*a*DNA *St. Dev.*	**18** *2*	**Low**	**3** *1*	**Very Low**

Additional Mg^{2+} in the mineral formation showed a negative effect on the transfection Brushite(Mg^{2+})-*c*DNA as the ratio decreasing one order of magnitude from M to L and V.L. orders.

7.8 EFFECT OF THE MINERAL SUBSTRATE OF THE TRANSFECTION VECTOR

Transfection efficiency of HAp, ACP (precursor of HAp) and CaOx was studied in the previous sections. Each of three cases split in two subcases: a) adsorbed DNA on already formed mineral particles and b) co-precipitated DNA with the mineral forming ions. We observed a positive transfection in all studied cases. However, the variability of transfection within the same day and inter-days was assessed as very high, justifying the use of a scale based on magnitude orders that allow to detect the significant differences in transfection efficiency when comparing several tested conditions (Summary in Table 30).

Table 30. Summary of transfection efficiency (RLU/µg protein) of naked DNA and HAp, ACP, CaOx with DNA adsorbed and co-precipitated and influence of Ca^{2+} and Mg^{2+} ions (n=3 at each run).

	24 h					48 h				
	Run 1	**Run 2**	**Run 3**	**Avg. (n=9)**	**Transfection**	**Run 1**	**Run 2**	**Run 3**	**Avg. (n=9)**	**Transfection**
Negative Control (n=3)	0	0	0	0	Negative	0	0	0	0	Negative
Desv. Est. (σ)	*0*	*0*	*0*			*0*	*0*	*0*		
Positive Control (PC)	11047 *1528*	26146 *2853*	23221 *3288*	20138	Very High	46416 *7356*	31325 *2158*	27829 *2175*	35190	Very High
Naked DNA	0 *0*	0 *0*	0 *0*	0	Negative	0 *0*	0 *0*	0 *0*	0	Negative
Naked DNA + Ca2+	714 *48*	9231 *518*	3297 *283*	4414	High	585 *22*	9942 *1633*	3278 *1203*	4602	High
Naked DNA + Mg2+	1 *1*	2 *2*	1 *0*	1	Very Low	1 *1*	2 *1*	2 *1*	2	Very Low
HAp-cDNA	0 *0*	3 *3*	4 *0*	3	Very Low	1 1	4 1	1 1	2	Very Low
HAp-cDNA(Ca2+)	6 *0*	106 *52*	456 *136*	189	Medium	209 *10*	82 *8*	903 *292*	398	Medium
HAp(Mg2+)-cDNA	2 *2*	2 *3*	2 *2*	2	Very Low	1 0	1 1	1 0	1	Very Low
HAp-aDNA	15 *5*	9 *5*	6 *2*	10	Low	49 *35*	25 *4*	6 *2*	27	Low
HAp-aDNA(Ca2+)	1815 *490*	187 *157*	95 *51*	699	Medium	7021 *726*	162 *65*	309 *230*	2497	High
HAp(Mg2+)-aDNA	16 *8*	54 *32*	27 *20*	35	Low	15 *3*	18 *5*	19 *6*	18	Low
CaOx-cDNA	1 *0*	7 *4*	5 *3*	4	Very Low	3 *1*	2 *0*	3 *1*	2	Very Low
CaOx-cDNA(Ca2+)	153 *15*	1443 *718*	2727 *372*	1441	High	328 *44*	1731 *197*	2461 *588*	1507	High
CaOx(Mg2+)-cDNA	7 *7*	3 *1*	5 *5*	5	Very Low	1 *1*	2 *1*	0 *0*	1	Very Low
CaOx-aDNA	27 *9*	13 *9*	12 *2*	17	Low	208 *76*	35 *23*	21 *9*	88	Low
CaOx-aDNA(Ca2+)	575 *419*	263 *59*	714 *147*	518	Medium	819 *406*	618 *162*	526 *144*	654	Medium
CaOx(Mg2+)-aDNA	19 *12*	20 *9*	21 *2*	20	Low	28 *14*	23 *4*	25 *3*	26	Low
ACP-cDNA	1227 *830*	13645 *1042*	11960 *3156*	8944	High	558 *251*	19996 *5556*	18886 *3568*	13147	Very High
ACP-cDNA(Ca2+)	310 *32*	273 *77*	966 *581*	516	Medium	286 *15*	338 *87*	1026 *286*	550	Medium
ACP(Mg2+)-cDNA	249 *33*	2465 *506*	1310 *192*	1478	High	154 *39*	4093 *1210*	1147 *564*	1798	High
ACP-aDNA	1191 *619*	7514 *3673*	13836 *2980*	7514	High	760 *378*	9595 *4562*	20897 *2255*	10417	Very High
ACP-aDNA(Ca2+)	305 *14*	256 *69*	1305 *600*	622	Medium	138 *63*	542 *102*	1340 *415*	674	Medium
ACP(Mg2+)-aDNA	510 *85*	2672 *977*	1077 *319*	1533	High	112 *40*	5851 *1274*	820 *179*	2261	High

ACP rated the highest, H at 24 h and V.H. at 48 h, compared to the values shown by HAp-*a*DNA and CaOx-*a*DNA that corresponded to L interval and HAp-*c*DNA and CaOx-*c*DNA that rated V.L. It is worth noting that the positive control rated V.H., higher compared to ACP, H at 24 h and equal at V.H. at 48 h, just for the effect of HEPES buffer that enhances the transfection of the reference vector (Figure 54).

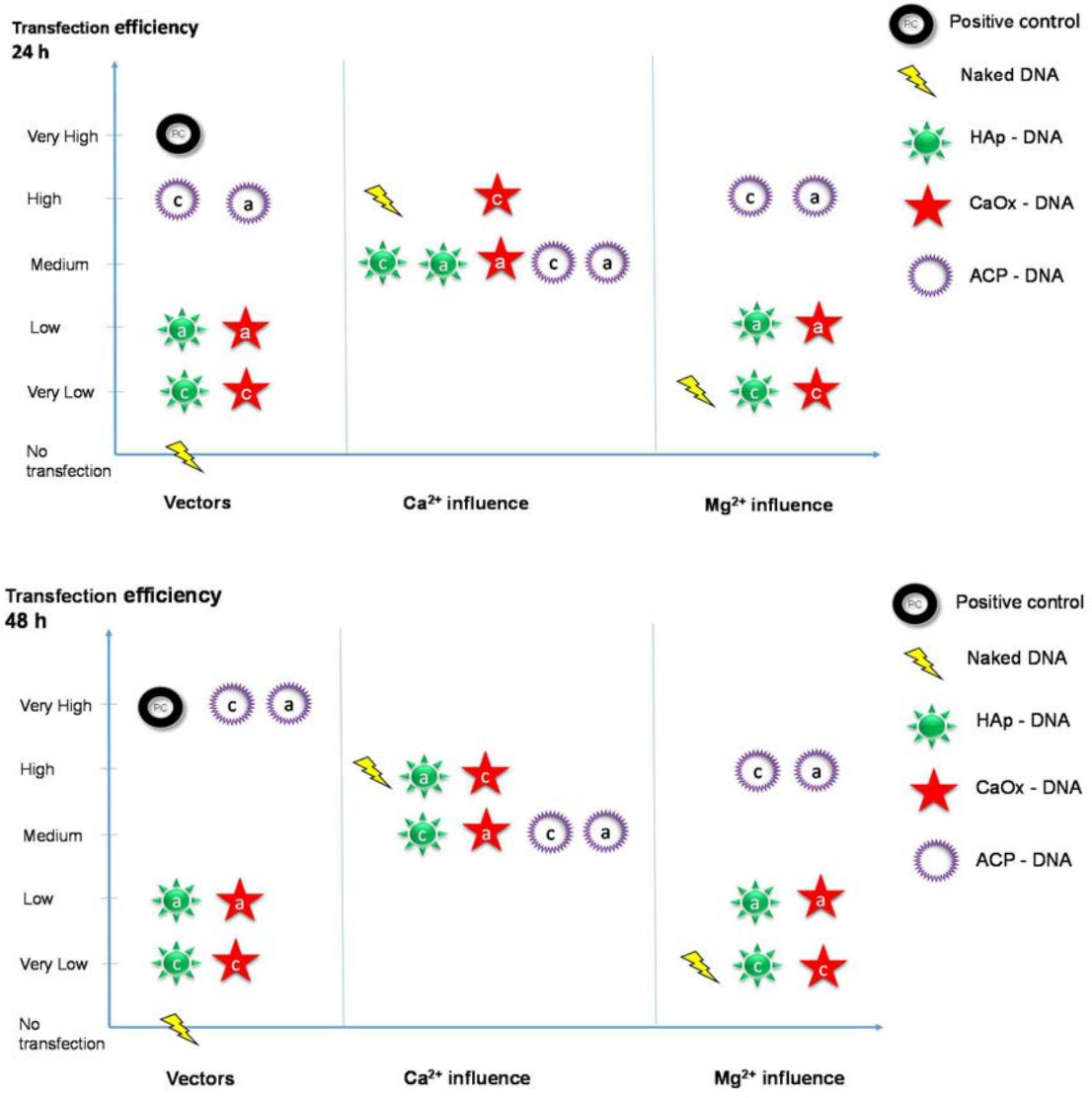

Figure 54. Transfection efficiency of Positive control (PC), naked DNA, HAp, CaOx, ACP at 24 and 48 h. Symbols in legend denote the mineral vectors prepared by DNA co-precipitation (c) and DNA adsorption (a).

After analyzing the HAp vector results (HAp-*c*DNA and HAp-*a*DNA), we observe that both types of *in vitro* chemically synthesized HAp vectors confirm the potential to transfect cells. Nevertheless, their transfection ratio is much lower than the PC and the ACP vectors.

DNA carried by transfection vectors was indirectly quantified by a bisBenzimide assay (Table 31).

Table 31. Quantification of free DNA in an initial DNA solution of 500 ng/400 µL in contact with mineral particles of HAp, ACP and CaOx. Percentage of DNA loaded in the mineral particle was obtained by subtracting measured free DNA concentration from the initial solution. DNA carried by transfection vectors was indirectly quantified by a bisBenzimide assay.

Transfection vectors	Free DNA (ng/ 400 µL)	Std. dev. σ	Carried DNA (ng/ 400 µL)	% DNA loaded
Negative control (Opti-MEM®)	0	*0*	N/A	N/A
Positive Control (CaP + HEPES)	174	*10*	326	65
Positive Control (CaP + HEPES) + Ca^{2+}	421	*85*	79	16
Positive Control (CaP + HEPES) + Mg^{2+}	192	*40*	308	62
Naked DNA	500	*23*	0	0
Naked DNA + Ca^{2+}	241	*121*	259	52
Naked DNA + Mg^{2+}	472	*22*	28	6
HAp-*c*DNA	19	*21*	481	96
HAp-*c*DNA + Ca^{2+}	149	*90*	351	70
HAp-*c*DNA + Mg^{2+}	263	*110*	237	47
HAp-*a*DNA	323	*22*	177	35
HAp-*a*DNA + Ca^{2+}	183	*41*	317	63
HAp-*a*DNA + Mg^{2+}	347	*46*	153	31
ACP-*c*DNA	211	*88*	289	58
ACP-*c*DNA + Ca^{2+}	197	*17*	303	61
ACP-*c*DNA + Mg^{2+}	214	*88*	286	57
ACP-*a*DNA	207	*31*	293	59
ACP-*a*DNA + Ca^{2+}	191	*67*	309	62
ACP-*a*DNA + Mg^{2+}	224	*122*	276	55
CaOx-*c*DNA	440	*37*	60	12
CaOx-cDNA + Ca^{2+}	127	*11*	373	75
CaOx-*c*DNA + Mg^{2+}	348	*52*	152	30
CaOx-*a*DNA	346	*15*	154	31
CaOx-*a*DNA + Ca^{2+}	117	*55*	383	77
CaOx-*a*DNA + Mg^{2+}	213	*10*	287	57

7.8.1.1 EFFECT OF ADDING Ca^{2+} AND Mg^{2+}

Particle size distribution and average of vectors were determined by DLS (Table 32). Results for as prepared HAp-*a*DNA show two populations, the averages centered at 88 ± 33 nm and 731 ± 262 nm, growing to 504 ± 125 nm and > 10 µm, respectively, after 30 min. A similar pattern occurs for HAp-*c*DNA, the average values of the two populations observed for as prepared samples, 75 ± 10 nm and 506 ± 311 nm, increasing to 7.8 ± 2.0 µm and > 10 µm after 30 min. Such an aggregation phenomena is expected to reduce the transfection efficiency when performing as transfection vectors. Indeed, 11.5 % of the HAp-*a*DNA particles exhibited a size smaller than 500 nm, decreasing to less than 0.2 % for HAp-*c*DNA.

Table 32. Particle size and percentage of particles below 500 nm vs above 500 nm (Γ_{500}).

Transfection vector	Time	Size	Γ_{500}
HAp-*a*DNA	0 min	88 ± 33 nm / 731 ± 262 nm*	0.115 ± 0.042*
HAp-*a*DNA	30 min	504 ± 125 nm / > 10 µm	0.032 ± 0.013
HAp-*a*DNA	60 min	711 ± 109 nm	0.026 ± 0.005
HAp-*a*DNA + $CaCl_2$	15 min	420 ± 108 nm / 2.6 ± 1.1 µm	0.094 ± 0.021
HAp-*a*DNA + $CaCl_2$	30 min	296 ± 116 nm / 4.6 ± 1.8 µm	0.048 ± 0.045
HAp-*a*DNA + $MgCl_2$	15 min	511 ± 201 nm / 1.6 ± 0.3 µm	0.017 ± 0.002
HAp-*a*DNA + $MgCl_2$	30 min	365 ± 109 nm / 1.8 ± 0.2 µm	0.005 ± 0.001
HAp-*c*DNA	0 min	75 ± 10 nm / 506 ± 311 nm	$0.002 \pm 1.4 \cdot 10^{-4}$
HAp-*c*DNA	30 min	7.8 ± 2.0 µm / > 10 µm	$0.0006 \pm 1 \cdot 10^{-4}$
HAp-*c*DNA	60 min	5.2 ± 0.3 µm	< l.d. **
HAp-*c*DNA + $CaCl_2$	15 min	406 ± 125 nm / 2.7 ± 0.9 µm	0.086 ± 0.016
HAp-*c*DNA + $CaCl_2$	30 min	456 ± 120 nm / 2.3 ± 1.8 µm / > 10 µm	0.068 ± 0.013
HAp-*c*DNA + $MgCl_2$	15 min	376 ± 156 nm / 4.7 ± 0.6 µm	0.105 ± 0.026
HAp-*c*DNA + $MgCl_2$	30 min	4.3 ± 0.6 µm	0.069 ± 0.021
ACP-*a*DNA	0 min	353 ± 135 nm / 2.0 ± 0.6 µm	0.310 ± 0.177
ACP-*a*DNA	30 min	1.5 ± 0.3 µm	0.072 ± 0.019
ACP-*a*DNA	60 min	1.2 ± 0.2 µm	0.047 ± 0.009
ACP-*a*DNA + $CaCl_2$	15 min	549 ± 123 nm / 4.7 ± 1.9 µm	0.083 ± 0.028
ACP-*a*DNA + $CaCl_2$	30 min	641 ± 20 nm / 1.5 ± 0.1 µm	0.102 ± 0.028
ACP-*a*DNA + $MgCl_2$	15 min	217 ± 38 nm / 713 ± 25 nm / 3.2 ± 0.1 µm	0.474 ± 0.134
ACP-*a*DNA + $MgCl_2$	30 min	284 ± 87 nm / 2.6 ± 0.1 µm	0.289 ± 0.071
ACP-*c*DNA	0 min	232 ± 135 nm / 744 ± 216 nm	0.613 ± 0.215
ACP-*c*DNA	30 min	1357 nm ± 0.3 µm	0.093 ± 0.016
ACP-*c*DNA	60 min	2264 nm ± 240 nm	0.060 ± 0.025
ACP-*c*DNA + $CaCl_2$	15 min	256 ± 24 nm / 2.5 ± 0.1 µm	0.179 ± 0.008
ACP-*c*DNA + $CaCl_2$	30 min	487 ± 203 nm / 4.8 ± 2.6 µm	0.080 ± 0.005
ACP-*c*DNA + $MgCl_2$	15 min	186 ± 40 nm / 625 ± 108 nm / 1.9 ± 0.4 µm	0.322 ± 0.177

ACP-*c*DNA + $MgCl_2$	30 min	301 ± 24 nm / 2.6 ± 0.5 µm	0.104 ± 0.043
CaOx-*a*DNA	0 min	264 ± 50 nm	0.140 ± 0.014
CaOx-*a*DNA	30 min	863 ± 140 nm	0.017 ± 0.005
CaOx-*a*DNA	60 min	3.0 ± 0.3 µm	< l.d. **
CaOx-*a*DNA + $CaCl_2$	15 min	577 ± 15 nm	0.075 ± 0.067
CaOx-*a*DNA + $CaCl_2$	30 min	773 ± 60 nm / 4.9 ± 0.6 µm	0.094 ± 0.024
CaOx-*a*DNA + $MgCl_2$	15 min	348 ± 56 nm / 7.5 ± 0.4 µm	0.007 ± 0.004
CaOx-*a*DNA + $MgCl_2$	30 min	517 ± 97 nm / 5.2 ± 0.6 µm / > 10 µm	0.004 ± 0.001
CaOx-*c*DNA	0 min	375 ± 137 nm	0.008 ± 0.007
CaOx-*c*DNA	30 min	1.1 ± 0.4 µm	$0.0008 \pm 1 \cdot 10^{-4}$
CaOx-*c*DNA	60 min	3.6 ± 0.2 µm	< l.d. **
CaOx-*c*DNA + $CaCl_2$	15 min	236 ± 46 nm / 1.6 ± 0.3 µm	0.156 ± 0.058
CaOx-*c*DNA + $CaCl_2$	30 min	178 ± 20 nm / 1.2 ± 0.1 µm	0.223 ± 0.030
CaOx-*c*DNA + $MgCl_2$	15 min	2.3 ± 0.7 µm / > 10 µm	< l.d. **
CaOx-*c*DNA + $MgCl_2$	30 min	3.4 ± 0.8 µm / > 10 µm	< l.d. **
HAp + DNA + HEPES	0 min	365 ± 224 nm / 2.7 ± 1.3 µm	0.036 ± 0.025
HAp + DNA + HEPES	15 min	428 ± 104 nm / 1.5 ± 0.4 µm	0.179 ± 0.080
HAp + DNA + HEPES	30 min	318 ± 42 nm / 1.9 ± 0.3 µm	0.268 ± 0.242
HAp + DNA + HEPES + Opti-MEM®	0 min	379 ± 16 nm / 2.4 ± 0.8 µm	0.149 ± 0.024
HAp + DNA + HEPES + Opti-MEM®	15 min	295 ± 38 nm / 0.9 ± 0.1 µm	0.186 ± 0.046
HAp + DNA + HEPES + Opti-MEM®	30 min	447 ± 259 nm / 1.1 ± 0.1 µm	0.222 ± 0.040

* Errors expressed in standard deviation
** < l.d. = below limit of detection

On the other hand, the temporal evolution of Z-potential values for HAp-*a*DNA and HAp-*c*DNA are displayed in (Figure 55a). The positive Z-potential of as prepared HAp-*a*DNA (23.7 ± 2.0 mV) corresponds to the counter cations of the Opti-MEM® media (1.8 mM Ca^{2+}) that neutralize the negative charge of the polyphosphates belonging to the adsorbed DNA.

Conversely, as prepared HAp-*c*DNA vector exhibits a negative Z-potential (–14.3 ± 4.1 mV), suggesting that the phosphate anions are the most exposed on the particle surface and, therefore, a change in the binding mode of the biomolecule. The origin of this change has been attributed to the templating effect of DNA, which affects the crystal growth pattern.[115] According to the DLVO electrostatic theory, the stability of a dispersion involving particles with charged surfaces depends on the balance between the attractive van der Waals forces (steric stabilization) and the electrical repulsion because of the net surface charge. In general, a Z-potential beyond 30 mV (positive or negative) indicates that the electrostatic repulsive

forces exceed the attractive steric forces and the system is kept in a relatively stable dispersed state in solution.

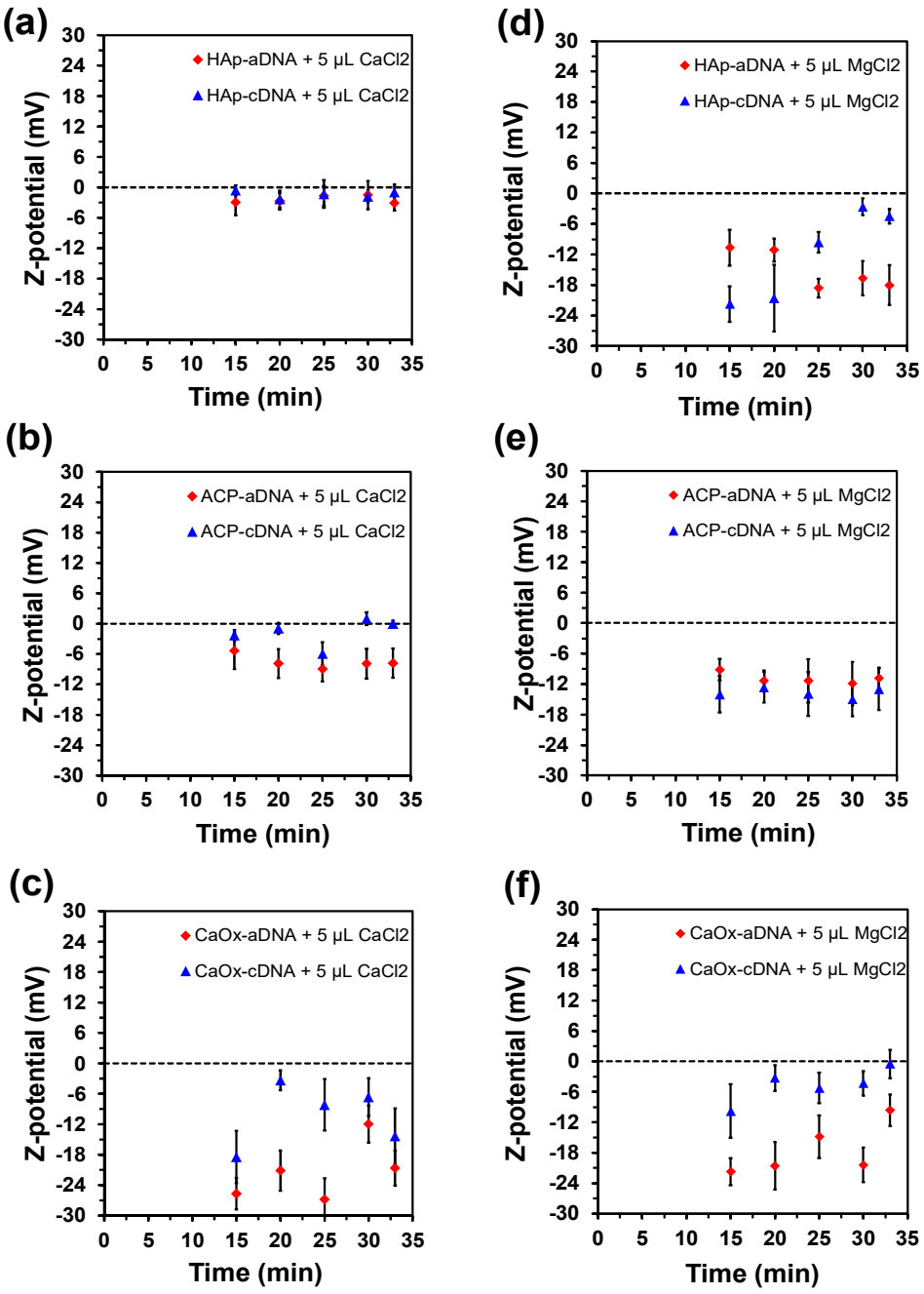

Figure 55. Z-potential dynamics of transfection vectors through time: a) HAp-*a*DNA(Ca^{2+}) (red) and HAp-*c*DNA(Ca^{2+}) (blue); b) ACP-*a*DNA(Ca^{2+}) (red) and ACP-*c*DNA(Ca^{2+}) (blue); c) CaOx-*a*DNA(Ca^{2+}) (red) and CaOx-*c*DNA(Ca^{2+}) (blue); d) HAp(Mg^{2+})-*a*DNA (red) and HAp(Mg^{2+})-*c*DNA (blue); e) ACP(Mg^{2+})-*a*DNA (red) and ACP(Mg^{2+})-*c*DNA (blue); f) CaOx(Mg^{2+})-*a*DNA (red) and CaOx(Mg^{2+})-*c*DNA (blue). Courtesy of UPC and B. Braun Surgical.

Z-potential of HAp-*a*DNA and HAp-*c*DNA does not fulfill such threshold value, which explains the previously discussed aggregation phenomena. Moreover, as a consequence of such aggregation processes that occur in the first minutes, the Z-potential of both HAp-*a*DNA and HAp-*c*DNA approaches to zero with increasing time, reaching values of –0.5 $\pm$ 0.5 mV and –2.9 $\pm$ 2.8 mV, respectively, after 30 minutes (min).

Two well-defined size populations were also observed for as prepared ACP-*a*DNA (353 $\pm$ 135 nm and 2.0 $\pm$ 0.6 µm) and ACP-*c*DNA (232 $\pm$ 135 nm and 744 $\pm$ 216 nm). Moreover, the Z-potential of such species was relatively low (1.8 $\pm$ 1.1 and –12.1 $\pm$ 1.1 mV for ACP-*a*DNA and ACP-*c*DNA, respectively), suggesting they are not able to form stable dispersions. Indeed, after 30 min the size of the particles increased up to 1.5 ± 0.3 µm and 1.3 ± 0.3 µm respectively, even though an unimodal distribution was observed for both species but showing a broad distribution curve. Inspection of temporal evolution of the Z-potential, which is shown in Figure 55b, indicates that ACP-*a*DNA follows a distinctive behavior compared to HAp vectors. More specifically, the Z-potential of as prepared particles decreased to –10.8 $\pm$ 0.8 mM after 15 min and, subsequently increased to –1.2 $\pm$ 0.5 mV after 30 min. This feature suggests that, at the initially of the aggregation process ($\leq$ 15 min) ACP evolves into a more ordered phase in which anions are preferentially exposed at the surface.

The size of as prepared CaOx-*a*DNA and CaOx-*c*DNA particles measured 264 $\pm$ 50 nm and 375 $\pm$ 137 nm, respectively, while their Z-potential was negative (–4.5 $\pm$ 0.6 mV and –2.1 $\pm$ 0.5 mV, respectively). As expected from such low values, the size of both kind of particles increases with time due to aggregation, after 30 min reaching average values up to 863 $\pm$ 140 nm and 1.1 $\pm$ 0.4 µm for CaOx-*a*DNA and CaOx-*c*DNA, respectively. Moreover, the Z-potential approaches zero with increasing time, as can be seen in Figure 55c.

Figure 56 represents the ratio of particles with a size lower than 500 nm with respect to agglomerates with a size higher than 500 nm (Γ_{500}= Particles < 500 nm / Particles > 500 nm * 100) after 30 min, which was determined by integrating the distribution profiles recorded for the different species. We note the highest percentage of small particles is achieved by ACP vectors at t=0, reaching to 61.3 % for ACP-*c*DNA, however after 30 min the percentage was lower than 10 %. CaOx vectors show a similar distribution compared to HAp.

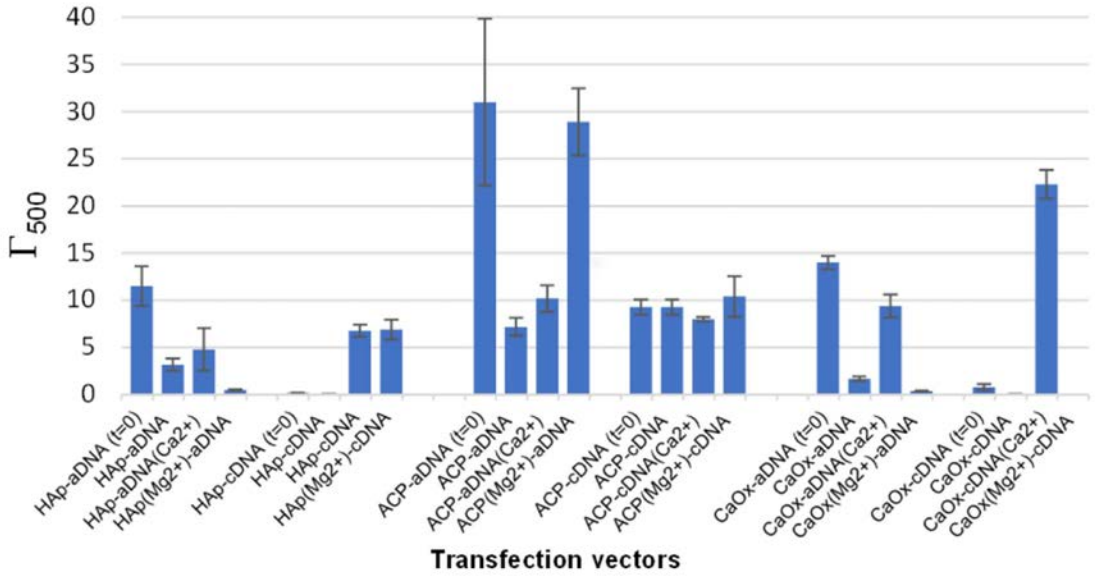

Figure 56. Percentage of particles below 500 nm (Γ500). First value of series (t=0) denotes the Γ500 value at the time of the transfection vector synthesis. All other values correspond to 30 minutes after vector synthesis.

The impact of adding Ca^{2+} in the solution is noticeable. The added cations on HAp vectors allow to keep the average particle size lower in both distributions, reducing by more than 40 % the average size of the lower distribution (296 $\pm$ 116 nm / 4.6 $\pm$ 1.8 µm) and keeping Γ_{500} = 4.8 % in HAp-aDNA(Ca^{2+}) after 30 min, an effect that is more significant in HAp-*c*DNA(Ca^{2+}) where the average size of the lower distribution is reduced by a factor higher than x10 (456 ± 125 nm/ 2.3 $\pm$ 1.8 µm) and Γ_{500} = 6.8 % indicates a delay in the aggregation process (Table 32).

A similar effect is observed for both ACP-*a*DNA(Ca^{2+}) and ACP-*c*DNA(Ca^{2+}), 641 $\pm$ 20 nm / 1.5 $\pm$ 0.1 µm and 487 $\pm$ 203 nm / 4.8 $\pm$ 2.6 µm respectively, but affected by a reduction factor of x2.6 and increasing Γ_{500} up to 10.2 % and 8.0 % respectively. Conversely, in CaOx-*c*DNA(Ca^{2+}) is observed a significant average size reduction by a factor of x6 (178 ± 20 nm / 1.2 ± 0.1 µm and an increase in the number of particles below 500 nm up to Γ_{500} = 22.3%. Z-potential measurements adding 50 µL, as used in the transfection protocol, were not feasible due to interference of such high Ca^{2+} concentration during the test measurements. However, Z-potential measures, using only 5 µL to reduce the Ca^{2+} in solution, show a stable similar trend

in HAp-*a*DNA(Ca^{2+}) and HAp-*c*DNA(Ca^{2+}) at –1.2 and –2.9 mV. ACP-*a*DNA(Ca^{2+}) displays lower values at 30 min (–7.9 mV) but ACP-*c*DNA(Ca^{2+}) stabilizes itself at almost at 0 mV. The most interesting trend is shown by CaOx-*a*DNA(Ca^{2+}) as is the lowest reaching at –15 mV at 30 min (Figure 55).

We focused on the effect of an exogenous burst of Ca^{2+} in the transfection media when additional Ca^{2+} was supplied once the particles were already formed. The first noticeable effect was that naked DNA with Ca^{2+} was able to transfect, rating H at 24 and 48 h. As expected Ca^{2+} ions should be able to interact with the negatively charged backbone of DNA, facilitating the endocytosis of the DNA. It is worth noting that the level of transfection is similar to the ACP despite no additional phosphate ions were supplied to naked DNA. On the other hand, an enhanced transfection ratio was observed for HAp-*a*DNA(Ca^{2+}) and HAp-*c*DNA(Ca^{2+}) and CaOx-*a*DNA(Ca^{2+}) and CaOx-*c*DNA(Ca^{2+}), resulting in an increment of two orders of magnitude for HAp and one for CaOx-*a*DNA(Ca^{2+}) and three for CaOx-*c*DNA(Ca^{2+}) at 48 h. Conversely, the additional Ca^{2+} showed a negative effect on the transfection ACP-*c*DNA(Ca^{2+}) and ACP-*a*DNA(Ca^{2+}), the ratio decreasing one order of magnitude from H to M at 24 h and two orders of magnitude from V.H. to M at 48 h (Table 30, Figure 54).

On the other hand, the size of particle when Mg^{2+} is incorporated in the HAp(Mg^{2+})-*a*DNA vectors decreases at about 30 % in lower population and by a factor of 4 in the higher (365 $\pm$ 109 nm / 1.8 $\pm$ 0.2 µm) after 30 minutes but the impact is also important in HAp(Mg^{2+})-*c*DNA obtaining a reduction of 50 % (4.3 $\pm$ 0.6 µm) compared to HAp-cDNA. Nevertheless, the Γ_{500} is quite similar and not above 7 % in any case (Table 32). Contrariwise, the impact on ACP(Mg^{2+})-*a*DNA shows approx. 20 % reduction (284 $\pm$ 87 nm / 2.6 $\pm$ 0.1 µm) but the Γ_{500} = 28.9 % is slightly lower. However, an increase of 30 % observed in ACP(Mg^{2+})-*c*DNA (301 $\pm$ 24 nm / 2.6 $\pm$ 0.5 µm) and a significant reduction by a factor of 6 in Γ_{500} up to 10.4 %. Finally, Mg^{2+} influence on CaOx results in an increase of x2 of the average size in CaOx(Mg^{2+})-*a*DNA (517 $\pm$ 97 nm / 5.2 $\pm$ 0.6 µm / > 10 µm) and a noticeable increase by a factor of x10 in CaOx(Mg^{2+})-*c*DNA (3.4 $\pm$ 0.8 µm / > 10 µm) being in both cases the percentage below 500 nm beyond the detection limit of the measurement. The dynamics of Z-potential are significantly different depending on the mineral. HAp-*a*DNA shows a decreasing trend from –10.65 mV (15 min) to –16.7 mV (30 min) but HAp-*c*DNA increases from –21.73 mV (15 min) to –2.6 mV (30

min). Conversely, Z-potential of ACP-*a*DNA remains higher than ACP-*c*DNA for the whole period until 30 min (–11.89 mV and –14.95 mV, respectively). The inverse relation (Figure 55) is observed for CaOx-*c*DNA where stays less negative than CaOx-*a*DNA through time (–4.30 mV and –20.38 mV after 30 min respectively). Mg^{2+} ions allowed naked DNA to transfect cells but only up to V.L. interval. Compared with Ca^{2+}, the effect is mild, unveiling that Ca^{2+} transfection enhancement is not only related to the positive charge of the ion. In the case of Mg^{2+} included in the mineral lattice as HAp(Mg^{2+})-*a*DNA and HAp(Mg^{2+})-*c*DNA and CaOx in the same conditions, the effect is almost negligible compared to the vector without Mg^{2+}. Finally, Mg^{2+} ions do not influence the transfection ratio of ACP vectors at 24 h but reduce to H at 48 h. As Figure 54 describes, the presence of Mg^{2+} keeps the ratio of both ACP(Mg^{2+})-*a*DNA and ACP(Mg^{2+})-*c*DNA in the H interval.

7.8.1.2 PRINCIPAL COMPONENT ANALYSIS

A principal component analysis (PCA) was performed to elucidate which are the variables that have positive associations with transfection efficiency ratio. The variables used for the analysis were: transfection ratio, average size, ratio of particles below 500 nm vs particles above 500 nm (Γ_{500}), Z-potential after 30 min, and DNA load carried by the transfection vector (Θ_{DNA}) (Table 33).

Table 33. Data set of Transfection ratio (0-10), Average size (nm), ratio of particles below 500 nm vs particles above 500 nm (Γ500), Z-potential (mV) and DNA (ng) contained in 50 µL of transfection vector solution.

Transfection vector	Transfection ratio	Average size (S) (nm)	Γ_{500} (%)	Z-potential (Z) (mV)	Θ_{DNA} (ng)
HAp-*a*DNA	L (4)	504	3.2	–0.48	22.1
HAp-*c*DNA	VL (2)	7830	0.6	–2.93	60.1
HAp-*a*DNA(Ca^{2+})	H (8)	296	4.8	–1.52	39.6
HAp-*c*DNA(Ca^{2+})	M (6)	456	6.8	–1.79	43.9
HAp(Mg^{2+})-*a*DNA	L (4)	365	0.5	–16.7	19.1
HAp(Mg^{2+})-*c*DNA	V.L. (2)	4325	6.9	–2.6	29.6
ACP-*a*DNA	V.H. (10)	1526	7.2	–1.2	36.6
ACP-*c*DNA	V.H. (10)	1357	9.3	–2.91	36.1
ACP-*a*DNA(Ca^{2+})	M (6)	641	10.2	–7.9	38.6

Transfection vector	Transfection ratio	Average size (S) (nm)	Γ_{500} (%)	Z-potential (Z) (mV)	Θ_{DNA} (ng)
ACP-*c*DNA(Ca^{2+})	M (6)	487	8	1	37.9
ACP(Mg^{2+})-*a*DNA	H (8)	284	28.9	−11.89	34.5
ACP(Mg^{2+})-*c*DNA	H (8)	301	10.4	−14.98	35.8
CaOx-*a*DNA	L (4)	863	1.7	−0.99	19.3
CaOx-*c*DNA	V.L. (2)	1100	0.8	−1.36	7.5
CaOx-*a*DNA(Ca^{2+})	M (6)	773	9.4	−11.99	47.9
CaOx-*c*DNA(Ca^{2+})	H (8)	178	22.3	−6.63	46.6
CaOx(Mg^{2+})-*a*DNA	L (4)	517	0.4	−20.38	35.9
CaOx(Mg^{2+})-*c*DNA	V.L. (2)	3400	0	−4.3	19.0

Results displayed in Table 34a show that proportion of variance explained by the three first components is 87.5 %. Therefore, we used three components for the PCA analysis. The first component (PC1) is mainly explained by the following variables: transfection (0.606), the most important contributing factor, followed by Γ_{500} (0.567) and Θ_{DNA} (0.282) unveiling a positive association among those three variables and indicating the high explicative power of Γ_{500} and Θ_{DNA} to understand the transfection process.

Table 34. Principal Component Analysis.

a) Eigenanalysis of the Correlation Matrix

Eigenvalue	2.1160	1.3095	0.9483	0.4449	0.1813
Proportion	0.423	0.262	0.190	0.089	0.036
Cumulative	0.423	0.685	0.875	0.964	1.000

b) Eigenvectors

Variable	PC1	PC2	PC3
Transfection rate	**0.606**	0.071	0.277
Average size (S)	-0.428	0.615	-0.166
Γ_{500}	0.567	0.138	0.055
Z-potential (Z)	-0.220	0.278	0.912
Θ_{DNA}	0.282	0.722	-0.247

However, a negative contribution is observed for average size (–0.428) and Z-potential (–0.220). Conversely, the second component (PC2) shows a positive association among Θ_{DNA} (0.722), average size (0.615) and Z-potential (0.278) linking the physicochemical features of the particles with the capacity of carrying DNA. The third component (PC3) denote positive

associations between Z-potential (0.912) and Transfection rate (0.277) but negative association with ʘDNA (–0.247) and average size (–0.166), so PC3 component primarily refers to the contribution of particle charge to transfection. The loading plot showing first and second component graphically the positive and negative associations (Figure 57) for the two first components.

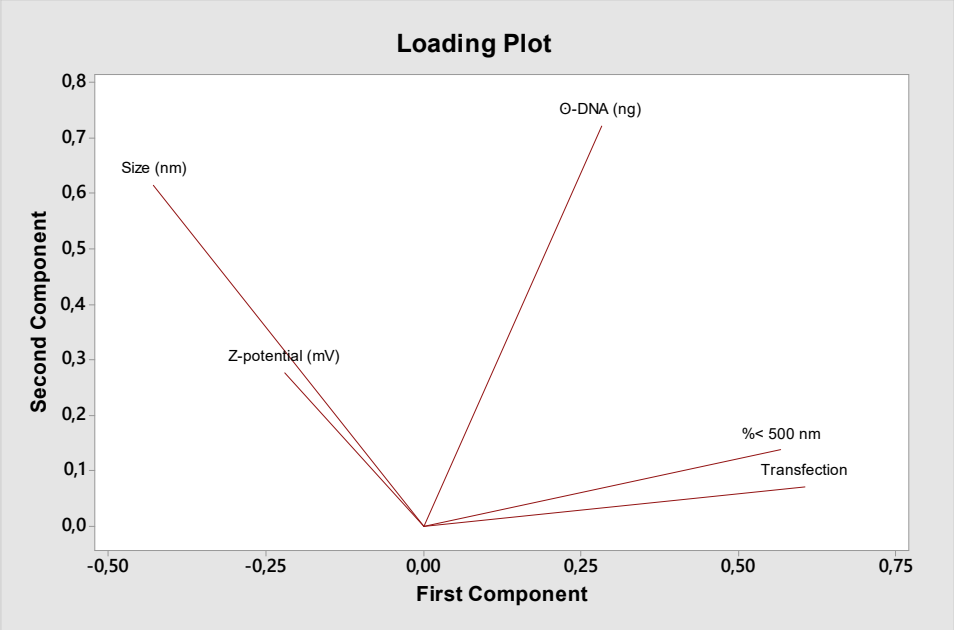

Figure 57. Principal Component Analysis. PCA loading plot representing the contribution of the variables to the first two components (PC1 and PC2).

7.9 DETERMINATION OF TRANSFECTION EFFICIENCY AFTER MIGRATION

In vitro transfection assays were conducted on A549 cells (ATCC® CCL-185™) after migration. Transfection vectors were forced to travel to certain distances (3 mm, 7 mm, 20 mm and 50 mm) within the range of breast multifocality definition (≤ 50 mm) by means of gravity. We used pDNA co-precipitated and absorbed on different carriers used in the previous sections made of hydroxyapatite (HAp), calcium oxalate (CaOx) and amorphous calcium phosphate (ACP). The general procedure for transfection studies is described on section Materials and Methods. The transfection efficiency of the nanoparticles above mentioned was evaluated using a luciferase reporter gene (nLuc) into A549 cells. Cells were seeded onto 24-wells with 40,000 cells per well for all experiments in an *in vitro* vertical migration setup (Figure 58).

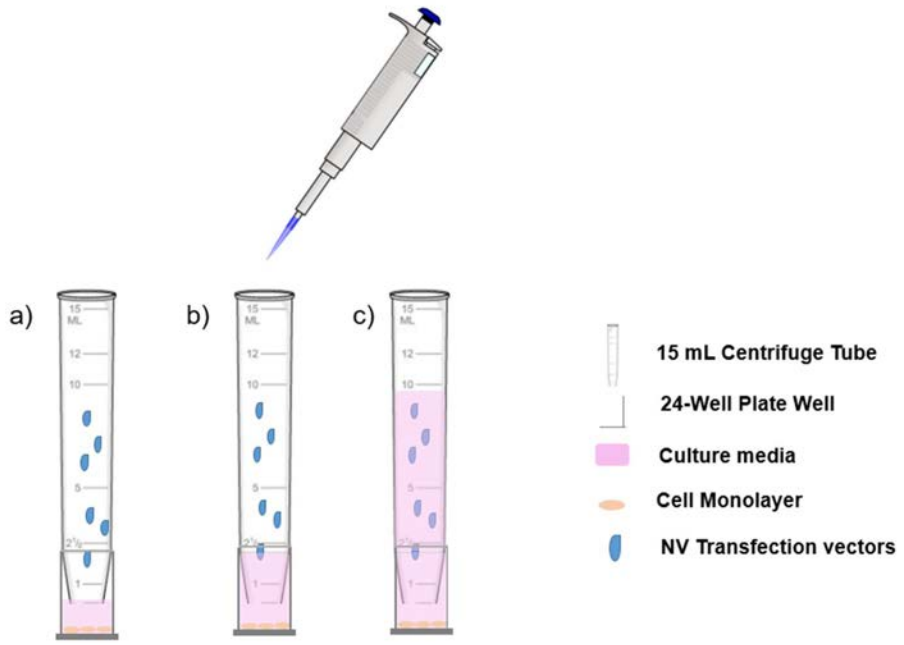

Figure 58. Scheme of the migration setup. The distance from the point where vectors were deposited to the cells was a) 7 mm, b) 20 mm, and c) 50 mm.

In this section we report how the distance from the vector synthesis location to the target cells influences the transfection efficiency ratio at defined distances: 3 mm, 7 mm, 20 mm and 50 mm (see Table 35 and Figure 59).

Table 35. Transfection efficiency (RLU/µg protein) of HAp, ACP, CaOx with DNA adsorbed and encapsulated vs. migration distance (n=3 at each run).

	24 h					48 h				
	Run 1	**Run 2**	**Run 3**	**Avg. (n=9)**	**Transfection**	**Run 1**	**Run 2**	**Run 3**	**Avg. (n=9)**	**Transfection**
Negative Control	0	0	0	0	Negative	0	0	0	0	Negative
PC 3 mm (ave. n=3)	11047	26146	23221	20138	Very High	46416	31325	27829	35190	Very High
Desv. Est. (σ)	*1528*	*2853*	*3288*			*7356*	*2158*	*2175*		
PC 7 mm	6535	26146	14710	15797	Very High	8344	31325	9007	16226	Very High
	360	*2853*	*2805*			*1076*	*2158*	*3075*		
PC 20 mm	1572	23570	2469	9204	High	1047	9513	2361	4307	High
	75	*9351*	*1999*			*41*	*4550*	*1212*		
PC 50 mm	275	9	334	206	Medium	39	16	93	49	Low
	21	*1*	*222*			*9*	*1*	*47*		
HAp-cDNA 3 mm	0	3	4	3	Very Low	1	4	1	2	Very Low
	0	*3*	*0*			*1*	*1*	*1*		
HAp-cDNA 7 mm	7	0	0	3	Very Low	14	0	1	5	Very Low
	5	*0*	*0*			*7*	*0*	*1*		
HAp-cDNA 20 mm	33	7	3	14	Low	17	1	1	6	Low
	19	*1*	*1*			*7*	*0*	*0*		
HAp-cDNA 50 mm	0	1	2	1	Very Low	0	2	0	1	Very Low
	0	*1*	*1*			*0*	*2*	*0*		
HAp-aDNA 3 mm	15	9	6	10	Low	49	25	6	27	Low
	5	*5*	*2*			*35*	*4*	*2*		
HAp-aDNA 7 mm	10	18	25	18	Low	25	23	30	26	Low
	7	*8*	*13*			*16*	*14*	*39*		
HAp-aDNA 20 mm	30	20	11	21	Low	21	13	22	18	Low
	3	*7*	*8*			*1*	*4*	*2*		
HAp-aDNA 50 mm	12	7	10	10	Low	10	5	11	8	Very Low
	3	*5*	*1*			*2*	*1*	*7*		
CaOx-cDNA 3 mm	1	7	5	4	Very Low	3	2	3	2	Very Low
	0	*4*	*3*			*1*	*0*	*1*		
CaOx-cDNA 7 mm	0	0	0	0	No Transfection	0	0	1	0	No Transfection
	0	*0*	*1*			*0*	*0*	*0*		
CaOx-cDNA 20 mm	1	2	4	2	Very Low	0	1	4	2	Very Low
	0	*0*	*2*			*0*	*2*	*3*		
CaOx-cDNA 50 mm	1	3	0	1	Very Low	0	1	0	0	No Transfection
	0	*2*	*0*			*0*	*1*	*0*		
CaOx-aDNA 3 mm	27	13	12	17	Low	208	35	21	88	Low
	9	*9*	*2*			*76*	*23*	*9*		
CaOx-aDNA 7 mm	34	11	8	18	Low	58	32	40	43	Low
	21	*2*	*3*			*7*	*13*	*17*		
CaOx-aDNA 20 mm	50	33	15	32	Low	49	35	20	35	Low
	11	*3*	*7*			*6*	*5*	*9*		
CaOx-aDNA 50 mm	15	9	18	14	Low	27	21	7	18	Low
	6	*4*	*12*			*2*	*6*	*5*		
ACP-cDNA 3 mm	1227	482	11960	4556	High	558	3075	18886	7507	High
	830	*32*	*3156*			*251*	*410*	*3568*		
ACP-cDNA 7 mm	4787	5079	13645	7837	High	7843	5833	19996	11224	Very High
	190	*1392*	*1042*			*3113*	*1252*	*5556*		
ACP-cDNA 20 mm	1	339	1703	681	Medium	41	602	907	517	Medium
	0	*66*	*582*			*3*	*35*	*372*		
ACP-cDNA 50 mm	0	32	37	23	Low	0	16	0	5	Very Low
	0	*4*	*35*			*0*	*1*	*0*		
ACP-aDNA 3 mm	1191	7514	13836	7514	High	760	9595	20897	10417	High
	619	*3673*	*2980*			*378*	*4562*	*2255*		
ACP-aDNA 7 mm	3729	4643	7514	5295	High	7131	2299	9595	6342	High
	761	*1147*	*3673*			*5166*	*201*	*9595*		
ACP-aDNA 20 mm	2	71	1299	457	Medium	19	353	626	333	Medium
	2	*22*	*474*			*1*	*41*	*655*		
ACP-aDNA 50 mm	14	0	62	25	Low	1	0	0	0	No transfection
	2	*0*	*58*			*0*	*0*	*0*		

Considering the V.H. ratio of the positive control at 3 mm, it is interesting to note the decrease of the transfection ratio with increasing migration distance. In both cases, transfection ratio

remains in V.H. up to 7 mm at 24 and 48 h. However, at 20 mm decreases to H (24 and 48 h) and at 50 mm to M (24 h) and L (48 h). These results confirm the feasibility of transfection at long distance after migration, indicating that the transfection is not exclusively a local effect.

The migration of HAp-*c*DNA and HAp-*a*DNA particles show a totally different pattern (Figure 59). The trend of transfection ratio through distance is flat instead of decreasing, although the efficiency ratio remains L for HAp-*a*DNA and in V.L. for HAp-*c*DNA. This is an important result that merits further discussion as it shows the capacity of HAp to protect DNA and transfect distant cells.

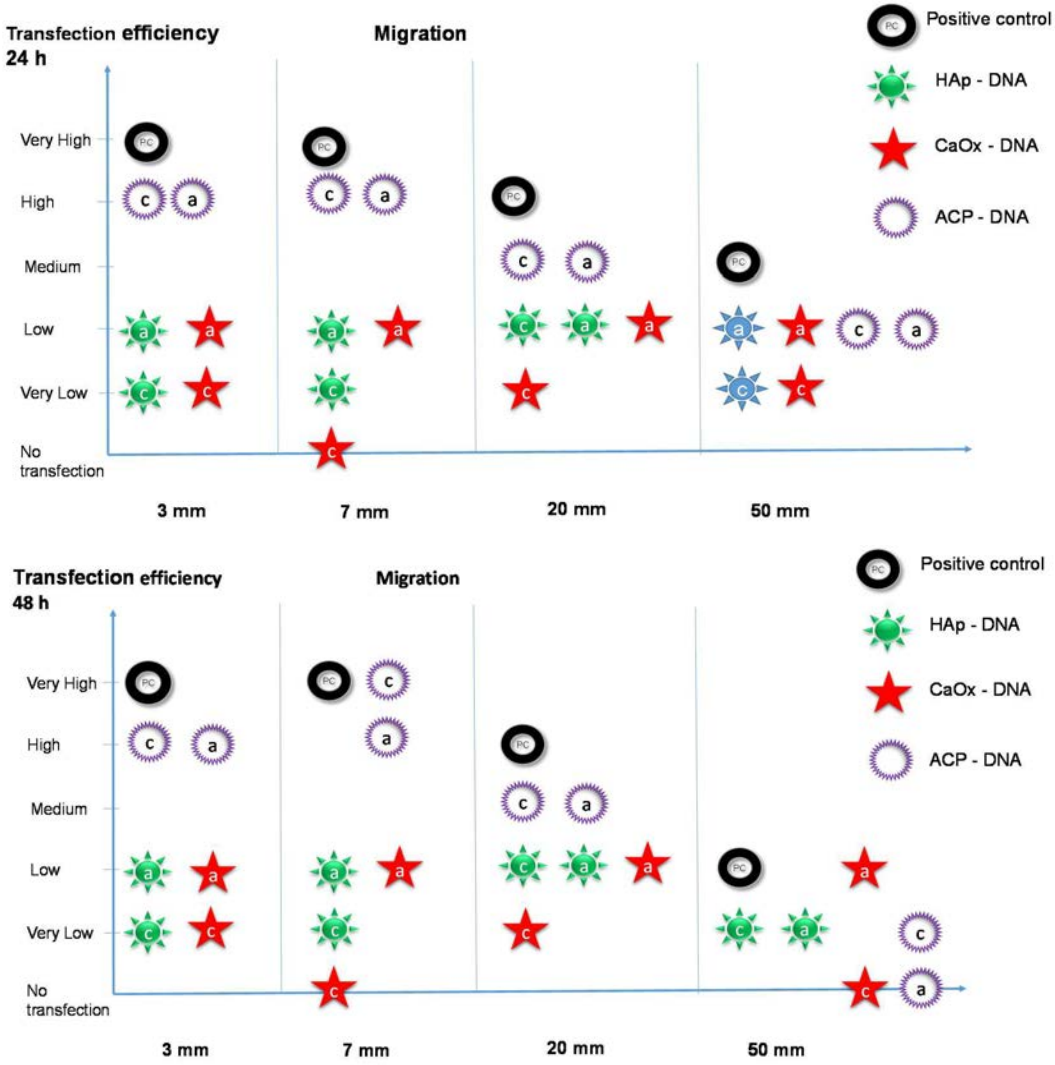

Figure 59. Transfection efficiency ratio of naked DNA, HAp, ACP, CaOx vectors at 24 and 48 hours vs migration distance. Symbols in legend denote the vector prepared by DNA co-precipitation (c) and DNA adsorption (a).

The cases of CaOx-*c*DNA and CaOx-*a*DNA show a similar tendency compared to HAp. As can be seen in Figure 59, it is maintained the capacity of transfection in L range for the CaOx-*a*DNA and V.L. or “No transfection” for the CaOx-*c*DNA. Nevertheless, the transfection at long distances is still feasible being observed less transfection at 48 h than at 24 h. Finally, the case of ACP shows an analogous profile compared to the PC. Again the H or V.H. (48 h) ratio observed at shorter distances (3 mm and 7 mm) decreases at longer distances, rating M at 20 mm. At 50 mm, ACP-*c*DNA shows L (24 h) or V.L. (48 h) and ACP-*a*DNA scores L (24 h) and “No transfection” (48 h).

DISCUSSION

8 DISCUSSION

8.1 TRANSFERENCE OF HYDROXYOLITE CONCEPTUAL BACKGROUND TO BREAST CANCER TISSUE CLINICAL SCENARIO

A few studies had been developed in search of basic mechanisms involved in the formation of hydroxyapatite (HAp) calcifications containing nucleic acids. Up until recently, no previous work had been reported at atomistic level, showing the thermodynamics of the synthesis of a hybrid system made of a nucleic acids on HAp calcifications. Such a conceptual work lead to the conclusion that Nature should be able to synthesize hydroxyolites in natural environments when some ions and the nucleic acid biopolymer converge in the same location and at the same time. Following that assumption, a Concept article was published by Turon et al. (2015)[116] describing natural scenarios that might result in the synthesis of those particles by a cell. It is worth noting that most of them were related to physical or chemical aggressions to the cells. The potential consequences of the generation of those hydroxyolite particles were enumerated in terms of their role as carriers of DNA or RNA that under the shell of HAp were protected against such aggressions. Here, we make use of that conclusion, as it explains that mineralization processes are ubiquitous and thermodynamically favored when constituting ions of HAp and the nucleic acids are in the same location and can interact freely. For that reason, following our approach, we hypothesized that hydroxyolites should be synthesized in natural environments, for instance in living tissue, and they should contain RNA or DNA, healthy or mutated, methylated or unmethylated. We looked for real scenarios where the synthesis of such hybrid systems could be feasible without human intervention. After a preliminary research, we found a first indirect evidence of the existence of hydroxyolites, reported by Weinbach and von Brand (1967)[242] fifty years ago. It was located inside of mitochondria where the authors described a calcification containing nitrogen and ribose that finally assigned to be RNA inside HAp.[242]

Very recently, Tsolaki and Bertazzo (2019)[243] described a parallel approach to the one we use in this thesis, in order to understand the pathological mineralization of living tissue by using methods based on materials science. They argue that mineralomics might lead to a deeper understanding of the role, mechanisms, and causes of mineral formation in soft tissue related

to some diseases (i.e. cardiovascular and ocular calcifications). As they mention, such a research pathway requires a multidisciplinary expertise to gather the hidden information behind calcifications, including organic and inorganic components, and to recognize how the physicochemical features of materials (i.e. morphology, composition, phase and crystallinity) is as relevant as cells and extracellular matrix are. A recent work of Vidavsky et al. (2018)[97] pursue to dive deeper in the biomineralization pathways using a 3D culture model of breast cancer microcalcifications. They aim to elucidate their role in cancer progression, trying to elucidate if such calcifications are related to a dystrophic mineralization or a bone-like mineral deposition. Their work focus on studying spheroids generated by several cell lines with different tumor progression. They concluded that concentration levels of alkaline phosphatase inversely correlated with malignancy potential but directly with osteopontin, supporting the idea that breast cancer calcifications are distinct from an osteogenic biomineralization.

Through this thesis, our purpose is to transfer such concepts inherited from Chemistry to Medicine in order to adapt them to the context of breast cancer. We focused on breast cancer as it shows evidence of HAp calcifications and a fingerprint of cell death processes related to the tumor evolution. Consequently, through the results reported in Chapter 7, we have demonstrated that DNA biomineralization occurs when DNA interacts with HAp forming ions (*i.e.* Ca^{2+}, PO_4^{3-}, OH^-). We note that several cell death mechanisms, such as necrosis and apoptosis, are associated with calcium and magnesium overload inside cellular compartments. Particularly interesting is the example of mitochondria, where DNA mutations are more often observed and where the formation of calcium phosphate precipitates containing organic matter had also been reported since long ago, during the decade of 1960s.[244] The release and fragmentation of DNA that frequently occurs during cell death in combination with the loss of functionality of the different organelles may induce the adsorption of DNA on HAp freshly formed. In the same manner, the co-precipitation of DNA with the excess of Ca^{2+} and PO_4^{3-} related to cell death process should lead to the formation of natural hydroxyolites. Such a combination of empirical evidences points towards the feasible the synthesis of natural hydroxyolites in the context of breast cancer. In addition, cells are expected to die due to the effect of physico-chemical aggressions. One of the most likely scenarios leading to cell death is the lack of oxygen supply as it can happen at the center of a

tumor due to insufficient irrigation resulting in a necrotized area. However, we can extend the list of attacks to the negative effect of radiation (i.e. UV or gamma) or related to the toxic effect of some chemicals, coming from the environment or as a result of the metabolic processes of the own cells under a chemical attack, as can be the generation by mitochondria of Reactive Oxygen Substances (ROS) under such circumstances. All of them are candidates to trigger cell death processes and consequently, generate natural hydroxyolites. Furthermore, we took into consideration that some authors guessed the presence of nucleic acids as RNA on HAp calcifications and others found indirect evidence through spectroscopic methods detecting amide bands on HAp microcalcifications that were assigned to both proteins and nucleic acids. All of them were based on pure empirical exploration, looking for correlation between of their chemical content with the evolution of the disease, but to our knowledge, there were no theoretical model based on the thermodynamics of the calcifications behind such research. They were more focused on the empirical analysis of chemical composition of the calcifications in an attempt to correlate it with the prognosis of the patients. In good agreement with our understanding of the current situation about the research related to the role of microcalcifications, O'Grady and Morgan (2018)[92] stated in their recent review "*There are no reports which attempt to bring together recent basic science research findings and current knowledge of the clinical significance of microcalcifications*". We aim to contribute to this field with a theoretical model that explains and predicts how microcalcifications are and how they behave, for instance, under the influence of an acidic environment.

In the previous chapters, we have introduced a synergistic theoretical-empirical approach in order to understand the origin and implications of hydroxyapatite microcalcifications found in living breast cancer tissue. Such an approach has been extremely fruitful because after transferring those theoretical concepts to the selected clinical scenario, we have confirmed the existence of natural hydroxyolites in breast cancer tissue, as predicted by the simulation studies. Moreover, consistent with our approach, we noted that hydroxyolites must have similar hybrid structures than non-viral vectors of transfection (NVT) and this means we introduce a new perspective about the role of traditional breast microcalcifications.[245] Thus, we have explored their ability to transfect cells using both DNA adsorbed in HAp chemically synthesized and HAp synthesized by a cell culture. The results of that line of research are of

outmost interest in terms of its potential impact, understanding how transfection processes might work when natural hydroxyolites are formed in the context of breast cancer and breast cancer multifocality. O'Grady and Morgan (2018)[92] also reviewed the biological effects of HAp microcalcifications. However, we note they did not mention the possibility that such microcalcifications could be related to non-viral vectors of transfection, and the transfection process by itself, as a potential explanatory factor of malignancy. A hypothesis we consider one of our contributions.

On the other hand, we used again the theoretical-empirical approach in order to understand the different role of microcalcifications observed in breast tissue. In section 7.3, we have explored whether type I calcifications, frequently observed in mammographic scans but more related to benign prognosis, could adsorb or encapsulate nucleic acids as we were interested in knowing if they could be considered a natural NVT as HAp. That study lead to increase our understanding about the role of calcium oxalate (CaOx), and more interesting about the role of Mg^{2+} ion. Our *in silico* studies predicted that DNA cannot be encapsulated in CaOx and that DNA can only be adsorbed on it when Mg^{2+} ion is not present. We confirmed such behavior through empirical *in vitro* studies later, confirming how powerful has been is the strategy we used by transferring concepts and techniques from one discipline to the other.

8.2 CHARACTERIZATION OF HYDROXYOLITE CALCIFICATIONS BY RAMAN SPECTROSCOPY

Raman spectroscopy has been proposed as a suitable technique to analyze biopsies, successfully distinguishing between calcium oxalate (CaOx, type I) and hydroxyapatite (HAp, type II) calcifications, and being able to identify additional ions and molecules that might enter in contact with them coming from the surrounding tissue. According to our literature review, some authors have used Raman spectroscopy to analyze the chemical composition of breast cancer calcifications. We highlight the contributions of Haka et al. (2002, 2005, 2009),[72,129,130] Shafer-Peltier et al. (2002),[134] Baker et al. (2007, 2010),[73,246] Kerssens et al. (2010),[136] Saha et al. (2011),[84] Brozek-Pluska et al. (2012),[131] Liang et al. (2014),[247] Sathyavathi et al. (2015),[248] Kunitake et al. (2018),[249] Lyng et al. (2019)[250] and as the ones who have been more active in the field. Recently, Gao et al. (2017)[123] reviewed the clinical application of Raman spectroscopy for breast cancer detection but not only focusing on microcalcifications. We use them as a framework for our discussion and to confirm our hypotheses and results about the existence of hydroxyolites in breast tumor tissue.

Saha et al. (2011)[84] noted that Raman analysis was able to detect microcalcifications <10 µm, which is one order of magnitude smaller than those that can be detected on mammography as its detection limit is around 100 µm. However, Kunitake et al. (2018)[249] detected calcifications smaller than 2 µm. In our own study, we confirm the detection of such small particles detecting calcifications in the submicrometric range as the detection limit of the Raman equipment we used was established within 200-500 nm. However, we focused on scanning calcifications up to 20 µm in order to facilitate the localization of DNA on their surface or interior. In parallel, we decided to analyze the smallest ones using fluorescent probes for DNA and HAp due to its high selectivity, and its lower detection limit. Although those results are not included in this thesis, they were consistent with the results obtained by Raman spectroscopy that we discuss here.

Shafer-Peltier et al. (2002)[134] reported an interesting aspect related to the preservation of samples to be analyzed by Raman. The standard fixation process of the tissue samples might alter the tissue proteins although did not affect the relatively inert mineral deposits in the calcifications. Sathyavathi et al. (2015)[248] were aligned with them and stated that preparation might can have a non-negligible impact on the spectrum interpretation. Formalin fixing and

paraffin embedding resulted in the appearance of a band at 1490 cm^{-1} that might reduce the amide-I peak (due to the formation of tertiary amides). Consistent with their conclusion and our own observations, we adopted a sample conservation protocol freezing tissue samples without using additives, as formalin or paraffin, in order to avoid the degradation or removal of nucleic acids that could end in damaging any natural hydroxyolite contained in the sample. Additionally, the fluorescence background on the Raman spectra, as a result of the paraffin method to fix the samples (used generally in Biobank samples handling and storage), is a drawback to be avoided. Our study shows that Raman spectroscopy on samples treated with OCT discriminate between the chemical composition of microcalcifications in breast diseases, easily identifying HAp and CaOx substrates. Moreover, the obtained data exhibit the efficacy of the sampling method making feasible the assessment of the chemical composition of HAp microcalcifications.

It is worth mentioning the initial work of Haka et al. (2002)[72] who described how type I and type II calcifications embedded in breast cancer tissue could be identified by Raman spectroscopy. They reported that CaOx dihydrate crystals were scarcely found in proliferative lesions, including carcinoma. A fact that we also observed as very few calcifications (4 %) were made of CaOx in our study, a ratio in good agreement with Scimeca et al. (2014)[100] who compiled several works where CaOx found in biopsied tissue ranged from 0.4 % to 28.8 %. Moreover, they inferred that HAp microcalcifications found in malign ducts typically contained lesser amount of calcium carbonate and a higher amount of proteins than those formed in benign ducts. Finally, they mentioned that such HAp calcifications contained, using their words, "*biological impurities*" but without describing their chemical identity, a fact that is of a high interest from the perspective of the hydroxyolite investigation we perform in this thesis. An interesting precedent for our purpose was reported by Baker et al. (2010),[246] who after analyzing a long series of patients using FTIR, reported IR vibrational modes that might be compatible with proteins, lipids or nucleic acids (DNA) in some breast HAp calcifications.

Since the seminal work of Haka et al. (2002),[72] the main bands used by the researchers in order to differentiate calcifications had been 912 cm^{-1} and 1477 cm^{-1} for CaOx and the most intense band of HAp in its spectrum located at 960 cm^{-1}. We note that the number of Raman studies focusing on HAp (n=7) is significantly higher than the studies reporting CaOx calcifications (n=2), most likely due to the difficulty of obtaining CaOx samples from biopsies

as they are used for diagnosis purposes. Additionally, the higher interest of HAp has been justified due to the worst prognosis associated with HAp and the easier accessibility to samples from extracted tumors after their assessment, that mainly contain HAp and not CaOx.

Through time, some contributions have tried to elucidate the identity of the organic matter deposited on the microcalcifications. The most complex part of the spectra to be interpreted belongs to the fingerprint of such molecules where different authors have reported different bands for the same substances as fat (1294, 1447, 1660, 1750, 2909 cm^{-1}),[251] collagen (1268, 1447, 1655, 2933, 3320 cm^{-1}),[252] proteins (1050, 1220, 1450, 1662, 2940 cm^{-1}), lipids (1130, 1301, 1450, 1660, 1742, 2854, 2888, 2940, 3009 cm^{-1}), phospholipids (1080 cm^{-1}), amino acids as phenylalanine (1004, 1026, 1153, 1182, 1585 cm^{-1}), tyrosine (1182 cm^{-1}) and tryptophan (1208, 1610, 1657 cm^{-1}), carotenoids (1004, 1158, 1518 cm^{-1}), cholesterol (1440, 1670,2838-2906 cm^{-1})[253] and nucleic acids.

Table 36. Raman studies focused on breast tissue. Bands reported for HAp and nucleic acids.

Raman studies on calcifications	HAp					Nucleic acids (NA or DNA)					
Haka et al.[72] (2002)	960	1028		1061	1075						
Haka et al.[129] (2005)	958-961		1040		1076						
Kerssens et al.[136] (2010)	960										
Saha et al.[84] (2011)	960										
Liang et al.[247] (2014, NA)	958							1072			1663
Sathyavathi et al.[248] (2015)	960										
Gao et al.[123] (2017)	960										
Kunitake et al.[249] (2018, DNA)	961					667-697	785-800	1081-1106	1336-1351	1573-1593	
Lyng et al.[250] (2019, NA)											1662
Thesis	**960**						**785**		**1372**	**1576**	

We note as can be seen in Table 36 that only two works mention that some of the microcalcifications were composed by the combination of nucleic acids and HAp: Liang et al. (2014)[247] and Kunitake et al. (2018),[249] although some others mentioned that such organic fingerprint could be compatible with some bands of nucleic acids or proteins, usually related to Amide I vibrational mode at ~1660 cm^{-1}.[254] Liang et al. (2014)[247] were the first to explicitly mention that HAp calcifications were associated only with nucleic acids but they selected two conflictive bands for such assignation, 1072 cm^{-1} (assigned by them to the phosphate skeleton

of nucleic acids, O-P-O) and the one at 1663 cm^{-1} (assigned by themselves to Amide I, α-helix, V(C=O) of proteinic collagens and elastins, and V(C=C) of lipids instead to v(C4=O) – T, G, C of that might correspond to nucleic acids). We note that the band at 1072 cm^{-1} is likely to be mixed up with CO_3^{2-} band, a frequent substituting ion in HAp, usually found within 1070-1080 cm^{-1} as reported by many authors as Haka et al. (2002, 2005),[72,129] Baker et al. (2007),[73] Kersens et al. (2010)[136] and Sathyawathi et al. (2015).[248] They reported the peak at 1080 cm^{-1} and it was assigned to the characteristic v1 vibration mode of carbonate from the HAp. Kerssens et al. (2010)[136] reported a reduction in HAp crystallinity caused by higher carbonate content because they observed a higher FWHM and a small peak shifts in the band 960 cm^{-1}. However, it may also be representative of the phosphate from nucleic acids or phospholipids in the tissue. On the other hand, the band at 1663 cm^{-1} might be confused with the strong protein band reported by Haka et al. (2002)[72] and Gao et al. (2017)[123] at 1664 cm^{-1}. Thus, such a risk might put to the question the univocal identification of nucleic acids. Gao et al. (2017)[123] only mention 1662 cm^{-1} as a useful band to identify nucleic acids in their review. We remark that band was useful to identify nucleic acids when we analyzed hydroxyolites synthesized *in vitro* in our laboratory (see section 7.2). However, it was not useful in the fresh tissue calcifications due to the mentioned interferences and overlapping with bands that are not possible to be assigned.

The most remarkable work for our research is the contribution of Kunitake et al. (2018)[249] who selected the following intervals 667-697, 785-800, 1081-1106, 1336-1351, 1373-1398, 1573-1593 cm^{-1} in order to map what they termed a "DNA-like" component deposited on calcifications diagnosed as high grade ductal carcinoma in situ (DCIS) and invasive cancer, the same kind of samples we used in this thesis as it presents a high ratio of calcifications (> 90%). We recall that the bands we selected to confirm the DNA presence in our study through the advanced MCR algorithm were 785, 1340, 1575 cm^{-1}, in perfect concurrence with their intervals despite the fact we performed our research a couple of years before their publication. We used advanced multivariate methods to analyze the spectra of calcifications imaged in the tissue sections. Specifically, Multivariate Curve Resolution (MCR) was used to deconvolve molecular components that are present in the studied calcifications, particularly we split the signal in three main components: HAp, DNA and others. In this way, molecular spectral components and their relative abundance maps can be plotted, providing

information about the composition and distribution of molecules in the tissue calcifications. After MCR analysis, the HAp calcifications showed a component that contained bands mainly assigned to DNA although often mixed with a few bands from other biomacromolecules such as lipids or proteins. The assignments on the DNA spectral component were validated by comparing the spectra of the molecular components obtained by MCR with the Raman database collected from HAp-DNA samples synthesized in the laboratory and DNA. On the other hand, DNA was not found in the samples that contained CaOx calcifications. This result merits further research as we discuss in the next section.

We consider the work of Kunitake and co-workers to be totally aligned with our research taken into consideration they unveiled the existence of hydroxyolites with DNA adsorbed. We reproduce in Figure 60B their finding where can be easily observed the natural hydroxyolites formed by the combination of HAp (blue) and DNA-like in yellow.

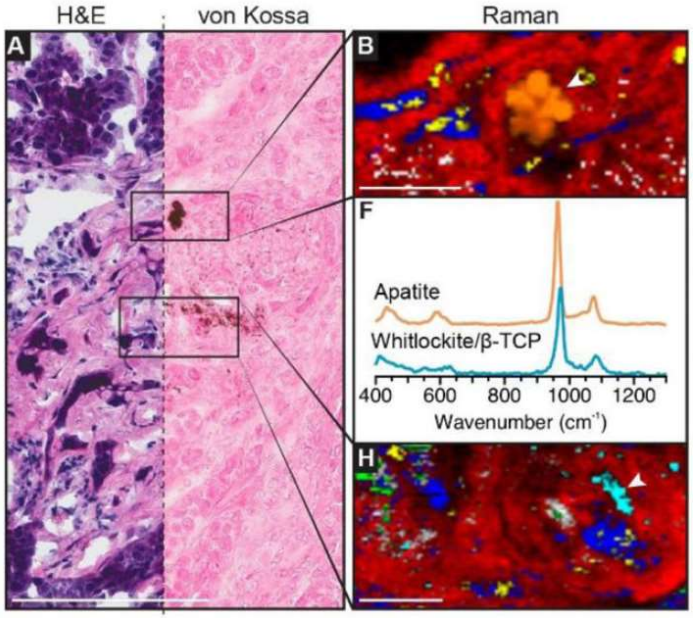

Figure 60. (B) Raman combination map corresponding to the upper region (apatite: orange; collagen: red; NCPs: blue; DNA-like: yellow; cholesterol-like: white). (H) Raman combination map of the lower region (whitlockite: cyan; collagen: red; NCP: blue; DNA-like: yellow; cholesterol-like: white; carotenoid: green). Figure extracted from Kunitake et al. (2018)[249] Reproduced with Elsevier Publisher permission.

It is worth emphasizing they did not look for the existence of hydroxyolites by encapsulation as they did not mention a Raman scan through Z-axis. For that reason, this thesis unveils for the first time, the existence of natural hydroxyolites containing DNA encapsulated.

Biomineralized DNA was revealed through the Z-axis scan we reported in section 7.2. Figure 60 confirms the presence of DNA in natural HAp calcifications, as predicted by the previous works of our group, and the model of DNA biomineralization described in our approach (section 2). We will discuss the potential role of such encapsulated DNA in section 8.4 and such a structure is deemed to be a non-viral vector of transfection.

Additionally, Kunitake et al. also looked for the presence of Mg^{2+} in the calcifications they analyzed. However, they do not report the association of such whitlockite calcifications with DNA. Kunitake et al. detected the presence of Mg^{2+} in calcifications to form whitlockite calcifications, $Ca_9Mg(PO_3OH)(PO_4)_6$ associated with the DNA-like component. An observation that confirms the interest of our further research about the role of Mg^{2+} in such calcifications. The presence of Mg^{2+} was also confirmed by Scimeca et al. (2014)[100] using an energy dispersive X-ray microanalysis of malignancy associated microcalcifications and by X-ray diffraction that showed a mix of whitlockite and magnesium substituted HAp. The role of Mg^{2+} is still unclear but apparently it correlates with malignant lesions confirming the interest of investigating more about it as we do in the following sections. Despite the fact that Shafer-Peltier et al. (2002)[134] were more focused on tissue components than on microcalcifications, they mentioned the existence of other calcium phosphates different from HAp in their spectra, probably they would be amorphous calcium phosphate (ACP) and Brushite as they are precursors of HAp. Such a finding opens, from our perspective, the possibility that other calcium phosphate phases might interact with nucleic acids and behave as non-viral vectors of transfection as we introduced in the objectives of this thesis.

Summarizing, we have achieved the goal of identifying natural hydroxyolites embedded in breast cancer tissue. Such finding confirms previous works of Liang et al. and particularly, the work Kunitake et al. who reported univocally the coexistence of nucleic acids and HAp. We note that they only reported hydroxyolites by adsorption and our work enlarge such result by revealing the existence of hydroxyolites by encapsulation that will enhance the protection of the encapsulated biopolymer. We consider after analyzing the findings reported in section 7.2. to validate the first hypothesis of this thesis: “Hydroxyolites, nucleic acids adsorbed or encapsulated in hydroxyapatite, are naturally synthesized in the context of a human breast cancer tumor”.

8.3 COMPARISON OF CALCIUM OXALATE AND HYDROXYAPATITE FEASIBILITY TO ADSORB AND ENCAPSULATE NUCLEIC ACIDS

Our published work (see Annex 3) renders a physico-chemical contribution to a long term debate in the medical community regarding if and why breast cancer patients with HAp-based microcalcifications have a worse prognosis compared to those showing mostly CaOx-based microcalcifications. The first part of the results presented in this section deals with the energetics and statistical mechanics of mineral···DNA complexation, and the second part proves that DNA can only be encapsulated without denaturalization in HAp-based matrices thus forming biominerals not only able to encapsulate and transport DNA but also to deliver it.[176]

Thus, the double helix is able to accommodate itself onto the HAp surface, independently of the methylation, by establishing a balance between the attractive and repulsive interactions between the phosphate groups of DNA and the Ca^{2+} and PO_4^{3-} ions of the mineral, respectively. The formation of such interactions is reflected in Figure 42c for R1A and DD, respectively, which display a representative snapshot of the dodecamer adsorbed onto HAp and compares the adsorbed double helix with a canonical one. The affinity of HAp towards the double helix of DNA has been attributed to the complementarity between the mineral and the phosphate groups of the DNA backbone, which were found to exhibit isomorphic planes.[114]

The RMSD calculated with respect to the canonical B-DNA used as starting point was close to 10 Å for both sequences, which is significantly higher than the values obtained for complexes with HAp. This is because of the repulsive interactions between the oxalate anions (Ox^{2-}) and the phosphate groups of the double helix that, in this case, are not shielded by the attractive interactions of the latter with the Ca^{2+} ions. Apparently, these results indicate that the geometry of CaOx is not appropriated to preserve the tertiary structure of the biological DNA when the latter is embedded inside of the nanopore.

Overall, these results indicate that the cavity generated in HAp allows B-DNA double helices encapsulation without producing mineral-induced stress, while the opposite situation is obtained when CaOx nanopores are studied. Although this feature might be related with the benign and malignancy cancer prognosis associated to CaOx and HAp microcalcifications,[81,210]

no experimental observation relating the medical diagnosis and the functionality of the genes linked to cancer disease has been reported yet.

For this purpose, these results unambiguously demonstrate that the mineralization of DNA from Ca^{2+}- and Ox^{2-}-containing solutions mainly occurs through the adsorption of the biomolecule on the surface of the formed CaOx particles, whereas the encapsulation of DNA inside such inorganic particles is very limited.

These and the previous $\Delta\Delta_{Gb}$ and $\Delta\Delta G_{hyd}$ differences indicate that the coordination of an extra Ox^{2-} with already Ox^{2-}-bound Ca^{2+} or Mg^{2+} instead of DNAp-bound Mg^{2+} is favored before the precipitation of any of the complexes may happen. In addition, $Ca^{2+}\cdots Ox^{2-}$ and $Ox^{2-}\cdots Ca^{2+}\cdots Ox^{2-}$ have much more favorable hydration than their corresponding Mg^{2+} counterparts. Finally, Mg^{2+} prefers to coordinate with two Ox^{2-} rather than with DNAp and Ox^{2-}, which enables CaOx and MgOx calcifications to grow DNA-free in the solution as previously confirmed by in the lab tests.

In summary, we systematically compared the mineralization of DNA in CaOx and HAp using a synergistic computational− experimental approach. With the latter material traditionally related with transfection of cells with nucleic acids and with the formation of microcalcifications inside living organisms, the biomedical application of DNA-based biominerals might be further improved by understanding the fundamental interactions associated to adsorption and encapsulation of such biomolecules in HAp and CaOx.

Using atomistic MD simulations, we studied DNA adsorption and encapsulation in CaOx and HAp. Although DNA can be adsorbed onto the most stable facet of the two minerals, important differences are found. HAp is able to preserve the DNA double helix because of the complementarity between their phosphate anions through isomorphic planes, while the repulsive interactions between the oxalate anions of CaOx and the polyphosphate backbone of the biomolecule cause the destabilization of the double helix.

Besides, DNA nucleates the growing of HAp when it is immersed in an ionic solution containing Ca^{2+}, Mg^{2+}, and PO_4^{3-} ions and encapsulates it inside HAp nanopores maintaining the stability of the double helix. The opposite behavior is observed when DNA is immersed in a Ca^{2+}, Mg^{2+}, and Ox^{2-} solution and encapsulated in CaOx pores: the minerals grow separately from DNA, and the double helix undergoes severe structural alterations. These theoretical results have

been corroborated experimentally by preparing DNA−HAp, DNA−CaOx, and DNA−MgOx complexes. Furthermore, QM calculations on model complexes in the aqueous solution show that Ca^{2+} ions prefer to coordinate with two Ox^{2-} than form triads involving an Ox^{2-} and a phosphate group from DNA.

8.4 DETERMINATION OF THE TRANSFECTION CAPABILITIES OF HYDROXYOLITES

Through the last decades, several articles dealt with transfection efficiency of non-viral vectors, particularly since viral vectors demonstrated to have some shortcomings and researchers recuperated the interest for non-viral vectors.[168,169] Among them, calcium phosphate are one of the most studied despite showing a low a transfection efficiency. Moreover, the transfection process of calcium phosphate is a well-studied process and several authors described many influencing factors that explain such a low transfection ratio and the poor reproducibility of the process,[184] for instance, due to cell type,[180] phase of the cell cycle,[181] reagent concentration, precipitation time, size of particles, mixing process, temperature,[144,156,164,182,183] presence of dispersants,[185] and soluble calcium ions that facilitate the DNA uptake and further endosomal escape.[186]

Based on Kunitake et al. (2018)[249] findings, who detected nucleic acid bands in HAp calcifications extracted from breast cancer tissue using Raman spectroscopy and our own results about the existence of such particles (Marro et al. (2021),[b] we concluded that transfection vectors are indeed created by Nature. We consider that is worth studying in detail the behavior of those vectors in order to understand the risks related to their existence in living tissue. Particularly interesting is the fact that they could be carriers of tumor DNA and they might act as non-viral vectors transfecting the surrounding cells or migrating agents able to transfect a distant tissue.

In this work, we aim to understand how such submicrometric calcifications found in breast cancer tissue in combination with nucleic acids adsorbed or encapsulated might behave in living tissue after being naturally formed. We did not intend to optimize the efficiency of such vectors. For that reason, we used a well-established transfection protocol, and the epithelial

[b]Marro, M., Rodríguez-Rivero, A. M., Araujo-Andrade, C., Fernández-Figueras, M.T., Pérez-Roca, L., Castellà, E., Navinés, J., Mariscal, A., Julián, J.F., Turon, P., & Loza-Alvarez, P. Unravelling the encapsulation of DNA and other biomolecules in HAp microcalcifications of human breast cancer tissues by Raman imaging. *Cancers.* 2021; *13*(11): 2658. https://doi.org/10.3390/cancers13112658

cell line A549 (widely used as a transfection host) in order to study how differences in the synthesis and composition of the vectors might affect the transfection efficiency ratio. The positive control (PC) used as a reference belongs to the calcium phosphate family but includes 4-(2-hydroxyethyl)-1-piperazineethanesulfonic acid (HEPES) buffer that acts as neutralizing agent of the negative charges of DNA, controls the pH during the particle synthesis and regulates the pH along the transfection process. Therefore, the PC efficiency ratio is optimized and scores V.H. Moreover, the transfection ratios obtained for all tested vectors show individual results with a high variability which has been accepted as a basis to understand how those natural vectors could behave inside of a living organism. As a result, we extrapolate their ability to transfect in a simplified *in vitro* model, without using facilitating additives, to the more complex physiological environment where a natural transfection could take place.

Focusing on the results reported in this work, we observe that the PC shows a transfection rate we classified as V.H. Conversely, the signal corresponding to the negative control (NC) is zero, thus, no transfection was observed. Therefore, we corroborate that the transfection protocol was correctly applied evidencing the feasibility of transfecting A549 cells. On the other hand, naked DNA does not show any transfection, as it is not able to cross the cell membrane due to its negative zeta potential (from -30 to -70 mV). This fact allows foreseeing that there will be no transfection in living tissue when naked DNA is released to the extracellular matrix, for instance, as a consequence of necrotic cell death processes, not only due to its negative zeta potential but also as a consequence of its large size. In addition, nuclease enzymes could degrade DNA in a short period of time, minimizing the risk of transfection. After analyzing the HAp vector results (HAp-*c*DNA and HAp-*a*DNA), we observe that both types of *in vitro* chemically synthesized HAp vectors confirm the potential to transfect cells. Nevertheless, their transfection ratio is much lower than the PC vectors.

However, after analyzing the results of the addition of Ca^{2+}, that enhance the transfection, we note the relevance of looking for factors that can provide an additional bursts of Ca^{2+} as it significantly enhances the transfection of naked DNA up to H interval. This result is coherent with other authors' work that mention Ca^{2+} ion as a key factor to enhance the transfection efficiency.[255,256] Furthermore, we point out that during the course of a cell death process, as it occurs in the center of a tumor, significant amounts of Ca^{2+} are likely to be released from the cell calcium storage sites, mainly from endoplasmic reticulum that might trigger the

synthesis of such natural vectors, increasing the likelihood of transfection. Additional Ca^{2+} added to the transfection vector solution is a highly influencing factor as it changed the performance of HAp vectors and the transfection capability of naked DNA. In both cases, the additional Ca^{2+} boosted the efficiency ratio of hydroxyolites. We note that in HAp-*a*DNA(Ca^{2+}), the extra calcium neutralized the negative charge and reduced the particle size average, increasing the likelihood of transfection as the vector fits in the optimal transfection window. The extra layer of calcium might have a favorable effect neutralizing the negative charge on the surface coming from the exposed phosphates in the HAp lattice or negative backbone of DNA, a fact that is not possible in the particles with DNA encapsulated as only can make the outer layer thicker. Additional Ca^{2+} ions increase the positive charge of the particle surface that will be compensated by an external corona of chloride ions in the outer solvation layer. As a consequence, the uptake by the cell is facilitated and the transfection enhanced. Nevertheless, we assume that Ca^{2+} should have an additional effect beyond the charge neutralization. Such effect could be related to the impairment of DNase inside the lysosomes that could facilitate the preservation of internalized DNA carried by the vector and further release into the cytosol. Bish et al.[168] reported that calcium phosphate nanoparticles can cross the cell membrane via calcium ion-mediated endocytosis. Furthermore, Truong et al.[257] proposed that CaP stimulates DNA cellular uptake involving either endocytosis of the membrane-bound DNA complex or enhanced permeabilization of the plasma membrane to facilitate DNA entry. However, Haberland et al.[258] indicated that it is possible to differentiate between the Ca^{2+} role in cellular uptake of H1 (or mediator)-DNA complexes and endocytotic release because both Ca^{2+} ions and CaP microprecipitates enhanced the transfection to similar levels.

On the other hand, we note that the presence of Cl^-, as Ca^{2+} counter ion, may play a role creating a thin layer of ions on the surface of adsorbed DNA. Chloride ions are engulfed together with the particle and become internalized in the endosome. Such an ion will help to increase the osmotic pressure inside the endosome that will result in the final release of the nucleic acid to the cytosol after endosome rupture. This fact has important consequences in terms of the role of natural hydroxyolites because the generation of the transfection vector might occur in two steps. The first would be the adsorption of the nucleic acid on an already formed HAp calcification, the second would be related to a further wave of Ca^{2+} and Cl^- ions

from adjacent dying cells that may reduce the average size of already existing submicrometric calcifications and neutralize the charges, enhancing transfection capabilities.

Transfection assays reveal three important features. Firstly, we note that the results of the negative control (NC) demonstrate that no luminescent signal is originated by cells and cell culture media in absence of reactants. Secondly, the positive control (PC) based on a standardized transfection vector made of calcium phosphate in combination with HEPES Buffer Solution (HBS) and luciferase pDNA supplied in the transfection kit resulted in a V.H. transfection rate at 24 and 48 hours, demonstrating the correct application of the transfection protocol and the feasibility of A549 cells transfection with the protocol used. Thirdly, naked DNA showed no luminescence signal above the threshold confirming that there is no transfection when DNA naked is used as a vector. We observed a positive transfection in all hydroxyolites studied. However, the variability of transfection within the same day and inter-days was assessed as very high, justifying the use of a scale based on magnitude orders that allow to detect the significant differences in transfection efficiency when comparing several tested conditions (Table 9). According to these results, HAp-*c*DNA and HAp-aDNA are capable to transfect A549 cells, showing hydroxyolites are able to introduce DNA inside target cells when it is absorbed or co-precipitated on them.

8.5 DETERMINATION OF Mg^{2+} ION EFFECT ON ADSORPTION, ENCAPSULATION AND TRANSFECTION OF HYDROXYOLITES

Magnesium is found in nature in many different environments and playing different roles (e.g. sea and fresh water, biological fluids, and biological minerals). Mg^{2+} content in hard tissues is relatively low (e.g., 1.23, 0.72, and 0.5–0.9 wt % in dentine, bone and cementum, respectively), but it plays an important function in terms of homeostasis and metabolism.[259] Despite a relatively large number of investigations, the influence of Mg^{2+} in breast cancer and its role in a hydroxyapatite (HAp) calcification remains unclear and results generate some controversy.[260]

Scimeca et al. (2014)[100] performed elemental microanalysis on breast microcalcifications. The presence of calcium oxalate (CaOx) was found in benign lesions in 81.8 % of cases, whereas in 97.7 % of malignant lesions were found complex forms of microcalcifications, identifying among them HAp containing Mg^{2+}. Such a substitution of Ca^{2+} by Mg^{2+} in HAp was detected a significant part of malignant lesions. Mg^{2+} incorporation into HAp hinders particle growth by replacement of Ca^{2+} by Mg^{2+}. Additionally, Mg^{2+} is related with the mineralization of tissues, stimulating osteoblast proliferation.[261] Mg^{2+} is a significant modulator of intracellular Ca^{2+} concentration and pH. Some authors hypothesized that pH is expected to be low in malignant tissue, thus impeding integration of Mg^{2+} into the apatite lattice resulting in the formation of whitlockite ($Ca_9Mg(PO_3OH)(PO_4)_6$). Such a mechanism would offer an explanation for the enlarged whitlockite presence in malignant cases, and also higher levels of Mg^{2+} in calcifications found in malignant lesions. Elevated levels of magnesium within calcifications might lead to lower carbonate levels in calcifications associated with breast cancer. High intracellular levels of Mg^{2+} could give an explanation about the low levels of CO_3^{2-} detected in calcifications associated with tumors, as the incorporation of CO_3^{2-} ions within the HAp lattice is influenced by the Mg^{2+} concentration incorporate during the crystallization. Participation of heavy metals salts has been described as involved in biomineralization of breast tissue.[262] Ions such as zinc, copper, iron, nickel and chromium can replace calcium ions in HAp, and the excessive accumulation has been suggested as a source of lipid peroxidation and the formation of hydrogen peroxide and superoxide anions, facilitating necrosis, apoptosis or inflammation of the tissue. Those factors may be also involved on the pathological biomineralization process.

Bertran et al. (2015)[205] studied the connections between the Mg^{2+} ions and DNA and confirmed that $Mg^{2+}\cdots$phosphate interactions in the inorganic solution are independent of the magnesium concentration, but the abundance of $Mg^{2+}\cdots$base direct interactions increases with the concentration of magnesium. The experimental observations achieved for DNA-CaOx, DNA-MgOx and DNA-HAp complexes are fully consistent with the computer simulations (see also section 7.3). MD simulations showed that, although DNA can be adsorbed onto the most stable facets of CaOx and, especially, HAp, its predominant role as nucleating template only occurs for HAp. On the other hand, Mg^{2+} ions tend to be located in the grooves of DNA, acting as counterions of the polyphosphate backbone. Nevertheless, MgOx particles are not appropriated to mineralize the DNA by superficial absorption or encapsulation.

In the context of transfection, we take into consideration that HAp aggregated precipitates usually result in low transfection efficiencies as the particles become too large to be endocytosed.[263] Turbidity of the solution where particles are being synthesized gives an indirect measure of the particle size and the easiness of the agglomeration. The turbidity of solutions containing DNA-HAp complexes (hydroxyolites) progressively decreased increasing the Mg^{2+} concentration (Figure 49). When Mg^{2+} was added previous to the formation of the precipitates, it was observed that Mg^{2+} affects the evolution of the precipitates reducing the particle size and even obstructing the precipitation of new particles.[264] Recently, there have been some interest in stabilizing other phases of calcium phosphate (tricalcium phosphate, amorphous calcium phosphate among others) with the intention to their solubility and improve their performance as a non-viral vectors for transfection by including other metallic ions (i.e. Al^{3+}, Zn^{2+}, Cd^{2+}, Ni^{2+}) but Mg^{2+} is the preferred for its biocompatibility.[143]

Cells cultured under mineralizing conditions, supplemented with magnesium chloride (Mg^{2+} concentration of 1.5 mM), demonstrated the anti-mineralization effect of magnesium.[96] To evaluate if elevated Mg^{2+} levels could impact the development of calcifications, cells were grown during 45 days in osteogenic cocktail media supplemented with magnesium chloride to yield a total Mg^{2+} concentration of 2 and 8 mM (Figure 51), displaying an almost 8 and 28-fold decrease in Alizarin Red quantification measurements ($p < 0.05$), respectively. Our results confirm[265] that a concentration Mg^{2+} of 8 mM almost inhibited the formation of microcalcifications.

Concerning Mg^{2+} effect, we considered the inclusion of Mg^{2+} ion in the transfection analysis of natural microcalcifications because Mg^{2+} is ubiquitous in physiological environments and its relationship with cancer disease is still controversial. Scott *et al.* (2017)[91] described that low Mg^{2+} levels in serum were found in breast cancer patients, suggesting that a high Ca/Mg ratio is a risk factor in breast cancer. Nevertheless, tumor cells accumulate Mg^{2+} even when its extracellular concentrations are low. On the other hand, in cell death processes (i.e. associated to apoptotic processes or by the hydrolysis of ATP), Mg^{2+} concentration is likely to be increased and can easily interact with calcium and phosphate to be part of a newly formed calcification. Previous results showed that Mg^{2+} ions stabilize the double helix of DNA, which might acts as a template of a HAp calcification that can become a natural non-viral vector of transfection. It was concluded that DNA is preferentially bound to Mg^{2+} when this ion is available in the mother solution displacing Ca^{2+} to other positions. Thus, Mg^{2+} shows preference to bind DNA in all circumstances but it does not prevent the biomineralization of DNA in HAp. Our results showed that the impact of Mg^{2+} in terms of transfection is very mild in comparison to Ca^{2+}, suggesting that the ion does not have a significant role in the regulation of the endocytosis pathways or it does not modify the behavior of the particle during the release of DNA in the cytosol or nucleus.

It is worth mentioning that mitochondria have the ability to precipitate HAp inside, there will be a regular capture of Mg^{2+} in these structures. On the other hand, in cell death processes (*i.e.* associated to apoptotic processes or by the hydrolysis of ATP), its concentration is likely to be increased and can easily interact with calcium and phosphate to be part of a newly formed calcification. In addition, we took into consideration previous results of our group indicating that Mg^{2+} ions stabilize the double helix of DNA, which might acts as a template of a HAp calcification that can become a natural non-viral vector of transfection.

A fact that allows the generation of hydroxyolites containing Mg^{2+} to be in close contact with DNA but also to be in the outer surface of the HAp particle as Mg^{2+} ions tend to migrate to the external layers of the calcification during the synthesis process of calcium phosphate precipitates and their reorganization to become HAp. However, when considering the same effect in CaOx calcifications it is worth recalling that DNA cannot be encapsulated in CaOx when Mg^{2+} binds to DNA. This is the circumstance to be expected in normal physiologic conditions. As a consequence, the adsorption or encapsulation of DNA in a CaOx calcification

is not expected to occur. However, it cannot be discarded that a depletion of Mg^{2+} can allow the formation of such transfection vectors we have tested. Furthermore, Mg^{2+} ions included in HAp lattice are not significantly affecting the transfection ratio in HAp(Mg^{2+})-*a*DNA and no increase is observed for HAp(Mg^{2+})-*c*DNA most probably, as reported in the literature, due to the reduction in particle size related to the inclusion of Mg^{2+} in the crystal lattice.[241] However, such effect is not related to a reduction in the particle size but could be attributed to a secondary mechanism associated with the neutralization of Z-potential and the absorption of Cl^- ions on the outer layer.[167] In regards of hydroxyolites by adsorption we observe that when Mg^{2+} undercovers the already formed HAp, there is not an enhancement of the transfection rate (Table 17), even a slight decrease is observed between HAp-*a*DNA and HAp(Mg^{2+})-*a*DNA remaining in the L rate interval.

Transfection results including vectors doped with magnesium lead to interesting conclusions. First, these transfection ratios are not enhanced as it happens when excess of calcium is used. All co-precipitation cases show a transfection rate in the range of L transfection rate and in the same range that hydroxyolites without any additive, showing that transfection is feasible but is not enhanced. Furthermore, we observe that Cl^- that may help the transfection process in the case of Ca^{2+} but this is not the case when Mg^{2+} become part of the transfection vector. On the other hand, the low size effect expected for the magnesium contained in the particles that may facilitate the uptake by the cells has not been observed.

8.6 DETERMINATION OF THE TRANSFECTION CAPABILITIES OF CALCIUM OXALATE (TYPE I)

Calcium oxalate (CaOx) calcifications, who are also found in breast cancer tissue, remained in a second line of interest as they have been more related to benign prognosis. Up to now, to the best of our knowledge, no other works have reported the role of CaOx as an *in vitro* or natural non-viral vector of transfection. In spite of the relevance of breast microcalcifications for the early detection and diagnostic of breast cancer, not many contributions have been focused on the investigation about the presence and role of CaOx in a tumor microenvironment. Although CaOx were related to carcinoma in situ lesions and invasive carcinomas[266] they were considered bystanders as they coexist with regular apatite calcifications.[267] CaOx calcifications are found in breast tissue, as mineral deposits related to breast epithelium, and in benign cysts, particularly in those presenting apocrine metaplasia or inside of dilated ducts.[90,268,269] They can be observed in breast biopsies under polarized light and with more sophisticated techniques as Raman spectroscopy and Energy-dispersive X-ray spectroscopy coupled with scanning electron microscope (SEM-EDS).[91,246] Although the mechanism behind their synthesis is not totally understood yet, some hypotheses have been proposed.[100,210] Furthermore, cells cannot metabolize the oxalate ion and, for that reason, it is observed as end product of some metabolic processes. Castellaro et al. (2015)[268] reported some evidences related to the long-term exposure of breast epithelial cells to oxalates, resulting in the transformation of normal breast cells to tumor cells. Oxalate ions make soluble salts with sodium and potassium but they precipitate as an insoluble salt when are paired with calcium ions. The exposure of living tissue to a CaOx deposits may induce some pathological scenarios.[270] The most studied are renal diseases, where CaOx is intended to affect epithelial cells by modifying their metabolic pathways, inducting early gene expression, upregulating and downregulating genes, re-initiating DNA synthesis,[271] and CaOx stimulates the production of IL-6 in human proximal tubular epithelial cells.[272]

To the best of our knowledge, this is the first work that evaluates the role of CaOx as an *in vitro* or natural non-viral vector of transfection. Here, we report the unveiled capabilities of CaOx as a new non-viral transfection vector. CaOx-*a*DNA and CaOx-*c*DNA show a L transfection ratio and both were able to transfect A549 cells. The transfection is also enhanced when additional Ca^{2+} is supplemented but not with Mg^{2+}. We recall that we

demonstrated in a previous work by synergistic theoretical-empirical studies that DNA cannot be encapsulated in CaOx.[273] For that reason, when co-precipitation route is used, CaOx clusters are expected to be formed in a first stage and the absorption of DNA on CaOx cluster will occur in a second stage.

The most interesting effect, in terms of transfection, occurs when CaOx particles are synthesized in a solution with an excess of Ca^{2+} ions supplied through $CaCl_2$ salt. Comparing both assays, with and without Ca^{2+} excess, we note that transfection of the co-precipitated vector was increased by a factor of three magnitude orders, a similar effect to the observed in the hydroxyolites transfection assay. Such a relevant increment emphasizes the relevance of additional Ca^{2+} and Cl^- concentration present in the mother solution. Thus, we confirm the important role of a Ca^{2+} excess and CaOx particles as potential facilitators of transfection in a living tissue. On the other hand, Mg^{2+} is expected to hinder the adsorption of DNA on the surface of the particle. Bertran et al.[205] studied the connections between the Mg^{2+} ions and DNA and confirmed that $Mg^{2+}\cdots$phosphate interactions in the inorganic solution are independent of the magnesium concentration. Molecular Dynamics simulations showed that, although DNA can be adsorbed onto the most stable facets of CaOx cannot template a crystal as it does in HAp.[205] In terms of transfection, Mg^{2+} effect on the CaOx vector is not observed as the transfection ratio is similar with and without. As DNA cannot be adsorbed on CaOx in presence of Mg^{2+}, we expect that the transfection observed in this assay would correspond to naked DNA with Mg^{2+} that leads to a similar level of transfection.[241]

Considering such a premise, under normal homeostatic concentration, no transfection driven by CaOx should occur in a physiological environment as Mg^{2+} is ubiquitous. Only under certain specific circumstances, CaOx calcification could become a transfection vector similar to the one we used for experimentation in the laboratory, for instance, in patients with a severe hypomagnesemia or in specific areas where Mg^{2+} would be depleted any reason. Nevertheless, the results of the transfection *in vitro* test open the door to consider CaOx as a natural transfection vector.

8.7 DETERMINATION OF THE TRANSFECTION CAPABILITIES OF HYDROXYAPATITE PRECURSORS

The transfection efficacy of hydroxyapatite (HAp) precursors as amorphous calcium phosphate (ACP) and Brushite (Bru; $CaHPO_4 \cdot 2H_2O$) was studied. Each of cases split in two subcases: a) adsorbed DNA on already formed mineral particles and b) co-precipitated DNA with the mineral forming ions. The interest of studying the behavior of ACP as transfection vector is that ACP is the first calcium phosphate phase to precipitate and can be one of the precursors of HAp calcification as usually observed in breast cancer biopsies.[109,274] We selected ACP for this transfection study because the likelihood to be naturally synthesized at physiological conditions is higher than other potential precursors such as Bru that have been studied in further analysis. It has been pointed out that its capacity of transfection depends on the exposed surface to the nucleic acid.

Gene delivery efficacy of nanocomposite spheres of DNA-ACP demonstrated to be better gene delivers than DNA–ACP nanocomposite layer by four orders of magnitude.[275] Our results confirm that submicrometric spherical (Figure 53) vectors using ACP-*c*DNA and ACP-*a*DNA are able to transfect A549 cells scoring as the highest. Likewise, due to the HEPES effect, we cannot extrapolate how ACP vectors could behave in a physiological environment. Hence, we included ACP, as it is still able to transfect without HEPES. Their average size fulfils the requirement for being a feasible transfection vector (353 nm and 232 nm in adsorbed and encapsulated, respectively) and their Z-potential indicate that they also will aggregate forming bigger particles (ACP-*c*DNA = –2.91 mV; ACP-*a*DNA = –1.2 mV).

The confirmation of their ability of being transfection vectors gains in importance as our results indicate the transfection process in an ACP calcification is more likely to occur during the first minutes after the initiation of the formation of the calcification. On the other hand, we observe a differential effect regarding the influence of adding Ca^{2+} compared to the previous analyzed vectors, as additional Ca^{2+} has a negative effect on their transfection efficiency. This fact is probably due to the observed increase in particle size (641 nm in ACP-*a*DNA(Ca^{2+}) and 487 nm in ACP-*c*DNA(Ca^{2+})) and a saturation of Ca^{2+} cell channels that might reduce the internalization of the particles containing DNA. On the other hand, no differences were observed when Mg^{2+} was included in the particle, suggesting that Mg^{2+} is not involved in the internalization process.

Transfection using polyphosphates is scarcely studied. They are known to be ancient precursors of orthophosphate PO_4^{3-} monomers due to the action of the enzyme alkaline phosphatase (ALP) that can participate in the construction of a HAp crystal.[276] Polyphosphates (PolyP) are old biopolymers spread in all types of organisms, their length varies from short chains of monomers to long chains with more than thousand units. They are degraded in less than 2 hours digestion by endopolyphosphatases and exopolyphosphatases that cleave within the polymer chain within or terminal phosphates respectively, being ALP one of the more potent enzyme cleaving the terminal one.[277] PolyP are known to be released by platelet granules (130 mM), usually within 60-100 residues, and recently has been demonstrated that PolyP associated to platelet membranes is forming nanospheres ranging 100-200 nm associated with Ca^{2+}[278,279] which is comparable to the size of synthetic non-viral vectors of transfection. PolyP play an important role in cell metabolism due to its high negative change and the ability for form complexes with Ca^{2+} ions. PolyP are found in significant quantities in bacteria and lower eukaryote providing energy storage. They participate in the gene expression regulation and protection against heavy metals that form complexes with them.[280]

On the other hand, pyrophosphate is also present in platelet granules (300 mM) and it is released together with the calcium stored in them when platelets are activated.[281,282] An interesting feature of pyrophosphate is that inhibits HAp formation but its effect is balanced by the action of ALP that leads to pyrophosphate hydrolysis and facilitates the HAp formation.[278,283] Furthermore, other sources of phosphate that can lead to HAp formation can be adenosine phosphates (AMP, ADP and ATP) as they can be released by hydrolysis of ATP or ADP[92] as HAp was formed by adding exogenous ATP to osteoblast cultures.[284]

In this subsection, we compare HAp based transfection with vectors made of DNA adsorbed on three different calcium polyphosphates with increasing number of monomers: calcium pyrophosphate (n=2), calcium triphosphate (n=3) and a long chain polyphosphate (n=25). The three of them show different behavior as only pyrophosphate is able to introduce the plasmid DNA adsorbed on the mineral in the cell but no transfection is observed in the case of triphosphate and polyphosphate. The explanation of such behavior must be found in the manner how DNA interact with them in the co-precipitation solution. Looking at the results of free DNA after the adsorption process we confirm that calcium pyrophosphate is able to retain all DNA available in the solution on its surface and therefore no free DNA is observed

in the solution. Conversely, sodium triphosphate is not able to adsorb DNA on its surface in any case, as a strong repulsive forces are expected between the polyphosphate DNA backbone and the intrinsic high negative charge of the triphosphate ion ($P_3O_{10}^{5-}$). We note that even in the presence of Ca^{2+} or Mg^{2+} the total amount of DNA is still free in the solution, meaning that it is not adsorbed on the triphosphate, therefore the transfection is not feasible as it happens in the case of naked DNA. The case of Graham polyphosphate salt is slightly different as it is able to bind the half of DNA on the solution but despite such adsorption the transfection is not possible. We suspect that the negative charge of the phosphate polymer hinders the internalization of the particle inside the cell.

The transfection efficiency of DNA adsorbed on pyrophosphate is in the range of L transfection, slightly inferior to the case of DNA adsorbed in HAp at 24 h rated as M. However, at 48 h the ratios are inverted and the transfection of pyrophosphate is much higher. Conversely, when n > 2, the capacity of transfection disappears and no transfection is observed in the case of calcium triphosphate and the polyphosphate. Furthermore, Bru-*c*DNA and Bru-*a*DNA are capable to transfect target cells. A M. transfection ratio is achieved when Brushite is co-precipitated (Bru-*c*DNA) form.

When an excess of calcium is added to the adsorption solution, an increase in the transfection ratio of CaPyr-*a*DNA(Ca^{2+}) is observed and the transfection rate is raised up to H, and also a positive effect is observed in the case of Bru-*a*DNA(Ca^{2+}). One of the most relevant results of the HAp precursors section is that pyrophosphate is even better transfection vector than DNA adsorbed on HAp, a finding that merits further research.

This result, together with the previous where DNA adsorbed in CaOx was able to transfect as well, suggesting that the particle by itself, as a DNA carrier, exerts a mechanical action on the cell membrane, facilitating the invagination of the membrane to end up in the internalization of the particle. The potential of calcium pyrophosphate for gene delivery has been successfully confirmed,[285] as such particles were able to show transfection efficiency comparable to hydroxyolites. Merits further research to look for such molecules in tumor microenvironment as their role as non-viral vector of transfection is currently almost unknown and might have a relevant role in diseases where ALP is downregulated. A failure of

ALP to break the PolyP in single monomers may lead to the extensive formation of dimers as pyrophosphate that could act as a DNA carriers.

8.8 EFFECT OF THE MINERAL SUBSTRATE OF TRANSFECTION VECTOR

The interest of studying the behavior of amorphous calcium phosphate (($Ca_3(PO_4)_2 \cdot nH_2O$); henceforth ACP) is based on the possibility they become a hydroxyapatite (HAp) calcification.[109,276] We selected ACP for the transfection study because they are likely to be synthesized at physiological conditions and they are consistent with the conceptual approach around natural vectors of transfection we pursue in this thesis. We discarded other potentially interesting calcium phosphate phases because they would require extreme synthesis conditions, as high temperature or high pH. ACP vectors are expected to end up as HAp, which is the most stable phase of calcium phosphate. Such a process takes a while and it is interesting to know if they have the potential to be vectors of transfection in that lapse of time. Particularly, in the first phase of precipitation until the particles become bigger enough to impede the transfection process. In addition, depending on the initial concentrations of calcium and phosphate ions in the mother solution, the precipitate can result in different Ca/P ratios (theoretical ratio for HAp is 1.67) and develop calcium or phosphate deficient HAp and contain some substituting impurities to compensate the missing Ca^{2+} or PO_4^{3-} ions.

ACP is often found as a transitory phase in aqueous systems during the synthesis of other calcium phosphates phases. ACP is the initial phase that precipitates from supersaturated solutions containing Ca^{2+}, PO_4^{3-} and is stable within pH 6.5-9.5. Through time it evolves to more stable phases, usually Brushite or HAp.[243,286,287,288] ACP may act as the nucleating agent of the crystallization of HAp. Electron microscopy shows the existence of spherical particles in ACP, ranging from 20 to 200 nm, but macroscopically an amorphous precipitate is formed. Additionally, some ions such as Mg^{2+}, CO_3^{2-} and $P_2O_7^{4-}$ being part of ACP are also observed in soft-tissue pathological calcifications[289] (e.g. heart-valve calcifications of uremic patients and breast microcalcifications). Concerning its capacity of transfection it has been reported that it depends on the exposed surface to the nucleic acid. Gene delivery efficacy of nanocomposite spheres of DNA-ACP demonstrated to be better gene delivers than filmy DNA–ACP nanocomposite layer by four orders of magnitude.[277]

Observing our own results in terms of aggregation and the time that particles fulfill the requirements for being a feasible transfection vector this section gains in importance as the transfection process is more likely to occur in the first minutes of the formation of the

calcification. At that time lapse, the synthesis of HAp under physiological constrains is less likely than other calcium phosphate phases. However, we cannot neglect that probably there is a continuum in transfection feasibility.

The average of the particle size of HAp-*c*DNA(~ 450 nm) at the time to enter into contact with the cells, is higher than the size of HAp-*a*DNA adsorbed (~ 220 nm), a fact that is aligned with the general rule that smaller particles transfect more easily that the bigger ones in the transfection range (20-500 nm) even though the optimal window is within 20-200 nm. On the other hand, the temporal evolution of Z-potential values for HAp-*a*DNA and HAp-*c*DNA are displayed in Figure 55. Freshly synthesized HAp-*c*DNA particles show a negative Z-potential (–14.3 ± 4.1 mV), similar to ACP-*c*DNA (–12.1 ± 3.6 mV), that shows a contrary sign to HAp-*a*DNA (+23.7 ± 2.0 mV). The Z-potential reaches to values of –0.48 ± 0.51 mV at 30 min, a result that is expected to have a significant impact in the aggregation process of those particles, increasing the size and, as a consequence, limiting the time window suitable for transfection. We observe that none of the hydroxyolites will remain stable in solution in the long-term and all of them tend to aggregate as their Z-potential is almost neutral after 30 min (Figure 55). On the other hand, Chen et al.[167] concluded that the more positive the charge of the particle, the higher their internalization in the cell. However, we have not confirmed such result in our study that is more aligned with Sokolova et al.,[170] which concluded that the charge does not play a critical role for explaining the transfection efficiency, since a linear increase of the transfection rate with the particle charge was not observed. Beyond that fact, Forest and Pourchez[290] proposed that the protein corona formed when the nanoparticles are in physiological environment drastically alters the Z-potential, which affects the cell behavior on nanoparticle uptake even proteins adsorbed on the particle can change after internalization due to new interactions.[291] Additionally, Z-potential shows a dependence with the pH being the highest at pH 7.8 that is close to the pH we use in the transfection study.[167] Nevertheless, their convergence to 0 mV demonstrates that the charge is not the primary factor for explaining differences in the transfection ratio, a fact that we confirmed with the PCA analysis.

Results for HAp-*a*DNA show two populations centered at 88 ± 33 nm and 731 ± 262 nm and the same pattern occur for HAp-*c*DNA 75 ± 10 nm and 506 ± 311 nm. We observe that all transfection vectors are within 250-450 nm after 30 minutes, being the adsorbed vectors the ones with smaller sizes. On the other hand, the Z-potential values obtained at different time

points are detailed in Table 33. Z-potential values show different trends depending on the vector and if DNA is co-precipitated or adsorbed. All obtained values are less than 30 mV that is considered the stability limit, hence, the particles will tend to aggregate through time and effect that can influence the transfection efficiency. It is worth mentioning that after 30 minutes the Z-potential converge to neutrality confirming the trend to aggregate quicker as the time goes by.

Furthermore, we note that the particle size of both CaOx-*a*DNA and CaOx-*c*DNA (264 nm and 375 nm, respectively) is in the feasible range of transfection but only the adsorbed show a significant part of them below 500 nm (T500=0.14). However, the Z-potential values of such particles are almost neutral, suggesting colloidal instability.

This thesis explored the basics of a potential spreading mechanism based on the adsorption or encapsulation of nucleic acids coming from tumor cells on natural vectors of transfection. We consider that in most cases, the nucleic acid, DNA or RNA carried by the calcifications would be released from healthy cells and will cause no harm to a new cell in case there would be a posterior transfection. However, when DNA or RNA from tumor cells becomes part of a natural HAp, ACP o CaOx calcification, the newly formed particles might carry tumor DNA containing specific gene mutations. Although the effects of such hypothetical transfection process are uncertain and merit further research, it could be related to the theory of genometastasis,[292,293] which explains that the circulating tumor DNA (ctDNA) might have the role of an intercellular messenger. Therefore, such ctDNA could be considered as a potential natural vector in combination with Ca^{2+} that could be delivered and integrated into the cell genome after transfection at distant locations leading to genetic instability or cell transformation.

8.9 DETERMINATION OF TRANSFECTION EFFICIENCY AFTER MIGRATION

This thesis intends to look for complementary mechanisms that could explain how tumor DNA can be distributed to the surrounding tissues. Interestingly, the possibility that tumors can spread through non-cellular mechanisms (i.e. exosomes, nucleosomes, naked cell-free DNA) has been recently reported opening new avenues for cancer researchers.[294,295] Recently, Rizwan et al.[296] stated that the relationship between the microcalcification status of breast cancer cells and their metastatic capabilities remains largely unexplored.

We studied the migration of transfection vectors, as a hypothetical mechanism of tumor DNA dissemination. We note that, to the best of our knowledge, the transfection of non-viral vectors after long distance migration has not been reported in the literature. Therefore, the study of natural vectors migration and subsequent transfection of cells situated to a certain distance merits further research to contribute to the understanding of a wide range of diseases related to calcifications. We are particularly interested in gathering information about the migration ability of such vectors in the context of breast cancer multifocality that refers to the appearance of various tumors in a specific area of tissue, a breast quadrant.[54] This is the reason why we restricted the migration interval up to 50 mm. However, we consider that the migration of such vectors could be feasible beyond such limit but it is out of the scope of this work.

Submicrometric and nanometric particles are expected to be able to migrate through living tissue if their size is small enough and/or they are driven by internal gradients (i.e. through vascular or lymphatic system). DNA adsorbed or encapsulated should remain protected and functional during migration until it reaches to the target cell, meaning that DNA is not separated from the carrier and/or degraded (i.e. nuclease enzymes) to the extreme that the transfection vector is disabled. We note that the migration through the extracellular matrix (ECM) is difficult due to its mesh-like organization.[297] The matrix barrier would block the migration of particles with diameters larger than the size of network space, while smaller particles are expected to cross it. Collagen fibrils are able to block particles larger than 20–40 nm. Inter fibrillary space would allow migration of particles up to 75–130 nm. Furthermore, it is important to note that nanoparticle interactions with ECM components are dependent on

their respective intrinsic properties (i.e. trafficking and uptake of nanoparticles are affected by their own charge and electric interactions with the ECM components).

After inspection of the results reported in Figure 59, we demonstrate that such transfection vectors are able to migrate and transfect up to 50 mm distance propelled in experimental conditions. Such a result indicates that transfection can occur at relatively long distance from the place where the vector was synthesized. Second, we observe that the positive control presents an inverse relationship between the rate of transfection efficiency and migration distance, following the rule “the longest the distance, the less the transfection rate”. We interpret such a result as a consequence of the aggregation process that reduces the amount of particles below 500 nm when particles reach to the cells.

Same pattern is observed when ACP vectors are forced to the migration setup, indicating that the presence of HEPES does not influence such behavior. Contrariwise, we observe a totally different profile concerning the HAp and CaOx vectors. In both cases, the transfection ratio remains in L (HAp-*a*DNA and CaOx-*a*DNA) and V.L. (HAp-*c*DNA) but the score is not affected by the distance as the ACP are. We interpret such result as consequence that the ratio of particles < 500 nm does not change reaching to cells with a similar proportion. The transfection at long distance empirically confirms the protective role of HAp on DNA, maintaining attached the nucleic acid to the particle and confirms that nucleic acid functionality is preserved as well. Merit further research to expose the particles to a trip containing degrading enzymes to test their influence on the transfection rate.

An interesting perspective about the role of breast cancer calcifications is that hydroxyolites containing tumor DNA which might be resilient in physiological environments by keeping DNA intact for a long time and thus protecting it from degradation as occurs with ctDNA. This fact might enable tumor DNA to migrate, travelling through tissue ducts, being disseminated locally (i.e. intramammary) or through a long distance (i.e. blood or lymphatic vessels), until it reaches to a distant tissue while maintaining its functionality and therefore, being feasible the cell transfection, fact that could lead to cell transformation. As a result of this hypothesis, the presence of tumor DNA on such calcifications in tumor tissue merits further research as it could be correlated with the progression and aggressiveness of the cancer disease.

LIMITATIONS AND FUTURE PROSPECTS

9 LIMITATIONS AND FUTURE PROSPECTS

9.1 LIMITATIONS OF THE STUDY

This thesis has some limitations we summarize in this section through the following concepts:

1. Theoretical framework

The transference of the theoretical framework is based on some premises that we validated using several *in silico* studies and by performing a preliminary empirical work we have described through this thesis. Nevertheless, we are conscious about the complexity of the physiological environment and living tissue and the numerous influencing factors that might play a role in the natural synthesis of hydroxyolites. For that reason, we note that more scenarios beyond the breast cancer are necessary to be identified in order to confirm the general process behind our hypothesis of the spontaneous synthesis of hydroxyolites.

2. Raman spectroscopy

Raman spectroscopy used to identify natural hydroxyolites has a limit of detection in the interval of 200 – 500 nm, just in the range of the hydroxyolites that are able to transfect. In that sense, we note that other techniques such as fluorescence specific probes must be used. Despite such results are not specifically displayed in this thesis, we confirmed by parallel assays the existence of such particles containing DNA using DAPI (i.e. Marro et al. (2021)) and in a separated experimental work, we used selective fluorescent probes to univocally identify the particles containing DNA and HAp in the transfection range.

3. Tissue samples from breast tumors

The classic treatment of preservation of samples with ethanol and paraffin might lead to desorption of the nucleic acids from the surface of the calcification, or even the dissolution of the particle. Additionally, such preservatives can introduce distortions or even masking the molecules of interest to be identified by the spectroscopic methods. For

that reason, extraction of fresh samples without any further treatment beyond their freezing were planned using the regular scheduled surgeries of the hospital. Samples from breast tumors were excised *in situ* from diagnosed patients going through surgery. Thus, the number of patients and consequently, the number of samples was limited along the lapse of time for their collection.

4. Ribonucleic acid

As explained in the corresponding section, we focused this thesis on the transfection behavior of the non-viral vectors by DNA and the different minerals studied but not in the vectors containing RNA. As exposed, from a theoretical perspective the synthesis of transfection vectors composed of RNA and HAp are equally feasible in the physiological context. The impact of such vectors can be totally different as the nucleic acid can be released in the cytosol and be ready to interact with the cellular mechanisms. Such research will be performed in future works of our research team as we consider it is as relevant as the vectors containing DNA studied here.

5. Cell lines

Concerning the number of target cell lines used in the transfection model, we acknowledge the need to include more cell lines to be transfected in order to compare the efficiency of the transfection vectors depending on the lineage of the cell. In this thesis we have given priority to make the transfection model as robust as possible by focusing our experimental work in performing an extensive number of replicates and testing a high number of conditions without varying the A549 as target cell in order to stablish a solid basis for future comparison. Such assays, which are beyond the scope of this thesis, are currently being performed and they will be part of the continuation of this thesis.

6. Migration models

We are aware that the migration model we describe in this thesis is the simplest model as it uses only the gravity as a driving force for to make the particles migrate through the transfection media. The fact that the cell growth media is used as a simulation of the real

tissue implies an enormous simplification that we only accept in order to demonstrate, as a basic proof of concept, that the transfection vectors are capable of remain functional despite they move to certain distance. Further research is needed in order to increase the complexity of the migration model and to study some influencing factors that might hinder the feasibility of the transfection process in real tissue.

All these factors, considered as a whole set of limitations, cannot be obviated when extracting conclusions of the work presented in this thesis. Taking into consideration the novelty of the concepts exposed in this work, we consider that the restrictions exposed above do not impair the conclusions we extract through the thesis and their acknowledgement reinforces the need of further research to understand better how such natural transfection vectors behave in a clinical scenario.

9.2 PROSPECTS FOR FUTURE RESEARCH

As a result of our investigation related to the role of hydroxyolites in the context of breast cancer multifocality, many topics were considered of interest but beyond the scope of this thesis. However, we briefly summarize them here because we consider they merit further research and some of them are already in the experimental phase:

1. Transfection studies using different cell lines.

   The extension of the transfection model using A549 cells to other cell lines, particularly to non-tumor breast cells is an ongoing investigation in order to determine the different behavior of the transfection vectors of amorphous calcium phosphate, hydroxyapatite and calcium oxalate in a transfection model closer to the clinical scenario of breast cancer. Preliminary results allow to detect differences being the hydroxyapatite vectors more efficient than calcium oxalate, a fact that merits a detailed investigation to elucidate the origin of such differences. In addition, other cell lines, as human mesenchymal stem cells are expected to be used as a target cell and to determine if the role of the mineralized transfection vectors show a better performance than the previous cell lines or even if they are able to differentiate the original cell.

2. Precursors of hydroxyapatite as transfection vectors.

   As shown in this thesis the interest of new natural transfection vectors is of high interest due to the potential synergistic effect with naked DNA released as a result of cell death processes. To our current knowledge, the impact of polyphosphates as transfection vector is a new area of interest unveiled in this thesis. Therefore, more detailed characterization of such transfection vectors, in particular pyrophosphate focused on its performance using different target cells. Such studies are needed in order to understand their role in different clinical contexts, not only in the breast cancer but also in different tumor processes where calcifications are not observed, as pyrophosphate is considered an inhibitor of hydroxyapatite calcifications.

3. Alkaline phosphatase influence on the generation of natural hydroxyolites.

   The enzyme alkaline phosphatase, among other enzymes able to cleave the polyphosphate chain, has a crucial role in regulating the amount of polyphosphate monomers released from the long chain polymers of such family usually released by α-granules of platelets or the polyphosphates already present in the cytosol as they are energy storage molecules. As free phosphates ions is a necessary but not sufficient condition for the generation of hydroxyolites, the molecules that are able to regulate the phosphate concentration are of high interest as they control the feasibility of hydroxyolite synthesis, particularly interesting in the context of the role of natural non-viral vector of transfection. Such processes merit further research as the down regulation of alkaline phosphatase has been associated to the apparition of tumors and metastatic processes despite its role is still unclear.

4. DNA sequencing of natural transfection vectors.

   Our findings reported in this thesis have open the opportunity to investigate which sequences of nucleic acids are contained in naturally formed hydroxyolites. Such research might shed light if hydroxyolites can be used as a diagnostic tool to foresee the progression of the disease depending on the kind of sequences that are adsorbed or encapsulated in such natural vectors.

5. Migration models.

   A deeper investigation is needed to better simulate the potential pathways that can be used by hydroxyolites to migrate from the original synthesis location to other surrounding cells and tissues. Therefore, new models that simulate the migration through the vascular and lymphatic tissue are expected to be developed to understand how such transfection vectors interact with the physiological environment that contains other molecules that can hinder or enhance the transfection feasibility (i.e. DNase that disable the DNA functionality or proteins that creates a corona effect that protects DNA from enzymatic attacks or facilitates the entrance of the vector inside the cell).

CONCLUSIONS

10 CONCLUSIONS

1. Hydroxyolites, hybrid particles composed of hydroxyapatite and nucleic acids, in particular when containing DNA adsorbed or co-precipitated, are able to transfect and introduce DNA inside target cells.

2. We establish a conceptual framework that allows the transference of concepts from Chemistry of materials (hydroxyolite model) to Biology and Medicine (breast cancer) in order to understand how natural transfection vectors are synthesized in living tissue.

3. We successfully identify DNA in hydroxyapatite microcalcifications found in freshly excised human breast tumors by combining advanced 3D Raman imaging algorithms with a Multivariate Curve Resolution (MCR) method.

4. We demonstrate the feasibility of DNA adsorption and encapsulation on hydroxyapatite, adsorption in calcium oxalate but not encapsulation by Molecular Dynamics independently of the methylation degree of the simulated DNA dodecamers. No adsorption of DNA in calcium oxalate is feasible when Mg^{2+} is present.

5. We confirm that an additional supply of Ca^{2+} ions to the transfection vectors plays a significant role enhancing the transfection efficiency of all vectors, in particular allows the transfection of naked DNA and significantly enhance the transfection efficiency of hydroxyolites.

6. We demonstrate that Mg^{2+} included in the mineral lattice does not have a significant effect enhancing transfection of hydroxyolites.

7. We unveil that calcium oxalate with adsorbed DNA is able to perform as a new non-viral transfection vector.

8. Hydroxyapatite precursors, amorphous calcium phosphate and calcium hydrogen phosphate (Brushite), are able to perform as non-viral vectors of transfection. Conversely, polyphosphates with more than two monomers ($n \geq 3$) are not able to perform as transfection vectors. Only calcium pyrophosphate ($n=2$) is able to transfect.

9. All transfection vectors potentially found in breast cancer microcalcification have the ability to transfect. The most efficient is amorphous calcium phosphate which is the fastest to be formed and the hydroxyapatite the most stable.

10. We demonstrate that DNA adsorbed or encapsulated in hydroxyapatite, amorphous calcium phosphate and calcium oxalate vectors can migrate up to 50 mm, within the range defined by breast multifocality, before transfecting target cells.

The results obtained in this thesis push forward the idea that nucleic acids adsorbed or encapsulated in hydroxyapatite microcalcifications are a fossilized fingerprints of tumor cells that retain information which might be useful to understand the progression of breast cancer disease. Moreover, submicrometric breast tissue hydroxyapatite calcifications might migrate and transfect distant cells.

ANNEXES

11 ANNEXES

ANNEX 1: RAMAN SPECTRAL DATABASE

- Complete Raman spectra of commercial hydroxyapatite (HAp, Sigma Aldrich, Ref. 04238). 1076 cm^{-1}, 1052 cm^{-1} (shoulder, sh), 1047 cm^{-1}, 1040 cm^{-1} (sh), and 1028 cm^{-1} bands arise from v3 PO_4, the very strong 962 cm^{-1} band arises from v1 PO_4, the 614 cm^{-1}, 607 cm^{-1}, 590 cm^{-1}, and 579 cm^{-1} bands arise from v4 PO_4, and the 447 cm^{-1} and 431 cm^{-1} bands arise from v2 PO_4.

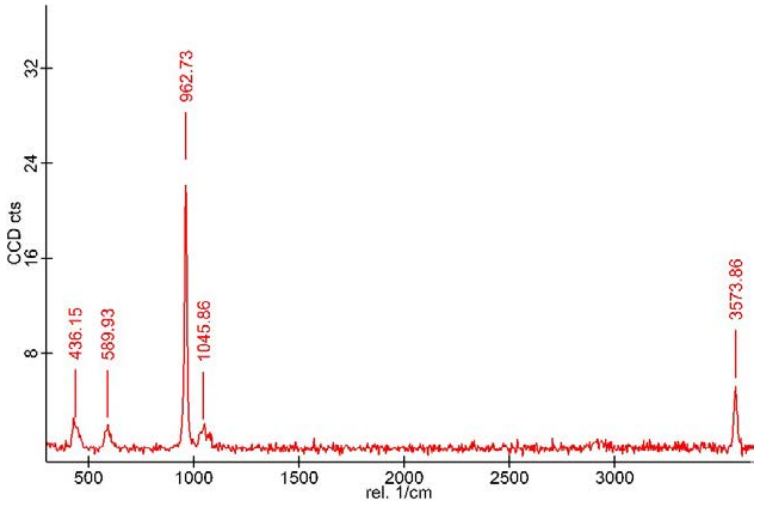

PRECURSORS OF HYDROXYAPATITE

It could be possible to find intermediates of the hydroxyapatite (HAp). In this case, calcium pyrophosphate, amorphous calcium phosphate (ACP) and Brushite, species has been considered to analyze.

- Raman spectra of calcium pyrophosphate (CaPyr, $Ca_2O_7P_2$, Sigma Aldrich, ≥ 99.9% trace metals basis, Ref. 401552).

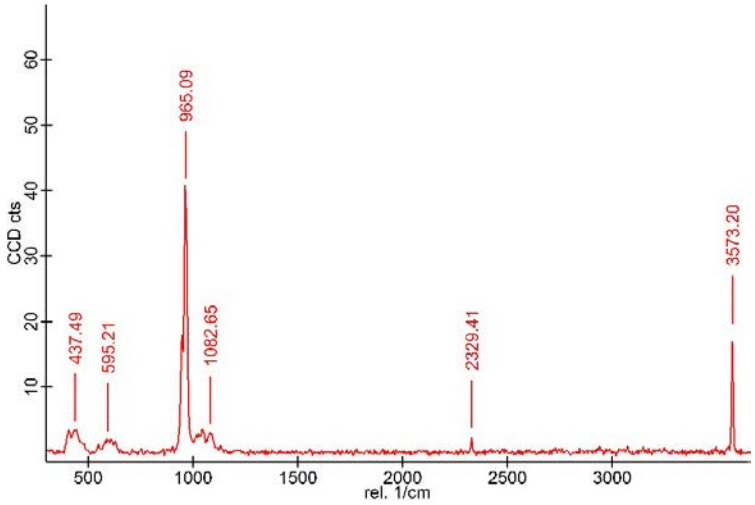

- Raman spectra of amorphous calcium phosphate (ACP, *in situ* synthetized). Courtesy of B. Braun - UPC.

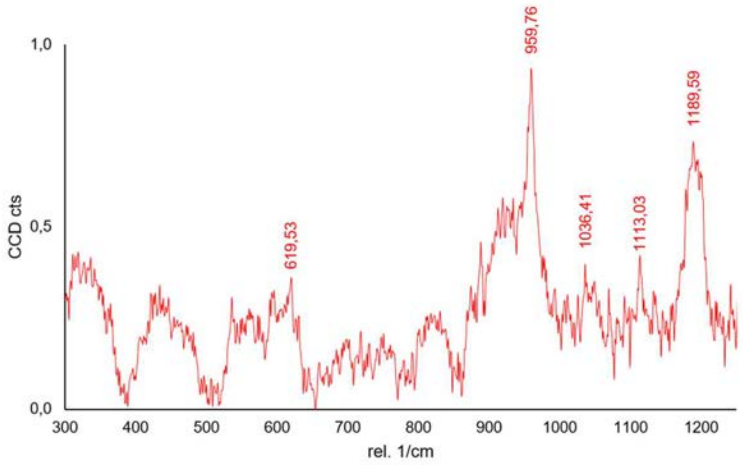

- Raman spectra of Brushite ($CaHPO_4 \cdot 2H_2O$, calcium hydrogen phosphate dihydrate, Ph. Eur., BP, USP, Scharlau, Ref. CA0210050). The v1 appears at 986 cm^{-1} the two bands at 1062 and 1081 cm^{-1} are recognized as components v3 mode. A band at 409 cm^{-1} may be assigned to v2. Bands at 584 and 525 cm^{-1} are assigned to v4 mode.

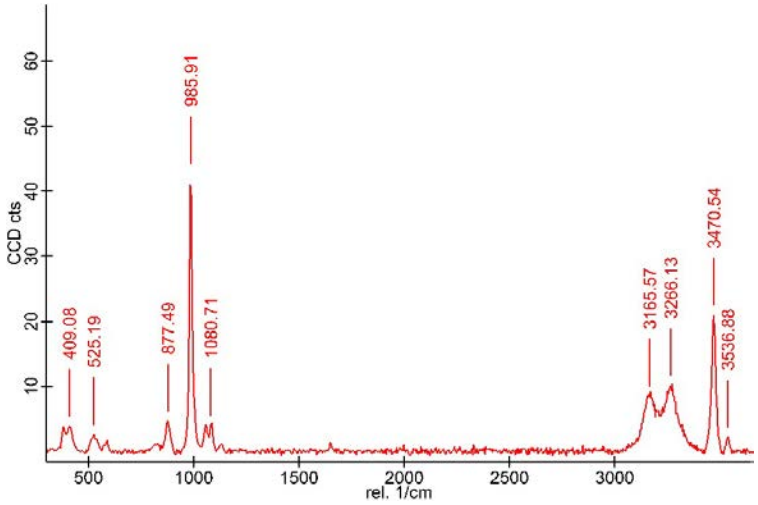

- Raman spectra of sodium phosphate monobasic monohydrated ($NaH_2PO_4 \cdot H_2O$, Sigma Aldrich Ref. 17844).

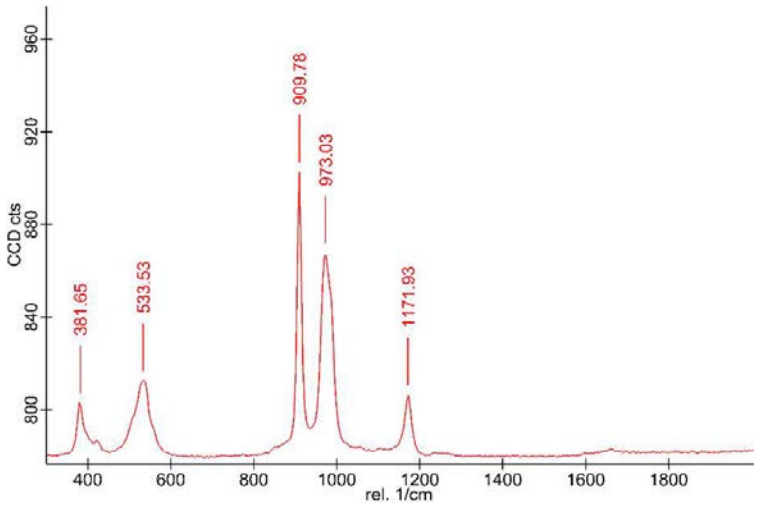

Moreover, according to literature[298] others are described as: amorphous carbon phosphate (950 cm^{-1}), dicalcium phosphate (878, 985 cm^{-1}), β-tricalcium phosphate (949, 970 cm^{-1}), octacalcium phosphate (958-965-970, 1010 cm^{-1}).

- Raman spectra of sodium triphosphate (ACROS, Ref. 393960250). Sodium triphosphate ($Na_5P_3O_{10}$) was measured in substitution of the calcium species, as no tripolyphosphate product more similar was found in the market.

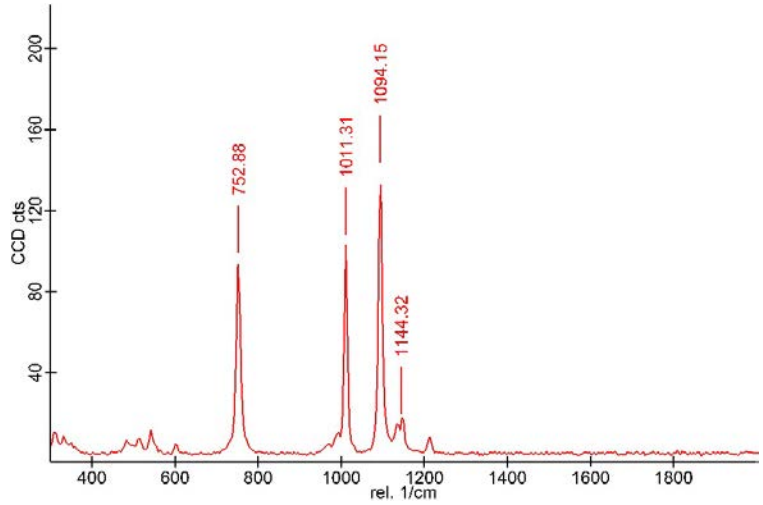

OXALATES (CaC_2O_4 $(H_2O)_X$)

- Raman spectra of calcium oxalate (Sigma Aldrich, Ref. 455997).

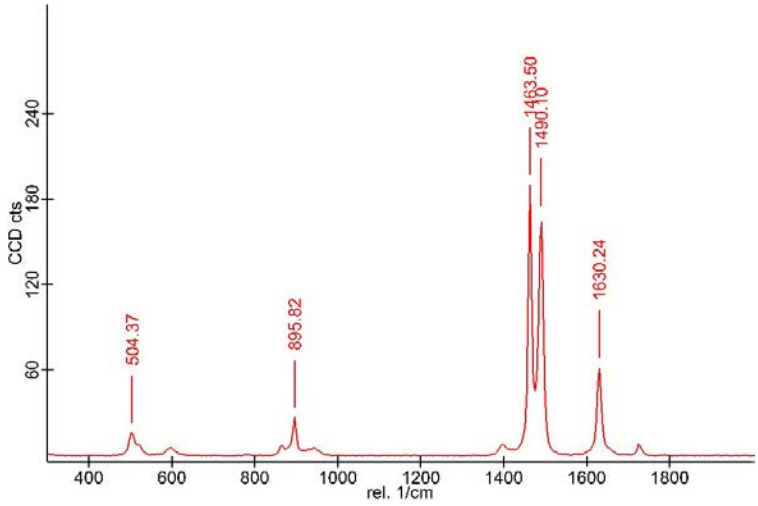

- Raman spectra of calcium oxalate hydrate (Sigma Aldrich, Ref. 289841). Vibrational features characteristic of calcium oxalate hydrated can be seen at 505 cm^{-1}, 895 cm^{-1}, 1463 -1490 cm^{-1}, and 1630 cm^{-1}. These Raman features are attributed to O-C-O in plane bending, C-C stretching, and C-O symmetric and asymmetric stretching respectively, and are consistent with previously published Raman spectra of calcium oxalate hydrated[299].

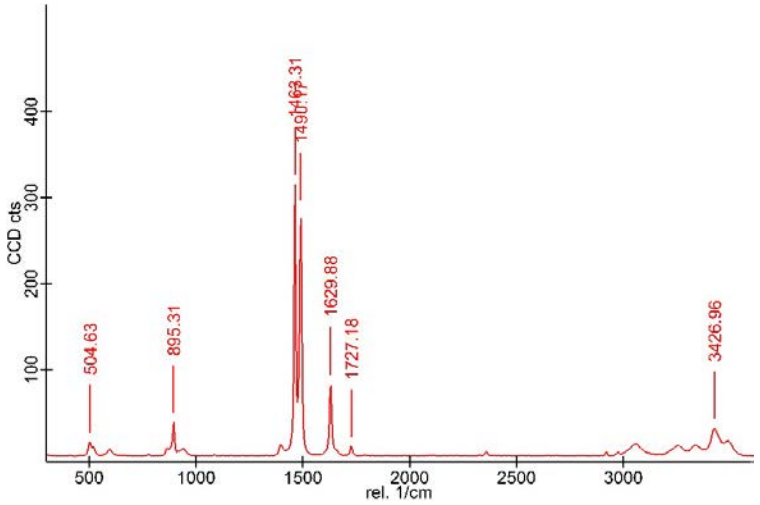

- Raman spectra of calcium oxalate dihydrate from synthesis. Raman features similar to calcium oxalate hydrate.

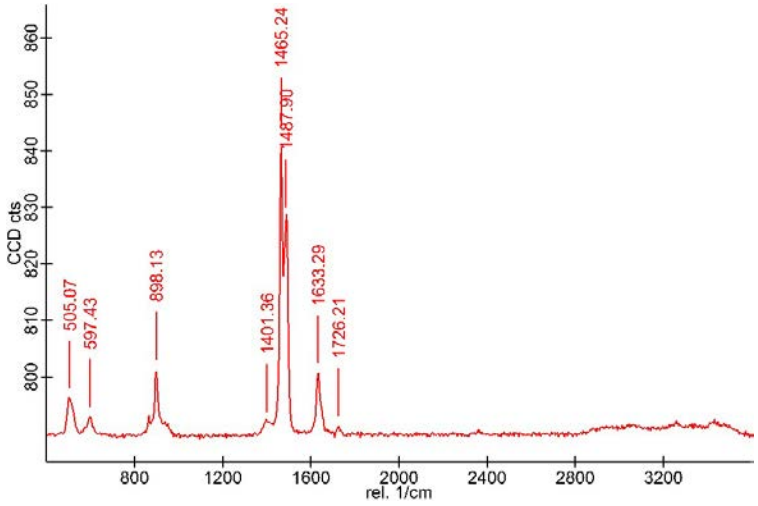

- Raman spectra of sodium oxalate 99.5 % (Sigma Aldrich, Ref. 223433). To distinguish form the sodium oxalate form, its spectra was analyzed. The characteristic lines at 960 cm^{-1} for hydroxyapatite and 1462 cm^{-1} for calcium oxalate were used for the analysis.

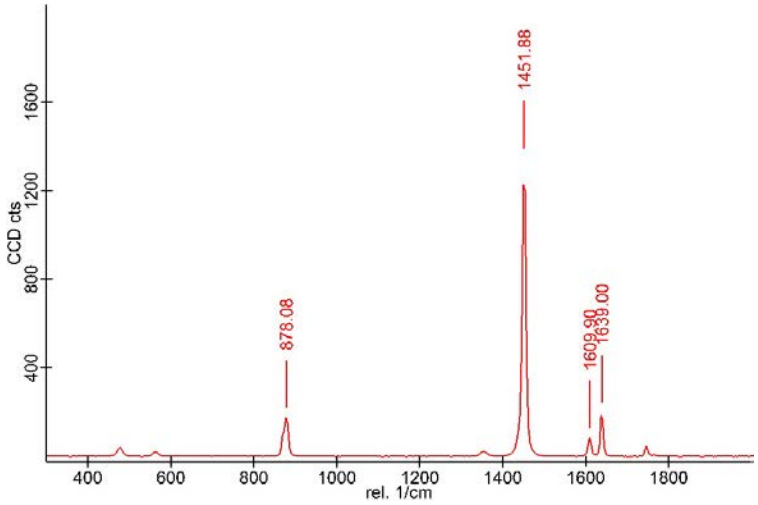

NUCLEIC ACIDS

- Raman spectra of RNA (Sigma Aldrich, Ref. Y0000662).

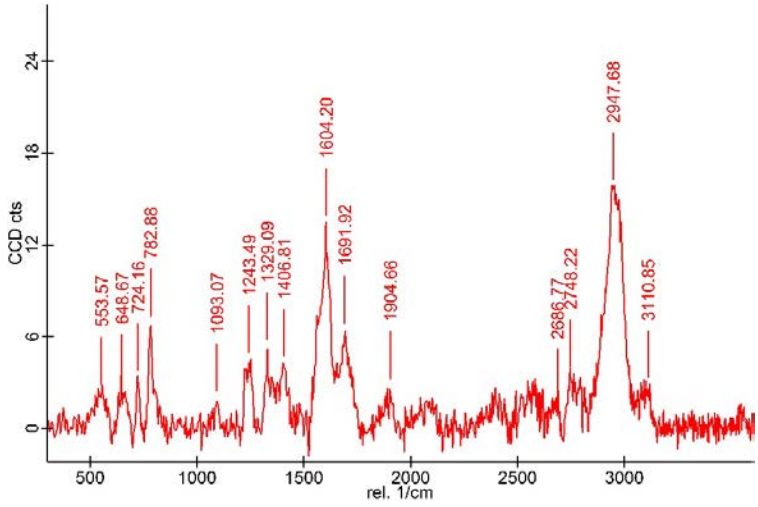

POLYPHOSPHATE (POLYP) SPECIES

- Raman spectra of sodium hexametaphosphate 65-70 % (Aldrich, Ref. 71600).

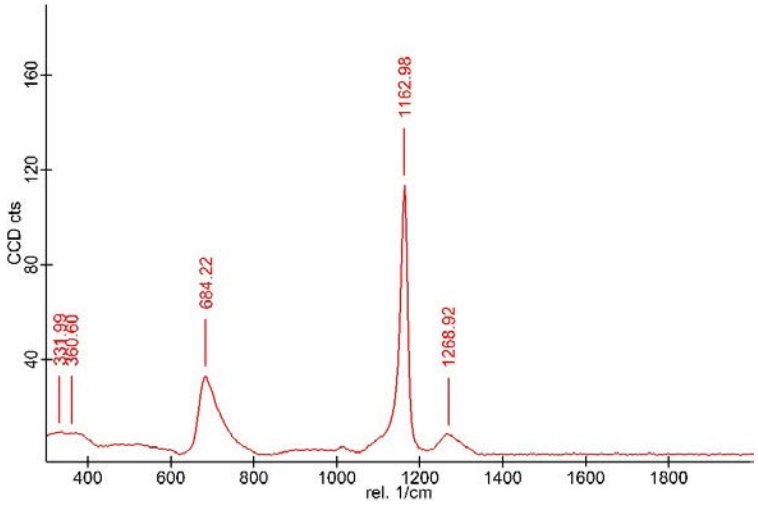

- Raman spectra of sodium hexametaphosphate +200 mesh 96% (Aldrich, Ref. 305553).

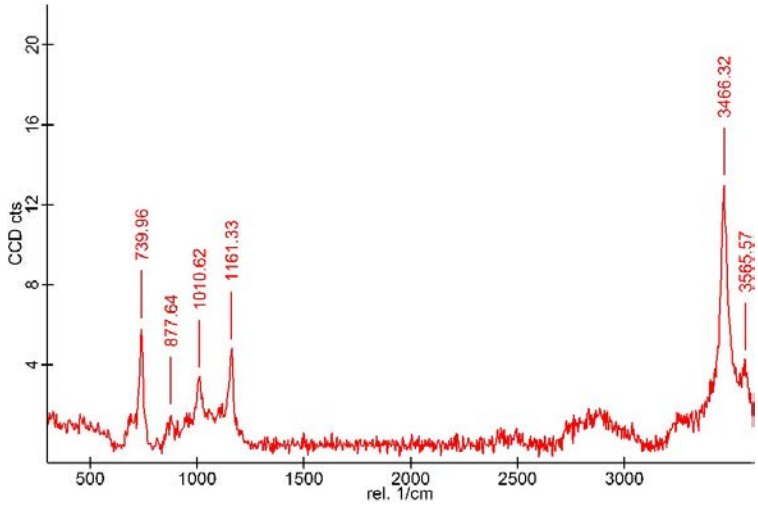

- Raman spectra of sodium polyphosphate (Graham's salt, Merck, Ref. 1.06529.1000).

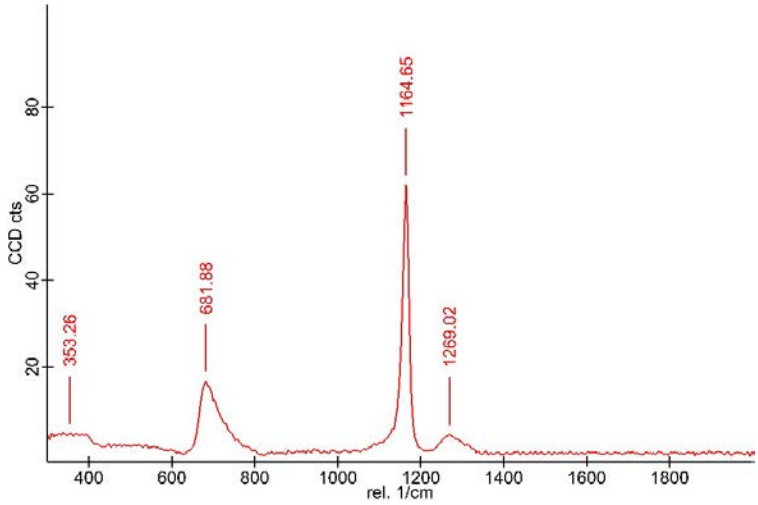

CALCIUM CARBONATE ($CaCO_3$)

- Raman spectra of calcium carbonate (Sigma Aldrich, Ref. 1002478705).

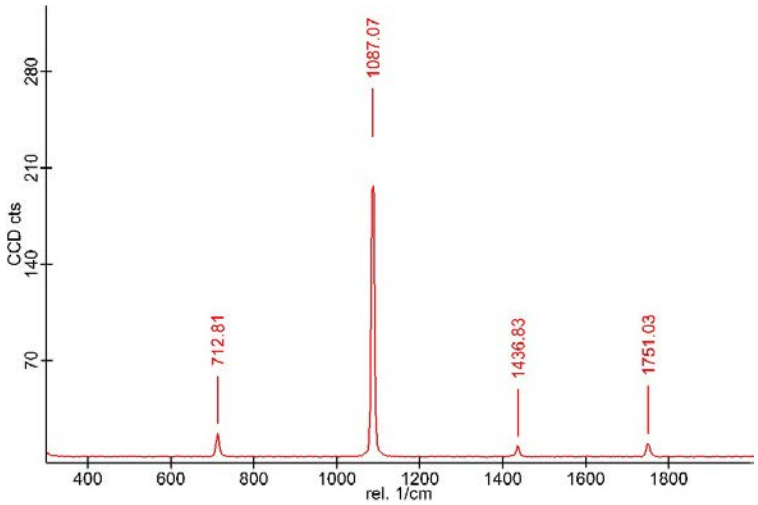

ADENOSINE 5'-TRIPHOSPHATE (ATP)

- Raman spectra of Adenosine 5'-triphosphate magnesium salt (Sigma Aldrich, Ref. A9187).

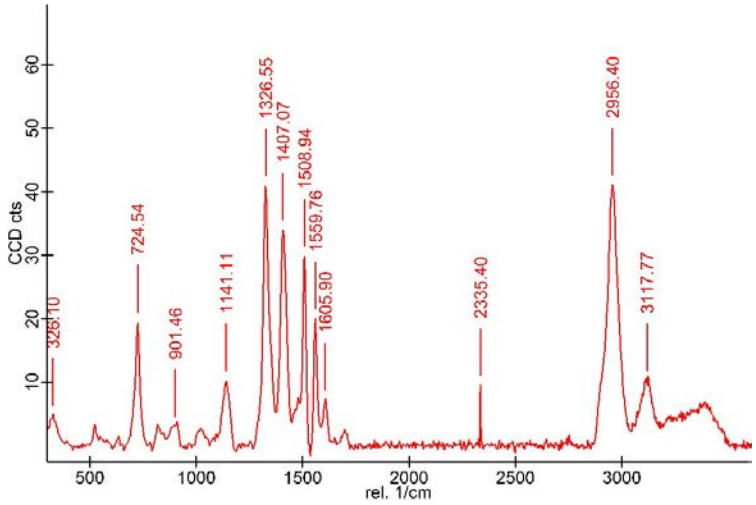

COLLAGEN

Raman bands in the collagen spectra corresponding to the C-C stretch of the collagen backbone (860 cm^{-1}), amide III (1249 cm^{-1}), CH_2/CH_3 bending (1455 cm^{-1}), and amide I (1671 cm^{-1}) were examined, according to found literature.[300]

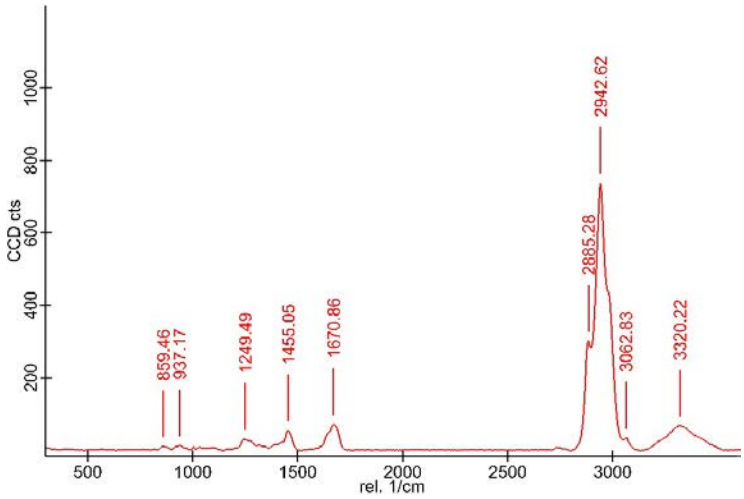

L-PHENYLALANINE

- Raman spectra of L-Phenylalanine (Sigma Aldrich, Ref.40541). 1003 cm^{-1} phenyl ring breathing.

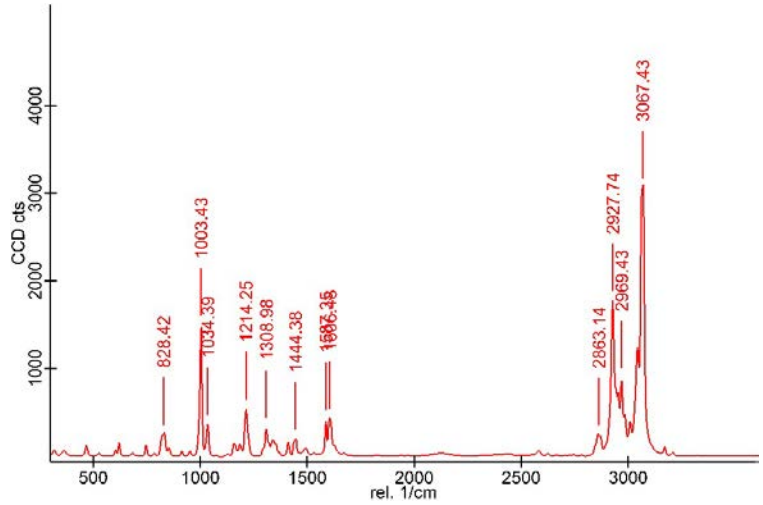

HYDROXYAPATITE (HAp) + POLYPHOSPHATES (POLYP) AND POLYP + Mg

- Raman spectra of hydroxyapatite synthetized with polyphosphates (red), and HAp synthetized with polyphosphates and Mg (1.5 %, blue).

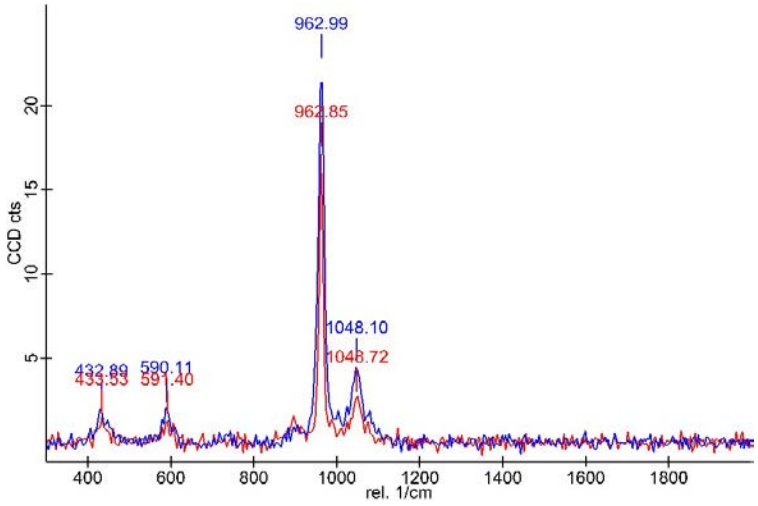

HYDROXYOLITES (HOLI)

- Raman spectra of HOLi with DNA adsorbed. Courtesy of UPC and B. Braun.

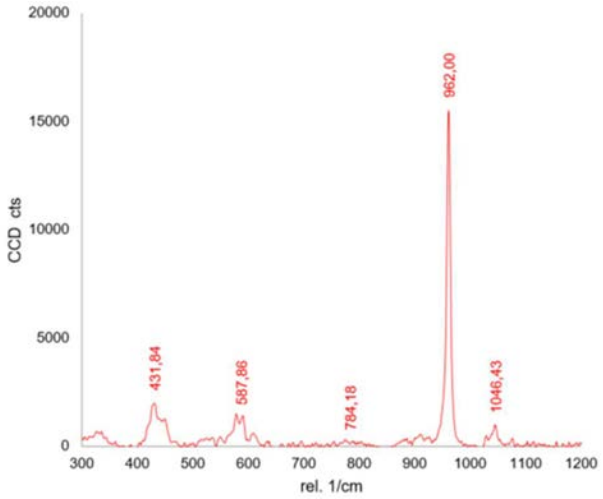

- Raman spectra of a DNA hydroxyolite on (001) facet.

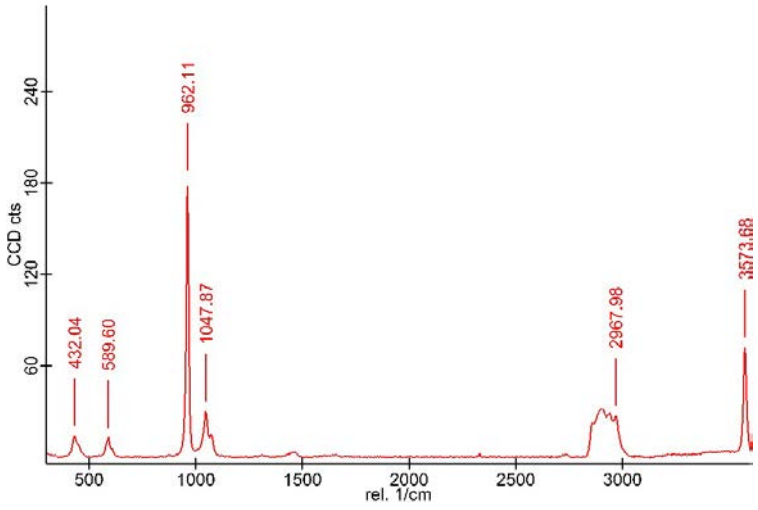

- Raman spectra of HOLi with DNA adsorbed on 010 Ca.

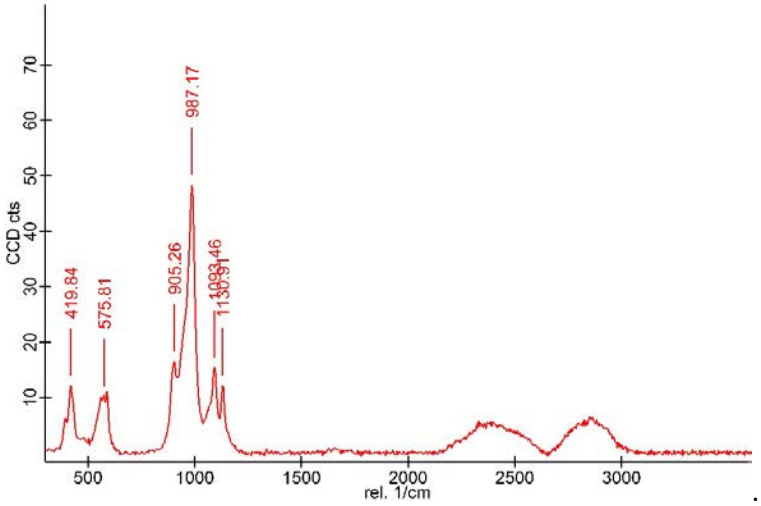

- Raman spectra of HOLi with DNA adsorbed in 010 Ca OH.

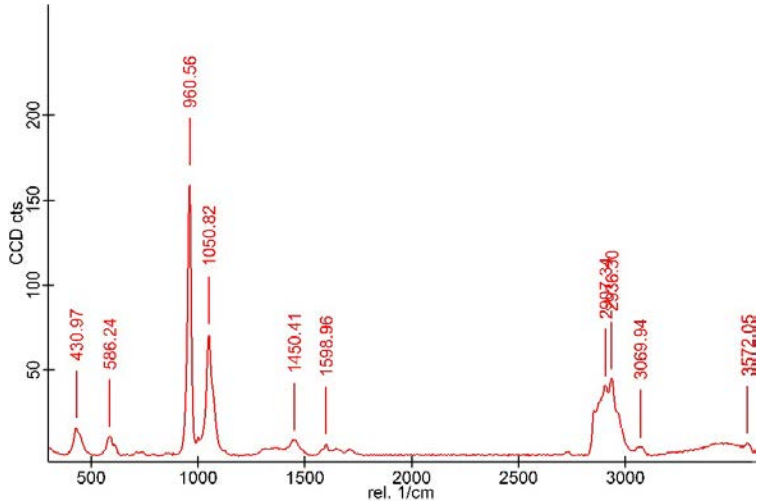

ANNEX 2: PATIENT CONSENT FORM TEMPLATE

Biobanc | IGTP | Germans Trias i Pujol Hospital | ICO Institut Català d'Oncologia

Consentiment per a la utilització de material biològic sobrant de l'assistència i les dades clíniques associades per a investigació

A l'Hospital Universitari Germans Trias i Pujol (HUGTP), igual que a la majoria d'hospitals, a més de la tasca assistencial, també es fa recerca. Les mostres que s'obtenen per al diagnòstic o tractament de les malalties, un cop utilitzades amb aquesta finalitat, encara poden ser útils i necessàries per a la investigació de cara a millorar el coneixement sobre les malalties i aconseguir la seva possible curació.

Per això, li sol·licitem l'autorització per utilitzar la informació clínica i el material biològic **sobrant** de les proves que, com a part de l'assistència normal, li hagin fet o li faran a l'HUGTP, sense que això li causi cap molèstia ni risc addicionals. **En cap cas no li practicaran més proves de les necessàries ni tampoc cap prova experimental.**

En el cas que hi doni l'autorització, aquest material biològic passarà a formar part del banc de mostres biològiques de l'hospital, anomenat Biobanc IGTP-HUGTP. Tot i així, vostè o la seva família podran disposar de les mostres quan sigui necessari per motius de salut, sempre que encara estiguin disponibles.

En tota cas, vostè (els menors d'edat, per mitjà del seu tutor o representant legal) podrà exercir els seus drets d'accés, rectificació, limitació, portabilitat, esborrat i objecció, i també obtenir informació sobre els projectes d'investigació en els quals s'hagin utilitzat les seves mostres dirigint-se a:

Responsable del tractament
Fundació Institut d'Investigació en Ciències de la Salut Germans Trias i Pujol
Carretera de Can Ruti. Camí de les Escoles s/n
08916, Badalona. Espanya
Tel. 93 497 8653 / 93 557 2831
Adreça electrònica: biobanc@igtp.cat; igtp@igtp.cat
Delegat de Protecció de dades: dpd@igtp.cat

Les mostres cedides només podran ser utilitzades amb finalitat d'investigació biomèdica, en estudis aprovats sempre pel Comitè d'Ètica de la Investigació de l'HUGTP i d'acord amb les lleis actuals. Es codificaran les mostres per a la seva utilització i les dades clíniques associades estaran custodiades d'acord amb la legislació vigent per tal de garantir la confidencialitat. En el cas que les mostres no s'hagin anonimitzat, només tindran accés a les dades personals els investigadors i les persones autoritzades que en garanteixin la confidencialitat.

El Biobanc podrà cedir les dades i mostres a investigadors d'altres centres, però sempre de forma codificada. La cessió haurà de ser aprovada pel Comitè Ètic d'Investigació Clínica. La cessió de mostres biològiques que vostè fa al Biobanc és gratuïta i voluntària.

En alguns casos es duran a terme estudis genètics amb les mostres donades, a partir de les quals es pot obtenir informació rellevant per a la seva salut i la dels seus familiars. En aquest cas, ens posarem en contacte amb vostè mitjançant les dades que figurin en el seu historial clínic. Naturalment, es respectarà el seu dret a decidir que no li comuniquin els resultats de la investigació en la qual hagin estat utilitzades les seves mostres.

Si vostè decideix signar aquest consentiment, també podrà revocar-lo lliurement en qualsevol moment sol·licitant-ho al responsable del tractament o al seu metge de referència a l'hospital. La revocació del consentiment no té cap repercussió negativa en l'assistència sanitària que vostè rep o pogués rebre. En cas de revocació, es destruiran les seves mostres i les dades associades dipositades al Biobanc. En cas d'acceptació, es conservaran indefinidament fins a la seva extinció.

En cas de tancament del Biobanc IGTP-HUGTP, la informació sobre la destinació de les seves mostres estarà a la seva disposició al Registre Nacional de Biobancs per a Investigació Biomèdica.

Autoritzo el Biobanc IGTP-HUGTP a emmagatzemar i utilitzar tant la informació clínica del meu historial mèdic com el material biològic sobrant de les proves que m'han fet o que m'han de fer, amb la finalitat de dur a terme projectes d'investigació, incloent la seva utilització en investigacions internacionals, **amb les següents restriccions**:

Descrigui les restriccions aquí _____ SÍ ☐ NO ☐

Desitjo que em siguin comunicats els resultats de la investigació **importants** per a la meva salut o la de la meva família SÍ ☐ NO ☐

Signatura del pacient (NHC .....)

Sr/Sra ..... NIF.....

o tutor o representant legal

Sr/Sra ..... NIF.....

Professional que informa:

Sr/Sra .....

Núm. de col·legiat .....

Badalona, de de 20

Model BBCI.2.08

ANNEX 3: PUBLICATIONS

ANNEX 3.1. BIOMINERALS FORMED BY DNA AND CALCIUM OXALATE OR HYDROXYAPATITE: A COMPARATIVE STUDY

Reprinted with permission from Revilla-Lopez, G., Rodríguez-Rivero, A. M., del Valle, L. J., Puiggali, J., Turon, P., & Alemán, C. Biominerals Formed by DNA and Calcium Oxalate or Hydroxyapatite: A Comparative Study. *Langmuir. 2019; 35* (36): 11912-11922. Copyright (2019) American Chemical Society.

https://doi.org/10.1021/acs.langmuir.9b01566

Abstract: "Biominerals formed by DNA and calcium oxalate (CaOx) or hydroxyapatite (HAp; the most important and stable phase of calcium phosphate) have been examined and compared using a synergistic combination of computer simulation and experimental studies. Molecular dynamics simulations show that: 1) the DNA double helix remains stable when it is adsorbed onto the most stable facet of HAp, whereas it undergoes significant structural distortions when it is adsorbed onto CaOx; 2) DNA acts as template for the nucleation and growth of HAp but not for the mineralization of CaOx; 3) the DNA double helix remains stable when it is encapsulated inside HAp nanopores but it becomes destabilized when the encapsulation occurs into CaOx nanopores. Furthermore, CaOx and HAp minerals containing DNA molecules inside and/or adsorbed on the surface have been prepared in the lab by mixing solutions containing the corresponding ions with fish sperm DNA. Characterization of the formed minerals, which has been focused on the identification of DNA using UV-vis spectroscopy, indicates that the tendency to adsorb and, especially, encapsulate DNA is much smaller for CaOx than for HAp, which is in perfect agreement with results from Molecular Dynamics simulations. Finally, quantum mechanical calculations have been performed to rationalize these results in terms of molecular interactions, results evidencing the high affinity of Ca^{2+} towards oxalate anions in aqueous environment".

LANGMUIR Article
Cite This: Langmuir 2019, 35, 11912−11922 pubs.acs.org/Langmuir

Biominerals Formed by DNA and Calcium Oxalate or Hydroxyapatite: A Comparative Study

Guillem Revilla-López,[†] Anna M. Rodríguez-Rivero,[‡,§] Luis J. del Valle,[†,∥] Jordi Puiggalí,[†,∥,⊥] Pau Turon,[*,‡] and Carlos Alemán[*,†,∥,⊥]

[†]Departament d'Enginyeria Química, EEBE, Universitat Politècnica de Catalunya, C/Eduard Maristany 10-14, Edif. I2, 08019 Barcelona, Spain

[‡]Research and Development, B. Braun Surgical, S.A., Ctra. de Terrassa 121, Rubí, 08191 Barcelona, Spain

[§]Universitat Autònoma de Barcelona. Campus de la UAB, Plaça Cívica, Bellaterra, 08193 Barcelona, Spain

[∥]Barcelona Research Center for Multiscale Science and Engineering, EEBE, Universitat Politècnica de Catalunya, C/Eduard Maristany 10-14, Edif. C, 08019 Barcelona, Spain

[⊥]Institute for Bioengineering of Catalonia (IBEC), The Barcelona Institute of Science and Technology, Baldiri Reixac 10-12, 08028 Barcelona, Spain

Supporting Information

ABSTRACT: Biominerals formed by DNA and calcium oxalate (CaOx) or hydroxyapatite (HAp), the most important and stable phase of calcium phosphate) have been examined and compared using a synergistic combination of computer simulation and experimental studies. The interest of this comparison stems from the medical observation that HAp- and CaOx-based microcalcifications are frequently observed in breast cancer tissues, and some of their features are used as part of the diagnosis. Molecular dynamics simulations show that (1) the DNA double helix remains stable when it is adsorbed onto the most stable facet of HAp, whereas it undergoes significant structural distortions when it is adsorbed onto CaOx; (2) DNA acts as a template for the nucleation and growth of HAp but not for the mineralization of CaOx; and (3) the DNA double helix remains stable when it is encapsulated inside HAp nanopores, but it becomes destabilized when the encapsulation occurs into CaOx nanopores. Furthermore, CaOx and HAp minerals containing DNA molecules inside and/or adsorbed on the surface have been prepared in the lab by mixing solutions containing the corresponding ions with fish sperm DNA. Characterization of the formed minerals, which has been focused on the identification of DNA using UV−vis spectroscopy, indicates that the tendency to adsorb and, especially, encapsulate DNA is much smaller for CaOx than for HAp, which is in perfect agreement with results from molecular dynamics simulations. Finally, quantum mechanical calculations have been performed to rationalize these results in terms of molecular interactions, evidencing the high affinity of Ca^{2+} toward oxalate anions in an aqueous environment.

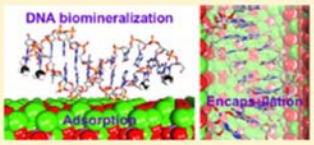

INTRODUCTION

The combination of DNA with nanomaterials (e.g., gold and metal oxide nanoparticles and carbon-based nanomaterials and minerals) to form hybrid systems is of fundamental interest for applications in DNA delivery, biosensors development, and nanotechnology.[1−8] Within this extensive field of research, the interaction of DNA with nanostructured calcium phosphate (CaP) is especially relevant because of its important biological implications. In particular, hydroxyapatite (HAp), which is probably the most important phase of CaP, is the main mineral of mammalian tooth enamel and bone[9] where it grows as nanosized mineral platelets at nucleating sites on a protein template.[10,11] Understanding the interaction between HAp and DNA has been found to be essential for biomedical field applications. For example, HAp nanoparticles (NPs) have been used for cell transfection as carriers of nucleic acids[12−15] and for purifying DNA from virus.[16]

On the other hand, spectroscopic studies on HAp microcalcifications formed inside living organisms (i.e., tumoral tissue) showed the contribution of vibrational modes of DNA, phospholipids, and proteins.[17] Such a finding is particularly relevant since HAp detection in breast cancer microcalcifications has been successfully used for screening and diagnostic purposes.[18−20] More specifically, such analyses concentrated on the chemical differentiation between two minerals: calcium oxalate (CaOx), usually associated with benign prognoses, and HAp, which is more frequently associated with malignancies.[21,22]

In recent years, the interaction between plasmid DNA and both nanostructured HAp, $Ca_{10}(PO_4)_6(OH)_2$, and amorphous CaP has been examined.[23−28] Results showed that DNA adsorption depends on the HAp morphology with NPs and fusiform nanorods adsorbing more DNA compared with flower-like and laminar nanocrystals.[23] Similar results were

Received: May 24, 2019
Revised: July 28, 2019
Published: August 2, 2019

DOI: 10.1021/acs.langmuir.9b01566
Langmuir 2019, 35, 11912−11922

obtained for polyphosphates, which mimicked the backbone of DNA.[24] Structural changes induced in plasmid DNA by the adsorption on HAp resulted in enhanced stabilization, increasing the resistance against enzymatic digestion.[23] Besides, the formation of HAp was found to be regulated by DNA, which acts as a template in a "biomineralization" process.[25−28] More specifically, the DNA backbone behaved as a very large nucleus for the growth of HAp surrounding the biomolecule.[28] Moreover, the utilization of HAp NPs as nonviral vectors for transfection has been demonstrated, proving that such inorganic particles are able to deliver DNA or RNA to a cell.[23,29−31] Interestingly, Mg^{2+} was found to play a unique role in the DNA−HAp biomineralization process since this ion has a very high affinity toward DNA, whereas in the initial stages of the particle nucleation process, it prefers to be located at the surface regions rather than at the core ones.[32]

This work renders a physical−chemical contribution to a long term debate in the medical community regarding if and why breast cancer patients with HAp-based microcalcifications have a worse prognosis compared to those showing mostly CaOx-based microcalcifications. The first part of the paper deals with the energetics and statistical mechanics of mineral··· DNA complexation, and the second part proves that DNA can only be encapsulated without denaturalization in HAp-based matrices thus forming biominerals not only able to encapsulate and transport DNA but also able to deliver it.[33] For this purpose, we have used a synergistic approach to compare DNA mineralization in HAp and CaOx. Particularly, the capacity of DNA to interact with HAp and CaOx has been examined theoretically and experimentally. Initially, molecular dynamics (MD) simulations have been carried out in order to analyze the adsorption of DNA onto the most stable facet of HAp and CaOx, the growing of HAp and CaOx minerals around the DNA template (i.e., the nucleating effect of DNA), and the stability of biominerals formed by DNA encapsulated inside nanopores of HAp or CaOx. After this, DNA−CaOx and DNA−HAp complexes have been synthesized in the laboratory and studied by UV−vis spectroscopy to compare the ability of these minerals to adsorb and encapsulate DNA. Finally, quantum mechanical (QM) calculations have been conducted to provide a comprehensive chemical explanation of the results derived from both MD simulations and UV−vis spectroscopy, which are fully consistent. It is worth mentioning that special attention has been given to the discussion of the biominerals involving CaOx, which have been much less studied than those that contain HAp, and to the role of Mg^{2+}.

METHODS

Molecular Dynamics. MD simulations were performed with the NAMD 2.6 software package.[34] In order to study the adsorption and encapsulation of DNA in CaOx and HAp, we took into consideration the clinical interest of hypomethylated and hypermethylated DNA sequences as they have been associated with the overexpression of genes or gene silencing linked to cancer diseases.[35−38] More specifically, two representative DNA dodecamers were selected to cover the full range of methylation: (a) the highly methylated dodecamer 5′-CG^{4}GTCG^{5}CCG^{6}TCG^7−3′ (hereafter, R1A) extracted from the RASSF1A gene and (b) the Dickerson dodecamer 5′-CGCGAATTCGCG-3′ (hereafter, DD) as a representative of unmethylated sequences. The DD is widely used as a DNA probe in experiments, working as a wildcard when no specific sequence is investigated. On the other hand, hypermethylation of the RASSF1A gene has been correlated with clinical and pathological characteristics of breast cancer and their clinical outcomes.[39] Charge neutralization was performed with the addition of Mg^{2+} counterions, which were located at the major groove of the double helix.[40]

Force-field parameters for DNA and phosphate anions were taken from ff99-SB,[41] Ca^{2+} parameters were from Bradbook et al.,[42] and parameters for Mg^{2+} were from Sorensen et al.[43] The TIP3P[44] water model was employed to describe explicit water molecules. In previous work, we used quantum mechanical calculations on model systems to demonstrate that such a combination of force-field parameters satisfactorily reproduce the interactions of DNA···HAp systems.[25] Bonding and van der Waals parameters for oxalate anions (Ox^{2-}) were extracted from the general Amber force-field (GAFF),[45] while charges were developed following the RESP[46] protocol and using ab initio HF/6-31G* calculations.

All productive MD runs were performed in the *NPT* ensemble at 298 K and 1 bar. Both temperature and pressure were controlled by the Berendsen thermobarostat.[47] Productive MD simulations were conducted using an integration time step of 2 fs. Representative structures were extracted every 500 steps. van der Waals interactions were evaluated with a cutoff of 10 Å and a switching distance at 8 Å. For electrostatic interactions, we computed the nontruncated electrostatic potential throughout Ewald summations, that is, the particle mesh Ewald (PME) method.[48] The real space term was determined by the van der Waals cutoff (10 Å), while the reciprocal term was estimated by interpolation of the effective charge into a charge mesh with a grid thickness of 5 points/volume unit. In all cases, bond lengths involving hydrogen were kept frozen by using the SHAKE algorithm.[49]

Adsorption of DNA. The HAp hexagonal unit cell with a $P6_3/m$ geometry ($a = b = 9.421$ Å, $c = 6.881$ Å, $\alpha = \beta = 90°$, and $\gamma = 120°$) and the 4e Wyckoff position occupied by two hydroxyl ions, each with 1/2 occupancy,[50] and the monohydrated CaOx monoclinic unit cell with a $P2_1/c$ geometry ($a = 6.316$ Å, $b = 14.541$ Å, $c = 10.116$ Å, $\alpha = \gamma = 90°$, and $\beta = 109°$)[51] were generated. These systems were cleaved to obtain the most stable facet of such minerals (see below). HAp and CaOx unit cells were expanded 6 and 4 times in the x and y directions, creating 6×6 and 4×4 supercells, respectively. The thickness of the supercell in the z axis entailed four- and two-layer slabs for HAp and CaOx, respectively. Afterward, both surfaces were solvated in the z direction with 17,756 and 12,532 water molecules for the (001) of HAp and the (100) of CaOx, respectively.

Initially, water and DNA coordinates were optimized through 5000 steps of conjugated gradient algorithm minimization. The resulting coordinates of the two systems underwent 0.5 ns of *NVT* molecular dynamics (MD) at 373 K with frozen coordinates for the DNA and the mineral. Final coordinates and velocities of the *NVT* run were used as inputs for 0.5 ns *NPT* (298 K, 1 bar) to equilibrate energy and water density (to 1 g/cm^3) in the volume occupied by the liquid and the DNA. The Berendsen thermobarostat[47] was employed at constant xy-plane areas and frozen DNA and mineral slab coordinates. Productive dynamics started from the latter output, keeping fixed only the mineral atoms. Trajectories were 150 ns long.

DNA in Solution. The R1A and DD double helices and Mg^{2+} counterions were solvated with 30,000 water molecules, and the density of the resulting system was equilibrated to 1 g/cm^3 following the same protocol used for the surface slabs in the adsorption simulations. Productive control dynamics was 150 ns long.

Nucleation of DNA Biominerals. As DNA methylation is not expected to play any role in the nucleation of biominerals, simulations were conducted using the R1A dodecamer only. The nucleation of CaOx around R1A was simulated considering, in addition of the dodecamer, 10 Mg^{2+}, 20 Ca^{2+}, 20 Ox^{2-} molecules, and 50,551 water molecules. The nucleation of HAp around the R1A was examined considering a system with 10 Mg^{2+}, 30 Ca^{2+}, 20 PO_4^{3-} molecules, and 51,675 water molecules.

Systems were previously equilibrated at the target temperature (298 K), pressure (1 atm), and density (1 g/cm^{-1}). For this purpose, 5000 steps of energy minimization were initially performed to relax structural tensions. After this, the solvent and ions were thermally relaxed by three consecutive runs, while the B-DNA was kept frozen: 0.5 ns of *NVT*-MD (volume conserved) at 500 K was used to

DOI: 10.1021/acs.langmuir.9b01566
Langmuir 2019, 35, 11912−11922

homogeneously distribute the solvent and ions in the box. Then, 0.5 ns of isothermal (298 K) and 0.5 ns of isobaric (1 atm and 298 K) relaxations were run. Finally, all of the atoms of the systems were submitted to 0.15 ns of steady heating until the target temperature was reached (298 K), 0.25 ns of *NVT*-MD at 298 K (thermal equilibration), and 0.5 ns of density relaxation (*NPT*-MD). After equilibration, productive MD simulations of 150 ns were conducted.

Encapsulation of DNA. The HAp hexagonal unit cell[50] and the monohydrated CaOx monoclinic unit cell[51] were used to construct supercells considering $6 \times 6 \times 7$ and $4 \times 4 \times 5$ unit cells, respectively. After this, a hole was generated in the center of each supercell with the dimensions of such a hole being defined by a DNA double helix. After several trials, we found that a hole of $2 \times 2 \times 7$ unit cells was the minimum required for both minerals to accommodate the double helix without severe steric contacts. In order to completely avoid unfavorable steric interactions between the apatite and the biomolecule, some additional atoms and groups of atoms were translated at their border regions allowing us to maintain the electroneutrality of the supercells. Then, R1A and DD double helices, which were arranged in the canonical B form, were embedded inside the pores. In order to maintain the electrical neutrality of the system, Mg^{2+} ions were put at the major groove of the double helix. Figure 1 depicts the starting models used to represent the DD double helix embedded into HAp and CaOx pores with the starting models for the R1A sequence being analogous to these ones.

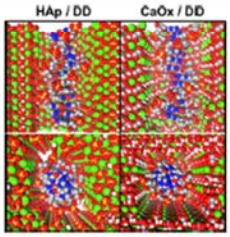

Figure 1. Axial and equatorial perspectives of the starting models used to represent the DD double helix embedded in HAp and CaOx nanopores.

In order to evaluate the stability of the encapsulated DNA models, both energy minimization and MD simulations were applied. Initially, all the models were minimized by applying 5×10^3 steps of the steepest descent to relax the more important conformational and structural tensions. Then, an MD run of 3.0 ns in the *NVT* ensemble (constant number of particles, volume, and temperature) at 298 K was carried out to equilibrate the four systems under study (i.e., R1A and DD encapsulated into HAp and CaOx) and eliminate small structural tensions. After such thermal relaxation, the saved coordinates were submitted to a new energy minimization by applying 5×10^3 steps of the steepest descent until energy convergence. In both energy minimizations and MD simulations, atoms contained in R1A and DD were only allowed to move from their positions with the coordinates of the mineral kept fixed at their crystallographic positions in all cases. Each system was calculated in triplicate considering starting points that differ in the orientation of the DNA inside the generated holes.

In Vitro Synthesis of Biominerals. *In Vitro Synthesis of DNA–CaOx and DNA–MgOx Complexes.* The synchronized dropwise (rate of 2 mL/min) addition of 10 mL of a solution of 0.04 M sodium oxalate (Sigma-Aldrich 99.5%, 223433) and 10 mL of 0.04 M $CaCl_2$ (Scharlab, CA01920500) to 0.06 g of fish sperm DNA (Sigma-Aldrich, 74782) was conducted under stirring at 75 °C for 5 h. Then, the resulting solutions were cooled to room temperature, centrifuged, and washed successively with molecular biology grade water (Millipore, H2OMB0506) twice and a 60/40 v/v mixture of ethanol–water (Ethanol, Scharlab ET0011000). A white powder with traces of pale orange was obtained after freeze-drying. Calcium chloride was replaced by $MgCl_2$ (Sigma-Aldrich, M8266) to obtain the DNA–MgOx system.

In Vitro Synthesis of DNA–HAp Complexes. Fish sperm DNA (0.1 g) was added to 15 mL of 0.3 M $(NH_4)_2HPO_4$ solution in deionized water. The pH of such solution was previously adjusted to 10 with aqueous ammonia. The mixture was added dropwise (rate of 2 mL/min) and under agitation (400 rpm) to 25 mL of 0.3 M $Ca(NO_3)_2$ solution in deionized water and the appropriate amount of aqueous ammonia to adjust the pH to 10. Temperature was maintained at 40 °C during the addition process. After that, the reaction mixture was stirred at 80 °C for 1.5 h and then naturally cooled to room temperature. The resultant suspension was aged for 24 h at room temperature. Then, the precipitate was separated by centrifugation and washed sequentially with deionized water and a 60/40 v/v mixture of ethanol–water (twice). A white powder was obtained after freeze-drying.

A UV-3600 (Shimadzu) UV–vis–NIR spectrophotometer controlled by UVProbe 2.31 software was used to record UV–vis spectra of DNA–CaOx, DNA–MgOx, and DNA–HAp complexes at room temperature in the 200–400 nm range with a bandwidth of 0.2 nm and a scan speed of 600 nm/min.

QM Calculations. QM calculations were performed using the Gaussian 09 software package.[52] Geometry optimization, solvation, and binding energy calculations were carried out with the hybrid functional B3LYP[53,54] combined with the 6-311G++(2d,2p) basis set. All geometry optimizations were carried out until a stationary point was reached. These were confirmed as minima by frequency analyses (i.e., no imaginary frequency was found). The gas-phase free energies were obtained at 298 K by correcting the energies with the zero-point energy and the thermal correction term and by evaluating the entropy using standard statistical thermodynamic methods. The SMD solvation method[55] was chosen to calculate the hydration free energy of the systems, ΔG_{hyd}, which was estimated as the difference between the free energies in the gas phase and aqueous solution. Binding energies, ΔG_b, were calculated as $\Delta G_b = G_{sol,c} - \Sigma_i G_{sol,i}$ where $G_{sol,c}$ is the free energy of the complex in the aqueous solution and $G_{sol,i}$ is the free energy of each component of the complex in the aqueous solution (i.e., *i* stands for each of the interacting component of the complex). All ΔG_b values were corrected by the base superposition error (BSSE) using the standard counterpoise protocol.

RESULTS AND DISCUSSION

Adsorption of DNA on the Mineral Surface. Initially, MD simulations were focused on the adsorption of R1A and DD sequences on the surfaces of the HAp and monohydrated CaOx minerals. We focused on the interaction formed when such dodecamers are adsorbed onto the most stable facet of HAp[56] and monohydrated CaOx,[57] which is the (001) and (100), respectively. Almora-Barrios et al.[58] reported that the calculated surface energies of the (001) and the average (010) surfaces are 1.01 and 1.32 J/m, respectively, indicating that the former is more stable than the latter in agreement with the previous literature.[59,60] Indeed, the less stable (010) surface, which was proposed to be much less populated than the (100), quickly accumulates more materials that grow out of the crystal morphology because of the reactivity associated to such instability. Besides, the (100) was identified by atomic force microscopy experiments not only as the most populated facet of CaOx[61,62] but also as the surface that forms the strongest interactions with carboxylate and amidinium groups, which are abundantly present in biomolecules, including DNA.[62]

Although the methylated and nonmethylated sequences showed a similar behavior when interacting separately with HAp or monohydrated CaOx, simulations demonstrated that the structural stability of DNA is totally different for each mineral. The stability of the adsorbed sequences was evaluated

DOI: 10.1021/acs.langmuir.9b01566
Langmuir 2019, 35, 11912–11922

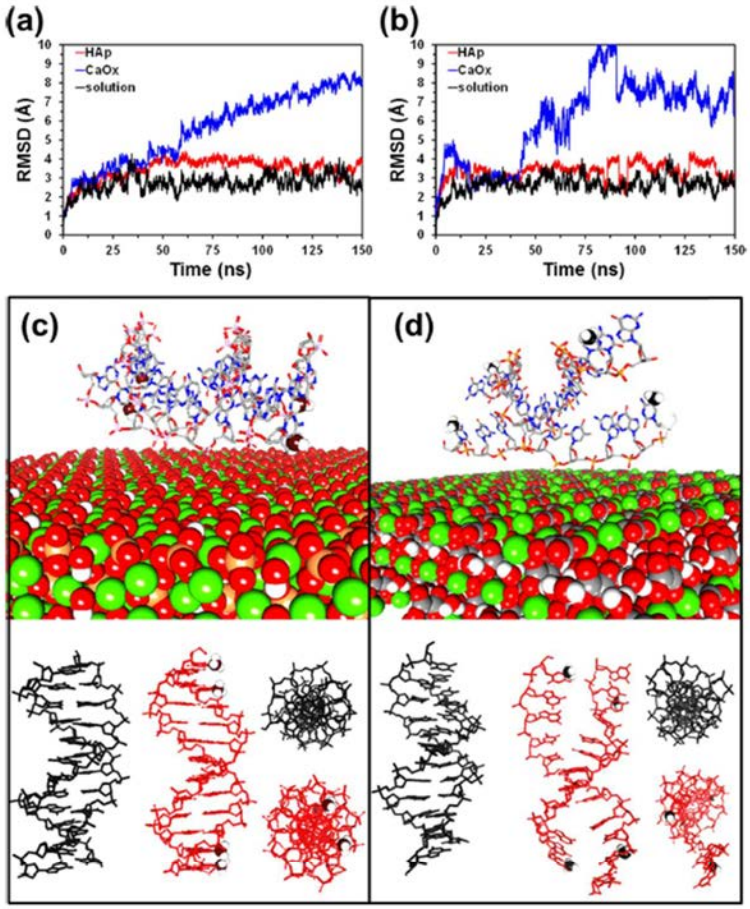

Figure 2. Comparison of DNA adsorption on HAp and monohydrated CaOx. Temporal evolution of the RMSD with respect to the canonical B-DNA double helix for (a) R1A (5′-CG^{4}GTCG^{5}CCG^{6}TCG^7-3′) and (b) DD (5′-CGCGAATTCGCG-3′) adsorbed onto the (001) HAp and (100) CaOx facets. The RMSD obtained for the DNA in aqueous solution has been included for comparison. Axial view of the R1A dodecamer adsorbed onto (c) the (001) surface of HAp and (d) the (100) surface of monohydrated CaOx. Oversized black balls highlight the position of carbon of methyl groups in the methylated DNA. For each system, the axial and equatorial views of the canonical double helix (in black) and the R1A double helix adsorbed onto the HAp or CaOx surface (in red) are compared at the bottom.

by examining the temporal evolution of the root mean square deviation (RMSD), which was calculated between each atom position of the B-DNA canonical double helix and the dodecamer structures recorded from MD trajectories. As shown below, the RMSD was converged for all systems preserving the B-DNA structure, whereas the RMSD was high enough to guarantee complete destructuration for all systems in which the double helix is lost. However, in the latter cases, convergence of the RMSD was not considered a requisite since the dynamics and structure of unfolded B-DNA is out of the scope of this work.

Figure 2a,b, which includes the results obtained in the aqueous solution (control), compares the RMSDs obtained for R1A and DD, respectively. The average RMSDs obtained for R1A and DD adsorbed onto the (001) HAp (3.5 ± 0.6 and 3.4 ± 0.4 Å, respectively) are close to those obtained for the same sequences in the aqueous solution (2.7 ± 0.5 and 2.7 ± 0.4 Å, respectively), evidencing that the B-DNA double helix remains stable when adsorbed onto HAp. Thus, the double helix is able to accommodate itself onto the HAp surface, independent of the methylation, by establishing a balance between the attractive and repulsive interactions between the phosphate groups of DNA and the Ca^{2+} and PO_4^{3-} ions of the mineral, respectively. The formation of such interactions is reflected in Figure 2c and Figure S1a for R1A and DD, respectively, which display a representative snapshot of the dodecamer adsorbed onto HAp and compare the adsorbed double helix with a canonical one. The affinity of HAp toward the double helix of

DOI: 10.1021/acs.langmuir.9b01566
Langmuir 2019, 35, 11912−11922

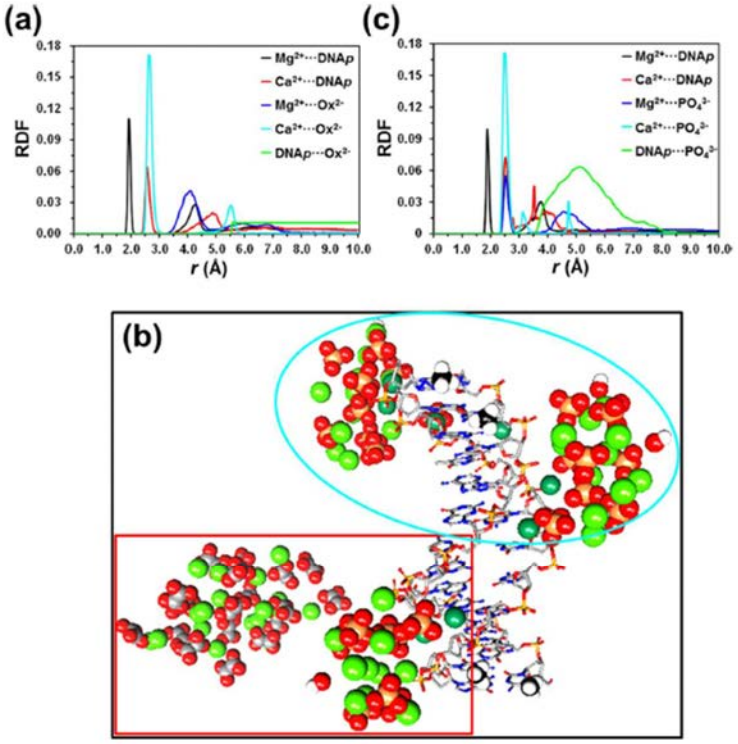

Figure 3. (a) RDFs extracted from the MD simulation of the solution containing R1A, water, Mg^{2+}, Ca^{2+}, and Ox^{2-}. DNA*p* refers to the DNA phosphate backbone. (b) Superposed snapshot extracted from the simulations with Ox^{2-} (red box) and PO_4^{3-} (blue ellipsoid) ions. (c) RDFs extracted from the MD simulation of the solution containing R1A, water, Mg^{2+}, Ca^{2+}, and PO_4^{3-}. In order to ensure that R1A···ion and ion···ion interactions had enough time for their formation (if possible), RDFs were calculated in all cases considering only the last 50 ns of productive simulations.

DNA has been attributed to the complementarity between the mineral and the phosphate groups of the DNA backbone, which were found to exhibit isomorphic planes.[25]

In contrast, the average RMSD increases progressively for the R1A and DD sequences adsorbed on the (100) facet of monohydrated CaOx, reaching, in both cases, values higher than 8 Å after 150 ns. Thus, the CaOx surface causes a drastic destabilization of the adsorbed double helix due to the electrostatic repulsions between Ox^{2-} and the polyphosphate DNA backbone, which are directly confronted. The effect of Ox^{2-}···polyphosphate repulsive interactions in the double helix is illustrated in Figure 2d and Figure S1b for R1A and DD, respectively. As it can be seen, electrostatic repulsions tend to deploy the DNA double helix, separating the two strands. This destabilizing effect is not offset by the water molecules of the internal monohydration layer, which practically does not interact with the superficial DNA.

Nucleation of DNA-Templated Biominerals. The behavior of R1A in an ionic solution to assess the feasibility of DNA to nucleate CaOx and/or HAp biominerals and act as a template was modeled using solution-like systems containing Ox^{2-} or PO_4^{3-} ions together with the DNA dodecamer, Ca^{2+}, and Mg^{2+}. Figure 3a shows the radial distribution functions (RDFs) derived from the simulation with Ox^{2-} for the following pairs: Mg^{2+}–DNA*p* (where DNA*p* refers to the center of masses of the phosphate groups from the DNA backbone), Ca^{2+}–DNA*p*, Mg^{2+}–Ox^{2-} (where Ox^{2-} refers to the center of masses of Ox^{2-} anions), Ca^{2+}–Ox^{2-}, and DNA*p*–Ox^{2-}. For a given pair, α–β, the RDF curve gives a measure of the relative probability that β resides at a radial distance r from α centered at the origin of coordinates.

The profile obtained for the Mg^{2+}–DNA*p* pair (black) shows a sharp peak at r = 1.9 Å, evidencing the high affinity of Mg^{2+} toward DNA. Besides, the first peak for the Ca^{2+}–DNA*p* pair, which appears at r = 2.6 Å, apparently displays a smaller area under the curve (red). On the other hand, the area under the Ca^{2+}–Ox^{2} peak at r = 2.6 Å (light blue) is much larger, reflecting that the attraction of Ca^{2+} by the Ox^{2-} is very favored in comparison to the affinity by the phosphate groups from DNA. Interestingly, Ox^{2-} anions do not exhibit any affinity toward DNA with an equiprobable distribution to be found once an exclusion threshold at r = 5.5 Å is exceeded.

Considering the possibility of forming triads like DNA*p*···X···Ox^{2-} where X refers to Ca^{2+} or Mg^{2+} coordination ions, analysis of the RDFs shows that Ca^{2+} cannot play this role. Once Ca^{2+} is bound to DNA*p* or to Ox^{2-}, it prefers the

DOI: 10.1021/acs.langmuir.9b01566
Langmuir 2019, 35, 11912–11922

interaction with surrounding explicit water molecules instead of forming the triad. Thus, the sum of the r values for the first peak of the Ca^{2+}–DNA*p* and Ca^{2+}–Ox^{2-} RDFs totals to 5.2 Å with this value being lower than the threshold distance of cation-mediated DNA*p*–Ox^{2-} carboxyl interaction (i.e., 5.5 Å). The addition of the distances associated to the first peak of Mg^{2+}–DNA*p* and Mg^{2+}–Ox^{2-} RDFs renders a value of 6.0 Å, which is higher than the cation-mediated threshold. However, the absence of peaks in the RDF of the DNA*p*–Ox^{2-} pair suggests that DNA*p*···Mg^{2+}···Ox^{2-} interactions are extremely weak in highly hydrated environments. The abovementioned tendencies are reflected in Figure 3b, which displays a snapshot from the MD simulation of the modeled system (red box). As it can be seen, Ox^{2-} anions tend to form clusters with Ca^{2+} cations separated from the DNA. Apparently, the polyphosphate groups from DNA do not play any significant role in the formation of CaOx.

Figure 3c displays the RDFs derived from the simulation with PO_4^{3-} for the Mg^{2+}–DNA*p*, Ca^{2+}–DNA*p*, Mg^{2+}–PO_4^{3-} (where PO_4^{3-} refers to the center of masses of PO_4^{3-} anions), Ca^{2+}–PO_4^{3-}, and DNA*p*–PO_4^{3-} pairs. The profiles obtained for Mg^{2+}–DNA*p* and Ca^{2+}–DNA*p* pairs (black and red, respectively) show a sharp peak at r = 1.9 and 2.5 Å, respectively. Thus, although the affinity of the DNA dodecamer toward Mg^{2+} is higher than toward Ca^{2+}, the latter ion interacts more with the phosphate groups of DNA than those in the simulation with Ox^{2-}. Besides, the Ca^{2+}–PO_4^{3-} profile shows a sharp peak at r = 2.5 Å (light blue), indicating that the attraction of Ca^{2+} by PO_4^{3-} anions and DNA*p* is very similar. However, the most important difference between simulations with Ox^{2-} and PO_4^{3-} is detected in the RDF calculated for the DNA*p*–PO_4^{3-} pair (green), which shows a broad peak centered at r = 5.00 Å. This peak evidences that PO_4^{3-} anions tend to be distributed around the DNA, which acts as a template and facilitates the growing of the mineral around it.

Moreover, in this case, the formation of both DNA*p*···Ca^{2+}···PO_4^{3-} and DNA*p*···Mg^{2+}···PO_4^{3-} triads is consistent with the peaks observed in the RDFs. Thus, the addition of the r values for the first peak of the Ca^{2+}–DNA*p* and Ca^{2+}–PO_4^{3-} RDFs sums 5.0 Å, which matches the maximum of the broad peak obtained for the DNA*p*–PO_4^{3-} RDF (i.e., 5.0 Å). Besides, the sum of the distances associated to the first peak of Mg^{2+}–DNA*p* and Mg^{2+}–PO_4^{3-} is 4.3 Å, which is within the area of the broad peak obtained for DNA*p*–PO_4^{3-}. These results indicate that PO_4^{3-} anions tend to form clusters around the polyphosphate backbone of DNA with repulsive interactions being shielded by the Ca^{2+} and Mg^{2+} ions located between them. This clustering distribution is shown in Figure 3b, which displays a representative snapshot from the MD simulation of the PO_4^{3-}-containing system (blue ellipsoid) superposed to that from simulation with Ox^{2-}. Overall, the formation of calcium phosphate clusters surrounding the DNA backbone is fully consistent with previous experimental observation in which the DNA was found to act as a template for the nucleation and growth of crystalline HAp.[28]

Encapsulation of DNA inside Mineral Nanopores. In order to elucidate if DNA can be present inside HAp and CaOx in microcalcifications, the encapsulation of R1A and DD in mineral nanopores was modeled. Figure 4 represents the structure of R1A and DD dodecamers embedded in HAp and CaOx nanopores after relaxation through energy minimizations and MD, as described in the Methods section.

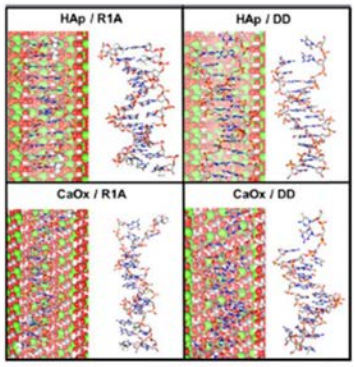

Figure 4. Axial perspective of the R1A and DD double helix embedded in HAp and CaOx nanopores after relaxation through energy minimization and MD. The double helix is also displayed without the mineral to show the different degrees of distortion induced by the minerals.

In the case of HAp, the DNA double helix occupies practically the whole pore, independent of its methylation degree. Although interactions with mineral ions induce some distortions in the backbone, the DD and R1A double helices with their intrastrand stacking and the interstrand hydrogen bonds are clearly preserved. This is illustrated in Figure 4, which also depicts the double helix without the mineral. As it can be seen, initial double helices do not undergo significant distortions, which is fully consistent with the simulations discussed in the previous subsection. Thus, the attractive interaction between the Ca^{2+} ions of HAp and the polyphosphate chain of the DNA allows maintaining the stability of the B-DNA inside the pore. The RMSD between the canonical double helix (i.e., the starting structure) and the relaxed double helix, which was calculated considering all the atoms, is relatively small: 1.9 and 3.5 Å for R1A and DD, respectively.

Relaxation of R1A and DD dodecamers embedded in CaOx induced drastic geometric distortions that affected significantly both the interstrand hydrogen bonds and the intrastrand π–π stacking, as displayed in Figure 4. Thus, the RMSD calculated with respect to the canonical B-DNA used as a starting point was close to 10 Å for both sequences, which is significantly higher than the values obtained for complexes with HAp. This is because of the repulsive interactions between the Ox^{2-} anions and the phosphate groups of the double helix that, in this case, are not shielded by the attractive interactions of the latter with the Ca^{2+} ions. Apparently, these results indicate that the geometry of CaOx is not appropriate for preserving the tertiary structure of the biological DNA when the latter is embedded inside the nanopore.

Overall, these results indicate that the cavity generated in HAp allows B-DNA double helices' encapsulation without producing mineral-induced stress, while the opposite situation is obtained when CaOx nanopores are studied. Although this feature might be related with the benign and malignancy cancer prognosis associated to CaOx and HAp microcalcifications,[21,22] no experimental observation relating the medical diagnosis and the functionality of the genes linked to cancer diseases has been reported yet.

DOI: 10.1021/acs.langmuir.9b01566
Langmuir 2019, 35, 11912−11922

Experimental DNA Mineralization. As a consequence of the previous in silico results, DNA mineralization with CaOx, magnesium oxalate (MgOx), and HAp was investigated forming DNA−CaOx, DNA−MgOx, and DNA−HAp complexes through the procedure described in the Methods section. It is worth noting that DNA was incorporated into aqueous inorganic solutions, and therefore the biomolecule could be absorbed onto the surface of the formed mineral particles or encapsulated into them. The nonphysiological conditions used in these experiments have been used as a proof of concept for the underlying physicochemical mechanism considering monohydrated CaOx and HAp, which are the minerals employed in the simulations. Thus, the conditions used for the in vitro synthesis of minerals have avoided mixed effects of other crystalline forms, for example, dihydrates and trihydrates in the case of CaOx and brushite, tricalcium phosphate, or amorphous calcium phosphate in the case of HAp.

Figure 5a compares the UV−vis spectra recorded for (a1) as-obtained DNA−CaOx samples, (a2) digested DNA−CaOx

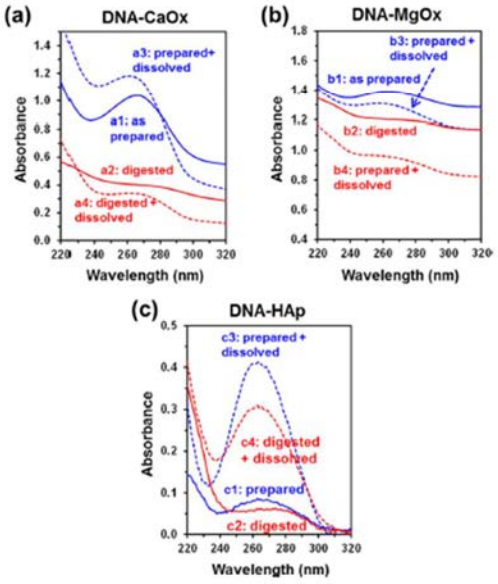

Figure 5. UV−vis absorption spectra of the (a) DNA−CaOx, (b) DNA−MgOx, and (c) DNA−HAp complexes. Spectra of as-prepared samples (#1, blue solid lines), samples digested with DNAase to eliminate DNA adsorbed on the surface (#2, red solid lines), dissolved as-prepared samples (#3, blue dashed lines), and dissolved digested samples (#4, red dashed lines) (# refers to a, b, or c).

samples in which superficially adsorbed DNA is removed by digesting as-obtained DNA−CaOx complexes with DNAase, (a3) as-obtained DNA−CaOx samples from a1 redissolved with sodium citrate (5 mM), and (a4) digested DNA−CaOx samples dissolved with sodium citrate (5 mM). The UV−vis spectrum of as-prepared DNA−CaOx complexes (a1) clearly demonstrates the presence of DNA since a characteristic absorption peak is observed at 266 nm. However, the absorbance at 266 nm decreases considerably after enzymatic degradation treatment (a2). This absorbance increases after dissolution of the as-obtained DNA−CaOx complexes (a3), while it remains very small when the digested samples are dissolved (a4). Overall, these results unambiguously demonstrate that the mineralization of DNA from Ca^{2+}- and Ox^{2-}-containing solutions mainly occurs through the adsorption of the biomolecule on the surface of the formed CaOx particles, whereas the encapsulation of DNA inside such inorganic particles is very limited.

To promote the affinity of Ox^{2-} toward DNA, DNA−MgOx complexes were prepared following the procedure previously used to obtain DNA−CaOx complexes (see Methods section). As the electrostatic binding of Mg^{2+} in the grooves of DNA is essential for the stability of the double helix, substitution of Ca^{2+} by Mg^{2+} was hypothesized to favor the mineralization of DNA. The UV−vis spectra recorded for as-prepared, digested, and dissolved DNA−MgOx samples are displayed in Figure 5b. Surprisingly, the absorption peak at 266 nm is very small for the as-obtained samples before and after dissolution (b1 and b3, respectively) and inexistent for the digested ones before and after dissolution (b2 and b4, respectively). Accordingly, the adsorption of DNA onto the mineral surface is lower for MgOx than for CaOx, whereas the DNA encapsulation was very limited in both cases. These experimental observations are fully consistent with MD simulations on the nucleation of DNA biominerals in which the formation of DNA*p*···Ca^{2+}···Ox^{2-} and DNA*p*···Mg^{2+}···Ox^{2-} interacting triads was not detected, indicating that Ox^{2-} anions hinder the mineralization of DNA, independent of the identity of the divalent metallic cation.

Conversely, UV−vis spectra obtained for DNA−HAp complexes shows the presence of both DNA absorbed on the surface and encapsulated inside the particles. Thus, the DNA absorption peak is clearly observed in as-prepared complexes before and after dissolution (c1 and c3, respectively) and in samples dissolved after digestion with the DNAase (c4). Interestingly, the absorbance is much higher for dissolved samples (c3 and c4) than that for as-prepared samples (c1 and c2), evidencing the very high tendency of HAp to grow surrounding the DNA molecule that acts as the nucleating template.

It is worth noting that the experimental observations achieved for DNA−CaOx, DNA−MgOx, and DNA−HAp complexes are fully consistent with the computer simulations discussed above. Thus, MD simulations showed that, although DNA can be adsorbed onto the most stable facets of CaOx and especially HAp, its predominant role as a nucleating template only occurs for HAp. On the other hand, Mg^{2+} ions tend to be located in the grooves of DNA, acting as counterions of the polyphosphate backbone. Nevertheless, MgOx particles are not appropriate for mineralizing the DNA by superficial absorption or encapsulation.

QM Calculations. Interactions between the different species involved in DNA−CaOx complexes were further studied to completely understand the poor affinity of DNA by CaOx in comparison to HAp. For this purpose, QM calculations in vacuum and within the framework of an implicit solvation model were performed on small representative model complexes involving two or three interacting species, which are depicted in Figure 6. The estimated ΔG_b and ΔG_{byd} values, which were calculated as indicated in the Methods section, are expected to complete the scenario described by classical MD simulations. The ΔG_b informs about the strength of the

DOI: 10.1021/acs.langmuir.9b01566
Langmuir 2019, 35, 11912−11922

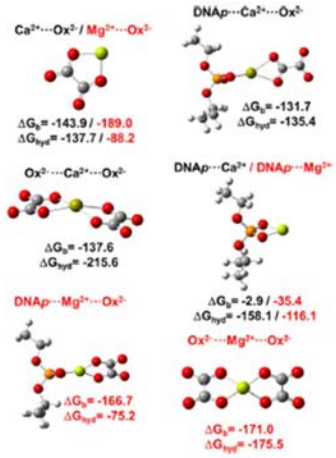

Figure 6. Quantum mechanics calculated binding free energy in the aqueous solution (ΔG_b, kcal/mol) and hydration free energy (ΔG_{hyd}, kcal/mol) for different complexes including either Ca^{2+} or Mg^{2+}, oxalate (Ox^{2-}), and DNA phosphates (*p*DNA): black letters stand for Ca^{2+} whereas red ones for Mg^{2+}. Calculations were performed within the SMD-B3LYP/6-311G++(2d,2p) framework.

interactions that maintain the species involved in the complex assembled in the aqueous solution, while ΔG_{hyd} gives the free energy change associated with the transfer of the complex between vacuum and bulk water. The ΔG_b and ΔG_{hyd} values included in Figure 6 completely support the conclusions derived from MD simulations and experimental observations.

First inspection of the ΔG_b and ΔG_{hyd} values reveals that the strength of the binding is more exothermic in complexes with Mg^{2+} than in those with Ca^{2+}, whereas hydration favors the latter with respect to the former. Careful analysis reveals that when differential energies are considered for the calculated complexes, this behavior can be explained. The ΔG_b is more attractive for Mg^{2+}···DNA*p* than for Ca^{2+}···DNA*p* (i.e., $\Delta\Delta G_b = -32.5$ kcal/mol), indicating that the phosphates from DNA tend to coordinate with Mg^{2+} instead of Ca^{2+} when both ions are present. The same trend is observed for Mg^{2+}···Ox^{2-} and Ca^{2+}···Ox^{2-} complexes with the strength of the binding being higher in the former than in the latter (i.e., $\Delta\Delta G_b = -46.0$ kcal/mol). However, ΔG_{hyd} indicates the opposite, the solvation being significantly more favored for complexes with Ca^{2+} than for those with Mg^{2+} (i.e., $\Delta\Delta G_{hyd} = -42.0$ and -49.5 kcal/mol for complexes with DNA*p* and Ox^{2-}, respectively). The balance between $\Delta\Delta G_b$ and $\Delta\Delta G_{hyd}$ values indicates that, in a solution containing all the considered species, Ox^{2-} preferentially interacts with Ca^{2+}, while DNA phosphate prefers Mg^{2+}.

Additional calculations on model complexes involving three interacting species provide complete understanding of the in-lab experiments described in the previous subsection for CaOx and MgOx. Thus, the strength of the binding in Ox^{2-}···Mg^{2+}···Ox^{2-} is stronger than in Ox^{2-}···Ca^{2+}···Ox^{2-} by $\Delta\Delta G_b = -33.4$ kcal/mol, while the hydration of the latter is favored with respect to that of the former by $\Delta\Delta G_{hyd} = -40.1$ kcal/mol. Therefore, the sum of these free energy gaps indicates that Ox^{2-} anions tend to surround and coordinate with Ca^{2+} instead of Mg^{2+}. Amazingly, this tendency is much more pronounced for DNA*p*···Mg^{2+}··· Ox^{2-} and DNA*p*···Ca^{2+}··· Ox^{2-} complexes. Thus, although the binding is favored in the former complex by $\Delta\Delta G_b = -35.0$, hydration stabilizes the latter by $\Delta\Delta G_{hyd} = -60.2$ kcal/mol. These and the previous $\Delta\Delta G_b$ and $\Delta\Delta G_{hyd}$ differences indicate that the coordination of an extra Ox^{2-} with already Ox^{2-}-bound Ca^{2+} or Mg^{2+} instead of DNA*p*-bound Mg^{2+} is favored before the precipitation of any of the complexes can happen. In addition, Ca^{2+}···Ox^{2-} and Ox^{2-}···Ca^{2+}···Ox^{2-} have much more favorable hydration than their corresponding Mg^{2+} counterparts. Finally, Mg^{2+} prefers to coordinate with two Ox^{2-} rather than with DNA*p* and Ox^{2-}, which enables CaOx and MgOx calcifications to grow DNA-free in the solution as previously confirmed by in-the-lab tests.

■ CONCLUSIONS

In summary, we systematically compared the mineralization of DNA in CaOx and HAp using a synergistic computational–experimental approach. With the latter material traditionally related with transfection of cells with nucleic acids and with the formation of microcalcifications inside living organisms, the biomedical application of DNA-based biominerals might be further improved by understanding the fundamental interactions associated to adsorption and encapsulation of such biomolecules in HAp and CaOx. Using atomistic MD simulations, we studied DNA adsorption and encapsulation in CaOx and HAp. Although DNA can be adsorbed onto the most stable facet of the two minerals, important differences are found. HAp is able to preserve the DNA double helix because of the complementarity between their phosphate anions through isomorphic planes, while the repulsive interactions between the oxalate anions of CaOx and the polyphosphate backbone of the biomolecule cause the destabilization of the double helix. Besides, DNA nucleates the growing of HAp when it is immersed in an ionic solution containing Ca^{2+}, Mg^{2+}, and PO_4^{3-} ions and encapsulates it inside HAp nanopores maintaining the stability of the double helix. The opposite behavior is observed when DNA is immersed in a Ca^{2+}, Mg^{2+}, and Ox^{2-} solution and encapsulated in CaOx pores: the minerals grow separately from DNA, and the double helix undergoes severe structural alterations. These theoretical results have been corroborated experimentally by preparing DNA–HAp, DNA–CaOx, and DNA–MgOx complexes. UV–vis spectra show that HAp is much more effective than CaOx and MgOx for DNA mineralization in terms of both adsorption and encapsulation. Furthermore, QM calculations on model complexes in the aqueous solution show that Ca^{2+} ions prefer to coordinate with two Ox^{2-} than form triads involving an Ox^{2-} and a phosphate group from DNA.

Another fundamental insight obtained in this work is that results described above are independent of the methylation degree of the simulated DNA dodecamers. This is very relevant in the medical context since CaOx and HAp breast cancer microcalcifications have been associated with more frequent benign and malignancy prognoses, respectively. Results derived from this study open a new concept that deserves further research, suggesting that HAp microcalcifications might be involved in the protection and transport of carcinogenic DNA.

DOI: 10.1021/acs.langmuir.9b01566
Langmuir 2019, 35, 11912–11922

■ ASSOCIATED CONTENT

Supporting Information

The Supporting Information is available free of charge on the ACS Publications website at DOI: 10.1021/acs.langmuir.9b01566.

An axial view of the DD dodecamer adsorbed onto the (001) surface of HAp and the (100) surface of monohydrated CaOx (PDF)

■ AUTHOR INFORMATION

Corresponding Authors

*E-mail: pau.turon@bbraun.com (P.T.).
*E-mail: carlos.aleman@upc.edu (C.A.).

ORCID

Pau Turon: 0000-0001-6354-9701
Carlos Alemán: 0000-0003-4462-6075

Notes

The authors declare no competing financial interest.

■ ACKNOWLEDGMENTS

Authors acknowledge MINECO-FEDER (nos. RTI2018-098951-B-I00 and RTI2018-101827-B-I00), Agència de Gestió d'Ajuts Universitaris i de Recerca (nos. 2017SGR359 and 2017SGR373), and B. Braun Surgical, S.A., for financial support. This work is integrated within a wider research project supported by B. Braun Surgical S.A., UPC, ICS, and ICFO. Support for the research of C.A. was received through the prize "ICREA Academia" for excellence in research funded by the Generalitat de Catalunya.

■ REFERENCES

(1) Tan, L. H.; Xing, H.; Lu, Y. DNA as a Powerful Tool for Morphology Control, Spatial Positioning, and Dynamic Assembly of Nanoparticles. *Acc. Chem. Res.* **2014**, *47*, 1881−1890.

(2) Zhou, W.; Saran, R.; Liu, J. Metal Sensing by DNA. *Chem. Rev.* **2017**, *117*, 8272−8325.

(3) Wang, H.; Yang, R.; Yang, L.; Tan, W. Nucleic Acid Conjugated Nanomaterials for Enhanced Molecular Recognition. *ACS Nano* **2009**, *3*, 2451−2460.

(4) Giljohann, D. A.; Seferos, D. S.; Daniel, W. L.; Massich, M. D.; Patel, P. C.; Mirkin, C. A. Gold Nanoparticles for Biology and Medicine. *Angew. Chem., Int. Ed.* **2010**, *49*, 3280−3294.

(5) Jones, M. R.; Seeman, N. C.; Mirkin, C. A. Programmable Materials and the Nature of the DNA Bond. *Science* **2015**, *347*, 1260901.

(6) Song, S.; Qin, Y.; He, Y.; Huang, Q.; Fan, C.; Chen, H.-Y. Functional Nanoprobes for Ultrasensitive Detection of Biomolecules. *Chem. Soc. Rev.* **2010**, *39*, 4234−4243.

(7) Liu, B.; Salgado, S.; Maheshwari, V.; Liu, J. DNA Adsorbed on Graphene and Graphene Oxide: Fundamental Interactions, Desorption and Applications. *Curr. Opin. Colloid Interface Sci.* **2016**, *26*, 41−49.

(8) Pautler, R.; Kelly, E. Y.; Huang, P.-J. J.; Cao, J.; Liu, B.; Liu, J. Attaching DNA to Nanoceria: Regulating Oxidase Activity and Fluorescence Quenching. *ACS Appl. Mater. Interfaces* **2013**, *5*, 6820−6825.

(9) Narasaraju, T. S. B.; Phebe, D. E. Some Physico-Chemical Aspects of Hydroxylapatite. *J. Mater. Sci.* **1996**, *31*, 1−21.

(10) Weiner, S.; Wagner, H. D. THE MATERIAL BONE: Structure-Mechanical Function Relations. *Annu. Rev. Mater. Sci.* **1998**, *28*, 271−298.

(11) Fratzl, P.; Gupta, H. S.; Paschalis, E. P.; Roschger, P. Structure and Mechanical Quality of the Collagen−Mineral Nano-Composite in Bone. *J. Mater. Chem.* **2004**, *14*, 2115−2123.

(12) Uskoković, V.; Uskoković, D. P. Nanosized Hydroxyapatite and other Calcium Phosphates: Chemistry of Formation and Application as Drug and Gene Delivery Agents. *J. Biomed. Mater. Res., Part B* **2011**, *96B*, 152−191.

(13) Kozlova, D.; Chernousova, S.; Knuschke, T.; Buer, J.; Westendorf, A. M.; Epple, M. Cell Targeting by Antibody-Functionalized Calcium Phosphate Nanoparticles. *J. Mater. Chem.* **2012**, *22*, 396−404.

(14) Olton, D.; Li, J.; Wilson, M. E.; Rogers, T.; Close, J.; Huang, L.; Kumta, P. N.; Sfeir, C. Nanostructured Calcium Phosphates (NanoCaPs) for Non-Viral Gene Delivery: Influence of the Synthesis Parameters on Transfection Efficiency. *Biomaterials* **2007**, *28*, 1267−1279.

(15) Wan, Y.; Wu, C.; Zuo, G.; Xiong, G.; Jin, J.; Guo, R.; Wang, Z.; Luo, H. Controlled Template Synthesis of Lamellar Hydroxyapatite Nanoplates as a Potential Carrier for Gene Delivery. *Mater. Chem. Phys.* **2015**, *156*, 238−246.

(16) Andrews-Pfannkoch, C.; Fadrosh, D. W.; Thorpe, J.; Williamson, S. J. Hydroxyapatite-Mediated Separation of Double-Stranded DNA, Single-Stranded DNA, and RNA Genomes from Natural Viral Assemblages. *Appl. Environ. Microbiol.* **2010**, *76*, 5039−5045.

(17) Baker, R.; Rogers, K. D.; Shepherd, N.; Stone, N. New Relationships between Breast Microcalcifications and Cancer. *Br. J. Cancer* **2010**, *103*, 1034−1039.

(18) Haka, A. S.; Shafer-Peltier, K. E.; Fitzmaurice, M.; Crowe, J.; Dasari, R. R.; Feld, M. S. Diagnosing Breast Cancer by Using Raman Spectroscopy. *Proc. Natl. Acad. Sci. U. S. A* **2005**, *102*, 12371−12376.

(19) Haka, A. S.; Shafer-Peltier, K. E.; Fitzmaurice, M.; Crowe, J.; Dasari, R. R.; Feld, M. S. Identifying Microcalcifications in Benign and Malignant Breast Lesions by Probing Differences in Their Chemical Composition using Raman Spectroscopy. *Cancer Res.* **2002**, *62*, 5375−5380.

(20) Tse, G. M.; Tan, P.-H.; Cheung, H. S.; Chu, W. C. W.; Lam, W. W. M. Intermediate to Highly Suspicious Calcification in Breast Lesions: A Radio-Pathologic Correlation. *Breast Cancer Res. Treat.* **2008**, *110*, 1−7.

(21) Frappart, L.; Boudeulle, M.; Boumendil, J.; Lin, H. C.; Martinon, I.; Palayer, C.; Mallet-Guy, Y.; Raudrant, D.; Bremond, A.; Rochet, Y.; Feroldi, J. Structure and Composition of Microcalcifications in Benign and Malignant Lesions of the Breast: Study by Light Microscopy, Transmission and Scanning Electron Microscopy, Microprobe Analysis, and X-Ray Diffraction. *Hum. Pathol.* **1984**, *15*, 880−889.

(22) Cox, R. F.; Hernandez-Santana, A.; Ramdass, S.; McMahon, G.; Harmey, J. H.; Morgan, M. P. Microcalcifications in Breast Cancer: Novel Insights into the Molecular Mechanism and Functional Consequence of Mammary Mineralisation. *Br. J. Cancer* **2012**, *106*, 525−537.

(23) del Valle, L. J.; Bertran, O.; Chaves, G.; Revilla-López, G.; Rivas, M.; Casas, M. T.; Casanovas, J.; Turon, P.; Puiggalí, J.; Alemán, C. DNA Adsorbed on Hydroxyapatite Surfaces. *J. Mater. Chem.* **2014**, *2*, 6953−6966.

(24) Rivas, M.; Casanovas, J.; del Valle, L. J.; Bertran, O.; Revilla-López, G.; Turon, P.; Puiggalí, J.; Alemán, C. An Experimental-Computer Modeling Study of Inorganic Phosphates Surface Adsorption on Hydroxyapatite Particles. *Dalton Trans.* **2015**, *44*, 9980−9991.

(25) Revilla-López, G.; Casanovas, J.; Bertran, O.; Turon, P.; Puiggalí, J.; Alemán, C. Modeling Biominerals Formed by Apatites and DNA. *Biointerphases* **2013**, *8*, 10.

(26) Takeshita, T.; Matsuura, Y.; Arakawa, S.; Okamoto, M. Biomineralization of Hydroxyapatite on DNA Molecules in SBF: Morphological Features and Computer Simulation. *Langmuir* **2013**, *29*, 11975−11981.

(27) Vasconcellos, K. B.; McHugh, S. M.; Dapsis, K. J.; Petty, A. R.; Gerdon, A. E. Biomimetic Nanoparticles with Polynucleotide and PEG mixed-monolayers Enhance Calcium Phosphate Mineralization. *J. Nanopart. Res.* **2013**, *15*, 1942.

DOI: 10.1021/acs.langmuir.9b01566
Langmuir 2019, 35, 11912−11922

(28) Bertran, O.; del Valle, L. J.; Revilla-López, G.; Chaves, G.; Cardús, L.; Casas, M. T.; Casanovas, J.; Turon, P.; Puiggalí, J.; Alemán, C. Mineralization of DNA into Nanoparticles of Hydroxyapatite. *Dalton Trans.* **2014**, *43*, 317−327.
(29) Klesing, J.; Chernousova, S.; Epple, M. Freeze-Dried Cationic Calcium Phosphate Nanorods as Versatile Carriers of Nucleic Acids (DNA, siRNA). *J. Mater. Chem.* **2012**, *22*, 199−204.
(30) Wu, G. J.; Zhou, L. Z.; Wang, K. W.; Chen, F.; Sun, Y.; Duan, Y. R.; Zhu, Y. J.; Gu, H. C. Hydroxylapatite Nanorods: An Efficient and Promising Carrier for Gene Transfection. *J. Colloid Interface Sci.* **2010**, *345*, 427−432.
(31) Zhu, S. H.; Huang, B. Y.; Zhou, K. C.; Huang, S. P.; Liu, F.; Li, Y. M.; Xue, Z. G.; Long, Z. G. Hydroxyapatite Nanoparticles As a Novel Gene Carrier. *J. Nanopart. Res.* **2004**, *6*, 307−311.
(32) Bertran, O.; del Valle, L. J.; Revilla-López, G.; Rivas, M.; Chaves, M.; Casas, M. T.; Casanovas, J.; Turon, P.; Puiggalí, J.; Alemán, C. Synergistic Approach to Elucidate the Incorporation of Magnesium Ions into Hydroxyapatite. *Chem. − Eur. J.* **2015**, *21*, 2537−2546.
(33) Betran, O.; Revilla-López, G.; Casanovas, J.; del Valle, L. J.; Turon, P.; Puiggalí, J.; Alemán, C. Dissolving Hydroxyolite: A DNA Molecule into Its Hydroxyapatite Mold. *Chem. − Eur. J.* **2016**, *22*, 6631−6636.
(34) Phillips, J. C.; Braun, R.; Wang, W.; Gumbart, J.; Tajkhorshid, E.; Villa, E.; Chipot, C.; Skeel, R. D.; Kalé, L.; Schulten, K. Scalable Molecular Dynamics with NAMD. *J. Comput. Chem.* **2005**, *26*, 1781−1802.
(35) Fleischer, T.; Tekpli, X.; Mathelier, A.; Wang, S.; Nebdal, D.; Dhakal, H. P.; Kleivi, K.; Sahlberg, K. K.; Schlichting, E; Oslo Breast Cancer Research Consortium (OSBREAC); Børresen-Dale, A. L.; Borgen, E.; Naume, B.; Eskeland, R.; Frigessi, A.; Tost, J.; Hurtado, A.; Kristensen, V. N. DNA Methylation at Enhancers Identifies Distinct Breast Cancer Lineages. *Nat. Commun.* **2017**, *8*, 1379.
(36) Si, X.; Zhao, Y.; Yang, C.; Zhang, S.; Zhang, X. DNA Methylation as a Potential Diagnosis Indicator for Rapid Discrimination of Rare Cancer Cells and Normal Cells. *Sci. Rep.* **2015**, *5*, 11882.
(37) Widschwendter, M.; Jones, P. A. DNA Methylation and Breast Carcinogenesis. *Oncogene* **2002**, *21*, 5462−5482.
(38) Mathe, A.; Wong-Brown, M.; Locke, W. J.; Stirzaker, C.; Braye, S. G.; Forbes, J. F.; Clark, S. J.; Avery-Kiejda, K. A.; Scott, R. J. DNA Methylation Profile of Triple Negative Breast Cancer-Specific Genes Comparing Lymph Node Positive Patients to Lymph Node Negative Patients. *Sci. Rep.* **2016**, *6*, 33435.
(39) Dammann, R.; Yang, G.; Pfeifer, G. P. Hypermethylation of the cpG Island of Ras Association Domain Family 1A (RASSF1A), a Putative Tumor Suppressor Gene from the 3p21.3 Locus, Occurs in a Large Percentage of Human Breast Cancers. *Cancer Res.* **2001**, *61*, 3105−3109.
(40) Gueroult, M.; Boittin, O.; Mauffret, O.; Etchebest, C.; Hartmann, B. Charge Neutralization was Performed with the Addition of Na^+ Counterions. *PLoS One* **2012**, *7*, No. e41704.
(41) Duan, Y.; Wu, C.; Chowdhury, S.; Lee, M. C.; Xiong, G.; Zhang, W.; Yang, R.; Cieplak, P.; Luo, R.; Lee, T.; Caldwell, J.; Wang, J.; Kollman, P. A Point-Charge Force Field for Molecular Mechanics Simulations of Proteins Based on Condensed-Phase Quantum Mechanical Calculations. *J. Comput. Chem.* **2003**, *24*, 1999−2012.
(42) Bradbrook, G. M.; Gleichmann, T.; Harrop, S. J.; Habash, J.; Raftery, J.; Kalb, J.; Yariv, J.; Hillier, I. H.; Helliwell, J. R. X-Ray and Molecular Dynamics Studies of Concanavalin-A Glucoside and Mannoside Complexes. Relating Structure to Thermodynamics of Binding. *J. Chem. Soc., Faraday Trans.* **1998**, *94*, 1603−1611.
(43) Allnér, O.; Nilsson, L.; Villa, A. Magnesium Ion−Water Coordination and Exchange in Biomolecular Simulations. *J. Chem. Theor Comput.* **2012**, *8*, 1493−1502.
(44) Jorgensen, W. L.; Chandrasekhar, J.; Madura, J. D.; Impey, R. W.; Klein, M. L. Comparison of Simple Potential Functions for Simulating Liquid Water. *J. Chem. Phys.* **1983**, *79*, 926−935.
(45) Wang, J.; Wolf, R. M.; Caldwell, J. W.; Kollman, P. A.; Case, D. A. Development and Testing of a General Amber Force Field. *J. Comput. Chem.* **2004**, *25*, 1157−1174.
(46) Bayly, C. I.; Cieplak, P.; Cornell, W.; Kollman, P. A. A Well-Behaved Electrostatic Potential Based Method Using Charge Restraints for Deriving Atomic Charges: The RESP Model. *J. Phys. Chem.* **1993**, *97*, 10269−10280.
(47) Berendsen, H. J. C.; Postma, J. P. M.; van Gunsteren, W. F.; DiNola, A.; Haak, J. R. Molecular Dynamics with Coupling to an External Bath. *J. Chem. Phys.* **1984**, *81*, 3684−3690.
(48) Darden, T.; York, D.; Pedersen, L. Particle Mesh Ewald: An *N*·log (*N*) Method for Ewald sums in Large Systems. *J. Chem. Phys.* **1993**, *98*, 10089−10092.
(49) Ryckaert, J.-P.; Ciccotti, G.; Berendsen, H. J. C. Numerical Integration of the Cartesian Equations of Motion of a System with Constraints: Molecular Dynamics of *n*-Alkanes. *J. Comput. Phys.* **1977**, *23*, 327−341.
(50) Stork, L.; Muller, P.; Dronskowski, R.; Ortlepp, J. R. Z. *Kristallogr.* **2005**, *220*, 201−205.
(51) Daudon, M.; Bazin, D.; André, G.; Jungers, P.; Cousson, A.; Chevallier, P.; Veéron, E.; Matzen, G. Examination of Whewellite Kidney Stones by Scanning Electron Microscopy and Powder Neutron Diffraction Techniques. *J. Appl. Cryst.* **2009**, *42*, 109−115.
(52) M Frisch, M. J.; Trucks, G. W.; Schlegel, H. B.; Scuseria, G. E.; Robb, M. A.; Cheeseman, J. R.; Scalmani, G.; Barone, V.; Mennucci, B.; Petersson, G. A.; Nakatsuji, H.; Caricato, M.; Li, X.; Hratchian, H. P.; Izmaylov, A. F.; Bloino, J.; Zheng, G.; Sonnenberg, J. L.; Hada, M.; Ehara, M.; Toyota, K.; Fukuda, R.; Hasegawa, J.; Ishida, M.; Nakajima, T.; Honda, Y.; Kitao, O.; Nakai, H.; Vreven, T.; Montgomery, J. A., Jr.; Peralta, J. E.; Ogliaro, F.; Bearpark, M.; Heyd, J. J.; Brothers, E.; Kudin, K. N.; Staroverov, V. N.; Kobayashi, R.; Normand, J.; Raghavachari, K.; Rendell, A.; Burant, J. C.; Iyengar, S. S.; Tomasi, J.; Cossi, M.; Rega, N.; Millam, J. M.; Klene, M.; Knox, J. E.; Cross, J. B.; Bakken, V.; Adamo, C.; Jaramillo, J.; Gomperts, R.; Stratmann, R. E.; Yazyev, O.; Austin, A. J.; Cammi, R.; Pomelli, C.; Ochterski, J. W.; Martin, R. L.; Morokuma, K.; Zakrzewski, V. G.; Voth, G. A.; Salvador, P.; Dannenberg, J. J.; Dapprich, S.; Daniels, A. D.; Farkas, Ö.; Foresman, J. B.; Ortiz, J. V.; Cioslowski, J.; Fox, D. J. *Gaussian 09, Revision A.1*;. Gaussian, Inc.: Wallingford CT, 2009.
(53) Becke, A. D. Density-Functional Thermochemistry. III. The Role of Exact Exchange. *J. Chem. Phys.* **1993**, *98*, 5648−5652.
(54) Lee, C.; Yang, W.; Parr, R. G. Development of the Colle-Salvetti Correlation-Energy Formula into a Functional of the Electron Density. *Phys. Rev. B* **1988**, *37*, 785−789.
(55) Marenich, A. V.; Cramer, C. J.; Truhlar, D. G. Universal Solvation Model Based on Solute Electron Density and on a Continuum Model of the Solvent Defined by the Bulk Dielectric Constant and Atomic Surface Tensions. *J. Phys. Chem. B* **2009**, *113*, 6378−6396.
(56) Mkhonto, D.; de Leeuw, N. H. A Computer Modelling Study of the Effect of Water on the Surface Structure and Morphology of fluorapatite: Introducing a $Ca_{10}(PO_4)_6F_2$ Potential Model. *J. Mater. Chem.* **2002**, *12*, 2633−2642.
(57) Di Tommaso, D.; Hernández, S. E. R.; Du, Z.; de Leeuw, N. H. Density Functional Theory and Interatomic Potential Study of Structural, Mechanical and Surface Properties of Calcium Oxalate Materials. *RSC Adv.* **2012**, *2*, 4664−4674.
(58) Almora-Barrios, N.; Austen, K. F.; de Leeuw, N. H. Density Functional Theory Study of the Binding of Glycine, Proline, and Hydroxyproline to the Hydroxyapatite (0001) and ($01\bar{1}0$) Surfaces. *Langmuir* **2009**, *25*, 5018−5025.
(59) Filgueiras, M. R. T.; Mkhonto, D.; de Leeuw, N. H. Computer Simulations of the Adsorption of Citric Acid at Hydroxyapatite Surfaces. *J. Cryst. Growth* **2006**, *294*, 60−68.
(60) de Leeuw, N. H.; Rabone, J. A. L. Molecular Dynamics Simulations of the Interaction of Citric Acid with the Hydroxyapatite (0001) and ($01\bar{1}0$) Surfaces in an Aqueous Environment. *CrystEngComm* **2007**, *9*, 1178−1186.

DOI: 10.1021/acs.langmuir.9b01566
Langmuir 2019, 35, 11912−11922

(61) Sandersius, S.; Rez, P. Morphology of Crystals in Calcium Oxalate Monohydrate Kidney Stones. *Urol. Res.* **2007**, *35*, 287−293.
(62) Sheng, X.; Jung, T.; Wesson, J.; Ward, M. D. Adhesion at Calcium Oxalate Crystal Surfaces and the Effect of Urinary Constituents. *Proc. Natl. Acad. Sci. U. S. A.* **2005**, *102*, 267−272.

SUPPORTING INFORMATION

Biominerals Formed by DNA and Calcium Oxalate or Hydroxyapatite: A Comparative Study

Guillem Revilla-López,[1] Anna M. Rodríguez-Rivero,[2,3] Luis J. del Valle,[1,4] Jordi Puiggalí,[1,4,5] Pau Turon[2,*] and Carlos Alemán[1,4,5,*]

[1] Departament d'Enginyeria Química, EEBE, Universitat Politècnica de Catalunya, C/Eduard Maristany 10-14, Edif. I2, 08019 Barcelona, Spain

[2] Research and Development, B. Braun Surgical, S.A. Ctra. de Terrassa 121, 08191 Rubí, Barcelona, Spain

[3] Universitat Autònoma de Barcelona. Campus de la UAB, Plaça Cívica, 08193 Bellaterra, Barcelona, Spain

[4] Barcelona Research Center for Multiscale Science and Engineering, EEBE, Universitat Politècnica de Catalunya, C/Eduard Maristany 10-14, Edif. C, 08019 Barcelona, Spain

[5] Institute for Bioengineering of Catalonia (IBEC), The Barcelona Institute of Science and Technology, Baldiri Reixac 10-12, 08028 Barcelona, Spain

[*] Correspondence to: pau.turon@bbraun.com and carlos.aleman@upc.edu

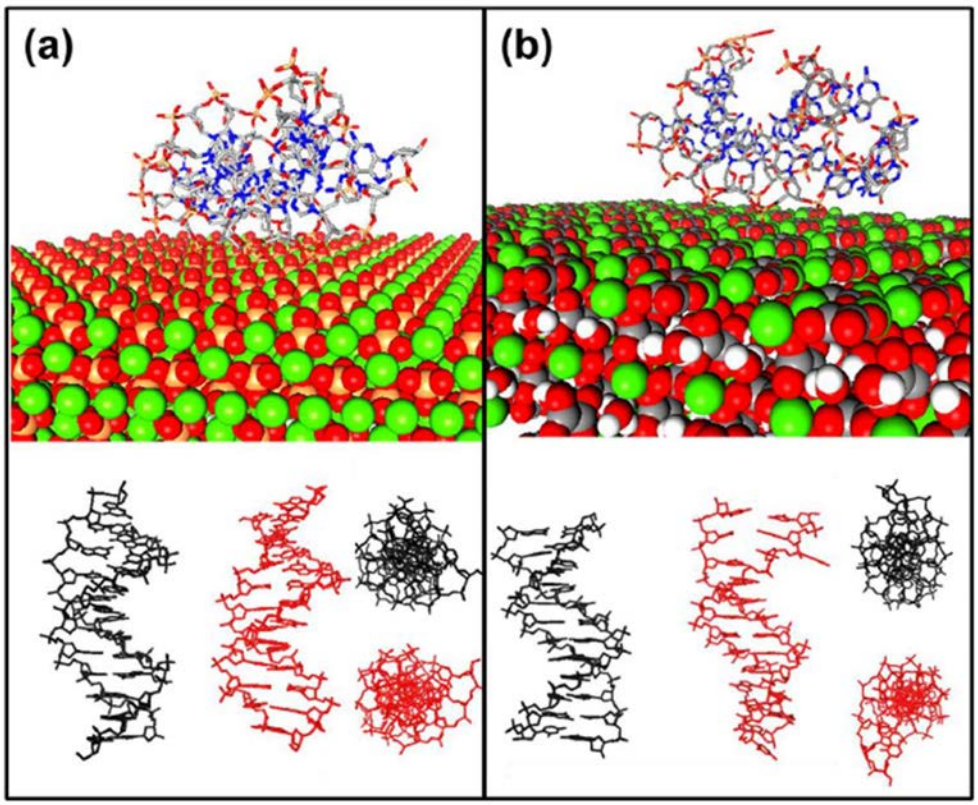

Figure S1. Axial view of the DD dodecamer adsorbed onto (a) the (001) surface of HAp and (b) the (100) surface of monohydrated CaOx. For each system, the axial and equatorial views of the canonical double helix (in black) and the R1A double helix adsorbed onto the HAp or CaOx surface (in red) are compared at the bottom.

ANNEX 3.2. UNRAVELLING THE ENCAPSULATION OF DNA AND OTHER BIOMOLECULES IN HAP MICROCALCIFICATIONS OF HUMAN BREAST CANCER TISSUES BY RAMAN IMAGING

Marro, M.; **Rodríguez-Rivero, A. M.**; Araujo-Andrade, C.; Fernández-Figueras, M. T.; Pérez-Roca, L.; Castellà, E.; Navinés, J.; Mariscal, A.; Julián, J. F.; Turon, P. and Loza-Alvarez, P. Unravelling the encapsulation of DNA and other biomolecules in HAp microcalcifications of human breast cancer tissues by Raman imaging. *Cancers.* 2021; *13*(11): 2658. https://doi.org/10.3390/cancers13112658

Abstract: "Microcalcifications are detected through mammography screening and, depending on their morphology and distribution (BI-RADS classification), they can be considered one of the first indicators of suspicious cancer lesions. However, the formation of hydroxyapatite (HAp) calcifications and their relationship with malignancy remains unknown. In this work, we report the most detailed three-dimensional biochemical analysis of breast cancer microcalcifications to date, combining 3D Raman spectroscopy imaging and advanced multivariate analysis in order to investigate in depth the molecular composition of HAp calcifications found in 26 breast cancer tissue biopsies. We demonstrate that DNA has been naturally adsorbed and encapsulated inside HAp microcalcifications. Furthermore, we also show the encapsulation of other relevant biomolecules in HAp calcifications, such as lipids, proteins, cytochrome C and polysaccharides. The demonstration of natural DNA biomineralization, particularly in the tumor microenvironment, represents an unprecedented advance in the field, as it can pave the way to understanding the role of HAp in malignant tissues."

cancers

MDPI

Article

Unravelling the Encapsulation of DNA and Other Biomolecules in HAp Microcalcifications of Human Breast Cancer Tissues by Raman Imaging

Monica Marro [1,*], Anna M. Rodríguez-Rivero [2,3], Cuauhtémoc Araujo-Andrade [1], Maria Teresa Fernández-Figueras [4,5], Laia Pérez-Roca [5], Eva Castellà [5], Jordi Navinés [5], Antonio Mariscal [5], Joan Francesc Julián [3,5], Pau Turon [2] and Pablo Loza-Alvarez [1,*]

1 ICFO—Institut de Ciencies Fotoniques, The Barcelona Institute of Science and Technology, Castelldefels, 08860 Barcelona, Spain; caraujo123@yahoo.com
2 Research and Development B. Braun Surgical, S.A.U. Ctra. de Terrassa, 121, Rubí, 08191 Barcelona, Spain; ana_maria.rodriguez_rivero@bbraun.com (A.M.R.-R.); pau.turon@bbraun.com (P.T.)
3 Campus de la UAB, Universitat Autònoma de Barcelona, Plaça Cívica, Bellaterra, 08193 Barcelona, Spain; 21127jji@gmail.com
4 Departament de Medicina, Facultat de Medicina i Ciències de la Salut, Universitat Internacional de Catalunya, Carrer de la Immaculada, 22, 08017 Barcelona, Spain; maiteffig@gmail.com
5 Institut de Recerca Germans Trias i Pujol (IGTP), Camí de les Escoles, s/n, 08916 Badalona, Spain; laiaproca@gmail.com (L.P.-R.); ecastella.germanstrias@gencat.cat (E.C.); drnavines@gmail.com (J.N.); mariscal.germanstrias@gencat.cat (A.M.)
* Correspondence: monica.marro@icfo.eu (M.M.); pablo.loza@icfo.eu (P.L.-A.)

Simple Summary: Although microcalcifications can be considered one of the first indicators of suspicious cancer lesions, depending on their morphology and distribution, the formation of hydroxyapatite calcifications and their relationship with malignancy remains unknown. In this work, we investigate in depth the biochemical composition of breast cancer microcalcifications, combining Raman spectroscopy imaging and advanced multivariate analysis. We demonstrate that DNA is naturally adsorbed and encapsulated inside hydroxyapatite found in breast cancer tissue. Furthermore, we also show the encapsulation of other relevant biomolecules such as lipids, proteins, cytochrome C and polysaccharides. The demonstration of the natural DNA biomineralization in cancer tissues represents an unprecedented advance in the field, as it can pave the way to understanding the role of hydroxyapatite in malignant tissues.

Abstract: Microcalcifications are detected through mammography screening and, depending on their morphology and distribution (BI-RADS classification), they can be considered one of the first indicators of suspicious cancer lesions. However, the formation of hydroxyapatite (HAp) calcifications and their relationship with malignancy remains unknown. In this work, we report the most detailed three-dimensional biochemical analysis of breast cancer microcalcifications to date, combining 3D Raman spectroscopy imaging and advanced multivariate analysis in order to investigate in depth the molecular composition of HAp calcifications found in 26 breast cancer tissue biopsies. We demonstrate that DNA has been naturally adsorbed and encapsulated inside HAp microcalcifications. Furthermore, we also show the encapsulation of other relevant biomolecules in HAp calcifications, such as lipids, proteins, cytochrome C and polysaccharides. The demonstration of natural DNA biomineralization, particularly in the tumor microenvironment, represents an unprecedented advance in the field, as it can pave the way to understanding the role of HAp in malignant tissues.

Keywords: microcalcifications; DNA mineralization; breast cancer; tumor microenvironment; Raman spectroscopy

Citation: Marro, M.; Rodríguez-Rivero, A.M.; Araujo-Andrade, C.; Fernández-Figueras, M.T.; Pérez-Roca, L.; Castellà, E.; Navinés, J.; Mariscal, A.; Julián, J.F.; Turon, P.; et al. Unravelling the Encapsulation of DNA and Other Biomolecules in HAp Microcalcifications of Human Breast Cancer Tissues by Raman Imaging. *Cancers* **2021**, *13*, 2658. https://doi.org/10.3390/cancers13112658

Academic Editor: Anupama Munshi

Received: 30 April 2021
Accepted: 25 May 2021
Published: 28 May 2021

1. Introduction

Breast cancer is by far the most frequent cancer diagnosed in women, with 2,088,849 new cases (11.6% of total diagnosed cancer) accounting for 626,679 deaths (6.6%) in 2018 [1]. However, the number of cancer survivors has been rapidly increasing due to improvements in early diagnosis and treatment efficacy (i.e., from 1989 to 2015, breast cancer death rates decreased by 39% in the US) [2–4]. Despite this positive trend, more efforts are needed to improve the basic understanding of the disease and the underlying cellular mechanisms in order to prevent its consequences.

Thanks to the introduction of mammographic screening programs, the early diagnosis of breast cancer has substantially improved during recent years, enabling the detection of lesions at a much earlier stage. Breast microcalcifications are often detected by means of mammographic scans, and depending on their size, morphology and distribution, they can be considered one of the first indicators of suspicious cancer lesions. Nowadays, microcalcifications are analyzed based on mammography images (BIRADS classification) and through histopathological assessments. Microcalcifications can be classified as type I or type II. Type I calcium oxalate (CaOx) microcalcifications are less frequent and are usually related to benign lesions [5–9]. Type II hydroxyapatite microcalcifications are frequently observed and normally associated with a worse prognosis [6,10–13]. In an effort to identify suspicious microcalcifications, several methods, such as deep learning [14], have been developed to analyze mammography scans. However, those methods are not able to provide information on the molecular composition of calcifications. Only one method, based on contrast-phase X ray tomography [15], has been reported to be able to discriminate between type I and type II calcifications in scans. However, FT-IR and Raman spectroscopy have been successfully used to investigate the adsorbed molecular composition of both types of calcifications, analyzing tissue biopsies extracted in the diagnosis phase or during surgery.

Despite multiple efforts, and many studies in the field, the mechanisms that lead to the formation of both types of microcalcifications are not completely understood, and HAp calcifications still attract the attention of researchers [10–20]. Traditionally, some authors focused on HAp morphology and its correlation with tumor features, whereas others focused on changes in its chemical composition (i.e., the presence of Mg^{2+} or the reduction of CO_3^{2-} content in its lattice, which were related to a poorer prognosis) [21,22]. In contrast, CaOx calcifications have received much less attention, even though their cytotoxicity and risk of carcinogenicity have been described [23,24]. O'Grady and Morgan (2018) recently reviewed breast cancer microcalcifications, covering a wide range of topics, from pathophysiology to diagnosis and prognosis [25]. However, there are few publications that have studied the biochemical composition of breast cancer calcifications and none of them describing the tridimensional structure [16,17,26–28]. Therefore, a method that is capable of investigating the biochemical composition in detail, along with the spatial distribution of biomolecules inside the calcification and the surrounding tissue, is a key objective in order to understand the formation of HAp calcifications and their associated worse prognosis.

Raman spectroscopy is an excellent technique for the detailed analysis of the biochemical content of tissues because of its high specificity, non-destructive nature and label-free approach [29–31]. Raman spectroscopy utilizes inelastic light scattering to extract vibrational molecular fingerprints of molecules present in the samples. It enables the simultaneously study of multiple molecular components present in a sample. Such an approach is not possible with other techniques such as fluorescence staining, which require the use of previously selected labels, making the study of several molecules in the same sample at the same time difficult. In addition, DNA fluorescent labels, such as DAPI, might not efficiently penetrate microcalcifications and the fluorescence bands may be shifted due to the interaction of the label with the microcalcification [32,33]. Consequently, the localization and identification of the molecular content in the microcalcification might not be feasible or sufficiently accurate with other techniques. In previous studies, Raman spectroscopy has been

demonstrated as an optimal technique to study breast tissue microcalcifications, because the Raman spectra of different calcium salts exhibit well defined signals with very distinct features. First, Haka et al. [6] showed that it was possible to identify different chemical compositions in benign and malignant breast microcalcifications using a single acquisition in the calcified region. Then, Stone et al. [7] successfully detected microcalcifications deeply buried in tissues by means of spatially offset Raman spectroscopy (SORS). Baker et al. reported a decrease in the carbonate content of HAp from benign to malignant calcifications using infrared spectroscopy [17]. Recently, it was shown that different inorganic compositions of microcalcifications correlate with histopathologic features [28]. Despite these efforts, the detailed tridimensional molecular composition adsorbed or encapsulated in such microcalcifications has never been studied. Specifically, the distribution of organic molecules in three dimensions has not yet been reported. In addition, previous Raman spectroscopic studies have considered a low number of calcifications and the analysis of their relationship with invasive tissues has been almost absent. Furthermore, due to the rich information collected by Raman spectroscopy, the biological interpretation of spectra has become complex, and many research works have not sufficiently analyzed the molecular information available. Recently, the use of advanced multivariate analysis methods has enabled the rigorous study of complex biological Raman spectra in detail [30,31].

In this paper, we describe a methodology that enables the investigation of the usual biochemical composition of HAp calcifications observed in human breast cancer tissues (Figure 1). We report the most detailed tridimensional study of breast cancer HAp microcalcifications to date, combining molecular Raman imaging of breast cancer tissue sections (n = 26 patients) with an advanced multivariate analysis method, multivariate curve resolution (MCR). The use of advanced data analysis enables the extraction of otherwise inaccessible molecular information encoded in the Raman spectra. Specifically, we focus on the study of the 3D molecular distribution of organic molecules in HAp microcalcifications. We show, for the first time, the spatial distribution of several molecular components (DNA, lipids, proteins, cytochrome C and polysaccharides) in the HAp calcifications extracted from a tumor microenvironment. Furthermore, this study is grounded on the most extensive Raman spectra analysis performed on breast tissue calcifications (more than 10,400 spectra).

Specifically, we show that DNA is encapsulated and adsorbed naturally in the HAp present in invasive cancer tissues. The natural biomineralization of DNA in breast cancer tissues would enable the preservation of this molecule for long periods of time, protecting it from enzymatic degradation [26,34–38]. This finding represents a major advance in the field, as it can pave the way to understanding the formation and the role of HAp calcifications in malignant tissues.

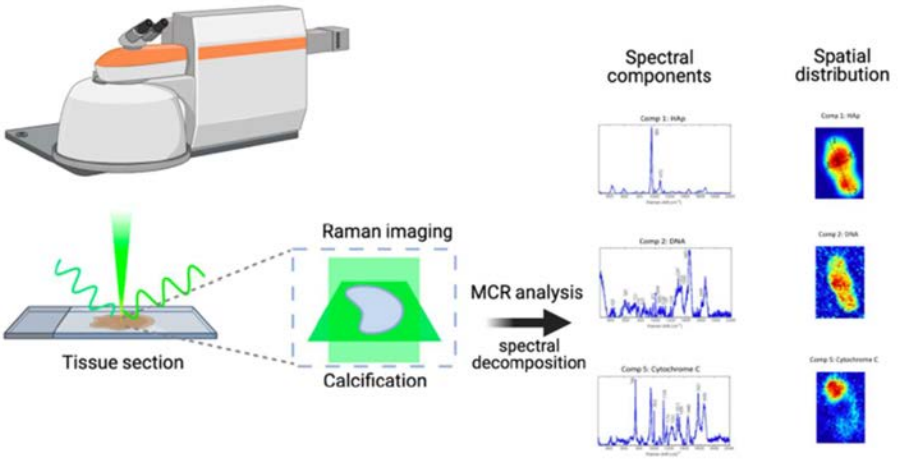

Figure 1. Workflow and experimental design: in this paper, we demonstrate a methodology that is capable of investigating the biochemical composition of HAp calcifications in human breast cancer tissues. First, we perform Raman imaging of breast cancer tissue sections (n = 26 patients), acquiring 2D images in perpendicular directions (xy, xz and yz) in order to retrieve 3D molecular information. Second, we use an advanced multivariate analysis method, multivariate curve resolution (MCR) to extract otherwise inaccessible molecular information encoded in the Raman spectra. Specifically, we decompose several spectral components, corresponding to organic molecules and their associated 3D molecular spatial distribution in HAp microcalcifications. Through this method, we show the presence and 3D spatial distribution of several molecular components (DNA, lipids, proteins, cytochrome C and polysaccharides) in the HAp calcifications extracted from cancer tissues.

2. Materials and Methods

2.1. Breast Tumor Samples

Samples and data from patients included in this study were provided by the IGTP-HUGTP Biobank, integrated in the Spanish National Biobank Network of Instituto de Salud Carlos III (PT13/0010/0009) and the Tumor Bank Network of Catalonia. The samples were processed following standard operating procedures with the appropriate approval of the Ethical and Scientific Committees (CCEBB IGTP-HUGTiP Request: BB14004 and evaluation Ref: BB-C-1402). Selected tissue specimens of the tumors were embedded in an optimal cutting temperature (OCT) compound and frozen in isopentane using a Bright Clini-RF freezer for 30 min after extraction.

Tissue sections from freshly excised human breast tumors (n = 26 patients) were studied (Table 1). Samples were diagnosed as infiltrating ductal and lobular carcinomas and microcalcifications were observed in previous mammography screenings.

Table 1. Summary of the microcalcifications measured by Raman spectroscopy found in the human breast cancer tissue sections analyzed. For each calcification, we specify the diagnosis, the type (Oxalate or HAp), content of DNA (according to Raman spectroscopy results), size, shape, and localization.

	Diagnosis	Oxalate	HAp	DNA	Size [a]	Shape [b]	Localisation [c]
1	Infiltrating ductal carcinoma (IDC)	No	Yes	Yes	m, D = 20 µm	S	t
2	Infiltrating ductal carcinoma (IDC)	No	Yes	Yes	m, D = 20 µm	R	t
3	Infiltrating ductal carcinoma (IDC)	No	Yes	No	m, D = 10 µm	S	t

Table 1. *Cont.*

	Diagnosis	Oxalate	HAp	DNA	Size [a]	Shape [b]	Localisation [c]
3	Infiltrating ductal carcinoma (IDC)	No	Yes	Yes	m	R	t
4	Infiltrating ductal carcinoma (IDC)	No	Yes	Yes	m, D = 20 µm	R	d
5	Infiltrating ductal carcinoma (IDC)	No	Yes	Yes	m, D = 20 µm	S	t
5	Infiltrating ductal carcinoma (IDC)	No	Yes	Yes	m, 30 × 20 µm	R	t
6	Infiltrating ductal carcinoma (IDC)	No	No	No	-	-	-
7	Infiltrating ductal carcinoma (IDC)	No	Yes	Yes	m, D = 10 µm	R	t
8	Infiltrating ductal carcinoma (IDC)	No	No	No	-	-	-
9	Infiltrating ductal carcinoma (IDC)	No	Yes	Yes	m, 25 × 15 µm	R	t
9	Infiltrating ductal carcinoma (IDC)	No	Yes	Yes	m, 20 µm	S	t
10	Infiltrating ductal carcinoma (IDC), multifocal	No	Yes	Yes	m, 30 µm	R	t
11	Infiltrating ductal carcinoma (IDC)	No	Yes	Yes	m	R	t
12	Infiltrating ductal carcinoma (IDC)	No	No	-	-	-	-
13	Infiltrating ductal carcinoma (IDC)	No	Yes	No	b	R	t
14	Infiltrating ductal carcinoma (IDC)	No	Yes	Yes (nc)	S	R	t
15	Infiltrating ductal carcinoma (IDC)	No	Yes	Yes	b	R	t
16	Infiltrating ductal carcinoma (IDC)	No	Yes	Yes	m, 100 µm	R	d
17	Infiltrating ductal carcinoma (IDC)	No	Yes	Yes	m, 40 × 50 µm	R	t
18	Infiltrating ductal carcinoma (IDC)	No	Yes	Yes	s, D = 7 µm	S	t
19	Infiltrating ductal carcinoma (IDC)	No	Yes	Yes	m	R	t
20	Infiltrating ductal carcinoma (IDC)	No	Yes	Yes	m	R	d
21	Infiltrating ductal carcinoma (IDC)	No	Yes	Yes	m	R	d
22	Infiltrating ductal carcinoma (IDC)	No	Yes	Yes	m, 20 × 10 µm	R	t
23	Infiltrating ductal carcinoma (IDC)	No	Yes	Yes	b	R	t
24	Infiltrating lobular carcinoma (ILC)	No	Yes	Yes	m, D = 20 µm	R	t
25	Infiltrating lobular carcinoma (ILC)	Yes	No	No	s	S	t
25	Infiltrating lobular carcinoma (ILC)	No	Yes	Yes	m	R	t
26	Infiltrating lobular carcinoma (ILC)	No	Yes	Yes	m	R	t

[a] Size: small, s (10 µm); medium, m (10 µm m 100 µm); big, b (100 µm). [b] Shape: rock, R; sphere, S; needle, N. [c] Localization: duct, d; tissue, t.

2.2. Raman Spectroscopy

Thawed tissue sections of 5 μm in thickness were measured in quartz slides after conditioning at room temperature for 30 min. An inVia Renishaw Raman microscope was used. A visible 532-nm laser excitation with 10 mW and a 50× objective lens was used. Raman images were acquired with 1 s acquisition time and 1-μm pixel size. For in-depth area acquisitions, a 0.5-μm pixel size was selected in the z direction.

2.3. Multivariate Analysis

To determine the chemical composition for the Raman images, we used multivariate curve resolution (MCR). For MCR analysis, a Matlab toolbox was used: PLS toolbox (from Eigenvector Research). Raman spectra were pre-processed before multivariate analysis. A background correction was performed using the baseline correction method; asymmetric least squares smoothing and an extended multiplicative scattering correction (EMSC) for multiplicative effects was applied [39].

First, an exploration of the spectral dataset was performed using principal component analysis (PCA). The initial number of components selected was the number in which the cumulative variance explained was more than 99%. Two independent analyses (PCA and MCR) were performed on the same dataset, which contained the spectra of the breast cancer tissues in rows. For the MCR-ALS algorithm, the protocol followed was as follows. First, the initial estimates were selected using the SIMPLISMA algorithm, which selects the purest rows (spectra) in the dataset; second, the iterative least squares calculation began with the addition of constraints (non-negativity of spectra and concentration matrices). Finally, the quality parameters from the MCR model were calculated—Lack of fit: $LOF = 100\sqrt{\frac{\sum_{i=1}^{n}\sum_{j=1}^{m} e_{i,j}^2}{\sum_{i=1}^{n}\sum_{j=1}^{m} d_{i,j}^2}}$ and the parameter: $R^2 = 100\frac{\sum_{i=1}^{n}\sum_{j=1}^{m} d_{i,j}^2 - \sum_{i=1}^{n}\sum_{j=1}^{m} e_{i,j}^2}{\sum_{i=1}^{n}\sum_{j=1}^{m} d_{i,j}^2}$ where $e_{i,j} = d_{i,j} - \hat{d}_{i,j}$ and $d_{i,j}$ is the original data matrix and $\hat{d}_{i,j}$ is calculated by means of the MCR-ALS algorithm.

2.4. Breast Tumor Sample Staining for Confocal Microscopy Imaging

OCT-fixed tissue section samples were rehydrated by immersing them in PBS for 15 min at room temperature and then staining them with DAPI.

2.5. In Vitro Synthesis of DNA-HAp Particles

Suspensions of HAp particles (5 mg·mL^{-1}) were prepared, following the procedure described elsewhere [34], and were subsequently sonicated to enhance the dispersion. DNA was extracted from 4T1-luc2 cells (Perkin Elmer, 124087). DNA-HAp complexes were formed to reach 1% DNA, on HAp w/w. DNA-HAp mixtures were incubated for 90 min at 37 °C and 200 rpm, shaking them with a vortex every 30 min. Complexes were separated from the solution by centrifugation at 10,000 rpm for 10 min. Sediments were re-suspended in 10 mL of sterile water.

3. Results

3.1. Molecular Raman Imaging and Advanced Multivariate Analysis of Tissue Calcifications

Revealing the presence and spatial distribution of biomolecules in microcalcifications might contribute to understanding their role in breast cancer tissue. In this paper, we applied an advanced multivariate analysis approach for the first time to Raman images to obtain new insights about the biomolecular content of breast cancer microcalcifications.

Raman spectral images were acquired from tissue sections of freshly excised human breast tumors (n = 26 patients). The measured samples were diagnosed as infiltrating ductal and lobular carcinomas. Microcalcifications were observed in previous mammographic scans. In Table 1, a detailed summary of the analyzed samples is presented.

We used MCR to fully extract the complex biomolecular information contained in the Raman spectra. As a result, we were able to deconvolve multiple molecular spectral

signatures that could be assigned to specific molecular components present in the studied calcifications. In addition, associated with those molecular spectral fingerprints, we retrieved the related concentration maps, showing the distribution of the molecular components along the area and volume of the sample studied (Figure 2). Therefore, through the use of this method, we provide information not only about the molecular composition but also about the spatial distribution of molecules contained in the tissue calcifications. As we studied Raman images in the tissue section plane and two perpendicular 2D sections, our multivariate analysis methodology enabled us to understand if a certain molecular component was located inside, on the surface of, or outside the microcalcfications. The results for a HAp calcification are shown in Figure 2.

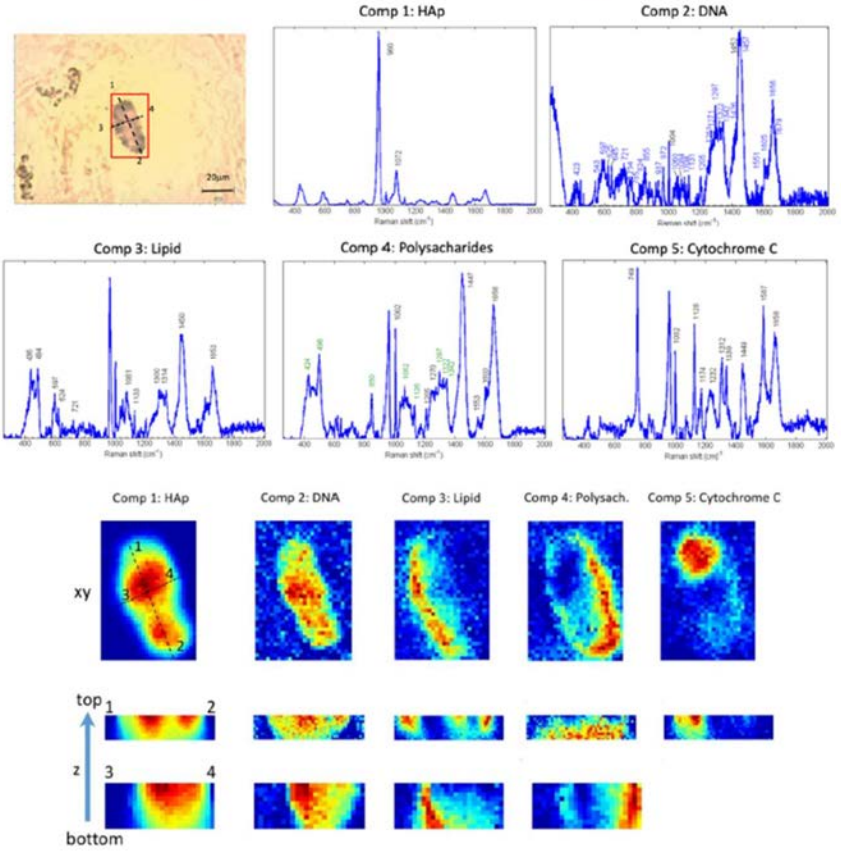

Figure 2. Raman spectral images show the presence of different molecular components in HAp tissue calcifications. Top left: Bright field image of a breast tissue section with a HAp calcification highlighted in the region of interest (red box). Raman images were taken from this area. Using the MCR algorithm, several molecular components were deconvolved from the spectra. In the first and second rows, the spectral signatures of the deconvolved molecular component are shown. For each component, its corresponding abundance maps are plotted in the bottom half of the Figure. The last two rows are perpendicular sections imaged to show the distribution of the molecules in depth inside the tissue. This microcalcification was found in tissue number 20 of Table 1. The assignment of bands for the different components was performed based on our constructed database and the literature [40–43].

A summary of the analyzed tissues can be found in Table 1. For each calcification, information about the size, shape, localization and molecular content is shown. We gathered the information about the size and the shape because the first radiological diagnosis is based not only on the presence of calcifications but also on the shape and distribution of the calcifications in the tissue, providing hints about the aggressiveness of the lesion.

We found HAp calcifications in 24 out of the 26 tissues studied (92.3%). In Figure 2, the results of an HAp calcification are shown (from tissue number 20 in Table 1). In Figure 2 a bright field image of the microcalcification is displayed, highlighting the area in which the Raman map was acquired. In total, five molecular spectral profiles were decomposed using the MCR-ALS algorithm. The associated abundance maps describing the distribution of the different molecular components in the area of the Raman image are shown below. Two perpendicular z-section Raman images were obtained to visualize the molecular content inside calcifications (last two rows of Figure 1). Component 1 has the spectral profile of HAp, defining the area of the calcification which correlates with the bright field image. The bands that confirm the assignment of this component to HAp are indicated in the spectra and are in agreement with the literature [22]. Component 2 contains a rich biological spectrum, having several bands in the fingerprint region, and is distributed inside the HAp calcification (plane (xy) and in depth (z) images from concentration maps). Components 3, 4 and 5 also have a rich spectral profile with bands that can be assigned to biological molecules. Components 2 and 5 are detected inside the tissue HAp calcification. However, Components 3 and 4 are found at the edges of the HAp calcification, indicating that they are adsorbed on the surface of the calcification. Such a pattern is repeated for almost all the HAp calcifications studied (24 out of 26, see Table 1), presenting biological content inside or adsorbed in the surface of the HAp calcifications (Figure 3). A further in-depth molecular assignment of the deconvolved MCR components is discussed in Sections 3.2 and 3.3. These results demonstrate that important biomolecules biomineralize in HAp calcifications. The observation that HAp mineralizes biological material could be related to its worse prognosis. Therefore, in the next section we investigate in depth the assignments of the biomolecular components found in HAp.

3.2. *Study of DNA Mineralization in HAp Microcalcifications*

Recent studies demonstrate that nucleic acids can be biomineralized and remain functional for long times [26], adsorbed or encapsulated in the mineral. Therefore, biomineralized DNA found in cancer tissues might have important implications, as biomineralized DNA is a hybrid system known for acting as a non-viral vector of transfection that has the ability to transfect to in vitro cells [38,44]. For this reason, we focused on studying in detail the presence and 3D distribution of DNA in microcalcifications.

3.2.1. Reference Raman Spectral Databases and Literature

To characterize and study the presence of DNA and other molecules in HAp calcifications, we measured the spectra of HAp crystals synthesized in the laboratory (Figure 4) and created a spectral database of bands assigned to DNA and other biomolecules that may be present in cancer tissues, based on the reports shown in literature [40–43]. HAp crystals exhibit a main band at 964 cm^{-1} and other smaller bands at 435, 592, 1050 and 1077 cm^{-1} (Figure 4). These observed bands are compatible with the ones reported in the literature [40]. The Raman spectra of DNA have been broadly studied and characterized and its main Raman bands have been reported [40,43].

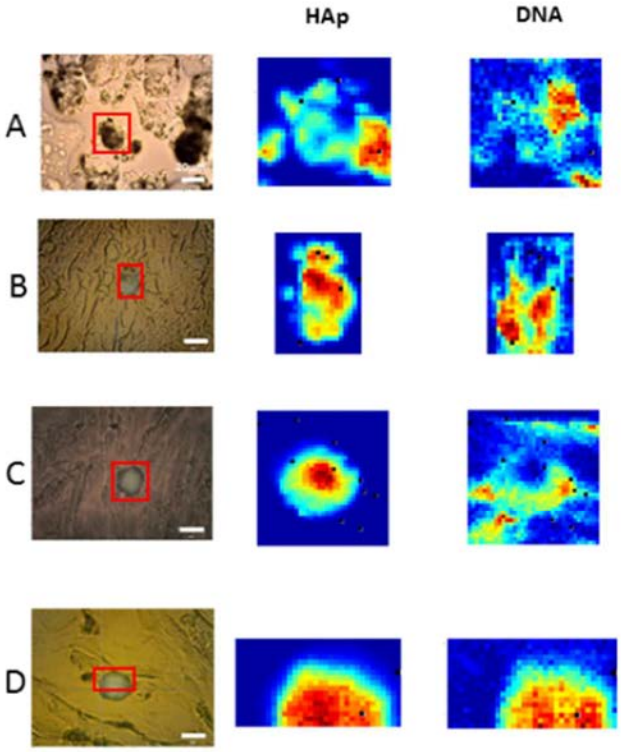

Figure 3. Raman spectral images of different breast cancer tissue sections showed the presence of DNA in HAp calcifications. First column: Bright field image of the breast tissue section imaged, with a HAp calcification highlighted in the region of interest (red box). Raman images were obtained from this area. Using the MCR algorithm, several molecular components were deconvolved from the spectra. The abundance maps of HAp and DNA molecular components are plotted in the second and third columns. Tissues (**A**–**D**) correspond to tissues 20, 22, 1 and 9 in Table 1.

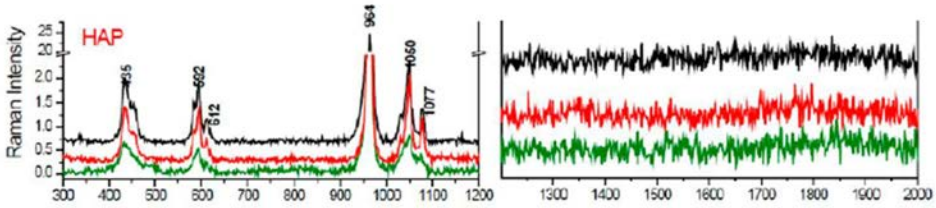

Figure 4. Raman spectrum of HAp synthetized in the laboratory.

3.2.2. Identification of DNA in HAp Calcifications Found in Breast Cancer Tissues

The spectral features obtained from the synthetic HAp crystals and the Raman databases of biomolecules found in the literature were used as a reference to study the Raman images acquired from the excised breast cancer samples. In Figure 2, the different spectral profiles of the components extracted by MCR-ALS algorithm are shown, specifying the position of the main Raman bands.

In Table 2, we summarize the bands and assignments of molecular component number 2 extracted from the MCR analysis of HAp calcification, shown in Figure 2. Assignments

were based on the literature [40,43]. More than 90% of the spectral band positions in component 2 correspond to the Raman bands also found in DNA.

Analyzing the distribution of Component 2 in the Raman imaging abundance maps (Figure 2), we can observe that DNA is present inside the HAp calcifications, as its spectra coincide with the spatial distribution of the HAp spectral component (Component 1). Z-sections along lines 1–2 and 3–4 confirm the presence of DNA inside the region of the HAp calcification. Therefore, we conclude that DNA is present and surrounded by HAp crystals in natural HAp calcifications found in breast cancer tissues.

The majority (92.3%) of HAp calcifications studied in breast cancer tissues contained DNA. Specifically, a DNA component was found in 91.3% of samples (23 patients) for infiltrating ductal carcinoma and 100% of samples (three patients) for lobular carcinoma. All details are shown in Table 1. In some cases, the presence of DNA was found more abundantly at the border of the microcalcifications, which indicates that DNA cannot only be encapsulated within, but must also be adhered to the surface of, the HAp calcification. Raman images of other analyzed breast cancer tissue sections are shown in Figure 3.

Table 2. Bands and assignments of molecular component number 2, extracted from MCR analysis of HAp calcification shown in Figure 2. Assignments were based on the literature [40,43].

Component 2: DNA			
Band/cm^{-1}	**Assignment**	**Band/cm^{-1}**	**Assignment**
1679	T, DNA base	1084	Phosphodiester groups in nucleic acids
1656	T, G, C (ring breathing modes of the DNA/RNA bases); amide I (protein); C=C lipids	1060	PO_2-stretching of DNA
1605	Cytosine (NH2)	1004	Phenylalanine
1551	Guanine	972	T, ribose, Phosphate monoester groups of phosphorylated proteins and cellular nucleic acids
1457	A, C, T DNA bases	937	G, A DNA bases
1452	CH_2 CH_3 deformation	855	Phosphate group
1426	Deoxyribose (B, Z marker)	824	O-P-O stretch DNA
1342	A, G DNA bases	785	U, T, C, O-P-O
1322	G, DNA base	754	T, DNA
1297	C, palmitic acid, CH_2	721	A, DNA base
1271	C, G DNA bases	645	G DNA base
1261	A, G, C DNA bases	625	A, T DNA bases
1205	A, T, ring breathing mode of DNA bases	597	C DNA base
1131	A DNA base	543	C DNA base
1104	O-P-O backbone stretch DNA, U	423	T, U DNA bases

3.2.3. Fluorescence Staining of Microcalcifications with DAPI

To confirm the presence of DNA with a different technique, we stained tissue sections with DAPI. Staining has several complications and limitations because dyes might not penetrate in an effective way inside the calcifications. For this reason, we used DAPI as a complementary technique to our work. Images of HAp calcifications were acquired at different depths (Figure 5). Figure 5A shows a HAp calcification stained with DAPI that has an elongated region in one extreme, which indicates the presence of DNA in this area. Going deeper into the sample, the end of the HAp calcification is encountered, and the plane of the surrounding tissue can be visualized (Figure 5B). This area contains cells, and we can observe the nucleus stained with DAPI, which confirms that the correct staining

procedure was used. Although fluorescence staining results are only reliable in mapping exposed DNA on the surface but not in the interior (because of the issues related to the penetration of the dye in the calcification and the fluorescence shifts), these results support the Raman results indicating that DNA is trapped inside HAp.

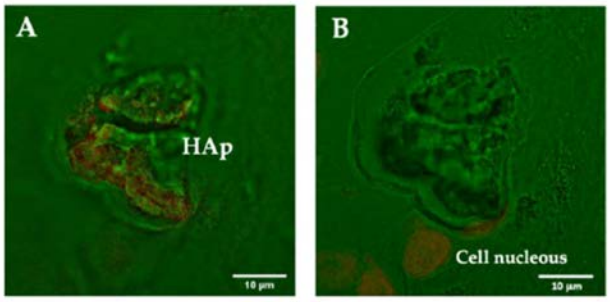

Figure 5. Confocal microscopy images of a breast cancer tissue section containing a HAp calcification at different depths: (**A**) image focused on the plane of the calcification, and (**B**) image focused on the plane of the surrounding cells in the tissue. DNA staining was performed with DAPI. Bright field (green) and DAPI (red). DAPI staining indicates the presence of DNA inside HAp calcifications and enables the visualization of the nucleus of the surrounding cells.

3.3. *Raman Images Reveal the Presence and Distribution of Biomolecules Inside HAp Calcifications*

Raman images in different optical sections (in x, y, z) confirmed that cancer tissue HAp calcifications contain several molecular components (Figure 2). Apart from the DNA, we found other molecular components present in the HAp tissue calcifications. The assignments of the bands of each spectral profile in Figure 2 are summarized in Table 3 and were assessed based on the literature [40–43].

First, Component 3 was extracted, presenting Raman bands at 436, 484, 597, 624, 721, 1081, 1133, 1300, 1314, 1450 and 1653 cm^{-1}. The majority of the Raman bands can be assigned to lipids [40,41,43]. According to the abundance map, this molecular component is present at the borders of the HAp (Figure 2). The two perpendicular z-section Raman images confirmed its localization at the surface of the calcification.

Second, Component 4 presents Raman bands at 424, 496, 850, 1002, 1062, 1126, 1205, 1270, 1297, 1322, 1342, 1447, 1553, 1603 and 1656 cm^{-1}. These bands can be assigned to polysaccharides (labeled in green) and proteins [40,43]. Component 4 is also present at the borders of the HAp calcification (Figure 2).

Finally, Component 5 presents bands (749, 1002, 1128, 1174, 1232, 1312, 1339, 1449, 1587 and 1658 cm^{-1}) that can be assigned to cytochrome C [42] (Figure 2). Thanks to the abundance maps in x-y and z we can confirm that this molecular component is located inside the HAp calcification.

These molecular components are common in most cells and human tissues. With these results, we are able to reveal the natural encapsulation or adhesion of relevant biological molecules in HAp microcalcifications of breast cancer tissues. The molecular information, together with the morphological distribution of the components in the calcification, could provide hints on how the calcification was initiated, indicating that many cellular and tissue molecular components might be biomineralized during calcification.

Table 3. Bands and assignments of molecular spectral components extracted from MCR analysis of the Raman image of the tissue HAp calcification shown in Figure 2. Assignments were based on the literature [40–43].

Component 3: Lipid		Component 4: Polysaccharides and Proteins		Component 5: Cytochrome C	
Band/cm^{-1}	Assignment	Band/cm^{-1}	Assignment	Band/cm^{-1}	Assignment
436	Cholesterol, cholesterol ester	424	Polysaccharide	749	Cytochrome C
597	Phosphatidylinositol	496	Glycogen	1002	Phenylalanine
624	Cholesterol ester	850	Polysaccharide	1128	Cytochrome C
721	Phosphatidylcholine, Sphingomyelin	1002	Phenylalanine	1174	CH tyrosine phenylalanine
1081	Phosphatidylcholine, membrane lipids	1062	C-C carbohydrates	1232	Amide III
1133	Membrane lipids (PC, PE, SM)	1126	Disaccharides, glucose, sucrose, C-O stretching carbohydrates	1312	Cytochrome C
1300	Membrane lipids (PC, PE)	1205	Amide III proteins	1339	tryptophan
1314	CH3CH2 twisting of lipid	1270	Amide III proteins	1449	C-H proteins
1450	CH (lipids and proteins)	1297	CH2 deformation	1587	Cytochrome C
1653	C=C lipids, proteins	1322	CH deformation proteins	1658	Amide I proteins
		1342	CH deformation protein and carbohydrates		
		1447	CH2 deformation proteins		
		1553	Tryptophan, Amide II		
		1603	Phenylalanine		
		1656	Amide I proteins		

4. Discussion

Microcalcifications are key features observed in breast mammography and, depending on the BIRADS classification method (based on morphological and distribution characteristics like shape and cluster organization), they are associated with a different degree of malignancy. However, the formation of HAp calcification in cancer tissues and its association with a worse prognosis is still not well understood. To address these questions, it is key to develop a method that is capable of investigating in detail the biochemical composition and the spatial distribution of biomolecules in the calcification and the surrounding tissue in a label-free approach. Raman spectroscopy has been shown to be a promising tool to characterize microcalcifications [5–7]. Specifically, a recent paper [28] showed that Raman spectroscopy of calcifications correlates with histopathology, while being more rapid and objective. Furthermore, RS would be able to be used for in depth measurements using SORS [7], or used in needle biopsies for the non-invasive future assessment of calcifications. However, despite the number of the studies in the field, there is a lack of in-depth chemical analysis of the content of microcalcifications exploiting the rich molecular information contained in Raman spectra.

In this study, we combined Raman imaging of breast cancer microcalcifications with advanced multivariate analysis (MCR-ALS). Such an approach enabled us to provide an in-depth analysis of the composition and distribution of different molecular components inside tissue calcifications, extracting meaningful biological information. Some previous studies have reported a low number of samples studied. Furthermore, most of them studied individual spectra at different sites on the calcification. Only two studies have recently used Raman imaging [27,28]. However, in [27], only one image was studied for exploration purposes, and in [28] the image spectra of calcifications were averaged, thus losing the spatial information. In general, in all studies, multivariate analysis has been

used to classify Raman spectra. Overall, all articles lack a multivariate analysis technique to study the rich molecular information that is contained in the Raman spectra in detail. In our work, we go a step further, extracting biological information from the Raman data.

The Raman spectra of biomolecules such as DNA, proteins, lipids, etc., have been largely characterized and reported [40–43]. However, biological samples such as tissues are complex because they contain mixtures of multiple biomolecules. In order to extract all the molecular information encoded in the Raman spectral images, we used MCR-ALS [30,31]. This multivariate algorithm enables the extraction of multiple components that are present in the sample studied. For each component, a molecular Raman spectral shape is retrieved and associated with the distribution or concentration of the molecular component along the spectra acquired. In this case, as we acquired images, we were able to reconstruct the 3D molecular distribution of the components along the microcalcification studied. This algorithm is of particular interest for biomedical analysis because relevant information about the identity of the molecules encrusted in those calcifications can be extracted. First, the algorithm does not require previous molecular information about the sample, and it is an unsupervised method. Second, the extracted spectral signatures of the different components could be assigned to Raman spectra of biological molecules. Therefore, by employing the MCR-ALS algorithm, we were able to retrieve spectral components that could be assigned to pure molecules or a combination of molecules that were present in the sample in the same locations. Thus, this enabled us to study the distribution and localization of different molecular components in the microcalcifications studied. Furthermore, as we obtained Raman images and two respective perpendicular *z*-sections, we were able to localize the different molecular components and study whether the molecules were located inside the calcification, adsorbed on its surface, or if they could be found outside it (in the surrounding tissue). Therefore, our methodology and work contribute novel results, adding important information to the state of the art, revealing information that is otherwise inaccessible with other techniques.

Raman spectroscopy studies on breast cancer microcalcifications have focused on the study of the inorganic content of calcifications. Only in few cases were organic components reported, but without an in-depth analysis [27,28]. However, our advanced multivariate methodology enabled us to concentrate on extracting for the first time different biological molecular components present in the breast microcalcifications. Therefore, the focus of our study is an in-depth analysis of biological material trapped in microcalcifications and its distribution in the calcification.

The first relevant result of this work is that HAp calcifications contain several molecular components that can be assigned to biological molecules distributed inside or adsorbed in the calcifications' volume. First, we observed that DNA is contained inside or adsorbed on the surface of HAp calcifications in a high percentage of cases (92.3%). The demonstration of the biomineralization of DNA in HAp is important because (a) recent studies demonstrated that DNA could be preserved in HAp for long periods of time [26], and (b) DNA can be transferred to a different cell after some time [38]. Therefore, these results represent a large step toward a deeper understanding of the formation and role of HAp calcifications and their association with a worse prognosis.

Another important finding that we report in this work is that HAp calcifications contain other significant biological molecules inside them or adsorbed on their surface. Molecules such as cytochrome C, lipids and polysaccharides were identified. This suggests that HAp calcifications could be formed as a result of specific cellular processes, in particular in a non-regulated cell death, where the uncontrolled release of calcium and phosphate ions in combination with DNA occurs and leads to the formation of necrotic microcalcifications. On the other hand, studies performed on tissue samples and in vitro on cultured cells demonstrated that microcalcification formation is a cell active process, influenced by the microenvironment and by the overexpression of bone matrix proteins (i.e., osteonectin and osteopontin) [16,28,45]. Both studies reported that active processes of microcalcification formation are significantly more represented in cases of malignancy. In

parallel, a retrospective study on patients referred for needle-guided biopsy reported that the formation of new microcalcifications significantly correlates with a high probability of ductal invasive carcinoma [46]. According to [28], the crystallinity and homogeneity of malignant microcalcifications that they found in their study could originate from a faster and more active process, stimulated by cancer and by its microenvironment. The presence of cytochrome C is considered to be a sign of cell apoptosis [47]. Cytochrome C is usually found in the extracellular space as a result of pathological conditions in which cell death occurs. The fact that cytochrome C is associated with HAp calcifications reinforces the hypothesis that the calcifications of HAp containing DNA are formed when cell death processes occur in the tumor. Thus, the Raman molecular fingerprint found in this study suggests that a pathological process is behind the origin of the natural biomineralization of DNA in tumor HAp calcifications.

Apart from the HAp calcifications measured, six different CaOx calcifications were analyzed, found in one infiltrating lobular carcinoma tissue sample (Figure S1). No traces of DNA were found inside the CaOx calcifications. Although it will be necessary to increase the number of samples analyzed, these data are consistent with the simulation results published recently [26] showing that the tendency to adsorb and especially encapsulate DNA is much smaller for CaOx than for HAp, particularly because Mg^{2+} hinders the adsorption of DNA on CaOx.

Raman imaging, together with the multivariate analysis methodology presented here, represents an important step forward in the field because new biological information can be obtained without requiring initial information about the composition of the sample. Furthermore, there is no need to use specifically developed immuno-labels to target the relevant molecules. The study of calcifications with immunofluorescence has some hurdles that must be considered in order to create a 3D mapping of the calcification. First, immunolabels may not penetrate the outer layer of the calcification, thus failing to reach certain parts of the biomineralized materials. Second, immunofluorescence requires a priori knowledge of the biological molecules existing in the sample in order to stain the tissue and image it. In this case, no prior information was known. Third, there is a limited number of immune labels that can be imaged, obtaining therefore only partial information. However, with our methodology, we demonstrated that tridimensional information on several biological molecular components could be extracted without the need for previous knowledge, minimizing the risk of perturbing the sample or the need to add chemicals that modify it. Therefore, new and otherwise inaccessible molecular information has been obtained, progressing the understanding of the association of HAp calcifications with malignancy and their role in cancer tissue.

5. Conclusions

In this paper we have presented a methodology that is capable of investigating the biochemical composition of HAp calcifications in human breast cancer tissue. We report the most detailed study on the biochemical analysis of breast cancer HAp microcalcifications to date, combining molecular Raman imaging of breast cancer tissue sections (n = 26 patients) with an advanced multivariate analysis method, multivariate curve resolution (MCR). The use of advanced data analysis has enabled the extraction of otherwise inaccessible molecular information encoded in the Raman spectra. Specifically, we focused on the detailed study of the 3D molecular distribution of organic molecules in HAp microcalcifications. We have shown for the first time the presence and spatial distribution of several molecular components (DNA, lipids, proteins, cytochrome C and polysaccharides) in the HAp calcifications extracted from living cancer tissue. Specifically, we have shown that DNA is encapsulated or adsorbed naturally in HAp calcifications present in invasive cancer tissues. The natural biomineralization of tumoral DNA in breast cancer tissues could enable the preservation of this molecule for long periods of time. This finding represents a substantial advance in the field as it can pave the way toward understanding the formation and the role of HAp calcifications in malignant tissues.

Supplementary Materials: The following are available online at https://www.mdpi.com/article/10.3390/cancers13112658/s1, Figure S1: Raman image of an oxalate calcification.

Author Contributions: Conceptualization, M.M. and P.T.; methodology, M.M.; software, M.M. and C.A.-A.; validation, M.M., A.M.R.-R. and C.A.-A.; formal analysis, M.M. and C.A.-A.; investigation, M.M. and A.M.R.-R.; resources, M.T.F.-F., L.P.-R., E.C., J.N., A.M., J.F.J. and P.T.; data curation, M.M., A.M.R.-R. and C.A.-A.; writing—original draft preparation, M.M.; writing—review and editing, M.M., A.M.R.-R., P.T. and P.L.-A.; visualization, M.M. and A.M.R.-R.; supervision, P.L.-A., P.T. and M.M.; project administration, P.T. and P.L.-A.; funding acquisition, P.T., P.L.-A. and M.M. All authors have read and agreed to the published version of the manuscript.

Funding: M.M., C.A.-A., P.L.-A. acknowledge financial support from the Spanish Ministry of Economy and Competitiveness through the "Severo Ochoa" program for Centres of Excellence in R&D (SEV-2015-0522), from Fundació Privada Cellex, Fundación Mig-Puig and from Generalitat de Catalunya through the CERCA program, EU H2020 LaserLab Europe grant 654148, and "Fundació La Marató de TV3" (Comprehensive molecular and microspectroscopic profiling of breast carcinomas and their resistance to neoadjuvant treatment). All authors acknowledge B. Braun Surgical, S.A. for financial support.

Institutional Review Board Statement: Not applicable.

Informed Consent Statement: Not applicable.

Data Availability Statement: Data are contained within the article or supplementary material.

Acknowledgments: Special thanks to E. Rodríguez, L.F. del Castillo, M. Jiménez, S. Santos, J. Osmond, S. Carrasco, S. Royo, P. Berto, C. Vilches, C. Alonso, J. Fernández-Llamazares, A. Ariza, M.A. Arbós, M. Quiles, Alastair Cunningham and C. Alemán. We want to thank IGTP, IGTP-HUGTP Biobank (Spanish National Biobanks Network of Instituto de Salud Carlos III (PT13/0010/0009)), Tumor Bank Network of Catalonia and their staff, and particularly the patients that consent to the use of their tissue samples. This work is integrated within a wider research project supported by B. Braun Surgical S.A. UPC, Institut de Ciencies Fotòniques (ICFO), and the Institut Català de la Salut (ICS) through the H. U. Germans Trias I Pujol and H. U. Vall d'Hebron.

Conflicts of Interest: The authors declare no conflict of interest.

References

1. Bray, F.; Ferlay, J.; Soerjomataram, I.; Siegel, R.L.; Torre, L.A.; Jemal, A. Global Cancer Statistics 2018: GLOBOCAN Estimates of Incidence and Mortality Worldwide for 36 Cancers in 185 Countries. *CA Cancer J. Clin.* **2018**, *68*, 394–424. [CrossRef]
2. Miller, K.D.; Siegel, R.L.; Lin, C.C.; Mariotto, A.B.; Kramer, J.L.; Rowland, J.H.; Stein, K.D.; Alteri, R.; Jemal, A. Cancer treatment and survivorship statistics, 2016. *CA Cancer J. Clin.* **2016**, *66*, 271–289. [CrossRef] [PubMed]
3. DeSantis, C.E.; Lin, C.C.; Mariotto, A.B.; Siegel, R.L.; Stein, K.D.; Kramer, J.L.; Alteri, R.; Robbins, A.S.; Jemal, A. Cancer treatment and survivorship statistics, 2014. *CA Cancer J. Clin.* **2014**, *64*, 252–271. [CrossRef] [PubMed]
4. DeSantis, C.E.; Ma, J.; Goding Sauer, A.; Newman, L.A.; Jemal, A. Breast cancer statistics, 2017, racial disparity in mortality by state. *CA Cancer J. Clin.* **2017**, *67*, 439–448. [CrossRef]
5. Haka, A.S.; Shafer-Peltier, K.E.; Fitzmaurice, M.; Crowe, J.; Dasari, R.R.; Feld, M.S. Diagnosing breast cancer by using Raman spectroscopy. *Proc. Natl. Acad. Sci. USA* **2015**, *102*, 12371–12376. [CrossRef]
6. Haka, A.S.; Shafer-Peltier, K.E.; Fitzmaurice, M.; Crowe, J.; Dasari, R.R.; Feld, M.S. Identifying microcalcifications in benign and malignant breast lesions by probing differences in their chemical composition using Raman spectroscopy. *Cancer Res.* **2002**, *62*, 5375–5380. [PubMed]
7. Stone, N.; Baker, R.; Rogers, K.; Parker, A.W.; Matousek, P. Subsurface probing of calcifications with spatially offset Raman spectroscopy (SORS): Future possibilities for the diagnosis of breast cancer. *Analyst* **2007**, *132*, 899–905. [CrossRef] [PubMed]
8. Gary, M.T.; Tan, P.H.; Cheung, H.S.; Chu, W.C.; Lam, W.W. Intermediate to highly suspicious calcification in breast lesions: A radio-pathologic correlation. *Breast Cancer Res. Treat.* **2008**, *110*, 1–7.
9. Scott, R.; Kendall, C.; Stone, N.; Rogers, K. Elemental vs. phase composition of breast calcifications. *Sci. Rep.* **2017**, *7*, 136. [CrossRef]
10. Frappart, L.; Boudeulle, M.; Boumendil, J.; Lin, H.C.; Martinon, I.; Palayer, C.; Mallet-Guy, Y.; Raudrant, D.; Bremond, A.; Feroldi, J. Structure and composition of microcalcifications in benign and malignant lesions of the breast: Study by light microscopy, transmission and scanning electron microscopy, microprobe analysis, and X-ray diffraction. *Hum. Pathol.* **1984**, *15*, 880–889. [CrossRef]
11. Tornos, C.; Silva, E.; El-Naggar, A.; Pritzker, K.P.H. Calcium oxalate crystals in breast biopsies. *Am. J. Surg. Pathol.* **1990**, *14*, 961–968. [CrossRef]

12. Radi, M.J. Calcium oxalate crystals in breast biopsies. An overlooked form of microcalcification associated with benign breast disease. *Arch. Pathol. Lab. Med.* **1989**, *113*, 1367–1369.
13. Winston, J.S.; Yeh, I.T.; Evers, K.; Friedman, A.K. Calcium oxalate is associated with benign breast tissue: Can we avoid biopsy? *Am. J. Clin. Pathol.* **1993**, *100*, 488–492. [CrossRef]
14. Yassin, N.I.R.; Omran, S.; El Houby, E.M.F.; Allam, H. Machine learning techniques for breast cancer computer aided diagnosis using different image modalities: A systematic review. *Comput. Methods Programs Biomed.* **2018**, *156*, 25–45. [CrossRef] [PubMed]
15. Wang, Z.; Hauser, N.; Singer, G.; Trippel, M.; Kubik-Huch, R.A.; Schneider, C.W.; Stampanoni, M. Non-invasive classification of microcalcifications with phase-contrast X-ray mammography. *Nat. Commun.* **2014**, *5*, 3797. [CrossRef] [PubMed]
16. Cox, R.F.; Hernandez-Santana, A.; Ramdass, S.; McMahon, G.; Harmey, J.H.; Morgan, M.P. Microcalcifications in breast cancer: Novel insights into the molecular mechanism and functional consequence of mammary mineralisation. *Br. J. Cancer* **2012**, *106*, 525–537. [CrossRef] [PubMed]
17. Baker RRogers, K.D.; Shepherd, N.; Stone, N. New relationships between breast microcalcifications and cancer. *Br. J. Cancer* **2010**, *103*, 1034–1039. [CrossRef] [PubMed]
18. Tabar, L.; Tony Chen, H.H.; Amy Yen, M.F.; Tot, T.; Tung, T.H.; Chen, L.S.; Duffy, S.W.; Smith, R.A. Mammographic tumor features can predict long-term outcomes reliably in women with 1–14-mm invasive breast carcinoma: Suggestions for the reconsideration of current therapeutic practice and the TNM classification system. *Cancer Interdiscip. Int. J. Am. Cancer Soc.* **2004**, *101*, 1745–1759. [CrossRef]
19. Cox, R.F.; Morgan, M.P. Microcalcifications in breast cancer: Lessons from physiological mineralization. *Bone* **2013**, *53*, 437–450. [CrossRef]
20. Scimeca, M.; Giannini, E.; Antonacci, C.; Pistolese, C.A.; Spagnoli, L.G.; Bonanno, E. Microcalcifications in breast cancer: An active phenomenon mediated by epithelial cells with mesenchymal characteristics. *BMC Cancer* **2014**, *14*, 286. [CrossRef]
21. Sathyavathi, R.; Saha, A.; Soares, J.S.; Spegazzini, N.; McGee, S.; Dasari, R.R.; Fitzmaurice, M.; Barman, I. Raman spectroscopic sensing of carbonate intercalation in breast microcalcifications at stereotactic biopsy. *Sci. Rep.* **2015**, *5*, 9907. [CrossRef] [PubMed]
22. Kerssens, M.M.; Matousek, P.; Rogers, K.; Stone, N. Towards a safe non-invasive method for evaluating the carbonate substitution levels of hydroxyapatite (HAP) in micro-calcifications found in breast tissue. *Analyst* **2010**, *135*, 3156–3161. [CrossRef] [PubMed]
23. Castellaro, A.M.; Tonda, A.; Cejas, H.H.; Ferreyra, H.; Caputto, B.L.; Pucci, O.A.; Gil, G.A. Oxalate induces breast cancer. *BMC Cancer* **2015**, *15*, 761. [CrossRef] [PubMed]
24. Sun, X.Y.; Ouyang, J.M.; Xu, M. Synthesis, characterization, and cytotoxicity assay of calcium oxalate dihydrate crystals in various shapes. *CrystEngComm* **2016**, *18*, 5463–5473. [CrossRef]
25. O'Grady, S.; Morgan, M.P. Microcalcifications in breast cancer: From pathophysiology to diagnosis and prognosis. *BBA Rev. Cancer* **2018**, *1869*, 310–320. [CrossRef]
26. Revilla-López, G.; Rodríguez-Rivero, A.; Valle, L.; Puiggalí, J.; Turon, P.; Alemán, C. Biominerals Formed by DNA and Calcium Oxalate or Hydroxyapatite: A Comparative Study. *Langmuir* **2019**, *3536*, 11912–11922. [CrossRef]
27. Kunitake, J.; Choi, S.; Nguyen, K.; Lee, M.; He, F.; Sudilovsky, D.; Morris, P.; Jochelson, M.; Hudis, C.; Muller, D.; et al. Correlative imaging reveals physiochemical heterogeneity of microcalcifications in human breast carcinomas. *J. Struct. Biol.* **2018**, *202*, 25–34. [CrossRef]
28. Vanna, R.; Morasso, C.; Marcinno, B.; Piccotti, F.; Torti, E.; Altamura, D.; Albasini, S.; Agozzino, M.; Villani, L.; Sorrentino, L.; et al. Raman Spectroscopy Reveals That Biochemical Composition of Breast Microcalcifications Correlates with Histopathologic Features. *Cancer Res.* **2020**, *80*, 1762–1772. [CrossRef] [PubMed]
29. Butler, H.J.; Ashton, L.; Bird, B.; Cinque, G.; Curtis, K.; Dorney, J. Using Raman spectroscopy to characterize biological materials. *Nat. Protoc.* **2016**, *11*, 664–687. [CrossRef]
30. Marro, M.; Nieva, C.; Sanz-Pamplona, R.; Sierra, A. Molecular monitoring of epithelial-to-mesenchymal transition in breast cancer cells by means of Raman spectroscopy. *Biochim. Biophys. Acta BBA Mol. Cell Res.* **2014**, *1843*, 1785–1795. [CrossRef]
31. Marro, M.; Nieva, C.; de Juan, A.; Sierra, A. Unravelling the metabolic progression of breast cancer cells to bone metastasis by coupling Raman spectroscopy and a novel use of MCR-ALS algorithm. *Anal. Chem.* **2018**, *90*, 5594–5602. [CrossRef]
32. Aschar-Sobbi, R.; Abramov, A.Y.; Diao, C.; Kargacin, M.E.; Kargacin, G.J.; French, R.J.; Pavlov, R. High Sensitivity, Quantitative Measurements of Polyphosphate Using a New DAPI-Based Approach. *J. Fluoresc.* **2008**, *18*, 859–866. [CrossRef] [PubMed]
33. Gomes, F.M.; Ramos, I.B.; Wendt, C.; Girard-Dias, W.; De Souza, W.; Machado, E.A.; Miranda, E.A.K. New insights into the in situ microscopic visualization and quantification of inorganic polyphosphate stores by 4X2019;, 6-diamidino-2-phenylindole (DAPI)-staining. *Eur. J. Histochem.* **2013**, *57*, e34.
34. Bertran, O.; del Valle, L.J.; Revilla-López, G.; Chaves, G.; Cardús, L.; Casas, M.T.; Casanovas, J.; Turon, P.; Puiggalí JAlemán, C. Mineralization of DNA into nanoparticles of hydroxyapatite. *Dalton Trans.* **2014**, *43*, 317–327. [CrossRef] [PubMed]
35. Revilla-López, G.; Casanovas, J.; Bertran, O.; Turon, P.; Puiggalí, J.; Alemán, C. Modeling biominerals formed by apatites and DNA. *Biointerphases* **2013**, *8*, 10. [CrossRef]
36. Turon, P.; Puiggalí, J.; Bertrán, O.; Alemán, C. Surviving mass extinctions through biomineralized DNA. *Chem. Eur. J.* **2015**, *21*, 18892–18898. [CrossRef]
37. Del Valle, L.J.; Bertran, O.; Chaves, G.; Revilla-López, G.; Rivas, M.; Casas, M.T.; Casanovas, J.; Turon, P.; Puiggalí, J.; Alemán, C. DNA adsorbed on hydroxyapatite surfaces. *J. Mater. Chem. B* **2014**, *2*, 6953–6966. [CrossRef]

38. Graham, F.L.; van der Eb, A.J. A new technique for the assay of infectivity of human adenovirus 5 DNA. *Virology* **1973**, *52*, 456–467. [CrossRef]
39. Eilers, P.H.; Boelens, H.F. Baseline correction with asymmetric least squares smoothing. *Leiden Univ. Med. Cent. Rep.* **2005**, *1*, 1–5.
40. Talari, A.; Movasaghi, Z.; Rehman, S.; Rehman, I. Raman Spectroscopy of Biological Tissues. *Appl. Spectrosc. Rev.* **2015**, *50*, 46–111. [CrossRef]
41. Czamara, K.; Majzner, K.; Pacia, M.Z.; Kochan, K.; Kaczora, A.; Baranskaa, M. Raman spectroscopy of lipids: A review. *J. Raman Spectrosc.* **2014**, *46*, 4–20. [CrossRef]
42. Brazhe, N.; Evlyukhin, A.; Goodilin, E.; Semenova, A.; Novikov, S.; Bozhevolnyi, S.; Chichkov, B.; Sarycheva, A.; Baizhumano, A.; Nikelshparg, E.; et al. Probing Cytochrome C in living mitochondria with surface enhanced Raman spectroscopy. *Sci. Rep.* **2015**, *5*, 13793. [CrossRef] [PubMed]
43. Gelder, J.; Gussem, K.; Vandenabeele, P.; Moens, L. Reference database of Raman spectra of biological molecules. *J. Raman Spectrosc.* **2007**, *38*, 1133–1147. [CrossRef]
44. Sokolova, V.; Epple, M. Inorganic Nanoparticles as Carriers of Nucleic Acids into Cells. *Angew. Chem. Int. Ed.* **2008**, *47*, 1382–1395. [CrossRef]
45. Bellahcene, A.; Castronovo, V. Increased expression of osteonectin and osteopontin, two bonematrix proteins, in human breast cancer. *Am. J. Pathol.* **1995**, *146*, 95–100. [PubMed]
46. Lev-Toaff, A.S.; Feig, S.A.; Saitas, V.L.; Finkel, G.C.; Schwartz, G.F. Stability of malignant breast microcalcifications. *Radiology* **1994**, *192*, 153–156. [CrossRef]
47. Eleftheriadis, T.; Pissas, G.; Liakopoulos, V.; Stefanidis, I. Cytochrome c as a Potentially Clinical Useful Marker of Mitochondrial and Cellular Damage. *Front. Immunol.* **2016**, *7*, 279. [CrossRef]

SUPPLEMENTARY MATERIAL

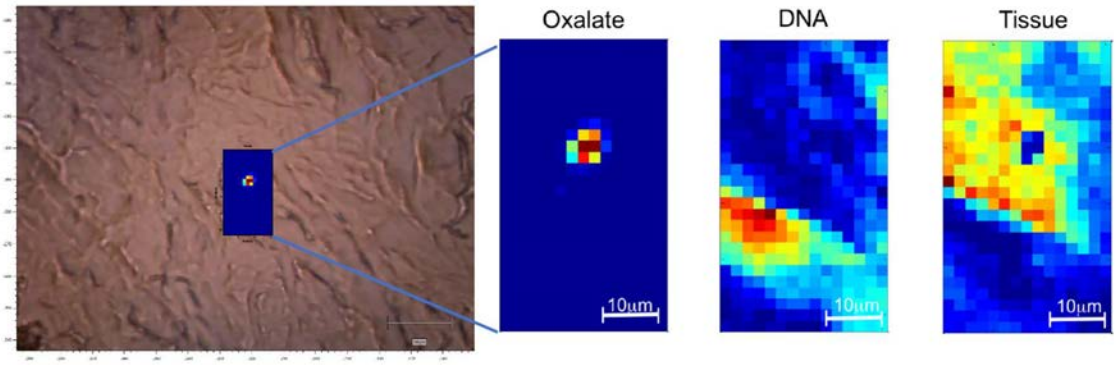

ANNEX 3.3. CELL TRANSFECTION MEDIATED BY BREAST CANCER NANOCALCIFICATIONS OF HYDROXYAPATITE AND CALCIUM OXALATE

Rodríguez-Rivero, A. M.; Rodríguez-Miguel, C.; Sans, J.; Alemán, C.; Julián, J. F. and Turon, P. Cell transfection mediated by breast cancer nanocalcifications of hydroxyapatite and calcium oxalate. 2021 (ready for submission).

Abstract: "Hydroxyapatite and calcium oxalate calcifications are frequently observed in breast tissue. Recently, it has been revealed that a subgroup of those calcifications contains nucleic acids adsorbed on their surface or encapsulated in their interior. Such particles are naturally formed when the nucleic acid and calcium, phosphate or oxalate ions are simultaneously present in a physiological environment. We propose that those hybrid systems, composed of a nucleic acid and a mineral, act as natural non-viral vectors of transfection and are able to deliver DNA to surrounding cells. Transfection processes have not been studied under the perspective of being a naturally formed vector in a physiological environment that can mineralize DNA and disseminate it to the surrounding tissue. In this work we investigate, under several in vitro conditions, the feasibility of such mineralization, migration and transfection processes with the aim to understand how hydroxyapatite, amorphous calcium phosphate and calcium oxalate transfection vectors behave in living tissue. We experimentally confirm that all studied vectors, both DNA adsorbed and co-precipitated, are able to transfect cells, being more efficient the amorphous calcium phosphate than hydroxyapatite and calcium oxalate. Moreover, they are more efficient when Ca^{2+} ions are added to the already formed vector. Conversely, Mg^{2+} has a minor effect. Finally, we study how such vectors are able to migrate and how the migration distance influences the transfection efficiency ratio."

Cell transfection mediated by breast cancer nanocalcifications of hydroxyapatite and calcium oxalate

Anna M. Rodríguez-Rivero,[1,2] Cristina Rodríguez-Miguel,[1] Jordi Sans,[3,4] Carlos Alemán[*],[3,4,5] Joan Francesc Julián[*],[2,6] Pau Turon[*,1]

[*]Corresponding authors

1. *Research and Development. B. Braun Surgical, S.A.U. Ctra. de Terrassa, 121. Rubí. Barcelona. Spain.*
2. *Universitat Autònoma de Barcelona. Campus de la UAB, Plaça Cívica, 08193 Bellaterra, Barcelona. Spain.*
3. *Departament d'Enginyeria Química, EEBE, Universitat Politècnica de Catalunya, C/ Eduard Maristany, 10-14, Ed. I2, 08019, Barcelona, Spain*
4. *Barcelona Research Center in Multiscale Science and Engineering, Universitat Politècnica de Catalunya, C/ Eduard Maristany, 10-14, 08019, Barcelona, Spain*
5. *Institute for Bioengineering of Catalonia (IBEC), The Barcelona Institute of Science and Technology, Baldiri Reixac 10-12, 08028 Barcelona Spain*
6. *Hospital Universitari Germans Trias i Pujol. Ctra del Canyet, s/n, 08916 Badalona, Barcelona. Spain.*

ABSTRACT

Hydroxyapatite and calcium oxalate calcifications are frequently observed in breast tissue. Recently, it has been revealed that a subgroup of those calcifications contains nucleic acids adsorbed on their surface or encapsulated in their interior. Such particles are naturally formed when the nucleic acid and calcium, phosphate or oxalate ions are simultaneously present in a physiological environment. We propose that those hybrid systems, composed of a nucleic acid and a mineral, act as natural non-viral vectors of transfection and are able to deliver DNA to surrounding cells. Transfection processes have not been studied under the perspective of being a naturally formed vector in a physiological environment that can mineralize DNA and disseminate it to the surrounding tissue. In this work we investigate, under several in vitro conditions, the feasibility of such mineralization, migration and transfection processes with the aim to understand how hydroxyapatite, amorphous calcium phosphate and calcium oxalate transfection vectors behave in living tissue. We experimentally confirm that all studied vectors, both DNA adsorbed and co-precipitated, are able to transfect cells, being more efficient the amorphous calcium phosphate than hydroxyapatite and calcium oxalate. Moreover, they are more efficient when Ca^{2+} ions are added to the already formed vector. Conversely, Mg^{2+} has a minor effect. Finally, we study how such vectors are able to migrate and how the migration distance influences the transfection efficiency ratio.

1. Introduction

Microcalcifications found in breast cancer tissue have been traditionally described as hydroxyapatite ($Ca_{10}(PO_4)_6(OH)_2$; HAp) and calcium oxalate (CaC_2O_4; CaOx).[1,2] However, a new subgroup of natural calcifications made of HAp containing nucleic acids (HAp-DNA and HAp-RNA), termed hydroxyolites,[3] have recently been reported.[4,5] Dystrophic calcifications

of HAp have often been related to cell death where a dysregulated process occurs.[6-9] The sudden release of calcium ions from endoplasmic reticulum in combination with existing phosphate ions in the cytoplasm usually results in calcium phosphate calcifications (i.e. amorphous calcium phosphate ($Ca_3(PO_4)_2 \cdot nH_2O$; ACP), brushite ($CaHPO_4 \cdot 2H_2O$; Bru) or HAp), as their solubility is extremely low. Recently, we studied how a nucleic acid influences such a precipitation process acting as a template to favour the DNA encapsulation or adsorption in the newly formed biomineral.[10] It is worth noting that a hybrid system made of a calcium phosphate and a nucleic acid synthesized in vitro is considered to be a transfection vector that can transfer the genetic information to a new cell.[11] The role of such microcalcifications as transfection vectors merits attention as they could be spreading agents of tumor DNA to the surrounding tissue as the mineral is able to protect the nucleic acid from enzymatic attacks keeping it functional.[12] To our knowledge, the feasibility and consequences of biomineralized DNA in calcium phosphates as natural non-viral vectors of transfection have not been considered in the context of breast cancer microcalcifications.

Since 1970s decade, synthetic particles containing calcium phosphate co-precipitated with DNA are known as in vitro non-viral vectors of transfection.[13,14] Calcium phosphate vectors are appreciated by their biocompatibility, low toxicity, low cost and easiness to transfect high amount of cells.[15-17] However, they are not considered highly efficient due to intrinsic characteristics and variability of the transfection process, and other approaches have been traditionally followed for curative purposes as gene therapy.[18] Nevertheless, throughout this process they can be used to modify the cell genome or to use the cell machinery to synthesize specific proteins.[19-22] Their formation in natural environments such as living tissue, particularly in cancer tissue, is still under intensive research. Focusing on breast calcifications, it has been recently reported the presence of DNA in natural HAp calcifications.[4] Consequently, we hypothesize that naturally formed calcium phosphate vectors in breast tissue might be able to

transfect by means of delivering nucleic acids to adjacent cells after migration and subsequently reproducing some tumor features of the primary tumor in the transfected cell.

On the other hand, CaOx calcifications have been related to disorders in metabolic processes despite their origin is not totally understood.[23] Recently, we empirically proved that DNA can be adsorbed in CaOx.[24] However, the well-established role for calcium phosphate as transfection vector has not been explored for CaOx and this is the reason why we include it in the study.

In this work, we investigate the transfection capacity of HAp, ACP and CaOx vectors in a controlled environment in order to understand how they could behave in a natural environment. We examine their physicochemical properties (i.e. particle size, percentage of particles with less than 500 nm and the dynamics of Z-potential) of each vector and how HAp, ACP and CaOx behave as transfection vectors in several scenarios. We analyze how a controlled addition of Ca^{2+} and Mg^{2+} ions in the vector synthesis microenvironment influences the transfection efficiency. Finally, we study how the migration distance to the target cell modifies the efficiency of the transfection process. We define the longest migration distance of the study as 50 mm, as it corresponds to the clinical scenario of multifocality that refers to the appearance of several tumors in the same breast quadrant.

2. Materials and Methods

2.1 Preparation of transfection vectors

HAp, ACP and CaOx transfection vectors were prepared by DNA co-precipitation or DNA adsorption on the mineral by mixing DNA with calcium (Ca^{2+}) , phosphate (PO_4^{3-}) or oxalate ($C_2O_4^{2-}$) according to the protocol described in Supplementary Information (SI) (SI.1.1a,b; SI.1.2a,b,c and SI.1.3a,b). The vectors (Figure 1) were named according to the inorganic substrate and the kind of interaction of DNA with the mineral, differentiating the co-precipitation (*c*) of DNA with the constituting ions (i.e. HAp-*c*DNA, ACP-*c*DNA, CaOx-*c*DNA) of the mineral from the DNA adsorbed (*a*) on the already formed particle (i.e. HAp-*a*DNA, ACP-*a*DNA, CaOx-*a*DNA).

The synthesis of vectors to assess the influence of additional Ca^{2+} in the solution containing the transfection vectors is described in SI (SI.1c; SI.2d; SI.3c). The resultant vectors were termed as HAp-*c*DNA(Ca^{2+}) and HAp-*a*DNA(Ca^{2+}) to denote that such additional Ca^{2+} ions were supplied to the already formed vectors, following the same language for ACP and CaOx. Finally, vectors synthesized by including Mg^{2+} in the mineral lattice, with the expectation that the ions would reduce the particle size, were prepared as detailed in SI (SI.1.1.d,e; SI.1.2.e; SI.1.3.d,e) and named as HAp(Mg^{2+})-*c*DNA and HAp(Mg^{2+})-*a*DNA to highlight that Mg^{2+} ions are included in the crystal structure, using the same terminology for ACP and CaOx.

2.2 Cell lines

A549 (ATCC® CCL-185™). Organism: *Homo sapiens*, human / Tissue: lung, epithelial / Disease: Carcinoma.

2.3 In vitro cell transfection

A549 cells (ATCC® CCL-185™, LGC Standards) were cultured in 75 cm^2 flasks in Dulbecco's modified Eagle's medium (DMEM, ThermoFisher, Ref. 31966021) supplemented

with 10% fetal bovine serum (Hi-FBS, ThermoFisher, Ref. 10082147), 1% Penicillin-Streptomycin (PenStrep, Sigma Aldrich, Ref. P4458) at 37 ºC in a humidified 5% CO_2-containing atmosphere. Cells were seeded at 40,000 cells per well into 24-well plates the day before transfection. Replacement of media with Opti-MEM® media (ThermoFisher, Ref. 11058021) without serum was done 2 hours before the transfection. Subsequently, the mineral–DNA systems were prepared as detailed previously. A conventional calcium phosphate transfection reagent containing HEPES buffer was used as a positive control (PC), meanwhile the negative control (NC) was obtained by cell culture media in absence of reactants. In addition, naked plasmid DNA was used to confirm that no transfection was feasible without the addition of the carrier under the experimental conditions described in this study. After addition of 50 μL of the incubated mixture (0.5 μg DNA) dropwise to each well (nanoparticles–DNA system, naked plasmid DNA, PC and NC, respectively), cells were incubated for 6 h at 37 ºC in a humidified 5% CO_2-containing atmosphere. Following incubation, the media was completely removed and 400 μL of fresh serum-supplemented media (DMEM, ThermoFisher, Ref. 11520556) were added per well. Each experiment was performed in triplicate and repeated in three independent days. Luciferase gene expression was monitored after cell lysis by using a commercial kit (Promega, Ref. N1110) and Cytation 5 microplate reader (BioTek), and according to manufacturer's instructions. Transfection efficiency was determined 24 and 48 h post-transfection, expressed as mean Relative Light Units (RLU) per microgram of cell protein (normalized against protein content), using a Pierce™ BCA protein assay kit. Transfection was monitored for all vectors through one week to determine the time of the transfection peak. As a result, 48 hours was the time point with the highest transfection efficiency for most of the cases, however, some of them showed the peak at 24 h (Table S1). Therefore, 24 and 48 h time points were selected to perform all the transfection assays.

2.4 Migration set-up

The transfection methodology described in the previous section was adapted in order to study how the migration distance of the vectors through the culture media affects the transfection rate. In this sense, the volume of Opti-MEM® media (ThermoFisher, Ref. 11058021) without serum added 2 hours before the transfection was adjusted to guarantee a migration distance of 3 mm (200 µL of Opti-MEM® media per well). An in vitro vertical migration setup was specifically designed for the assay to perform 7, 20 and 50 mm migration distance tests (Figure S1). The set-up was built using 24-well plates assembled with conical sterile polypropylene tubes in order to ensure a defined migration distance before entering in contact with the target cells seeded at the bottom of the well. The transfection procedure was identical to that described previously. Opti-MEM® media (ThermoFisher, Ref. 11058021) was used to fill the tube until the selected migration distance. 50 µL of the incubated mixture corresponding to each vector was added dropwise to each well.

2.5 Statistics

All series of average size (S), percentage of particles below 500 nm (Γ_{500}), Z-potential (Z), and free DNA (C_{DNA}) measurements were performed in triplicate. For each time point, the average and standard deviation were calculated. Furthermore, due to the intrinsic characteristics of the transfection assay, mostly related to the kind of cells, their life cycle and the internalization process of transfection vectors, a significant variability among replicates is expected that makes difficult the interpretation of the quantitative results. For that reason, assays were performed three independent days by triplicate each condition. Average and standard deviation (n–1) of the each test were calculated to compare the daily series. Average of the all data was calculated to classify the transfection ratio in intervals. The transfection efficiency intervals, which have been classified by magnitude orders as very low (V.L.), low (L), medium (M), high (H) and very high (V.H.) are defined in Table S2 included in SI.

Principal Components Analysis (PCA) was performed in Minitab® v.18.1 statistic software package.

3. Results

Raman spectra (SI.2) were performed in order to confirm the mineral composition of the HAp, ACP and CaOx vectors (Figure S2). DNA carried by transfection vectors was indirectly quantified by a bisBenzimide assay (SI.3, Table S3). Particle size distribution and average of vectors was determined by DLS (SI.4, Table S4). Results for as prepared HAp-*a*DNA show two populations, the averages centered at 88 ± 33 nm and 731 ± 262 nm, growing to 504 ± 125 nm and > 10 μm, respectively, after 30 min. A similar pattern occurs for HAp-*c*DNA, the average values of the two populations observed for as prepared samples, 75 ± 10 nm and 506 ± 311 nm, increasing to 7.8 ± 2.0 μm and > 10 μm after 30 min. Such an aggregation phenomena is expected to reduce the transfection efficiency when performing as transfection vectors. Indeed, 11.5 % of the HAp-*a*DNA particles exhibited a size smaller than 500 nm, decreasing to less than 0.2 % for HAp-*c*DNA (Figure 2, Table S4). On the other hand, the temporal evolution of Z-potential values for HAp-*a*DNA and HAp-*c*DNA are displayed in Figure 3a. The positive Z-potential of as prepared HAp-*a*DNA (23.7 ± 2.0 mV) corresponds to the counter cations of the OPTIMEM media (1.8 mM $Ca^{2+)}$ that neutralize the negative charge of the polyphosphates belonging to the adsorbed DNA.

Conversely, as prepared HAp-cDNA vector exhibits a negative Z-potential (–14.3 ± 4.1 mV), suggesting that the phosphate anions are the most exposed on the particle surface and, therefore, a change in the binding mode of the biomolecule. The origin of this change has been attributed to the templating effect of DNA, which affects the crystal growth pattern [10]. According to the DLVO electrostatic theory, the stability of a dispersion involving particles with charged surfaces depends on the balance between the attractive van der Waals forces

(steric stabilization) and the electrical repulsion because of the net surface charge. In general a Z-potential beyond 30 mV (positive or negative) indicates that the electrostatic repulsive forces exceed the attractive steric forces and the system is kept in a relatively stable dispersed state in solution. The Z-potential of HAp-aDNA and HAp-cDNA does not fulfill such threshold value, which explains the previously discussed aggregation phenomena. Moreover, as a consequence of such aggregation processes that occur in the first minutes, the Z-potential of both HAp-aDNA and HAp-cDNA approaches to zero with increasing time, reaching values of –0.5 ± 0.5 mV and –2.9 ± 2.8 mV, respectively, after 30 minutes (min).

Two well-defined size populations were also observed for as prepared ACP-*a*DNA (353 ± 135 nm and 2.0 ± 0.6 μm) and ACP-*c*DNA (232 ± 135 nm and 744 ± 216 nm). Moreover, the Zpotential of such species was relatively low (1.8 ± 1.1 and –12.1 ± 1.1 mV for ACP-*a*DNA and ACP-*c*DNA, respectively), suggesting they are not able to form stable dispersions. Indeed, after 30 min the size of the particles increased up to 1.5 ± 0.3 μm and 1.3 ± 0.3 μm respectively, even though an unimodal distribution was observed for both species but showing a broad distribution curve. Inspection of temporal evolution of the Z-potential, which is shown in Figure 3b, indicates that ACP-*a*DNA follows a distinctive behavior compared to HAp vectors. More specifically, the Z-potential of as prepared particles decreased to –10.8 ± 0.8 mM after 15 min and, subsequently increased to –1.2 ± 0.5 mV after 30 min. This feature suggests that, at the initially of the aggregation process (≤ 15 min) ACP evolves into a more ordered phase in which anions are preferentially exposed at the surface.

The size of as prepared CaOx-*a*DNA and CaOx-*c*DNA particles measured 264 ± 50 nm and 375 ± 137 nm, respectively, while their Z-potential was negative (–4.5 ± 0.6 mV and –2.1 ± 0.5 mV, respectively). As expected from such low values, the size of both kind of particles increases with time due to aggregation, after 30 min reaching average values up to 863 ± 140

nm and 1.1 ± 0.4 μm for CaOx-*a*DNA and CaOx-*c*DNA, respectively. Moreover, the Z-potential approaches zero with increasing time, as can be seen in Figure 3c.

Figure 2 represents the ratio of particles with a size lower than 500 nm with respect to agglomerates with a size higher than 500 nm (Γ_{500}= Particles < 500 nm / Particles > 500 nm * 100) after 30 min, which was determined by integrating the distribution profiles recorded for the different species. We note the highest percentage of small particles is achieved by ACP vectors at t=0, reaching to 61.3% for ACP-*c*DNA, however after 30 min the percentage was lower than 10 %. CaOx vectors show a similar distribution compared to HAp.

Transfection assays reveal three important features, which are represented in Figure 4 and summarized in Table S5. Firstly, we note that NC assay demonstrates that no luminescence signal was originated by cells and cell culture media in absence of reactants. Secondly, PC based on a standardized transfection vector made of calcium phosphate in combination with HEPES Buffer Solution (HBS) and luciferase pDNA supplied in the transfection kit scored the highest transfection rate (V.H.) at 24 and 48 h, indicating the correct application of the transfection protocol and the feasibility of A549 cells transfection with the protocol used. Thirdly, naked DNA showed no luminescence signal above the threshold confirming that there is no transfection when DNA naked is used as a vector.

The transfection efficacy of HAp, ACP (precursor of HAp) and CaOx was studied. Each of three cases split in two subcases: a) adsorbed DNA on already formed mineral particles and b) co-precipitated DNA with the mineral forming ions. We observed a positive transfection in all studied cases. However, the variability of transfection within the same day and inter-days was assessed as very high, justifying the use of a scale based on magnitude orders that allow to detect the significant differences in transfection efficiency when comparing several tested conditions (Table S2).

3.1. Effect of the mineral substrate of transfection vector

The type of vector is a determinant factor in regards of its ability to transfect in good agreement with previous results reported in the literature. ACP rated the highest, H at 24 h and V.H. at 48 h, compared to the values shown by HAp-*a*DNA and CaOx-*a*DNA that corresponded to L interval and HAp-*c*DNA and CaOx-*c*DNA that rated V.L. It is worth noting that the positive control rated V.H., higher compared to ACP, H at 24 h and equal at V.H. at 48 h, just for the effect of HEPES buffer that enhances the transfection of the reference vector (Figure 4).

3.2. Effect of adding Ca^{2+} and Mg^{2+}

The impact of adding Ca^{2+} in the solution is noticeable. The added cations on HAp vectors allow to keep the average particle size lower in both distributions, reducing by more than 40 % the average size of the lower distribution (296 ± 116 nm / 4.6 ± 1.8 μm) and keeping Γ_{500} = 4.8% in HAp-*a*DNA(Ca^{2+}) after 30 min, an effect that is more significant in HAp-*c*DNA(Ca^{2+}) where the average size of the lower distribution is reduced by a factor higher than x10 (456 ± 125 nm/ 2.3 ± 1.8 μm) and Γ_{500} = 6.8 % indicates a delay in the aggregation process (Table S4). A similar effect is observed for both ACP-*a*DNA(Ca^{2+}) and ACP-*c*DNA(Ca^{2+}), 641 ± 20 nm / 1.5 ± 0.1 μm and 487 ± 203 nm / 4.8 ± 2.6 μm respectively, but affected by a reduction factor of x2.6 and increasing Γ_{500} up to 10.2% and 8.0% respectively. Conversely, in CaOx cDNA(Ca^{2+}) is observed a significant average size reduction by a factor of x6 (178 ± 20 nm / 1.2 ± 0.1 μm and an increase in the number of particles below 500 nm up to Γ_{500} = 22.3%. Z-potential measurements adding 50 μL, as used in the transfection protocol, were not feasible due to interference of such high Ca^{2+} and Cl^- concentration during the test measurements. However, Zpotential measures, using only 5 μL to reduce the ion concentration in the solution, show a stable similar trend in HAp-*a*DNA(Ca^{2+}) and HAp-*c*DNA(Ca^{2+}) at –1.2 and –2.9 mV. ACPaDNA(Ca^{2+}) displays lower values at 30 min (–7,9 mV) but ACP-cDNA(Ca^{2+}) stabilizes

itself at almost at 0 mV. The most interesting trend is shown by CaOx-*a*DNA(Ca^{2+}) as is the lowest reaching at –15 mV at 30 min (Figure S3).

We focused on the effect of an exogenous burst of Ca^{2+} in the transfection media when additional Ca^{2+} was supplied once the particles were already formed. The first noticeable effect was that naked DNA with Ca^{2+} was able to transfect, rating H at 24 and 48 h. As expected Ca^{2+} ions should be able to interact with the negatively charged backbone of DNA, facilitating the endocytosis of the DNA. It is worth noting that the level of transfection is similar to the ACP despite no additional phosphate ions were supplied to naked DNA. On the other hand, and enhanced transfection ratio was observed for HAp-*a*DNA(Ca^{2+}) and HAp-*c*DNA(Ca^{2+}) and CaOx-*a*DNA(Ca^{2+}) and CaOx-*c*DNA(Ca^{2+}), resulting in an increment of two orders of magnitude for HAp and one for CaOx-*a*DNA(Ca^{2+}) and three for CaOx-*c*DNA(Ca^{2+}) at 48 h. Conversely, the additional Ca^{2+} showed a negative effect on the transfection ACP-*c*DNA(Ca^{2+}) and ACP-*a*DNA(Ca^{2+}), the ratio decreasing one order of magnitude from H to M at 24 h and two orders of magnitude from V.H. to M at 48 h (Figure 4).

On the other hand, the size of particle when Mg^{2+} is incorporated in the HAp(Mg^{2+})-*a*DNA vectors decreases at about 30 % in lower population and by a factor of 4 in the higher (365 ± 109 nm / 1.8 ± 0.2 μm) after 30 minutes but the impact is also important in HAp(Mg^{2+})-*c*DNA obtaining a reduction of 50 % (4.3 ± 0.6 μm) compared to HAp-*c*DNA. Nevertheless, the Γ_{500} is quite similar and not above 7% in any case (Table S4). Contrariwise, the impact on ACP(Mg^{2+})- *a*DNA shows aprox 20% reduction (284 ± 87 nm / 2.6 ± 0.1 μm) but the Γ_{500} = 28.9% is slightly lower. However, an increase of 30% observed in ACP(Mg^{2+})-*c*DNA (301 ± 24 nm / 2.6 ± 0.5 μm) and a significant reduction by a factor of 6 in Γ_{500} up to 10.4%. Finally, Mg^{2+} influence on CaOx results in an increase of x2 of the average size in CaOx(Mg^{2+})-*a*DNA (517 ± 97 nm / 5.2 ± 0.6 μm / > 10 μm) and a noticeable increase by a factor of x10 in CaOx(Mg^{2+})-*c*DNA (3.4 ± 0.8 μm / > 10 μm) being in both cases the percentage below 500 nm

beyond the detection limit of the measurement. The dynamics of Z-potential are significantly different depending on the mineral. HAp-*a*DNA shows a decreasing trend from –10.65 mV (15 min) to –16.7 mV (30 min) but HAp-*c*DNA increases from –21.73 mV (15 min) to –2.6 mV (30 min). Conversely, Zpotential of ACP-*a*DNA remains higher than ACP-*c*DNA for the whole period until 30 min (– 11.89 mV and –14.95 mV, respectively). The inverse relation (Figure S3) is observed for CaOx*c*DNA where stays less negative than CaOx-*a*DNA through time (–4.30 mV and –20.38 mV after 30 min respectively). Mg^{2+} ions allowed naked DNA to transfect cells but only up to V.L. interval. Compared with Ca^{2+}, the effect is mild, unveiling that Ca^{2+} transfection enhancement is not only related to the positive charge of the ion. In the case of Mg^{2+} included in the mineral lattice as HAp(Mg^{2+})-*a*DNA and HAp(Mg^{2+})-*c*DNA and CaOx in the same conditions, the effect is almost negligible compared to the vector without Mg^{2+}. Finally, Mg^{2+} ions do not influence the transfection ratio of ACP vectors at 24 h but reduce to H at 48 h. As Figure 4 describes, the presence of Mg^{2+} keeps the ratio of both ACP(Mg^{2+})-*a*DNA and ACP(Mg^{2+})-*c*DNA in the H interval.

A principal component analysis was performed to elucidate which are the variables that have positive associations with transfection efficiency ratio (Figure 5). The variables used for the analysis were: transfection rate, average size, Γ_{500}, Z-potential after 30 min and DNA load carried by the transfection vector (Θ_{DNA}) (Table S3). Results displayed in Table 2a show that proportion of variance explained by the three first components is 87.5%. Therefore, we used three components for the PCA analysis. The first component (PC1) is mainly explained by the following variables: transfection (0.606), the most important contributing factor, followed by Γ_{500} (0.567) and Θ_{DNA} (0.282) unveiling a positive association among those three variables and indicating the high explicative power of Γ_{500} and Θ_{DNA} to understand the transfection process. However, a negative contribution is observed for average size (–0.428) and Z-potential (–0.220). Conversely, the second component (PC2) shows a positive association among Θ_{DNA}

(0.722), average size (0.615) and Z-potential (0.278) linking the physicochemical features of the particles with the capacity of carrying DNA. The third component (PC3) denote positive associations between Z-potential (0.912) and Transfection rate (0.277) but negative association with ΘDNA (–0.247) and average size (–0.166), so PC3 component primarily refers to the contribution of particle charge to transfection. The loading plot showing first and second component graphically the positive and negative associations (Figure 5) for the two first components.

3.3. Effect of migration distance

In this section we report how the distance from the vector synthesis location to the target cells influences the transfection efficiency ratio at defined distances: 3 mm, 7 mm, 20 mm and 50 mm (Figure S1 and Table S6).

Considering the V.H. score of the positive control at 3 mm, it is interesting to note the decrease of the transfection ratio with increasing migration distance (Figure 6). In both cases, transfection ratio remains in V.H. up to 7 mm at 24 and 48 h. However, at 20 mm decreases to H (24 and 48 h) and at 50 mm to M (24 h) and L (48 h). These results confirm the feasibility of transfection at long distance after migration, indicating that the transfection is not exclusively a local effect.

The migration of HAp-*c*DNA and HAp-*a*DNA particles shows a totally different pattern (Figure 6). The trend of transfection ratio through distance is flat instead of decreasing, although the efficiency ratio remains L for HAp-*a*DNA and in V.L. for HAp-*c*DNA. This is an important result that merits further discussion as it shows the capacity of HAp to protect DNA and transfect distant cells. The cases of CaOx-*c*DNA and CaOx-*a*DNA exhibit a similar tendency compared to HAp. As can be seen in Figure 6, it is maintained the capacity of transfection in L range for the CaOx-*a*DNA and V.L. or "No transfection" for the CaOx-*c*DNA.

Nevertheless, the transfection at long distances is still feasible being observed less transfection at 48 h than at 24 h. Finally, the case of ACP shows an analogous profile compared to the PC. Again the H or V.H. (48 h) ratio observed at shorter distances (3 mm and 7 mm) decreases at longer distances, rating M at 20 mm. At 50 mm, ACP-*c*DNA shows L (24 h) or V.L. (48 h) and ACP-*a*DNA scores L (24 h) and "No transfection" (48 h).

4. Discussion

Through last decades, several articles dealt with transfection efficiency of non-viral vectors in vitro synthesized, particularly since viral vectors demonstrated to have some shortcomings and researchers recuperated the interest for non-viral vectors [25,26]. Among them, calcium phosphates are one of the most studied despite showing a relatively low transfection efficiency. Moreover, the transfection process of calcium phosphate is a well-studied process and several authors described many influencing factors that explain such a low transfection ratio and the poor reproducibility of the process [27]. For instance, due to cell type [28], phase of the cell cycle [29], reagent concentration, precipitation time, size of particles, mixing process, temperature [20,21,30-32], presence of dispersants [33], and soluble calcium ions that facilitate the DNA uptake and further endosomal escape [34]. Instead, CaOx calcifications, which are also found in breast cancer tissue, remained in a second line of interest as they have been more related to benign prognosis. Furthermore, to our knowledge, there are no study reports on the use of CaOx as a transfection vector. Thus, we confirm the feasibility of CaOx as a transfection vector.

In this work, we aim to understand how such submicrometric calcifications found in breast cancer tissue in combination with nucleic acids adsorbed or encapsulated might behave in living tissue after being naturally formed. We did not intend to optimize the efficiency of such vectors. For that reason, we used a well-established transfection protocol and the epithelial cell line A549 widely used as a transfection host in order to study how differences in the synthesis

and composition of the vectors might affect the transfection efficiency ratio. The positive control used as a reference belongs to the calcium phosphate family but includes 4-(2-hydroxyethyl)-1- piperazineethanesulfonic acid (HEPES) buffer that acts as neutralizing agent of the negative charges of DNA, controls the pH during the particle synthesis and regulates the pH along the transfection process. Therefore, the PC efficiency ratio is optimized and scores V.H.. Likewise, due to the HEPES effect, we cannot extrapolate how ACP vectors could behave in a physiological environment. Hence, we included ACP, as a precursor of HAp, as it is still able to transfect without HEPES. Moreover, the transfection ratios obtained for all tested vectors show individual results with a high variability which has been accepted as a basis to understand how those natural vectors could behave inside of a living organism. We extrapolate their ability to transfect in a simplified in vitro model, without using facilitating additives, to hypothesize their transfection behavior in more complex physiological environment where a natural transfection process could take place.

Based on Kunitake et al.[4] findings, who detected nucleic acid bands in HAp calcifications extracted from breast cancer tissue and our own previous research [24], we concluded that transfection vectors are indeed created by nature. We consider that is worth studying in detail the behavior of those vectors in order to understand the risks related to their existence in living tissue. Particularly noteworthy is the fact that they could be carriers of tumor DNA and they might act as non-viral vectors transfecting the surrounding cells or migrating agents able to transfect distant tissues.

Focusing on the results reported in this work, we note that naked DNA did not show any transfection, as it is not able to cross the cell membrane due to its high negative zeta potential (from –30 to –70 mV). This fact allows foreseeing that there will be no transfection in living tissue when only naked DNA is released to the extracellular matrix, for instance, as a consequence of necrotic cell death processes, not only due to its negative zeta potential but also

as a consequence of its large size. In addition, nuclease enzymes usually found in lysosomes and with an ubiquitous tissue distribution could degrade any exogenous DNA internalized by a cell in a short period of time, minimizing the risk of transfection. However, after analyzing the results of the addition of Ca^{2+}, that enhance the transfection efficiency, we note the relevance of looking for factors that can provide additional bursts of Ca^{2+} ions as it significantly enhances the transfection rate of naked DNA. This result is coherent with other authors' work that mention Ca^{2+} ion as a key factor to enhance the transfection efficiency as it can form DNA complexes by an electrostatic interaction of the negative phosphate backbone and Ca^{2+} ions [35,36]. Despite this effect is not totally understood, we note that some authors report that most nuclease enzymes are Ca^{2+} dependent and their activity can be reduced in the presence of an excess of Ca^{2+} that impairs the cleavage performance [37,38]. Furthermore, during the course of a cell death process, as it occurs in the center of a tumor, significant amounts of Ca^{2+} are likely to be released from cell calcium storage sites, mainly from endoplasmic reticulum, that might trigger the synthesis of such natural vectors, increasing the likelihood of further transfection. The same enhancing effect occurs in presence of already formed vectors made of phosphates HAp, ACP or CaOx. On the other hand, we observe that Mg^{2+} ions are also able to enhance the transfection of naked DNA but not at the same ratio of Ca^{2+}, remaining the transfection efficiency at low levels. Thus, we confirm that the neutralizing charge effect of Ca^{2+} and Mg^{2+} on polyphosphate DNA backbone is not the only factor that facilitates the transfection efficiency.

4.1. Hydroxyapatite

After analyzing the hydroxyapatite vector results (HAp-*c*DNA and HAp-*a*DNA), we observe that both types of in vitro chemically synthesized hydroxyapatite vectors confirm the potential to transfect cells. Nevertheless, their transfection ratio is much lower than the PC and

the ACP vectors. HAp-*a*DNA, despite containing less quantity of DNA on the particle (Table S3), results in a higher transfection ratio than HAp-*c*DNA, showing that transfection with DNA adsorbed is slightly more efficient than when DNA is co-precipitated. This effect that can be related to the smaller particle size, 7.8 μm and 504 ± 125 nm for HAp-*c*DNA and HAp-*a*DNA, respectively, at the time of coming into contact with the cells. The Z-potential of the particles gives an additional clue about the stability of the particles in solution and their internalization process (Figure 3). Freshly synthesized HAp-*c*DNA particles show a negative Z-potential (–14.3 ± 4.1 mV), similar to ACP-*c*DNA (–12.1 ± 3.6 mV), that shows a contrary sign to HAp-*a*DNA (+23.7 ± 2.0 mV). The Z-potential reaches to values of –0.48 ± 0.51 mV at 30 min, a result that is expected to have a significant impact in the aggregation process of those particles, increasing the size and, as a consequence, limiting the time window suitable for transfection. We observe that none of the hydroxyolites will remain stable in solution in the long-term and all of them tend to aggregate as their Z-potential is almost neutral after 30 min (Figure 3). On the other hand, Chen et al.[39] concluded that the more positive the charge of the particle, the higher their internalization in the cell. However, we have not confirmed such result in our study that is more aligned with Sokolova et al. [16], which concluded that the charge does not play a critical role for explaining the transfection efficiency. Beyond that fact, Forest and Pourchez [40] proposed that the protein corona formed when the nanoparticles are in physiological environment drastically alters the Z-potential, which affects the cell behavior on nanoparticle uptake. Additionally, Z-potential shows a dependence with the pH being the highest at pH 7.8 that is close to the pH we use in the transfection study [25,39]. Nevertheless, their convergence to 0 Mv demonstrates that the charge is not the primary factor for explaining differences in the transfection ratio, a fact that we confirmed with the PCA analysis.

Additional Ca^{2+} added to the transfection vector solution is a highly influencing factor as it changed the performance of HAp vectors and the transfection capability of naked DNA.

In both cases, the additional Ca^{2+} boosted the efficiency ratio of hydroxyolites. We note that in HAp*a*DNA(Ca^{2+}), the extra calcium neutralized the negative charge and reduced the particle size average, increasing the likelihood of transfection as the vector fits in the optimal transfection window. Nevertheless, we assume that Ca^{2+} should have an additional effect beyond the charge neutralization, as this effect is not observed when Mg^{2+} is added to HAp-*a*DNA as the transfection score remains in L. Such effect could be related to the impairment of DNase inside the lysosomes that could facilitate the preservation of internalized DNA carried by the vector and further release into the cytosol. Furthermore, Mg^{2+} ions included in HAp lattice are not significantly affecting the transfection ratio in HAp(Mg^{2+})-*a*DNA and no increase is observed for HAp(Mg^{2+})-*c*DNA. However, such effect is not related to a reduction in the particle size but could be attributed to a secondary mechanism associated with the neutralization of Z-potential and the absorption of Cl^- ions on the outer layer [41]. Bish et al. reported that calcium phosphate (CaP) nanoparticles can cross the cell membrane via calcium ion-mediated endocytosis [25]. Furthermore, Truong et al. proposed that CaP stimulates DNA cellular uptake involving either endocytosis of the membrane-bound DNA complex or enhanced permeabilization of the plasma membrane to facilitate DNA entry [42]. However, Haberland et al.[43] indicated that it is possible to differentiate between the Ca^{2+} role in cellular uptake of H1 (or mediator)-DNA complexes and endocytotic release because both Ca^{2+} ions and CaP microprecipitates enhanced the transfection to similar levels.

The presence of Cl^-, as Ca^{2+} counter ion, may play a role creating a thin layer of ions on the surface of adsorbed DNA. Chloride ions are engulfed together with the particle and become internalized in the endosome. Such an ion will help to increase the osmotic pressure inside the endosome that will result in the final release of the nucleic acid to the cytosol after endosome rupture. This fact has important consequences in terms of the role of natural hydroxyolites because the generation of the transfection vector might occur in two steps. The

first would be the adsorption of the nucleic acid on an already formed HAp calcification, the second would be related to a second wave of Ca^{2+} and Cl^{-} ions from adjacent dying cells that may reduce the average size of already existing submicrometric calcifications and neutralize the charges, enhancing transfection capabilities.

Concerning Mg^{2+} effect, we considered the inclusion of Mg^{2+} ion in the transfection analysis of natural microcalcifications because Mg^{2+} is ubiquitous in physiological environments and its relationship with cancer disease is still controversial. Scott et al.[44] described that low Mg^{2+} levels in serum were found in breast cancer patients, suggesting that a high Ca/Mg ratio is a risk factor in breast cancer. Nevertheless, tumor cells accumulate Mg^{2+} even when its extracellular concentrations are low. In cell death processes (*i.e.* associated to apoptotic processes or by the hydrolysis of ATP) Mg^{2+} concentration is likely to be increased and can easily interact with calcium and phosphate to be part of a newly formed calcification. Previous results showed that DNA was preferentially bound to Mg^{2+} when this ion is available in the mother solution, displacing Ca^{2+} to other positions. Thus, Mg^{2+} shows preference to bind DNA in all circumstances but it does not prevent the biomineralisation of DNA in HAp. Scimeca *et al.* [45] performed elemental microanalysis on breast microcalcifications. The presence of HAp was observed in 97.7% of malignant lesions and identifying Mg^{2+} inside of those HAp microcalcifications. Our results showed that the impact of Mg^{2+} in terms of transfection is very mild in comparison to Ca^{2+}, suggesting that the ion does not have a significant role in the regulation of the endocytosis pathways or it does not modify the behaviour of the particle during the release of DNA in the cytosol or nucleus.

4.2. Calcium oxalate

In spite of the relevance of breast microcalcifications for the early detection and diagnostic of breast cancer, not many contributions have been focused on the investigation about the

presence and role of CaOx in a tumor microenvironment. Although CaOx were related to carcinoma in situ lesions and invasive carcinomas [23], they were considered bystanders as they coexist with regular apatite calcifications [46]. CaOx calcifications are found in breast tissue, as mineral deposits related to breast epithelium, and in benign cysts, particularly in those presenting apocrine metaplasia or inside of dilated ducts [47,48]. They can be observed in breast biopsies under polarized light and with more sophisticated techniques as Raman spectroscopy and Energy-dispersive X-ray spectroscopy coupled with scanning electron microscope (SEM-EDS) [44,49]. Although the mechanism behind their synthesis is not totally understood yet, some hypotheses have been proposed [45,50]. Furthermore, cells cannot metabolize the oxalate ion and, for that reason, it is observed as end product of some metabolic processes. Castellaro et al.[23] reported some evidences related to the long-term exposure of breast epithelial cells to oxalates, resulting in the transformation of normal breast cells to tumor cells.

To the best of our knowledge, this is the first work that evaluates the role of CaOx as an in vitro or natural non-viral vector of transfection. Here, we report the unveiled capabilities of CaOx as a new non-viral transfection vector. CaOx-*a*DNA and CaOx-*c*DNA show a L transfection ratio and both were able to transfect A549 cells. The transfection is also enhanced when additional Ca^{2+} is supplemented but not with Mg^{2+}. We recall that we demonstrated in a previous work by synergistic theoretical-empirical studies that DNA cannot be encapsulated in CaOx [24]. For that reason, when co-precipitation route is used, CaOx clusters are expected to be formed in a first stage and the absorption of DNA on CaOx cluster will occur in a second stage. We note that the particle size of both CaOx-*a*DNA and CaOx-*c*DNA (264 nm and 375 nm, respectively) is in the feasible range of transfection but only the adsorbed show a significant part of them below 500 nm (Γ_{500}=0.14). However, the Z-potential values of such particles are almost neutral, suggesting colloidal instability.

The most interesting effect, in terms of transfection, occurs when CaOx particles are synthesized in a solution with an excess of Ca^{2+} ions supplied through $CaCl_2$ salt. Comparing both assays, with and without Ca^{2+} excess, we note that transfection of the co-precipitated vector was increased by a factor of three magnitude orders, a similar effect to the observed in the hydroxyolites transfection assay. Such a relevant increment emphasizes the relevance of additional Ca^{2+} and Cl^- concentration present in the mother solution. Thus, we confirm the important role of a Ca^{2+} excess and CaOx particles as potential facilitators of transfection in a living tissue. On the other hand, Mg^{2+} is expected to hinder the adsorption of DNA on the surface of the particle. Bertran et al.[51] studied the connections between the Mg^{2+} ions and DNA and confirmed that $Mg^{2+}\cdots$phosphate interactions in the inorganic solution are independent of the magnesium concentration. Molecular Dynamics simulations showed that, although DNA can be adsorbed onto the most stable facets of CaOx cannot template a crystal as it does in HAp [24]. In terms of transfection, Mg^{2+} effect on the CaOx vector is not observed as the transfection ratio is similar with and without. As DNA cannot be adsorbed on CaOx in presence of Mg^{2+}, we expect that the transfection observed in this assay would correspond to naked DNA with Mg^{2+} that leads to a similar level of transfection [41].

4.3. Amorphous Calcium Phosphate

The interest of studying the behaviour of ACP as transfection vector is that ACP is the first calcium phosphate phase to precipitate and can be one of the precursors of HAp calcification as usually observed in breast cancer biopsies [52,53]. We selected ACP for this transfection study because the likelihood to be naturally synthesized at physiological conditions is higher than other potential precursors such as brushite ($CaHPO_4 \cdot 2H_2O$) that have been studied in further analysis. It has been pointed out that its capacity of transfection depends on the exposed surface to the nucleic acid. Gene delivery efficacy of nanocomposite spheres

of DNA-ACP demonstrated to be better gene delivers than filmy DNA–ACP nanocomposite layer by four orders of magnitude [54]. Our results confirm that submicrometric spherical (Figure S4) vectors using ACP-*c*DNA and ACP-*a*DNA are able to transfect A549 cells scoring as the highest. Although its ratio is lower than the positive control is much higher compared to HAp-DNA and CaOx-DNA. Their average size fulfils the requirement for being a feasible transfection vector (353 nm and 232 nm in adsorbed and encapsulated, respectively) and their Z-potential indicate that they also will aggregate forming bigger particles (ACP-*c*DNA = –2,91 mV; ACP-*a*DNA = –1.2 mV). The confirmation of their ability of being transfection vectors gains in importance as our results indicate the transfection process in an ACP calcification is more likely to occur during the first minutes after the initiation of the formation of the calcification. On the other hand, we observe a differential effect regarding the influence of adding Ca^{2+} compared to the previous analysed vectors, as additional Ca^{2+} has a negative effect on their transfection efficiency. This fact is probably due to the observed increase in particle size (641 nm in ACP-*a*DNA(Ca^{2+}) and 487 nm in ACP-*c*DNA(Ca^{2+})) and a saturation of Ca^{2+} cell channels that might reduce the internalization of the particles containing DNA. On the other hand, no differences were observed when Mg^{2+} was included in the particle, suggesting that Mg^{2+} is not involved in the internalization process.

4.4. Migration of transfection vectors

This work intends to look for complementary mechanisms that could explain how tumor DNA can be distributed to the surrounding tissues. Interestingly, the possibility that tumors can spread through non-cellular mechanisms (i.e. exosomes, nucleosomes, naked cell-free DNA) has been recently reported opening new avenues for cancer researchers [55,56]. Recently, Rizwan et al.[57] stated that the relationship between the microcalcification status of breast cancer cells and their metastatic capabilities remains largely unexplored.

In this section, we study the migration of transfection vectors, as a hypothetical mechanism of tumor DNA dissemination. We note that, to the best of our knowledge, the transfection of non-viral vectors after long distance migration has not been reported in the literature. Therefore, the study of natural vectors migration and subsequent transfection of cells situated to a certain distance merits further research to contribute to the understanding of a wide range of diseases related to calcifications. We are particularly interested in gathering information about the migration ability of such vectors in the context of breast cancer multifocality that refers to the appearance of various tumors in a specific area of tissue, a breast quadrant [58]. This is the reason why we restricted the migration interval up to 50 mm. However, we consider that the migration of such vectors could be feasible beyond such limit but it is out of the scope of this work.

Submicrometric and nanometric particles are expected to be able to migrate through living tissue if their size is small enough and/or they are driven by internal gradients (i.e. through vascular or lymphatic system). DNA adsorbed or encapsulated should remain protected and functional during migration until it reaches to the target cell, meaning that DNA is not separated from the carrier and/or degraded (i.e. nuclease enzymes) to the extreme that the transfection vector is disabled. We note that the migration through the extracellular matrix (ECM) is difficult due to its mesh-like organization [59]. The matrix barrier would block the migration of particles with diameters larger than the size of network space, while smaller particles are expected to cross it. Collagen fibrils are able to block particles larger than 20–40 nm. Inter fibrillary space would allow migration of particles up to 75–130 nm. Furthermore, it is important to note that nanoparticle interactions with ECM components are dependent on their respective intrinsic properties (i.e. trafficking and uptake of nanoparticles are affected by their own charge and electric interactions with the ECM components).

After inspection of the results reported in Figure 4, we demonstrate that such transfection vectors are able to migrate and transfect up to 50 mm distance propelled in experimental conditions. Such a result indicates that transfection can occur at relatively long distance from the place where the vector was synthesized. Second, we observe that the positive control presents an inverse relationship between the rate of transfection efficiency and migration distance, following the rule "the longest the distance, the less the transfection rate". We interpret such a result as a consequence of the aggregation process that reduces the amount of particles below 500 nm when particles reach to the cells.

Same pattern is observed when ACP vectors are forced to the migration setup, indicating that the presence of HEPES does not influence such behaviour. Contrariwise, we observe a totally different profile concerning the HAp and CaOx vectors. In both cases, the transfection ratio remains in L (HAp-*a*DNA and CaOx-*a*DNA) and V.L. (HAp-*c*DNA) but the score is not affected by the distance as the ACP are. We interpret such result as consequence that the ratio of particles < 500 nm does not change reaching to cells with a similar proportion. The transfection at long distance empirically confirms the protective role of HAp on DNA, maintaining attached the nucleic acid to the particle and confirms that nucleic acid functionality is preserved as well. Merit further research to expose the particles to a trip containing degrading enzymes to test their influence on the transfection rate.

5. Conclusions and outcomes

Transfection vectors are of high interest due to their capacity to modify the genome of target cells. Moreover, the confirmation that nature is able to create such vectors inside living organisms opens a new field of research, in particular related to cancer disease where tumor DNA can be spread by such natural vectors. We have confirmed that ACP, HAp and CaOx are able to introduce DNA inside target cells when it is adsorbed or co-precipitated on them. ACP,

the first that is synthesized in a physiological environment is the one who has the highest transfection ratio. On the other hand, we have confirmed that an additional burst Ca^{2+} plays a significant role enhancing the transfection of naked DNA, HAp and CaOx vectors. Conversely, Mg^{2+} does not have a significant role enhancing their transfection. Finally, we have demonstrated that such vectors can migrate up to 50 mm before transfecting the target cells.

This work explores the basics of a potential spreading mechanism based on the adsorption or encapsulation of nucleic acids coming from tumor cells on natural vectors of transfection. We consider that in most cases, the nucleic acid, DNA or RNA, which can be carried by the calcifications would be released from healthy cells and will cause no harm to a new cell in case there is a transfection. However, when DNA or RNA from tumor cells becomes part of a natural HAp, ACP o CaOx calcification, the newly formed particle carries tumor specific genetic alterations. Although the effects of such hypothetical transfection process are uncertain and merit further research, it could be related to the theory of genometastasis [60,61], which claims that the circulating tumor DNA (ctDNA) might have the role of an intercellular messenger. Thus, considered such ctDNA as a natural vector in combination with Ca^{2+} could be either integrate into the genome after transfection of a healthy cell leading to genetic instability or cell transformation at distant locations.

An interesting perspective about the role of breast cancer calcifications is that hydroxyolites containing tumor DNA which might be resilient in physiological environments by keeping DNA intact for a long time and thus protecting it from degradation as occurs with ctDNA. This fact might enable tumor DNA to migrate, travelling through tissue ducts, being disseminated locally (i.e. intramammary glands) or through a long distance (i.e. blood or lymphatic vessels), until it reaches to a distant tissue while maintaining its functionality and therefore, being feasible the cell transfection, fact that could lead to cell transformation. As a result of this hypothesis, the presence of tumor DNA on such calcifications in tumor tissue

merits further research as it could be correlated with the progression and aggressiveness of the cancer disease.

Author Contributions

Anna M. Rodríguez-Rivero: methodology, validation, formal analysis and review. Cristina Rodríguez-Miguel: methodology, validation, formal analysis and review. Jordi Sans: methodology, validation, formal analysis, review, Figure 1 and graphical abstract design. Carlos Alemán: conceptualization, review, editing and supervision. Joan Francesc Julián: conceptualization, review, editing and supervision. Pau Turon: conceptualization, writing, project administration and supervision.

Conflicts of interest

There are no conflicts to declare.

Acknowledgements

Authors acknowledge financial support from B. Braun Melsungen AG, B. Braun Surgical, S.A.U, MINECO/FEDER (RTI2018-098951-B-I00), the Agència de Gestió d'Ajuts Universitaris i de Recerca (2017SGR359). Support for the research of C.A is grateful to ICREA Academia program for excellence in research. Authors thank Dr. Meinrad Lugan, Dr. Hans-Otto Maier and Dr. Sonja Rauschschwalbe for supporting the OLi project. This work is integrated within a wider research project supported by B. Braun Surgical S.A.U, UPC, ICS and ICFO.

References

1. S. O'Grady and M. P. Morgan, *BBA-Reviews on Cancer*. **1869 (**2018)2, 310-320.

2. S. Gosling, R. Scott, C. Greenwood, P. Bouzy, J. Nallala, I.D. Lyburn, N. Stone and K. Rogers, *J. Mammary Gland Biol. Neoplasia.* **24** (2019) 333–342.

3. P. Turon, J. Puiggalí, O. Bertrán and C. Alemán, *Chemistry - A European Journal*. **21** (2015) 18892 – 18898.

4. J.A.M.R Kunitake, S. Choi, K.X. Nguyen, M.M. Lee, F. He, D. Sudilovsky, P.G. Morris, M.S. Jochelson, C.A. Hudis, D.A. Muller, P. Fratzl, C. Fischbach, A. Masicj and L.A. Estroff, *J. Struct. Biol.* **202** (2018) 25–34.

5. L. Liang, C. Zheng, H. Zang, S. Xu, Z. Zhang, C. Hu, L. Bi, Z. Fan, B. Han and W. Xu, *Spectrochim. Acta A Mol. Biomol. Spectrosc.* **132** (2014) 397–402.

6. G.J. Rockley, *Br. Med. J.* **2** (1965) 633–636.

7. H. Fujita, M. Yamamoto, T. Ogino, H. Kobuchi, N. Ohmoto, E. Aoyama, T. Oka, T. Nakanishi, K. Inoue and J. Sasaki, *Cell Biochem. Funct*. **32** (2014) 77–86.

8. J.M. Chenga, S.H. Tirumania, K.W. Kima, S.S. Saboo, J.C. Baez and A.B. Shinagare, *Cancer Imaging*. **13** (2013) 4, 527539.

9. K.L. Eales, K.E.R. Hollinshead and D.A. Tennant, *Oncogenesis*. **5** (2016) e190, 1-8.

10. O. Bertran, L. J. del Valle, G. Revilla-López, G. Chaves, L. Cardús, M. T. Casas, J. Casanovas, P. Turon, J. Puiggalí and C. Alemán, *Dalton Trans.* 43 (2014) 1, 317-327.

11. V. Sokolova and M. Epple, *Angew. Chem., Int. Ed.*, 47 (2008) 8, 1382-1395.

12. L. J. del Valle, O. Bertran, G. Chaves, G. Revilla-López, M. Rivas, M. T. Casas, J. Casanovas, P. Turon, J. Puiggalí and C. Alemán, *J. Mater. Chem. B*. **2 (2014)** 6953-6966.

13. F.L. Graham and A.J. van der Eb, *Virology*. **52 (1973)** 456–467.

14. V. Sokolova, O. Prymak, W. Meyer-Zaika, H. Colfen, H. Rehage, A. Shukla and M. Epple, *Materwiss. Werkstofftech*. 37 (2006) 441–445.

15. L. Kaestner, A. Scholz and P. Lipp, *Bioorg. Med. Chem. Lett.* 25 (2015) 1171–1176.

16. V. Sokolova, I. Radtke, R. Heumann and M. Epple, *Biomaterials.* 27 (2006) 16, 3147- 3153.

17. Y. Xie, Y. Chen, M. Sun and O. Ping, *Curr. Pharm. Biotechnol.* 14 (2013) 918-925.

18. D. Ibraheem, A. Elaissari and H. Fessi, *Int. J. Pharm.* 459 (2014) 70– 83.

19. T. Liu, A. Tang, G. Zhang, Y. Chen, J. Zhang, S. Peng and A. Cai, *Cancer Biother. Radiopharm.* 20 (2005) 2, 141-149.

20. D. Lee, K. Upadhye and P.N. Kumta, *Mater. Sci. Eng. B.* 177 (2012) 3, 289–302.

21. D. Olton, J. Li, M.E. Wilson, T. Rogers, J. Close, L. Huang, P.N. Kumta and C. Sfeir, *Biomaterials*. 28 (2007) 6, 1267-79.

22. P.N. Kumta, C. Sfeir, D.H. Lee, D. Olton and D. Choi, *Acta Biomater.*1 (2005) 65–83.

23. A.M. Castellaro, A. Tonda, H.H. Cejas, H. Ferreyra, B.L. Caputto, O.A. Pucci and G.A. Gil, *BMC Cancer*. 15 (2015) 1, 1-13.

24. G. Revilla-López, A.M. Rodríguez-Rivero, L.J. del Valle, J. Puiggalí, P. Turon, C. Alemán, *Langmuir.* 35 (2019) 11912−11922.

25. S. Bisht, G. Bhakta, S. Mitra and A. Maitra, *Int. J. Pharm.* 288 (2005) 1, 157-168.

26. E. Blanco, H. Shen and M. Ferrari, *Nat. Biotechnol.* 33 (2015) 9, 941.

27. W. Song and D.K. Lahiri, *Nucleic Acids Res.* 23 (1995) 17, 3609-3611.

28. J.L. Santos, D. Pandita, J. Rodrigues, A.P. Pêgo, P.L. Granja and H. Tomás, *Curr. Gene Ther,* 11 (2011) 1, 46-57.

29. F. Grosjean, P. Batard, M. Jordan, F.M. Wurm, *Cytotechnology* 38 (2002) 1-3, 57-62.

30. M. Epple, K. Ganesan, R. Heumann, J. Klesing, A. Kovtun, S. Neumann and V. Sokolova, *J. Mater. Chem*. 20 (2010) 18–23.

31. A. Gigante, M. Li, S. Junghänel, C. Hirschhäuser, S. Knauer and C. Schmuck, *MedChemComm*. 10 (2019) 1692-1718.

32. X. Cao, W. Deng, Y. Wie, W. Su, Y. Yang, Y. Wie, J. Yu and X. Xu, *Int. J. Nanomedicine*. 6 (2011) 3335–3349.

33. M.A. Khan, V.M. Wu, S. Ghosh and V. Uskoković, *J. Colloid Interface Sci*. 471 (2016) 48–58.

34. S. Choi, X. Yu, L. Jongpaiboonkit, S.J. Hollister and W.L. Murphy, *Sci. Rep.*, 3 (2013) **3**, 1567.

35. T.M. Acri, N.Z. Laird, S. M. Geary, A. K. Salem and K. Shin, *J Tissue Eng Regen Med*. 13 (2019) 2256-2265.

36. V.I. Kulkarni, V. S. Shenoy, S.S. Dodiya, T.H. Rajyaguru and R.R. Murthy, *Expert Opin Drug Deliv*. 3 (2006) 2, 235-245.

37. C.Y. Chen, S.C. Lu and T.H. Liao, *Protein Sci.* 11 (2002) 659–668.

38. C.Q. Pan and R.A. Lazarus, *Protein Sci.* 8 (1999) 1780–1788.

39. L. Chen, J.M. Mccrate, J. C-M Lee and H. Li, *Nanotechnology*. 22 (2011) 10, 105708.

40. V. Forest and J. Pourchez, *Mater. Sci. Eng. C*. 70 (2017) 889–896.

41. J.M. Riley, H. Kim, T.D. Averch and H.J. Kim, *J. Endourol.* 27 (2013) 12.

42. L. Truong-Le, S.M. Walsh, E. Schweibert, H.Q. Mao, W.B. Guggino, J.T. August and K.W. Leong, *Arch Biochem Biophys*. 361 (1999) 47-56.

43. A. Haberland, T. Knaus, S.V. Zaitsev, R. Stahn, A.R. Mistry, C. Coutelle, H. Haller and M. Bonttger, *Biochim Biophys Acta*. 1445 (1999) 21-30.

44. R. Scott, C. Kendall, N. Stone, and K. Rogers, *Sci. Rep.* 7 (2017) 136.

45. M. Scimeca, E. Giannini, C. Antonacci, C. A. Pistolese, L. G. Spagnoli and E. Bonanno, *BMC cancer*. 14 (2014) 286.

46. N. Singh, J. Theaker, *J Clin Pathol.* 52 (1999) 145–6.

47. J.E. Gonzalez, R.G. Caldwell and J. Valaitis, *Am J Surg Pathol*. 15 (1991) 586-91.

48. J. S. Winston, I. T. Yeh, K. Evers and A. K. Friedman, *Am. J. Clin. Pathol*. 100 (1993) 488 492.

49. R. Baker, P. Matousek, K.L. Ronayne, A.W. Parker, K. Rogers and N. Stone, *Analyst.* 132 (2007) 1, 48-53.

50. R.F. Cox, A. Hernandez-Santana, S. Ramdass, G. McMahon, J.H. Harmey and M.P. Morgan, *Br J Cancer*. 106 (2012) 525–37.

51. O. Bertran, L. J. Valle, G. Revilla- López, M. Rivas, G. Chaves, M. T. Casas, J. Puiggalí, P. Turon and C. Aleman, *Chem. Eur. J.* 21 (2015) 2537-2546.

52. Y.H. Tseng, C.Y. Mou and J.C.C. Chan, *J. Am. Chem. Soc*. 128 (2006) 6909.

53. S.V. Dorozhkin, M. Epple, Angew. Chem. – Int. Ed. 41 (2002) 3130.

54. A. Oyane, H. Araki, M. Nakamura, Y. Shimizu, Q.T.H. Shubhra, A. Ito and H. Tsurushima, *Colloids Surf. B*. 141 (2016) 519–527.

55. B. K. Thakur, H. Zhang, A. Becker, I. Matei, Y. Huang, B. Costa-Silva, Y. Zheng, A. Hoshino, H. Brazier, J. Xiang, C. Williams, R. Rodriguez-Barrueco, J.M. Silva, W. Zhang, S. Hearn, O. Elemento, N. Paknejad, K. Manova-Todorova, K. Welte, J. Bromberg, H. Peinado and D. Lyden, *Cell Res.* 24 (2014) 766-769.

56. A. Kustanovich, R. Schwartz, T. Peretz and A. Grinshpun, *Cancer Biol Ther*. 20 (2019) 1057-1067.

57. A. Rizwan, S. K. Paidi, C. Zheng, M. Cheng, I. Barman and K. Glunde, *Sci. Rep.* 8 (2018) 1-10.

58. S.P. Lyncj, X. Lei, L. Hsu, F. Meric-Bernstam, T.A. Buchholz, H. Zhang, G.N. Hortobágy, A.M. González-Angulo and V. Valero, *The Oncologist*. 18 (2013) 1167–1173.

59. A.B. Engin, D. Nikitovic, M. Neagu, P. Henrich-Noack, A. Oana Docea, M.I. Shtilman, K. Golokhvast and A.M. Tsatsakis, *Part. Fibre Toxicol.* 14 (2017) 22.

60. D.C. García-Olmo, R. Ruiz-Piqueras and D. García-Olmo, *Histol Histopathol*. 19 (2004) 575–83.

61. Z . Chen, A. Fadiel, F. Naftolin, K.D. Eichenbaum and Y. Xia, *Med Hypotheses*. 65 (2005) 956–61.

Table 1. Data set of Transfection ratio (0-10), Average size (nm), ratio of particles below 500 nm vs particles above 500 nm (Γ_{500}), Z-potential (mV) and DNA (ng) contained in 50 µL of transfection vector solution.

Transfection vectors	Transfection ratio	Average size (S) (nm)	Γ_{500} (%)	Z-potential (Z) (mV)	Θ_{DNA} (ng)
HAp-*a*DNA	L (4)	504	3.2	–0.48	22.1
HAp-*c*DNA	VL (2)	7830	0.6	–2.93	60.1
HAp-*a*DNA(Ca^{2+})	H (8)	296	4.8	–1.52	39.6
HAp-*c*DNA(Ca^{2+})	M (6)	456	6.8	–1.79	43.9
HAp(Mg^{2+})-*a*DNA	L (4)	365	0.5	–16.7	19.1
HAp(Mg^{2+})-*c*DNA	V.L. (2)	4325	6.9	–2.6	29.6
ACP-*a*DNA	V.H. (10)	1526	7.2	–1.2	36.6
ACP-*c*DNA	V.H. (10)	1357	9.3	–2.91	36.1
ACP-*a*DNA(Ca^{2+})	M (6)	641	10.2	–7.9	38.6
ACP-*c*DNA(Ca^{2+})	M (6)	487	8	1	37.9
ACP(Mg^{2+})-*a*DNA	H (8)	284	28.9	–11.89	34.5
ACP(Mg^{2+})-*c*DNA	H (8)	301	10.4	–14.98	35.8
CaOx-*a*DNA	L (4)	863	1.7	–0.99	19.3
CaOx-*c*DNA	V.L. (2)	1100	0.8	–1.36	7.5
CaOx-*a*DNA(Ca^{2+})	M (6)	773	9.4	–11.99	47.9
CaOx-*c*DNA(Ca^{2+})	H (8)	178	22.3	–6.63	46.6
CaOx(Mg^{2+})-*a*DNA	L (4)	517	0.4	–20.38	35.9
CaOx(Mg^{2+})-*c*DNA	V.L. (2)	3400	0	–4.3	19.0

Table 2. Principal Components Analysis.

Table 2a. Eigenanalysis of the Correlation Matrix

Eigenvalue	2.1160	1.3095	0.9483	0.4449	0.1813
Proportion	0.423	0.262	0.190	0.089	0.036
Cumulative	0.423	0.685	0.875	0.964	1.000

Table 2b. Eigenvectors

Variable	PC1	PC2	PC3
Transfection rate	0.606	0.071	0.277
Average size (S)	-0.428	0.615	-0.166
Γ_{500}	0.567	0.138	0.055
Z-potential (Z)	-0.220	0.278	0.912
Θ_{DNA}	0.282	0.722	-0.247

CAPTION TO FIGURES

Figure 1. Figurative representation of HAp, CaOx and ACP transfection vectors. A) DNA adsorbed on HAp (001) facet (HAp-*a*DNA); B) DNA adsorbed on CaOx (100) facet (CaOx-*a*DNA); C) DNA adsorbed on amorphous calcium phosphate clusters (ACP-*a*DNA); D) DNA co-precipitated with stoiquiometric Ca^{2+} and PO_4^{3-} to form HAp-*c*DNA; E) DNA co-precipitated with Ca^{2+} and oxalate ($C_2O_4^{2-}$) to form CaOx-*c*DNA; DNA co-precipitated with Ca^{2+} and PO_4^{3-} to form ACP-*c*DNA.

Figure 2. Percentage of particles below 500 nm (Γ_{500}). First value of series (t=0) denotes the Γ_{500} value at the time of the transfection vector synthesis. All other values correspond to 30 minutes after vector synthesis.

Figure 3. Z-potential dynamics of transfection vectors through time (0-32 minutes): a) HAp-*a*DNA (red) and HAp-*c*DNA (blue); b) ACP-*a*DNA (red) and ACP-*c*DNA (blue); c) CaOx-*a*DNA (red) and CaOx-*c*DNA (blue).

Figure 4. Transfection efficiency ratio of naked DNA, HAp, ACP and CaOx vectors at 24 and 48 hours. Symbols in legend denote the vector prepared by DNA co-precipitation (*c*) and DNA adsorption (*a*).

Figure 5. Principal Component Analysis. PCA loading plot representing the contribution of the variables to the first two components (PC1 and PC2).

Figure 6. Transfection efficiency ratio of naked DNA, HAp, ACP, CaOx vectors at 24 and 48 hours vs migration distance. Symbols in legend denote the vector prepared by DNA co-precipitation (*c*) and DNA adsorption (*a*).

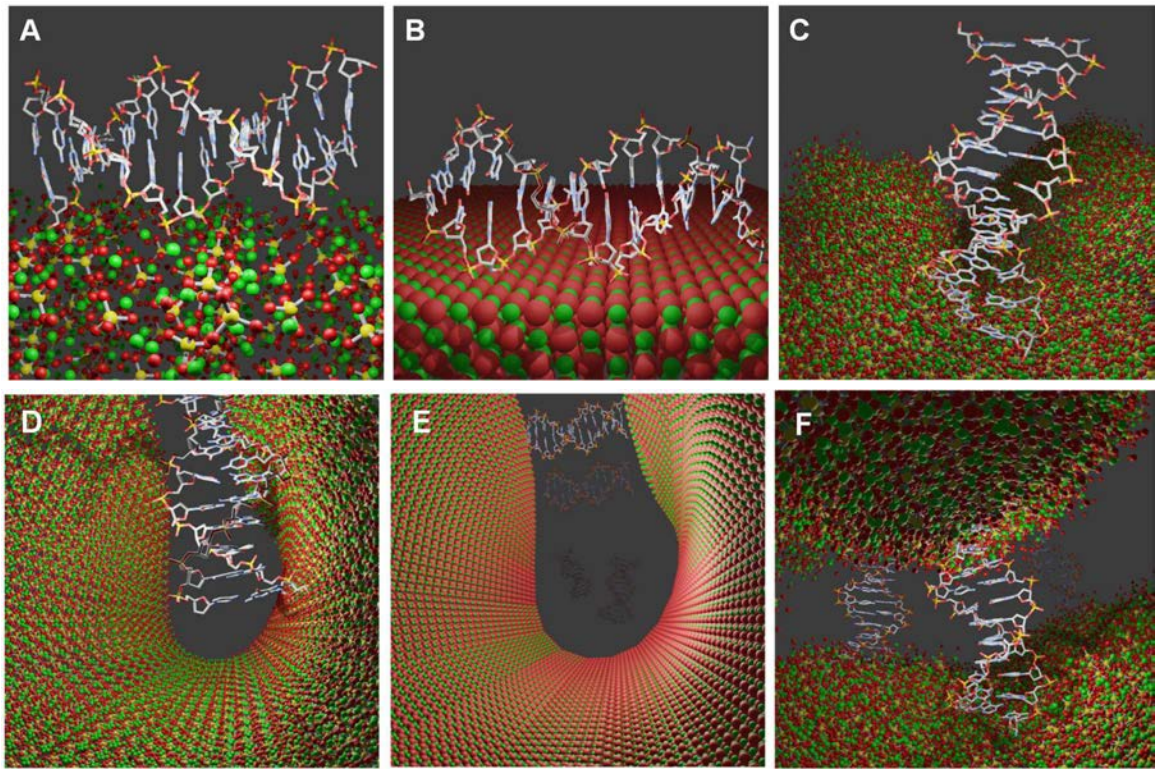

Figure 1

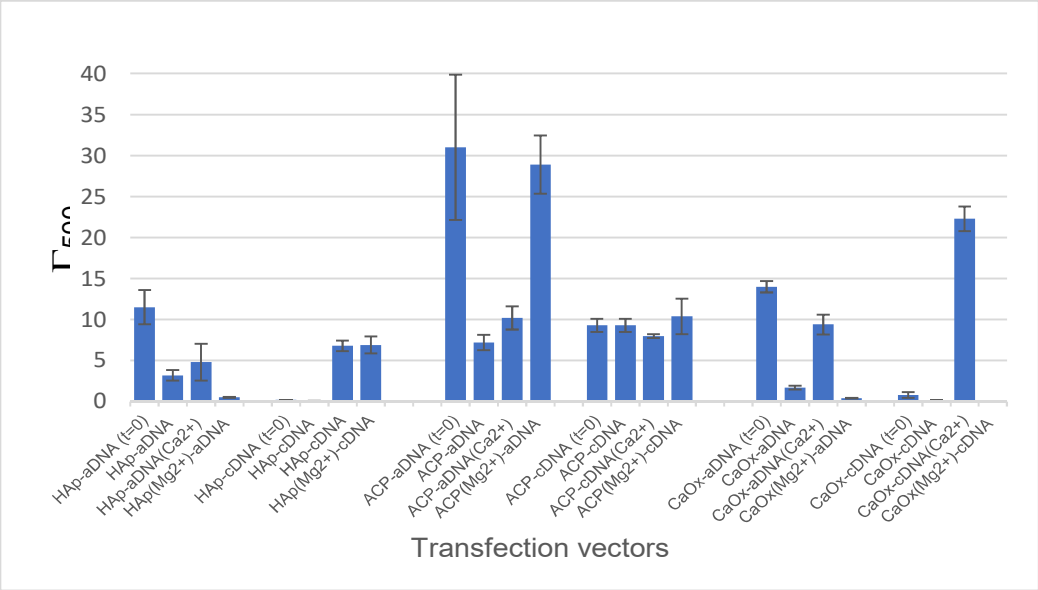
40
35
30
25
20
15
10
5
0
HAp-aDNA (t=0)
HAp-aDNA
HAp-aDNA(Ca2+)
HAp(Mg2+)-aDNA
HAp-cDNA (t=0)
HAp-cDNA
HAp-cDNA
HAp(Mg2+)-cDNA
ACP-aDNA (t=0)
ACP-aDNA
ACP-aDNA(Ca2+)
ACP(Mg2+)-aDNA
ACP-cDNA (t=0)
ACP-cDNA
ACP-cDNA(Ca2+)
ACP(Mg2+)-cDNA
CaOx-aDNA (t=0)
CaOx-aDNA
CaOx-aDNA(Ca2+)
CaOx(Mg2+)-aDNA
CaOx-cDNA (t=0)
CaOx-cDNA
CaOx-cDNA(Ca2+)
CaOx(Mg2+)-cDNA
Transfection vectors

Figure 2

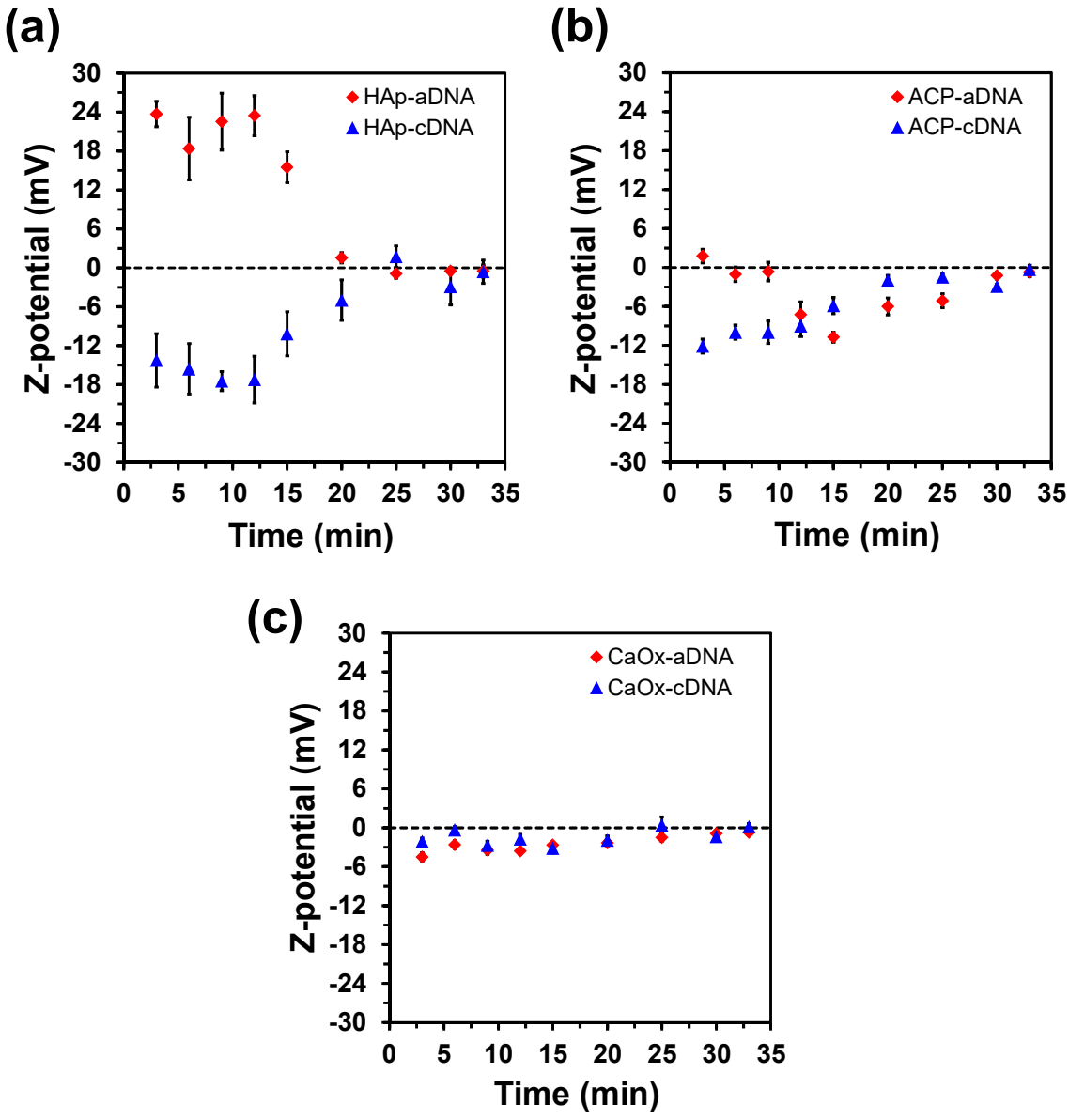
(a)
HAp-aDNA
HAp-cDNA
Z-potential (mV)
Time (min)
(b)
ACP-aDNA
ACP-cDNA
Z-potential (mV)
Time (min)
(c)
CaOx-aDNA
CaOx-cDNA
Z-potential (mV)
Time (min)

Figure 3

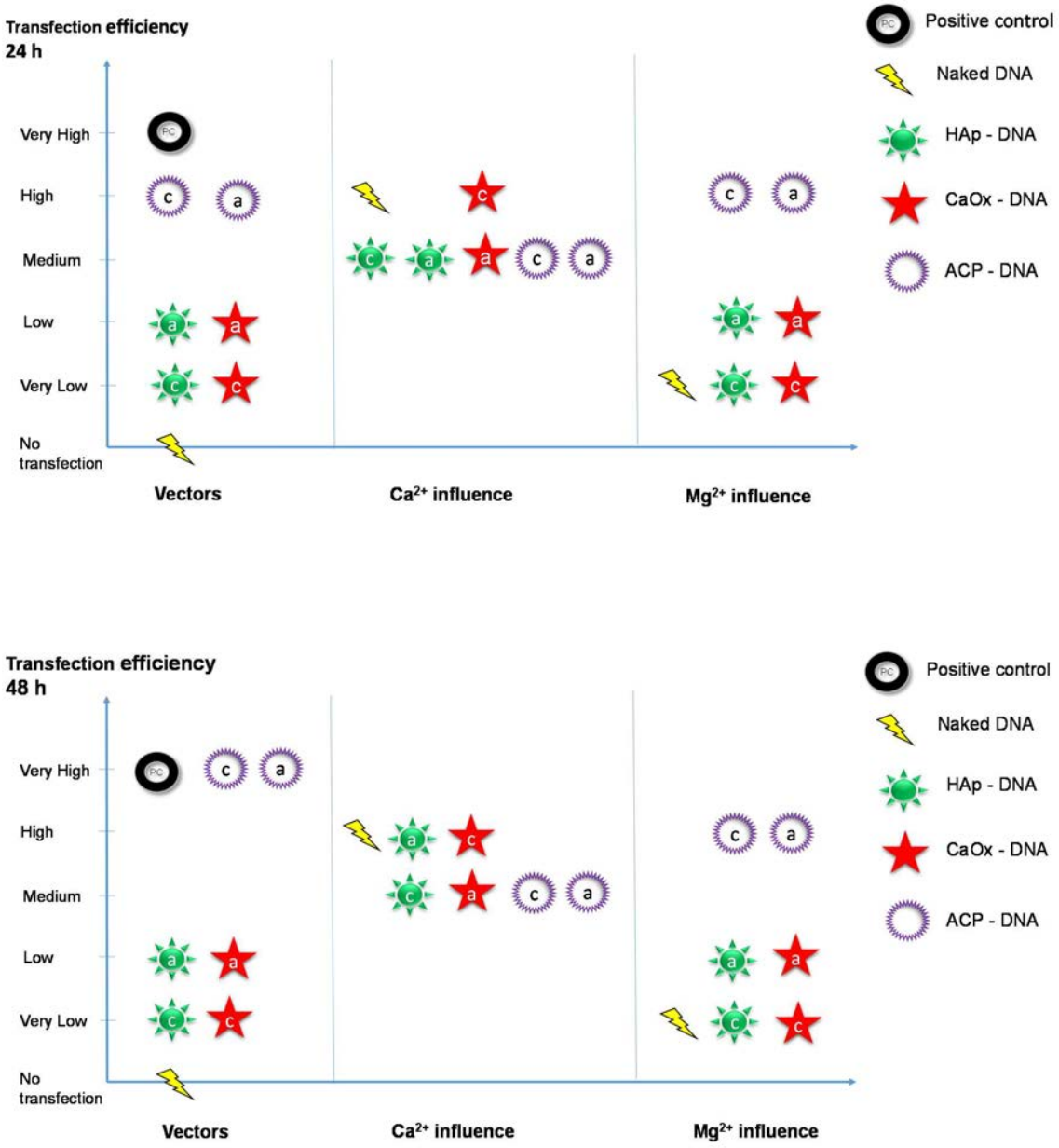
Transfection efficiency
24 h
Very High
High
Medium
Low
Very Low
No transfection
Vectors
Ca2+ influence
Mg2+ influence
Positive control
Naked DNA
HAp - DNA
CaOx - DNA
ACP - DNA
Transfection efficiency
48 h
Very High
High
Medium
Low
Very Low
No transfection
Vectors
Ca2+ influence
Mg2+ influence
Positive control
Naked DNA
HAp - DNA
CaOx - DNA
ACP - DNA

Figure 4

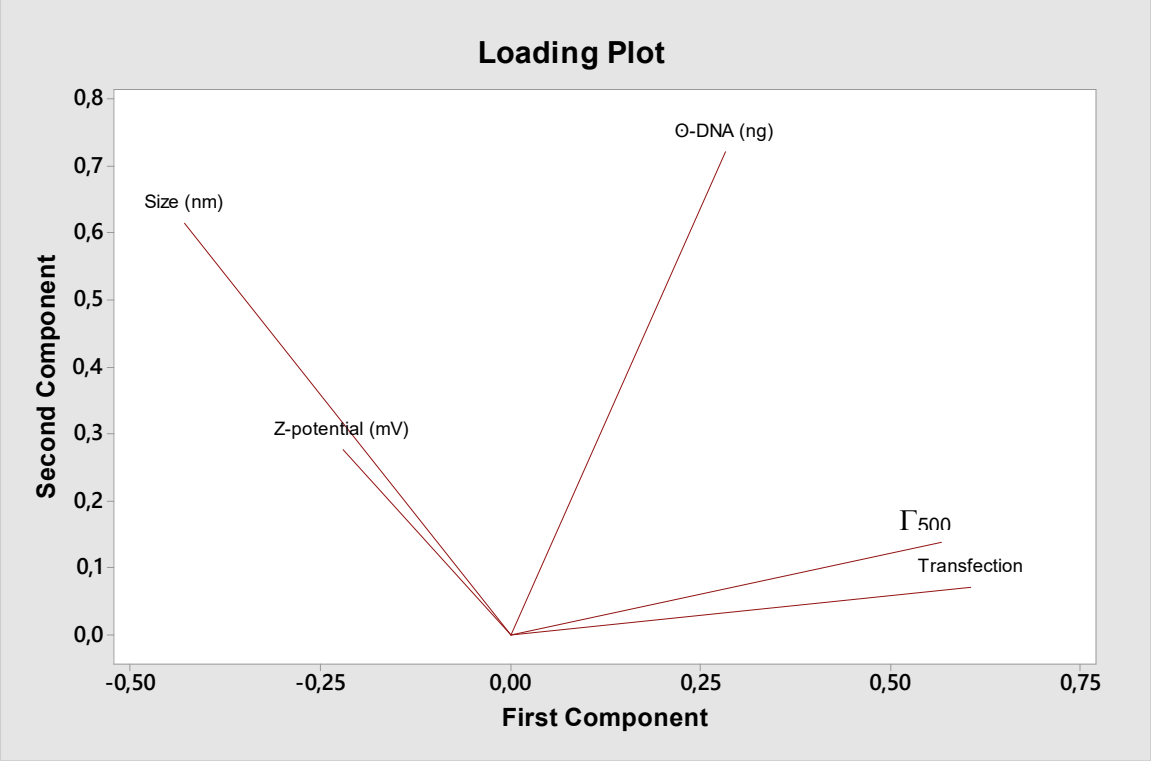
Loading Plot
Second Component
First Component
0,8
0,7
0,6
0,5
0,4
0,3
0,2
0,1
0,0
-0,50
-0,25
0,00
0,25
0,50
0,75
Size (nm)
Θ-DNA (ng)
Z-potential (mV)
Γ500
Transfection

Figure 5

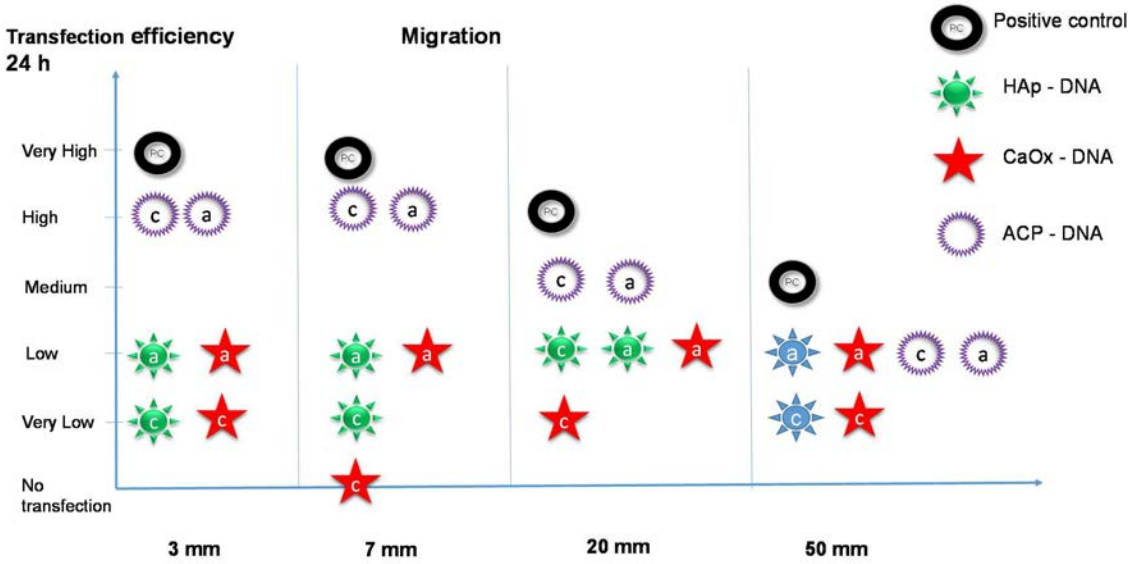
Transfection efficiency
24 h
Migration
Positive control
HAp - DNA
CaOx - DNA
ACP - DNA
Very High
High
Medium
Low
Very Low
No transfection
3 mm
7 mm
20 mm
50 mm

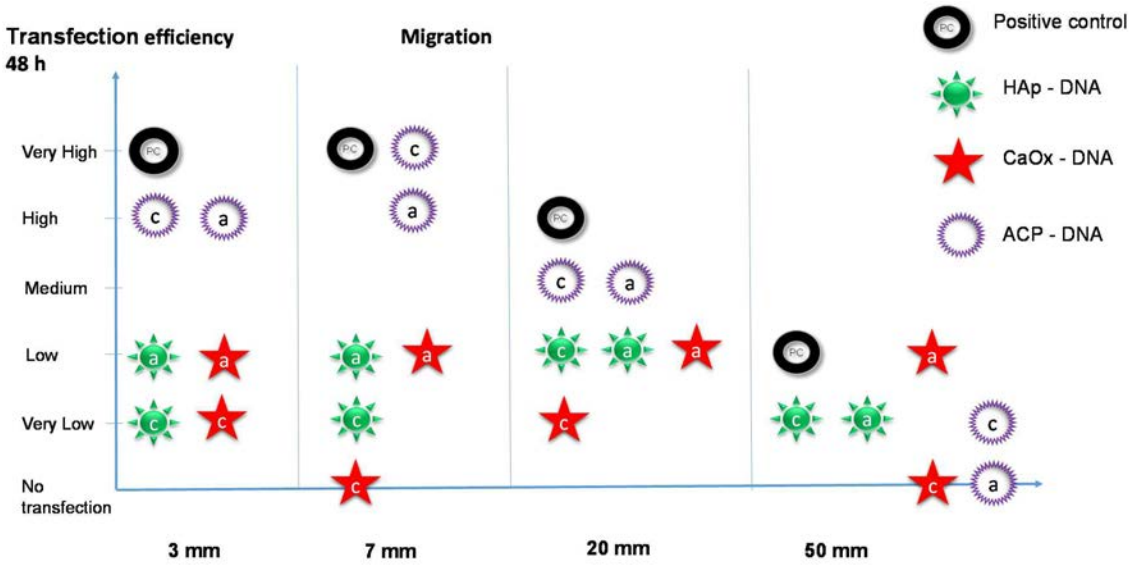
Transfection efficiency
48 h
Migration
Positive control
HAp - DNA
CaOx - DNA
ACP - DNA
Very High
High
Medium
Low
Very Low
No transfection
3 mm
7 mm
20 mm
50 mm

Figure 6

Supplementary Information

Cell transfection mediated by breast cancer nanocalcifications of hydroxyapatite and calcium oxalate

Anna M. Rodríguez-Rivero,[1,2] Cristina Rodríguez-Miguel,[1] Jordi Sans,[3,4] Carlos Alemán*,[3,4,5,] Joan Francesc Julián*,[2,6] Pau Turon*,[1]

*Corresponding authors

Corresponding authors:

carlos.aleman@upc.edu, 21127jji@gmail.com, pau.turon@bbraun.com,

1. Research and Development. B. Braun Surgical, S.A.U. Ctra. de Terrassa, 121. Rubí. Barcelona. Spain.

2. Universitat Autònoma de Barcelona. Campus de la UAB, Plaça Cívica, 08193 Bellaterra, Barcelona. Spain.

3. Departament d'Enginyeria Química, EEBE, Universitat Politècnica de Catalunya, C/ Eduard Maristany, 10-14, Ed. I2, 08019, Barcelona, Spain

4. Barcelona Research Center in Multiscale Science and Engineering, Universitat Politècnica de Catalunya, C/ Eduard Maristany, 10-14, 08019, Barcelona, Spain

5. Institute for Bioengineering of Catalonia (IBEC), The Barcelona Institute of Science and Technology, Baldiri Reixac 10-12, 08028 Barcelona Spain

6. IGTP. Research Institute. Hospital Universitari Germans Trias i Pujol. Camí de les Escoles, s/n, 08916 Badalona, Barcelona. Spain.

Materials and Methods

SI.1 Preparation of transfection vectors

a) Hydroxyapatite

• HAp-*c*DNA. DNA co-precipitated with HAp. Hydroxyapatite nanoparticles containing DNA encapsulated (HAp-*c*DNA) were synthesized by co-precipitation *in situ* from a solution of 500 mM calcium nitrate tetrahydrate ($Ca(NO_3)_2 \cdot 4\ H_2O$); Sigma Aldrich, Ref. C4955) and 500 mM diammonium hydrogen phosphate ($(NH_4)_2HPO_4$; Sigma Aldrich, Ref. 09839), adjusting volumes to achieve a molar relation Ca/P = 1.67. 0.5 µg of plasmid DNA (NanoLuc™, a pNL vector using a pGL4-based backbone; Promega, Ref. N1091; see Figure S1) was added during the hydroxyapatite nanoparticles *in situ* preparation, and the HAp-DNA system was then diluted with Opti-MEM® media (ThermoFisher, Ref. 11058021).

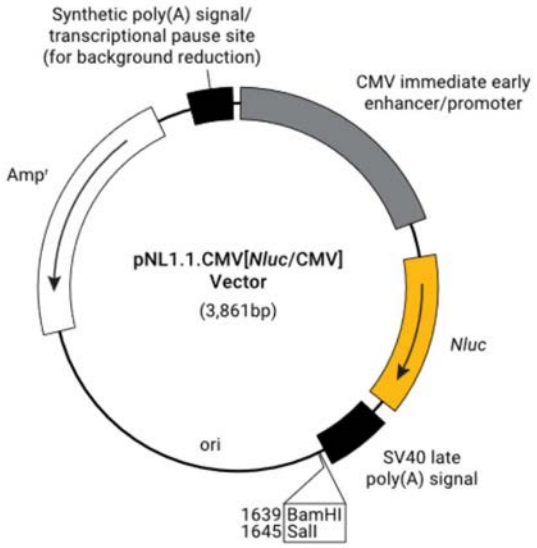

Figure S1. pNL1.1.CMV[*Nluc*/CMV] Vector map and sequence reference points.[1]

• HAp-*a*DNA. DNA adsorbed on HAp. To obtain HAp particles with adsorbed DNA, 0.5 µg of plasmid DNA (NanoLuc™, a pNL vector using a pGL4-based backbone; Promega,

Ref. N1091) was added to 1 M hydroxyapatite particles suspension and diluted with Opti-MEM® media (ThermoFisher, Ref. 11058021). 1 M hydroxyapatite (Sigma Aldrich, Ref.289396) solution was prepared using water for molecular biology (Merck Millipore, Ref.H20MB0506).

• HAp-*c*DNA(Ca^{2+}) and HAp-*a*DNA(Ca^{2+}). Exogenous Ca^{2+} was supplied to hydroxyolitevectors once the particles were already formed through the addition of $CaCl_2$ to reach aconcentration of 0.0524M $CaCl_2$.

• HAp(Mg^{2+})-*c*DNA. *30 % Mg doped Hydroxyapatite – DNA system*. 0.5 µg of plasmidDNA (NanoLuc™, a pNL vector using a pGL4-based backbone; Promega, Ref. N1091) was added to 0.15 mol of 1 M magnesium dichloride ($MgCl_2$; Sigma Aldrich, Ref.1002071925). 0.35 mol of 0.5 M calcium nitrate tetrahydrate ($Ca(NO_3)_2 \cdot 4\ H_2O$); SigmaAldrich, Ref. C4955) and 0.5 M diammonium hydrogen phosphate ($(NH_4)_2HPO_4$; SigmaAldrich, Ref. 09839), adjusting volumes to achieve a molar relation Ca/P = 1.67, wereadded to the solution and diluted with Opti-MEM® media (ThermoFisher, Ref. 11058021).

• HAp(Mg^{2+})-*a*DNA. *30 % Mg doped Hydroxyapatite – DNA system*. 0.5 µg of plasmidDNA (NanoLuc™, a pNL vector using a pGL4-based backbone; Promega, Ref. N1091was added to 0.15 mol of 1 M Magnesium dichloride ($MgCl_2$; Sigma Aldrich, Ref.1002071925). Then, this mixture was added to 1 M hydroxyapatite particles suspensionand diluted with Opti-MEM® media (ThermoFisher, Ref. 11058021).

b) Amorphous calcium phosphate

• Positive control (PC). *DNA co-precipitated HAp and HEPES.* Amorphous calcium phosphate was synthesized using the "Calcium Phosphate Transfection Kit"(ThermoFisher, Ref. K278001) and according to the manufacturer's instructions.[1,2]

Briefly, 0.5 µg of plasmid DNA (NanoLuc™, a pNL vector using a pGL4-based backbone; Promega, Ref. N1091) was mixed directly with a concentrated solution of 2 M calcium dichloride ($CaCl_2$) and water for molecular biology (Merck Millipore, Ref. H20MB0506). This mixture was then added dropwise to a HEPES Buffered Saline (HBS) solution in a ratio 1:1, and diluted with Opti-MEM® media (ThermoFisher, Ref. 11058021) while bubbling air through the solution over 1-2 minutes. The final solution was incubated at room temperature for 30 minutes prior to use.

- ACP-*c*DNA. DNA co-precipitated with ACP. The procedure was identical to that previously described but replacing the volume of HBS by a solution of 274 mM sodium chloride (NaCl; Scharlab, Ref. SO02250500), 10 mM potassium chloride (KCl; Scharlab, Ref. PO02000500) and 1.4 mM disodium hydrogen phosphate (Na_2HPO_4; Sigma Aldrich, Ref. 795410).
- ACP-*a*DNA. DNA adsorbed on ACP. According to the proportions detailed in the "Calcium Phosphate Transfection Kit" (ThermoFisher, Ref. K278001), a solution of 2M calcium dichloride ($CaCl_2$; Scharlab, Ref. CA01920500) and water for molecular biology (Merck Millipore, Ref. H20MB0506) was mixed with 274 mM sodium chloride (NaCl; Scharlab, Ref. SO02250500), 10 mM potassium chloride (KCl; Scharlab, Ref. PO02000500) and 1.4 mM disodium hydrogen phosphate (Na_2HPO_4; Sigma Aldrich, Ref. 795410) in a ratio 1:1. Then, the mixture was added dropwise to 0.5 µg of plasmid DNA (NanoLuc™, a pNL vector using a pGL4-based backbone; Promega, Ref. N1091) and diluted with Opti-MEM® media (ThermoFisher, Ref. 11058021) while bubbling air through the solution over 1-2 minutes. The final solution was then incubated at room temperature for 30 minutes prior to use.
- PC(Ca^{2+}), ACP-*c*DNA(Ca^{2+}) and ACP-*a*DNA(Ca^{2+}) with additional exogenous source of Ca^{2+}. Ca^{2+} was supplied once the particles were already formed through the final addition of $CaCl_2$ in a concentration of 0.0524M $CaCl_2$.

• PC(Mg^{2+}), ACP(Mg^{2+})-*c*DNA and ACP(Mg^{2+})-*a*DNA. *30 % Mg doped Amorphous calcium phosphate (with or without HEPES) – DNA system.* Particles were synthesized using the "Calcium Phosphate Transfection Kit" (ThermoFisher, Ref. K278001) following the methodology previously detailed for each particle, but adding 0.15 mol of 1 M magnesium dichloride ($MgCl_2$; Sigma Aldrich, Ref. 1002071925) to 0.5 µg of plasmid DNA (NanoLuc™, a pNL vector using a pGL4-based backbone; Promega, Ref. N1091) prior to the addition of the rest of reagents.

c) Calcium oxalate

• CaOx-*c*DNA. DNA co-precipitated with CaOx. Calcium oxalate nanoparticles were synthesized from a solution of 0.04 M sodium oxalate ($Na_2C_2O_4$; Sigma Aldrich, Ref. 223433) and 0.04 M calcium chloride ($CaCl_2$; Scharlab, Ref. CA01920500), adjusting volumes to reach a molar relation Ca/Ox = 1. 0.5 µg of plasmid DNA (NanoLuc™, a pNL vector using a pGL4-based backbone; Promega, Ref. N1091) was added during the calcium oxalate nanoparticles *in situ* preparation, and the calcium oxalate-DNA system was then diluted with Opti-MEM® media (ThermoFisher, Ref. 11058021).

• CaOx-*a*DNA. DNA adsorbed on CaOx. 0.5 µg of plasmid DNA (NanoLuc™, a pNL vector using a pGL4-based backbone; Promega, Ref. N1091) was added to 1 M calcium oxalate suspension and diluted with Opti-MEM® media (ThermoFisher, Ref. 11058021). 1 M calcium oxalate (Sigma Aldrich, Ref. 455997) solution was prepared using water for molecular biology (Merck Millipore, Ref. H20MB0506).

• CaOx-*c*DNA(Ca^{2+}) and CaOx-*a*DNA(Ca^{2+}) with additional exogenous source of Ca^{2+}.Ca^{2+} was supplied once the particles were already formed through the final addition of $CaCl_2$ in a concentration of 0.0524M $CaCl_2$.

• CaOx(Mg^{2+})-*c*DNA. *30 % Mg doped Calcium oxalate – DNA system.* 0.5 µg of plasmid DNA (NanoLuc™, a pNL vector using a pGL4-based backbone; Promega, Ref. N1091)was added

to 0.012 mol of 1 M magnesium dichloride ($MgCl_2$; Sigma Aldrich, Ref. 1002071925). 0.028 M sodium oxalate ($Na_2C_2O_4$; Sigma Aldrich, Ref. 223433) and 0.04 M calcium chloride ($CaCl_2$; Scharlab, Ref. CA01920500), adjusting volumes to reach a molar relation Ca/Ox = 1, were added to the solution and diluted with Opti-MEM® media (ThermoFisher, Ref. 11058021).

- CaOx(Mg^{2+})-*a*DNA. *30 % Mg doped Hydroxyapatite – DNA system*. 0.5 µg of plasmid DNA (NanoLuc™, a pNL vector using a pGL4-based backbone; Promega, Ref. N1091) was added to 0.15 mol of 1 M magnesium dichloride ($MgCl_2$; Sigma Aldrich, Ref. 1002071925). Then, this mixture was added to 1 M calcium oxalate suspension and diluted with Opti-MEM® media (ThermoFisher, Ref. 11058021).

SI.2. Raman spectroscopy

Raman spectra of HAp, CaOx, ACP (see Figure S2) were obtained using a Confocal Raman Microscopy System (inVia Renishaw). A 532 nm laser was used for excitation and the laser power was 80 mW 0.1 s (large scan area) which is focused onto the sample via a microscope with 10x or 50x objective. A piezo stage was used to move the sample in order to obtain the Raman spectra. A spectrum was recorded at every point, with a scan area according to the size of the calcification.

SI.3. Measurement of DNA carried by transfection vectors

Total DNA free in solution was determined by a bisBenzimide H 33258 assay (Hoechst 33258) using a DNA Quantitation Kit (Sigma-Aldrich®, Catalog number DNAQF), according to the instructions provided by the manufacturer and measured using a microplate reader (Cytation 5, Biotek Instruments, Inc.) at ambient temperature, and at a wavelength of 360 nm excitation and 460 nm emission. Hoechst 33258 assay requires a DNA standard calibration curve to determine the DNA content of samples. Transfection vectors were prepared containing 500 ng in 400 µL DNA in all cases.

SI.4. Particle size (DLS) and Z-potential

Measurements were performed on a NanoBrook 90Plus Zeta equipped with an AQ-1321 cell for the zeta potential measurement. The synthesized samples were re-suspended and diluted 5,000 times in ultrapure milli-Q water (Millipore) and 1 mM KCl water solution respectively. Before DNA absorption of HAp-*a*DNA, ACP-*a*DNA and CaOx-*a*DNA samples, supensions were sonicated for 10 minutes. Particle size (DLS) was set to collect and average data every 3 minutes and Zeta potential (ELS) was obtained from averaging two series of 10 measurements to ensure representative data. All measurements were performed at room temperature.

SI.5. Bicinchoninic acid (BCA) Protein assay

Pierce™ BCA Protein Assay Kit (ThermoFisher, Ref. 23225) was used to measure total protein concentration from cell lysate according to manufacturer's instructions. First, a set of diluted Albumin (BSA) Standards was prepared using a working range from 20 to 2,000 µg/mL.
Then, 25 µL of each standard or unknown sample was pipetted into a clear 96-microplate well.200 µL of the working reagent (50:1, Reagent A:B) was added to each well. The plate was mixed thoroughly on a plate shaker for 30 seconds, covered and incubated at 37 °C. After 30 minutes, the plate was cooled to RT, and the absorbance was measured at 562 nm on a plate reader. The standard curve was used to determine the protein concentration of each unknown sample.

Table S1. Transfection efficiency of HAp, ACP, CaOx through time with DNA adsorbed and encapsulated through time (n=3 at each time point)

	24 h	48 h	72 h	1 week
Negative Control (NC)	0	0	0	0
Positive Control (PC) 3 mm	22078 *583*	75792 *2525*	29998 *5847*	5017 *495*
HAp-*c*DNA 3 mm	2 *1*	8 *2*	1 *0*	0 *0*
HAp-*a*DNA 3 mm	26 *11*	61 *79*	3 *2*	0 *0*
ACP-*c*DNA 3 mm	18347 *4332*	8364 *2458*	1128 *683*	184 *28*
ACP-*a*DNA 3 mm	16556 *4221*	12452 *3294*	1142 *193*	255 *151*
CaOx-*c*DNA 3 mm	8 *6*	6 *6*	1 *1*	0 *0*
CaOx-*a*DNA 3 mm	37 *7*	57 *15*	52 *57*	13 *8*

Table S2. Intervals of transfection efficiency by magnitude order

Transfection efficiency	RLU/µg protein	Score
No transfection	0	0
Very Low (V.L.)	1 – 9	2
Low (L)	10 – 99	4
Medium (M)	100 – 999	6
High (H)	1,000 – 9,999	8
Very high (V.H.)	10,000 – 99,999	10

Table S3. Quantification of free DNA in an initial DNA solution of 500 ng/400 µL in contact with mineral particles of HAp, ACP and CaOx. Percentage of DNA loaded in the mineral particle was obtained by subtracting measured free DNA concentration from the initial solution (n=3 at each point).

Transfection vectors	Free DNA (ng/ 400 µL)	Std. dev. σ	Carried DNA (ng/ 400 µL)	% DNA loaded
Negative control (OptiMEM)	0	0	N/A	N/A
Positive Control (CaP + HEPES)	174	10	326	65
Positive Control (CaP + HEPES) + Ca^{2+}	421	85	79	16
Positive Control (CaP + HEPES) + Mg^{2+}	192	40	308	62
Naked DNA	500	23	0	0
Naked DNA + Ca^{2+}	241	121	259	52
Naked DNA + Mg^{2+}	472	22	28	6
HAp-*c*DNA	19	21	481	96
HAp-*c*DNA + Ca^{2+}	149	90	351	70
HAp-*c*DNA + Mg^{2+}	263	110	237	47
HAp-*a*DNA	323	22	177	35
HAp-*a*DNA + Ca^{2+}	183	41	317	63
HAp-*a*DNA + Mg^{2+}	347	46	153	31
ACP-*c*DNA	211	88	289	58
ACP-*c*DNA + Ca^{2+}	197	17	303	61
ACP-*c*DNA + Mg^{2+}	214	88	286	57
ACP-*a*DNA	207	31	293	59
ACP-*a*DNA + Ca^{2+}	191	67	309	62
ACP-*a*DNA + Mg^{2+}	224	122	276	55
CaOx-*c*DNA	440	37	60	12
CaOx-*c*DNA + Ca^{2+}	127	11	373	75
CaOx-*c*DNA + Mg^{2+}	348	52	152	30
CaOx-*a*DNA	346	15	154	31
CaOx-*a*DNA + Ca^{2+}	117	55	383	77
CaOx-*a*DNA + Mg^{2+}	213	10	287	57

Table S4. Particle size and percentage of particles below 500 nm vs above 500 nm (Γ_{500}).

Transfection vector	Time	Size	Γ_{500}
HAp-aDNA	0 min	88 ± 33 nm / 731 ± 262 nm*	0.115 ± 0.042*
HAp-aDNA	30 min	504 ± 125 nm / > 10 µm	0.032 ± 0.013
HAp-aDNA	60 min	711 ± 109 nm	0.026 ± 0.005
HAp-aDNA + $CaCl_2$	15 min	420 ± 108 nm / 2.6 ± 1.1 µm	0.094 ± 0.021
HAp-aDNA + $CaCl_2$	30 min	296 ± 116 nm / 4.6 ± 1.8 µm	0.048 ± 0.045
HAp-aDNA + $MgCl_2$	15 min	511 ± 201 nm / 1.6 ± 0.3 µm	0.017 ± 0.002
HAp-aDNA + $MgCl_2$	30 min	365 ± 109 nm / 1.8 ± 0.2 µm	0.005 ± 0.001
HAp-cDNA	0 min	75 ± 10 nm / 506 ± 311 nm	$0.002 \pm 1.4 \cdot 10^{-4}$
HAp-cDNA	30 min	7.8 ± 2.0 µm / > 10 µm	$0.0006 \pm 1 \cdot 10^{-4}$
HAp-cDNA	60 min	5.2 ± 0.3 µm	< l.d.**
HAp-cDNA + $CaCl_2$	15 min	406 ± 125 nm / 2.7 ± 0.9 µm	0.086 ± 0.016
HAp-cDNA + $CaCl_2$	30 min	456 ± 120 nm / 2.3 ± 1.8 µm / > 10 µm	0.068 ± 0.013
HAp-cDNA + $MgCl_2$	15 min	376 ± 156 nm / 4.7 ± 0.6 µm	0.105 ± 0.026
HAp-cDNA + $MgCl_2$	30 min	4.3 ± 0.6 µm	0.069 ± 0.021
ACP-aDNA	0 min	353 ± 135 nm / 2.0 ± 0.6 µm	0.310 ± 0.177
ACP-aDNA	30 min	1.5 ± 0.3 µm	0.072 ± 0.019
ACP-aDNA	60 min	1.2 ± 0.2 µm	0.047 ± 0.009
ACP-aDNA + $CaCl_2$	15 min	549 ± 123 nm / 4.7 ± 1.9 µm	0.083 ± 0.028
ACP-aDNA + $CaCl_2$	30 min	641 ± 20 nm / 1.5 ± 0.1 µm	0.102 ± 0.028
ACP-aDNA + $MgCl_2$	15 min	217 ± 38 nm / 713 ± 25 nm / 3.2 ± 0.1 µm	0.474 ± 0.134
ACP-aDNA + $MgCl_2$	30 min	284 ± 87 nm / 2.6 ± 0.1 µm	0.289 ± 0.071
ACP-cDNA	0 min	232 ± 135 nm / 744 ± 216 nm	0.613 ± 0.215
ACP-cDNA	30 min	1357 nm ± 0.3 µm	0.093 ± 0.016
ACP-cDNA	60 min	2264 ± 240 nm	0.060 ± 0.025
ACP-cDNA + $CaCl_2$	15 min	256 ± 24 nm / 2.5 ± 0.1 µm	0.179 ± 0.008
ACP-cDNA + $CaCl_2$	30 min	487 ± 203 nm / 4.8 ± 2.6 µm	0.080 ± 0.005
ACP-cDNA + $MgCl_2$	15 min	186 ± 40 nm / 625 ± 108 nm / 1.9 ± 0.4 µm	0.322 ± 0.177
ACP-cDNA + $MgCl_2$	30 min	301 ± 24 nm / 2.6 ± 0.5 µm	0.104 ± 0.043
CaOx-aDNA	0 min	264 ± 50 nm	0.140 ± 0.014
CaOx-aDNA	30 min	863 ± 140	0.017 ± 0.005
CaOx-aDNA	60 min	3.0 ± 0.3 µm	< l.d.**
CaOx-aDNA + $CaCl_2$	15 min	577 ± 15 nm	0.075 ± 0.067
CaOx-aDNA + $CaCl_2$	30 min	773 ± 60 nm / 4.9 ± 0.6 µm	0.094 ± 0.024
CaOx-aDNA + $MgCl_2$	15 min	348 ± 56 nm / 7.5 ± 0.4 µm	0.007 ± 0.004
CaOx-aDNA + $MgCl_2$	30 min	517 ± 97 nm / 5.2 ± 0.6 µm / > 10 µm	0.004 ± 0.001
CaOx-cDNA	0 min	375 ± 137 nm	0.008 ± 0.007
CaOx-cDNA	30 min	1.1 ± 0.4 µm	$0.0008 \pm 1 \cdot 10^{-4}$
CaOx-cDNA	60 min	3.6 ± 0.2 µm	< l.d.*
CaOx-cDNA + $CaCl_2$	15 min	236 ± 46 nm / 1.6 ± 0.3 µm	0.156 ± 0.058
CaOx-cDNA + $CaCl_2$	30 min	178 ± 20 nm / 1.2 ± 0.1 µm	0.223 ± 0.030
CaOx-cDNA + $MgCl_2$	15 min	2.3 ± 0.7 µm / > 10 µm	< l.d.**
CaOx-cDNA + $MgCl_2$	30 min	3.4 ± 0.8 µm / > 10 µm	< l.d.**
HAp + DNA + HEPES	0 min	365 ± 224 nm / 2.7 ± 1.3 µm	0.036 ± 0.025
HAp + DNA + HEPES	15 min	428 ± 104 nm / 1.5 ± 0.4 µm	0.179 ± 0.080
HAp + DNA + HEPES	30 min	318 ± 42 nm / 1.9 ± 0.3 µm	0.268 ± 0.242
HAp + DNA + HEPES + Optimem	0 min	379 ± 16 nm / 2.4 ± 0.8 µm	0.149 ± 0.024
HAp + DNA + HEPES + Optimem	15 min	295 ± 38 nm / 0.9 ± 0.1 µm	0.186 ± 0.046
HAp + DNA + HEPES + Optimem	30 min	447 ± 259 nm / 1.1 ± 0.1 µm	0.222 ± 0.040

* Errors expressed in standard deviation

** < l.d. = below limit of detection

Table S5. Transfection efficiency of naked DNA and HAp, ACP, CaOx with DNA adsorbed and encapsulated and influence of Ca2+ and Mg2+ ions (RLU/ug protein).

	24 h					48 h				
	Run 1	Run 2	Run 3	Avg. (n=9)	Transfection	Run 1	Run 2	Run 3	Avg. (n=9)	Transfection
Negative Control (n=3)	0	0	0	0	No transfection	0	0	0	0	No transfection
Desv. Est. (σ)	*0*	*0*	*0*			*0*	*0*	*0*		
Positive Control (PC)	11047	26146	23221	20138	Very High	46416	31325	27829	35190	Very High
	1626	*3563*	*3266*			*7366*	*2166*	*2176*		
Naked DNA	0	0	0	0	Negative	0	0	0	0	Negative
	0	*0*	*0*			*0*	*0*	*0*		
Naked DNA + Ca2+	714	9231	3297	4414	High	585	9942	3278	4602	High
	46	*616*	*263*			*22*	*1533*	*1203*		
Naked DNA + Mg2+	1	2	1	1	Very Low	1	2	2	2	Very Low
	1	*2*	*0*			*1*	*1*	*1*		
HAp-cDNA	0	3	4	3	Very Low	1	4	1	2	Very Low
	0	*3*	*0*			1	1	1		
HAp-cDNA(Ca2+)	6	106	456	189	Medium	209	82	903	398	Medium
	0	*62*	*136*			*10*	*6*	*292*		
HAp(Mg2+)-cDNA	2	2	2	2	Very Low	1	1	1	1	Very Low
	2	*3*	*2*			0	1	0		
HAp-aDNA	15	9	6	10	Low	49	25	6	27	Low
	6	*6*	*2*			*36*	*4*	*2*		
HAp-aDNA(Ca2+)	1815	187	95	699	Medium	7021	162	309	2497	High
	490	*167*	*61*			*726*	*66*	*230*		
HAp(Mg2+)-aDNA	16	54	27	35	Low	15	18	19	18	Low
	6	*32*	*20*			*3*	*6*	*6*		
CaOx-cDNA	1	7	5	4	Very Low	3	2	3	2	Very Low
	0	*4*	*3*			*1*	*0*	*1*		
CaOx-cDNA(Ca2+)	153	1443	2727	1441	High	328	1731	2461	1507	High
	16	*716*	*372*			*44*	*197*	*666*		
CaOx(Mg2+)-cDNA	7	3	5	5	Very Low	1	2	0	1	Very Low
	7	*1*	*6*			*1*	*1*	*0*		
CaOx-aDNA	27	13	12	17	Low	208	35	21	88	Low
	9	*9*	*2*			*76*	*23*	*9*		
CaOx-aDNA(Ca2+)	575	263	714	518	Medium	819	618	526	654	Medium
	419	*69*	*147*			*406*	*162*	*144*		
CaOx(Mg2+)-aDNA	19	20	21	20	Low	28	23	25	26	Low
	12	*9*	*2*			*14*	*4*	*3*		
ACP-cDNA	1227	13645	11960	8944	High	558	19996	18886	13147	Very High
	630	*1042*	*3166*			*261*	*6666*	*3666*		
ACP-cDNA(Ca2+)	310	273	966	516	Medium	286	338	1026	550	Medium
	32	*77*	*681*			*16*	*67*	*266*		
ACP(Mg2+)-cDNA	249	2465	1310	1478	High	154	4093	1147	1798	High
	33	*606*	*192*			*39*	*1210*	*664*		
ACP-aDNA	1191	7514	13836	7514	High	760	9596	20897	10417	Very High
	619	*3673*	*2960*			*376*	*4662*	*2266*		
ACP-aDNA(Ca2+)	305	256	1305	622	Medium	138	542	1340	674	Medium
	14	*69*	*600*			*63*	*102*	*416*		
ACP(Mg2+)-aDNA	510	2672	1077	1533	High	112	5851	820	2261	High
	66	*977*	*319*			*40*	*1274*	*179*		

Table S6. Transfection efficiency of HAp, ACP, CaOx with DNA adsorbed and encapsulated vs. migration distance.

	24 h					48 h				
	Run 1	Run 2	Run 3	Avg. (n=9)	Transfection	Run 1	Run 2	Run 3	Avg. (n=9)	Transfection
Negative Control	0	0	0	0	No transfection	0	0	0	0	No transfection
PC 3 mm (ave. n=3)	11047	26146	23221	20138	Very High	46416	31325	27829	35190	Very High
Desv. Est. (σ)	*1528*	*2853*	*3288*			*7356*	*2158*	*2175*		
PC 7 mm	6535	26146	14710	15797	Very High	8344	31325	9007	16226	Very High
	360	*2853*	*2805*			*1076*	*2158*	*3075*		
PC 20 mm	1572	23570	2469	9204	High	1047	9513	2361	4307	High
	75	*9351*	*1900*			*41*	*4550*	*1212*		
PC 50 mm	275	9	334	206	Medium	39	16	93	49	Low
	21	*1*	*222*			*9*	*1*	*47*		
HAp-cDNA 3 mm	0	3	4	3	Very Low	1	4	1	2	Very Low
	0	*3*	*0*			*1*	*1*	*1*		
HAp-cDNA 7 mm	7	0	0	3	Very Low	14	0	1	5	Very Low
	5	*0*	*0*			*7*	*0*	*1*		
HAp-cDNA 20 mm	33	7	3	14	Low	17	1	1	6	Low
	19	*1*	*1*			*7*	*0*	*0*		
HAp-cDNA 50 mm	0	1	2	1	Very Low	0	2	0	1	Very Low
	0	*1*	*1*			*0*	*2*	*0*		
HAp-aDNA 3 mm	15	9	6	10	Low	49	25	6	27	Low
	5	*5*	*2*			*35*	*4*	*2*		
HAp-aDNA 7 mm	10	18	25	18	Low	25	23	30	26	Low
	7	*8*	*13*			*16*	*14*	*39*		
HAp-aDNA 20 mm	30	20	11	21	Low	21	13	22	18	Low
	3	*7*	*8*			*1*	*4*	*2*		
HAp-aDNA 50 mm	12	7	10	10	Low	10	5	11	8	Very Low
	3	*5*	*1*			*2*	*1*	*7*		
CaOx-cDNA 3 mm	1	7	5	4	Very Low	3	2	3	2	Very Low
	0	*4*	*3*			*1*	*0*	*1*		
CaOx-cDNA 7 mm	0	0	0	0	No Transfection	0	0	1	0	No Transfection
	0	*0*	*1*			*0*	*0*	*0*		
CaOx-cDNA 20 mm	1	2	4	2	Very Low	0	1	4	2	Very Low
	0	*0*	*2*			*0*	*2*	*3*		
CaOx-cDNA 50 mm	1	3	0	1	Very Low	0	1	0	0	No Transfection
	0	*2*	*0*			*0*	*1*	*0*		
CaOx-aDNA 3 mm	27	13	12	17	Low	208	35	21	88	Low
	9	*9*	*2*			*76*	*23*	*9*		
CaOx-aDNA 7 mm	34	11	8	18	Low	58	32	40	43	Low
	21	*2*	*3*			*7*	*13*	*17*		
CaOx-aDNA 20 mm	50	33	15	32	Low	49	35	20	35	Low
	11	*3*	*7*			*6*	*5*	*9*		
CaOx-aDNA 50 mm	15	9	18	14	Low	27	21	7	18	Low
	6	*4*	*12*			*2*	*6*	*5*		
ACP-cDNA 3 mm	1227	482	11960	4556	High	558	3075	18886	7507	High
	830	*32*	*3156*			*251*	*410*	*3568*		
ACP-cDNA 7 mm	4787	5079	13645	7837	High	7843	5833	19996	11224	Very High
	190	*1392*	*1042*			*3113*	*1252*	*5556*		
ACP-cDNA 20 mm	1	339	1703	681	Medium	41	602	907	517	Medium
	0	*66*	*582*			*3*	*35*	*372*		
ACP-cDNA 50 mm	0	32	37	23	Low	0	16	0	5	Very Low
	0	*4*	*35*			*0*	*1*	*0*		
ACP-aDNA 3 mm	1191	7514	13836	7514	High	760	9595	20897	10417	High
	619	*3673*	*2080*			*378*	*4562*	*2255*		
ACP-aDNA 7 mm	3729	4643	7514	5295	High	7131	2299	9595	6342	High
	761	*1147*	*3673*			*5166*	*201*	*9595*		
ACP-aDNA 20 mm	2	71	1299	457	Medium	19	353	626	333	Medium
	2	*22*	*474*			*1*	*41*	*655*		
ACP-aDNA 50 mm	14	0	62	25	Low	1	0	0	0	No transfection
	2	*0*	*58*			*0*	*0*	*0*		

Figure S1. Scheme of the migration setup. A549 cells were seeded on the lower compartment. The distance from the point where vectors were deposited to the cells was: a) 7 mm, b) 20 mm and c) 50 mm.

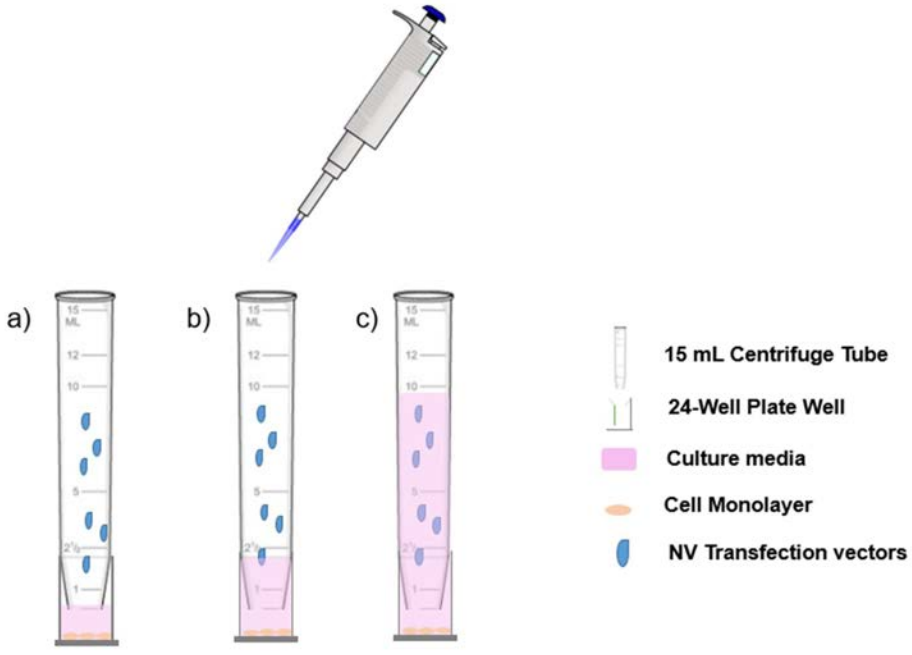

Figure S2. Raman spectra of the different vectors used in the study. The characteristic vibrational bands of CaOx (■) can be clearly distinguished from the four v1-4 vibrational modes of HAp corresponding to the P-O vibrations. The asymmetric widening of the main peak v1 is characteristic from ACP phase (*).

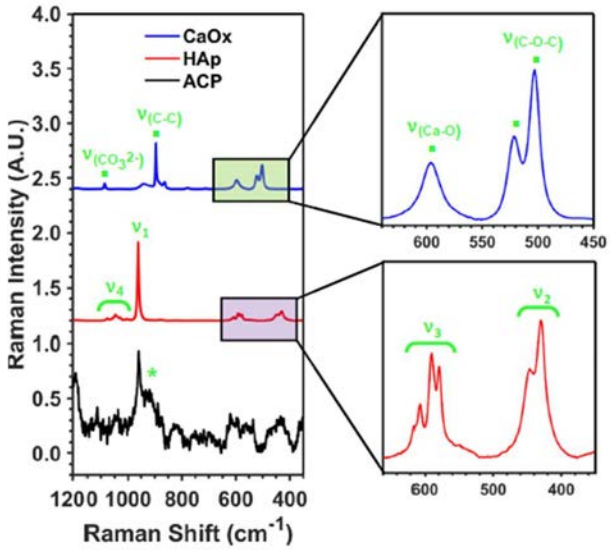

Figure S3. Z-potential dynamics of transfection vectors through time: a) HAp-aDNA(Ca2+) (red) and HAp-cDNA(Ca2+) (blue); b) ACP-aDNA(Ca2+) (red) and ACP-cDNA(Ca2+) (blue); c)CaOx-aDNA(Ca2+) (red) and CaOx-cDNA(Ca2+) (blue); d) HAp(Mg2+)-aDNA (red) andHAp(Mg2+)-cDNA (blue); e) ACP(Mg2+)-aDNA (red) and ACP(Mg2+)-cDNA (blue); f)CaOx(Mg2+)-aDNA (red) and CaOx(Mg2+)-cDNA (blue).

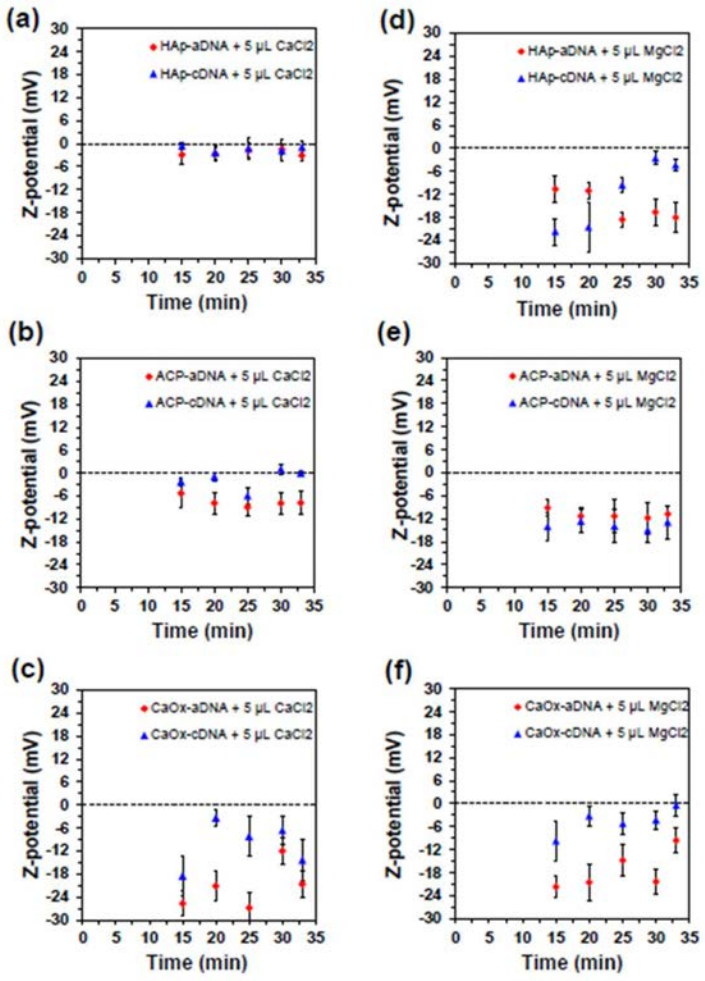

Figure S4. SEM micrograph of the ACP simple synthesized. The inset confirms the spherical morphology of the initial ACP particle.

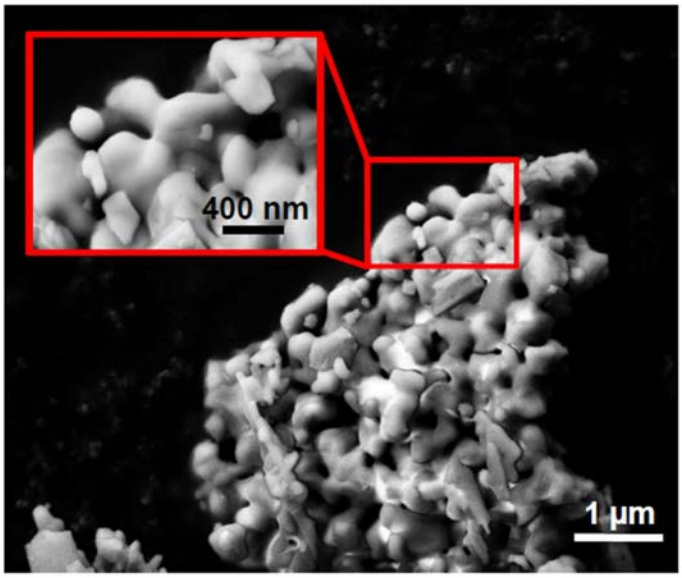

References

1. Promega. https://www.promega.es/products/luciferase-assays/genetic-reporter-vectorsand-cell-lines/promoter-driven-control-nanoluc-luciferase-vectors/?catNum=N1091

(accessed March 13th 2021).

2. M. Wigler, S. Silverstein, L.S. Lee, A. Pellicer, Y. Cheng, R. Axel. *Cell.* 11 (1977) 1,

223-232.

TOC. Graphical abstract

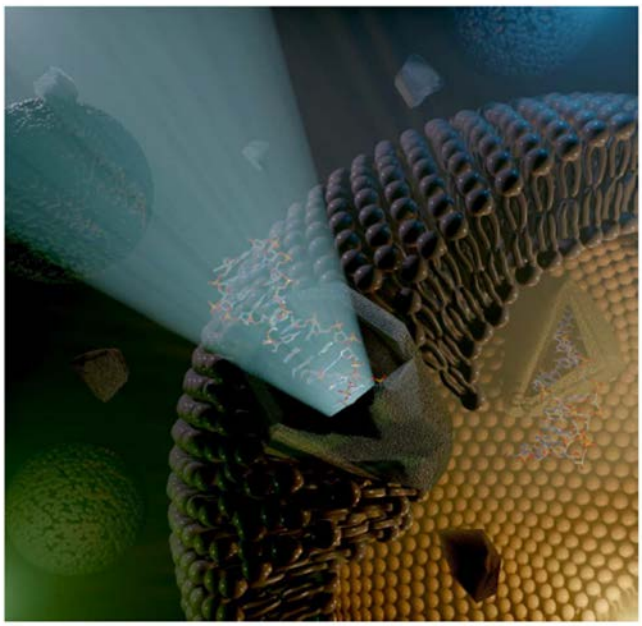

REFERENCES

12 REFERENCES

[1] Siegel, R. L., Miller, K. D., & Jemal, A. Cancer statistics, 2020. *CA: a cancer journal for clinicians*. 2020; *70*(1): 7-30.

[2] Galceran, J., Ameijide, A., Carulla, M., Mateos, A., Quirós, J. R., Rojas, D., et al. Cancer incidence in Spain, 2015. *Clinical and Translational Oncolog.* 2017; *19*(7): 799-825.

[3] Department of Health, *Generalitat de Catalunya*. Data obtained from October 2017.

[4] Stewart, B. W. K. P., & Wild, C. P. World cancer report 2014. *Health*. 2017.

[5] McPherson, K., Steel, C., & Dixon, J. M. ABC of breast diseases: breast cancer—epidemiology, risk factors, and genetics. *BMJ: British Medical Journal*. 2000; *321*(7261): 624.

[6] Key, T. J., Verkasalo, P. K., & Banks, E. Epidemiology of breast cancer. *The lancet oncology.* 2001; *2*(3): 133-140.

[7] Mansfield, C. M. A review of the etiology of breast cancer. *Journal of the National Medical Association.* 1993; *85*(3): 217.

[8] Schulz, M., Hoffmann, K., Weikert, C., Nöthlings, U., Schulze, M. B., & Boeing, H. Identification of a dietary pattern characterized by high-fat food choices associated with increased risk of breast cancer: the European Prospective Investigation into Cancer and Nutrition (EPIC)-Potsdam Study. *British journal of nutrition*. 2008; *100*(5): 942-946.

[9] McDonald, J. A., Goyal, A., & Terry, M. B. Alcohol intake and breast cancer risk: weighing the overall evidence. *Current breast cancer reports*. 2013; *5*(3): 208-221.

[10] Gray, J., Evans, N., Taylor, B., Rizzo, J., & Walker, M. State of the evidence: the connection between breast cancer and the environment. *International journal of occupational and environmental health*. 2009; *15*(1): 43-78.

[11] Rohan, T. E., Heo, M., Choi, L., Datta, M., Freudenheim, J. L., Kamensky, V., et al. Body fat and breast cancer risk in postmenopausal women: a longitudinal study. *Journal of cancer epidemiology*. 2013; Vol 2013.

[12] Million Women Study Collaborators. Breast cancer and hormone-replacement therapy in the Million Women Study. *The Lancet*. 2003; *362*(9382): 419-427.

[13] Mørch, L. S., Skovlund, C. W., Hannaford, P. C., Iversen, L., Fielding, S., & Lidegaard, Ø. Contemporary Hormonal Contraception and the Risk of Breast Cancer. *New England Journal of Medicine*. 2017; *377*(23): 2228-2239.

[14] Collaborative Group on Hormonal Factors in Breast Cancer. Breast cancer and breastfeeding: collaborative reanalysis of individual data from 47 epidemiological studies in 30 countries, including 50 302 women with breast cancer and 96 973 women without the disease. *The Lancet.* 2002; *360*(9328): 187-195.

[15] Collaborative Group on Hormonal Factors in Breast Cancer. Menarche, menopause, and breast cancer risk: individual participant meta-analysis, including 118 964 women with breast cancer from 117 epidemiological studies. *The lancet oncology.* 2012; *13*(11): 1141-1151.

[16] Antoniou, A., Pharoah, P. D., Narod, S., Risch, H. A., Eyfjord, J. E., Hopper, J. L., et al. Average risks of breast and ovarian cancer associated with BRCA1 or BRCA2 mutations detected in case series unselected for family history: a combined analysis of 22 studies. *The American Journal of Human Genetics*. 2003; *72*(5): 1117-1130.

[17] King, M. C., Marks, J. H., & Mandell, J. B. Breast and ovarian cancer risks due to inherited mutations in BRCA1 and BRCA2. *Science*. 2003; *302*(5645): 643-646.

[18] Kuchenbaecker, K. B., Hopper, J. L., Barnes, D. R., Phillips, K. A., Mooij, T. M., Roos-Blom, M. J., et al. Risks of breast, ovarian, and contralateral breast cancer for BRCA1 and BRCA2 mutation carriers. *Jama*. 2017; *317*(23): 2402-2416.

[19] Donninger, H., Vos, M. D., & Clark, G. J. The RASSF1A tumor suppressor. *Journal of cell science*. 2007; *120*(18): 3163-3172.

[20] Esteller, M., & Herman, J. G. Cancer as an epigenetic disease: DNA methylation and chromatin alterations in human tumors. *The Journal of Pathology: A Journal of the Pathological Society of Great Britain and Ireland*. 2002; *196*(1): 1-7.

[21] Esteller, M. Epigenetics in cancer. *New England Journal of Medicine*. 2008; *358*(11): 1148-1159.

[22] Rodríguez-Paredes, M., & Esteller, M. Cancer epigenetics reaches mainstream oncology. *Nature medicine*. 2011; *17*(3): 330-339.

[23] Rodríguez-Miguel, C., Moral, R., Escrich, R., Vela, E., Solanas, M., & Escrich, E. The role of dietary extra virgin olive oil and corn oil on the alteration of epigenetic patterns in the rat DMBA-induced breast cancer model. *PLoS One*. 2015; *10*(9): e0138980.

[24] Robertson, K. D. DNA methylation, methyltransferases, and cancer. *Oncogene.* 2001; *20*(24): 3139.

[25] Davalos, V., Martinez-Cardus, A., & Esteller, M. The epigenomic revolution in breast cancer: from single-gene to genome-wide next-generation approaches. *The American journal of pathology*. 2017; *187*(10): 2163-2174.

[26] Geahigan, K. B., Meints, G. A., Hatcher, M. E., Orban, J., & Drobny, G. P. The dynamic impact of CpG methylation in DNA. *Biochemistry*. 2000; *39*(16): 4939-4946.

[27] Maresca, A., Zaffagnini, M., Caporali, L., Carelli, V., & Zanna, C. DNA methyltransferase 1 mutations and mitochondrial pathology: is mtDNA methylated? *Frontiers in genetics.* 2015; *6*: 90.

[28] Kelly, J. G., Najand, G. M., & Martin, F. L. Characterisation of DNA methylation status using spectroscopy (mid-IR versus Raman) with multivariate analysis. *Journal of biophotonics*. 2011; *4*(5): 345-354.

[29] Daura-Oller, E., Cabre, M., Montero, M. A., Paternain, J. L., & Romeu, A. Specific gene hypomethylation and cancer: new insights into coding region feature trends. *Bioinformation*. 2009; *3*(8): 340.

[30] Guo, Y., Pakneshan, P., Gladu, J., Slack, A., Szyf, M., & Rabbani, S. A. Regulation of DNA methylation in human breast cancer effect on the urokinase-type plasminogen activator gene production and tumor invasion. *Journal of Biological Chemistry*. 2002; *277*(44): 41571-41579.

[31] Du, Z., Ma, K., Sun, X., Li, A., Wang, H., Zhang, L., et al. Methylation of RASSF1A gene promoter and the correlation with DNMT1 expression that may contribute to esophageal squamous cell carcinoma. *World journal of surgical oncology*. 2015; *13*(1): 141.

[32] Barnadas, A., Algara, M., Cordoba, O., Casas, A., Gonzalez, M., Marzo, M., et al. Recommendations for the follow-up care of female breast cancer survivors: a guideline of the Spanish Society of Medical Oncology (SEOM), Spanish Society of General Medicine (SEMERGEN), Spanish Society for Family and Community Medicine (SEMFYC), Spanish Society for General and Family Physicians (SEMG), Spanish Society of Obstetrics and Gynecology (SEGO), Spanish Society of Radiation Oncology (SEOR), Spanish Society of Senology and Breast Pathology (SESPM), and Spanish Society of Cardiology (SEC). *Clinical and Translational Oncology*. 2017: 1-8.

[33] Ferro, T., & Pérez, J. P. *Necesidades de información en el cáncer de mama y de atención en la supervivencia*. Federacion Española de Cáncer de Mama. 2013.

[34] Weigelt, B., Geyer, F. C., & Reis-Filho, J. S. Histological types of breast cancer: how special are they? *Molecular oncology.* 2010; *4*(3): 192-208.

[35] Burstein, H. J., Polyak, K., Wong, J. S., Lester, S. C., & Kaelin, C. M. Ductal carcinoma in situ of the breast. *New England Journal of Medicine*. 2004; *350*(14): 1430-1441.

[36] Shin, S. U., Lee, J., Kim, J. H., Kim, W. H., Song, S. E., Chu, A., et al. Gene expression profiling of calcifications in breast cancer. *Scientific reports*. 2017; *7*(1): 11427.

[37] Rudas, M., Neumayer, R., Gnant, M. F. X., Mittelböck, M., Jakesz, R., & Reiner, A. p53 protein expression, cell proliferation and steroid hormone receptors in ductal and lobular in situ carcinomas of the breast. *European journal of cancer*. 1997; *33*(1): 39-44.

[38] Gospodarowicz, M. K., Brierley, J. D., & Wittekind, C. (Eds.). *TNM classification of malignant tumors*. John Wiley & Sons. 2017.

[39] Perou, C. M., Sørlie, T., Eisen, M. B., Van De Rijn, M., Jeffrey, S. S., Rees, C. A., et al. Molecular portraits of human breast tumors. *Nature.* 2000; *406*(6797): 747.

[40] Prat, A., Pineda, E., Adamo, B., Galván, P., Fernández, A., Gaba, L., et al. Clinical implications of the intrinsic molecular subtypes of breast cancer. *The Breast.* 2015; *24*: S26-S35.

[41] Parker, J. S., Mullins, M., Cheang, M. C., Leung, S., Voduc, D., Vickery, T., et al. Supervised risk predictor of breast cancer based on intrinsic subtypes. *Journal of clinical oncology.* 2009; *27*(8): 1160.

[42] Anderson, W. F., Rosenberg, P. S., Prat, A., Perou, C. M., & Sherman, M. E. How many etiological subtypes of breast cancer: two, three, four, or more? *Journal of the National Cancer Institute*. 2014; *106*(8): 165.

[43] Yersal, O., & Barutca, S. Biological subtypes of breast cancer: Prognostic and therapeutic implications. *World journal of clinical oncology*. 2014; *5*(3): 412.

[44] Sørlie, T., Perou, C. M., Tibshirani, R., Aas, T., Geisler, S., Johnsen, H., et al. Gene expression patterns of breast carcinomas distinguish tumor subclasses with clinical implications. *Proceedings of the National Academy of Sciences.* 2001; *98*(19): 10869-10874.

[45] Lehmann, B. D., Bauer, J. A., Chen, X., Sanders, M. E., Chakravarthy, A. B., Shyr, Y., & Pietenpol, J. A. Identification of human triple-negative breast cancer subtypes and preclinical models for selection of targeted therapies. *The Journal of clinical investigation.* 2011; *121*(7): 2750-2767.

[46] Tabár, L., & Dean, P. B. A new era in the diagnosis and treatment of breast cancer. *The breast journal.* 2010; *16*(s1).

[47] Fajdic, J., Djurovic, D., Gotovac, N., & Hrgovic, Z. Criteria and procedures for breast conserving surgery. *Acta Informatica Medica*. 2013; *21*(1): 16.

[48] Goldhirsch, A., Wood, W. C., Senn, H. J., Glick, J. H., & Gelber, R. D. Meeting highlights: international consensus panel on the treatment of primary breast cancer. *JNCI: Journal of the National Cancer Institute*. 1995; *87*(19): 1441-1445.

[49] Treatment of Early-Stage Breast Cancer. *NIH Consens Statement*. 1990; 18-21;8(6): 1-19.

[50] Zahoor, S., Haji, A., Battoo, A., Qurieshi, M., Mir, W., & Shah, M. Sentinel lymph node biopsy in breast cancer: a clinical review and update. *Journal of breast cancer*. 2017; *20*(3): 217.

[51] Julián, J. F., Navinés, J., Botey, M., Pascual, I., Balibrea, J. M., Fernández-Llamazares, J., ... & Mariscal, A. Reconstrucción de la mama con gel de plaquetas en la cirugía conservadora del cáncer. *Cirugía Española*. 2012; *90*(9): 582-588.

[52] Oh, J. L. Multifocal or multicentric breast cancer: understanding its impact on management and treatment outcomes. In *Methods of cancer diagnosis, therapy and prognosis.* 2008; Springer, Dordrecht: 583-587.

[53] Rezo, A., Dahlstrom, J., Shadbolt, B., Rodins, K., Zhang, Y., & Davis, A. J. Tumor size and survival in multicentric and multifocal breast cancer. *The Breast.* 2011; *20*(3): 259-263.

[54] Lynch, S. P., Lei, X., Hsu, L., Meric-Bernstam, F., Buchholz, T. A., Zhang, H., et al. Breast cancer multifocality and multicentricity and locoregional recurrence. *The oncologist.* 2013; *18*(11): 1167-1173.

[55] Martínez, A. M., Roselló, I. V., Gómez, A. S., Catanese, A., Molina, M. P., Suarez, M. S., et al. Advantages of preoperative localization and surgical resection of metastatic axillary lymph nodes using magnetic seeds after neoadjuvant chemotherapy in breast cancer. *Surgical Oncology*. 2021; *36*: 28-33.

[56] Early Breast Cancer Trialists' Collaborative Group. Effects of radiotherapy and of differences in the extent of surgery for early breast cancer on local recurrence and 15-year survival: an overview of the randomised trials. *The Lancet*. 2005; *366*(9503): 2087-2106.

[57] Van Tienhoven, G., Voogd, A. C., Peterse, J. L., Nielsen, M., Andersen, K. W., Mignolet, F., et al. Prognosis after treatment for loco-regional recurrence after mastectomy or breast conserving therapy in two randomised trials (EORTC 10801 and DBCG-82TM). *European Journal of Cancer*. 1999; *35*(1): 32-38.

[58] Tsoutsou, P. G., Vozenin, M. C., Durham, A. D., & Bourhis, J. How could breast cancer molecular features contribute to locoregional treatment decision making? *Critical reviews in oncology/hematology*. 2017; *110:* 43-48.

[59] Hanahan, D., & Weinberg, R. A. Hallmarks of cancer: the next generation. *Cell.* 2011; *144*(5): 646-674.

[60] Nguyen, D. X., Bos, P. D., & Massagué, J. Metastasis: from dissemination to organ-specific colonization. *Nature Reviews Cancer*. 2009; *9*(4): 274.

[61] Paget, S. The distribution of secondary growths in cancer of the breast. *The Lancet.* 1889; *133*(3421): 571-573.

[62] Kang, Y. New tricks against an old foe: molecular dissection of metastasis tissue tropism in breast cancer. *Breast disease*. 2007; *26*(1): 129-138.

[63] Weigelt, B., Peterse, J. L., & Van't Veer, L. J. Breast cancer metastasis: markers and models. *Nature reviews cancer*. 2005; *5*(8): 591.

[64] Lambert, A. W., Pattabiraman, D. R., & Weinberg, R. A. Emerging biological principles of metastasis. *Cell*. 2017; *168*(4): 670-691.

[65] Olmo, D. G., Olmo, D. G., Ontanon, J., Martinez, E., & Vallejo, M. Tumor DNA circulating in the plasma might play a role in metastasis. The hypothesis of the genometastasis. *Histology and histopathology.* 1999; *14*(4): 1159-1164.

[66] Weichselbaum, R. R. The 46th David A. Karnofsky Memorial Award Lecture: Oligometastasis—From Conception to Treatment. *Journal of Clinical Oncology.* 2018; *36*(32): 3240-3250.

[67] Hui, L., & Chen, Y. Tumor microenvironment: Sanctuary of the devil. *Cancer letters.* 2015; *368*(1): 7-13.

[68] Korkaya, H., Liu, S., & Wicha, M. S. Breast cancer stem cells, cytokine networks, and the tumor microenvironment. *The Journal of clinical investigation.* 2011; *121*(10): 3804-3809.

[69] Salomon A. Beiträge zur Pathologie und Klinik der Mammakarzinome. *Arch. Klin. Chir.* 1913; 101: 573–668.

[70] Bhargava, S., & Bhargava, S. K. Differential diagnosis in radiology. 2014. Jaypee brothers.

[71] Henrot, P., Leroux, A., Barlier, C., & Génin, P. Breast microcalcifications: the lesions in anatomical pathology. *Diagnostic and interventional imaging.* 2014; *95*(2): 141-152.

[72] Haka, A. S., Shafer-Peltier, K. E., Fitzmaurice, M., Crowe, J., Dasari, R. R., & Feld, M. S. Identifying microcalcifications in benign and malignant breast lesions by probing differences in their chemical composition using Raman spectroscopy. *Cancer research*. 2002; *62*(18): 5375-5380.

[73] Baker, R., Rogers, K. D., Shepherd, N., & Stone, N. New relationships between breast microcalcifications and cancer. *British journal of cancer.* 2010; *103*(7): 1034.

[74] Morgan, M. P., Cooke, M. M., Christopherson, P. A., Westfall, P. R., & McCarthy, G. M. Calcium hydroxyapatite promotes mitogenesis and matrix metalloproteinase expression in human breast cancer cell lines. *Molecular Carcinogenesis: Published in cooperation with the University of Texas MD Anderson Cancer Center*. 2001; *32*(3): 111-117.

[75] Rao, A. A., Feneis, J., Lalonde, C., & Ojeda-Fournier, H. A pictorial review of changes in the BI-RADS fifth edition. *Radiographics*. 2016; *36*(3): 623-639.

[76] ACR BI-RADS Atlas® 5th Edition.

[77] Monda, L. A. Differentiation of breast calcifications. *Radiologic technology*. 2001; *72*(6): 532-532.

[78] Tabár, L., & Dean, P. B. Thirty years of experience with mammography screening: a new approach to the diagnosis and treatment of breast cancer. *Breast Cancer Research.* 2008; *10*(4): S3.

[79] Tabár, L., Dean, P. B., Chen, T. H. H., Yen, A. M. F., Chiu, S. Y. H., Tot, T., et al. The impact of mammography screening on the diagnosis and management of early-phase breast cancer. In *Breast Cancer*. Springer New York; 2014.

[80] Holme, T. C., Reis, M. M., Thompson, A., Robertson, A., Parham, D., Hickman, P., & Preece, P. E. Is mammographic microcalcification of biological significance? *European journal of surgical oncology: the journal of the European Society of Surgical Oncology and the British Association of Surgical Oncology*. 1993; *19*(3): 250-253.

[81] Frappart, L., Boudeulle, M., Boumendil, J., Lin, H. C., Martinon, I., Palayer, C., et al. Structure and composition of microcalcifications in benign and malignant lesions of the breast: study by light microscopy, transmission and scanning electron microscopy, microprobe analysis, and X-ray diffraction. *Human pathology.* 1984; *15*(9): 880-889.

[82] Morgan, M. P., Cooke, M. M., & McCarthy, G. M. Microcalcifications associated with breast cancer: an epiphenomenon or biologically significant feature of selected tumors? *Journal of mammary gland biology and neoplasia.* 2005; *10*(2): 181-187.

[83] Tornos, C., Silva, E., El-Naggar, A., & Pritzker, K. P. H. Calcium oxalate crystals in breast biopsies. *Am J Surg Pathol.* 1990; *14*(10): 961-968.

[84] Saha, A., Barman, I., Dingari, N. C., McGee, S., Volynskaya, Z., Galindo, L. H., et al. Raman spectroscopy: a real-time tool for identifying microcalcifications during stereotactic breast core needle biopsies. *Biomedical optics express.* 2011; *2*(10): 2792-2803.

[85] Zhang, J., Wang, L., & Putnis, C. V. Underlying Role of Brushite in Pathological Mineralization of Hydroxyapatite. *The Journal of Physical Chemistry B.* 2019; *123*(13): 2874-2881.

[86] Johnsson, M. S. A., & Nancollas, G. H. The role of brushite and octacalcium phosphate in apatite formation. *Critical Reviews in Oral Biology & Medicine*. 1992; *3*(1): 61-82.

[87] Damaghi, M., Wojtkowiak, J. W., & Gillies, R. J. pH sensing and regulation in cancer. *Frontiers in physiology*. 2013; *4*: 370.

[88] Radi, M. J. Calcium oxalate crystals in breast biopsies. An overlooked form of microcalcification associated with benign breast disease. *Archives of pathology & laboratory medicine*. 1989; *113*(12): 1367-1369.

[89] Winston, J. S., Yeh, I. T., Evers, K., & Friedman, A. K. Calcium oxalate is associated with benign breast tissue: can we avoid biopsy? *American journal of clinical pathology*. 1993; *100*(5): 488-492.

[90] Clemenceau, A., Michou, L., Diorio, C., & Durocher, F. Breast Cancer and Microcalcifications: An Osteoimmunological Disorder? *International Journal of Molecular Sciences*. 2020; *21*(22): 8613.

[91] Scott, R., Kendall, C., Stone, N., & Rogers, K. Elemental vs. phase composition of breast calcifications. *Scientific reports*. 2017; *7*(1): 136.

[92] O'Grady, S., & Morgan, M. P. Microcalcifications in breast cancer: From pathophysiology to diagnosis and prognosis. *Biochimica et Biophysica Acta (BBA)-Reviews on Cancer*. 2018; *1869*(2): 310-320.

[93] Cox, R. F., & Morgan, M. P. Microcalcifications in breast cancer: Lessons from physiological mineralization. *Bone.* 2013; *53*(2): 437-450.

[94] Cox, R. F., Jenkinson, A., Pohl, K., O'Brien, F. J., & Morgan, M. P. Osteomimicry of mammary adenocarcinoma cells in vitro; increased expression of bone matrix proteins and proliferation within a 3D collagen environment. *PLoS One*. 2012; *7*(7): e41679.

[95] Langenbach, F., & Handschel, J. Effects of dexamethasone, ascorbic acid and β-glycerophosphate on the osteogenic differentiation of stem cells in vitro. *Stem cell research & therapy*. 2013; *4*(5): 117.

[96] O'Grady, S., & Morgan, M. P. Deposition of calcium in an in vitro model of human breast tumor calcification reveals functional role for ALP activity, altered expression of osteogenic genes and dysregulation of the TRPM7 ion channel. *Scientific reports*. 2019; *9*(1): 542.

[97] Vidavsky, N., Kunitake, J. A., Chiou, A. E., Northrup, P. A., Porri, T. J., Ling, L et al. Studying biomineralization pathways in a 3D culture model of breast cancer microcalcifications. *Biomaterials*. 2018; *179*: 71-82.

[98] Bellahcene, A., & Castronovo, V. Increased expression of osteonectin and osteopontin, two bone matrix proteins, in human breast cancer. *The American journal of pathology*. 1995; *146*(1): 95.

[99] Scimeca, M., Antonacci, C., Toschi, N., Giannini, E., Bonfiglio, R., Buonomo, C. O., et al. Breast osteoblast-like cells: A reliable early marker for bone metastases from breast cancer. *Clinical breast cancer*. 2018; *18*(4): e659-e669.

[100] Scimeca, M., Giannini, E., Antonacci, C., Pistolese, C. A., Spagnoli, L. G., & Bonanno, E. Microcalcifications in breast cancer: an active phenomenon mediated by epithelial cells with mesenchymal characteristics. *BMC cancer*. 2014; *14*(1): 286.

[101] Alarmo, E. L., Pärssinen, J., Ketolainen, J. M., Savinainen, K., Karhu, R., & Kallioniemi, A. BMP7 influences proliferation, migration, and invasion of breast cancer cells. *Cancer letters*. 2009; *275*(1): 35-43.

[102] Bailey, J. M., Singh, P. K., & Hollingsworth, M. A. Cancer metastasis facilitated by developmental pathways: Sonic hedgehog, Notch, and bone morphogenic proteins. *Journal of cellular biochemistry*. 2007; *102*(4): 829-839.

[103] Sharma, T., Radosevich, J. A., Pachori, G., & Mandal, C. C. A molecular view of pathological microcalcification in breast cancer. *Journal of mammary gland biology and neoplasia*. 2016; *21*(1-2): 25-40.

[104] Mori, K., Emoto, M., & Inaba, M. Fetuin-A: a multifunctional protein. *Recent patents on endocrine, metabolic & immune drug discovery*. 2011; *5*(2): 124-146.

[105] Heiss, A., DuChesne, A., Denecke, B., Grötzinger, J., Yamamoto, K., Renné, T., & Jahnen-Dechent, W. Structural basis of calcification inhibition by α2-HS glycoprotein/fetuin-A formation of colloidal calciprotein particles. *Journal of Biological Chemistry.* 2003; *278*(15): 13333-13341.

[106] Mostaghaci, B., Loretz, B., & Lehr, C. M. Calcium phosphate system for gene delivery: historical background and emerging opportunities. *Current pharmaceutical design*. 2016; *22*(11): 1529-1533.

[107] Sokolova, V., & Epple, M. Biological and medical applications of calcium phosphate nanoparticles. *Chemistry–A European Journal*. 2021.

[108] Awasthi, S., Pandey, S. K., Arunan, E., & Srivastava, C. A review on hydroxyapatite coatings for the biomedical applications: experimental and theoretical perspectives. *Journal of Materials Chemistry B*. 2020.

[109] Dorozhkin, S. V., & Epple, M. Biological and medical significance of calcium phosphates. *Angewandte Chemie International Edition*. 2002; *41*(17): 3130-3146.

[110] Rivas, M., Del Valle, L. J., Rodríguez-Rivero, A. M., Turon, P., Puiggalí, J., & Alemán, C. Loading of antibiotic into biocoated hydroxyapatite nanoparticles: smart antitumor platforms with regulated release. *ACS biomaterials science & engineering*. 2018; *4*(9): 3234-3245.

[111] Francis, M. D., & Webb, N. C. Hydroxyapatite formation from a hydrated calcium monohydrogen phosphate precursor. *Calcified tissue research*. 1970; *6*(1): 335-342.

[112] Scott, R., Stone, N., Kendall, C., Geraki, K., & Rogers, K. Relationships between pathology and crystal structure in breast calcifications: an in situ X-ray diffraction study in histological sections. *NPJ breast cancer*. 2016; *2*: 16029.

[113] Mandel, S., & Tas, A. C. Brushite (CaHPO4· 2H2O) to octacalcium phosphate (Ca8 (HPO4) 2 (PO4) 4· 5H2O) transformation in DMEM solutions at 36.5° C. *Materials Science and Engineering: C*. 2010; *30*(2): 245-254.

[114] Revilla-López, G., Casanovas, J., Bertran, O., Turon, P., Puiggalí, J., & Alemán, C. Modeling biominerals formed by apatites and DNA. *Biointerphases*. 2013; *8*(1): 10.

[115] Bertran O., del Valle L.J., Revilla-López G., Chaves G., Cardús L., Casas M.T., et al. Mineralization of DNA into nanoparticles of hydroxyapatite. *Dalton Transactions*. 2014; *43*(1): 317-327.

[116] Turon, P., Puiggalí, J., Bertrán, O., & Alemán, C. Surviving mass extinctions through biomineralized DNA. *Chemistry–A European Journal*. 2015; *21*(52): 18892-18898.

[117] del Valle, L. J., Bertran, O., Chaves, G., Revilla-López, G., Rivas, M., Casas, M. T., et al. DNA adsorbed on hydroxyapatite surfaces. *Journal of Materials Chemistry B*. 2014; *2*(40): 6953-6966.

[118] Ghita, A., Matousek, P., & Stone, N. High sensitivity non-invasive detection of calcifications deep inside biological tissue using Transmission Raman Spectroscopy. *Journal of biophotonics*. 2018; *11*(1): e201600260.

[119] Tschandl, P., Rinner, C., Apalla, Z., Argenziano, G., Codella, N., Halpern, A., et al. Human–computer collaboration for skin cancer recognition. *Nature Medicine*. 2020; *26*(8): 1229-1234.

[120] Rey-Barroso, L., Burgos-Fernández, F. J., Delpueyo, X., Ares, M., Royo, S., Malvehy, J., et al. Visible and extended near-infrared multispectral imaging for skin cancer diagnosis. *Sensors*. 2018; *18*(5): 1441.

[121] Gareau, D. S., Browning, J., Da Rosa, J. C., Suarez-Farinas, M., Lish, S., Zong, A. M., et al. Deep learning-level melanoma detection by interpretable machine learning and imaging biomarker cues. *Journal of biomedical optics*. 2020; *25*(11): 112906.

[122] Stremersch, S., Marro, M., Pinchasik, B. E., Baatsen, P., Hendrix, A., De Smedt, S. C., et al. Identification of individual exosome-like vesicles by surface enhanced raman spectroscopy. *Small*. 2016; *12*(24): 3292-3301.

[123] Gao, P., Han, B., Du, Y., Zhao, G., Yu, Z., Xu, W., et al. The clinical application of Raman spectroscopy for breast cancer detection. *Journal of Spectroscopy*, 2017.

[124] Notingher, I., Verrier, S., Romanska, H., Bishop, A. E., Polak, J. M., & Hench, L. L. In situ characterisation of living cells by Raman spectroscopy. *Spectroscopy*. 2002; *16*(2): 43-51.

[125] Chiang, Y. H., Wu, S. H., Kuo, Y. C., Chen, H. F., Chiou, A., & Lee, O. K. Raman spectroscopy for grading of live osteosarcoma cells. *Stem Cell Research & Therapy.* 2015; *6*(1): 81.

[126] Bilal, M., Bilal, M., Tabassum, S., Saleem, M., Mahmood, H., Sarwar, U., et al. Optical screening of female breast cancer from whole blood using Raman spectroscopy. *Applied spectroscopy*. 2017; *71*(5): 1004-1013.

[127] Nieva, C., Marro, M., Santana-Codina, N., Rao, S., Petrov, D., & Sierra, A. The lipid phenotype of breast cancer cells characterized by Raman microspectroscopy: towards a stratification of malignancy. *PloS one*. 2012; *7*(10): e46456.

[128] Marro, M., Nieva, C., Sanz-Pamplona, R., & Sierra, A. Molecular monitoring of epithelial-to-mesenchymal transition in breast cancer cells by means of Raman spectroscopy. *Biochimica et Biophysica Acta (BBA)-Molecular Cell Research.* 2014; *1843*(9): 1785-1795.

[129] Haka, A. S., Shafer-Peltier, K. E., Fitzmaurice, M., Crowe, J., Dasari, R. R., & Feld, M. S. Diagnosing breast cancer by using Raman spectroscopy. *Proceedings of the National Academy of Sciences.* 2005; *102*(35): 12371-12376.

[130] Haka, A. S., Volynskaya, Z. I., Gardecki, J. A., Nazemi, J., Shenk, R., Wang, N., et al. Diagnosing breast cancer using Raman spectroscopy: prospective analysis. *Journal of biomedical optics*. 2009; *14*(5): 054023.

[131] Brozek-Pluska, B., Musial, J., Kordek, R., Bailo, E., Dieing, T., & Abramczyk, H. Raman spectroscopy and imaging: applications in human breast cancer diagnosis. *Analyst*. 2012; *137*(16): 3773-3780.

[132] Abramczyk, H., & Brozek-Pluska, B. Raman imaging in biochemical and biomedical applications. Diagnosis and treatment of breast cancer. *Chemical reviews.* 2013; *113*(8): 5766-5781.

[133] Haka, A. S., Volynskaya, Z., Gardecki, J. A., Nazemi, J., Lyons, J., Hicks, D., et al. In vivo margin assessment during partial mastectomy breast surgery using Raman spectroscopy. *Cancer research*. 2006; *66*(6): 3317-3322.

[134] Shafer-Peltier, K. E., Haka, A. S., Fitzmaurice, M., Crowe, J., Myles, J., Dasari, R. R., & Feld, M. S. Raman microspectroscopic model of human breast tissue: implications for breast cancer diagnosis in vivo. *Journal of Raman Spectroscopy*. 2002; *33*(7): 552-563.

[135] Stone, N., & Matousek, P. Advanced transmission Raman spectroscopy: a promising tool for breast disease diagnosis. *Cancer Research*. 2008; *68*(11): 4424-4430.

[136] Kerssens, M. M., Matousek, P., Rogers, K., & Stone, N. Towards a safe non-invasive method for evaluating the carbonate substitution levels of hydroxyapatite (HAP) in micro-calcifications found in breast tissue. *Analyst*. 2010; *135*(12): 3156-3161.

[137] Tonannavar, J., Deshpande, G., Yenagi, J., Patil, S. B., Patil, N. A., & Mulimani, B. G. Identification of mineral compositions in some renal calculi by FT Raman and IR spectral analysis. *Spectrochimica Acta Part A: Molecular and Biomolecular Spectroscopy.* 2016; *154:* 20-26.

[138] Anguela, X. M., & High, K. A. Entering the modern era of gene therapy. *Annual review of medicine*. 2019; *70*: 273-288.

[139] Dunbar, C. E., High, K. A., Joung, J. K., Kohn, D. B., Ozawa, K., & Sadelain, M. Gene therapy comes of age. *Science*. 2018; *359*:6372.

[140] Noguchi, P. Risks and benefits of gene therapy. *New England Journal of Medicine.* 2003; *348*(3): 193-194.

[141] Kimmelman, J. Recent developments in gene transfer: risk and ethics. *Bmj*. 2005; *330*(7482): 79-82.

[142] Ragusa, A., García, I., & Penadés, S. Nanoparticles as nonviral gene delivery vectors. *IEEE transactions on nanobioscience.* 2007; *6*(4): 319-330.

[143] Lee, D., Upadhye, K., & Kumta, P. N. Nano-sized calcium phosphate (CaP) carriers for non-viral gene deilvery. *Materials Science and Engineering: B*. 2012; *177*(3): 289-302.

[144] Ridi, F., Meazzini, I., Castroflorio, B., Bonini, M., Berti, D., & Baglioni, P. Functional calcium phosphate composites in nanomedicine. *Advances in Colloid and Interface Science*. 2017; *244*: 281-295.

[145] Sokolova, V., & Epple, M. Inorganic nanoparticles as carriers of nucleic acids into cells. *Angewandte chemie international edition*. 2008; *47*(8): 1382-1395.

[146] Kim, T. K., & Eberwine, J. H. Mammalian cell transfection: the present and the future. *Analytical and bioanalytical chemistry*. 2010; *397*(8): 3173-3178.

[148] Kaestner, L., Scholz, A., & Lipp, P. Conceptual and technical aspects of transfection and gene delivery. *Bioorganic & medicinal chemistry letters*. 2015; *25*(6): 1171-1176.

[149] Keles, E., Song, Y., Du, D., Dong, W. J., & Lin, Y. Recent progress in nanomaterials for gene delivery applications. *Biomaterials science*. 2016; *4*(9): 1291-1309.

[150] Yin, H., Kanasty, R. L., Eltoukhy, A. A., Vegas, A. J., Dorkin, J. R., & Anderson, D. G. Non-viral vectors for gene-based therapy. *Nature Reviews Genetics*. 2014; *15*(8): 541.

[151] Pouton, C. W., & Seymour, L. W. Key issues in non-viral gene delivery. *Advanced drug delivery reviews*. 2001; *46*(1-3): 187-203.

[152] Kawabata, K., Takakura, Y., & Hashida, M. The fate of plasmid DNA after intravenous injection in mice: involvement of scavenger receptors in its hepatic uptake. *Pharmaceutical research*. 1995; *12*(6): 825-830.

[153] Wolff, J. A., & Budker, V. The mechanism of naked DNA uptake and expression. *Advances in genetics*. 2005; *54:* 1-20.

[154] Bergsmedh, A., Szeles, A., Henriksson, M., Bratt, A., Folkman, M. J., Spetz, A. L., & Holmgren, L. Horizontal transfer of oncogenes by uptake of apoptotic bodies. *Proceedings of the National Academy of Sciences*. 2001; *98*(11): 6407-6411.

[155] Mintzer, M. A., & Simanek, E. E. Nonviral vectors for gene delivery. *Chemical reviews*. 2009; *109*(2): 259-302.

[156] Gigante, A., Li, M., Junghänel, S., Hirschhäuser, C., Knauer, S., & Schmuck, C. Non-viral transfection vectors: are hybrid materials the way forward? *Medchemcomm*. 2019; *10*(10): 1692-1718.

[157] Ramamoorth, M., & Narvekar, A. Non viral vectors in gene therapy-an overview. *Journal of clinical and diagnostic research: JCDR.* 2015; *9*(1): GE01.

[158] Graham, F. L., & van der Eb, A. J. A new technique for the assay of infectivity of human adenovirus 5 DNA. *Virology*. 1973; *52*(2): 456-467.

[159] Alexander, H. E., Koch, G., Mountain, I. M., & Van Damme, O. Infectivity of ribonucleic acid from poliovirus in human cell monolayers. *The Journal of experimental medicine*. 1958; *108*(4): 493.

[160] Vaheri, A., & Pagano, J. S. Infectious poliovirus RNA: a sensitive method of assay. *Virology*. 1965; *27*(3): 434-6.

[161] Maleki Dizaj, S., Barzegar-Jalali, M., Zarrintan, M. H., Adibkia, K., & Lotfipour, F. Calcium carbonate nanoparticles as cancer drug delivery system. *Expert opinion on drug delivery*. 2015; *12*(10): 1649-1660.

[162] Sarda, S., Errassifi, F., Marsan, O., Geffre, A., Trumel, C., & Drouet, C. Adsorption of tranexamic acid on hydroxyapatite: Toward the development of biomaterials with local hemostatic activity. *Materials Science and Engineering: C*. 2016; *66*: 1-7.

[163] McCrudden, C. M., & McCarthy, H. O. Current status of gene therapy for breast cancer: progress and challenges. *The application of clinical genetics*. 2014; *7*: 209.

[164] Cao, X., Deng, W., Wei, Y., Su, W., Yang, Y., Wei, Y., et al. Encapsulation of plasmid DNA in calcium phosphate nanoparticles: stem cell uptake and gene transfer efficiency. *International journal of nanomedicine*. 2011; *6*: 3335.

[165] Han, Y., Li, S., Cao, X., Yuan, L., Wang, Y., Yin, Y., et al. Different inhibitory effect and mechanism of hydroxyapatite nanoparticles on normal cells and cancer cells in vitro and in vivo. *Scientific reports*. 2014; *4*: 7134.

[166] Chowdhury, E. H., & Akaike, T. High performance DNA nano-carriers of carbonate apatite: multiple factors in regulation of particle synthesis and transfection efficiency. *International journal of nanomedicine*. 2007; *2*(1): 101.

[167] Chen, L., Mccrate, J. M., Lee, J. C., & Li, H. The role of surface charge on the uptake and biocompatibility of hydroxyapatite nanoparticles with osteoblast cells. *Nanotechnology*. 2011; *22*(10): 105708.

[168] Bisht, S., Bhakta, G., Mitra, S., & Maitra, A. pDNA loaded calcium phosphate nanoparticles: highly efficient non-viral vector for gene delivery. *International journal of pharmaceutics*. 2005; *288*(1): 157-168.

[169] Blanco, E., Shen, H., & Ferrari, M. Principles of nanoparticle design for overcoming biological barriers to drug delivery. *Nature biotechnology*. 2015; *33*(9): 941.

[170] Sokolova, V. V., Radtke, I., Heumann, R., & Epple, M. Effective transfection of cells with multi-shell calcium phosphate-DNA nanoparticles. *Biomaterials*. 2006; *27*(16): 3147-3153.

[171] Xie, Y., Chen, Y., Sun, M., & Ping, Q. A mini review of biodegradable calcium phosphate nanoparticles for gene delivery. *Current pharmaceutical biotechnology.* 2013; *14*(10): 918-925.

[172] Keller, M. Lipidic carriers of RNA/DNA oligonucleotides and polynucleotides: What a difference a formulation makes! *Journal of controlled release*. 2005; *103*(3): 537-540.

[173] Olton, D. Y., Close, J. M., Sfeir, C. S., & Kumta, P. N. Intracellular trafficking pathways involved in the gene transfer of nano-structured calcium phosphate-DNA particles. *Biomaterials*. 2011; *32*(30): 7662-7670.

[174] Batard, P., Jordan, M., & Wurm, F. Transfer of high copy number plasmid into mammalian cells by calcium phosphate transfection. *Gene*. 2001; *270*(1-2): 61-68.

[175] Giger, E. V., Castagner, B., Räikkönen, J., Mönkkönen, J., & Leroux, J. C. siRNA transfection with calcium phosphate nanoparticles stabilized with PEGylated chelators. *Advanced healthcare materials*. 2013; *2*(1): 134-144.

[176] Bertran, O., Revilla-López, G., Casanovas, J., del Valle, L. J., Turon, P., Puiggalí, J., & Alemán, C. Dissolving hydroxyolite: A DNA molecule into its hydroxyapatite mold. *Chemistry–A European Journal*. 2016; *22*(19): 6631-6636.

[177] Liang, W., & Lam, J. K. Endosomal escape pathways for non-viral nucleic acid delivery systems. *Molecular regulation of endocytosis*. 2012: 429-456.

[178] Jordan, M., Schallhorn, A., & Wurm, F. M. Transfecting mammalian cells: optimization of critical parameters affecting calcium-phosphate precipitate formation. *Nucleic acids research*. 1996; *24*(4): 596-601.

[179] Lechardeur, D., Verkman, A. S., & Lukacs, G. L. Intracellular routing of plasmid DNA during non-viral gene transfer. *Advanced drug delivery reviews*. 2005; *57*(5): 755-767.

[180] Santos, J., Pandita, D., Rodrigues, J., P Pego, A., L Granja, P., & Tomás, H. Non-viral gene delivery to mesenchymal stem cells: methods, strategies and application in bone tissue engineering and regeneration. *Current gene therapy*. 2011; *11*(1): 46-57.

[181] Grosjean, F., Batard, P., Jordan, M., & Wurm, F. M. S-phase synchronized CHO cells show elevated transfection efficiency and expression using CaPi. *Cytotechnology*. 2002; *38*(1-3): 57-62.

[182] Epple, M., Ganesan, K., Heumann, R., Klesing, J., Kovtun, A., Neumann, S., & Sokolova, V. J. J. C. Application of calcium phosphate nanoparticles in biomedicine. *Journal of Materials Chemistry*. 2010; *20*(1): 18-23.

[183] Olton, D. Y., Close, J. M., Sfeir, C. S., & Kumta, P. N. Intracellular trafficking pathways involved in the gene transfer of nano-structured calcium phosphate-DNA particles. *Biomaterials*. 2011; *32*(30): 7662-7670.

[184] Song, W., & Lahiri, D. K. Efficient transfection of DNA by mixing cells in suspension with calcium phosphate. *Nucleic acids research*. 1995; *23*(17): 3609.

[185] Khan, M. A., Wu, V. M., Ghosh, S., & Uskoković, V. Gene delivery using calcium phosphate nanoparticles: optimization of the transfection process and the effects of citrate and poly (L-lysine) as additives. *Journal of colloid and interface science.* 2016; *471:* 48-58.

[186] Choi, S., Yu, X., Jongpaiboonkit, L., Hollister, S. J., & Murphy, W. L. Inorganic coatings for optimized non-viral transfection of stem cells. *Scientific reports*. 2013; *3:* 1567.

[187] Salimzadeh, L., Jaberipour, M., Hosseini, A., & Ghaderi, A. Non-viral transfection methods optimized for gene delivery to a lung cancer cell line. *Avicenna journal of medical biotechnology*. 2013; *5*(2): 68.

[188] Orrantia, E., & Chang, P. L. Intracellular distribution of DNA internalized through calcium phosphate precipitation. *Experimental cell research*. 1990; *190*(2): 170-174.

[189] Roy, I., Mitra, S., Maitra, A., & Mozumdar, S. Calcium phosphate nanoparticles as novel non-viral vectors for targeted gene delivery. *International Journal of Pharmaceutics.* 2003; *250*(1): 25-33.

[190] Sokolova, V., Kozlova, D., Knuschke, T., Buer, J., Westendorf, A. M., & Epple, M. Mechanism of the uptake of cationic and anionic calcium phosphate nanoparticles by cells. *Acta biomaterialia*. 2013; *9*(7): 7527-7535.

[191] Turon, P., del Valle, L. J., Alemán, C., & Puiggalí, J. Biodegradable and Biocompatible Systems Based on Hydroxyapatite Nanoparticles. *Applied Sciences*. 2017; *7*(1): 60.

[192] Sambrook, J., & Russell, D. W. Calcium-phosphate-mediated transfection of eukaryotic cells with plasmid DNAs. *Cold Spring Harbor Protocols.* 2006; (1): pdb-prot3871.

[193] Kirchenbuechler, I., Kirchenbuechler, D., & Elbaum, M. Correlation between cationic lipid-based transfection and cell division. *Experimental cell research.* 2016; *345*(1): 1-5.

[194] Chernousova, S., & Epple, M. Live-cell imaging to compare the transfection and gene silencing efficiency of calcium phosphate nanoparticles and a liposomal transfection agent. *Gene Therapy*. 2017; *24*(5): 282-289.

[195] Epple, M., Ganesan, K., Heumann, R., Klesing, J., Kovtun, A., Neumann, S., & Sokolova, V. Application of calcium phosphate nanoparticles in biomedicine. *Journal of Materials Chemistry*. 2010; *20*(1): 18-23.

[196] Chowdhury, E. H., Maruyama, A., Kano, A., Nagaoka, M., Kotaka, M., Hirose, S., et al. pH-sensing nano-crystals of carbonate apatite: effects on intracellular delivery and release of DNA for efficient expression into mammalian cells. *Gene*. 2006; *376*(1): 87-94.

[197] Frayssinet, P., Rouquet, N., & Mathon, D. Bone cell transfection in tissue culture using hydroxyapatite microparticles. *Journal of Biomedical Materials Research Part A: An Official Journal of The Society for Biomaterials, The Japanese Society for Biomaterials, and The Australian Society for Biomaterials and the Korean Society for Biomaterials*. 2006; *79*(2): 225-228.

[198] Zhao, M., Li, J., Chen, D., & Hu, H. A Valid Bisphosphonate Modified Calcium Phosphate-Based Gene Delivery System: Increased Stability and Enhanced Transfection Efficiency In Vitro and In Vivo. *Pharmaceutics*. 2019; *11*(9): 468.

[199] Zhang, L. J., Liu, H. G., Feng, X. S., Zhang, R. J., Zhang, L., Mu, Y. D., et al. Mineralization mechanism of calcium phosphates under three kinds of Langmuir monolayers. *Langmuir*. 2004; *20*(6): 2243-2249.

[200] Cohrs, R. J., Martin, T., Ghahramani, P., Bidaut, L., Higgins, P. J., & Shahzad, A. Translational medicine definition by the European Society for Translational Medicine. 2015.

[201] Ozin, G. A. Morphogenesis of biomineral and morphosynthesis of biomimetic forms. *Accounts of Chemical Research*. 1997; *30*(1): 17-27.

[202] Wolf, S. G., Frenkiel, D., Arad, T., Finkel, S. E., Kolter, R., & Minsky, A. DNA protection by stress-induced biocrystallization. *Nature*. 1999; *400*(6739): 83-85.

[203] Krupyanskii, Y. F., Loiko, N. G., Sinitsyn, D. O., Tereshkina, K. B., Tereshkin, E. V., Frolov, I. A., et al. Biocrystallization in bacterial and fungal cells and spores. *Crystallography Reports.* 2018; *63*(4): 594-599.

[204] Kachroo, A. H. Order in stress—Lessons from the inanimate world. *Journal of Biosciences.* 2004; *29*(4): 369-372.

[205] Bertran, O., Valle, L. J. D., Revilla-López, G., Rivas, M., Chaves, G., Casas, M. T., et al. Synergistic approach to elucidate the incorporation of magnesium ions into hydroxyapatite. *Chemistry–A European Journal*. 2015; *21*(6): 2537-2546.

[206] Casanovas, J., Revilla-López, G., Bertran, O., Del Valle, L. J., Turon, P., Puiggalí, J., & Alemán, C. Restricted puckering of mineralized RNA-like riboses. *The Journal of Physical Chemistry B.* 2014; *118*(19): 5075-5081.

[207] Kovtun, A., Heumann, R., & Epple, M. Calcium phosphate nanoparticles for the transfection of cells. *Bio-medical materials and engineering.* 2009; *19*(2-3): 241-247.

[208] Kalantari, F., Miao, D., Emadali, A., Tzimas, G. N., Goltzman, D., Vali, H., et al. Cellular and molecular mechanisms of abnormal calcification following ischemia–reperfusion injury in human liver transplantation. *Modern pathology*. 2007; *20*(3): 357-366.

[209] Gajdos, C., Tartter, P. I., Bleiweiss, I. J., Hermann, G., de Csepel, J., Estabrook, A., & Rademaker, A. W. Mammographic appearance of nonpalpable breast cancer reflects pathologic characteristics. *Annals of surgery*. 2002; *235*(2): 246.

[210] Cox, R. F., Hernandez-Santana, A., Ramdass, S., McMahon, G., Harmey, J. H., & Morgan, M. P. Microcalcifications in breast cancer: novel insights into the molecular mechanism and functional consequence of mammary mineralisation. *British journal of cancer*. 2012; *106*(3): 525-537.

[211] Stomper, P. C., & Connolly, J. L. Ductal carcinoma in situ of the breast: correlation between mammographic calcification and tumor subtype. *AJR. American journal of roentgenology*. 1992; *159*(3): 483-485.

[212] Gary, M. T., Tan, P. H., Cheung, H. S., Chu, W. C., & Lam, W. W. Intermediate to highly suspicious calcification in breast lesions: a radio-pathologic correlation. *Breast cancer research and treatment*. 2008; *110*(1): 1-7.

[213] Movasaghi, Z., Rehman, S., & Rehman, I. U. Raman spectroscopy of biological tissues. *Applied Spectroscopy Reviews*. 2007; *42*(5): 493-541.

[214] Caspers, P. J., Lucassen, G. W., Carter, E. A., Bruining, H. A., & Puppels, G. J. In vivo confocal Raman microspectroscopy of the skin: noninvasive determination of molecular concentration profiles. *Journal of Investigative Dermatology*. 2001; *116*(3): 434-442.

[215] Luo, D., & Saltzman, W. M. Synthetic DNA delivery systems. *Nature biotechnology.* 2000; *18*(1): 33-37.

[216] Labhasetwar, V., Bonadio, J., Goldstein, S. A., & Levy, R. J. Gene transfection using biodegradable nanospheres: results in tissue culture and a rat osteotomy model. *Colloids and Surfaces B: Biointerfaces*. 1999; *16*(1): 281-290.

[217] Gaumet, M., Vargas, A., Gurny, R., & Delie, F. Nanoparticles for drug delivery: the need for precision in reporting particle size parameters. *European Journal of Pharmaceutics and Biopharmaceutics*. 2008; *69*(1): 1-9.

[218] Peeters, L., Sanders, N. N., Braeckmans, K., Boussery, K., Van de Voorde, J., De Smedt, S. C., & Demeester, J. Vitreous: a barrier to nonviral ocular gene therapy. *Investigative Ophthalmology and Visual Science*. 2005; *46*(10): 3553.

[219] Rivas, M., Casanovas, J., del Valle, L. J., Bertran, O., Revilla-López, G., Turon, P., et al. An experimental-computer modeling study of inorganic phosphates surface adsorption on hydroxyapatite particles. *Dalton Transactions*. 2015; *44*(21): 9980-9991.

[220] Kumta, P. N., Sfeir, C., Lee, D. H., Olton, D., & Choi, D. Nanostructured calcium phosphates for biomedical applications: novel synthesis and characterization. *Acta Biomaterialia*. 2005; *1*(1): 65-83.

[221] De Aza, P. N., Guitian, F., Santos, C., De Aza, S., Cusco, R., & Artus, L. Vibrational properties of calcium phosphate compounds. 2. Comparison between hydroxyapatite and β-tricalcium phosphate. *Chemistry of Materials*. 1997; *9*(4): 916-922.

[222] Markovic, M., Fowler, B. O., & Tung, M. S. Preparation and comprehensive characterization of a calcium hydroxyapatite reference material. *Journal of research of the National Institute of Standards and Technology*. 2004; *109*(6): 553.

[223] Chandra, G. K., Eklouh-Molinier, C., Fere, M., Angiboust, J. F., Gobinet, C., Van-Gulick, L., et al. Probing in vitro ribose induced DNA-glycation using Raman microspectroscopy. *Analytical chemistry*. 2015; *87*(5): 2655-2664.

[224] Han, Y., Han, L., Yao, Y., Li, Y., & Liu, X. Key factors in FTIR spectroscopic analysis of DNA: the sampling technique, pretreatment temperature and sample concentration. *Analytical Methods*. 2018; *10*(21): 2436-2443.

[225] Mkhonto, D., & de Leeuw, N. H. A computer modelling study of the effect of water on the surface structure and morphology of fluorapatite: introducing a Ca10(PO4)6F2 potential model. *Journal of Materials Chemistry*. 2002; *12*(9): 2633-2642.

[226] Di Tommaso, D., Hernández, S. E. R., Du, Z., & de Leeuw, N. H. Density functional theory and interatomic potential study of structural, mechanical and surface properties of calcium oxalate materials. *RSC advances.* 2012; *2*(11): 4664-4674.

[227] Almora-Barrios, N., Austen, K. F., & de Leeuw, N. H. Density functional theory study of the binding of glycine, proline, and hydroxyproline to the hydroxyapatite (0001) and (0110) surfaces. *Langmuir*. 2009; *25*(9): 5018-5025.

[228] Filgueiras, M. R. T., Mkhonto, D., & de Leeuw, N. D. Computer simulations of the adsorption of citric acid at hydroxyapatite surfaces. *Journal of crystal growth*. 2006; *294*(1): 60-68.

[229] De Leeuw, N. H., & Rabone, J. A. L. Molecular dynamics simulations of the interaction of citric acid with the hydroxyapatite (0001) and (0110) surfaces in an aqueous environment. *CrystEngComm*. 2007; *9*(12): 1178-1186.

[230] Sandersius, S., & Rez, P. Morphology of crystals in calcium oxalate monohydrate kidney stones. *Urological research*. 2007; *35*(6): 287-293.

[231] Sheng, X., Jung, T., Wesson, J. A., & Ward, M. D. Adhesion at calcium oxalate crystal surfaces and the effect of urinary constituents. *Proceedings of the National Academy of Sciences.* 2005; *102*(2): 267-272.

[232] Zaheer, A., Murshed, M., De Grand, A. M., Morgan, T. G., Karsenty, G., & Frangioni, J. V. Optical imaging of hydroxyapatite in the calcified vasculature of transgenic animals. *Arteriosclerosis, thrombosis, and vascular biology*. 2006; *26*(5): 1132-1136.

[233] Mizrahi, D. M., Ziv-Polat, O., Perlstein, B., Gluz, E., & Margel, S. Synthesis, fluorescence and biodistribution of a bone-targeted near-infrared conjugate. *European journal of medicinal chemistry*. 2011; *46*(10): 5175-5183.

[234] Nadar, R. A., Margiotta, N., Iafisco, M., van den Beucken, J. J., Boerman, O. C., & Leeuwenburgh, S. C. Bisphosphonate-functionalized imaging agents, anti-tumor agents and nanocarriers for treatment of bone cancer. *Advanced healthcare materials.* 2017; *6*(8): 1601119.

[235] Martin, R. M., Leonhardt, H., & Cardoso, M. C. DNA labeling in living cells. *Cytometry Part A: the journal of the International Society for Analytical Cytology*. 2005; *67*(1): 45-52.

[236] Sato, T., Ishii, T., & Okahata, Y. In vitro gene delivery mediated by chitosan. Effect of pH, serum, and molecular mass of chitosan on the transfection efficiency. *Biomaterials*. 2001; *22*(15): 2075-2080.

[237] Feng, X., Tang, Y., Duan, X., Liu, L., & Wang, S. Lipid-modified conjugated polymer nanoparticles for cell imaging and transfection. *Journal of Materials Chemistry*. 2010; *20*(7): 1312-1316.

[238] Gao, X., & Huang, L. A novel cationic liposome reagent for efficient transfection of mammalian cells. *Biochemical and biophysical research communications*. 1991; *179*(1): 280-285.

[239] Pedraza, C. E., Bassett, D. C., McKee, M. D., Nelea, V., Gbureck, U., & Barralet, J. E. The importance of particle size and DNA condensation salt for calcium phosphate nanoparticle transfection. *Biomaterials*. 2008; *29*(23): 3384-3392.

[240] Chowdhury, E. H., Megumi, K., Harada, I., Kundu, A. K., & Akaike, T. Dramatic effect of Mg^{2+} on transfecting mammalian cells by DNA/calcium phosphate precipitates. *Analytical biochemistry*. 2004; *1*(328): 96-97.

[241] Riley, J. M., Kim, H., Averch, T. D., & Kim, H. J. Effect of magnesium on calcium and oxalate ion binding. *Journal of Endourology*. 2013; *27*(12): 1487-1492.

[242] Weinbach, E. C., & von Brand, T. Formation, isolation and composition of dense granules from mitochondria. *Biochimica et Biophysica Acta (BBA)-General Subjects.* 1967; *148*(1): 256-266.

[243] Tsolaki, E., & Bertazzo, S. Pathological Mineralization: The Potential of Mineralomics. *Materials*. 2019; *12*(19): 3126.

[244] Chinopoulos, C., & Adam-Vizi, V. Mitochondrial Ca2+ sequestration and precipitation revisited. *The FEBS journal*. 2010; *277*(18): 3637-3651.

[245] Bonfiglio, R., Scimeca, M., Urbano, N., Bonanno, E., & Schillaci, O. Breast microcalcifications: Biological and diagnostic perspectives. 2018: 3097-3099.

[246] Baker, R., Matousek, P., Ronayne, K. L., Parker, A. W., Rogers, K., & Stone, N. Depth profiling of calcifications in breast tissue using picosecond Kerr-gated Raman spectroscopy. *Analyst*. 2007; *132*(1): 48-53.

[247] Liang, L., Zheng, C., Zhang, H., Xu, S., Zhang, Z., Hu, C., et al. Exploring type II microcalcifications in benign and premalignant breast lesions by shell-isolated nanoparticle-enhanced Raman spectroscopy (SHINERS). *Spectrochimica Acta Part A: Molecular and Biomolecular Spectroscopy*. 2014; *132*: 397-402.

[248] Sathyavathi, R., Saha, A., Soares, J. S., Spegazzini, N., McGee, S., Dasari, R. R., et al. Raman spectroscopic sensing of carbonate intercalation in breast microcalcifications at stereotactic biopsy. *Scientific reports*. 2015; *5*(1): 1-12.

[249] Kunitake, J. A., Choi, S., Nguyen, K. X., Lee, M. M., He, F., Sudilovsky, D., et al. Correlative imaging reveals physiochemical heterogeneity of microcalcifications in human breast carcinomas. *Journal of structural biology*. 2018; *202*(1): 25-34.

[250] Lyng, F. M., Traynor, D., Nguyen, T. N. Q., Meade, A. D., Rakib, F., Al-Saady, R., et al. Discrimination of breast cancer from benign tumors using Raman spectroscopy. *PLoS One*. 2019; *14*(2): e0212376.

[251] Yang, H., Irudayaraj, J., & Paradkar, M. M. Discriminant analysis of edible oils and fats by FTIR, FT-NIR and FT-Raman spectroscopy. *Food Chemistry*. 2005; *93*(1): 25-32.

[252] Gullekson, C., Lucas, L., Hewitt, K., & Kreplak, L. Surface-sensitive Raman spectroscopy of collagen I fibrils. *Biophysical journal*. 2011; *100*(7): 1837-1845.

[253] Hanlon, E. B., Manoharan, R., Koo, T., Shafer, K. E., Motz, J. T., Fitzmaurice, M., et al. Prospects for in vivo Raman spectroscopy. *Physics in Medicine & Biology*. 2000; *45*(2): R1.

[254] McEwen, G. D., Wu, Y., Tang, M., Qi, X., Xiao, Z., Baker, S. M., et al. Subcellular spectroscopic markers, topography and nanomechanics of human lung cancer and breast cancer cells examined by combined confocal Raman microspectroscopy and atomic force microscopy. *Analyst*. 2013; *138*(3): 787-797.

[255] Acri, T. M., Laird, N. Z., Geary, S. M., Salem, A. K., & Shin, K. Effects of calcium concentration on nonviral gene delivery to bone marrow-derived stem cells. *Journal of Tissue Engineering and Regenerative Medicine.* 2019; *13*(12): 2256-2265.

[256] Kulkarni, V. I., Shenoy, V. S., Dodiya, S. S., Rajyaguru, T. H., & Murthy, R. R. Role of calcium in gene delivery. *Expert Opinion on Drug Delivery*. 2006; *3*(2): 235-245.

[257] Truong-Le, V. L., Walsh, S. M., Schweibert, E., Mao, H. Q., Guggino, W. B., August, J. T., & Leong, K. W. Gene transfer by DNA–gelatin nanospheres. *Archives of Biochemistry and Biophysics*. 1999; *361*(1): 47-56.

[258] Haberland, A., Knaus, T., Zaitsev, S. V., Stahn, R., Mistry, A. R., Coutelle, C., et al. Calcium ions as efficient cofactor of polycation-mediated gene transfer. *Biochimica et Biophysica Acta (BBA)-Gene Structure and Expression.* 1999; *1445*(1): 21-30.

[259] Quamme, G. A. Renal handling of magnesium: drug and hormone interactions. *Magnesium*. 1986; *5*(5-6): 248-272.

[260] Castiglioni, S., & Maier, J. A. Magnesium and cancer: a dangerous liason. *Magnesium Research*. 2011; *24*(3): 92-100.

[261] Abed, E., & Moreau, R. Importance of melastatin-like transient receptor potential 7 and magnesium in the stimulation of osteoblast proliferation and migration by PDGF. *American Journal of Physiology-Cell Physiology*. 2009.

[262] Romaniuk, A. M., Lyndin, M. S., Moskalenko, R. A., Hortynska, O. M., & Lyndina, Y. M. The role of heavy metal salts in pathological biomineralization of breast cancer tissue. *Adv. Clin Exp Med.* 2016; *25*(5): 907-910.

[263] Wang, K. W., Zhou, L. Z., Sun, Y., Wu, G. J., Gu, H. C., Duan, Y. R., et al. Calcium phosphate/PLGA-mPEG hybrid porous nanospheres: A promising vector with ultrahigh gene loading and transfection efficiency. *Journal of Materials Chemistry*. 2010; *20*(6): 1161-1166.

[264] Cacciotti, I., Bianco, A., Lombardi, M., & Montanaro, L. Mg-substituted hydroxyapatite nanopowders: synthesis, thermal stability and sintering behaviour. *Journal of the European Ceramic Society*. 2009; *29*(14): 2969-2978.

[265] Xu, J., Bai, Y., Jin, J., Zhang, J., Zhang, S., Cui, L., & Zhang, H. Magnesium modulates the expression levels of calcification-associated factors to inhibit calcification in a time-dependent manner. *Experimental and therapeutic medicine*. 2015; *9*(3): 1028-1034.

[266] Castellaro, A. M., Tonda, A., Cejas, H. H., Ferreyra, H., Caputto, B. L., Pucci, O. A., & Gil, G. A. Oxalate induces breast cancer. *BMC cancer*. 2015; *15*(1): 1-13.

[267] Martin, H. M., Bateman, A. C., & Theaker, J. M. Calcium oxalate (Weddellite) crystals within ductal carcinoma in situ. *Journal of clinical pathology*. 1999; *52*(12): 932.

[268] Singh, N., & Theaker, J. M. Calcium oxalate crystals (Weddellite) within the secretions of ductal carcinoma in situ--a rare phenomenon. *Journal of clinical pathology*. 1999; *52*(2): 145-146.

[269] Gonzalez, J. E., Caldwell, R. G., & Valaitis, J. Calcium oxalate crystals in the breast. Pathology and significance. *The American journal of surgical pathology*. 1991; *15*(6): 586-591.

[270] Ruiz-Agudo, E., Burgos-Cara, A., Ruiz-Agudo, C., Ibañez-Velasco, A., Cölfen, H., & Rodriguez-Navarro, C. A non-classical view on calcium oxalate precipitation and the role of citrate. *Nature communications*. 2017; *8*(1): 1-10.

[271] Koul, S., Khandrika, L., Meacham, R. B., & Koul, H. K. Genome wide analysis of differentially expressed genes in HK-2 cells, a line of human kidney epithelial cells in response to oxalate. *PLoS One*. 2012; *7*(9): e43886.

[272] Huang, M. E. I. Y. I., Chaturvedi, L. S., Koul, S., & Koul, H. K. Oxalate stimulates IL-6 production in HK-2 cells, a line of human renal proximal tubular epithelial cells. *Kidney international.* 2005; *68*(2): 497-503.

[273] Revilla-López G, Rodríguez-Rivero A. M., Valle L, Puiggalí J, Turon P, Alemán C. Biominerals formed by DNA and calcium oxalate or hydroxyapatite: a comparative study. *Langmuir*. 2019; *35*(36): 11912-11922.

[274] Tseng, Y. H., Mou, C. Y., & Chan, J. C. Solid-state NMR study of the transformation of octacalcium phosphate to hydroxyapatite: a mechanistic model for central dark line formation. *Journal of the American Chemical Society*. 2006; *128*(21): 6909-6918.

[275] Oyane, A., Araki, H., Nakamura, M., Shimizu, Y., Shubhra, Q. T., Ito, A., & Tsurushima, H. Controlled superficial assembly of DNA–amorphous calcium phosphate nanocomposite spheres for surface-mediated gene delivery. *Colloids and Surfaces B: Biointerfaces*. 2016; *141*: 519-527.

[276] Harmey, D., Hessle, L., Narisawa, S., Johnson, K. A., Terkeltaub, R., & Millán, J. L. Concerted regulation of inorganic pyrophosphate and osteopontin by akp2, enpp1, and ank: an integrated model of the pathogenesis of mineralization disorders. *The American journal of pathology*. 2004; *164*(4): 1199-1209.

[277] Morrissey, J. H., Choi, S. H., & Smith, S. A. Polyphosphate: an ancient molecule that links platelets, coagulation, and inflammation. *Blood, The Journal of the American Society of Hematology*. 2012; *119*(25): 5972-5979.

[278] Verhoef, J. J., Barendrecht, A. D., Nickel, K. F., Dijkxhoorn, K., Kenne, E., Labberton, L., et al. Polyphosphate nanoparticles on the platelet surface trigger contact system activation. *Blood, The Journal of the American Society of Hematology*. 2017; *129*(12): 1707-1717.

[279] Donovan, A. J., Kalkowski, J., Smith, S. A., Morrissey, J. H., & Liu, Y. Size-controlled synthesis of granular polyphosphate nanoparticles at physiologic salt concentrations for blood clotting. *Biomacromolecules*. 2014; *15*(11): 3976-3984.

[280] Abramov, A. Y., Fraley, C., Diao, C. T., Winkfein, R., Colicos, M. A., Duchen, M. R., et al. Targeted polyphosphatase expression alters mitochondrial metabolism and inhibits calcium-dependent cell death. *Proceedings of the National Academy of Sciences*. 2007; *104*(46): 18091-18096.

[281] Jardín, I., López, J. J., Pariente, J. A., Salido, G. M., & Rosado, J. A. Intracellular calcium release from human platelets: different messengers for multiple stores. *Trends in cardiovascular medicine*. 2008; *18*(2): 57-61.

[282] Weitz, J. I., & Fredenburgh, J. C. Platelet polyphosphate: the long and the short of it. *Blood, The Journal of the American Society of Hematology.* 2017; *129*(12): 1574-1575.

[283] Addison, W. N., Azari, F., Sørensen, E. S., Kaartinen, M. T., & McKee, M. D. Pyrophosphate inhibits mineralization of osteoblast cultures by binding to mineral, up-regulating osteopontin, and inhibiting alkaline phosphatase activity. *Journal of Biological Chemistry*. 2007; *282*(21): 15872-15883.

[284] Nakano, Y., Addison, W. N., & Kaartinen, M. T. ATP-mediated mineralization of MC3T3-E1 osteoblast cultures. *Bone*. 2007; *41*(4): 549-561.

[285] Danilevich, V. N., Mulyukin, A. L., Machulin, A. V., Sorokin, V. V., & Kozlov, S. A. Structural variability of DNA-containing Mg-pyrophosphate microparticles: optimized conditions to produce particles with desired size and morphology. *Journal of Biomolecular Structure and Dynamics.* 2019; *37*(4): 918-930.

[286] Gadaleta, S. J., Paschalis, E. P., Betts, F., Mendelsohn, R., & Boskey, A. L. Fourier transform infrared spectroscopy of the solution-mediated conversion of amorphous calcium phosphate to hydroxyapatite: new correlations between X-ray diffraction and infrared data. *Calcified tissue international*. 1996; *58*(1): 9-16.

[287] Lotsari, A., Rajasekharan, A. K., Halvarsson, M., & Andersson, M. Transformation of amorphous calcium phosphate to bone-like apatite. *Nature communications*. 2018; *9*(1): 1-11.

[288] Ibsen, C. J., Chernyshov, D., & Birkedal, H. Apatite formation from amorphous calcium phosphate and mixed amorphous calcium phosphate/amorphous calcium carbonate. *Chemistry–A European Journal*. 2016; *22*(35): 12347-12357.

[289] Vidavsky, N., Kunitake, J. A., & Estroff, L. A. Multiple Pathways for Pathological Calcification in the Human Body. *Advanced Healthcare Materials*. 2021; *10*(4): 2001271.

[290] Forest, V., & Pourchez, J. Preferential binding of positive nanoparticles on cell membranes is due to electrostatic interactions: A too simplistic explanation that does not take into account the nanoparticle protein corona. *Materials Science and Engineering: C*. 2017; *70*: 889-896.

[291] Cedervall, T., Lynch, I., Lindman, S., Berggård, T., Thulin, E., Nilsson, H., et al. Understanding the nanoparticle–protein corona using methods to quantify exchange rates and affinities of proteins for nanoparticles. *Proceedings of the National Academy of Sciences*. 2007; *104*(7): 2050-2055.

[292] García-Olmo, D. C., & Ruiz-Piqueras, R. Circulating nucleic acids in plasma and serum (CNAPS) and its relation to stem cells and cancer metastasis: state of the issue. *Histology and histopathology*. 2004.

[293] Chen, Z., Fadiel, A., Naftolin, F., Eichenbaum, K. D., & Xia, Y. Circulation DNA: biological implications for cancer metastasis and immunology. *Medical hypotheses.* 2005; *65*(5): 956-961.

[294] Thakur, B. K., Zhang, H., Becker, A., Matei, I., Huang, Y., Costa-Silva, B., et al. Double-stranded DNA in exosomes: a novel biomarker in cancer detection. *Cell research*. 2014; *24*(6): 766-769.

[295] Kustanovich, A., Schwartz, R., Peretz, T., & Grinshpun, A. Life and death of circulating cell-free DNA. *Cancer biology & therapy*. 2019; *20*(8): 1057-1067.

[296] Rizwan, A., Paidi, S. K., Zheng, C., Cheng, M., Barman, I., & Glunde, K. Mapping the genetic basis of breast microcalcifications and their role in metastasis. *Scientific reports*. 2018; *8*(1): 1-10.

[297] Engin, A. B., Nikitovic, D., Neagu, M., Henrich-Noack, P., Docea, A. O., Shtilman, M. I., et al. Mechanistic understanding of nanoparticles' interactions with extracellular matrix: the cell and immune system. *Particle and fibre toxicology*. 2017; *14*(1): 1-16.

[298] Gras, P., Rey, C., Marsan, O., Sarda, S., & Combes, C. Synthesis and characterisation of hydrated calcium pyrophosphate phases of biological interest. *European Journal of Inorganic Chemistry*. 2013; 34: 5886-5895.

[299] Kontoyannis, C. G., Bouropoulos, N. C., & Koutsoukos, P. G. Raman spectroscopy: a tool for the quantitative analysis of mineral components of solid mixtures. The case of calcium oxalate monohydrate and hydroxyapatite. *Vibrational spectroscopy*. 1997; *15*(1): 53-60.

[300] Esmonde-White, K. Raman spectroscopy of soft musculoskeletal tissues. *Applied spectroscopy*. 2014; *68*(11): 1203-1218.